frontiers | Research Topics

Multi-scale fluid physics in oceanic flows: New insights from laboratory experiments and numerical simulations

Edited by
Shi-Di Huang, Houshuo Jiang, Shengqi Zhou, Yeping Yuan and Claudia Cenedese

Published in
Frontiers in Marine Science

ISSN 1664-8714
ISBN 978-2-8325-3771-8
DOI 10.3389/978-2-8325-3771-8

About Frontiers

Frontiers is more than just an open access publisher of scholarly articles: it is a pioneering approach to the world of academia, radically improving the way scholarly research is managed. The grand vision of Frontiers is a world where all people have an equal opportunity to seek, share and generate knowledge. Frontiers provides immediate and permanent online open access to all its publications, but this alone is not enough to realize our grand goals.

Frontiers journal series

The Frontiers journal series is a multi-tier and interdisciplinary set of open-access, online journals, promising a paradigm shift from the current review, selection and dissemination processes in academic publishing. All Frontiers journals are driven by researchers for researchers; therefore, they constitute a service to the scholarly community. At the same time, the *Frontiers journal series* operates on a revolutionary invention, the tiered publishing system, initially addressing specific communities of scholars, and gradually climbing up to broader public understanding, thus serving the interests of the lay society, too.

Dedication to quality

Each Frontiers article is a landmark of the highest quality, thanks to genuinely collaborative interactions between authors and review editors, who include some of the world's best academicians. Research must be certified by peers before entering a stream of knowledge that may eventually reach the public - and shape society; therefore, Frontiers only applies the most rigorous and unbiased reviews. Frontiers revolutionizes research publishing by freely delivering the most outstanding research, evaluated with no bias from both the academic and social point of view. By applying the most advanced information technologies, Frontiers is catapulting scholarly publishing into a new generation.

What are Frontiers Research Topics?

Frontiers Research Topics are very popular trademarks of the *Frontiers journals series*: they are collections of at least ten articles, all centered on a particular subject. With their unique mix of varied contributions from Original Research to Review Articles, Frontiers Research Topics unify the most influential researchers, the latest key findings and historical advances in a hot research area.

Find out more on how to host your own Frontiers Research Topic or contribute to one as an author by contacting the Frontiers editorial office: frontiersin.org/about/contact

Multi-scale fluid physics in oceanic flows: New insights from laboratory experiments and numerical simulations

Topic editors

Shi-Di Huang — Southern University of Science and Technology, China
Houshuo Jiang — Woods Hole Oceanographic Institution, United States
Shengqi Zhou — South China Sea Institute of Oceanology, Chinese Academy of Sciences (CAS), China
Yeping Yuan — Zhejiang University, China
Claudia Cenedese — Woods Hole Oceanographic Institution, United States

Citation

Huang, S.-D., Jiang, H., Zhou, S., Yuan, Y., Cenedese, C., eds. (2024). *Multi-scale fluid physics in oceanic flows: New insights from laboratory experiments and numerical simulations*. Lausanne: Frontiers Media SA.
doi: 10.3389/978-2-8325-3771-8

Table of contents

frontiers | Frontiers in Marine Science

TYPE Editorial
PUBLISHED 04 January 2024
DOI 10.3389/fmars.2023.1361265

OPEN ACCESS

EDITED AND REVIEWED BY
Ming Li,
University of Maryland, College Park, United States

*CORRESPONDENCE
Claudia Cenedese
ccenedese@whoi.edu
Shi-Di Huang
huangsd@sustech.edu.cn
Houshuo Jiang
hsjiang@whoi.edu
Yeping Yuan
yyping@zju.edu.cn
Sheng-Qi Zhou
sqzhou@scsio.ac.cn

RECEIVED 25 December 2023
ACCEPTED 27 December 2023
PUBLISHED 04 January 2024

CITATION
Cenedese C, Huang S-D, Jiang H, Yuan Y and Zhou S-Q (2024) Editorial: Multi-scale fluid physics in oceanic flows: new insights from laboratory experiments and numerical simulations.
Front. Mar. Sci. 10:1361265.
doi: 10.3389/fmars.2023.1361265

Editorial: Multi-scale fluid physics in oceanic flows: new insights from laboratory experiments and numerical simulations

Claudia Cenedese[1]*, Shi-Di Huang[2]*, Houshuo Jiang[3]*, Yeping Yuan[4]* and Sheng-Qi Zhou[5]*

[1]Physical Oceanography Department, Woods Hole Oceanographic Institution, Woods Hole, MA, United States, [2]Department of Mechanics and Aerospace Engineering and Center for Complex Flows and Soft Matter Research, Southern University of Science and Technology, Shenzhen, China, [3]Department of Applied Ocean Physics and Engineering, Woods Hole Oceanographic Institution, Woods Hole, MA, United States, [4]Ocean College, Zhejiang University, Zhoushan, China, [5]State Key Laboratory of Tropical Oceanography, South China Sea Institute of Oceanology, Chinese Academy of Sciences, Guangzhou, China

KEYWORDS

oceanic flows, multi-scale fluid dynamics, interaction between flow and topology, air-sea interaction, table-top experiment, numerical simulation

Editorial on the Research Topic

Multi-scale fluid physics in oceanic flows: new insights from laboratory experiments and numerical simulations

Oceanic flows are characterized by various physical processes that occur over a wide range of spatial-temporal scales, such as eddies, tides, waves, convections, plumes, and turbulent mixing. These flows have great impacts on the oceanic environment (physical, chemical, biological, and ecological) and the global climate, so a comprehensive understanding of their dynamical mechanisms is crucial. However, because of the often-harsh oceanic environment and associated technical difficulties, revealing the multi-scale, multi-physical dynamics of oceanic flows via field measurements remains a considerable challenge. In this context, laboratory experiments and numerical simulations, which can be conducted under precisely-controlled conditions with a relatively low cost, become useful tools for tackling this problem.

This Research Topic collects a total of fifteen articles that provide valuable insights into the multi-scale dynamics of oceanic flows, using laboratory experiments and numerical simulations. While the oceanic flows investigated in these articles involve a diverse range of physical processes, they can be broadly classified into two groups: (1) interaction between oceanic flows and topography and (2) air-sea interaction.

For the first group of studies, one well recognized example is the interaction between internal tides and topography, which is believed to play an important role in maintaining the meridional overturning circulation through contributing a large amount of diapycnal mixing. Thanks to the rapid development in computational power and techniques, this process can be numerically simulated in more detail than before. For example, compared to

early studies that mostly used idealized topography and considered all the tidal constituents in the numerical models, modern high-resolution simulations allow researchers to adopt realistic topography in the models and study the influence of different tidal constituents separately. These issues are exactly the focuses of Tang et al. and Wang et al. Their studies provide a more detailed energy budget of internal tides and the effects of larger-scale currents on internal tides during the generation and propagation processes, which is important in developing ocean models with high accuracy.

Compared to the extensive studies of the interaction between internal tides and topography, how the bottom topography affects the meridional overturning in deep oceans has received less attention. By conducting novel laboratory experiments of rotating horizontal convection, Zhang et al. observed that even without spatial variation of mixing intensity, the existence of a meridional ridge can strongly alter both the pattern and the strength of the overturning circulation. This finding not only provides a fresh perspective to explore the overturning circulation via field measurements and modeling studies, but also raises a new question on the influence of bottom topography on the overturning circulation.

While the answer to the question above is subject to future studies, the effect of a sloping bottom on buoyant plumes is becoming clear. Through laboratory experiments on a rotating table, Yuan et al. revealed that bottom-attached river plumes trapped near the coast inhibit offshore freshwater transport on one hand, and promote coastal current transport on the other. The interaction between buoyant plumes and topography is also crucial in the deep sea. By investigating the dispersion of hydrothermal plumes in a complex flow field arising from the interaction with a pronounced seafloor, Xu and German showed that tidal forcing has a notable influence on the plume dispersion by inducing an anti-cyclonic circulation near the region with large topographic features. These findings are useful for modeling bio-geo-chemical processes in oceans.

The significant role of topography on oceanic flows can be found in more situations. Examples collected in this Research Topic include the influence of multiple islands on western boundary currents (Li et al.), the sub-meso-scale motions in coastal regions with shallow water (Si et al.), and the effect of large-scale suspended mussel farms on the tidally induced water circulation (Zhong et al.). These studies not only provide a more comprehensive understanding of the multi-scale dynamics of oceanic flows, but also reflect the current trend in this research field: moving towards more complex physical processes occurring at smaller scales.

The second major topic in this Research Topic is air-sea interaction. One important issue is the role of tropical cyclones, one of the key drivers of upper ocean dynamics. In contrast to previous studies that are mostly based on the statistics of multiple tropical cyclones, Chu et al. focused on the influence of an individual event on the ocean dynamics. Somewhat surprisingly, they found that even a low-intensity cyclone can pronouncedly alter the thermohaline structure by amplifying Kelvin waves in the equatorial regions. It is even more surprising to realize that, according to the large-eddy simulations by Falor et al., surface evaporation can result in a significant diurnal variation in the thermohaline structure by enhancing the irreversible mixing throughout the day. These findings can lead to a better prediction of the key variables in upper oceans and help to improve the parameterizations in ocean modeling.

Improving model parameterizations not only requires a better understanding of the dynamics driving air-sea interaction, but also calls for new methods to analyze the involved processes quantitatively. For example, it is notoriously difficult to quantify the relative contribution of wind forcing and surface buoyancy flux to the upper ocean dynamics. By proposing a new scaling method, Cen et al. found that the turbulent kinetic energy dissipation rate at the mixing layer base exhibits a universal similarity, in spite of variable dynamic states. The new scaling parameter, given by a nonlinear combination of wind-shear-driven dissipation rate and surface buoyancy flux, could potentially simplify model parameterizations. Another long-standing issue in the study of air-sea interaction is how to establish the wind-wave relation, which is often contaminated by the existence of swells. In the work by Gao et al., a probability-based approach was proposed to extract the swell information without knowing the wave spectrum *a priori*. Compared with previous empirical relations in the literature, this method is more practical in distinguishing swells from wind waves.

Besides new methods for data analysis, the present Research Topic also collects a few articles that propose novel perspectives to understand oceanic phenomena. One of such studies is the work of Zhang & Xie. Noticing the similarity between the amplitude equation of near-inertial waves and the Schrödinger equation, they interpreted the large-scale concentration of near-inertial waves in anticyclones as a combined effect of energy conservation and uncertainty principle. It is quite interesting and even astonishing to see that oceanic phenomena can be explained by the basic concepts of quantum mechanics. Another interesting study is carried out by Azminuddin et al. By using a Lagrangian particle tracking method, they quantitatively explored the destination of the New Guinea Coastal Undercurrent and the associated water mass transformation. Although their tracer release experiment method is not new, it is not until recently that researchers can use this technique to disclose the pathways of deep waters. This could help to solve the puzzle of upwelling that goes back decades: where and how deep-ocean waters rise back to the surface to keep the overturning circulation going?

Finally, we end this Editorial by highlighting the work of Moscoso et al.. They showed that even table-top experiments built with LEGO modules can reproduce the multi-scale dynamics that are essential in deep ocean convection. Although these experiments just confirm the existing theories and do not provide any new insight, they are very useful for popular science education. In particular, these low-cost and elegant experiments may inspire young people to pursue careers in physical oceanography in the future. In this context, we hope this Research Topic can not only stimulate further innovative investigations and the next generation of ocean models, but also

act as a source for inspiring the next generation of physical oceanographers.

Author contributions

CC: Writing – review & editing. S-DH: Writing – original draft, Writing – review & editing. HJ: Writing – review & editing. YY: Writing – review & editing. S-QZ: Writing – review & editing.

Acknowledgments

We thank all the authors and reviewers for their valuable contributions to this Research Topic.

Conflict of interest

The authors declare that the research was conducted in the absence of any commercial or financial relationships that could be construed as a potential conflict of interest.

Publisher's note

frontiers | Frontiers in Marine Science

TYPE Original Research
PUBLISHED 23 August 2022
DOI 10.3389/fmars.2022.973155

OPEN ACCESS

EDITED BY
Houshuo Jiang,
Woods Hole Oceanographic Institution, United States

REVIEWED BY
Andrea Cucco,
National Research Council (CNR), Italy
Craig Stevens,
National Institute of Water and Atmospheric Research (NIWA), New Zealand

*CORRESPONDENCE
Jun Lin
jlin@shou.edu.cn

SPECIALTY SECTION
This article was submitted to Physical Oceanography, a section of the journal Frontiers in Marine Science

RECEIVED 19 June 2022
ACCEPTED 25 July 2022
PUBLISHED 23 August 2022

CITATION
Zhong W, Lin J, Zou Q, Wen Y, Yang W and Yang G (2022) Hydrodynamic effects of large-scale suspended mussel farms: Field observations and numerical simulations. *Front. Mar. Sci.* 9:973155. doi: 10.3389/fmars.2022.973155

Hydrodynamic effects of large-scale suspended mussel farms: Field observations and numerical simulations

Wei Zhong[1], Jun Lin[1,2]*, Qingping Zou[3], Ying Wen[1], Wei Yang[1] and Guanlin Yang[1]

[1]College of Marine Ecology and Environment, Shanghai Ocean University, Shanghai, China, [2]Engineering Technology Research Center of Marine Ranching, Shanghai Ocean University, Shanghai, China, [3]The Lyell Centre for Earth and Marine Science and Technology, Institute for Infrastructure and Environment, Heriot-Watt University, Edinburgh, United Kingdom

The hydrodynamic effects of the largest suspended mussel farms in the East China Sea near Gouqi Island, was investigated using a high-resolution 3D ocean model and field observations. To capture the 3D farm effects on hydrodynamics, an additional depth dependent momentum sink term was introduced in the model. The model results compared well with the field observations. The present model and observational results indicate that the presence of farms reduces the flow by more than 79%, 55%, and 34% in the upper, middle, and bottom layers at the farm center, respectively. According to the harmonic analysis of predicted current, mussel farms reduce the magnitude of the semidiurnal tidal current and also alter the magnitude and direction of the diurnal tidal current. The blockage by the farm weakens the Eulerian residual tidal current within the farm in the NE-SW direction, while strengthens that at the edge of the farm in the SE-NW direction. Cross sections, Sec1 and Sec2 are perpendicular to these two major residual currents and intercept with the center of the farm from SE to NW and from NE to SW respectively. The farm effect on the total water flux over a month through the Sec2 displays a semi-lunar periodic oscillation and is one order of magnitude smaller than that at Sec1. An asymmetry tidal current was observed in the farm north of Gouqi Island. The field observation of vertical profiles of current suggests that the thickness of surface canopy boundary layer can reach 5 m upstream from the farm during flood tide, increases gradually downstream up to 10 m under the cumulative influences of the farm. And a wake zone was observed downstream from the farm during flood tide. Better understanding of farm-induced hydrodynamic effects provides insight into how to optimize farm layouts based on local hydrodynamics, to maximize farm productivity and minimize environmental impacts.

KEYWORDS

suspended mussel aquaculture, blocking effect, momentum sink, ECOM-si, drag of canopy

1 Introduction

Global aquaculture production has grown dramatically over the past 50 years to meet the rising demand for food (Mustafa et al., 2017; Garlock et al., 2019). The global shellfish production attained 17.5 million tons in live weight with a value of USD 29.2 billion in 2018, accounting for 56.2% of the total aquaculture production. As the largest producer of aquaculture bivalves in the world, China produced 14.4 million tons, which is 82% of worldwide shellfish production (FAO, 2020). Gouqi Island is located in the East China Sea, just south-east of Shanghai and east of Hangzhou. As one of the top mussel producer in China, the island features a 12 km^2 mussel farm with an annual production of more than 180, 000 tons.

The 'off-bottom' cultivation with raft, pole, and longline is commonly used for mussel aquaculture to prevent predation by predators such as crabs and starfish. The longline aquaculture system employed in the mussel farms of Gouqi Island, is the most used technology since it requires the least amount of infrastructure (Mascorda Cabre et al., 2021). This farming system forms a suspended canopy and acts as a porous medium in the water column. Suspended canopy such as aquaculture farms on hydrodynamics has received much less attention than submerged or emergent canopy (Plew, 2011a; O'Donncha et al., 2015). Nevertheless, the hydrodynamic effects of suspended canopy is of fundamental importance (Grant and Bacher, 2001; Plew et al., 2005; Stevens et al., 2008; Delaux et al., 2011; O'Donncha et al., 2013, O'Donncha et al., 2015; Duarte et al., 2014; Aguiar et al., 2015; Filgueira et al., 2015; Konstantinou et al., 2015; Lin et al., 2016; Filgueira, 2018; Liu and Huguenard, 2020).

At Gouqi Island, there has been increased in conflicts over coastal space in recent years, as the space suitable for aquaculture has been gradually used up. Accordingly, the fishermen repeatedly lengthen the mussel ropes and raise the stocking density, which causes overstocking. The production and quality of mussels, however, have not increased with the expansion of the aquaculture unit. In addition, the complex flow patterns near the island have led to significant geographical variation in the yield of mussel farms. Therefore, the mussel farms on Gouqi Island needs a comprehensive farming plan to optimize the farming layout and enhance overall productivity and quality.

The hydrodynamics modifications by the aquaculture structures has significant effect on the growth of cultured populations especially non-feeding mussels. The suspended canopy layer inhibits the surface layer water flow, therefore, change the circulation pattern inside and around the farm (Konstantinou et al., 2015; Lin et al., 2016; Konstantinou and Kombiadou, 2020; Liu and Huguenard, 2020). The flow responses to the presence of farm in turn affect the mussel food availability through increased water residence time and nutrient depletion, therefore, the carrying capacity of ecosystem (Byron et al., 2011a; Byron et al., 2011b; Anaïs et al., 2020; Gao et al., 2020). Quantifications of effect of suspended farms on circulation is critical in evaluating carrying capacity, ecosystem sustainable and effective management of the aquaculture activities (Filgueira et al., 2015; Froján et al., 2018; Konstantinou and Kombiadou, 2020).

The objective of this study is to investigate the hydrodynamic effects of a large-scale suspended mussel farms using, *in-situ* and navigational field observations and 3D ocean circulation numerical model that incorporate the farm effect. Ocean models have become a popular tool to assess the environmental effects and interactions among open water aquaculture systems (Reid et al., 2018; Broch et al., 2020). Thus, a high-resolution three-dimensional hydrodynamic model, Estuarine Coastal Ocean Model semi-implicit (ECOM-si) (Wu and Zhu, 2010; Wu et al., 2011) of Gouqi Island is also developed to further explore the hydrodynamic processes related to farms. To incorporate the blockage effect of the suspended farms into the model, a depth dependent momentum sink term representing the loss of momentum is added to the momentum equations of the model (Roc et al., 2013; Yang et al., 2013; Li et al., 2017; O'Hara Murray and Gallego, 2017). Introduction to the geographic location and farm configurations of Gouqi Island, field observations and numerical model are presented in section 2. In section 3, the field observations, are analyzed to provide insight into the hydrodynamic effects of the farm. In section 4, the model results are compared against the field observations to evaluate the model performance. In section 5, the model results of farm effects on tides are highlighted and discussed. Implications of the present study and future research needs are summarized in section 6.

2 Methods

2.1 Study site

Gouqi Island is known as the hometown of mussels in China. It has the largest mussel farming area in the East China Sea, with an aquaculture area of 12 km^2. It has a subtropical climate, with an average surface water temperature ranges between 17 and 19°C. It is dominated by a semidiurnal tide with a spring tidal range of approximately 2.5 m and neap tidal range of 1.0 m. The western part of the farm is influenced by the runoff of the Changjiang and Qiantang rivers (Figure 1A), while the eastern part of the farm is affected by the Taiwan warm current and Zhebei upwelling, which leads to a large horizontal salinity gradient from the east to the west of the farm (Zhang et al., 2008). A significant amount of nutrients is transported in the aquaculture area by river runoff and strong tidal current, which raises the primary productivity and supplies the farm with a rich food source. Typhoons frequently pass by Gouqi Island and pose a serious threat to the aquaculture infrastructure and personnel. In order to minimize the typhoon damages to the aquaculture facilities, most mussel farms are

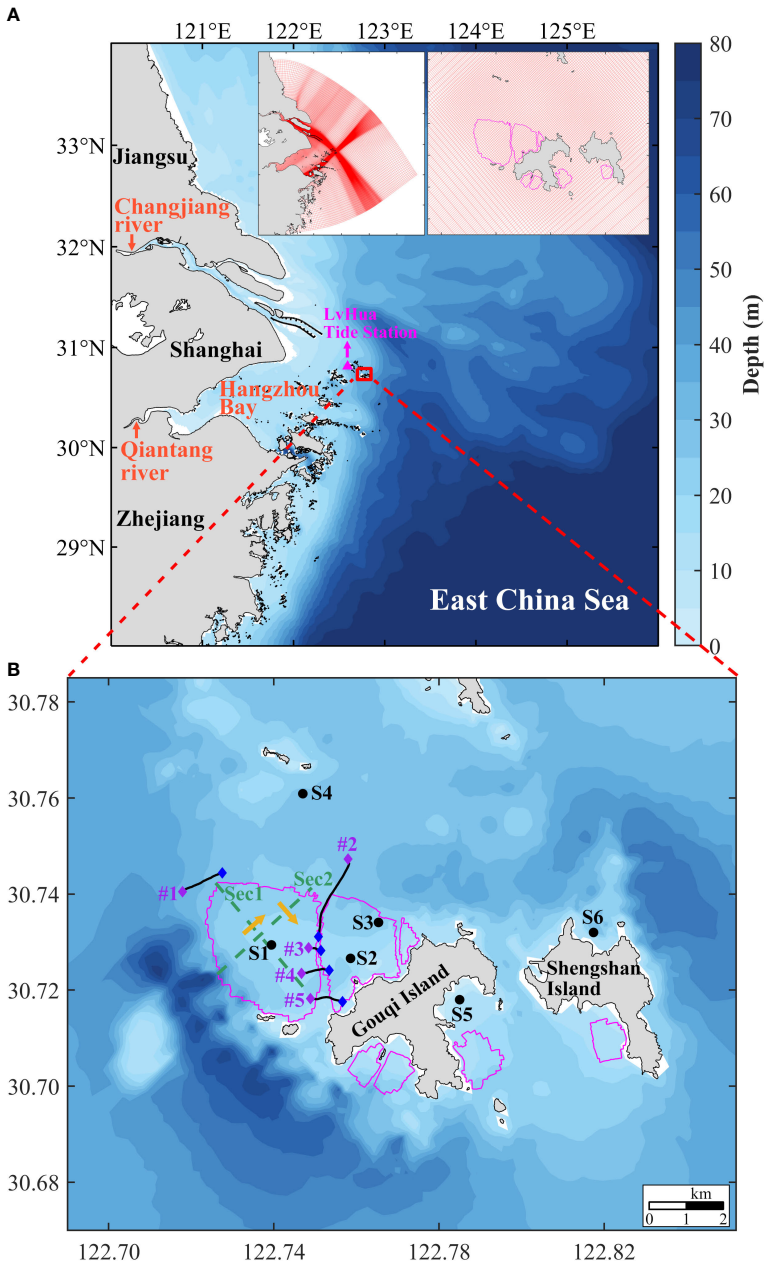

FIGURE 1
Map of the study area, field stations and model grid system. **(A)** Geographic location of Gouqi Island. The model domain and mesh. Pink triangle indicates the location of LvHua Tide Station (30°49′N,122°36′E). Red rectangle indicates the range of Gouqi Island area. **(B)** Field observation stations (S1 to S6). The orange arrows show the positive direction of water transport across Sec1 and Sec2 indicated in green dashed lines. The black lines indicate the boat cruise route #1 to #5 for ADCP measurements. The purple and blue diamond are the starting and end point, respectively. The pink lines indicate the borderlines of suspended mussel farms.

located to the northwest of Gouqi Island (Figure 1B) which protect the farms from most typhoons come from the southeast. Additionally, a suitable water depth of ~ 20 m and a reasonably close operational distance is convenient for fishermen.

There are seven mussel farming zones in Gouqi Island area (Figure 1B). The largest one is to the northwest of the island with 6.76 km^2 (Figure 2A). A suspended aquaculture system is used for mussel farms. The suspended aquaculture system consists of buoys, lanyards, suspended sleeves (aquaculture lines with mussels attached), and longlines used to attach sleeves in the vertical direction (Figure 2C) (Lin et al., 2016). The mussel farms in Gouqi Island are owned by different individuals, which complicate the layouts both within and across the aquaculture units. And it is difficult to count the actual number of mussel sleeves during the field observations.

Making use of the Google Earth high-resolution remote-sensing image, we estimated that a typical aquaculture unit is roughly 7200 m^2 (90m×80m) (Figure 2B), with 20 rows and 90 mussel sleeves in each row. We assumed that the mussel sleeves are evenly distributed across the model grid. Therefore, in the model, the mussel sleeves density is approximately 4 m^2 $sleeves^{-1}$.

2.2 Field observations

In order to investigate the hydrodynamic effects due to mussel farms in Gouqi Island area, *in-situ* observations of velocity fields and tidal elevations were conducted during spring and neap tidal conditions. An Acoustic Doppler Current Profiler (ADCP) was installed on buoys at the field station S1, S2, S3 and S4 (Figure 1B). Current profiles were measured with a 0.5 m vertical bin using a 500 Hz Teledyne RD Instrument (RDI). The measurements were conducted at S1 for 96 hours starting on July 21, 2020 (spring tide), at S2 for 72 hours starting on July 25, 2020 (neap tide), at S3 for 48 hours starting on March 10, 2021 (spring tide), and at S4 for 25 hours starting on November 5, 2018 (spring tide).

Furthermore, five boat cruise observations were also conducted across mussel farms using a navigational ADCP (Nortek, 1000Hz) mounted on a boat with a 0.2 m vertical bin. The #1 boat cruise track lies in the northwest of Gouqi Island (Figure 1B), from southwest to northeast and away from the farm, nearly paralleling to the coast of the island. The ADCP data was collected for about 7 minutes on July 10, 2021 during

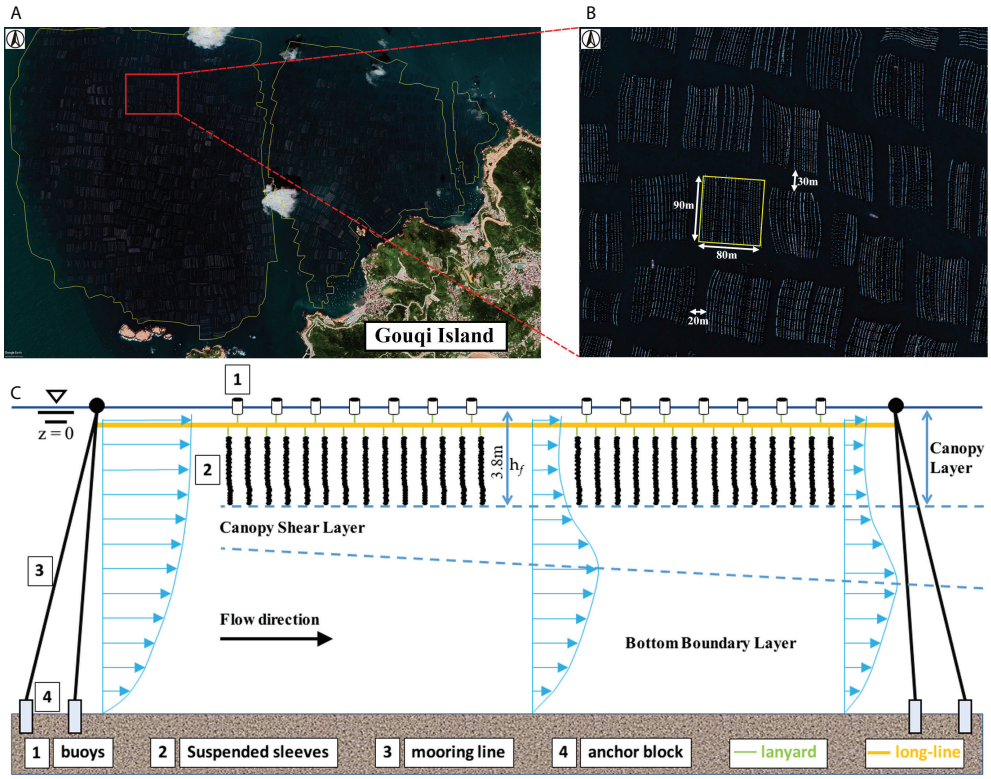

FIGURE 2
(A) Satellite view of farms at the north of Gouqi Island from Google Earth, August 20, 2018. **(B)** A zoom-in satellite view of a local farming region that shows the configuration of mussel farms. A typical aquaculture unit of mussel farms outlined by the yellow line. **(C)** Side view of the components of aquaculture facilities. Three layer flow structures exist around the facility. h_f is the farm penetration depth.

spring tide. The #2 boat cruise track is located in the north of Gouqi Island (Figure 1B), stretching from outside to inside of the farm. The ADCP data was collected for about 17 minutes on June 29, 2021 during neap tide. The #3, #4 and #5 boat cruise is located across the waterway between the two major farms (Figure 1B). The ADCP data was collected for about 2, 4 and 5 minutes respectively on July 10, 2021 during spring tide.

The tidal elevation data were collected every 5 minutes at S4, S5 and S6 stations in Figure 1B using a RBR wave tidal gauge. At S4, the tidal data was collected from November 5, 2018 to November 10, 2018. At S5, the tidal data was collected from July 19, 2020 to July 29, 2020. And at S6, the tidal data was collected from November 9, 2018 to November 11, 2018. Also, the tide elevation data at Lvhua tidal station (30°49′N, 122°36′ E) from the National Marine Information Center (https://www.cnss.com.cn/tide) was also used to verify the present model results of tidal elevation from July 18, 2020 to July 31, 2020.

2.3 Numerical model

2.3.1 Model description

In this study, an Estuarine Coastal Ocean Model semi-implicit (ECOM-si) developed by Blumberg (1994) and improved by Wu and Zhu (2010) was used to simulate the hydrodynamic conditions of mussel farms around Gouqi Island. The model uses an orthogonal curvilinear coordinate system that accommodates complicated coastlines. Wu and Zhu (2010) developed a robust third-order advection scheme to reduce the numerical oscillations in solving the transport equations. To increase the computational efficiency, the time step was set to vary automatically based on the Courant-Friedrich-Levy (CFL) criterion (Wu et al., 2011).

In order to quantify the mussel farms blockage effect in the transport equations, the water flux at a given transect is calculated by applying the following equation (Wu et al., 2006; Lin et al., 2015):

$$WR(t)|_{\Gamma}\int_{-d}^{\zeta}\left(\int_{0}^{L}V_n(x,y,z,t)|_{\Gamma}d\xi\right)\quad dz \tag{1}$$

where $WR(t)|_{\Gamma}$ is the water volume flux, with a unit of cubic meters per second, perpendicular to a given transect Γ.

The direction of positive water transport is defined in Figure 1B, d is the local still water depth, ζ is the surface water level, L is the length of the transect Γ, d_{ξ} is the line segment along the transect Γ, $V_n(x,y,z,t)$ is the horizontal velocity component perpendicular to the transect Γ

The accumulated total water flux over a time period is calculated by integrating (1) (Zhang et al., 2022):

$$\widetilde{WR}(t)|_{\Gamma}=\int_{t_0}^{t_f}\int_{-d}^{\zeta}\left(\int_{0}^{L}V_n(x,y,z,t)|_{\Gamma}d\xi\right)\quad dz\quad d\tau \tag{2}$$

where $\tau\in[t_0,t_f]$ is the time interval, t_0 the initial time, and t_f the final time.

The model domain included the Changjiang River Estuary, the Hangzhou Bay, and part of the East China Sea (Figure 1A). A curvilinear orthogonal coordinate was employed in the horizontal direction, and the sigma coordinate was used in the vertical direction. The horizontal mesh grid was refined to 336×256 cells with the highest spatial resolution of 100 m inside the mussel farms. The model was divided into 35 layers in the vertical direction with refinement in the aquaculture surface layer and the bottom layer. At the offshore open boundary, the model was driven by 16 tidal constituents (M_2, S_2, N_2, K_2, K_1, O_1, P_1, Q_1, MU_2, NU_2, T_2, L_2, $2N_2$, J_1, M_1 and OO_1), with amplitude and phase from the TPXO7.1 dataset (http://g.hyyb.org/archive/Tide/TPXO/TPXO_WEB/global.html). The annual average discharge of the Changjiang River was set to 30000 m^3s^{-1}. A variable time step was taken according to the instantaneous CFL criteria at each time step, with the maximum time step of 30s and the minimum time step of 10s. Only tidal currents were considered in the present study. Wind driven currents and the effects of density stratification (baroclinic force) on circulation were not considered.

In this study, two numerical model cases were carried out. For case 1, the blocking effects of the mussel farms was considered. For case 2, the computations were done without the mussel farms. The time duration of the simulation was 66 days from 14 July, 2020 to 20 September, 2020. We also conducted another numerical experiment for the simulation period between 1 November, 2018 and 15 November, 2018.

2.3.2 Momentum sink term for farm effects

A drag coefficient is often introduced into ocean numerical models to represent the blocking effects of marine aquaculture structures, such as kelp ropes (Shi and Wei, 2009; Shi et al., 2011). The drag coefficient applied at the surface and bottom layer may only influence the flow around the boundary layer, which is not the case of mussel sleeves. Hence, a depth-dependent momentum sink term was added to the momentum conservation equation to adequately represent the suspended structures in the water column (Yang et al., 2013; Beudin et al., 2017; Li et al., 2017; O'Hara Murray and Gallego, 2017). In this study, the blocking effect of suspended mussel farms was modeled using the additional sink term (O'Hara Murray and Gallego, 2017) as:

$$F_u=-C_T W_k L_\sigma n\frac{1}{2}\rho_0 u\left|\vec{V}\right| \tag{3}$$

$$F_v = -C_T W_k L_\sigma n \frac{1}{2} \rho_0 v \left| \vec{V} \right| \quad (4)$$

where F_u and F_v are the additional sink term for the x and y direction momentum equation per unit area, C_T is the drag coefficient of the suspended mussel farms which determines the strength of the sink term, W_k and L_σ is the width and height of each aquaculture components, n is the number of aquaculture components in a cell, $|\vec{V}|$ is the magnitude of the velocity in a cell.

The W_k and L_σ are used to represent the vertical difference in momentum sink caused by different components of the aquaculture facilities (Table 1). The C_T was set to 1 (Beudin et al., 2017; Liu and Huguenard, 2020). The value of n was determined by the cell area and the area occupied by each sleeve (4 m^2 $sleeves^{-1}$). The width of mussel sleeve was measured during harvest, and the variation of sleeve width in different mussel growth stage is not considered in this study.

TABLE 1 Geometric parameters of the aquaculture facility components.

Mussel farm components	W_k(m)	L_σ(m)
Buoys	0.5	0.3
Lanyard	0.125	0.3
Long-line	0.25	0.2
Lanyard	0.125	0.2
Suspended sleeves	0.25	2.8

W_k and L_σ is the width and height of each aquaculture components.

3 Field observation results

3.1 *In-situ* measurements of current

A series of field observations were conducted to examine the impact of mussel farms on the vertical variation of flow field. The results of *in-situ* observations of vertical profiles of current by ADCP mounted to a buoy at S1, S2 and S3 station were shown in Figure 3. The tidal current direction at three stations is almost the same during flood tide, which was southwest, but different during ebb tide (Figure 3). At S1 station, the ebb current is in the southeast direction, and the flood current is greater than the ebb current by about 0.1m/s (Figure 3B). However, at S2 station, the ebb current is in the northeast direction, and the flood current is smaller than the ebb current by about 0.2 m/s (Figure 3C). At S3 station at the edge of farm, the ebb current is in the east direction (Figure 3D). The flood current is also greater than the ebb current at S3 station, which is consistent with S1 station. It is evident that an asymmetry tidal current field was observed in the north farming area.

S3 station is less affected by the farm since it is located at the edge of farm, the flow velocity of canopy layer thus reached 0.5 m/s during flood and ebb tide (Figure 3D). However, at S1 and S2

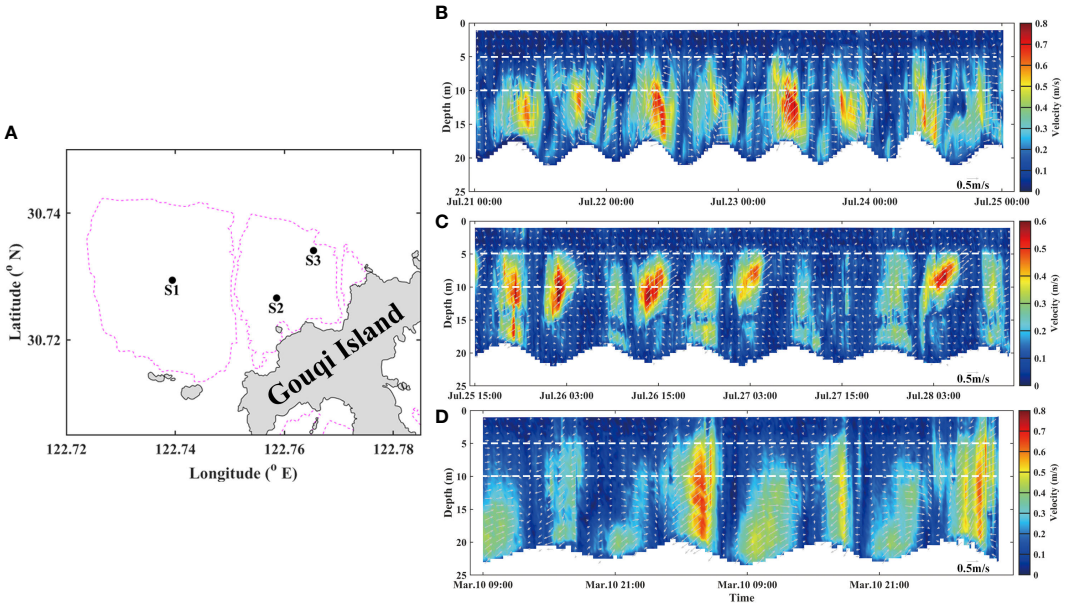

FIGURE 3
In-situ observed vertical profile of current collected by the ADCP mounted to a buoy for S1, S2 and S3 station. **(A)** Station location diagram. Time series of vertical current profile **(B)** at S1 during spring tide, from July 21, 2020 for 96 hours. **(C)** at S2 during neap tide, from July 25, 2020 for 72 hours. **(D)** at S3 during spring tide, from March 10, 2021 for 48 hours. The gray arrows indicate the horizontal direction and magnitude of tidal current.

station located inside the farm, under the cumulative blockage influences of farm, the thickness of surface canopy boundary layer is maintained at about 5 m, and can be greater than 10 m when the hydrodynamic is weakened. The spatiotemporal variation of natural hydrodynamics environment in the aquaculture area cause significant spatiotemporal variation of surface canopy boundary layer thickness by suspended aquaculture facilities.

3.2 Moving-boat ADCP current measurements

In addition to *in-situ* measurements, we also carried out a series of current measurements using ADCP mounted to a moving boat. The velocity profiles produced by suspended canopies such as mussel ropes and kelp may be divided into three layers: a bottom boundary layer, a canopy shear layer (i.e., a structure-induced boundary layer), and an internal canopy layer (Plew, 2011a; Cheng et al., 2019).The measured current profile outside and inside the farm (Figure 4) shows that the velocity is reduced in the upper water column, and the thickness of surface canopy boundary layer increased entering the farming area, up to about 10 m (Figure 4). The flow within the surface canopy boundary layer is attenuated by the drag force of suspended mussel farms.

A region of flow recirculation behind an object, a wake zone, may form downstream from the mussel farm (Plew et al., 2005; Plew et al., 2006; Cornejo et al., 2014; Tseung et al., 2015; Qiao, 2016), where lower velocity is present. The wake zone consists of, a steady wake zone with approximately constant velocity and a

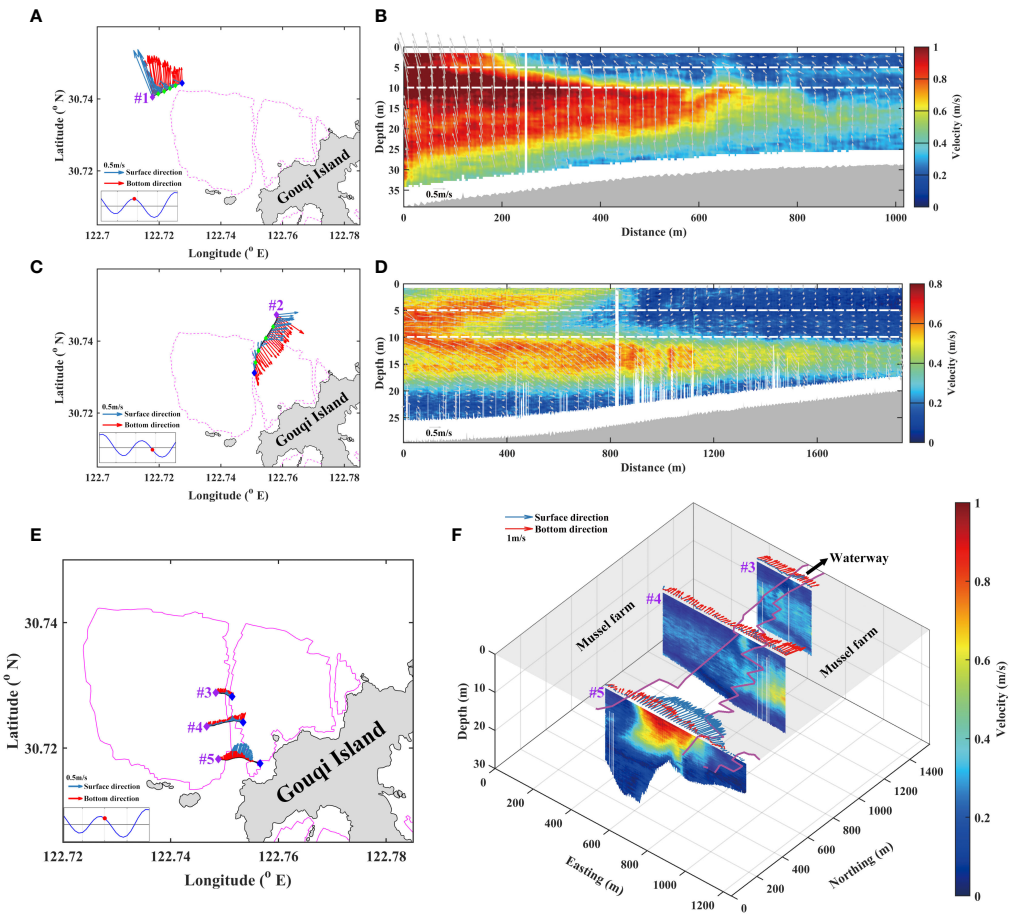

FIGURE 4
Observed vertical profiles of flow for transect lines #1, #2, #3, #4 and #5 collected by ADCP mounted to a boat. Pink lines indicate the borderlines of mussel farms. The insert plot is the time series of tidal elevation at Shengshan Tide station (122°28′E,30°43′N) with the red dot indicate the time instant of the tidal elevation. Blue and red arrows show the current vector at the surface and bottom, respectively. The gray arrows in **(B, D)** indicate the horizontal tidal current vector. The purple and blue diamond is the starting and end point of boat cruises respectively. The green diamonds in **(A, C)** indicate observation point of 400 meters intervals. **(A)** Transect line #1 & **(C)** Transect line #2 & **(E)** Transect line #3, #4 and #5 location diagram. **(B)** Vertical current profile along transect line #1 on July 10, 2021 during spring tide. **(D)** Vertical current profile along transect line #2 on June 29, 2021 during neap tide. **(F)** Vertical current profile along transect line #3, #4 and #5 on July 10, 2021 during spring tide within 30 minutes for 2 minutes, 4 minutes and 5 minutes, respectively.

velocity recover zone where velocity increases downstream (Tseung et al., 2015). The results show that the wake zone occurred in the surface layer (Figure 4) with a thickness increasing closer to the farming area, up to 10 m.

In order to assess whether the current layout of central waterway in the north of Gouqi Island is suitable, we conducted three current profile observations from west to east along the waterway (Figure 4). The observed current profile at transect line #5 show that the horizontal velocity of the whole water column at the waterway is large with a maximum value of about 1m/s (Figure 4) due to the reduced cross section for flow to pass through by the farm. Due to the cumulative flow attenuation by the aquaculture facilities, the current at transect line #3 is smaller than that at line #4 which in turn is smaller than that at line #5 from south to north (Figure 4). The observations indicated that the spatiotemporal variation of natural hydrodynamic conditions around the farm have an important impact on that of tidal current within the farm. As a results, the hydrodynamic effect of large-scale aquaculture farm in the field has a sophisticated temporal and spatial variations.

4 Model validation

4.1 Tidal elevation

Tidal elevation measurements at S4, S5, S6 and the Lvhua Tide Station were used to validate the model results. Skill score (SS) and correlation coefficient (CC) were calculated to quantify the model-data comparison.

$$SS = 1 - \frac{\sum_{i=1}^{N}(x_m - x_o)^2}{\sum_{i=1}^{N}(|x_m - \overline{x_m}| + |x_o - \overline{x_o}|)^2} \quad (5)$$

$$CC = \frac{\sum_{i=1}^{N}(x_m - \overline{x_m})(x_o - \overline{x_o})}{\left[\sum_{i=1}^{N}(x_m - \overline{x_m})^2 \sum_{i=1}^{N}(x_o - \overline{x_o})^2\right]^{1/2}} \quad (6)$$

where N is the number of samples for the time series, x_m and x_o are the predicted and observed tidal elevation respectively, $\overline{x_m}$ and $\overline{x_o}$ are the average of the variables.

The simulated and observed time series of tidal elevation at 4 stations are compared in Figure 5. Model performances quantified by SS and CC as follows: >0.65 excellent, 0.65–0.5 very good, 0.5–0.2 good, <0.2 poor (Wu et al., 2011). The root-mean-square error (RMSE) was also used to judge the accuracy of model results:

$$RMSE = \left[\sum_{i=1}^{N}\frac{(x_m - x_o)^2}{N}\right]^{1/2} \quad (7)$$

The SS and CC of model results are greater than 0.98 at all stations, and the RMSE is less than 0.2, which indicates that the simulated tidal elevations accurately reproduced the observed tidal elevations (Table 2).

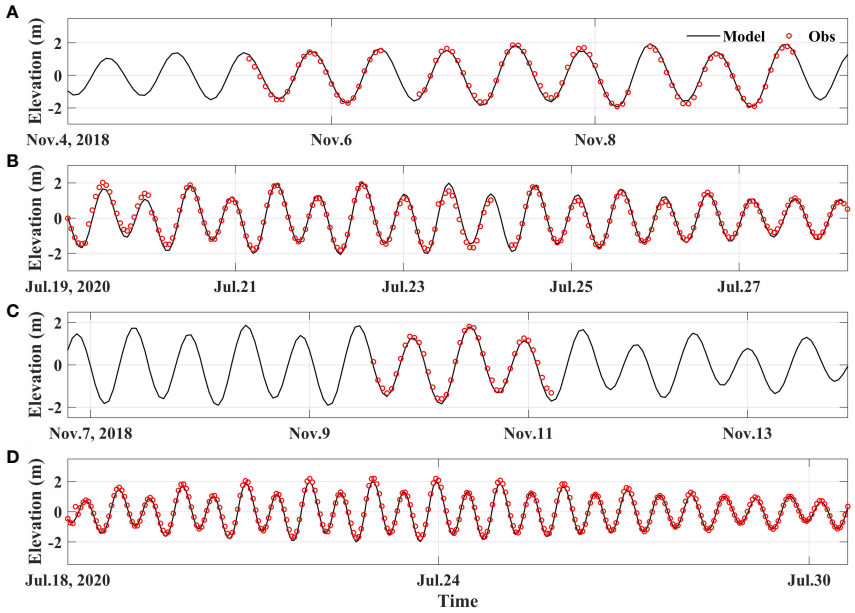

FIGURE 5
Model-data comparisons of tidal elevations at **(A)** S4 outside the farm, north of farm, **(B)** S5 outside the farm, south of Gouqi Island, **(C)** S6 north of Shengshan Island and **(D)** LvHua Tide Station (30°49′N, 122°36′E).

TABLE 2 The model-data comparisons of tidal elevation.

Field Station	SS	CC	RMSE
S4	0.996	0.992	0.156
S5	0.992	0.985	0.197
S6	0.993	0.998	0.180
Lvhua Tide Station	0.994	0.995	0.144

SS is skill score. CC is correlation coefficient. RMSE denotes root-mean-square error.

4.2 Tidal current

Simulated tidal currents were evaluated against observed data collected at S1 in the center of the mussel farm and S4 outside the mussel farm across the mussel farm (Figure 6). The skill score (SS), correlation coefficient (CC) and root-mean-square error (RMSE) are listed in Table 3. The SS and CC of surface and middle layer at S4 are both greater than 0.8 and the RMSE are less than 0.3, which are excellent scores. At S1, the model accuracies of middle and bottom layer are better than that of the surface layer. The SS and CC at S4 are better than those at S1 throughout the water column, whereas the RMSE at S1 is better than that of S4. The reason is probably that the surface layer flow velocity is consistently less than 0.2 m/s at S1 (Figure 7A), which is difficult to simulate.

As stated previously, the effect of mussel farms was represented by assigning W_k and L_σ values individually to the sigma layers. The values of W_k and L_σ were determined by the field measurements. However, the horizontal spatial distribution of mussel farm is not uniform in the field, but limited by mesh resolution, the model

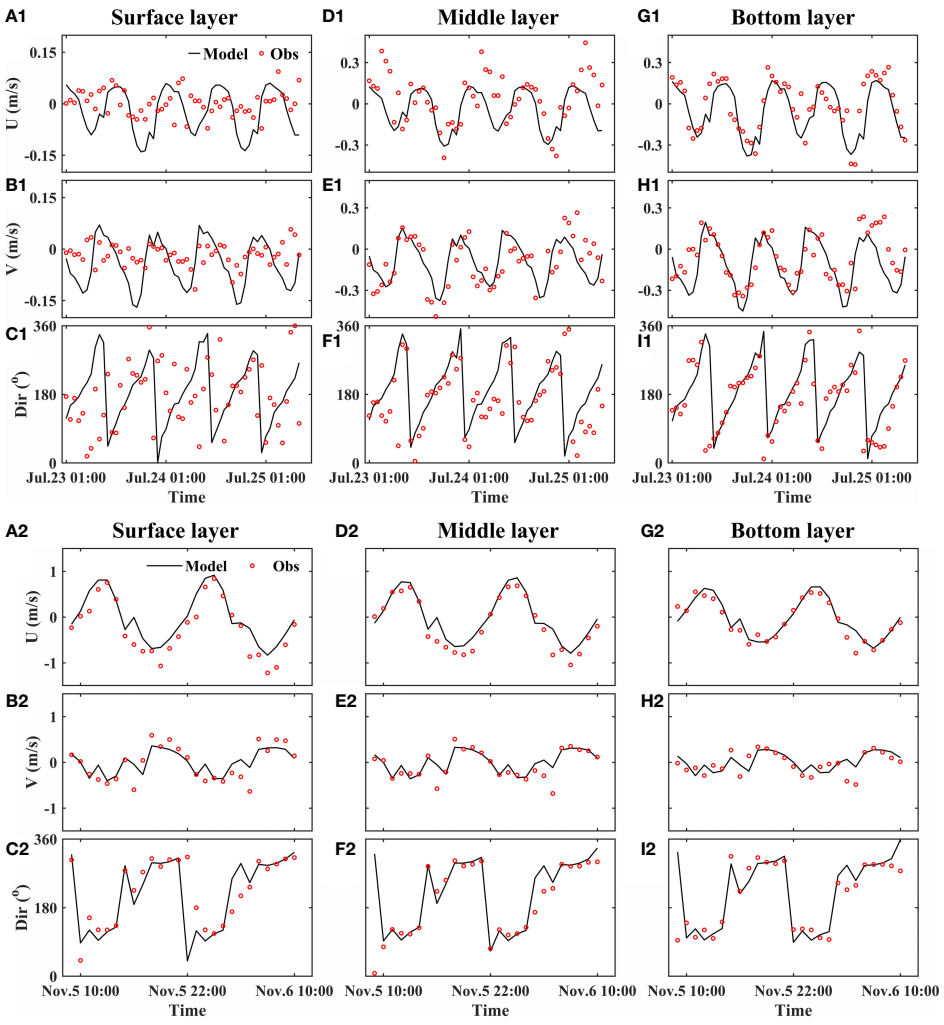

FIGURE 6
Model-data comparisons of tidal current velocity components and direction at S1 (A1-I1) inside the farm and S4 (A2-I2) outside the farm: (Upper) u in the x-direction, (Middle) v in the y-direction, (Lower) direction of current. **(A–C)** surface layer. **(D–F)** middle layer. **(G–I)** bottom layer.

TABLE 3 The model-data comparisons of tidal current.

Station	Depth	Velocity component	SS	CC	RMSE
S1	0.1 d	u	0.423	0.230	0.069
		v	0.454	0.348	0.067
	0.5 d	u	0.704	0.566	0.162
		v	0.843	0.794	0.137
	0.9 d	u	0.866	0.772	0.130
		v	0.851	0.746	0.130
S4	0.1 d	u	0.932	0.948	0.289
		v	0.853	0.813	0.228
	0.5 d	u	0.960	0.959	0.209
		v	0.875	0.825	0.183
	0.9 d	u	0.960	0.931	0.165
		v	0.767	0.638	0.187

SS is the skill score. CC is the correlation coefficient. RMSE denotes the root-mean-square error. d is the local total still water depth.

TABLE 4 The average relative difference of velocity R_U (%) between with (U_1) and without farm (U_2).

Depth (m)	Field Station	U_1(m/s)	U_2 (m/s)	R_U (%)
0.1 d (upper layer)	S1	0.08	0.42	-79
	S2	0.09	0.45	-80
0.5 d (mid layer)	S1	0.18	0.40	-55
	S2	0.18	0.44	-58
0.8 d (lower layer)	S1	0.24	0.36	-34
	S2	0.24	0.39	-38

d is the total still depth at field station S1 and S2 inside the farm (see Figure 1B).

cannot exactly represent each mussel farm. The mussel stocking density also have a significant influence on the flow field (Tseung et al., 2015; Xu and Dong, 2018). All these factors make the simulation of surface layer flow in the farm difficult.

The model results suggest that it is difficult to reproduce the complex three-dimensional flow structure inside suspended mussel farms using the present model. A CFD model such as that developed by Chen and Zou (2019) for fluid interaction with flexible suspended canopy are needed to fully resolve the 3D flow patterns within the farm. The flow pattern and its temporal variation, however, are well captured (Figure 7), thus the model can be used to study the hydrodynamic effects of large-scale suspended mussel farms around Gouqi Island. In addition, the simulation results demonstrate that the additional momentum sink term is suitable for modelling the effects of suspended mussel farms.

5 Model results of mussel farm effects on tides

5.1 Tidal current

Large scale suspended mussel farms may attenuate the local ocean circulation considerably (Stevens et al., 2008; Campbell and Hall, 2019; Liu and Huguenard, 2020). The model is run with and without the mussel farms to assess the impacts of farms on the tidal currents. The tidal currents at depth = 0.1d where d is local water depth with and without farm during flood and ebb phase are shown in Figure 8.

The main farm effect is the substantial reduction of surface flow during both flood and ebb tide. During flood tide, the tidal

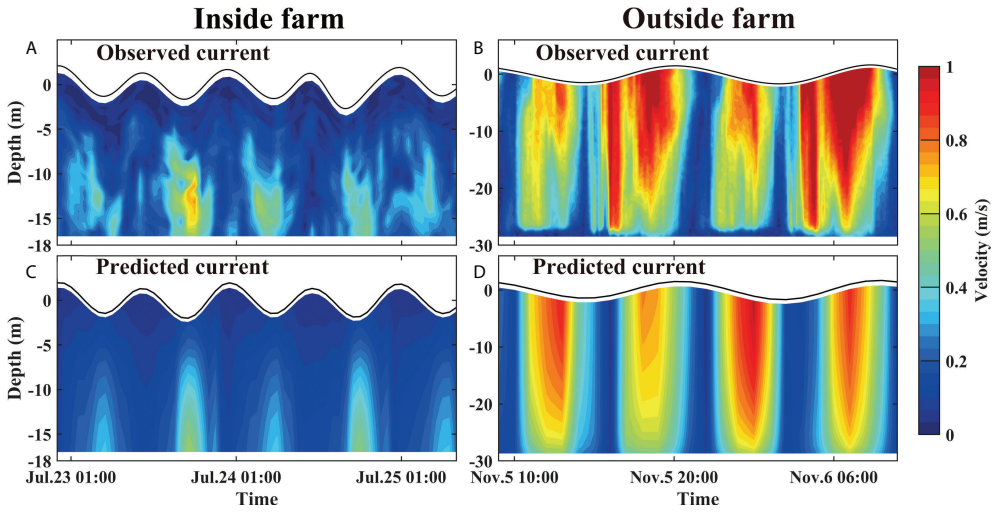

FIGURE 7
Model-data comparisons of time series of current profile at S1 station inside the farm (Left) and S4 station outside the farm (Right). **(A)** observed & **(C)** predicted current profile at S1. **(B)** observed & **(D)** predicted current profile at S4.

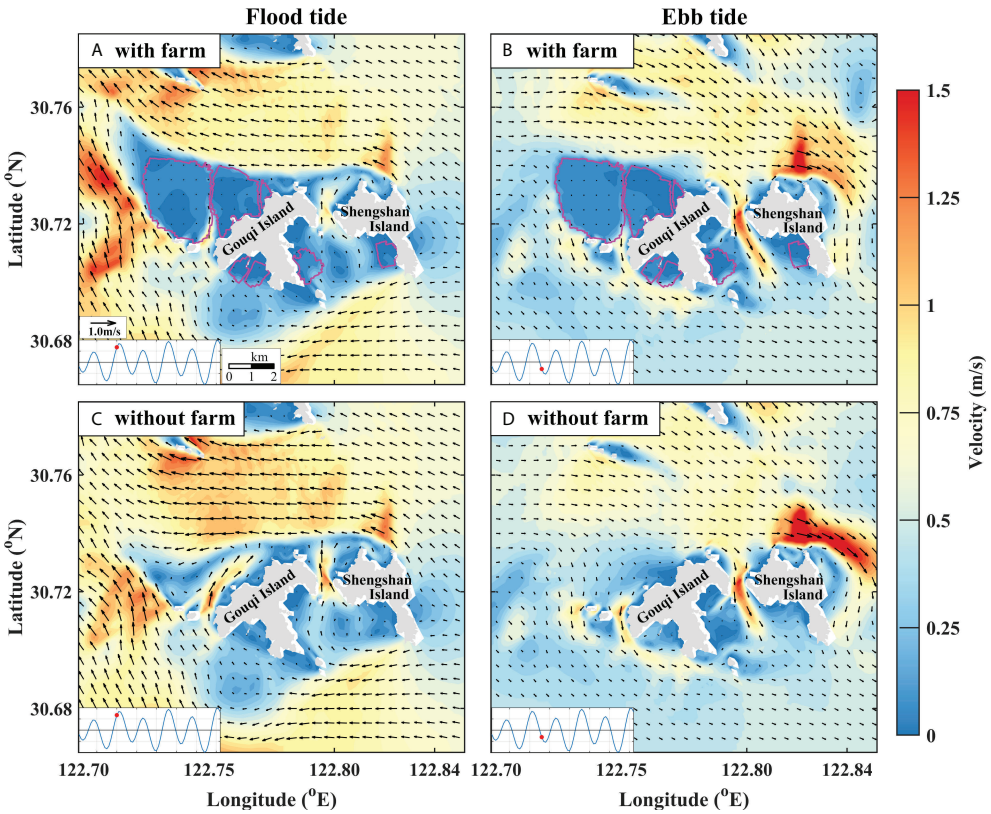

FIGURE 8
Predicted instantaneous surface layer (depth=0.1d, where d is local depth) flow field. **(A, B)** with and **(C, D)** without mussel farms during flood (Left) and ebb (Right) tide. The pink lines indicate the borderlines of the farm. The insert plot is the time series of the observed tidal elevation at Shengshan Tide station (122°28′E,30°43′N) with the red dot indicates the time instant of tidal elevation shown in the plot.

current from the east to the west at the north of Gouqi Island is weakened by the farm, whereas the tidal current from the southeast to the northwest at the west of the largest mussel farm is strengthened (Figures 8A, C). When the suspended mussel farms were removed, the tidal currents at the northeast of Shengshan Island and the west of Gouqi Island are strengthened, and the tidal currents at the middle of the islands is weakened (Figure 8C, D). The model results show that a wake zone appeared downstream from the farming area, the northwest of Gouqi Island during the flood tide (Figure 8A), under the combined influence of islands and aquaculture facilities. Therefore, we carried out moving-boat ADCP current profile observations (Figure 4) along a transect parallel to the coast of island outside the northwest farm during flood tide, when the tidal current direction is northwest that is consistent with the numerical results. These results indicate that the impact of suspended mussel farms is not limited to the immediate farm area, but extended to the local circulation outside the farms, which has significant implication on the ecosystem.

In order to quantify the degree of tidal current reduction around farms, the relative difference of tidal current velocity between with and without farm was evaluated by the following equation (Wu et al., 2014):

$$R_U = \frac{U_1 - U_2}{U_2} \times 100\,\% \tag{8}$$

where U_1 and U_2 is the average tidal current velocity over tidal cycles of with farm and without farm. U is defined as:

$$U = \frac{1}{T}\int\left[\frac{1}{A}\int\int|u|dxdy\right]dt \tag{9}$$

where T is the averaging period (T = 58 days), A is the area of water layer, $|\ u\ |$ is the magnitude of instantaneous tidal current velocity.

S1 and S2 stations inside the farm (see Figure 1B) were selected to represent the velocity change due to the mussel farms in water column (Table 4). The tidal current decrease is by more than 79%, 55% and 34% in the upper layer (depth=0.1d, where d is local water depth), middle layer (depth=0.5d) and lower layer

(depth=0.8d) respectively, which is consistent with the previous study (Lin et al., 2016).

5.2 Tidal ellipse

A harmonic analysis (T-Tide toolbox: Pawlowicz et al., 2002) for tidal currents of with and without farm case was conducted to obtain the amplitudes and phases of M_2 (principal lunar semi-diurnal), S_2 (principal solar semi-diurnal), K_1 (lunar diurnal) and O_1 (lunar diurnal) tidal constituents. Figure 9 presents the tidal ellipse at depth=0.1d where d is local water depth with and without farm. The semi major and minor axis of tidal ellipse represent the maximum and minimum current velocity within one period for the tidal constituent respectively. And the inclination of major and minor axis is equivalent to the orientation of the maximum and minimum current induced by each tidal constituent respectively.

M_2 is the dominant tidal component around Gouqi Island. In the aquaculture farm at the north of Gouqi Island, without farm, the tidal current is in the southwest direction. At the edge of the farm, the tidal current gradually changes to the west direction, and so does S_2 tidal constituent. The farm has little effect on the tidal current in the eastern area of Shengshan Island. The tidal ellipse of semidiurnal tide in the northeast area of Shengshan Island is almost perpendicular to that of diurnal tide. The semidiurnal tide comes from the southeast of the island, while that of diurnal tide comes from the northeast of the island. Due to the shelter effect of islands, the tides are divided into two branches, which lead to the complicated tidal currents around Gouqi Island.

The farm has a direct impact on the major axis and inclination of four tidal constituent ellipses, and its scope of influence can extend to a certain distance away from the farming area. The ellipse inclination variation of diurnal tide caused by the farm is greater than that of semidiurnal tide especially to the west of Gouqi Island (Figure 9). In case of K1, tidal constituent

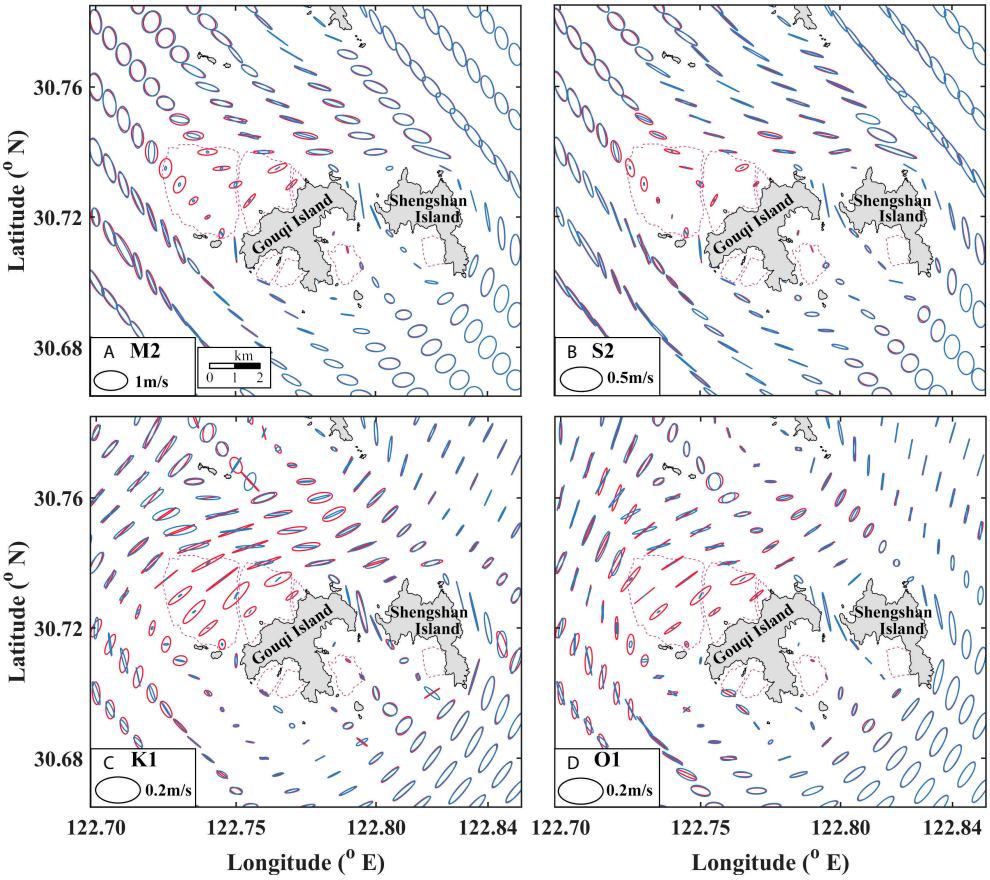

FIGURE 9
Modeled tidal ellipse in the surface layer (depth=0.1d, where d is local depth) with (blue) and without (red) farm. **(A)** M_2 semi-tide. **(B)** S_2 semi-tide. **(C)** K_1 diurnal tide. **(D)** O_1 diurnal tide. The pink dash lines indicate the borderlines of mussel farms.

the blockage of farms changes the major axis of ellipse from northeast-southwest (NE-SW) to northwest-southeast (NW-SE) degenerating to rectilinear motion to the west of Gouqi Island (Figure 9C). Similar effects are observed for the O1 tidal constituent. (Figure 9D).

The variation of semidiurnal tides due to the farm is significantly enhanced within the farm but not so outside the farm (Figures 9A, B). The length of major axes is shortened inside the farm, and the reduction is the largest for the M_2 tidal constituent. Besides, the influence of mussel farms on tides at the south of Gouqi Island is weaker than that at the north of Gouqi Island due to the fact that the former is weakened by the island with lower tidal current velocity, while the latter is adjacent to the open ocean with higher tidal current velocity.

5.3 Residual tidal current and water transport

The farm may affect both the magnitude and direction of the tidal current of the four tidal components which are both important for water transport. Therefore, in order to understand the major net water transport direction around Gouqi Island, the Euler residual tidal current was derived from model results. The Euler residual tidal current is derived an arithmetically averaged the tidal current to filter out the periodic oscillating component (Lee et al., 2017). In this study, the model results with and without farm for 58 days were averaged to obtain the Euler residual tidal current for surface layer (depth=0.1d where d is local water depth) and bottom layer (depth=0.8d). The Euler residual tidal current of with and without farm were presented in Figure 10.

With farm, a major residual current transport is observed around the farm, the northwest of Gouqi Island flowing from southeast (SE) to northwest (NW) (Figure 10A). Without farm, an additional residual current transport is observed flowing from northeast (NE) to southwest (SW) within the farm at the north of Gouqi Island (Figure 10C). The NE to SW residual tidal current also appears in the bottom layer with and without farm but the latter is stronger than that of the former (Figure 10B). The direction of the two residual tidal current is perpendicular to each other, and the magnitude of the residual tidal current outside the farm is greater than that inside the farm (Figures 10C, D). The presence of farm not only weaken the surface and bottom residual transport inside the farm, but also strengthened the residual transport at the north of the farm (Figure 10E). Moreover, the bottom layer residual transport is also strengthened inside the farm (Figure 10F). Overall, it is evident that the presence of mussel farms intensifies the residual transport in the SE to NW direction but weakens that in the NE to SW direction (Figures 10E, F).

Based on the residual transport pattern, Sec1 and Sec2 (see Figures 10E, F) were set up to estimate the change in the net water flux in the aquaculture area by the presence of farm. The Sec1 cuts the largest farm into almost two halves from SE to NW with a length of 3.6 km, and the Sec2 cuts the largest farm into two halves from NE to SW with a length of 3 km. The time evolution of water flux and the sum of the water flux along two transects over a month calculated by the Eq. (1) and (2) were shown in Figure 11.

The time series of water flux (Figure 11) through two transects have a semidiurnal periodicity. The maximum water flux with farm through Sec1 are 2.9×10^4 m^3 s^{-1} and 2.0×10^4 m^3 s^{-1} during spring and neap tides, respectively. Without farm, the maximum water flux through Sec1 is 5.7 $\times10^4$ m^3 s^{-1} during spring tide, indicating the farm reduce the water flux by~ 49%. The water flux with farm through Sec2 is ~ 1.9 $\times10^4$ m^3 s^{-1} and 0.4 $\times10^4$ m^3 s^{-1} during spring and neap tides respectively, smaller than that at Sec1. The maximum water flux without farm through Sec2 is 4.6 $\times10^4$ m^3 s^{-1} during spring tide, indicating the farm reduce the water flux by ~59%, greater than that at Sec1.

The total water flux over a month at Sec1 is negative with and without farm showing a NE to SW transport (Figure 11), which is consistent with the direction of residual currents in Figure 10. The maximum difference in the total water flux over a month with and without farm at Sec1 can reach 2.8×10^7 m^3 (Figure 11). The total water flux at Sec1 indicates that the farm greatly alters the amount of water transport, but not the main direction of water transport. The total water flux over a month at Sec2 with and without farm is also negative indicating offshore transport from SE to NW (Figure 11). The maximum difference in total water flux over a month with and without farm at Sec2 is 5.2×10^6 m^3, smaller than that of at Sec1 (Figure 11). The total water flux difference over a month displays a semi-lunar periodicity at Sec2 but not at Sec1 (Figure 11). The total water flux difference over a month at Sec2 is positive during the transition between spring and neap tide with a maximum before neap tide, but become negative during the transition between neap and spring tide. This is likely due to the enhanced bottom layer tidal current shown in Figure 10F.

6 Application and further discussion

Several studies have established a comprehensive decision-making system for key aquaculture strategies (Ferreira et al., 2008; Ferreira et al., 2009; Ibarra et al., 2014; Konstantinou and Kombiadou, 2020), such as farm layout, optimized stocking density, and carrying capacity estimation, which is critical for overall farm production. Neglecting farm drag may underestimate seston depletion within the farm (Plew, 2011b; O'Donncha et al., 2013), and overestimate of carrying capacity. As a result, the hydrodynamic effect of large-scale aquaculture facilities is critical for aquaculture decision-making.

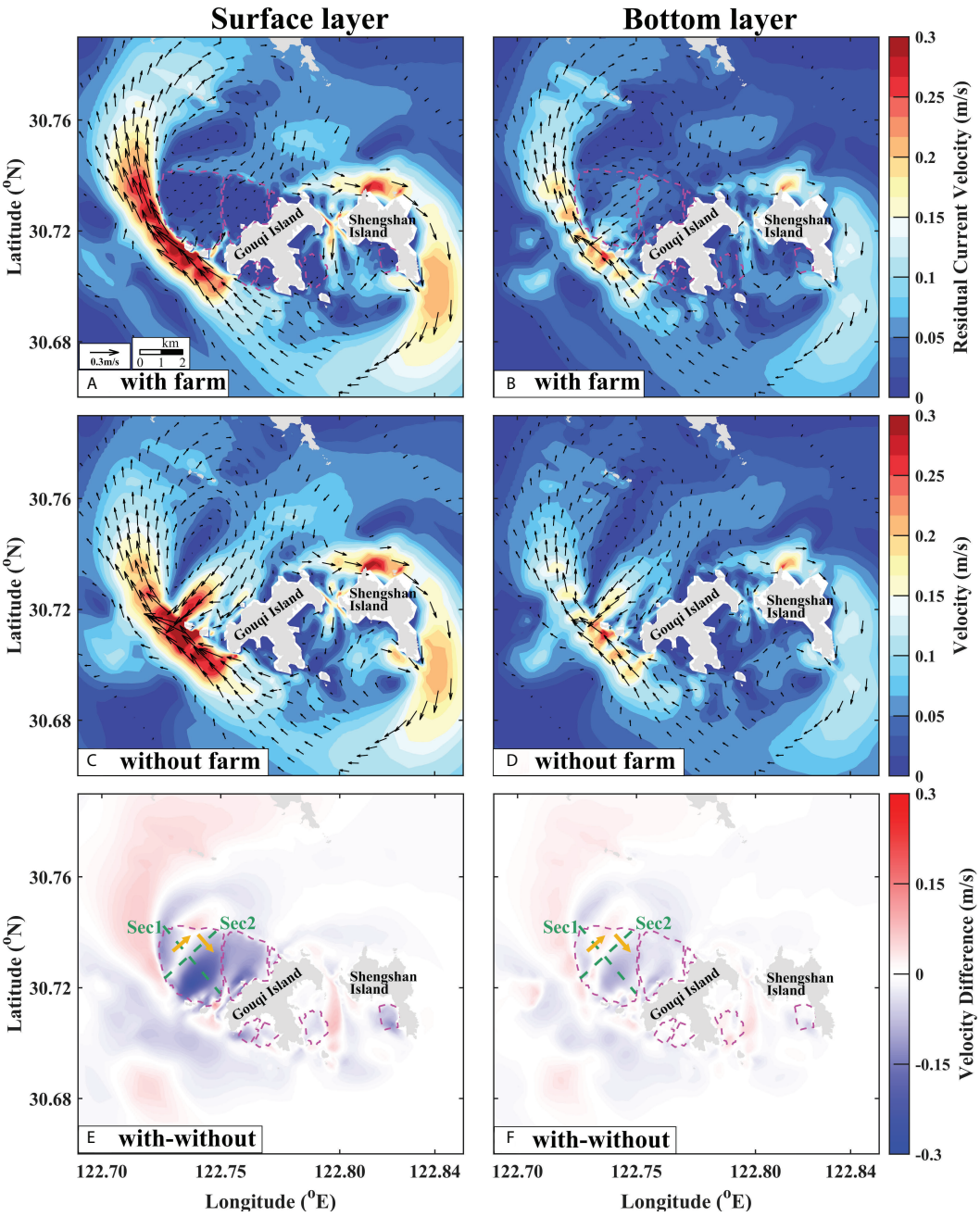

FIGURE 10
Modeled Eulerian residual tidal current. **(A, B)** with and **(C, D)** without mussel farms at the surface (Left, depth=0.1d, where d is local depth) and bottom (Right, depth=0.8d) layer. **(E, F)** is the difference of residual current with and without farm at the surface (Left) and bottom (Right) layer. The orange arrows show the positive direction of water transport across Sec1 and Sec2 in the figure. Pink dash lines indicate the borderlines of mussel farms.

The farm is a suspended canopy made of distributed elements that act as a porous media to flow. Flow disturbances of suspended canopy generally presents reduced flow velocity within the canopy, and increased flow beneath the canopy (Plew et al., 2005; Plew, 2011a; Newell and Richardson, 2014; Wu et al., 2014; Wu et al., 2022; Qiao, 2016; O'Donncha et al., 2017). Due to differences in geographic environment, faming size, farm layout and species farmed, the current velocity decrease in the canopy layer varies from farm to farm. For kelp farms, the reduction of average surface current velocity is around 40% in a

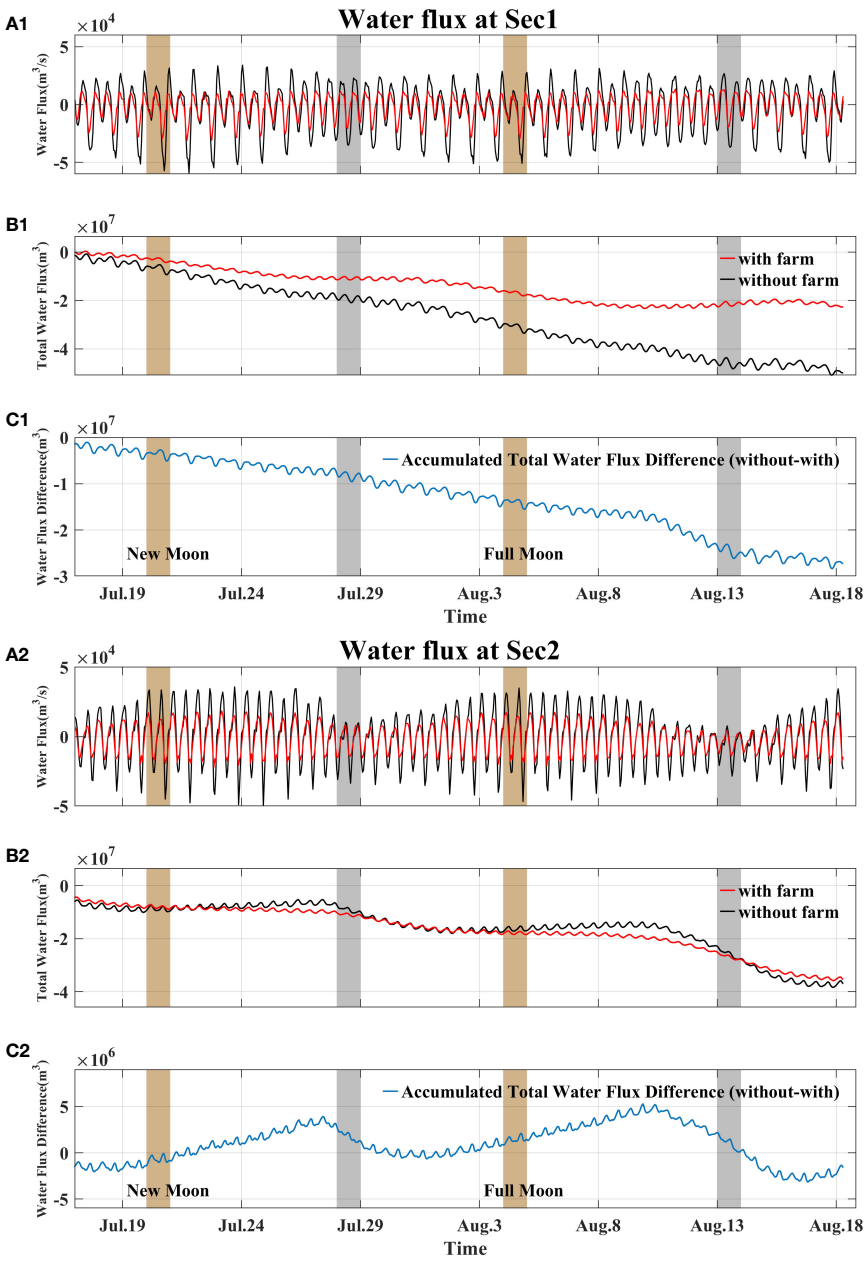

FIGURE 11
Water flux through Sec1 (A1-C1) and Sec2 (A2-C2). **(A)** water flux with (red) and without (black) farm. **(B)** accumulated total water flux with (red) and without (black) farm. **(C)** difference of total water flux with and without farm. The brown and grey box indicate time interval of 24 hours during spring and neap tide, respectively.

bay (Shi et al., 2011). As little as 25% reduction of current within the suspended canopy have been found (O'Donncha et al., 2013; Hulot et al., 2020).

The thickness of the canopy shear layer is proportional to the drag force induced by the aquaculture facilities and the depth ratios (canopy length to water depth) (Plew, 2011a; Qiao, 2016). Our field observations revealed the presence of a surface canopy boundary layer inside the farm. And its thickness progressively increase with increasing distance downstream. Given the relatively intense aquaculture density (4 m^2 $sleeve^{-1}$) on Gouqi Island, this is mainly due to the cumulative effect of flow attenuation by the farming facilities. The surface canopy boundary layer can also be seen in a large-scale suspended cage fish farm of ~ 300 km^2 at Sansha Bay (Lin et al., 2019;

Jiang et al., 2022), where cage-induced drag on the flow field may reach a depth up to 20 m in rather deep channels (30~40 m).

The tidal ellipse results described above in section 5.2 provides guidance for farm-scale layout optimization. For example, within the farm, the orientation of the aquaculture facilities shall be parallel to the major axis of the tidal ellipse, i.e., the direction of flood and ebb tides, in order to minimize the flow resistance of the farm, and therefore increase the water exchange rate. The moving-boat ADCP observations of current profile throughout the waterway indicate the same strategy (Figure 4F). Strong current is observed on the east side of transect #4, and that the ebb flow direction is southwest, which is consistent with the findings of tidal ellipses. The waterway channel's primary function right now is to make it easier for ships and fisherman to operate on the farm. On the other hand, the channel is a crucial passage for off-site replenishment of high biomass water, supplying food for mussel. Therefore, the layout of waterway should minimize the blockage effect of aquaculture facility, so that the high biomass seawater outside the farm can be transported into the farming area in time for the mussel growth, thereby improving the production and quality of aquaculture. This shall be taken into account for farm unit layout design in the future.

The major goal of this paper is to use field measurements and numerical models to investigate the hydrodynamic effects by a large-scale suspended mussel farm. In order to incorporate the blockage effects of aquaculture facility into large scale ocean models, such as ECOM-si, an appropriate drag coefficient of the suspended mussel farms is necessary. In this study, the drag coefficient is chosen based on the previous study (Beudin et al., 2017; Liu and Huguenard, 2020). Thus, more studies are required to provide improved drag coefficients through small scale computational fluid dynamics (CFD) simulations such as those of Chen & Zou (2019), field observations and laboratory experiments. Furthermore, the impacts of aquaculture facilities on tides are the main concern of this study, other physical processes such as stratification, turbulent mixing, and waves (Plew et al., 2006; Stevens and Petersen, 2011; Zhu et al., 2020)-are the subjects of future research. To determine the ideal distance between farm blocks, it is also important to consider how aquaculture farms may affect the primary production of the surrounding sea area which will be the worthwhile future works.

7 Summary

The influence of mussel farms on the flow structures near Gouqi Island was investigated using a three-dimensional ocean model and field observations. Model-data comparisons show that the additional sink terms in the momentum equations of ECOM-si adequately capture the blocking effect of large-scale suspended mussel farms. Comparisons of model results with and without farms indicate that the presence of mussel farms reduces the velocity by more than 79%, 55% and 34% in the upper, the middle, and the bottom layer at the center of farms, respectively. Tidal harmonic analysis demonstrate that mussel farms affect both the major axis and inclination of four major tidal constituent ellipses (M2, S2, K1 and O1) at much larger area than the farm area. The farm reduces the velocity magnitude of semidiurnal tide, but change both the magnitude and direction of diurnal tide, as well.

The residual currents from nonlinear interactions of tidal currents play a key role in the transport of material, such as seston and sediment. The SE to NW surface residual flow along the west border of the farm is strengthened, while the NE to SW surface residual flow inside the farm is weakened. To quantify the residual current around the farm, two cross sections, Sec 1 and Sec 2 are selected and they are perpendicular to the two major residual current and cut through the center of the farm. Sec 1 cuts the largest farm into two halves from SE to NW with a length of 3.6 km, and the Sec 2 cuts the largest farm into two halves from NE to SW with a length of 3 km. The water flux reduction by mussel farms through Sec1 and Sec2 can reach 49% and 59% respectively. In addition, the difference in the total water flux at Sec1 with and without farms reaches up to 2.8×10^7 m^3 with the major water transport direction in NE to SW. At Sec2, the total water flux difference displays a semi-lunar periodicity, positive during the transition from spring to neap tide and negative during the transition from neap to spring tide. The total offshore water transport at Sec2 may be increased by mussel farms by up to 5.2×10^6 m^3, an order of magnitude smaller than that of at Sec1.

The field observation revealed tidal asymmetry in the farm at the north of Gouqi Island. The flood currents are stronger than the ebb currents at field station S1 inside the farm and S3, while the opposite is true at field station S2 inside the farm. The thickness of the surface canopy boundary layer formed by suspended mussel farms has large spatiotemporal variations due to the heterogeneity in natural hydrodynamics within the farm. The observed current velocity profiles show that the thickness of the surface canopy boundary layer is maintained at about 5 m inside the farm, but may become larger than 10 m when the hydrodynamic is weakened by the cumulative blocking effect. And a wake zone was observed downstream the northwest farming area, which becomes larger closer to the farming area.

The present model can be a robust tool for farm site selection or farm extension and configuration by estimating the hydrodynamic changes by mussel farm and guide the production management decisions. The mussel farm needs to comply with the natural hydrodynamic conditions at the site and minimize the blocking effect on the water exchange between the water body inside and outside the farm, so that the suspended particulate organic matter in the farm can be replenished in time, which is essential for healthy mussel growth.

Data availability statement

The raw data supporting the conclusions of this article will be made available by the authors, without undue reservation.

Author contributions

WZ and YW conducted the numerical experiments and wrote the first draft of the manuscript. QZ and WZ analyzed the results and revised the manuscript. WY and GY collected and analyzed the field observation data. JL conceived the idea, designed the experiments, and revised the manuscript. All authors contributed extensively to the interpretation of results and approved the submitted version.

Funding

This research was supported by National Key R&D Program of China (2018YFD0900905 and 2019YFD0901302). This study was also funded by the project of "Study on the germplasm, environment and culture strategy of mussel culture in sea area around Gouqi Island", Shengsi County, Zhejiang Province.

Acknowledgments

The authors thank Changsheng Chen, Jianrong Zhu and Hui Wu for their generosity allowing us to use the modified ECOM-si model. We thank Hidekatsu Yamazaki and Hui Wu for their comments on the content. The authors acknowledge Xingchen Wu, Yiguo Tan, Mingbo Sun and Jianshi Liu for deploying and retrieving the instruments used in this investigation.

Conflict of interest

The authors declare that the research was conducted in the absence of any commercial or financial relationships that could be construed as a potential conflict of interest.

Publisher's note

References

Aguiar, E., Piedracoba, S., Alvarez-Salgado, X. A., and Labarta, U. (2015). Circulation of water through a mussel raft: clearance area vs. idealized linear flows. *Rev. Aquacul.* 9, 3–22. doi: 10.1111/raq.12099

Anaïs, A., Adélaïde, A., Jean-Claude, G., Oihana, L., Philippe, A., and Nabila, G. (2020). Assessment of carrying capacity for bivalve mariculture in subtropical and tropical regions: the need for tailored management tools and guidelines. *Rev. Aquacult.*, 12, 1721–1735. doi: 10.1111/raq.12406

Beudin, A., Kalra, T. S., Ganju, N. K., and Warner, J. C. (2017). Development of a coupled wave-flow-vegetation interaction model. *Comput. Geosci.* 100, 76–86. doi: 10.1016/j.cageo.2016.12.010

Blumberg, A. (1994). *A primer for ECOM-si. technical report of HydroQual*, Vol. 66. Mahwah, N.J.: Technical Report of HydroQual.

Broch, O. J., Klebert, P., Michelsen, F. A., and Alver, M. O. (2020). Multiscale modelling of cage effects on the transport of effluents from open aquaculture systems. *PloS One* 15, e0228502. doi: 10.1371/journal.pone.0228502

Byron, C., Link, J., Costa-Pierce, B., and Bengtson, D. (2011a). Calculating ecological carrying capacity of shellfish aquaculture using mass-balance modeling: Narragansett bay, Rhode island. *Ecol. Model.* 222, 1743–1755. doi: 10.1016/j.ecolmodel.2011.03.010

Byron, C., Link, J., Costa-Pierce, B., and Bengtson, D. (2011b). Modeling ecological carrying capacity of shellfish aquaculture in highly flushed temperate lagoons. *Aquaculture* 314, 87–99. doi: 10.1016/j.aquaculture.2011.02.019

Campbell, M. D., and Hall, S. G. (2019). Hydrodynamic effects on oyster aquaculture systems: a review. *Rev. Aquacult.* 11, 896–906. doi: 10.1111/raq.12271

Cheng, W., Sun, Z., and Liang, S. (2019). Numerical simulation of flow through suspended and submerged canopy. *Adv. Water Resour.* 127, 109–119. doi: 10.1016/j.advwatres.2019.01.008

Chen, H., and Zou, Q.-P. (2019). Eulerian–Lagrangian flow-vegetation interaction model using immersed boundary method and OpenFOAM. *Adv. Water Resour.* 126, 176–192. doi: 10.1016/j.advwatres.2019.02.006

Cornejo, P., Sepúlveda, H. H., Gutiérrez, M. H., and Olivares, G. (2014). Numerical studies on the hydrodynamic effects of a salmon farm in an idealized environment. *Aquaculture* 430, 195–206. doi: 10.1016/j.aquaculture.2014.04.015

Delaux, S., Stevens, C. L., and Popinet, S. (2011). High-resolution computational fluid dynamics modelling of suspended shellfish structures. *Environ. Fluid. Mech.* 11, 405–425. doi: 10.1007/s10652-010-9183-y

Duarte, P., Alvarez-Salgado, X. A., Fernández-Reiriz, M. J., Piedracoba, S., and Labarta, U. (2014). A modeling study on the hydrodynamics of a coastal embayment occupied by mussel farms (Ria de Ares-betanzos, NW Iberian peninsula). *Estuar. Coast. Shelf. Sci.* 147, 42–55. doi: 10.1016/j.ecss.2014.05.021

FAO (2020). *The state of world fisheries and aquaculture 2020* Sustainability in action. (Rome). doi: 10.4060/ca9229en

Ferreira, J. G., Hawkins, A. J. S., Monteiro, P., Moore, H., Service, M., Pascoe, P. L., et al. (2008). Integrated assessment of ecosystem-scale carrying capacity in shellfish growing areas. *Aquaculture* 275, 138–151. doi: 10.1016/j.aquaculture.2007.12.018

Ferreira, J. G., Sequeira, A., Hawkins, A. J. S., Newton, A., Nickell, T. D., Pastres, R., et al. (2009). Analysis of coastal and offshore aquaculture: Application of the FARM model to multiple systems and shellfish species. *Aquaculture* 289, 32–41. doi: 10.1016/j.aquaculture.2008.12.017

Filgueira, R. (2018). Identifying the optimal depth for mussel suspended culture in shallow and turbid environments. *J. Sea. Res.* 132, 15–23. doi: 10.1016/j.seares.2017.11.006

Filgueira, R., Comeau, L. A., Guyondet, T., McKindsey, C. W., and Byron, C. J. (2015). "Modelling carrying capacity of bivalve aquaculture: A review of definitions and methods," in *Encyclopedia of sustainability science and technology*. Ed. R. A. Meyers (New York, NY: Springer New York), 1–33. doi: 10.1007/978-1-4939-2493-6_945-1

Froján, M., Castro, C. G., Zúñiga, D., Arbones, B., Alonso-Pérez, F., and Figueiras, F. G. (2018). Mussel farming impact on pelagic production and respiration rates in a coastal upwelling embayment (Ría de vigo, NW Spain). *Estuar. Coast. Shelf. Sci.* 204, 130–139. doi: 10.1016/j.ecss.2018.02.025

Gao, Y., Fang, J., Lin, F., Li, F., Li, W., Wang, X., et al. (2020). Simulation of oyster ecological carrying capacity in sanggou bay in the ecosystem context. *Aquacul. Int.* 28, 2059–2079. doi: 10.1007/s10499-020-00576-3

Garlock, T., Asche, F., Anderson, J., Bjørndal, T., Kumar, G., Lorenzen, K., et al. (2019). A global blue revolution: Aquaculture growth across regions, species, and countries. *Rev. Fish. Sci. Aquacul.* 28, 107–116. doi: 10.1080/23308249.2019.1678111

Grant, J., and Bacher, C. (2001). A numerical model of flow modification induced by suspended aquaculture in a Chinese bay. *Can. J. Fish. Aquat. Sci.* 58, 1003–1011. doi: 10.1139/f01-027

Hulot, V., Saulnier, D., Lafabrie, C., and Gaertner-Mazouni, N. (2020). Shellfish culture: a complex driver of planktonic communities. *Rev. Aquacult.* 12, 33–46. doi: 10.1111/raq.12303

Ibarra, D. A., Fennel, K., and Cullen, J. J. (2014). Coupling 3-d eulerian biophysics (ROMS) with individual-based shellfish ecophysiology (SHELL-e): A hybrid model for carrying capacity and environmental impacts of bivalve aquaculture. *Ecol. Model.* 273, 63–78. doi: 10.1016/j.ecolmodel.2013.10.024

Jiang, X., Tu, J., and Fan, D. (2022). The influence of a suspended cage aquaculture farm on the hydrodynamic environment in a semienclosed bay, SE China. *Front. Mar. Sci.* 8. doi: 10.3389/fmars.2021.779866

Konstantinou, Z. I., and Kombiadou, K. (2020). Rethinking suspended mussel-farming modelling: Combining hydrodynamic and bio-economic models to support integrated aquaculture management. *Aquaculture* 523, 735179. doi: 10.1016/j.aquaculture.2020.735179

Konstantinou, Z. I., Kombiadou, K., and Krestenitis, Y. N. (2015). Effective mussel-farming governance in Greece: Testing the guidelines through models, to evaluate sustainable management alternatives. *Ocean. Coast. Manage.* 118, 247–258. doi: 10.1016/j.ocecoaman.2015.05.011

Lee, S. B., Li, M., and Zhang, F. (2017). Impact of sea level rise on tidal range in Chesapeake and Delaware bays. *J. Geophys. Res. Ocean.* 122, 3917–3938. doi: 10.1002/2016JC012597

Li, X., Li, M., McLelland, S. J., Jordan, L.-B., Simmons, S. M., Amoudry, L. O., et al. (2017). Modelling tidal stream turbines in a three-dimensional wave-current fully coupled oceanographic model. *Renewable Energy* 114, 297–307. doi: 10.1016/j.renene.2017.02.033

Lin, H., Chen, Z., Hu, J., Cucco, A., Sun, Z., Chen, X., et al. (2019). Impact of cage aquaculture on water exchange in sansha bay. *Cont Shelf. Res.* 188, 103963. doi: 10.1016/j.csr.2019.103963

Lin, J., Li, C., Boswell, K. M., Kimball, M., and Rozas, L. (2015). Examination of winter circulation in a northern gulf of Mexico estuary. *Estuar Coast.* 39, 879–899. doi: 10.1007/s12237-015-0048-y

Lin, J., Li, C., and Zhang, S. (2016). Hydrodynamic effect of a large offshore mussel suspended aquaculture farm. *Aquaculture* 451, 147–155. doi: 10.1016/j.aquaculture.2015.08.039

Liu, Z., and Huguenard, K. (2020). Hydrodynamic response of a floating aquaculture farm in a low inflow estuary. *J. Geophys. Res.: Ocean.* 125, e2019JC015625. doi: 10.1029/2019jc015625

Mascorda Cabre, L., Hosegood, P., Attrill, M. J., Bridger, D., and Sheehan, E. V. (2021). Offshore longline mussel farms: a review of oceanographic and ecological interactions to inform future research needs, policy and management. *Rev. Aquacul.* 13, 1864–1887. doi: 10.1111/raq.12549

Mustafa, S., Estim, A., AI-Azad, S., Shaleh, S. R. M., and Shapawi, R. (2017). Aquaculture sustainability: Multidisciplinary perspectives and adaptable models for seafood security. *J. Fish. Aquacul. Dev.* 126. doi: 10.29011/JFAD-126/100026

Newell, C. R., and Richardson, J. (2014). The effects of ambient and aquaculture structure hydrodynamics on the food supply and demand of mussel rafts. *J. Shellfish. Res.* 33, 257–272. doi: 10.2983/035.033.0125

O'Donncha, F., Hartnett, M., and Nash, S. (2013). Physical and numerical investigation of the hydrodynamic implications of aquaculture farms. *Aquacul. Eng.* 52, 14–26. doi: 10.1016/j.aquaeng.2012.07.006

O'Donncha, F., Hartnett, M., and Plew, D. R. (2015). Parameterizing suspended canopy effects in a three-dimensional hydrodynamic model. *J. Hydraulic. Res.* 53, 714–727. doi: 10.1080/00221686.2015.1093036

O'Donncha, F., James, S. C., and Ragnoli, E. (2017). Modelling study of the effects of suspended aquaculture installations on tidal stream generation in cobscook bay. *Renewable Energy* 102, 65–76. doi: 10.1016/j.renene.2016.10.024

O'Hara Murray, R., and Gallego, A. (2017). A modelling study of the tidal stream resource of the pentland firth, Scotland. *Renewable Energy* 102, 326–340. doi: 10.1016/j.renene.2016.10.053

Pawlowicz, R., Beardsley, B., and Lentz, S. (2002). Classical tidal harmonic analysis including error estimates in MATLAB using T_TIDE. *Comput. Geosci.* 28, 929–937. doi: 10.1016/S0098-3004(02)00013-4

Plew, D. R. (2011a). Depth-averaged drag coefficient for modeling flow through suspended canopies. *J. Hydraul. Eng.* 137, 234–247. doi: 10.1061/(ASCE)HY.1943-7900.0000300

Plew, D. R. (2011b). Shellfish farm-induced changes to tidal circulation in an embayment, and implications for seston depletion. *Aquacul. Environ. Interact.* 1, 201–214. doi: 10.3354/aei00020

Plew, D. R., Spigel, R. H., Stevens, C. L., Nokes, R. I., and Davidson, M. J. (2006). Stratified flow interactions with a suspended canopy. *Environ. Fluid. Mech.* 6, 519–539. doi: 10.1007/s10652-006-9008-1

Plew, D. R., Stevens, C. L., Spigel, R. H., and Hartstein, N. D. (2005). Hydrodynamic implications of Large offshore mussel farms. *IEEE J. Ocean. Eng.* 30, 95–108. doi: 10.1109/joe.2004.841387

Qiao, J. D. (2016). Flow structure and turbulence characteristics downstream of a spanwise suspended linear array. *Environ. Fluid. Mech.* 16, 1021–1041. doi: 10.1007/s10652-016-9465-0

Reid, G. K., Dumas, A., and Chopin, T. B. R. (2020). Performance measures and models for open-water integrated multi-trophic aquaculture. *Rev. Aquacul.* 12, 47–75. doi: 10.1111/raq.12304

Roc, T., Conley, D. C., and Greaves, D. (2013). Methodology for tidal turbine representation in ocean circulation model. *Renewable Energy* 51, 448–464. doi: 10.1016/j.renene.2012.09.039

Shi, J., and Wei, H. (2009). Simulation of hydrodynamic structures in a semi-enclosed bay with dense raft-culture. *Periodic. Ocean. Univ. China (Chinese)* 39, 1181–1187. doi: 10.16441/j.cnki

Shi, J., Wei, H., Zhao, L., Yuan, Y., Fang, J., and Zhang, J. (2011). A physical–biological coupled aquaculture model for a suspended aquaculture area of China. *Aquaculture* 318, 412–424. doi: 10.1016/j.aquaculture.2011.05.048

Stevens, C., and Petersen, J. (2011). Turbulent, stratified flow through a suspended shellfish canopy: implications for mussel farm design. *Aquacult. Environ. Interact.* 2, 87–104. doi: 10.3354/aei00033

Stevens, C., Plew, D., Hartstein, N., and Fredriksson, D. (2008). The physics of open-water shellfish aquaculture. *Aquacul. Eng.* 38, 145–160. doi: 10.1016/j.aquaeng.2008.01.006

Tseung, H. L., Kikkert, G. A., and Plew, D. (2015). Hydrodynamics of suspended canopies with limited length and width. *Environ. Fluid. Mech.* 16, 145–166. doi: 10.1007/s10652-015-9419-y

Wu, Y., Chaffey, J., Law, B., Greenberg, D. A., Drozdowski, A., Page, F., et al. (2014). A three-dimensional hydrodynamic model for aquaculture: a case study in the bay of fundy. *Aquacul. Environ. Interact.* 5, 235–248. doi: 10.3354/aei00108

Wu, H., and Zhu, J. (2010). Advection scheme with 3rd high-order spatial interpolation at the middle temporal level and its application to saltwater intrusion in the changjiang estuary. *Ocean. Model.* 33, 33–51. doi: 10.1016/j.ocemod.2009.12.001

Wu, H., Zhu, J., Chen, B., and Chen, Y. (2006). Quantitative relationship of runoff and tide to saltwater spilling over from the north branch in the changjiang estuary: A numerical study. *Estuar. Coast. Shelf. Sci.* 69, 125–132. doi: 10.1016/j.ecss.2006.04.009

Wu, H., Zhu, J., Shen, J., and Wang, H. (2011). Tidal modulation on the changjiang river plume in summer. *J. Geophys. Res.* 116, C08017. doi: 10.1029/2011jc007209

Wu, Y., Law, B., Ding, F., and Flaherty-Sproul, M.O. (2022). Modeling the effect of cage drag on particle residence time within fish farms in the Bay of Fundy. *Aquac Environ Interact.* 14, 163–179.

Xu, T.-J., and Dong, G.-H. (2018). Numerical simulation of the hydrodynamic behaviour of mussel farm in currents. *Ship. Offshore. Struct.* 13, 835–846. doi: 10.1080/17445302.2018.1465380

Yang, Z., Wang, T., and Copping, A. E. (2013). Modeling tidal stream energy extraction and its effects on transport processes in a tidal channel and bay system using a three-dimensional coastal ocean model. *Renewable Energy* 50, 605–613. doi: 10.1016/j.renene.2012.07.024

Zhang, Q., Li, C., Huang, W., Lin, J., Hiatt, M., and Rivera-Monroy, V. H. (2022). Water circulation driven by cold fronts in the wax lake delta (Louisiana, USA). *JMSE* 10, 415. doi: 10.3390/jmse10030415

Zhang, S. Y., Wang, L., and Wang, W. D. (2008). Algal communities at gouqi island in the zhoushan archipelago, China. *J. Appl. Phycol.* 20, 853–861. doi: 10.1007/s10811-008-9338-0

Zhu, L., Huguenard, K., Zou, Q-P., Fredriksson, D. W., and Xie, D. (2020). Aquaculture farms as nature-based coastal protection: Random wave attenuation by suspended and submerged canopies. *Coast. Eng.* 160, 103737. doi: 10.1016/j.coastaleng.2020.103737

frontiers | Frontiers in Marine Science

TYPE Original Research
PUBLISHED 03 November 2022
DOI 10.3389/fmars.2022.1035135

OPEN ACCESS

EDITED BY
François G. Schmitt,
UMR8187 Laboratoire d'océanologie et de géosciences (LOG), France

REVIEWED BY
Ming-Huei Chang,
National Taiwan University, Taiwan
Ru Chen,
Tianjin University, China

*CORRESPONDENCE
Shuang-Xi Guo
sxguo@scsio.ac.cn

SPECIALTY SECTION
This article was submitted to Physical Oceanography, a section of the journal Frontiers in Marine Science

RECEIVED 02 September 2022
ACCEPTED 17 October 2022
PUBLISHED 03 November 2022

CITATION
Cen X-R, Guo S-X, Wang Y and Zhou S-Q (2022) Similarity of the turbulent kinetic energy dissipation rate distribution in the upper mixed layer of the tropical Indian Ocean. *Front. Mar. Sci.* 9:1035135. doi: 10.3389/fmars.2022.1035135

Similarity of the turbulent kinetic energy dissipation rate distribution in the upper mixed layer of the tropical Indian Ocean

Xian-Rong Cen[1,2,3], Shuang-Xi Guo[1,3]*, Yan Wang[4] and Sheng-Qi Zhou[1,3]

[1]State Key Laboratory of Tropical Oceanography, South China Sea Institute of Oceanology, Chinese Academy of Sciences, Guangzhou, China, [2]School of Industrial Design and Ceramic Art, Foshan University, Foshan, China, [3]Southern Marine Science and Engineering Guangdong Laboratory (Guangzhou), Guangzhou, China, [4]Department of Ocean Science and Center for Ocean Research in Hong Kong and Macau, Hong Kong University of Science and Technology, Hong Kong, Hong Kong SAR, China

Turbulence within the upper ocean mixed layer plays a key role in various physical, biological, and chemical processes. Between September and November 2011, a dataset of 570 vertical profiles of the turbulent kinetic energy (TKE) dissipation rate, as well as conventional hydrological and meteorological data, were collected in the upper layer of the tropical Indian Ocean. These data were used to statistically analyze the vertical distribution of the TKE dissipation rate in the mixed layer. The arithmetic-mean method made the statistical TKE dissipation rate profile more scattered than the median and geometric-mean methods. The statistical TKE dissipation rate were respectively scaled by the surface buoyancy flux and the TKE dissipation rate at the mixed-layer base. It was found that the TKE dissipation rate scaled by that at the mixed-layer base exhibited better similarity characteristics than that scaled by the surface buoyancy flux, whether the stability parameter $D/|L_{MO}|$ was greater or less than 10, indicating that the TKE dissipation rate at the mixed-layer base is a better characteristic scaling parameter for reflecting the intrinsic structure of the TKE dissipation rate in the mixed layer, where D and L_{MO} are respectively the mixed-layer thickness and the Monin-Obukhov length scale. The parameterization of the TKE dissipation rate at the mixed-layer base on the shear-driven dissipation rate and the surface buoyancy flux was further explored. It was found that the TKE dissipation rate at the mixed-layer base could be well fitted by a linear combination of three terms: the wind-shear-driven dissipation rate, the surface buoyancy flux, and a simple nonlinear coupling term of these two .

KEYWORDS

turbulent mixing, dissipation rate, tropical indian ocean, mixed layer, similarity

1 Introduction

The upper part of the ocean is directly mixed by momentum and buoyancy fluxes from the atmosphere. This mixing produces a turbulent and homogeneous layer with a thickness of tens to hundreds of meters, commonly referred to as the upper ocean mixed layer (Kantha and Clayson, 2000; Pellichero et al., 2017). The upper ocean mixed layer acts as a buffer between the atmosphere and the interior ocean and affects oceanic dynamic processes at various scales and eventually global climate change (Macdonald and Wunsch, 1996; Kantha and Clayson, 2000; Esters et al., 2018; Qiu et al., 2019; Meredith and Garabato, 2021). For example, turbulence in the mixed layer generally dominates mass and energy exchange between the atmosphere and the ocean (Qiu et al., 2016; Evans et al., 2018), adjusts the spatial distributions of various materials and water masses in the upper ocean (Esters et al., 2017), and facilitates absorption of excess heat and carbon dioxide from the atmosphere (Sabine et al., 2004). The mixed layer is also where certain water masses form through dynamic processes such as subduction and deep convection. These processes can further impact the water mass properties of the deeper ocean and hence the Meridional Overturning Circulation (Kostov et al., 2014; Zhang and Wang, 2018).

Turbulence plays an important role in the formation and evolution of the mixed layer. The associated turbulent structures are assumed to be controlled by energy input and exchange from the atmosphere. There are three main types of this external energy source (Thorpe, 2005). The first is wind stress, which drives turbulence by vertical mean-current shear based on the Kelvin-Helmholtz instabilities and transfers the momentum flux downward in the mixed layer (Callaghan et al., 2014). Based on the theory of the turbulent boundary layer, it is assumed that the vertical distribution of the wind-shear-driven dissipation rate satisfies the classical “law of the wall” (D'Asaro, 2014). The second source is the surface wave field. The dynamic processes of the surface wave field, such as wave-breaking and Langmuir convection, modify the turbulence characteristics of the upper ocean and convert the energy of the wave field into TKE (Thorpe, 2005; Wain et al., 2015). It has been reported that the surface wave field can significantly enhance turbulence only in the top few meters of the ocean (Gemmrich and Farmer, 2004). In this depth range, however, collected turbulence data in field observations are often contaminated by the vibration and wake of the vessel (Oakey and Elliott, 1982; Lombardo and Gregg, 1989; Brainerd and Gregg, 1993). The third source is surface buoyancy flux. During nighttime, surface cooling promotes the transfer of ocean heat to the atmosphere, thus convective instability leads to turbulent flows in the mixed layer (hereafter, the oceanic heat loss is defined as the positive buoyancy flux). In contract to the surface wave field driving turbulence within the top few meters, the surface buoyancy flux can convectively drive turbulence from the sea surface to the base of the mixed layer. However, during daytime, the ocean is heated by penetrating solar radiation, and the surface buoyancy flux acts as a sink for turbulence, which initiates stable stratification near the surface and thus suppresses turbulence (Anis and Moum, 1994; Moulin et al., 2018).

The TKE dissipation rate, ϵ, acts as an important sink in the energy budget of the global ocean. It balances the energy input to the ocean from external forcing (Wunsch and Ferrari, 2004; Ferrari and Wunsch, 2009). Regardless of the top few meters, which are dominated by surface waves, the mixed layer is thought to be affected mainly by wind-induced current shear and buoyancy flux, and the vertical distribution of TKE dissipation rate in the mixed layer has been widely studied and parameterized by a linear combination of the shear-driven dissipation rate and surface buoyancy flux (Lombardo and Gregg, 1989; Tedford et al., 2014; Esters et al., 2017; Esters et al., 2018). Field observations have indicated that in the mixed layer the TKE dissipation rate first decreases rapidly beneath the sea surface, and then remains relatively uniform towards the mixed-layer base (Shay and Gregg, 1986; Lombardo and Gregg, 1989; Anis and Moum, 1994; Moum and Rippeth, 2009). To identify the similarity structure of TKE dissipation rate in the mixed layer, it has usually been rendered dimensionless by surface buoyancy flux, J_b^0, and has been found to be convergentin some ocean regions and in the atmosphere (Shay and Gregg, 1986; Moum and Rippeth, 2009; D'Asaro, 2014). These results have significantly expanded the understanding of turbulence structures in the mixed layer. Nonetheless, the choice of surface buoyancy flux as the scaling parameter may have some inherent flaws. For example, during daytime, surface buoyancy flux is inapplicable because it is negative and suppresses turbulence in the mixed layer. Moreover, when using only surface buoyancy flux to make TKE dissipation rate dimensionless, the contribution of wind-induced current shear is explicitly omitted, which may fail to produce a true intrinsic structure of TKE dissipation rate in the mixed layer (Anis and Moum, 1994; Lozovatsky et al., 2005). These issues motivate the search for a more appropriate parameter to characterize ϵ in the mixed layer.

In this paper, we attempt to propose a new characteristic parameter to reflect the intrinsic similarity structure of the TKE dissipation rate in the mixed layer. This parameter is available all day long, and its relationship with wind-induced current shear and surface buoyancy flux is systematically examined using the present dataset collected in the tropical Indian Ocean.

2 Theory and methods

2.1 Shear-driven dissipation rate ϵ_s

The oceanic surface wind-induced current shear stress τ_0, as a function of the wind speed at a reference height and the drag coefficient, can be expressed (Jones and Toba, 2001) as

$$\tau_0 = \rho_a C_D U_{10}^2 \tag{1}$$

where ρ_a is the air density, C_D is the drag coefficient, and U_{10} is the wind speed at a height of 10 m above the sea surface. Typical values of C_D are on the order of 10^{-3} and depend on wind speed. The calculation of C_D is based on version 3.0 of the Coupled Ocean-Atmosphere Response Experiment (COARE 3.0) bulk algorithm (Fairall et al., 1996; Fairall et al., 2003; Edson et al., 2013), which can be accessed at *ftp://ftp1.esrl.noaa.gov/BLO/Air-Sea/bulkalg/cor3_0/*. The friction velocity on the sea side, u_*, which is a characteristic velocity reflecting boundary shear effect, is defined as

$$u_* = \sqrt{\tau_0/\rho} \tag{2}$$

where ρ is the density of seawater.

When only wind stress is applied, based on the flat rigid-wall approximation of the ocean surface, in the upper boundary layer, the vertical distribution of the horizontal mean velocity U satisfies the classical logarithmic law (Esters et al., 2018)

$$U = \frac{u_*}{\kappa}\ln\left(\frac{z}{z_0}\right), \tag{3}$$

where z_0 is the roughness length of the sea surface boundary layer, z is distance from the sea surface, and κ=0.41 is the von Karman constant. This formula gives the velocity shear as $\frac{\partial U}{\partial z} = \frac{u_*}{\kappa z}$. Thus, the dissipation rate dominated by wind stress alone follows the so-called "law of the wall" as

$$\epsilon_s = \overline{u'w'}\frac{\partial U}{\partial z} = \frac{u_*^3}{\kappa z}, \tag{4}$$

where $\overline{u'w'} = u_*^2$ reflects the balance between near-surface Reynolds stress and surface wind stress, and u' and w' are the fluctuating velocities in the horizontal and vertical directions.

2.2 Buoyancy flux J_b^0

The oceanic surface buoyancy flux, which is affected by both heat and mass exchange between the atmosphere and ocean, is defined (Shay and Gregg, 1986; Thorpe, 2005) as

$$J_b^0 = \frac{gQ_p}{\rho_0}, \tag{5}$$

where g is the gravitational acceleration, ρ_0 is the reference density of seawater, and Q_p is the density flux, which is made up of contributions from temperature flux F_T and freshwater flux F_S as

$$Q_P = \rho(\alpha F_T + \beta F_S) \tag{6}$$

Here, $F_T = -Q_{net}/\rho_w C_p$ and $F_S = (E-P)S/(1-\frac{S}{1000})$, where α and β are the thermal expansion and saline contraction coefficients respectively. C_p represents the specific heat of seawater, and E, P, and S represent evaporation, precipitation, and sea surface salinity respectively. Q_{net}, the net radiative heat flux at the ocean surface, is given (Shay and Gregg, 1986) by the sum of the incoming shortwave radiation (SW), longwave radiation (LW), sensible heat (SH), and latent heat (LH) as

$$Q_{net} = SW + LW + SH + LH \tag{7}$$

E, P, SW, and LW were measured directly by the onboard meteorological observation system, and SH and LH were computed using the general flux algorithm of COARE 3.0 (Fairall et al., 2003), which has been wildly used to estimate sensible and latent heat in the air-sea interaction community with accuracy within 5% for wind speed of 0-10 m s^{-1} and 10% for wind speed of 10-20 m s^{-1}, guaranteeing a reasonable evaluation of J_b^0.

2.3 TKE dissipation rate ϵ

TKE dissipation rate ϵ characterizes the conversion intensity of turbulent energy into heat through fluid viscous forces. In isotropic turbulence, ϵ is defined (Wolk et al., 2002) as

$$\epsilon = \frac{15}{2}\nu\overline{\left(\frac{\partial u}{\partial z}\right)^2} = \frac{15}{2}\nu\int_0^\infty \varphi(k)dk, \tag{8}$$

where ν is Molecular viscosity coefficient, and $\frac{\partial u}{\partial z}$ is the velocity shear and directly measured by the shear probe mounted on the microstructure profiler. $\varphi(k)$ is the shear spectrum in wavenumber (k) space, which were transformed from the frequency (f) space based on Taylor's frozen turbulence hypothesis for each vertical segment.

Considering the observation noise in the high wave number region, the observed shear spectrum $\varphi(k)$ is fitted with the theoretical Nasmyth spectrum $\varphi_N(k)$ and extrapolated to high and low wavenumbers for each segment. $\varphi_N(k)$ is given (Bluteau et al., 2016) by

$$\varphi_N(k) = \frac{8.05(k/k_\nu)^{1/3}}{1+(20.6k/k_\nu)^{3.715}}, \tag{9}$$

where $k_\nu = (\in/\nu^3)^{1/4}$ is Kolmogorov wavenumber. Thus, ϵ is then obtained by integrating the fitted Nasmyth spectrum over the full extrapolated wavenumber range (Moum et al., 1995).

2.4 Determination of the mixed layer depth

The mixed layer has a relatively homogeneous distribution of temperature, salinity, and density, resulting from turbulent mixing driven by the surface forcing. Its thickness, called as the mixed layer depth (MLD), is a basic scale in the study of the turbulent energy budget within the mixed layer. The threshold method, which is based on the changes in temperature and density or in their gradients, is a simple and extensively employed method to identify the MLD (Brainerd and Gregg, 1995; de Boyer Montégut et al., 2004). However, this method is somewhat subjective and not suitable for different regions and seasons (Brainerd and Gregg, 1995; de Boyer Montégut et al., 2004; Holte and Talley, 2009). Whereafter, some relatively objective methods were proposed, such as the curvature method (Lorbacher et al., 2006), split-merge method (Thomson and Fine, 2003), maximum angle method (Chu and Fan, 2011), and relative variance method (Huang et al., 2018). Huang et al. (2018) compared these objective methods and found that they have their own advantages in different regions and environments. In this study, the MLD is determined from the density profiles with the maximum angle method, which is based on the maximum angle between two depth vectors of the profile (de Boyer Montégut et al., 2004; Chu and Fan, 2011).

2.5 ϵ/J_b^0 in the mixed layer

The input of surface energy makes the upper mixed layer be approximately vertically uniform layer. However, the energy flux varies with increasing depth as it transports downwards, resulting in a variable vertical structure of turbulence in the mixed layer. Based on the energy budget, the TKE dissipation rate ϵ is commonly used to represent turbulence in the mixed layer. Generally, the vertical structure of the nondimensionalized TKE dissipation rate, ϵ/J_b^0 , versus nondimensionalized depth, z/D, has been widely investigated in the previous literature, where z is depth and D is the thickness of the mixed layer. This normalization method for ϵ basically requires that data be available at night, i.e., $J_b^0 > 0$, which is favorable for convective mixing in the mixed layer. For example, Shay and Gregg (1986) performed a statistical analysis of ϵ/J_b^0 using microstructure data collected in the Bahamas and the Gulf Stream warm core ring. They found that in the uppermost layer (5–10 m), the TKE dissipation rate ϵ was exceptionally high. This thin layer with enhanced ϵ was thought to be generated mainly by wind forcing and/or surface wave breaking. Below this thin layer, ϵ was nearly uniform in the mixed layer, with an average ϵ/J_b^0 of 0.61 in the Bahamas and 0.72 in the Gulf Stream warm core ring. Lombardo and Gregg (1989) carried out a mixed-layer dynamic experiment at (34°N, 127°W), located in the outer reaches of the California Current. They found that the average value of ϵ/J_b^0 in the mixed layer was 0.58. Anis and Moum (1994) analyzed a mixed-layer dataset collected in the Pacific Ocean in 1987. They found that ϵ/J_b^0 decreased in an almost linear fashion with increasing depth in the lower half of the mixed layer, with a slight increase at the base of the mixed layer (i.e., near z/D~1). In a recent study Esters et al. (2018) statistically analyzed the scaled ϵ in mixed layer and found ϵ/J_b^0 were scattered ($0.1 < \epsilon/J_b^0 < 100$) in five different surveyed sea areas. To address this inconsistency of ϵ/J_b^0 and explore the similarity of ϵ in the mixed layer, in this study we try to propose a new characteristic parameter, TKE dissipation rate at the mixed-layer base ϵ_D, to normalize ϵ.

2.6 Data description

The observational dataset was acquired during an international field campaign, called the Cooperative Indian Ocean Experiment on Intraseasonal Variability in the Year 2011 (CINDY2011). This field campaign was part of the Dynamics of the Madden-Julian Oscillation (DYNAMO) program. For detailed information on CINDY2011, please refer to Yoneyama et al. (2013). The present study used only the on-board data collected by the research vessel *MIRAI*, which was stationed at (8°S, 80.5°E) (shown with the star in Figure 1). This measurement covered two periods, 30 September to 24 October and 30 October to 28 November 2011.

The oceanic surface meteorological data collected on *MIRAI* included air and sea surface temperatures, wind speed at 10 m height, evaporation, precipitation, and solar radiation, and had a temporal resolution of 10 minutes. The wind profile was measured by a 915-MHz wind profiler (Yoneyama et al., 2013). Using the method described in the last section, the time series of wind stress τ_0 and buoyancy flux J_b^0 are shown in Figures 2A, B. It is found that J_b^0 is positive and nearly constant at night except for the time of sunset and sunrise. During daytime, the heat gain is dominated by short-wave radiation, and J_b^0 varies sharply, increasing from zero after sunrise, reaching its maximum value near noon, and returning to zero again before sunset.

Conventional hydrographic instruments, including conductivity-temperature-depth (CTD) and the Lowered Acoustic Doppler Current Profiler (LADCP), were deployed down to 500 m every 3 h (Figures 2C–F). These data were postprocessed into vertical bins of 1 m for the CTD and 2 m for the LADCP. The base of the mixed layer is marked as the white curve in Figures 2E–G. It is of the order of magnitude of tens of meters in depth and shows obvious diurnal variations. This diurnal variation of MLD is one of the most important features of mixed layer. During the nighttime, cooling increases density of the surface water, which sinks and causes rapid turbulent convection, resulting in the increase of the MLD. While during the daytime, surface heating causes restratification and suppresses the turbulent convection, resulting in the decrease of the MLD (Imberger, 1985).

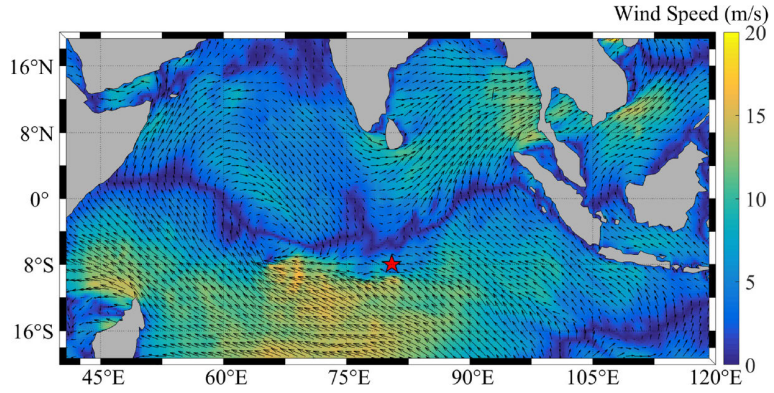

FIGURE 1
Map of the tropical Indian Ocean. The red star shows the fixed site where the dataset used in this study was collected. The contour and vector indicate the wind field at 10 m height above the sea surface on 30 September 2011 (i.e., the first day of the field campaign), which is from the ECMWF ERA5 reanalysis wind data at https://cds.climate.copernicus.eu/cdsapp#!/dataset/reanalysis-era5-pressure-levels?tab=overview.

After each cast of CTD/LADCP, two microstructure profiles were measured consecutively by a Turbulence Ocean Microstructure Acquisition Profiler (TurboMAP) for the upper 300 m. To avoid contamination by vessel-generated motion, the microstructure data for the uppermost 10 m were discarded in post-processing analysis. Briefly, the observed shear spectra were fitted with the Nasmyth spectrum for each 2-m vertical segment, and then ϵ was obtained by integrating the fitted spectrum over the full extrapolated wavenumber range (Moum et al., 1995) [for further details of estimating ϵ, refer to Wolk et al. (2002)]. Figure 2G shows the time series of ϵ profiles.

Note, as shown in Figure 2F, that a water-mass intrusion with low temperature and low salinity occurred in the upper layer (0–100 m) from DoY (day of year) 315 (11 November 2011, see the dashed line in Figure 2F), which was also described by Seiki et al. (2013). This lateral dominant process was beyond the scope of this study, and all the datasets after that day were excluded. Therefore, a total of 285 CTD/LADCP and 570 microstructure profiles were included in the final analysis. For consistency, the microstructure data were further averaged according to the CTD profile time stamps. This complete, high-resolution dataset for both atmospheric and oceanic states made it possible to quantitatively analyze the dynamics of the ocean mixed layer.

3 Results

3.1 ϵ scaled with the surface buoyancy flux, J_b^0

Although the previous studies show that the nondimensionalized TKE dissipation rate ϵ/J_b^0 does not reflect very good similarity structure in mixed layer, we still first followed and examined the previous literature to study ϵ/J_b^0 in the mixed layer during nighttime ($J_b^0 > 0$) for the present dataset. The dataset includes 183 original ϵ profiles overall. Each profile was divided into vertical bins with size $0.05z/D$. In each bin, the median, geometric-mean, and arithmetic-mean values and their corresponding 50% confidence intervals (i.e., the first and third quartiles) were calculated. Figure 3A shows ϵ/J_b^0 versus z/D using these three statistical averaging methods. The median and geometric-mean values were found to agree roughly with each other, but significantly differed from the arithmetic-mean values. This is because the median and geometric-mean values represent a typical value of the dataset, and are not shewed by a small proportion of extremely large ϵ in the mixed layer. Moreover, the arithmetic-mean values were more scattered than the other statistical average values. To quantitatively evaluate which statistic gave the best representation of the present dataset, a scatter index SI was defined as

$$SI = std\left(\frac{\epsilon}{J_b^0} - smooth\left(\frac{\epsilon}{J_b^0}, 5\right)\right), \tag{10}$$

where std denotes the standard deviation and $smooth$ denotes a low-pass filter with a moving average over five data points. SI was 0.058, 0.046, and 0.28 for the three statistical averages of median, geometric mean, and arithmetic mean values respectively. The SI values of the arithmetic mean were remarkably larger than those of the other averages. Such large values of SI may have been caused by individual outlier data points that could not be smoothed by the arithmetic mean method. For simplicity, median values were mainly used to represent the statistical average of the dataset.

Figure 3A shows that ϵ/J_b^0 sharply decreased with increasing z/D from the surface to depth $z/D \approx 0.5$. This result is consistent with those in previous studies (Shay and Gregg, 1986; Lombardo and Gregg, 1989). Below $z/D \approx 0.5$, the median and arithmetic mean

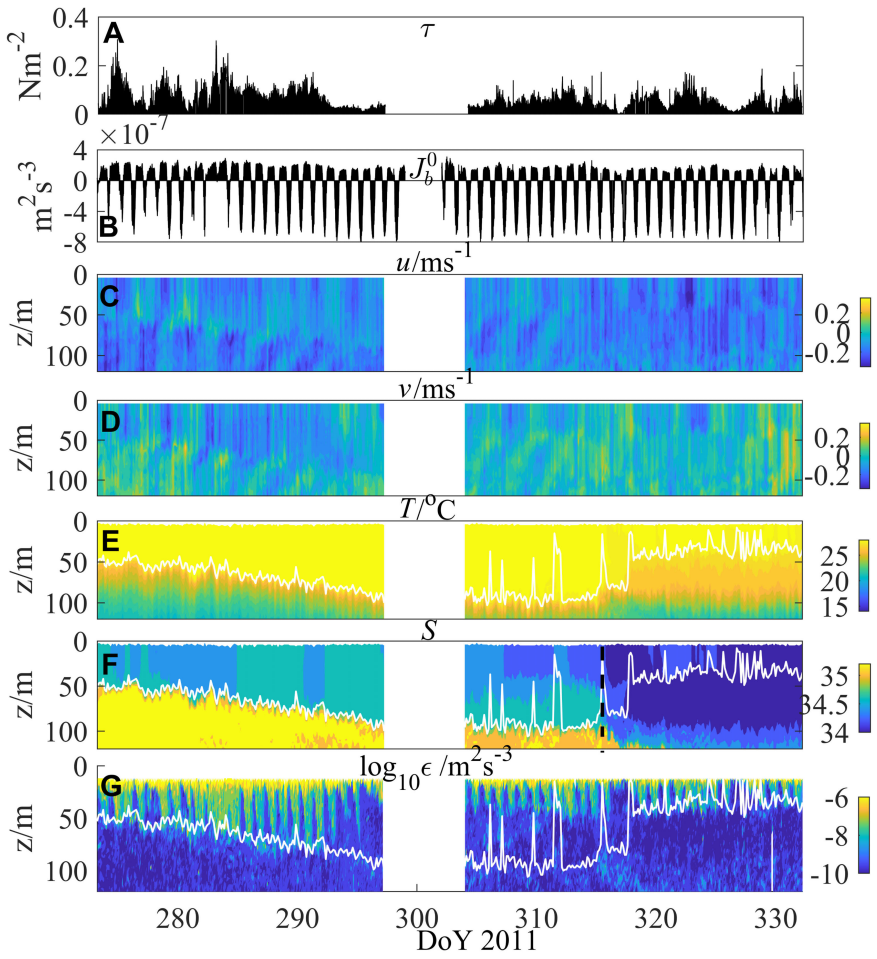

FIGURE 2
Time series of **(A)** wind stress, **(B)** surface buoyancy flux, **(C)** zonal current, **(D)** meridional current, **(E)** temperature, **(F)** salinity, and **(G)** TKE dissipation rate at the observation site. The white curves denote the base of the mixed layer. The black dashed line in **(F)** indicates that the data after DoY 315 (November 11) were not used due to the intrusion of a low-salinity water mass in the upper layer.

values of ϵ/J_b^0 were roughly uniform, with magnitudes of ~10^{-2} and 0.32, respectively. Shay and Gregg (1986) performed two experiments on convectively driven mixing and concluded that ϵ/J_b^0 slightly decreased with increasing z/D by no more than a factor of 3 in most of the lower part of the mixed layer, with an average value of 0.66. The arithmetic mean values of ϵ/J_b^0 in the lower half of the mixed layer in the present dataset were almost half those in the datasets of Shay and Gregg (1986), which implies that a larger fraction of the energy input from atmospheric forcing might have been dissipated in the upper part of the mixed layer.

Neglecting the influences of swells, surface wave breaking, and Langmuir cells, a classical length scale, called the Monin-Obukhov scale, was developed to compare the relative contributions of surface wind stress and buoyancy flux to turbulence in the mixed layer, as described (Monin and Yaglom, 1971; Grachev and Fairall, 1997) by

$$L_{MO} = -\frac{u_*^3}{\kappa J_b^0}, \tag{11}$$

where the numerator u_*^3 is proportional to the input of wind power. L_{MO} is negative in destabilizing conditions (during nighttime) and positive in stabilizing conditions (during daytime). $|L_{\mathrm{MO}}|$ represents a characteristic scale at which depth both processes, surface wind stress and buoyancy flux, have comparable importance in turbulence production. The mixed-layer depth D is generally greater than $|L_{\mathrm{MO}}|$. Wind stress dominates turbulence production in the depth range $0< z \ll |L_{\mathrm{MO}}|$, whereas buoyancy flux plays a dominant role in turbulence production in the range $|L_{\mathrm{MO}}| \ll z\ D$ (Lombardo and Gregg, 1989). Hence, the ratio $D/|L_{\mathrm{MO}}|$ can be considered as a stability parameter to characterize convective instability in the mixed layer (Shay and Gregg, 1986).

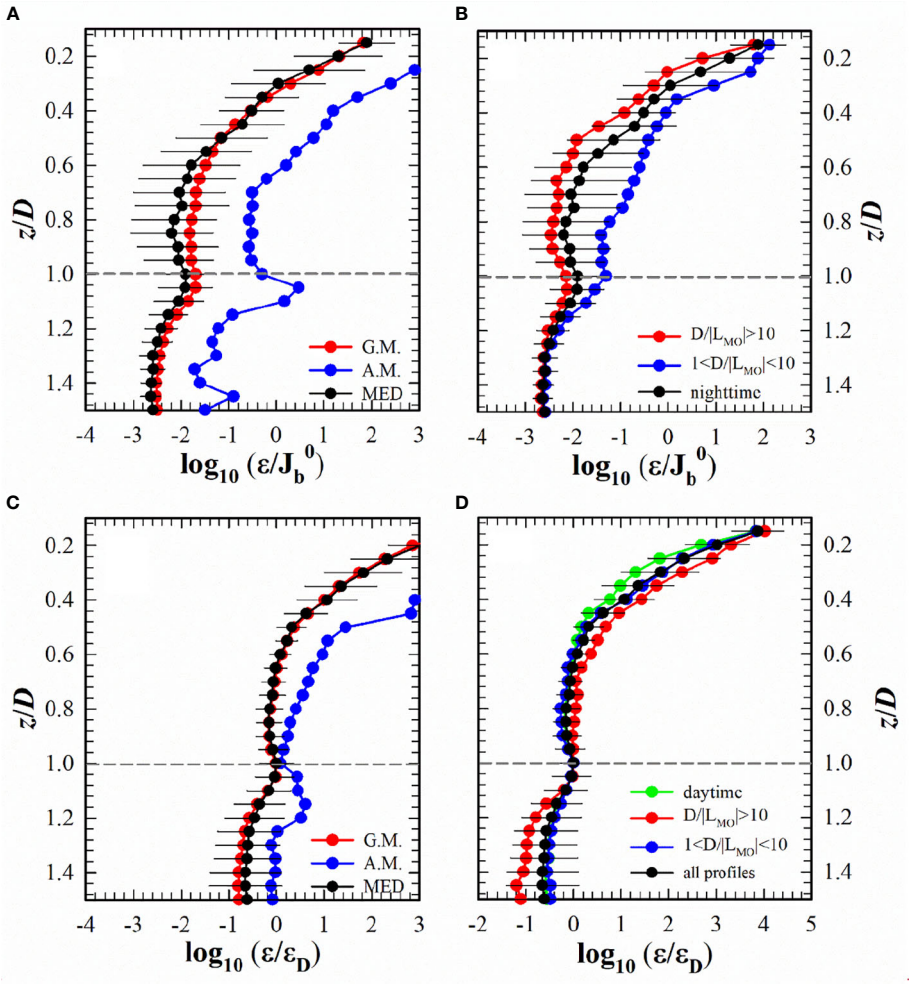

FIGURE 3
(A) ϵ/J_b^0 versus z/D in semi-log coordinates using different statistical methods, geometric-mean (G.M.), arithmetic-mean (A.M.), and median (MED), for all nighttime profiles. **(B)** Median ϵ/J_b^0 versus z/D for all nighttime profiles (black) and for nighttime profiles with $D/|L_{MO}| > 10$ (red) and $1< D/|L_{MO}|< 10$ (blue). **(C)** ϵ/ϵ_D versus z/D in semi-log coordinates using different statistical methods for all profiles. **(D)** Median ϵ/ϵ_D versus z/D for all profiles (black), daytime profiles (green), and nighttime profiles with $D/|L_{MO}| > 10$ (red) and $1< D/|L_{MO}|< 10$ (blue). The error bars, only draw representatively on one profile, denote the 50% confidence intervals. The vertical dashed lines in **(A, B)** denote ϵ/J_b^0=0.58 proposed in Lombardo and Gregg (1989). The horizontal dashed lines in **(A–D)** denote z = D.

Figure 3B shows the median profiles of ϵ/J_b^0 versus z/D for all 183 original nighttime profiles (black), of which 95 profiles satisfy $D/|L_{MO}| > 10$ (red) and 84 profiles satisfy $1< D/|L_{MO}|< 10$ (blue). The left four profiles satisfy $D/|L_{MO}|< 1$, which implies that turbulent mixing was dominated by wind stress, and were neglected in the present analysis. When $D/|L_{MO}| > 10$, ϵ/J_b^0 decreased rapidly until $z/D = 0.5$ and became roughly uniform below $z/D = 0.5$ in the mixed layer. This result confirms the argument of Lombardo and Gregg (1989), who proposed that surface buoyancy flux dominates turbulence in the mixed layer when $D >> |L_{MO}|$ and leads to a distinguishing feature of uniform ϵ with depth. When $1< D/|L_{MO}|< 10$, wind stress and surface buoyancy flux jointly dominate turbulence production in the mixed layer. In such conditions, ϵ/J_b^0 gradually decreases towards the lower part of the mixed layer. In general, the median all-nighttime profiles are well represented by the profiles under $\frac{D}{|L_{MO}|} > 10$, which implies that turbulence in the mixed layer was more likely dominated by buoyancy-induced convection during the observation period. Moreover, our data also supports that $D/|L_{MO}| \approx 10$ is a dynamical transition, which will be discussed in Section 5.

3.2 ϵ scaled with the dissipation rate at the mixed layer base, ϵ_D

As mentioned above, ϵ in the mixed layer has generally been scaled by J_b^0 to study its statistical characteristics. However, both surface wind stress and buoyancy flux might have made contributions to the turbulence of the mixed layer. Scaling ϵ by J_b^0 alone may lead to poor exhibition of its characteristic structure, especially in the case when wind stress dominates turbulent mixing. This flaw is indicated in Figure 3B, where the profiles of ϵ/J_b^0 change markedly as $D/|L_{\mathrm{MO}}|$ varies (the red and blue lines). Moreover, during the daytime, the surface buoyancy flux J_b^0 is negative, and it is usually trapped in the upper part of the mixed layer (Thompson et al., 2019). This is why ϵ/J_b^0, to the authors' knowledge, has rarely been used in the daytime in past studies. Hence, a more appropriate parameter is needed to characterize ϵ in the mixed layer.

Considering that the depth z is usually scaled by the mixed-layer depth D to study ϵ distributions in the mixed layer (Shay and Gregg, 1986; Lombardo and Gregg, 1989; Anis and Moum, 1994; Moum and Rippeth, 2009; Belcher et al., 2012), in this study we chose to use the TKE dissipation rate at depth D (i.e., the base of the mixed layer), ϵ_{D}, instead of J_b^0, as a parameter to scale ϵ. This choice has two main advantages. First, unlike J_b^0, which is one of the driving parameters, ϵ_{D} is expected to be a response parameter reflecting the combined contributions of surface wind stress, buoyancy flux, waves, and other processes. Secondly, the structural representation of ϵ is not limited to nighttime when using ϵ_{D} as the scaled parameter.

As in Figures 3A, C shows the three statistical-average profiles of $\epsilon/\epsilon_{\mathrm{D}}$. Again, as expected, the arithmetic mean profile significantly deviates from both the median and the geometric mean profiles, indicating that the median (or geometric mean) profile might be more appropriate for revealing the vertical distribution of ϵ in the mixed layer.

Figure 3D show the median profiles of $\epsilon/\epsilon_{\mathrm{D}}$ versus z/D for all 285 profiles (black), the 102 daytime profiles (green), and the 179 nighttime profiles, separated into 95 profiles satisfying $D/|L_{\mathrm{MO}}| >$ 10 (red) and 84 profiles satisfying $1< D/|L_{\mathrm{MO}}|< 10$ (blue). The four profiles demonstrate a very good similarity within the measurement scatter range. By contrast, as shown in Figure 3B, the three profiles of ϵ/J_b^0 show much different structures when $D/|L_{\mathrm{MO}}|$ is within different ranges. Besides, comparing the error bars in Figures 3B, D shows that $\epsilon/\epsilon_{\mathrm{D}}$ is much less scattered than ϵ/J_b^0. These results provide evidence that ϵ_{D} is a better candidate to characterize the intrinsic structure and similarity of ϵ in the mixed layer, regardless whether wind stress or surface buoyancy flux dominates turbulent mixing.

In addition, Figures 3B, D show a local maximum near the base of the mixed layer, and when $D/|L_{\mathrm{MO}}| > 10$, i.e., the mixed layer is convectively driven by surface buoyancy flux, the local peak is more pronounced than that when $1< D/|L_{\mathrm{MO}}|< 10$. This feature was also observed by Anis and Moum (1994) and was attributed to enhanced shear levels by entrainment at the base of the mixed layer.

4 Discussion: Parameterization of ϵ_{D}

It is known that the variation of ϵ usually depends on the strength of atmospheric forcing. Neglecting the influence of surface waves and assuming that atmospheric forcing can reach the mixed-layer base, it is expected that ϵ_{D} will be mainly affected by wind stress and surface buoyancy flux. However, how to quantitatively parameterize their contributions to ϵ_{D} remains unclear. This problem is the main concern of this subsection.

The parameterization study of ϵ_{D}, to the authors' knowledge, has not been reported so far. Previous investigations mainly focused on parameterization of bulk ϵ within the mixed layer with a linear combination of both the shear-driven dissipation rate ϵ_{s} and the surface buoyancy flux J_b^0 (Lombardo and Gregg, 1989; Tedford et al., 2014; Esters et al., 2017; Esters et al., 2018). For example, with the field-observation dataset for nighttime convective cooling of the Mixed Layer Dynamics Experiment in October 1986 at the site (34°N, 127°W), Lombardo and Gregg (1989) (hereafter denoted as LG89) suggested that ϵ over the depth range of $0.25D$ to $0.8D$ can be written as

$$\epsilon_{LG89} = 1.53\epsilon_s + 0.50J_b^0 \tag{12}$$

Esters et al. (2018) (hereafter denoted as Est18) analyzed five datasets collected from under-ocean conditions and fitted a linear formula for depths deeper than the Langmuir stability length as:

$$\epsilon_{Est18} = 0.57(\epsilon_s + J_b^0) \tag{13}$$

with different coefficients from ϵ_{LG89}. Assume that the linear combination for ϵ in the mixed layer can extend to depth D, that is,

$$\epsilon_D = A\epsilon_{s\_D} + BJ_b^0 \tag{14}$$

where A and B are undetermined constants and $\epsilon_{\mathrm{s\_D}}$ is ϵ_{s} at the mixed-layer base. When both sides of Eq. (14) are divided by $\epsilon_{\mathrm{s\_D}}$, the result is:

$$\frac{\epsilon_D}{\epsilon_{s\_D}} = A + B\frac{D}{|L_{MO}|} \tag{15}$$

Figure 4 shows $\frac{\epsilon_D}{\epsilon_{s\_D}}$ versus $\frac{D}{|L_{MO}|}$ for all nighttime profiles (gray squares). We divided all these data points into 14 bins with equal interval of $\log_{10}\frac{D}{|L_{MO}|}$, and the median value in each bin was obtained (black squares). When $D/|L_{MO}|< 12$, the median points slowly decreased with $D/|L_{MO}|$ from 1 to 0.1, but when $D/|L_{MO}| > 12$, they rapidly increased to 40. This unique transition at

$\frac{D}{|L_{MO}|} \approx 12$ was also found in Lombardo and Gregg (1989), above which the turbulence is mainly dominated by the buoyancy flux and below which the turbulence is dominated by both the wind-induced current shear and buoyancy flux.

We fitted these bin points (black squares) with Eq. (15), getting the coefficients A=-0.88 and B=0.032, as shown by the red line in Figure 4. The determination coefficient of this fitting is 0.03. It can only well represent the bin points when $\frac{D}{|L_{MO}|} > 20$ (When $D/|L_{MO}| < 20$ the fitted line is negative). For comparison, Eqs. (12) and (13) were also shown with gray line and gray dashed line, respectively. These two lines could also not describe the present observation data, especially for the data when $\frac{D}{|L_{MO}|} > 30$.

The linear combination for ϵ_D (Eq. (14) or (15)) could not well fit the present dataset to a certain extent, and much less does it reflect the transition character at $\frac{D}{|L_{MO}|} \approx 12$. Moreover, when both wind stress and surface buoyancy flux are simultaneously driving turbulence in the mixed layer, their contributions to ϵ may be intercoupling, which implies that the linear combination of ϵ_{s_D} and J_b^0 for ϵ_D may not be an appropriate choice. To consider nonlinear coupling from wind stress and surface buoyancy flux, an extra nonlinear term $\sqrt{\epsilon_{s\_D} J_b^0}$ was added to Eq. (14) to give

$$\epsilon_D = A\prime \epsilon_{s\_D} + B\prime J_b^0 + C\prime \sqrt{\epsilon_{s\_D} J_b^0} \tag{16}$$

where A' , B' , and C' are undetermined constants. Referring to the definition of L_{MO}, Eq. (16) can be equivalently written as:

$$\frac{\epsilon_D}{\epsilon_{s\_D}} A\prime + B\prime \frac{D}{|L_{MO}|} + C\prime \sqrt{\frac{D}{|L_{MO}|}} \tag{17}$$

The dataset was fitted using Eq. (17), shown as the red solid line in Figure 4, with constants $A' = 0.65$, $B' = 0.33$, and $C' = -0.26$. The determination coefficient is 0.31, much better than that of the linear fitting (Eq. (15)). Moreover, the fitting of Eq. (17) can well reflect the transition character of the data points at $\frac{D}{|L_{MO}|} \approx 12$. It is worth noting that the coefficient C' is negative, implying an opposite coupling effect of wind-induced current shear and buoyancy flux on turbulence kinetic energy dissipation rate. The mechanism behind this requires further research.

Although Eq. (17) could well fitted the present dataset collected from CINDY2011 in the tropical Indian Ocean, it is empirical and whether it can be extended to other sea areas needs further examination. However, this idea opens a window for further study of the interaction between the wind-driven stress and buoyancy fluxes in the mixed layer.

5 Summary

An observational dataset collected from CINDY2011 at the station (8°S, 80.5°E) in the tropical Indian Ocean was used to analyze statistically the vertical distribution of the TKE dissipation rate ϵ in the mixed layer. This dataset contains time series of high-resolution meteorological data, conventional hydrographic data, and turbulence microstructure data covering the whole mixed layer. The profiles of ϵ were statistically averaged using three methods. The arithmetic-mean method was significantly affected by individual outlier data and produced a more scattered ϵ profile. To examine the vertical distribution of ϵ in the mixed layer, ϵ was respectively scaled by the surface buoyancy flux J_b^0 and the TKE

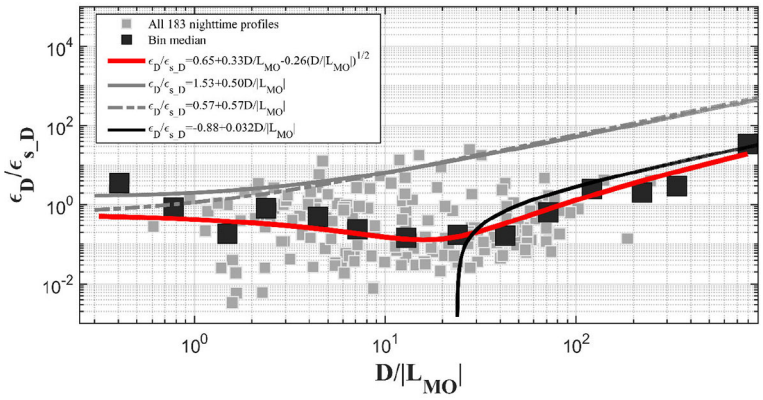

FIGURE 4
$\frac{\epsilon_D}{\epsilon_{s\_D}}$ versus $\frac{D}{|L_{MO}|}$ for all nighttime profiles (gray squares). The black squares denote the median values of 14 bins for all nighttime profiles, and they are fitted with Eqs. (15) and (17) as shown by the black and red solid lines, respectively. The gray line and gray dashed line denote the Eqs. (12) and (13), respectively.

dissipation rate at the mixed-layer base ϵ_D for comparison. When the parameter ϵ_D was used, the dissipation rate ϵ showed similar vertical distributions in the mixed layer under different dynamic conditions (Figure 3D). This result indicates that ϵ follows a universal vertical structure within the mixed layer with ϵ_D as an intrinsic parameter. The parameterization of ϵ_D on shear-driven dissipation rate ϵ_{s_D} and the surface buoyancy flux J_b^0 was further quantitatively explored. The comparison indicated that a linear combination $\frac{\epsilon_D}{\epsilon_{s\_D}} = 0.65 + 0.33\frac{D}{|L_{MO}|} - 0.26\sqrt{\frac{D}{|L_{MO}|}}$ could better describe the variation trend and transition features of $\frac{\epsilon_D}{\epsilon_{s\_D}}$ (Figure 4), in which the nonlinear term reflected the intercoupling characteristics between wind stress and buoyancy flux. The present study could be beneficial to our understanding of turbulence in the upper ocean boundary layer and might provide a reference for numerical modeling of the oceanic mixed layer.

Data availability statement

The original contributions presented in the study are included in the article/supplementary files. Further inquiries can be directed to the corresponding author.

Author contributions

SG and XC collected and analysed the field observation data and wrote the manuscript. SZ and YW provided advice and revised the manuscript. All authors contributed to the article and approved the submitted version.

Funding

This work was funded by National Key Research and Development Plan of China (2021YFC3101305, 2021YFC3101303), National Natural Science Foundation of China (91952106, 12172369), Southern Marine Science and Engineering Guangdong Laboratory (Guangzhou) (GML2019ZD0304, SMSEGL20SC01), and the research grants from State Key Laboratory of Tropical Oceanography (LTOZZ2001). The R/V *MIRAI* data were collected as part of the CINDY2011/DYNAMO project, which was sponsored by DOE, JAMSTEC, NASA, NOAA, NSF, and ONR. The CINDY2011 observational dataset used in this paper is available at https://www.jamstec.go.jp/cindy/obs/obs.html.

Conflict of interest

The authors declare that the research was conducted in the absence of any commercial or financial relationships that could be construed as a potential conflict of interest.

Publisher's note

All claims expressed in this article are solely those of the authors and do not necessarily represent those of their affiliated organizations, or those of the publisher, the editors and the reviewers. Any product that may be evaluated in this article, or claim that may be made by its manufacturer, is not guaranteed or endorsed by the publisher.

References

Anis, A., and Moum, J. N. (1994). Prescriptions for heat flux and entrainment rates in the upper ocean during convection. *J. Physs. Oceanogr.* 24 (10), 2142–2155. doi: 10.1175/1520-0485(1994)024<2142:PFHFAE>2.0.CO;2

Belcher, S. E., Grant, A. L. M., Hanley, K. E., Baylor, F-K, Van Roekel, L., Sullivan, P. P., et al. (2012). A global perspective on langmuir turbulence in the ocean surface boundary layer. *Geophys. Res. Lett.* 39 (18), L18605. doi: 10.1029/2012GL052932

Bluteau, C. E., Jones, N. L., and Ivey, G. (2016). Estimating turbulent dissipation from microstructure shear measurements using maximum likelihood spectral fitting over the inertial and viscous subranges. *J. Atmos. Oceanic. Technol.* 33, 713–722. doi: 10.1175/JTECH-D-15-0218.1

Brainerd, K. E., and Gregg, M. C. (1993). Diurnal restratification and turbulence in the oceanic surface mixed layer: 1. observations. *J. Geophys. Res-Oceans.* 98 (C12), 22645–22656. doi: 10.1029/93JC02297

Brainerd, K. E., and Gregg, M. C. (1995). Surface mixed and mixing layer depths. *Deep. Sea. Res.-PT. I.* 42 (9), 1521–1544. doi: 10.1016/0967-0637(95)00068-H

Callaghan, A. H., Ward, B., and Vialard, J. (2014). Influence of surface forcing on near-surface and mixing layer turbulence in the tropical Indian ocean. *Deep-Sea. Res. PT. I.* 94, 107–123. doi: 10.1016/j.dsr.2014.08.009

Chu, P. C., and Fan, C. (2011). Maximum angle method for determining mixed layer depth from seaglider data. *J. Oceanogr.* 67 (2), 219–230. doi: 10.1007/s10872-011-0019-2

D'Asaro, E. A. (2014). Turbulence in the upper-ocean mixed layer. *Annu. Rev. Mar. Sci.* 6, 101–115. doi: 10.1146/annurev-marine-010213-135138

de Boyer Montégut, C., Madec, G., Fischer, A. S., Lazar, A, and Iudicone, D. (2004). Mixed layer depth over the global ocean: An examination of profile data and a profile-based climatology. *J. Geophys. Res-Oceans.* 109 (C12), C12003. doi: 10.1029/2004JC002378

Edson, J. B., Jampana, V., Weller, R. A., Bigorre, S.P., Plueddemann, A.J., Fairall, C.W., et al. (2013). On the exchange of momentum over the open ocean. *J. Physs. Oceanogr.* 43 (8), 1589–1610. doi: 10.1175/JPO-D-12-0173.1

Esters, L., Breivik, Ø., Landwehr, S., Doeschate ten, A., Sutherland, G., Christensen, K.H., et al. (2018). Turbulence scaling comparisons in the ocean surface boundary layer. *J. Geophys. Res-Oceans.* 123 (3), 2172–2191. doi: 10.1002/2017JC013525

Esters, L., Landwehr, S., Sutherland, G., Bell, T.G., Christensen, K.H., Saltzman, E.S., et al. (2017). Parameterizing air-sea gas transfer velocity with dissipation. *J. Geophys. Res-Oceans.* 122 (4), 3041–3056. doi: 10.1002/2016JC012088

Evans, D. G., Lucas, N. S., Hemsley, V., Frajka-Williams, E., , A., Naveira Garabato, C., Martin, A., et al. (2018). Annual cycle of turbulent dissipation estimated from seagliders. *Geophys. Res. Lett.* 45 (19), 10,560–10,569. doi: 10.1029/2018GL079966

Fairall, C. W., Bradley, E. F., Hare, J. E., Grachev, A.A., and Edson, J.B.. (2003). Bulk parameterization of air–sea fluxes: Updates and verification for the COARE algorithm. *J. Climate* 16 (4), 571–591. doi: 10.1175/1520-0442(2003)016<0571:BPOASF>2.0.CO;2

Fairall, C. W., Bradley, E. F., Rogers, D. P., Edson, J.B., and Young, G.S.. (1996). Bulk parameterization of air-sea fluxes for tropical ocean-global atmosphere

coupled-ocean atmosphere response experiment. *J. Geophys. Res-Oceans.* 101 (C2), 3747–3764. doi: 10.1029/95JC03205

Ferrari, R., and Wunsch, C. (2009). Ocean circulation kinetic energy: Reservoirs, sources, and sinks. *Ann. Rev. Fluid. Mech.* 41, 253–282. doi: 10.1146/annurev.fluid.40.111406.102139

Gemmrich, J. R., and Farmer, D. M. (2004). Near-surface turbulence in the presence of breaking waves. *J. Physs. Oceanogr.* 34 (5), 1067–1086. doi: 10.1175/1520-0485(2004)034<1067:NTITPO>2.0.CO;2

Grachev, A. A., and Fairall, C. W. (1997). Dependence of the monin–obukhov stability parameter on the bulk Richardson number over the ocean. *J. Appl. Meteorol.* 36 (4), 406–414. doi: 10.1175/1520-0450(1997)036<0406:DOTMOS>2.0.CO;2

Holte, J., and Talley, L. (2009). A new algorithm for finding mixed layer depths with applications to argo data and subantarctic mode water formation. *J. Atmos. Ocean. Tech.* 26 (9), 1920–1939. doi: 10.1175/2009JTECHO543.1

Huang, P. Q., Lu, Y. Z., and Zhou, S. Q. (2018). An objective method for determining ocean mixed layer depth with applications to WOCE data. *J. Atmos. Ocean. Tech.* 35 (3), 441–458. doi: 10.1175/JTECH-D-17-0104.1

Imberger, J. (1985). The diurnal mixed layer 1. *Limnol. Oceanogr.* 30 (4), 737–770. doi: 10.4319/lo.1985.30.4.0737

Jones, I. S., and Toba, Y. (Eds.) (2001). *Wind stress over the ocean* (Cambridge, England, GB: Cambridge University Press).

Kantha, L. H., and Clayson, C. A. (2000). *Small scale processes in geophysical fluid flows* (San Francisco, California, USA: Elsevier).

Kostov, Y., Armour, K. C., and Marshall, J. (2014). Impact of the Atlantic meridional overturning circulation on ocean heat storage and transient climate change. *Geophys. Res. Lett.* 41 (6), 2108–2116. doi: 10.1002/2013GL058998

Lombardo, C. P., and Gregg, M. C. (1989). Similarity scaling of viscous and thermal dissipation in a convecting surface boundary layer. *J. Geophys. Res-Oceans.* 94 (C5), 6273–6284. doi: 10.1029/JC094iC05p06273

Lorbacher, K., Dommenget, D., Niiler, P. P., and Köhl, A.. (2006). Ocean mixed layer depth: A subsurface proxy of ocean-atmosphere variability. *J. Geophys. Res-Oceans.* 111 (C7), C07010. doi: 10.1029/2003JC002157

Lozovatsky, I., Figueroa, M., Roget, E., Fernando, H. J. S., and Shapovalov, S.. (2005). Observations and scaling of the upper mixed layer in the north Atlantic. *J. Geophys. Res-Oceans.* 110 (C5), C05013. doi: 10.1029/2004JC002708

Macdonald, A. M., and Wunsch, C. (1996). An estimate of global ocean circulation and heat fluxes. *Nature* 382 (6590), 436–439. doi: 10.1038/382436a0

Meredith, M., and Garabato, A. N. (Eds.) (2021). *Ocean mixing: Drivers, mechanisms and impacts* (London, England, GB, Elsevier).

Monin, A. S., and Yaglom, A. M. (1971). *Statistical fluid mechanics* Vol. Vol. 1 (Cambridge: MIT Press), 766–769.

Moulin, A. J., Moum, J. N., and Shroyer, E. L. (2018). Evolution of turbulence in the diurnal warm layer. *J. Physs. Oceanogr.* 48 (2), 383–396. doi: 10.1175/JPO-D-17-0170.1

Moum, J. N., Gregg, M. C., Lien, R. C., and Carr, M.E.. (1995). Comparison of turbulence kinetic energy dissipation rate estimates from two ocean microstructure profilers. *J. Atmos. Ocean. Tech.* 12 (2), 346–366. doi: 10.1175/1520-0426(1995)012<0346:COTKED>2.0.CO;2

Moum, J. N., and Rippeth, T. P. (2009). Do observations adequately resolve the natural variability of oceanic turbulence? *J. Mar. Syst.* 77 (4), 409–417. doi: 10.1016/j.jmarsys.2008.10.013

Oakey, N. S., and Elliott, J. A. (1982). Dissipation within the surface mixed layer. *J. Physs. Oceanogr.* 12 (2), 171–185. doi: 10.1175/1520-0485(1982)012<0171:DWTSML>2.0.CO;2

Pellichero, V., Sallée, J. B., Schmidtko, S., Roquet, F., and Charrassin, J.-B.. (2017). The ocean mixed layer under southern ocean sea-ice: Seasonal cycle and forcing. *J. Geophys. Res-Oceans.* 122 (2), 1608–1633. doi: 10.1002/2016JC011970

Qiu, C., Cui, Y., Ren, J., Wang, Q., Huo, D., Wu, J., et al. (2016). Characteristics of the surface mixed layer depths in the northern south China Sea in spring. *J. Oceanogr.* 72 (4), 567–576. doi: 10.1007/s10872-016-0351-7

Qiu, C., Huo, D., Liu, C., Cui, Y., Su, D., Wu, J., et al. (2019). Upper vertical structures and mixed layer depth in the shelf of the northern south China Sea. *Cont. Shelf. Res.* 174, 26–34. doi: 10.1016/j.csr.2019.01.004

Sabine, C. L., Feely, R. A., Gruber, N., Key, R.M., Lee, K., Bullister, J.L., et al. (2004). The oceanic sink for anthropogenic CO_2. *Science* 305 (5682), 367–371. doi: 10.1126/science.10974

Seiki, A., Katsumata, M., Horii, T., Hasegawa, T., Richards, K.J., Yoneyama, K., et al. (2013). Abrupt cooling associated with the oceanic rossby wave and lateral advection during CINDY2011. *J. Geophys. Res-Oceans.* 118 (10), 5523–5535. doi: 10.1002/jgrc.20381

Shay, T. J., and Gregg, M. C. (1986). Convectively driven turbulent mixing in the upper ocean. *J. Physs. Oceanogr.* 16 (11), 1777–1798. doi: 10.1175/1520-0485(1986)016<1777:CDTMIT>2.0.CO;2

Tedford, E. W., MacIntyre, S., Miller, S. D., and Czikowsky, M. J.. (2014). Similarity scaling of turbulence in a temperate lake during fall cooling. *J. Geophys. Res-Oceans.* 119 (8), 4689–4713. doi: 10.1002/2014JC010135

Thompson, E. J., Moum, J. N., Fairall, C. W., and Rutledge, S.A.. (2019). Wind limits on rain layers and diurnal warm layers. *J. Geophys. Res-Oceans.* 124 (2), 897–924. doi: 10.1029/2018JC014130

Thomson, R. E., and Fine, I. V. (2003). Estimating mixed layer depth from oceanic profile data. *J. Atmos. Ocean. Tech.* 20 (2), 319–329. doi: 10.1175/1520-0426(2003)020<0319:EMLDFO>2.0.CO;2

Thorpe, S. A. (2005). *The turbulent ocean* (Cambridge, England, GB, Cambridge University Press).

Wain, D. J., Lilly, J. M., Callaghan, A. H., Yashayaev, I., and Ward, B.. (2015). A breaking internal wave in the surface ocean boundary layer. *J. Geophys. Res-Oceans.* 120 (6), 4151–4161. doi: 10.1002/2014JC010416

Wolk, F., Yamazaki, H., Seuront, L., and Lueck, R.G.. (2002). A new free-fall profiler for measuring biophysical microstructure. *J. Atmos. Ocean. Tech.* 19 (5), 780–793. doi: 10.1175/1520-0426(2002)019<0780:ANFFPF>2.0.CO;2

Wunsch, C., and Ferrari, R. (2004). Vertical mixing, energy, and the general circulation of the oceans. *Ann. Rev. Fluid. Mech.* 36, 281–314. doi: 10.1146/annurev.fluid.36.050802.122121

Yoneyama, K., Zhang, C., and Long, C. N. (2013). Tracking pulses of the madden–Julian oscillation. *B. Am. Meteorol. Soc* 94 (12), 1871–1891. doi: 10.1175/BAMS-D-12-00157.1

Zhang, Y., and Wang, W. (2018). Convection: a neglected pathway for downward transfer of wind energy in the oceanic mixed layer. *J. Oceanol. Limnol.* 36 (4), 1189–1197. doi: 10.1007/s00343-018-7081-1

frontiers | Frontiers in Marine Science

TYPE Original Research
PUBLISHED 21 November 2022
DOI 10.3389/fmars.2022.1053964

OPEN ACCESS

EDITED BY
Shengqi Zhou,
South China Sea Institute of Oceanology (CAS), China

REVIEWED BY
Lei Zhou,
Shanghai Jiao Tong University, China
Xiaobiao Xu,
Florida State University, United States
Fei Wang,
Southern University of Science and Technology, China

*CORRESPONDENCE
Wei Wang
wei@ouc.edu.cn

SPECIALTY SECTION
This article was submitted to Physical Oceanography, a section of the journal Frontiers in Marine Science

RECEIVED 26 September 2022
ACCEPTED 07 November 2022
PUBLISHED 21 November 2022

CITATION
Zhang Y, Zhang Z and Wang W (2022) Rotating horizontal convection with meridional ridges.
Front. Mar. Sci. 9:1053964.
doi: 10.3389/fmars.2022.1053964

Rotating horizontal convection with meridional ridges

Yu Zhang, Zhengguang Zhang and Wei Wang*

Physical Oceanography Laboratory/Frontier Science Center for Deep Ocean Multispheres and Earth System (FDOMES), Ocean University of China and Qingdao National Laboratory for Marine Science and Technology, Qingdao, China

According to recent studies, the large-scale effect of bottom topography on the ocean overturning circulation can be considered as a result of bottom enhancement of turbulent mixing in the abyssal ocean. Here we show, using laboratory experiments of rotating horizontal convection, that even without spatial variation of mixing intensity, oceanic meridional ridges can strongly impact both the strength and the pattern of the overturning in some fundamental ways. For example, as suggested by experimental results, the existence of the mid-Atlantic ridge can lead to the formation of another deep jet, like the deep western boundary current (DWBC), along the ridge's eastern edge as a pathway for southward export of newly formed deep water. In response to this interior (mid-basin) jet and the associated isopycnal displacement, adiabatic flow structures may occur in upper and lower layers, including two opposing jets located respectively above and below the interior DWBC. Though unable to contribute to the overturning, they can probably affect transport along isopycnals. In the latitudinal band of the Antarctic Circumpolar Current without side boundary but with multiple ridges lying over the bottom, multiple interior DWBCs may develop preferentially along higher ridges, carrying the Antarctic Bottom Water into the northern latitudes. Moreover, the overturning cell or the strong jets can migrate vertically with the grow or decay of the ridge. Therefore, presumably strong variations of both ocean circulation and stratification may have occurred more than once during the past millions of years, as consequences of plate tectonic evolution, and have caused substantial changes of earth climate.

KEYWORDS

rotating, horizontal convection, meridional overturning circulation, meridional ridge, deep western boundary current

1 Introduction

The overturning circulation plays an important role in transporting and storing heat, freshwater, and carbon in the global ocean. Understanding what determines the structure and strength of this circulation is key to assessing the ocean's ability in regulating climate change. Over the past few decades, the influence of bottom topography on the

overturning has been gaining increasing interest, but most studies on the topic centers around the small-scale turbulent process and its topographic enhancement. In the current paper, we extend the discussion to the large-scale effects of topography. Our laboratory experiments of rotating horizontal convection suggest that even without spatial variation of mixing intensity meridional ridges alone can strongly affect both the strength and the three-dimensional structure of the overturning. Horizontal convection (hereinafter HC) is the name for flow resulting from buoyancy variation imposed along a horizontal boundary of a fluid (Stern, 1975). According to Sandström's theorem (Sandström, 1908), the persistent large-scale circulation of HC cannot exist without intense turbulent mixing in the deep ocean. Over a long period of time, this theorem was widely accepted until Rossby for the first time demonstrated a steady large-scale circulation in a rectangular non-rotating tank subject to differential heating applied along the bottom (Rossby, 1965). Since then, HC has been regarded as a simple model to study the overturning. Effects of various factors including earth rotation were investigated for a better match to the reality (Miller, 1968; Beardsley and Festa, 1972; Hignett et al., 1981; Rossby, 1998; Park and Whitehead, 1999; Coman et al., 2006; Hughes and Griffiths, 2008; Whitehead and Wang, 2008; Tailleux and Rouleau, 2010; Ilicak and Vallis, 2012; Stewart, 2012; Barkan et al., 2013; Wang et al., 2016). Nevertheless, considering apparent discrepancies between the reality and the idealized model, it remains a question of to what extent physical understanding achieved from HC studies can be applied to the real ocean.

Part of the answer lies in a recent paper by Zhang et al. (2016) about new laboratory experiments of rotating HC in a zonally closed annular gap that can be viewed as a 360°-wide basin. High-resolution three-dimensional measurements of both temperature and velocity field make possible an accurate analysis of the dynamical balance. Although some non-dimensional parameters are quite different from their oceanic values, experimental results show remarkable similarities to the real ocean including a strong deep western boundary current (DWBC) exporting newly formed water mass from the convecting region and weak zonal flow directed away from the western boundary. More importantly, the flow adjusts itself in such a way that in the deep ocean contours of large-scale potential vorticity (PV hereinafter), as mostly determined by stratification of the fluid, are meridionally aligned near the western boundary. The DWBC is therefore allowed to flow along PV contours with little dynamical constraint. According to the existing knowledge about the ocean circulation, the planetary β effect dominates the PV distribution and causes the formation of the western boundary jets, being viscous and flowing across PV contours. Compared with this classical view, the along-PV feature of the experimental DWBC is, at the first glance, surprising and doubtful. However, it is confirmed to be indeed the case for the North Atlantic basin by observational evidence. Although currently a satisfactory theory explaining the similarity between the experiments and the ocean is not available, the similarity itself gives us confidence in the applicability of the former.

We are thus motivated to further investigate issues of the overturning using lab experiments. Ocean topography is of particular interest because of topographic enhancement of abyssal turbulent mixing as suggested by increasingly-convincing observational evidence in the past few decades (Wunsch and Ferrari, 2004; Garrett and Kunze, 2007; Polzin et al., 1997; St. Laurent et al., 2012; Waterman et al., 2013; Waterhouse et al., 2014). More recently, a new paradigm has been proposed and suggests that the cross-density upwelling, by which the overturning cell is closed, occurs predominantly in the boundary layer along the bottom slope (Ferrari et al., 2016; McDougall and Ferrari, 2017; de Lavergne et al., 2017). Furthermore, knowledge about the impact of topography can help us understand how topographic changes induced by plate tectonic evolution have changed the ocean circulation and climate through the geological history.

Using lab experiments in an annular gap with partial-depth ridges, we gain new insights into the overturning and its relation to ocean ridges. Despite uniform distribution of intensity of diapycnal mixing, ocean ridges can affect the overturning in three main ways. First of all, the DWBC develops not only along the eastern side of the side boundary, but also along eastern sides of meridional ridges, thus leading to an interior pathway for deep or bottom water transport. Secondly, both above and below DWBCs (both along the side boundary and ridges), a meridional jet develops, flowing opposite to that in the middle. Both jets are adiabatic and geostrophic, with little contribution to the overturning but probably large impacts on isopycnal transport. Thirdly, following the grow or decay of ridges as occurred in the past millions of years, the overturning cell and DWBCs migrate in the vertical direction, causing substantial changes not only in the flow field but in the stratification of the deep ocean.

2 Materials and methods

2.1 Theoretical considerations

Several parameters are commonly considered relevant for HC and rotating HC (Hignett et al., 1981),

$$Rayleigh\ \ number:\ R_a = \frac{BL^3}{\upsilon\kappa}$$

$$Prandtl\ \ number:\ P_r = \frac{\upsilon}{\kappa}$$

$$Ekman\ \ number:\ E = \frac{\upsilon}{2\Omega L^2}$$

$$Aspect\ \ ratio:\ \sigma = \frac{H}{L} \tag{1}$$

Here B is the maximum buoyancy contrast imposed on the base of the annular gap, L is the characteristic horizontal length scale.

Keeping these parameters in mind, we begin with the linear Boussinesq equations for a rotating system at the steady state:

$$-fv = -\frac{1}{\rho_0}\frac{\partial p}{\partial x} + v\frac{\partial^2 u}{\partial z^2}$$

$$fu = -\frac{1}{\rho_0}\frac{\partial p}{\partial y} + v\frac{\partial^2 v}{\partial z^2}$$

$$0 = -\frac{1}{\rho_0}\frac{\partial p}{\partial z} + b$$

$$u\frac{\partial b}{\partial x} + v\frac{\partial b}{\partial y} + w\frac{\partial b}{\partial z} = \kappa\nabla^2 b$$

$$\frac{\partial u}{\partial x} + \frac{\partial v}{\partial y} + \frac{\partial w}{\partial z} = 0 \tag{2}$$

where b denotes buoyancy, f=2Ω is the Coriolis parameter of the system with the rotating axes pointing upward, and only vertical friction is considered. In the thin boundary layer along the bottom where the differential buoyancy forcing is applied, the gradient of buoyancy is dominated by its vertical component, hence the buoyancy equation can be simplified as

$$w\frac{\partial b}{\partial z} = \kappa\frac{\partial^2 b}{\partial z^2} \tag{3}$$

Cross differentiating horizontal momentum equations leads to great simplification of the above array of equations:

$$f^2\frac{\partial w}{\partial z} + v^2\frac{\partial^5 w}{\partial z^5} + v\nabla_h^2\frac{\partial b}{\partial z} = 0 \tag{4}$$

$$w\frac{\partial b}{\partial z} = \kappa\frac{\partial^2 b}{\partial z^2}, \tag{5}$$

where ∇_h is the del in horizontal. Dimensionalizing the system with the horizontal length scale, L, vertical length scale, δ, buoyancy scale, b, we obtain the scaling for w:

$$w \sim \frac{\kappa}{\delta} \tag{6}$$

Applying this scaling in non-dimensionalizing Eq.4 leads to

$$\left(\frac{f^2\delta^4}{v^2}\right)\frac{\partial w}{\partial z} + \frac{\partial^5 w}{\partial z^5} + \left(\frac{\delta^5 R_a}{L^5}\right)\frac{\partial b}{\partial z} = 0 \tag{7}$$

where w, z, and b are non-dimensional. Apparently in this equation describing the flow vorticity in the boundary layer, relative roles of stretching of the water column and the buoyancy forcing are measured respectively by two non-dimensional parameters in brackets. Equating the second parameter with one yields the well-known scaling law for the boundary layer thickness,

$$\delta \sim \frac{L}{R_a^{1/5}} \tag{8}$$

The first parameter is related to the ratio of two thickness,

$$\frac{f^2\delta^4}{v^2} = \left(\frac{\delta}{d}\right)^4 = Q^2, \tag{9}$$

where $d \equiv \sqrt{v/f}$ is the scaling of the Ekman layer thickness. Equation (9) is often written as the square of Q, a parameter widely considered by many to govern the rotating convection system (Hignett et al., 1981; Park and Whitehead, 1999; Barkan et al., 2013; Hussam et al., 2014; Sheard et al., 2016). We admit that regarding Eq. 7 the increase of Q from zero to finite or large value demonstrates the strengthening of rotation. However, its utility is limited by the fact that Eq. 7 as a differential equation itself does not encompass many other effects such as boundaries, which sometimes can be essential (Zhang et al., 2016), and topography, as will be discussed in the present study. It is actually the PV that is more essential in disclosing basic physics of the circulation, and according to Ertel's formula PV is defined as

$$q = \frac{(\omega + 2\boldsymbol{\Omega})}{\rho}\cdot\nabla\rho, \tag{10}$$

where ω+2Ω is the absolute vorticity with ω being the relative vorticity. By definition, the overturning stream function, $\psi(r,z)$, is the zonally as well as vertically integrated quantity of the meridional velocity,

$$\psi(r,z) = \int_z^H \bar{v}(r,z)dz \tag{11}$$

where $\bar{v}(r,z)$ is the zonally integrated meridional velocity. How the existence of a side boundary changes the overturning strength can be understood from Eq. 2, the momentum equation for the zonal velocity. Integrating Eq. 2 along a given latitude of a zonally periodic domain, the term of pressure gradient force $\frac{\partial p}{\partial x}$ makes no contribution, and all the meridional component of the flow cannot exist without friction. Nevertheless, in the presence of a meridional wall, a net pressure difference remains after zonal integration, balancing the Coriolis force to support a geostrophic component of the flow, and therefore enhancing the strength of the overturning circulation.

2.2 Apparatus and experimental configuration

2.2.1 Apparatus

We applied the differential buoyancy forcing at the bottom of an annular gap by maintaining a radially varying distribution

of temperature. The annular gap, bounded by two coaxial Plexiglas cylinders with heights of 154 mm, was filled with ethylene glycol to a depth of H = 120 mm (Figure 1A). At 20°C, it has density ρ_0=1115 kg/m^3, thermal expansion coefficient α=5.7×10^{-4} K^{-1}, kinematic viscosity υ=14.4 × 10^{-6} m^2/s, thermal diffusivity κ=0.9 ×10^{-7} m^2/s, thermal conductivity κ_c=0.258 W/m/K, and heat capacity C_p=2.49×10^3 J/kg/K (see Table 1). The inner cylinder is a clear one with the outer radius a = 15 mm. The outer cylinder has inner radius b = 180 mm and thickness 2 mm. Both cylinders were secured to a d = 10 mm thick copper plate, which was heated at the centre and cooled near its outer edge by recirculating water through two circular channels cut inward of the copper plate from below. Water circulating in the central channel was pumped out of a hot circulator bath with the target temperature T_h ; while that in the outer channel was from a cold bath with temperature T_c . The two circulators used were Thermo Scientific EZ COOL 80, powerful enough to maintain temperature to the target value with an accuracy of ±0.1 K. Thermal conduction through the metal plate established a smooth conductive transition between the heating and cooling regions, leading to a radial temperature profile. Similar methods of maintaining a temperature distribution along the boundary have been adopted by many laboratory studies (Hignett et al., 1981; Pedlosky et al., 1997; Whitehead and Pedlosky, 2000; Mullarney et al., 2004). In our experiments, the heat flux through the copper base is much greater than that through the fluid, so the base temperature, T_b , was able to be decoupled from the fluid motion, remaining axisymmetric in space as well as stable in time with small perturbations on the order of $O(10^{-2})$ K in the equilibrium state. It also decreases logarithmically with r at the lowest order because of the near constancy of the radial heat flux through the base. With axisymmetric base temperatures, none of our experiments showed vulnerability to instabilities, which, as suggested by several recent studies, can be potentially incited with zonal perturbations of boundary conditions (Winters and Barkan, 2013; Barkan et al., 2013; Sheard et al., 2016).

The lid of the tank was made of 25 mm thick Plexiglas, rested on the four sidewalls and in no direct contact with the fluid below. An inner lid made of 2 mm thick Plexiglas was placed on the top of the fluid, providing the solid top boundary condition mimicking that of the ocean bottom.

To reduce as much as possible the heat exchange with the environment, the cylinders with the copper base was snugly contained in a tank made of Plexiglas with a thickness of 15 mm. Immediately adjacent to its four sidewalls, the tank was further encased with double-walled glass. A high vacuum of 2×10^{-7} bar was maintained in the small gap with a thickness of 0.25 mm

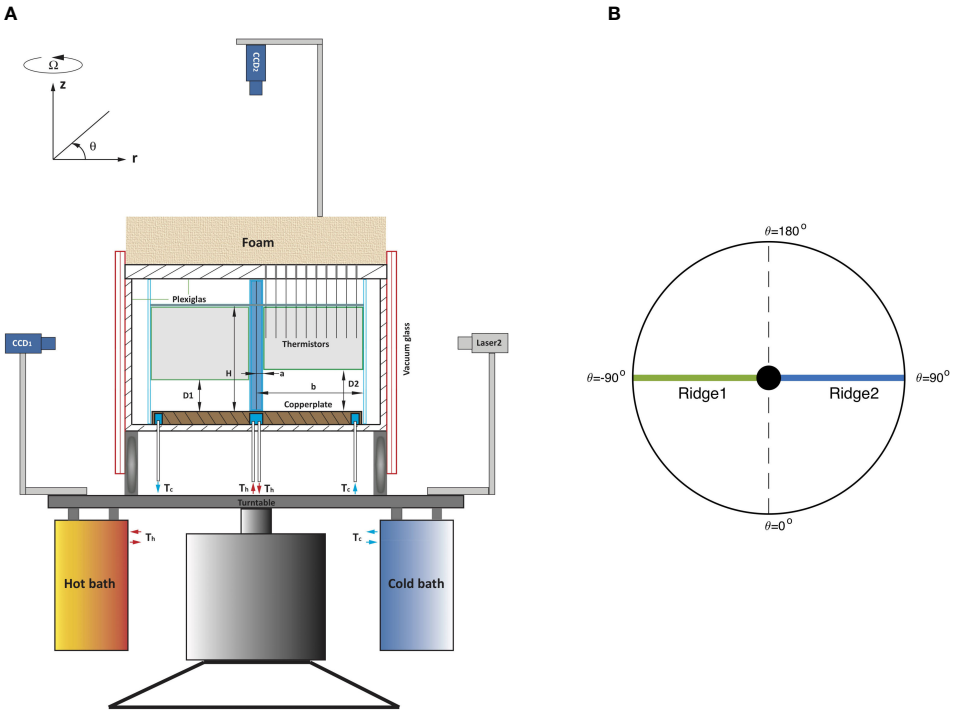

FIGURE 1
(A) A schematic view of the experimental apparatus. The working fluid was contained in the open region bounded by two thin-walled cylindrical tubes. The fluid was heated and cooled at its lower boundary by two baths as described in the text. **(B)** A schematic top view of the annulus with two ridges.

TABLE 1 Notation and parameter values.

Name	Definition
a	outer radius of the inner cylinder (15 mm)
b	inner radius of the outer cylinder (180 mm)
H	depth of the working fluid (120 mm)
r	radial distance
z	height
θ	polar angle
ρ	density
T	temperature
ρ_0	density at 20°C (1115 kg/m^3)
α	coefficient of thermal expansion (5.7×10^{-4}/K)
υ	kinematic viscosity (14.4×10^{-6} m^2/s)
κ	thermal diffusivity (0.9×10^{-7} m^2/s)
κ_c	thermal conductivity (0.258 W/m/K)
C_p	heat capacity (2.49×10^3 J/kg/K)
Ω	rotation rate of the turntable
T_c	temperature of the cold bath
T_h	temperature of the warm bath
ΔT	maximum imposed temperature difference on the base
ω	relative vorticity
f	Coriolis parameter
β	meridional gradient of Coriolis parameter

between its inner and outer walls. In addition, the tank was further covered with 60 mm thick rubber foam. All these measures helped to keep good insulation of the apparatus; the heat loss through the enclosure boundaries is negligible compared with that through the fluid.

On the lids and along different rays passing through the axial central line of the inner cylinder, there were arrays of holes that had a diameter of 3 mm and were separated 10 mm apart. Through these holes, thermistor probes were traversed vertically, measuring temperature with an accuracy of about ±0.01 K. The upper ends of the probes were attached to a horizontal rack, which could be not only moved vertically but also turned azimuthally to measure temperatures at different depths and along different radial directions.

Velocities of the fluid were measured with two sets of PIV (particle image velocimetry) systems, one for velocity measurement on the horizontal plane (Laser2 and CCD2 in Figure 1A) and the other for the vertical plane (CCD1 and Laser1 which was not shown in Figure 1A). Each PIV set consisted of a semiconductor laser with a power of 2 W at a wavelength of 532 nm and a digital CCD camera with a spatial resolution of 3296 × 2472 pixels for horizontal and 1920 × 1080 pixels for vertical respectively. Lasers with necessary optical components were used to produce a green light sheet with a thickness of 3 mm. The working fluid was seeded with silver-coated hollow glass spheres with a diameter of 0.01 mm. These particles that traverse the light sheet are nearly neutrally buoyant and could suspend in the fluid for over 200 hr. CCD cameras were used to acquire images, following which each pair of images could be translated into a velocity vector field. Motorized linear stages were used to traverse both lasers and cameras so that the velocity fields on horizontal/vertical planes could be measured as desired.

The tank containing the working fluid was levelled and centred on a 110 cm×110 cm turntable, whose rotation rate Ω could be changed smoothly between 3 and 30 rpm with an accuracy of 0.05%. Also mounted on the table were equipment for temperature and velocity measurements including the thermistor rack and the PIV system.

2.2.2 Procedure and measurements

Since the main focus of the current study is the effects of meridional ridges with rotation, we decided to have experiments with the same parameter settings (Ω = 10 rpm, ΔT = 6°C), but different geometries. Under such configurations, those non-dimensional parameters discussed in Section 2.1 have constant values: R_a=1.2×10^8 , Pr = 160, and $Q \approx 2.3$. As listed in Table 2, the experiments performed and investigated are divided into two sets, a single-ridged set and a two-ridged set. In the first set, a partial-depth meridional ridge with various vertical lengths was attached to the inner cylinder extending downward from the top lid with distance to the bottom denoted as D_1 (Figure 1A for side view and Figure 1B for top view). In the second set, two meridional ridges (180° apart, with distances to the bottom denoted respectively as D_1 and D_2 were installed.

A cylindrical polar coordinate system (r,θ,z) was used in analyzing results. The system has the origin located at the centre

TABLE 2 Experimental data and computed values for the non-dimensional parameters. D_1 and D_2 denote respectively the depth of the first (RidgeL) and the second ridge (RidgeR), as illustrated in Figure 2.

Name	D_1 [mm]	D_2 [mm]
ExpOPEN	120	120
ExpR0	0	120
ExpR30	30	120
ExpR50	50	120
ExpR70	70	120
ExpR30R0	30	0
ExpR50R0	50	0
ExpR70R0	70	0
ExpR50R30	50	30
ExpR50R40	50	40
ExpR50R50	50	50
ExpR50R60	50	60
ExpR50R70	50	70

The 'depth' of the ridge is defined as the distance from the ridge's lower edge to the bottom. The parameter R_0 is the Rossby number, defined as $R_0 = \frac{U}{2\Omega L}$ (Pedlosky 1987), is less than 10^{-3} in all experiments. Values of parameters are rpm] and ΔT=6°C.

of the copper plate, the radial direction directed outwards from the origin, the azimuthal direction directed anti-clockwise when viewed from above and the polar axis directed upward from the base. For convenience, we sometimes used "zonal" and "meridional" to refer to azimuthal and radial directions.

Three-dimensional distribution of horizontal velocity and temperature were measured for all experiments. For velocity measurement, the horizontal light sheet created by Laser2 was traversed downward from the top to the bottom of the fluid and stopped every 2.5 mm for a period of 5 minutes. During this period, 1201 images were taken by CCD2 at a sampling rate of 4 Hz, yielding 1200 instantaneous velocity fields.

For temperature measurements, 36 radial sections were taken sequentially in 10° increments of the polar angle. For each section, thermistor probes were traversed downward through holes in the lid, and stopped every 2.5 mm. At each depth, temperatures were measured at 16 equally spaced radial locations between r = 25 mm and r = 175 mm in a period of 20 seconds and at a sampling rate of 0.5 Hz.

All experiments were carried out for long enough time to ensure that the quasi-equilibrium state had been achieved, after which measurements were made for analysis.

3 Results

Under the current configuration where a radially-decreasing temperature field is prescribed along the lower boundary, the tank can be viewed as an upside-down ocean with its "abyss" being close to the top lid and the "surface" adjacent to the bottom of the tank (copper plate). The "north-pole" of the experimental ocean, where strong convection takes place nearby, is at the centre of the annulus. The clockwise direction (top view) around the annulus is also referred to as "west" in following discussions. The isothermal surfaces of the experimental ocean are parallel with isopycnal surfaces since the fluid density is only dependent on temperature that is variable.

For a no-ridge case (ExpOPEN), the overturning cell is characterized by a northward (inward) flow in the bottom boundary layer feeding deep convection (the near bottom part of the thick green line with negative value in Figure 2) and an interior (outward) flow away from the deep convection region towards the cooling end. An important result of Zhang et al. (2016) is the existence of two distinct types of the interior flow in association with two contrasting potential vorticity (PV) distributions in presence of different geometries. In a zonally open annular gap, like the flat bottomed Antarctic Circumpolar Current (ACC) region, the absence of meridional boundaries makes impossible the existence of geostrophic meridional flow, and induces axisymmetric distribution of both temperature (density) and PV that vary only in the meridional (radial) direction. As constrained by the law of PV conservation, the meridional component of the flow, axisymmetric as well, can only be supported by non-conservative processes. However, when the annular gap was changed into a closed 360°-wide basin with a full-depth radial ridge acting as side boundaries (ExpR0), the flow field adjusts itself by sloping isothermal (isopycnal) surfaces against the ridge and hence aligning PV contours along the "western" boundary. A relatively strong,

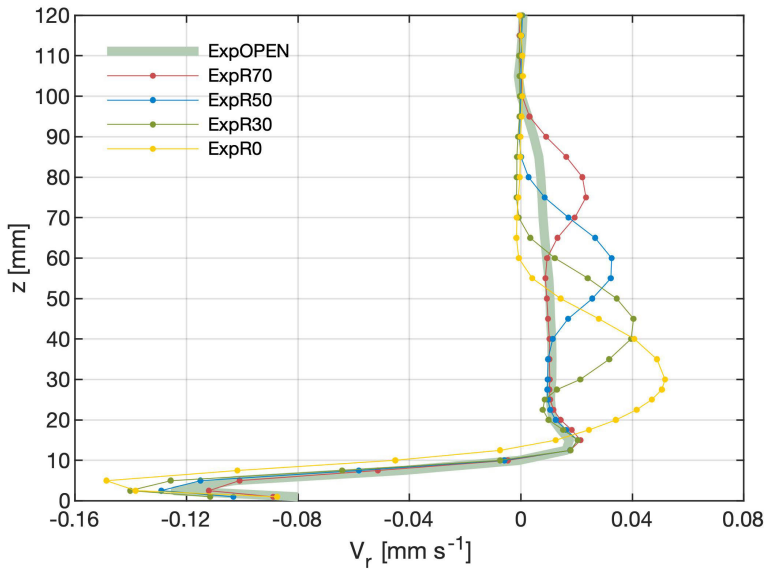

FIGURE 2
Vertical distribution of the zonally-averaged meridional velocity [mm/s] at r = 60 mm in single-ridged cases with various depth D_1.

geostrophic jet is therefore allowed by the law of PV; it transports newly-formed water away from the inner cylinder (outward or southward), and the strength of the MOC is much greater than that in the no-ridge case. Being analogous to the oceanic deep western boundary current (DWBC), this experimental interior jet is also referred to as DWBC in following discussions.

The above result revealed the significance of PV and meanwhile drew attention to the question of what eternally determines its distribution, since PV is not an independent variable known a prior but a consequence of intrinsic physics. Besides geometry, we speculate that topography, particularly meridional ridges may also be capable of exerting strong impacts at the large scale, as once suggested by an idealized modelling study of the meridional overturning circulation (MOC) (Toggweiler and Bjornsson, 2000). To verify this conjecture, we used partial-depth ridges that were attached to the top lid with a gap from the bottom to mimic ocean ridges, and carried out a series of rotating HC experiments.

3.1 Effects of a single ridge

3.1.1 The height and the strength of the MOC cell

For a meridional ridge with non-zero depth D_1, defined as the distance from the ridge to the bottom of the tank, the whole domain is divided in the vertical into two sub-regions: a zonally open one below the ridge and a zonally closed one above. The lower region is geometrically similar to an open channel like ACC, whereas the upper region is a basin.

In all single partial-ridge cases, the zonally integrated meridional flow, especially that in the interior above the bottom boundary layer, shows similarly contrasting features in the two sub-regions. In the open region, the meridional flow is ageostrophic, weak and spanning a wide vertical range, as in the axisymmetric, no-ridge case (ExpOPEN in Figure 2). In the closed region, the partial-depth ridge still acts as side boundaries, though only for the upper part of the water column. By supporting zonal pressure difference across the basin, it enables a concentrated jet structure like DWBC in the full-depth ridge case (ExpR0 in Figure 2).

As the ridge has its depth increased from zero (ExpR0) to leave a larger gap below, the vertical expanse of the open region is enlarged whereas that of the closed region is decreased. Correspondingly, the ageostrophic meridional flow expands in the vertical while the geostrophic jet migrates upward with the ridge and meanwhile diminishes in both vertical range and the strength. Taking ExpOPEN and ExpR0 as the two limiting cases, results of partial-ridge cases reveal a smooth transition in between. The MOC cell is at the lowest level with the largest strength in the full-depth ridge case (ExpR0), and declines linearly with D_1 (Figure 3).

The tendency of the MOC cell, particularly the DWBC, to "seek" the ridge has strong implications for the real ocean. First of all, we expect the existence of DWBC not only along the western boundary, but also along the mid-ocean ridges. Secondly, through the entire geological history characterized by complicated seafloor evolution, the DWBC probably has migrated up- or downward following the grow or decay of ocean ridges, which presumably has contributed to substantial changes in both ocean and climate.

3.1.2 The three-jet structure related to DWBC

The outward DWBC is remarkable on the curve of the zonally integrated meridional transport or the MOC (Figure 2), but it is not the only prominent feature in the three-dimensional flow field. In the case of a full-depth ridge (ExpR0), there is another reversing jet, though much weaker compared with the DWBC, along the western boundary above the DWBC (Figure 4A). Apparently this second jet transfers water inward but does not have remarkable effects on the overturning (thin green line in Figure 2). This fact suggests that the jet is part of a horizontal gyre that is dominantly adiabatic: what is transported inward within the thin jet along the boundary is almost all returned along the same isopycnal surface by much weaker and broader outward flow away from the boundary. The explanation for this jet is as follows. In association with the DWBC, the isopycnal surfaces above and below are slanted respectively up- and downward, forming a bulge-like structure along the boundary where PV is particularly low (Figure 5). This is a structure co-generated by the thermal forcing and the ridge. It in turn pushes isopycnals further up or down in the water column in opposite directions, and the weak jet above the DWBC is a consequence of slanting isopycnals at that level. Hence, this reversing jet is not independent but an accompanying feature of isopycnal structures related to DWBC, and is adiabatic in nature. By the same token, the isopycnals below the DWBC are pushed downward, leading to another reversing jet which, though embedded within the bottom boundary layer, is still noticeable in Figure 4A.

When the ridge is lifted upward well above the bottom boundary layer, the reversing jet above the DWBC remains more or less the same as that in the full-depth ridge case. However, the one below the DWBC, is enlarged substantially in both size and magnitude, extending all the way from the lower edge of the ridge to the bottom boundary layer (Figure 4B). At the first glance, this strong reversing jet is puzzling since it appears in the open region. However, considering the mechanism behind the reversing jet above the DWBC, the formation of this lower one can be understood in the similar way.

This three-jet structure consisting of the DWBC sandwiched between two reversing adiabatic jets can be seen more clearly in the vector plots of ExpR50 (Figure 6).

At z = 65 mm (Figure 6C) where the domain is closed, the horizontal circulation is anti-clockwise (top view) within the

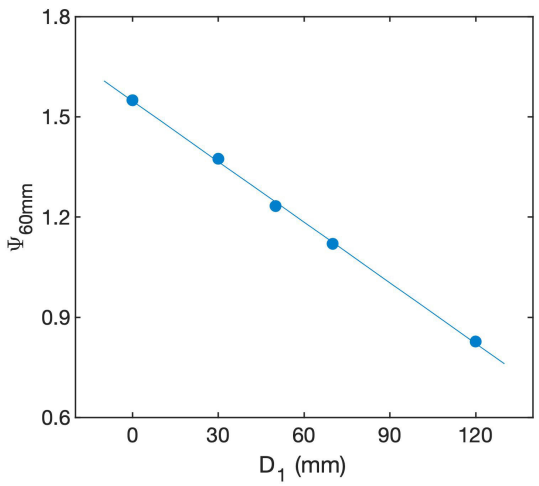

FIGURE 3
Variation of MOC strength at r = 60 mm in single-ridged cases with various ridge depth D_1.

basin. From the "northeastern" corner, the newly formed water flows westward around the inner cylinder, southward along the ridge as the DWBC, and then turns eastward along the exterior rim. The flow magnitude progressively weakens, indicating the existence of a strong diapycnal or diabatic component.

Above the DWBC at z =95 mm (Figure 6D), the domain is also closed and the basin-wide circulation is in the opposite direction to that below, characterized with another noticeable inward jet along the ridge that also can be seen in Figure 4B.

Below the ridge at z = 30 mm where the domain is open (Figure 6B), water parcels flow clockwise around the inner cylinder; as it approaches the longitudes of the partial-depth ridge, it first slowly turns to the south and then makes a sharp turn back to the north right below the ridge, corresponding to the lower reversing jet in Figure 4B. Along the streamlines, the amplitude of the horizontal flow does not change very much, consistent with the adiabatic nature of the flow at this level.

Further down to the upper edge of the bottom boundary layer at z =15 mm (Figure 6A), the flow becomes anti-clockwise around the inner cylinder, same as that in the boundary layer.

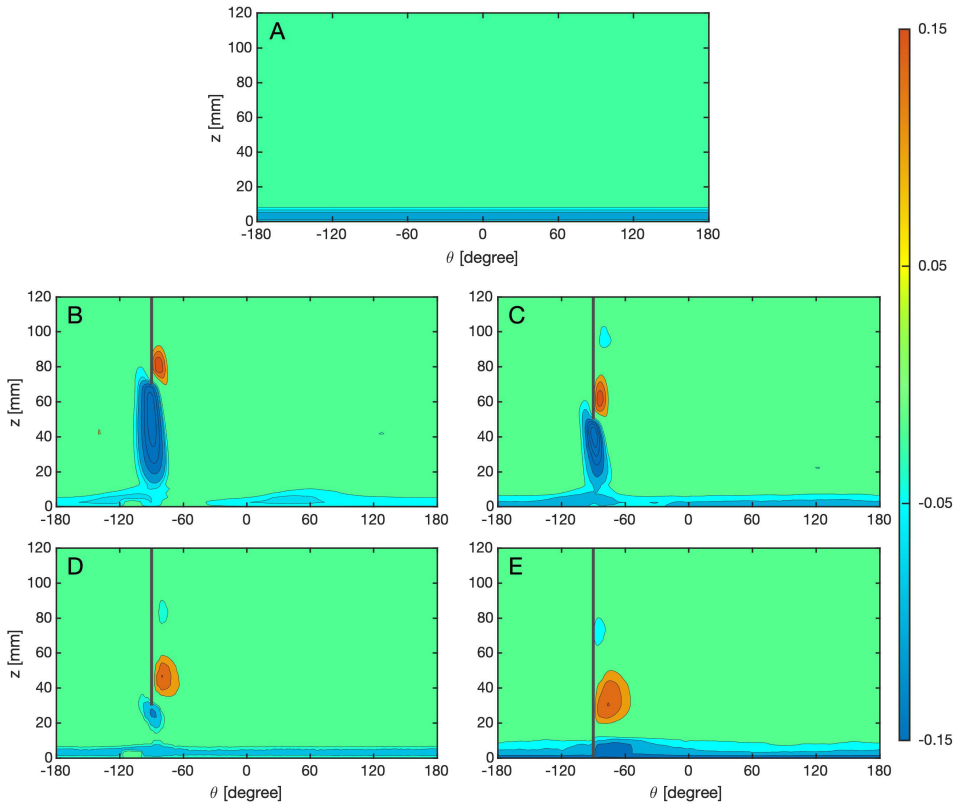

FIGURE 4
$\theta - z$ distribution of the meridional velocity [mm/s] at r = 120 mm in cases with a partial-depth ridge with different D_1 **(A)** no-ridge case (ExpOPEN), **(B)** 70 mm (ExpR70) **(C)** 50 mm (ExpR50) **(D)** 30 mm (ExpR30) **(E)** 0 mm (ExpR0). The outward (southward) flow is indicated by red, while the northward flow in blue.

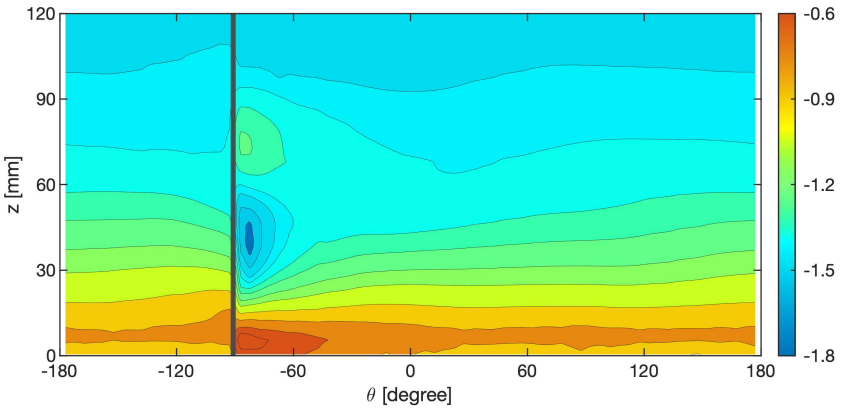

FIGURE 5
$\theta - z$ distribution of PV in log scale at r = 120 mm in ExpR0.

A local clockwise eddying flow appears with its west edge under the ridge.

As what have been described, the exclusive feature of the partial-depth ridge is the existence of the jet structure along the longitude of the ridge in the 'open' region. In other words, though the ridge is partial in depth, the along-ridge jet structure exists through the water column, with alternating flowing directions. It is a systematic and baroclinic response to the ridge. Taking the isopycnal variations in association with the DWBC as a "topography", the other two jets and the associated isopycnal variations can be understood as for a baroclinic Taylor column.

3.2 Effects of two ridges

It becomes clear that DWBCs can develop along both full- and partial-depth ridges. Then a question arises as to what will happen if more than one ridge exists, like the co-existence of the side boundary and the mid-ocean ridge in the Atlantic basin, or the distribution of multiple partial-depth ridges in the ACC region.

As shown in Figure 7, adding a partial-depth ridge to a closed basin does not do much to affect the original overturning cell in association with the western boundary. However, a second DWBC would develop along the eastern edge of the ridge. Consequently, the total strength of the overturning is to some extent enhanced, but the strength of this second MOC cell is dependent on the ridge's depth. It is weak as the ridge's depth is increased, and finally disappears when the ridge is too high above. For example, a DWBC is supported along a single partial-depth ridge with D_1=70 *mm* (Figure 2), but is hardly seen along the same ridge within a closed basin (Figure 7C). This is because as shown in the single-ridge cases the DWBC supported by the "western boundary" (a full-depth ridge) is significantly stronger than that along any partial-depth ridges, so are the related isopycnal variations. In a closed basin the existence of a primary DWBC along the western boundary makes the isopycnals above slope upward and those below downward against the boundary, acting as a large-scale background condition. With the addition of a partial-depth ridge, its DWBC, if exists, resides at a level higher than the primary DWBC and also tries to prop up isopycnals locally. This means isopycnals at levels between the two DWBCs receive two opposite impacts: a tendency of being raised upward by the primary DWBC and a tendency of being pressed down by the second DWBC. As a result of the competition between the two tendencies, the second DWBC will not appear when the related isopycnal variations are too small.

What this implies is that in the North Atlantic basin, whether the dense water can be exported along the ridge's eastern edge depends on its relative depth to that of the primary DWBC along the western boundary. If the mid-Atlantic ridge is lowered down, there probably would be no interior path anymore.

Therefore, we would naturally expect that in presence of multiple partial-depth ridges in a zonally open channel like the latitudinal band of ACC, the resulting flow filed regarding the MOC is determined by the relation among different ridges. This conjecture is confirmed by a series of two-ridge experiments. As shown in Figure 8, the ridge closest to the lower boundary has the strongest DWBC and the two ridges have exactly the same overturning when they have the same height. These are two features that can be easily understood. Interestingly, with two different ridges, the bigger the difference of their heights, the larger the difference of their overturning strengths. This again means the flow as well as the associated isopycnal variations along the shorter ridge with bigger D_1 is dominated by those

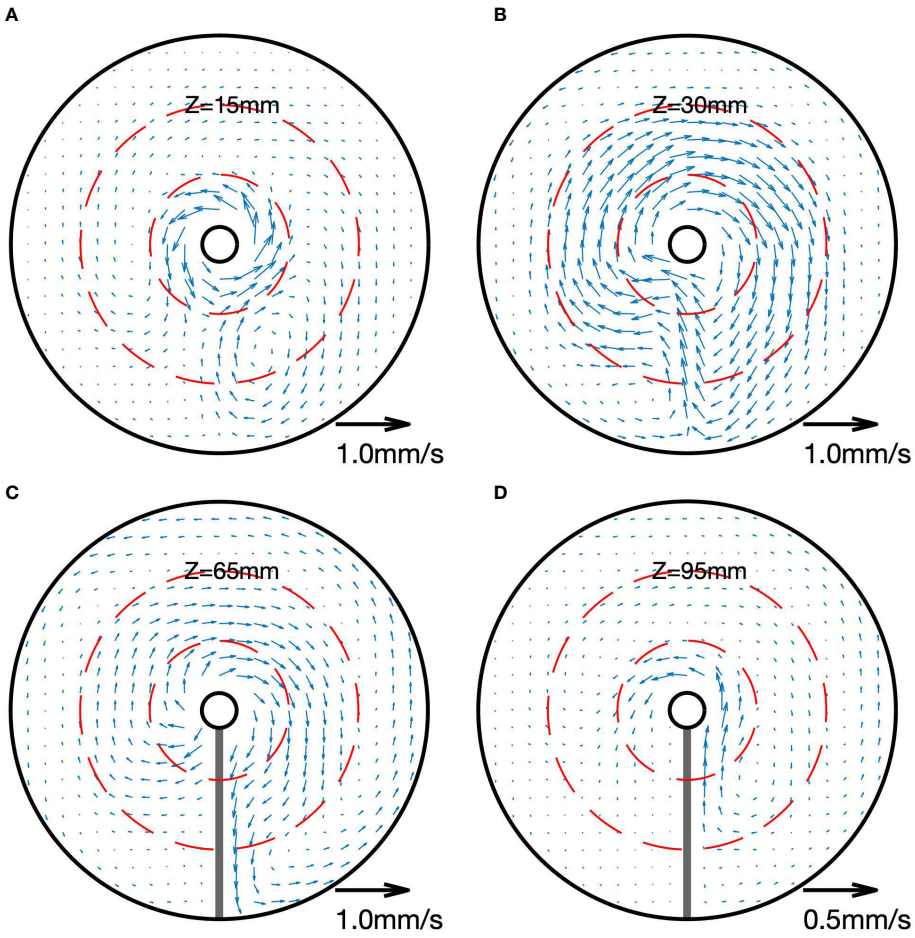

FIGURE 6
Horizontal velocity vectors of ExpR50 at **(A)** z = 15 mm, **(B)** z = 30 mm, **(C)** z = 65 mm and **(D)** z=95 mm above the bottom. The circles at r = 60 mm and r = 120 mm are denoted by red dashed lines.

along the ridge with smaller D_1. When the shorter ridge is too high above the lower DWBC along the other ridge, it can hardly support a second outward jet.

The overall strength of the overturning circulation, as indicated by the stream function at r=120 mm in Figure 9, generally declines with the increasing depth of the ridge, consistent with above results for single-ridge cases. Whether this result is applicable to the real ocean awaits more direct observational evidence in the future.

4 Conclusion and discussions

One remarkable feature of bottom topography, as realized over the past few decades, is the local and substantial enhancement of turbulent mixing (Polzin et al., 1997; Waterman et al., 2013; Waterhouse et al., 2014). According to a recent argument and as a result of this topographic strengthening, the overturning is deeply affected at the large scale: the abyssal upwelling occurs predominantly within a thin boundary layer along the bottom slope, whereas the interior region nearby is characterized by downwelling; the two are comparable in magnitude with a residual balancing that is generated and sinks from the surface (Ferrari et al., 2016; McDougall and Ferrari, 2017; de Lavergne et al., 2017). This is an example of how topography matters for the large-scale baroclinic flow, but it is probably not the only way. As reported in the paper, without spatial variation of diapycnal mixing, ocean ridges can still have impacts on both strength and pattern of the overturning, some of which are fundamental.

Applying experimental results to the real ocean, following features could be presumed. In the North Atlantic Basin, due to the existence of the mid-Atlantic ridge, deep water could be transported southward, in addition to the route along the western boundary, *via* an interior path along the ridge's eastern edge. The depth of this interior jet may migrate

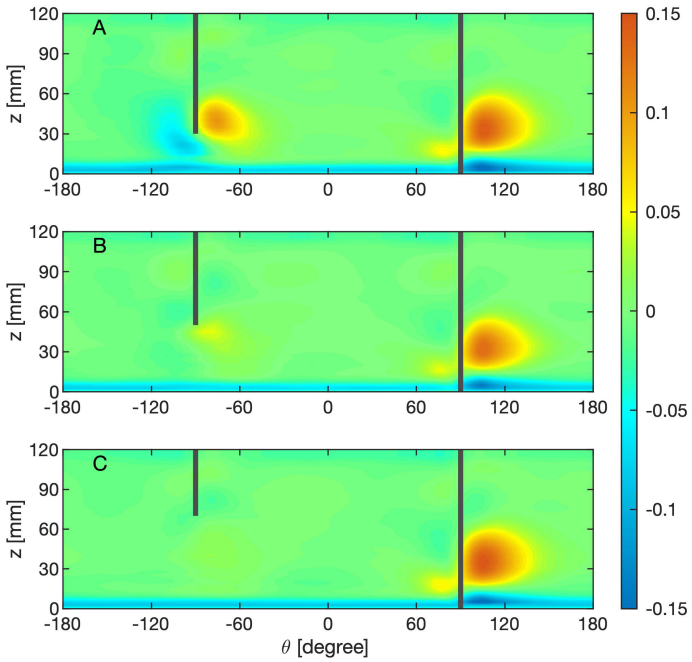

FIGURE 7
$\theta - z$ distribution of the meridional velocity [mm/s] at r = 120 mm in cases with a full radial barrier and a partial ridge with D_1 equal to **(A)** 30 mm, **(B)** 50 mm, and **(C)** 70 mm.

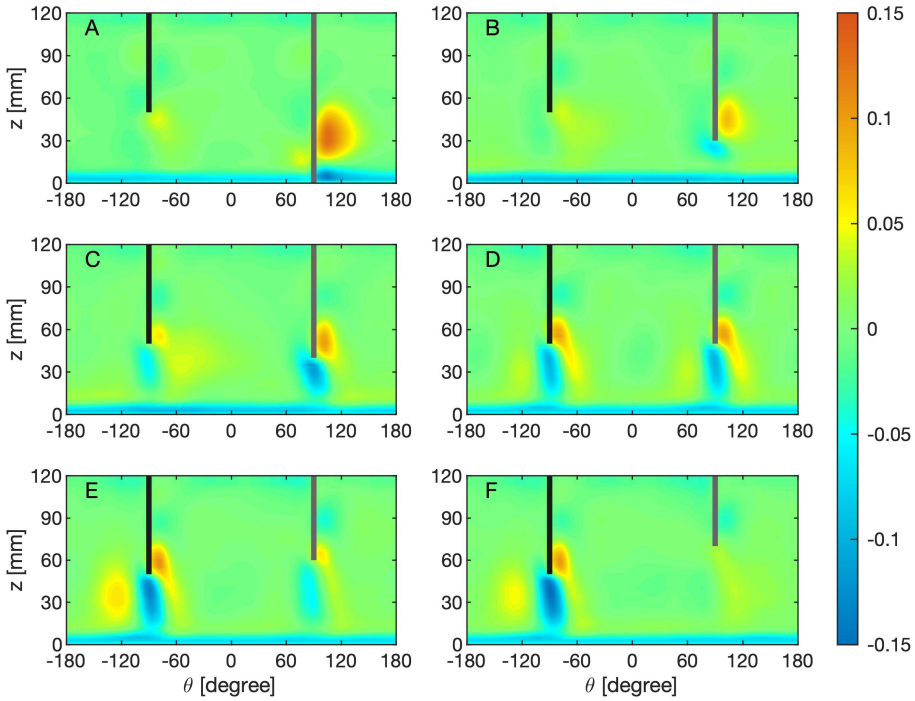

FIGURE 8
$\theta - z$ distribution of the meridional velocity [mm/s] at r = 120 mm with two ridges that have D1 = 50 mm and variable D2. **(A)** D2 = 0 mm; **(B)** D2 = 30 mm; **(C)** D2 = 40 mm; **(D)** D2 = 50 mm; **(E)** D2 = 60 mm; **(F)** D2 = 70 mm.

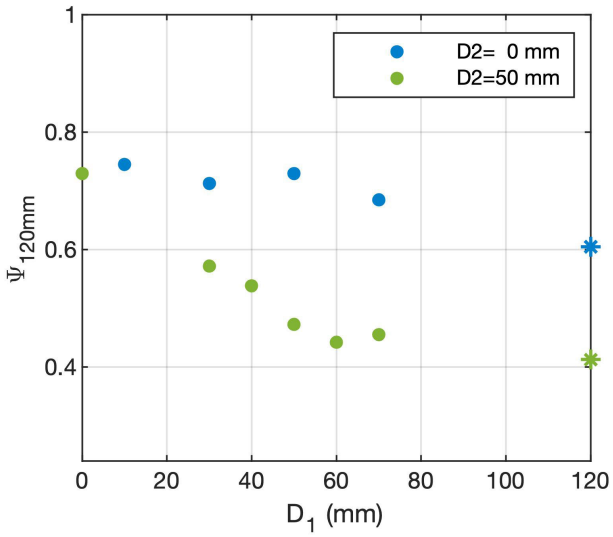

FIGURE 9
The MOC strength at r = 120 mm for two-ridge cases with variable D_1 for D_2 = 0 mm (blue dots) and D_2 = 50 mm (green dots). The cases denoted by stars are actually single-ridge cases since the full depth of the working fluid is 120 mm.

vertically, upward with increasing strength following the grow of the ridge or downward with decreasing strength following the decay of the ridge. Meanwhile, the formation of this second overturning cell can lead to adiabatic responses in the upper and lower layer, including a local horizontal meander above the ridge, and another opposing jet below the middle jet in the abyss.

However, in the latitudinal band of the Antarctic Circumpolar Current where the ocean bottom is characterized by complex topographic features including multiple meridionally oriented ridges, the transporting path of the Antarctic Bottom Water would be preferentially along higher ridges. With the grow of ridges as induced by plate tectonic evolution in the geological history, the overturning in association with the bottom water would be strengthened, accompanied by changes of stratification in the abyssal ocean which may then have strong impacts on the earth climate (Zachos et al., 2001; Scher and Martin, 2006).

All these conjectures gained from laboratory experiments, some of which are already found consistent with oceanic situation, are valuable in guiding future research in observational or modelling studies of the overturning circulation. The current results also raise some new questions, such as how, compared with ridges (or side boundary), the bottom slope can influence the circulation. Answers to these issues will finally lead us to a more comprehensive understanding of the nature of the ocean overturning.

Data availability statement

The raw data supporting the conclusions of this article will be made available by the authors, without undue reservation.

Author contributions

YZ and WW conceived the project, carried out experiments, and analyzed the data. YZ wrote the manuscript. ZZ reviewed and edited the manuscript. All authors contributed to the article and approved the submitted version.

Funding

This work was supported by the National Natural Science Foundation through Grants 42288101 and 41876007.

Conflict of interest

The authors declare that the research was conducted in the absence of any commercial or financial relationships that could be construed as a potential conflict of interest.

Publisher's note

References

Barkan, R., Winters, K. B., and Smith, S. G. L. (2013). Rotating horizontal convection. *J. Fluid Mech.* 723, 556–586. doi: 10.1017/jfm.2013.136

Beardsley, R. C., and Festa, J. F. (1972). A numerical model of convection driven by a surface stress and non-uniform horizontal heating. *J. Phys. Oceanogr.* 2, 444–455. doi: 10.1175/1520-0485(1972)002<0444:ANMOCD>2.0.CO;2

Coman, M. A., Griffiths, R. W., and Hughes, G. O. (2006). Sandström's experiments revisited. *J. Mar. Res.* 64, 783–796. doi: 10.1357/002224006779698413

de Lavergne, C., Madec, G., Roquet, F., Holmes, R. M., and McDougall, T. J. (2017). Abyssal ocean overturning shaped by seafloor distribution. *Nature* 9, 181–186. doi: 10.1029/2012GL052952

Ferrari, R., Mashayek, A., McDougall, T. J., Nikurashin, M., and Campin, J.-M. (2016). Turning ocean mixing upside down. *J. Phys. Oceanogr.* 46 (7), 2239–2261. doi: 10.1175/JPO-D-15-0244.1

Garrett, C., and Kunze, E. (2007). Internal tide generation in the deep ocean. *Annu. Rev. Fluid Mech.* 39, 57–58. doi: 10.1146/annurev.fluid.39.050905.110227

Hignett, P., Ibbetson, A., and Killworth, P. D. (1981). On rotating thermal convection driven by non-uniform heating from below. *J. Fluid Mech.* 109, 161–187. doi: 10.1017/S0022112081000992

Hughes, G. O., and Griffiths, R. W. (2008). Horizontal convection. *Annu. Rev. Fluid Mech.* 40, 185–208. doi: 10.1146/annurev.fluid.40.111406.102148

Hussam, W. K., Tsai, T. K., and Sheard, G. J. (2014). The effect of rotation on radial horizontal convection and nusselt number scaling in a cylindrical container. *Int. J. Heat Mass Transf.* 77, 46–59. doi: 10.1016/j.ijheatmasstransfer.2014.05.007

Ilicak, M., and Vallis, G. K. (2012). Simulations and scaling of horizontal convection. *Tellus A* 64, 118377. doi: 10.3402/tellusa.v64i0.18377

McDougall, T. J., and Ferrari, R. (2017). Abyssal upwelling and downwelling driven by near-boundary mixing. *J. Phys. Oceanogr.* 47 (2), 261–283. doi: 10.1175/JPO-D-16-0082.1

Miller, R. C. (1968). *A thermally convecting fluid heated nununiformly from below* (Cambridge: Mass. Inst. Technol.).

Mullarney, J. C., Griffiths, R. W., and Hughes, G. O. (2004). Convection driven by differential heating at a horizontal boundary. *J. Fluid Mech.* 516, 181–209. doi: 10.1017/S0022112004000485

Park, Y. G., and Whitehead, J. A. (1999). Rotating convection driven by differential bottom heating. *J. Phys. Oceanogr.* 29, 1208–1220. doi: 10.1175/1520-0485(1999)029<1208:RCDBDB>2.0.CO;2

Pedlosky, J. (1987). *Geophysical Fluid Dynamics* (New York: Springer).

Pedlosky, J., Whitehead, J. A., and Veitch, G. (1997). Thermally driven motions in a rotating stratified fluid: theory and experiment. *J. Fluid Mech.* 339, 391–411. doi: 10.1017/S0022112097005168

Polzin, K. L., Toole, J. M., Ledwell, J. R., and Schmitt, R. W. (1997). Spatial variability of turbulent mixing in the abyssal ocean. *Science* 276, 93–96. doi: 10.1126/science.276.5309.93

Rossby, T. (1965). On thermal convection driven by non-uniform heating from below: an experimental study. *Deep-Sea Res.* 12, 9–16. doi: 10.1016/0011-7471(65)91336-7

Rossby, T. (1998). Numerical experiments with a fluid heated non-uniformly from below. *Tellus* 50 (2), 242–257. doi: 10.3402/tellusa.v50i2.14523

Sandström, J. W. (1908). Dynamishce versuche mit merrwasser. *Ann. Hydrogr. Marit. Meteorol.* 36, 6–23.

Scher, H. D., and Martin, E. E. (2006). Timing and climatic consequences of the opening of drake passage. *Science* 312, 428–430. doi: 10.1126/science.1120044

Sheard, G. J., Hussam, W. K., and Tsai, T. (2016). Linear stability and energetics of rotating radial horizontal convection. *J. Fluid Mech.* 795, 1–35. doi: 10.1017/jfm.2016.193

Stern, M. E. (1975). *Ocean circulation physics* (New York: Academic).

Stewart, K. D. (2012). *The effect of sills and mixing on the meridional overturning circulation* (Canberra: Australian National University).

St. Laurent, L. C., Garabato, A. C. N., Ledwell, J. R., Thurnherr, A. M., Toole, J. M., and Watson, A. J. (2012). Turbulence and diapycnal mixing in drake passage. *J. Phys. Oceanogr.* 42, 2143–2125. doi: 10.1175/JPO-D-12-027.1

Tailleux, R., and Rouleau, L. (2010). The effect of mechanical stirring on horizontal convection. *Tellus* 62 (2), 138–153. doi: 10.1111/j.1600-0870.2009.00426.x

Toggweiler, J. R., and Bjornsson, H. (2000). Drake passage and paleoclimate. *J. Quat. Sci.* 15, 319–328. doi: 10.1002/1099-1417(200005)15:4<319::AID-JQS545>3.0.CO;2-C

Wang, F., Huang, S.-D., Zhou, S.-Q., and Xia, K.-Q. (2016). Laboratory simulation of the geothermal heating effects on ocean overturning circulation. *J. Geophys. Res.: Ocean.* 121, 7589–7598. doi: 10.1002/2016JC012068

Waterhouse, A. F., MacKinnon, J. A., Nash, J. D., Alford, M. H., Kunze, E., Simmons, H. L., et al. (2014). Clobal pattern of diapycnal mixing from measurement of the turbulent dissipation rate. *J. Phys. Oceanogr.* 44, 1854–1872. doi: 10.1175/JPO-D-13-0104.1

Waterman, S., Garabato, A. C. N., and Polzin, K. L. (2013). Internal waves and turbulence in the Antarctic circumpolar current. *J. Phys. Oceanogr.* 43, 259–282. doi: 10.1175/JPO-D-11-0194.1

Whitehead, J. A., and Pedlosky, J. (2000). Circulation and boundary layers in differentially heated rotating stratified fluid. *Dynam. Atmos. Ocean.* 31, 1–21. doi: 10.1016/S0377-0265(99)00026-3

Whitehead, J. A., and Wang, W. (2008). A laboratory model of vertical ocean circulation driven by mixing. *J. Phys. Oceanogr.* 38, 1091–1106. doi: 10.1175/2007JPO3805.1

Winters, K. B., and Barkan, R. (2013). Available potential energy density for boussinesq fluid flow. *J. Fluid Mech.* 714, 476–488. doi: 10.1017/jfm.2012.493

Wunsch, C., and Ferrari, R. (2004). Vertical mixing, energy, and the general circulation of the oceans. *Annu. Rev. Fluid Mech.* 36, 281–314. doi: 10.1146/annurev.fluid.36.050802.122121

Zachos, J., Pagani, M., Sloan, L., Thomas, E., and Billips, K. (2001). Trends, rhythms, and aberrations in global climate 65 ma to present. *Science* 292, 686–693. doi: 10.1126/science.1059412

Zhang, Y., Chen, C., Zhang, Z., and Wang, W. (2016). Rotating horizontal convection and the potential vorticity constraint. *J. Fluid Mech.* 803, 72–93. doi: 10.1017/jfm.2016.513

frontiers | Frontiers in Marine Science

TYPE Original Research
PUBLISHED 25 November 2022
DOI 10.3389/fmars.2022.1047446

OPEN ACCESS

EDITED BY
Yeping Yuan,
Zhejiang University, China

REVIEWED BY
Jihai Dong,
Nanjing University of Information Science and Technology, China
Zhiqiang Liu,
Southern University of Science and Technology, China

*CORRESPONDENCE
Tao Wang
taowang@ouc.edu.cn

SPECIALTY SECTION
This article was submitted to Physical Oceanography, a section of the journal Frontiers in Marine Science

RECEIVED 18 September 2022
ACCEPTED 08 November 2022
PUBLISHED 25 November 2022

CITATION
Si X, Wang T and Wang Y (2022) Temporal and spatial characteristics of submesoscale motions in the Bohai Sea. *Front. Mar. Sci.* 9:1047446. doi: 10.3389/fmars.2022.1047446

Temporal and spatial characteristics of submesoscale motions in the Bohai Sea

Xueying Si[1], Tao Wang[1*] and Yanping Wang[2,3]

[1]Key Laboratory of Marine Environment and Ecology, Ocean University of China, Qingdao, China, [2]Beijing Institute of Applied Meteorology, Beijing, China, [3]State Key Laboratory of Geo-Information Engineering, Xi'an, China

Submesoscale motions are ubiquitous in the ocean, playing a significant role in energy transfer, mass transport, and biogeochemical processes. However, little attention has been drawn to the submesoscale dynamics in shallow coastal waters. In the present study, submesoscale motions in the Bohai Sea, a typical shallow sea with mean depth of about 18 m, are studied using a validated high-resolution (~ 500 m) model based on Regional Oceanic Modeling System (ROMS). The results show that submesoscale structures in the Bohai Sea are mainly located in the shallow coastal regions, the Bohai Strait, the areas around islands and headlands, and mostly tend to be parallel to the isobaths. The periodic variations of submesoscale motions are closely related to the tidal, spring-neap, and seasonal cycles in the Bohai Sea. The spring-neap variations of submesoscale motions are mainly attributed to the curl of vertical mixing, which is stronger during spring tides than neap tides. Compared with winter, the stronger background horizontal and vertical density variance in summer are conducive to frontogenesis, resulting in more active submesoscale motions. The results in this study are expected to contribute to enriching our knowledge about submesoscale dynamics in shallow coastal seas.

KEYWORDS

Bohai Sea, submesoscale motions, tides, frontogenesis, coastal dynamics

1 Introduction

Submesoscale motions, with horizontal scales of 0.1-10 km, vertical scales of 0.01-1 km, and time scales of several hours to days, are significant in the forward energy cascade from large to small scale dynamics in the ocean (McWilliams, 2016). They are often featured with strong horizontal convergence, vertical velocity, and turbulent mixing, hence have significant effects on the transport of materials in the ocean (such as spilled oil and plastics), exchange of heat and momentum, and biogeochemical processes (Poje et al., 2014; Mahadevan, 2016; Lévy et al., 2018; Wang et al., 2022). Their primary generation mechanisms include mixed layer instabilities (Boccaletti et al.,

2007; Fox-Kemper et al., 2008), frontogenesis (Hoskins, 1982; McWilliams et al., 2009; Zhan et al., 2022), and topographic wakes (D'Asaro, 1988; Gula et al., 2016; Yu et al., 2016). Previous studies on submesoscale motions have mostly focused on the deep ocean, including the generation mechanisms (e.g., Thomas et al., 2008; McWilliams et al., 2009), momentum balances (e.g., Capet et al., 2008; Dong et al., 2020), spatio-temporal variabilities (e.g., Callies et al., 2015; Esposito et al., 2021; Liu et al., 2021), and effects on biogeochemical processes (e.g., Lévy et al., 2001; Mahadevan, 2016; Wang et al., 2021a), while the studies on submesoscale motions in shallow coastal waters are relatively rare. In coastal seas, there are multiple factors that may have significant effects on the formation, evolution, and destruction of submesoscale motions, such as complex shorelines, tidal currents, local circulations, river discharge, winds, solar radiation, and bottom boundary layer (e.g., Dauhajre and McWilliams, 2018; Wang et al., 2021b). The dominant factors may vary in different coastal systems, thus resulting in various spatial and temporal variabilities.

The Bohai Sea is a typical semi-enclosed shallow sea affected strongly by bathymetry, tides, monsoons and winds. Tides not only lead to periodic movements of seawater, but they also have been verified as important driving forces of subtidal water exchange and mass transport in the Bohai Sea (Wei et al., 2004). The averaged depth of the Bohai Sea is about 18 m (Zhao and Wei, 2005), so the water movement is inevitably affected by bottom friction. The complex coastlines and islands may induce horizontal shear of velocity, which could trigger submesoscale fronts (Dauhajre et al., 2017; Li et al., 2022). It also has a typical monsoon climate characteristic, including the seasonal variations of heat flux and winds (Wei et al., 2020). Therefore, submesoscale motions may be affected by the bathymetry, tides, winds, and some other factors in the Bohai Sea. Although some previous studies reported tidal fronts in some local bays of the Bohai Sea (Hickox et al., 2000; Zhao et al., 2001; Zhang et al., 2020), there is a lack of understanding of the spatio-temporal variabilities of submesoscale motions and their mechanisms.

In the present study, we conducted a realistic high-resolution numerical simulation with the Regional Oceanic Modeling System (ROMS) to investigate the spatio-temporal characteristics of submesoscale motions and the dominant factors in the Bohai Sea. Although the submesoscale roles in the Bohai Sea have not been well studied, a few studies have found that they can redistribute marine organisms, floating oil, plastics, and other oceanic pollutants, and have significant impact on phytoplankton and primary production in some other regional seas (Poje et al., 2014; D'Asaro et al., 2018; Wang et al., 2022). Therefore, the results are expected to contribute to improving our understanding of submesoscale dynamics in coastal seas and providing a reference for the biogeochemical and environmental studies in the frontal zones of the Bohai Sea. The model set-up is described and the model results are validated in section 2. In section 3, temporal and spatial variations of the submesoscale motions in the Bohai Sea are described in detail. The mechanisms for the spatial, spring-neap, and seasonal variations are analyzed in section 4, followed by the conclusions summarized in section 5.

2 Materials and methods

2.1 Model setup

In this study, we investigate the submesoscale motions in the Bohai Sea using a high-resolution numerical simulation based on the Regional Oceanic Modeling System (ROMS). The model domain and bathymetry are shown in Figure 1. The model has a 500-m horizontal resolution with orthogonal curvilinear grids and 20 sigma layers in the vertical. The bathymetry is constructed from the SKKU data (Choi et al., 2002), modified by the depth information in the Chuanxun website (https://www.shipxy.com/), and smoothed to avoid aliasing whenever the bathymetric data are available at higher resolution than the computation grid. The shorelines have changed a lot due to sea reclamation and sea level rise (Li et al., 2013), so they are manually modified according to the MODIS satellite image on August 26, 2016. The initial temperature and salinity fields are obtained from the climatological World Ocean Atlas (WOA) dataset. The initial values of sea surface height and velocities are set to zero. The 1-hourly surface forcing data are derived from the ERA5 dataset produced by the European Centre for Medium-Range Weather Forecasts (ECMWF) with a horizontal resolution of 0.25° x 0.25°, including the 10 m wind speed, shortwave radiation, longwave radiation, sea-level pressure, 2 m air temperature, 2 m dew-point temperature, and precipitation. The latent and sensible heat fluxes are calculated by bulk formula (Fairall et al., 1996). Two major rivers, including the Yellow River and the Liaohe River, are considered in the model. We apply the daily Yellow River discharge from the Station Lijin released by the Yellow River Conservancy of the Ministry of Water Resources (http://www.yrcc.gov.cn/) and Liaohe River discharge released by the Ministry of Water Resources of the People's Republic of China (http://www.mwr.gov.cn/sj/tjgb/zghlnsgb). The eastern open boundary conditions are interpolated from the output of a validated NEMO model with a horizontal resolution of 1/36° (Li et al., 2020). The boundary conditions consist of a Flather type scheme for the barotropic mode and a mixed radiation-nudging type scheme for both the tracer fields (temperature and salinity) and baroclinic velocities. The tidal forcing data are from the TPXO 8.0 tide model of Oregon State University (OSU), which provides nine tidal constituents (M_2, S_2, N_2, K_2, K_1, O_1, P_1, Q_1, and M_4). The vertical mixing of tracers and momentum is calculated based on the K-profile parameterization (KPP) (Large et al., 1994). The model is run from January 1, 2015 to December 31, 2016. Since the equilibration time is less than a year,

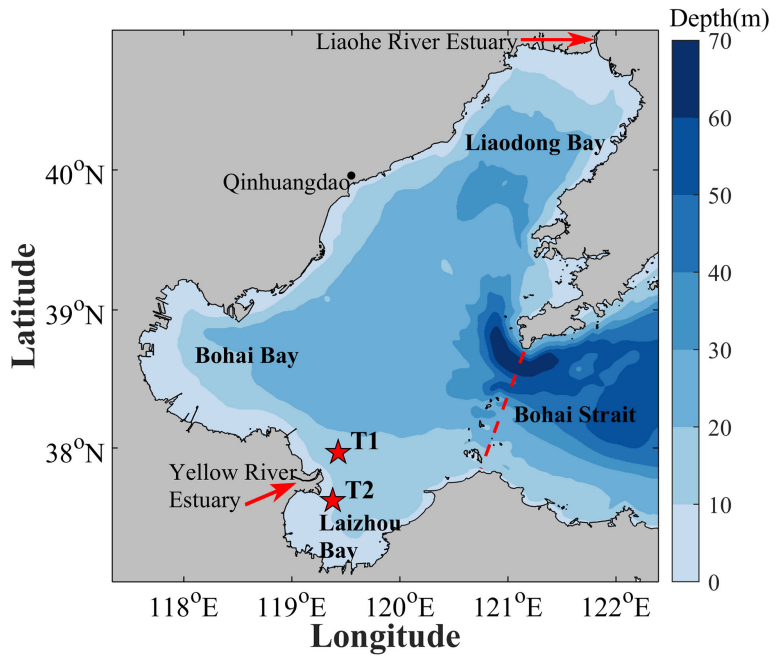

FIGURE 1
Topography of the model domain. Red stars indicate the *in-situ* observation stations (T1, T2) for validating the model simulated surface currents.

instantaneous model outputs at 1-hour intervals in 2016 are analyzed to study the submesoscale motions.

2.2 Model validation

Tides, sea surface temperature (SST), and temperature fronts simulated by the ROMS model are validated with *in-situ* and satellite observations to evaluate the accuracy of the model results.

Tidal harmonic analysis of the simulated water level in 2016 is conducted by t-tide toolbox to obtain the co-tidal charts of the main tidal constituents M_2 and K_1 in the Bohai Sea (Figure 2). The M_2 constituent has two amphidromic points located near the Yellow River estuary and Qinhuangdao, respectively. The K_1 constituent has one amphidromic point located in Bohai Strait. The amplitudes, phases, and amphidromic points are generally consistent with those in the Editorial Board for Marine Atlas, with small difference of the location of the amphidromic point for M_2 constituent (Chen and Editorial Board for Marine Atlas, 1993). The small difference is mainly attributed to the changes of the bathymetry induced by sea reclamation and sea level rise in recent years (Wei et al., 2020).

Surface currents are further validated against the *in-situ* observed data at Stations T1 and T2 (Yu et al., 2021). The time of the observations is from 19:00 on June 5 to 20:00 on June 6, 2016. The results show that the model simulated surface velocities have conspicuous characteristics of semidiurnal tide and are almost consistent in magnitudes and directions with the observations (Figure 3). The formula of skill proposed by Wilmott (1981), previously applied in the validations of many numerical simulations (e.g., Warner et al., 2005; Ralston et al., 2010) is applied to evaluate the consistency between the observed and model simulated currents. The skill is calculated by

$$\boldsymbol{skill} = \mathbf{1} - \frac{\sum_{i=1}^{N}(\boldsymbol{M_i} - \boldsymbol{O_i})^2}{\sum_{i=1}^{N}\left(\left|\boldsymbol{M_i} - \overline{\boldsymbol{O_i}}\right| + \left|\boldsymbol{O_i} - \overline{\boldsymbol{O_i}}\right|\right)^2} \quad (1)$$

where M_i and O_i indicate the model and observation results, respectively. Overbar indicates time mean. Perfect agreement between model results and observations yields a skill of one and complete disagreement yields a skill of zero. The skills of U and V are all around 0.9 at both stations, which indicate that the simulated results are in agreement with the observations.

Frontogenesis is one primary mechanism for the generation of submesoscale motions. To validate the model simulated fronts, the horizontal SST gradient $|\nabla_h T|$ and frontal probability are calculated to compare with the satellite observed results. Daily MODIS-Aqua Level-3 SST data (https://oceancolor.gsfc.nasa.gov/) with a 4-km spatial resolution are employed for verifying the modeled SST fronts. Although there are missing data in some Level-3 products due to clouds, the available SST data are applicable to study the SST fronts (Castelao and Wang, 2014; Wang et al., 2015). For comparison, the modeled SST are daily and spatially averaged

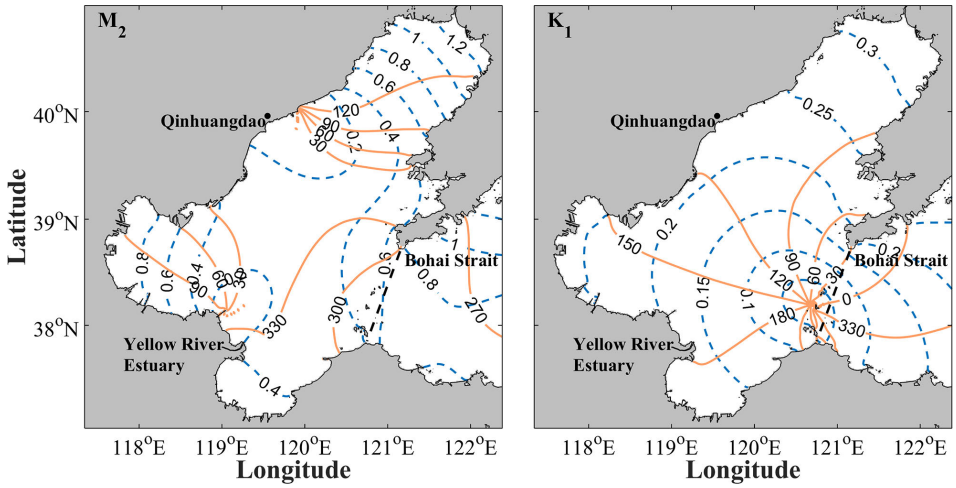

FIGURE 2
Co-tidal charts of the M_2 and K_1 constituents in the Bohai Sea. Blue dashed and orange solid lines indicate the tidal amplitudes (m) and phases (°), respectively.

in 4-km windows before calculating $|\nabla_h T|$ and frontal probability. The horizontal SST gradient $|\nabla_h T|$ is calculated at each grid based on all daily remote sensing and modeled SST in 2016. In the present study, the regions with $|\nabla_h T| > 5 \times 10^{-5}$ ° C/m are defined as SST fronts. We take the number of days a grid quantified as a front, and divide this value by the days that there is a valid value at the grid in the whole year of 2016, yielding a probability of detecting a front.

As shown in Figure 4, the modeled annually averaged $|\nabla_h T|$ and frontal probability are both consistent with the results from the satellite data. The small difference between the model and satellite results is perhaps partly attributed to the higher model resolution (~500 m) than MODIS-Aqua Level-3 SST product (~4 km), so stronger fronts, especially submesoscale fronts, can be better resolved by numerical model, leading to higher $|\nabla_h T|$ and frontal probability. We also have attempted to set other thresholds to compute the frontal probability, such as 8×10^{-5} °C/m and 1×10^{-4} °C/m, and the results show that the numerical simulation is consistent with the satellite data (not shown for brevity). Although the 4-km satellite products could not resolve submesoscale structures well enough, the consistence between the model simulated and satellite observed SST fronts proves the capabilities of the model to depict the general spatio-temporal distribution of SST fronts.

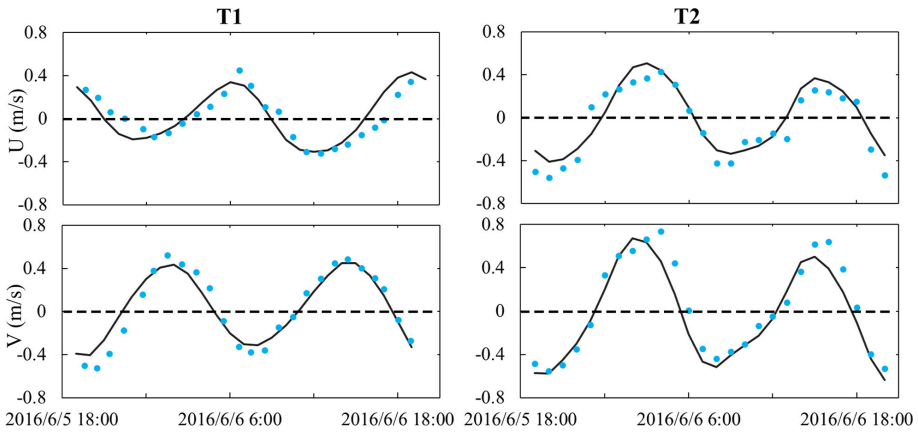

FIGURE 3
Validation of surface currents at Stations T1 and T2. Black solid lines and blue dots indicate the model simulated and *in-situ* observed results, respectively. Positive values indicate eastward or northward directions.

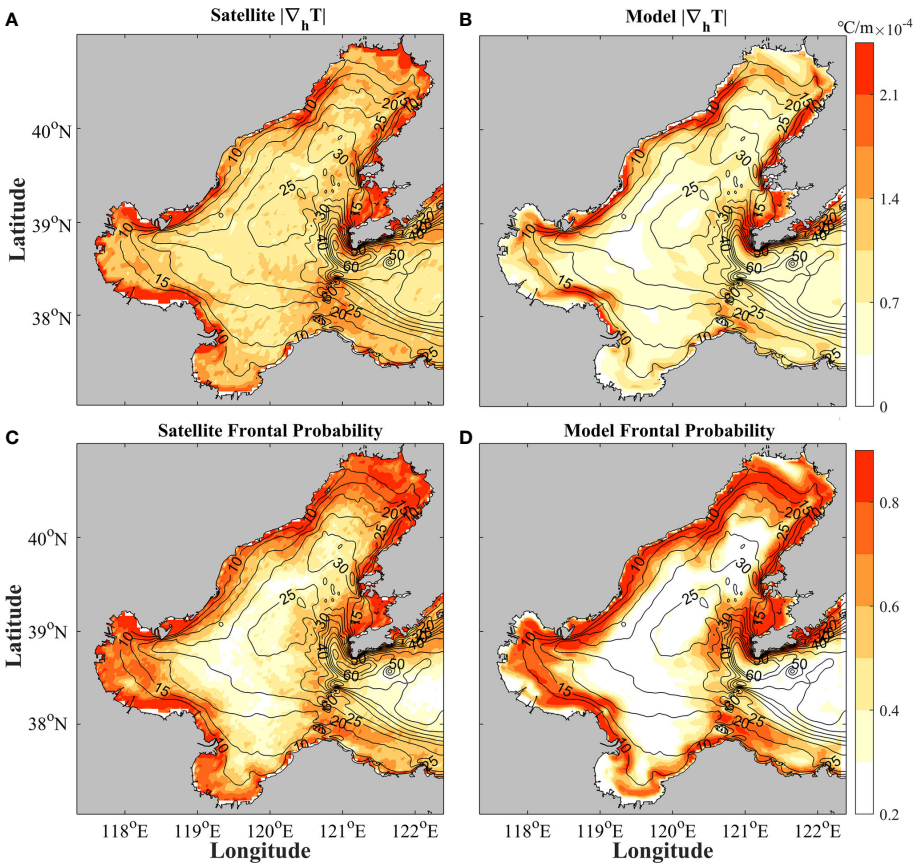

FIGURE 4
Annually averaged $|\nabla_h T|$ and frontal probability quantified with the **(A, C)** satellite and **(B, D)** model data. Black contours indicate isobaths (m) with an interval of 5 m.

Furthermore, the instantaneous satellite images of SST and ocean color with a higher resolution (~1 km) (https://optics.marine.usf.edu) are compared with the simulation results. Affected by frequent cloud cover, there are many missing values in the instantaneous satellite images. Some snapshots with good coverage are selected to compare with the model results. Two examples are presented in Figure 5. The model simulated horizontal distribution of SST (Figure 5A) is roughly identical to the satellite result (Figure 5B), including the features of the cold waters in the east of the Bohai Bay, the south of the Liaodong Bay, and near the Bohai Strait. The abrupt spatial changes of SST are corresponding to fronts, which are often corresponding to the clear boundaries of water color. The waters with abrupt SST changes in the model results (Figure 5C) resemble the satellite water color image (Figure 5D), demonstrating the good performance of the model in simulating the horizontal characteristics of SST and fronts in the Bohai Sea. The images in other days give similar results (not shown for brevity).

In the present study, we mainly focus on surface fronts, so SST and ocean color are used to validate the model results. We do not validate sea surface salinity (SSS), although it also has effects on the density (buoyancy) fronts. One reason is that there is no high-resolution satellite observed SSS. The other reason is that in most regions of the Bohai Sea, surface density fronts are mainly controlled by SST, as shown in the following analysis.

According to Barkan et al. (2017), Turner angle (Tu) is calculated to investigate the T–S relations based on the model results. The formula is as follows:

$$R_x = \frac{\alpha \partial T/\partial x}{\beta \partial S/\partial x},\ R_y = \frac{\alpha \partial T/\partial y}{\beta \partial S/\partial y} \tag{2}$$

$$Tu_x = arctan(R_x),\ Tu_y = arctan(R_y) \tag{3}$$

where α and β are the expansion and contraction coefficients of potential temperature (T) and salinity (S). Turner angles values in the range $(0<|Tu|<\pi/4)$ represent salinity dominated, and values in the range $(\pi/4<|Tu|<\pi/2)$ represent regions where temperature is dominated. It is found that the value and distribution of Tu_x and Tu_y are highly consistent (not shown for brevity). Two examples of Tu_x in winter and summer are

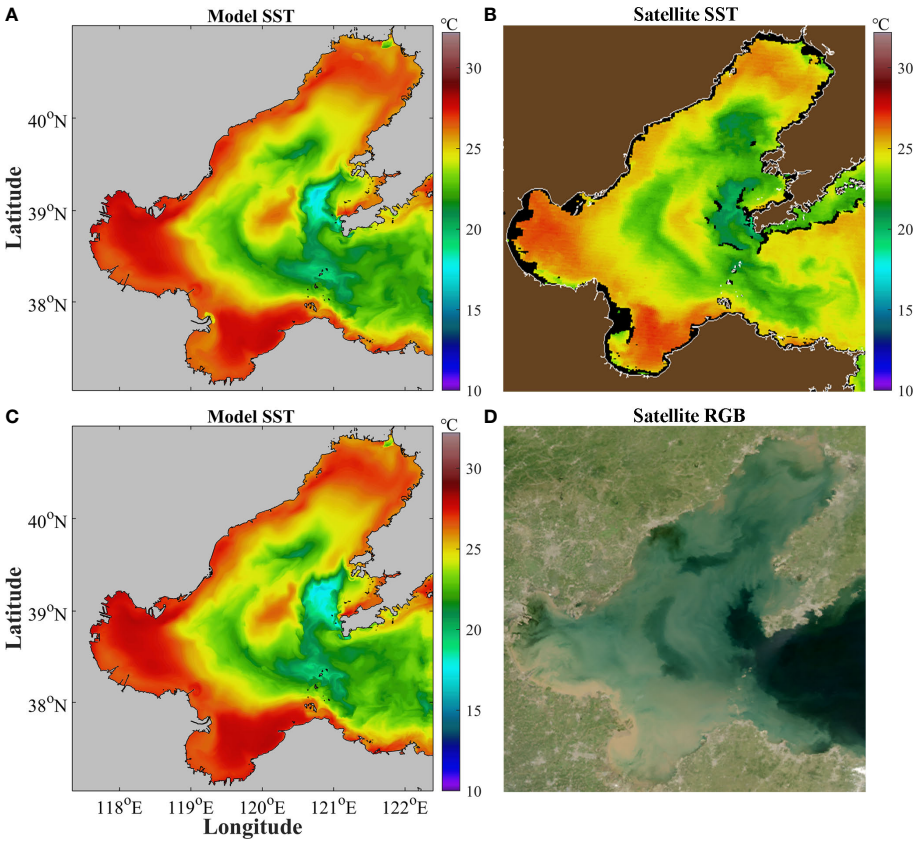

FIGURE 5
Comparison between the model and satellite images. **(A)** Model simulated SST at 17:00 on August 26, 2016; **(B)** Satellite observed SST at 17:25 on August 26, 2016; **(C)** Model simulated SST at 5:00 on August 26, 2016; **(D)** Satellite observed Red-Green-Blue (RGB) true-color composite image at 5:25 on August 26, 2016. The satellite images are from the Optical Oceanography Lab in University of South Florida. The RGB map in **(D)** is from normalized water-leaving radiance at 547 nm (R), 488 nm (G), and 443 nm (B) images, and is used to identify various ocean water types, from shallow (bright), sediment-rich (brownish), phytoplankton-rich (darkish), CDOM-rich (colored dissolved organic matter) (darkish), to blue waters (bluish) (Hu et al., 2005).

shown in Figure 6. The relatively small values of Tu_x in the bays (Figure 6) indicate that salinity is an important factor, which is mainly due to the influence of the river outflows. However, the values of Tu_x in most of the Bohai Sea are greater than $\pi/4$ (Figure 6), indicating that temperature generally dominated. In addition, the locations of SSS fronts are usually aligned with SST fronts (Wang et al., 2021b). Therefore, it is reasonable to verify that the model results and fronts by temperature (Figures 4, 5).

3 Results

3.1 Spatial distribution of submesoscale motions

Submesoscale motions are often featured with strong vertical vorticity $\zeta = v_x - u_y$ ($\zeta/f \sim 1$), horizontal divergence $\delta = u_x + v_y$, horizontal velocity gradient $|\nabla_h U| = \sqrt{u_x^2 + v_x^2 + u_y^2 + v_y^2}$, and horizontal buoyancy gradient $|\nabla_h b| = \sqrt{b_x^2 + b_y^2}$, where (u, v) are the horizontal velocity components in the (eastward, northward) directions; subscripts (x, y) indicate horizontal derivatives; $b = -g\frac{\rho}{\rho_0}$ is the buoyancy. Snapshots of these indicators in the Bohai Sea at the corresponding time of Figure 5C are shown in Figure 7.

The spatial distributions of the submesoscale indicators are roughly consistent with each other. Shallow coastal waters, the Bohai Strait, and the areas around islands exhibit more active submesoscale motions than other regions (Figure 7). High values of the submesoscale indicators are also found in the central area of the Bohai Sea due to the intrusion of cold water (Figure 5C). These high-value areas are primarily along isobaths, and resemble the sharp changes of water color (Figure 5D). Submesoscale motions near the Yellow River and Liaohe River estuaries differ from most of the other submesoscale processes in their higher magnitude of $|\nabla_h b|$. This is mainly associated with the river outflow, resulting in

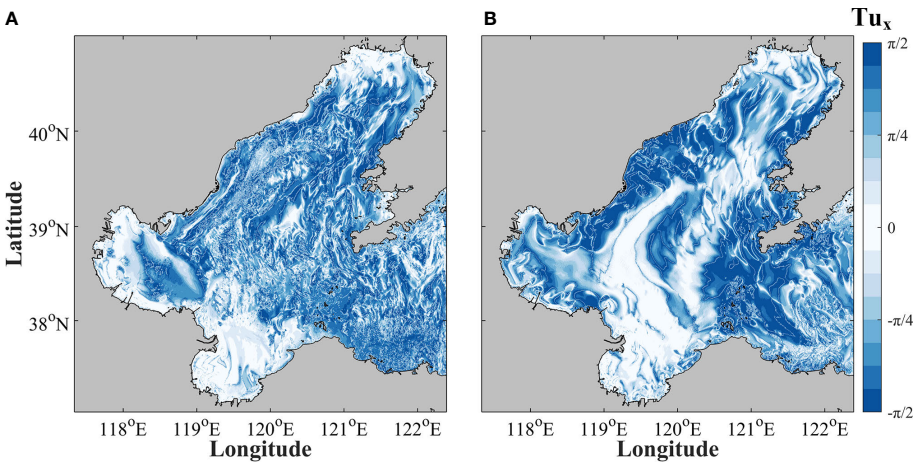

FIGURE 6
Model simulated Tu_x at **(A)** 12:00 on July 20, 2016, and **(B)** 12:00 on December 20, 2016.

large horizontal salinity and buoyancy gradients, and complex frontal structures.

The submesoscale motions in the Bohai Sea are potentially affected by multiple factors such as winds, bottom boundary layer, river discharge, and tidal currents, hence resulting in spatial and temporal variabilities. To investigate the spatial and temporal characteristics of the submesoscale motions in a whole year, we calculate the temporal root-mean-square (RMS)

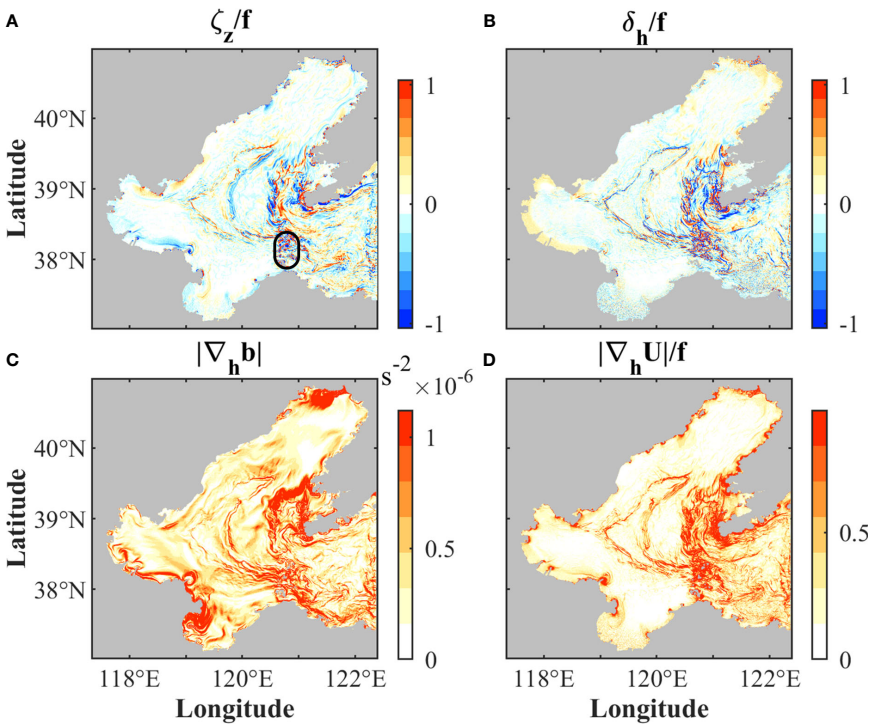

FIGURE 7
Instantaneous fields of **(A)** vertical vorticity normalized by the Coriolis frequency ζ/f , **(B)** divergence normalized by the Coriolis frequency δ/f, **(C)** absolute value of horizontal buoyancy gradient $|\nabla_h b|$, and **(D)** absolute value of horizontal velocity gradient normalized by the Coriolis frequency $|\nabla_h U|/f$, at the corresponding time of Figure 5C. The black ellipse in **(A)** indicates the region with a few islands.

and spatial RMS values of the submesoscale indicators (ζ, δ, $|\nabla_h b|$, and $|\nabla_h U|$), respectively.

The temporal RMS values of submesoscale indicators (ζ, δ, $|\nabla_h b|$, and $|\nabla_h U|$) at each grid cell (901 x 910 grids in total) are calculated using instantaneous model outputs at 1-hour intervals in the whole year of 2016 (8784 time points in total). Although the locations and intensities of the submesoscale motions vary with time under the effects of tidal currents, bathymetry, monsoons, and so on, there are some general spatial characteristics. According to the spatial distributions of the temporal RMS (Figure 8), during most time in one year, submesoscale motions are pervasively distributed in the shallow coastal waters, near the estuaries, the Bohai Strait, and the areas around islands, corresponding to the instantaneous features shown in Figure 7.

In the regions with sharp changes of water depth, such as the northern Bohai Bay, the east and west sides of the Liaodong Bay, and the northern Bohai Strait, the temporal RMS values are significantly high. It is consistent with the frontal probability (Figure 4D), indicating the high occurrence probability of submesoscale motions in these regions all year round. The magnitude of $|\nabla_h b|$ near the estuarine mouths is much larger than the other areas due to the effects of freshwater from the rivers, but the along-coast frontal structure is perspicuous after changing the range of color bar (bottom subplot in Figure 8C). The strain field induced by the complex topography can promote the formation and development of the submesoscale motions, so there are high RMS values of ζ, δ, $|\nabla_h b|$, and $|\nabla_h U|$ in the regions nearby the Bohai Strait and islands. Therefore, compared with the central region of the Bohai Sea, submesoscale motions are more ubiquitous and complex near the Bohai Strait.

3.2 Temporal variations of submesoscale motions

To investigate the temporal variations of submesoscale motions, the spatial RMS values of submesoscale indicators (ζ, δ, $|\nabla_h b|$, and $|\nabla_h U|$) at each moment (8784 time points in 2016) are calculated (Figure 9). The spatial RMS values of horizontal strain rate $S = \sqrt{u_x^2 + v_y^2 + \frac{1}{2}(u_y + v_x)^2}$ and surface kinetic energy KE=$\rho(u^2+v^2)/2$ are also calculated to study their relationships with submesoscale motions. To eliminate the influences of the open boundaries, the regions on the east of 122°E are removed when calculating the spatial RMS values.

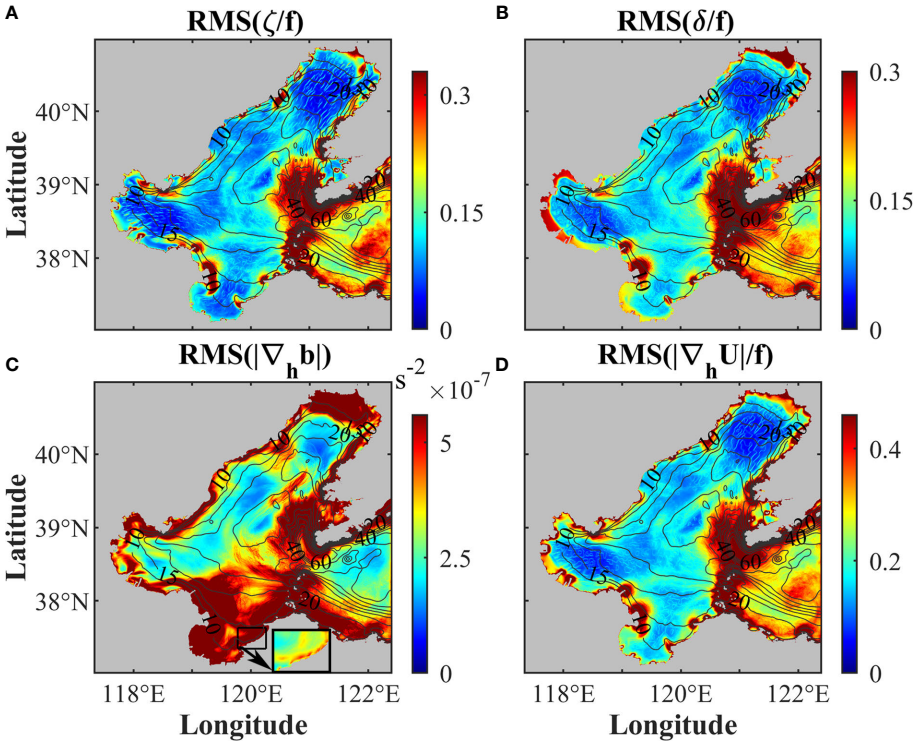

FIGURE 8
Temporal RMS of surface **(A)** ζ/f , **(B)** δ/f , **(C)** $|\nabla_h b|$, and **(D)** $|\nabla_h U|/f$. Black contours indicate isobaths (m) with an interval of 5 m. The subplot in the bottom of panel **(C)** indicates the temporal RMS of $|\nabla_h b|$ inside the black box with the color bar range of 0 to 1.2 x 10^{-6} s^{-2}. The subplot is used to show that the nearshore fronts tend to be parallel to the coast.

The submesoscale indicators (ζ, δ, and $|\nabla_h U|$) almost exhibit the same temporal variability as horizontal strain and *KE* (Figure 9A). The peaks at 28 and 14.5 days and 25.8, 23.9, 12.4, 12, 8.2, and 6.2 hours shown in the power spectra (Figure 9B) are consistent with the periods or double of the periods of the main tidal constituents in the Bohai Sea (e.g., spring-neap, O_1, K_1, M_2, S_2, M_3, and M_4). Those indicate that tides are significant controlling factors of the temporal variations of submesoscale motions in the Bohai Sea. The spring-neap tide cycle is the most apparent feature of the temporal variations of the submesoscale motions (Figure 9A). River outflow leads to strong horizontal buoyancy gradients near the estuaries during most time (Figure 8C), which has significant effects on the spatial RMS values, so $|\nabla_h b|$ shows less obvious periodical variation compared with the other submesoscale indicators (Figure 9A). Nevertheless, the horizontal buoyancy gradient $|\nabla_h b|$ also has the variation with a period of 14.6 days (Figure 9B). In addition to the tidal cycles, seasonal variations are also apparent in the spatial RMS values of submesoscale motions, with the highest in summer. The spatial RMS values increase in spring and reach the maximum in early August, indicating that the submesoscale motions in the Bohai Sea are more active in summer.

4 Discussion

As described in Section 3, the submesoscale motions in the Bohai Sea have significant spatial, spring-neap and seasonal variabilities. To explain these variabilities, the generation mechanisms and dominant factors of the submesoscale motions are analyzed in this section.

4.1 Mechanisms for the generation of vorticity

Based on time series of the spatial RMS values (Figure 9A), we selected three cases to explain the spring-

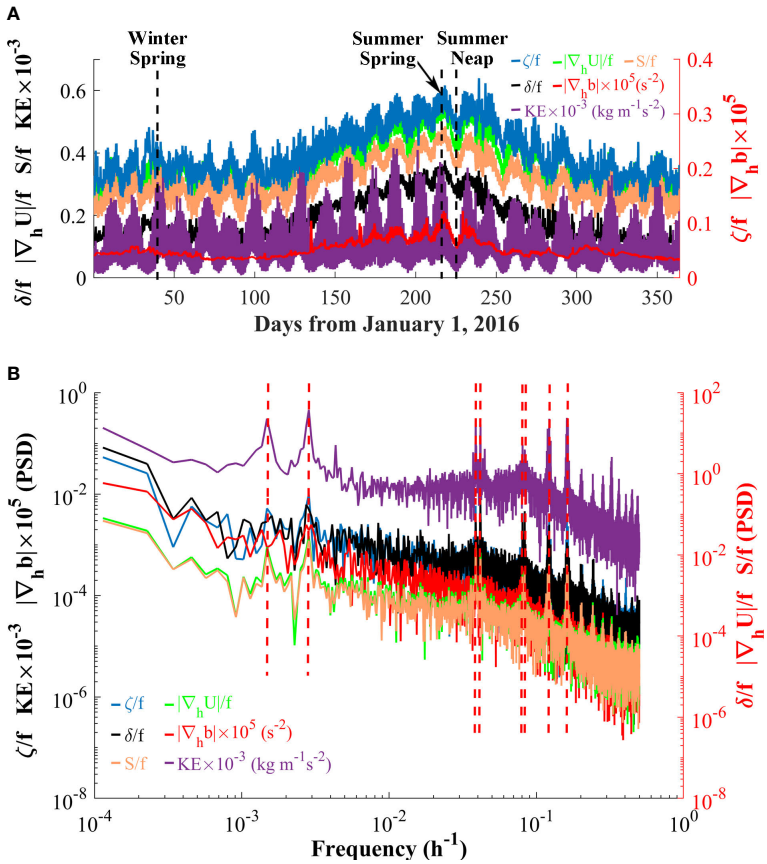

FIGURE 9
(A) Time series and **(B)** power spectra of the spatial RMS values of surface *ζ/f*, *δ/f*, $|\nabla_h b|$, $|\nabla_h U/f|$, *S/f*, and *KE* in 2016. Vertical dashed black lines in **(A)** represent the corresponding time of the cases in maximum spring and minimum neap tides in summer, and maximum spring tide in winter shown in Figures 10-14. Vertical dashed red lines in **(B)** indicate the locations of peaks.

neap and winter-summer variabilities of the submesoscale motions. Cases during the other periods give similar results (not shown for brevity). To get more detailed information about the spatial, spring-neap, and summer-winter variations of submesoscale processes, the instantaneous fields of submesoscale indicators (ζ, δ, $|\nabla_h b|$, and $|\nabla_h U|$) from three cases are presented in Figure 10. The results illustrate that the submesoscale indicators in spring tides in summer are enhanced in general compared with the neap tides. In spring tides, there are active submesoscale motions in the central area of the Bohai Sea, the Bohai Strait, and the northern Laizhou Bay. During spring tides in winter, submesoscale motions are even less active than neap tides in summer. The results during other tidal cycles in 2016 also resemble those shown in Figure 10.

One fundamental feature of the submesoscale processes is that they have vertical vorticities those are close to *f*. To study how the high vertical vorticities are generated, we calculated the terms in the vertical vorticity equation based on the model output data. The vertical vorticity equation can be obtained by taking the curls of the horizontal momentum equations and expressed by:

$$\frac{D\zeta}{Dt} = \underbrace{-(\zeta+f)\delta}_{F_{div}} + \underbrace{\left[\frac{\partial}{\partial x}\frac{\partial}{\partial z}\left(A\frac{\partial v}{\partial z}\right) - \frac{\partial}{\partial y}\frac{\partial}{\partial z}\left(A\frac{\partial u}{\partial z}\right)\right]}_{F_{mix}} + \underbrace{\left(\frac{\partial w}{\partial y}\frac{\partial u}{\partial z} - \frac{\partial w}{\partial x}\frac{\partial v}{\partial z}\right)}_{F_{tilt}} \underbrace{-\left[\frac{\partial}{\partial x}\left(\frac{1}{\rho}\frac{\partial P}{\partial y}\right) - \frac{\partial}{\partial y}\left(\frac{1}{\rho}\frac{\partial P}{\partial x}\right)\right]}_{F_{pres}} \quad (4)$$

where $\zeta = v_x - u_y$ is vertical vorticity; (*u*, *v*, *w*) are the components of velocity in the three-dimensional field; *f* indicates the Coriolis frequency; *p* and *p* are the pressure and density, respectively; *A* is the parameterized vertical viscosity. The left term indicates the rate of change of the relative vorticity following a water parcel. All right terms represent the processes that generate or dissipate the relative vorticity, that is, the sources and sinks of the relative vorticity. The first term on the right F_{div} indicates the effect of horizontal divergence δ . The second term F_{mix} describes the role of vertical mixing. The third term F_{tilt}, often called as the tilting term, describes the influence of a horizontal gradient of vertical velocity in transforming vorticity from a horizontal direction to vertical direction. The last term F_{pres} represents the generation of vorticity by pressure gradient.

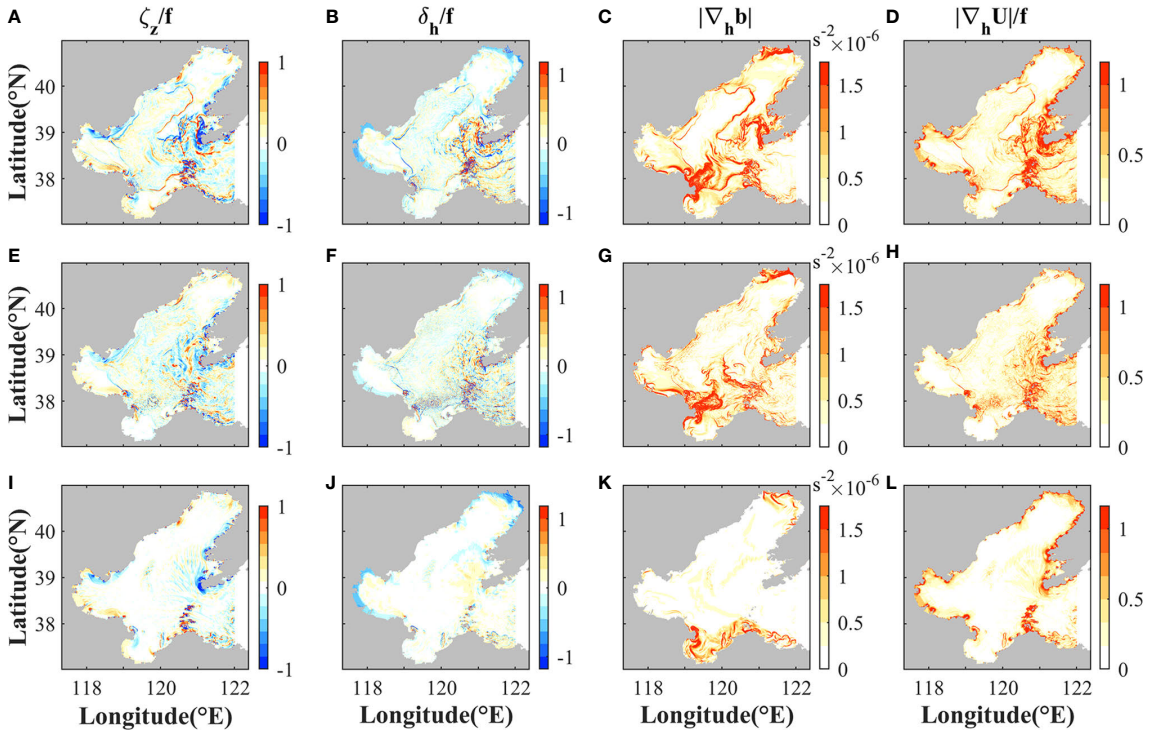

FIGURE 10
Distributions of the submesoscale indicators **(A, E, I)** ζ/f, **(B, F, J)** δ/f, **(C, G, K)** $|\nabla_h b|$, and **(D, H, L)** $|\nabla_h U/f|$ during (top) maximum spring tide and (middle) minimum neap tide in summer, and (bottom) maximum spring tide in winter. The corresponding time is noted in Figure 9A. These snapshots are chosen at the time with maximum *KE* in the corresponding tidal cycles.

Based on the model output, the magnitudes of the right terms are calculated to quantify their contributions to the change of vertical vorticity (Figure 11). The terms F_{div} and F_{mix} are found to be much larger than F_{tilt} and F_{pres} in the Bohai Sea (not shown for brevity), so the horizontal divergence and vertical mixing terms are dominant in generating or dissipating relative vorticity.

The distributions of the divergence term F_{div} coincide with vorticity and divergence (Figure 10). Strong divergence or convergence tends to occur in frontal regions (Figure 10) (Barkan et al., 2019). Therefore, compared with neap tides, the divergence term F_{div} is stronger during spring tides in summer due to more and stronger submesoscale fronts being generated. In winter, submesoscale fronts are much less active than summer, hence F_{div} is small. In addition to F_{div}, the curl of vertical mixing F_{mix} is also a primary source for vertical vorticity. As shown in Figure 11, the magnitude of F_{mix} is comparable to F_{div}. During spring tides, large magnitude of F_{mix} mainly occurs in the regions with sharp changes of depth and behind headlands and islands.

In shallow waters, the sources of vertical mixing may come from surface and bottom frictions. The regions with large magnitude of F_{mix} are generally near the coasts (Figure 11), where water depth is less than 30 m. To explore the mechanisms for F_{mix}, two typical cross-front sections during maximum

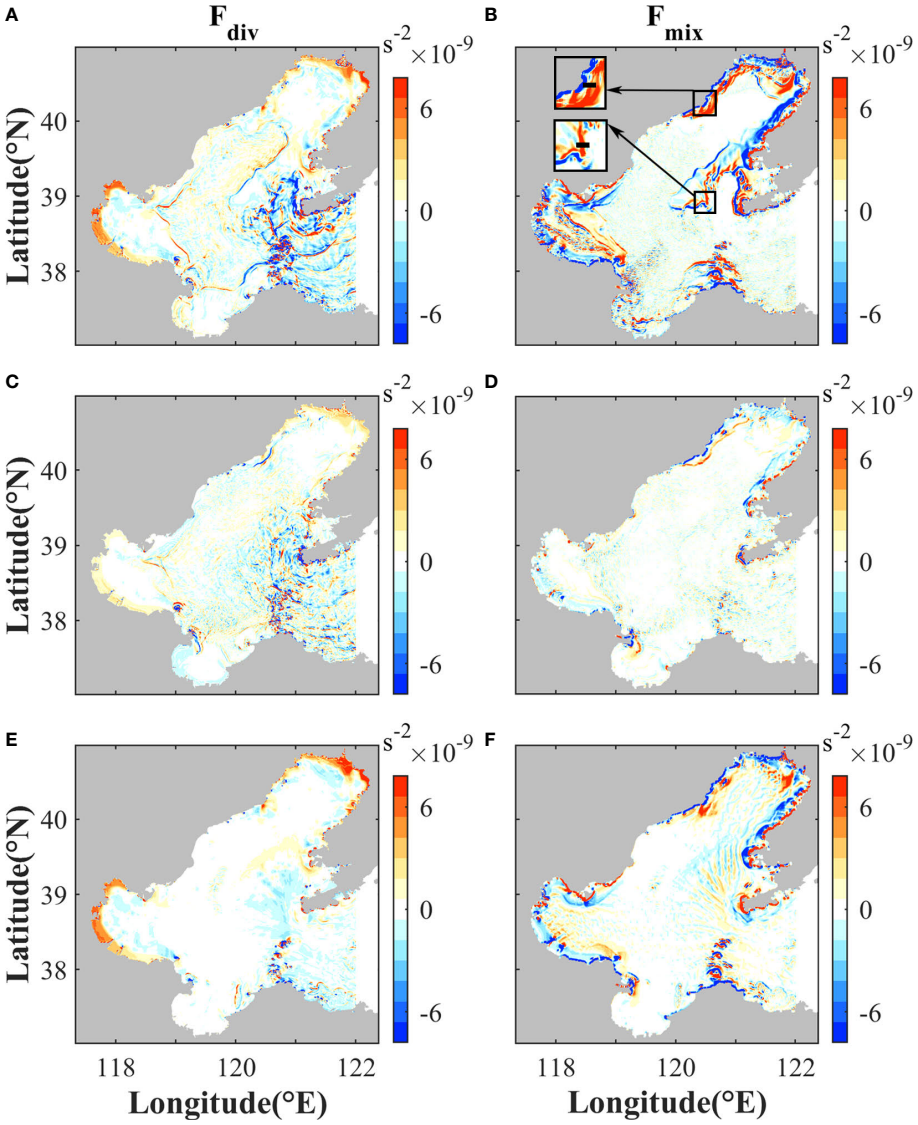

FIGURE 11
Magnitudes of **(A, C, E)** F_{div} and **(B, D, F)** F_{mix} in Eq. (4) during (top) maximum spring tide and (middle) minimum neap tide in summer, and (bottom) maximum spring tide in winter. The time is the same as Figure 10. The subplots are used to show the locations of sections in Figure 12.

spring tide in summer are selected to study the vertical variation of shear stress. The magnitude of shear stress is calculated by $\tau = A\sqrt{(\frac{\partial u}{\partial z})^2 + (\frac{\partial v}{\partial z})^2}$, where A indicates the vertical viscosity. As shown in Figure 12, shear stresses on both sides of the fronts decrease monotonically from bottom to surface, indicating that bottom friction dominates in the vertical mixing. Wind-induced friction does not dominate because there is no local maximum of shear stress at surface.

Across the front in the coastal area of the Liaodong Bay, temperature is almost homogeneous vertically (Figures 12A, B). The horizontal gradient of shear stress near surface is mainly due to the change of water depth across the front. In the central of the Bohai Sea, there is no apparent change of water depth across the front (Figure 12C, D). However, water is strongly stratified in the eastern side and almost homogeneous in the western side. The strong stratification in the eastern side inhibits vertical propagation of the bottom shear stress, hence resulting in much smaller stress near surface than the western side. In both cases shown in Figure 12, the horizontal change of the near-surface shear stress across the fronts leads to the curl of vertical mixing, hence inducing vertical vorticity. Other sections across the fronts with large magnitudes of F_{mix} show similar results (not shown for brevity).

Therefore, bottom friction has an important effect on vorticity due to the limited water depth in coastal seas. The curl of bottom shear stress is related to the change of water depth near the coasts (O'Donnell, 2010; Wang et al., 2022), so the distribution of F_{mix} is related to the topographic changes to some extent. This is unlike the situation in the deep water regions, where surface friction induced by winds is generally more important than bottom friction for the generation of surface submesoscale motions (McWilliams et al., 2015).

During spring tides, the magnitude and curl of bottom stress are large due to strong tidal velocity. Thus, F_{mix} is strong to generate high vorticity in the regions with sharp changes of depth and behind headlands and islands. Once generated, high vorticities and fronts would be advected under the effects of background tidal currents. Due to the strong divergence and convergence in frontal regions, F_{div} also plays a primary role for further evolution of vorticity. After vorticity and fronts are advected away from the regions with sharp topographic changes, F_{mix} is no longer as important as F_{div}. This is why F_{mix} does not coincide with vorticity in the central Bohai Sea. During neap tides, due to weak tidal currents, the curl of vertical mixing is smaller than spring tides, so submesoscale motions are less active.

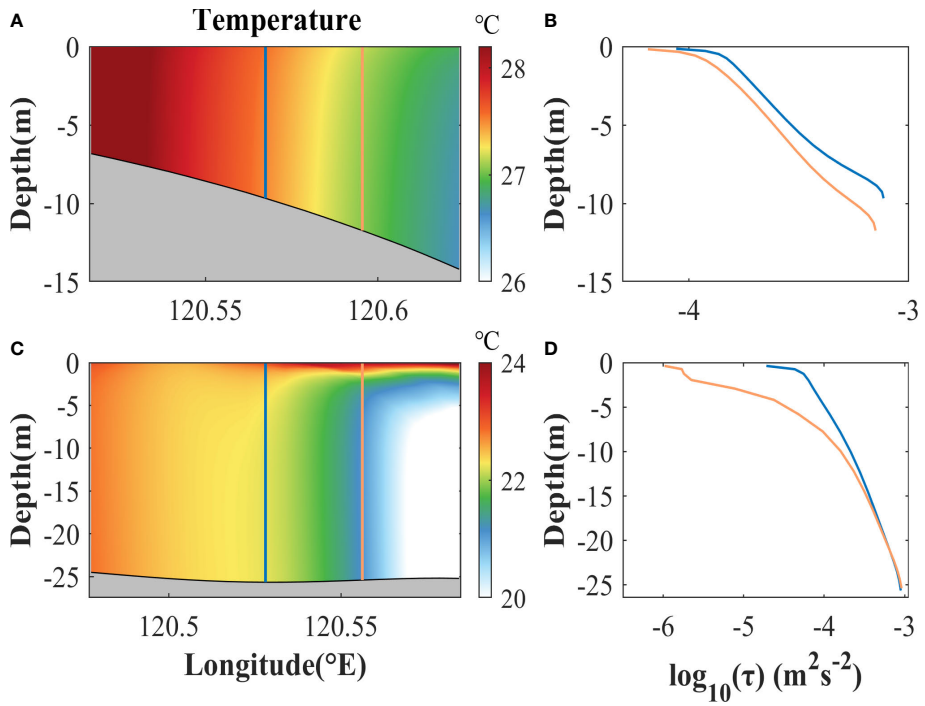

FIGURE 12
(A, B) Instantaneous fields of temperature and profiles of shear stresses in a cross-front section in the coastal area of the Liaodong Bay during maximum spring tide in summer. **(C, D)** as **(A, B)**, but indicate the results in a cross-front section in the central of the Bohai Sea. The locations of the profiles in **(B, D)** are corresponding to the blue and orange lines in **(A, C)**, respectively. The time is the same as the top panels of Figure 10. The locations of the vertical sections are shown as the black lines in the subplots of Figure 11B, respectively.

As for the seasonal variation, although the curl of bottom stress and vertical mixing are high during spring tides in winter, the magnitudes of F_{div} are much smaller than that in summer, so vorticities are much less active. Because F_{div} is related to fronts (McWilliams, 2016; Wang et al., 2021b), frontogenesis is analyzed in the following to study the mechanisms for the seasonal variation.

4.2 Frontogenesis

As discussed above, submesoscale fronts are much less active in winter than summer, and this is the main reason for lower vorticity. Frontogenesis is associated with the evolution processes of horizontal buoyancy and velocity gradients (McWilliams, 2021; Wang et al., 2021b). In previous studies on submesoscale motions, the frontogenetic tendency equation for horizontal buoyancy gradients has been demonstrated to be informative for frontogenesis of submesoscale fronts and filaments (Gula et al., 2014; Barkan et al., 2019). To find out the reasons for seasonal variation of submesoscale structures and get further detailed information about the mechanism responsible for fronts, we calculate the terms in the Lagrangian frontogenetic tendency equation to study the sources and sinks of the horizontal buoyancy gradients. In the present study, the frontogenetic tendency equation for horizontal buoyancy gradient $|\nabla_h b|$ is applied, which can be derived by taking horizontal derivatives of the tracer transport equations. The frontogenetic tendency equation for horizontal buoyancy gradient can be written as

$$\frac{1}{2}\frac{D|\nabla_h b|^2}{Dt} = \underbrace{\left[-u_x b_x^2 - v_y b_y^2 - \left(u_y + v_x\right) b_x b_y\right]}_{T_{adv}} \underbrace{- b_z \nabla_h w \cdot \nabla_h b}_{T_w} + \underbrace{\nabla_h \left[\frac{\partial}{\partial z}\left(K_z \frac{\partial b}{\partial z}\right)\right] \cdot \nabla_h b}_{T_{dv}} + \underbrace{\nabla_h [D_h] \cdot \nabla_h b}_{T_{dh}} \tag{5}$$

where $\frac{1}{2}\frac{D|\nabla_h b|^2}{Dt}$ indicates the time rate of change of horizontal buoyancy gradient in a Lagrangian reference frame (Gula et al., 2014). The right-side terms of the equation include horizontal advection term T_{adv}, vertical advection term T_w, vertical mixing term T_{dv}, and horizontal mixing term T_{dh}. The symbols (u, v, w) indicate the velocity components in the three-dimensional field; subscripts (x, y, z) indicate horizontal and vertical derivatives; K indicates parameterized vertical diffusivity; D_h indicates the horizontal buoyancy diffusion. Snapshots of the primary tendency terms are shown in Figure 13. It is found that horizontal mixing term T_{dh} is not dominant, so it is not shown.

The spatial distributions of the three tendency terms are basically consistent with the submesoscale indicators (Figure 10). Frontogenetic tendency terms near the estuaries are high due to high $|\nabla_h b|$. The tendency terms are much greater in summer than those in winter (Figure 13). All of the three terms could be positive or negative in different parts of the fronts (Figure 13), indicating that they could be frontogenetic or frontolytic. We account for the contributions of the three terms to frontogenesis, and find that their contributions are comparable during summer. While during winter, frontogenesis is mainly induced by the horizontal advection and vertical mixing terms near the coasts.

Horizontal advection term T_{adv} represents the effects of horizontal strain field on sharpening or weakening the preexisting horizontal buoyancy gradients. Although the convergence associated with secondary circulations plays a primary role in the horizontal strain field when fronts have been formed, horizontal velocity strain is generally induced by the deformation of background currents when fronts are triggered at early stage (Barkan et al., 2019; Wang et al., 2021b). Therefore, to induce T_{adv} at early stage, there should be preexisting background horizontal buoyancy gradients and deformation of background currents. Compared with winter, there is much more horizontal density variance in summer (Figure 14). This is mainly attributed to two reasons. First, the high river runoff induces high salinity and density variance near the river mouths in summer, while runoff is low during winter. Second, cold water intrudes into the central Bohai Sea from the Bohai Strait in summer (Figure 5), and induces high temperature and density variance in the Bohai Strait and central Bohai Sea. Therefore, although the strength of surface currents in winter is comparable to that in summer and the topography would induce strong flow deformation (Figure 14), fronts are easier to be triggered under the effects of T_{adv} in summer due to stronger background horizontal density variance. After fronts are generated, the convergence at fronts will have positive feedback to T_{adv}, resulting in further sharpening the fronts (Barkan et al., 2019; Wang et al., 2021b).

Vertical advection and mixing terms (T_w and T_{dv}) represent the effects of horizontal gradients of vertical velocity and mixing in transforming buoyancy gradient from a vertical direction to horizontal direction, respectively. Thus, vertical buoyancy (density) gradient is primary for inducing T_w and T_{dv}. As shown in Figures 14B, D, the vertical density gradient in summer is much stronger than that in winter, so it could provide more sources for inducing T_w and T_{dv}. In addition, the sharp horizontal changes of stratification in summer are mostly consistent with the regions where fronts occur, indicating the important roles of the vertical processes in frontogenesis.

As discussed above, strong background horizontal and vertical density gradients in summer provide favorable conditions for frontogenesis under the effects of T_{adv}, T_w, and T_{dv}. As fronts are generated and evolve, the convegence and divergence near fronts will have effects on the magnitude of vertical vorticity. Therefore, compared to winter, more and

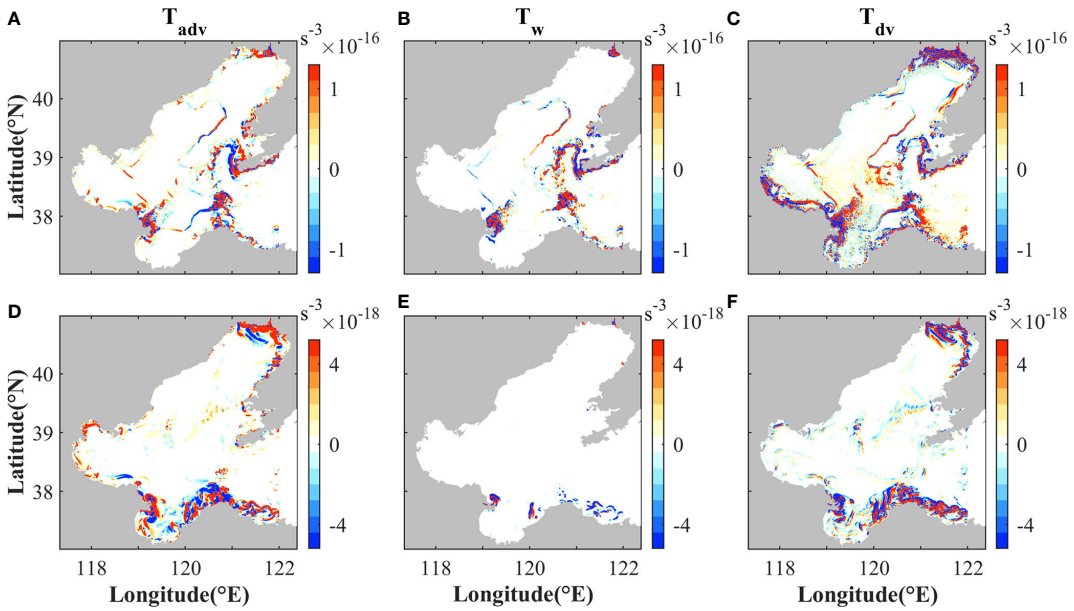

FIGURE 13
Magnitudes of the frontogenetic tendency terms **(A, D)** T_{adv}, **(B, E)** T_w, and **(C, F)** T_{dv} in Eq. (5) during (top) maximum spring tide in summer and (bottom) winter. The corresponding time is noted in Figure 9A.

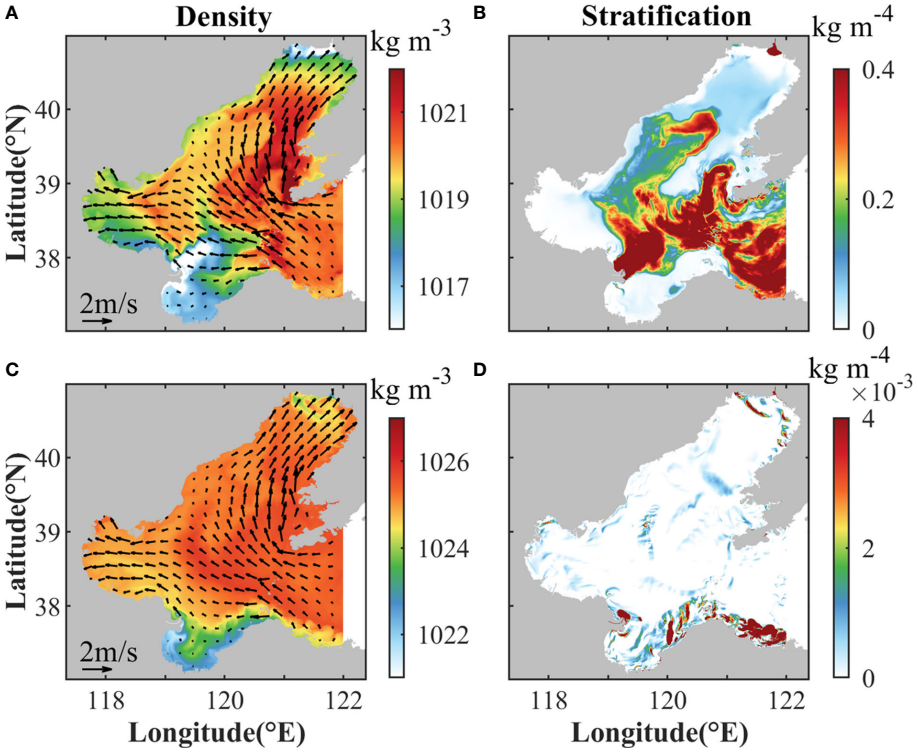

FIGURE 14
(A, C) Surface density and **(B, D)** stratification in the upper layer during (top) maximum spring tide in summer and (bottom) winter. The time is the same as Figure 13. The arrows in **(A, C)** indicate horizontal velocities in the upper layer. Stratification is quantified as the absolute value of vertical density gradient between surface and 5 m depth.

stronger fronts are generated in summer and induce stronger divergence term F_{div} for generating vertical vorticity.

5 Conclusions

In this study, a high-resolution numerical simulation is conducted to investigate the temporal and spatial characteristics of submesoscale motions in the Bohai Sea and explore their mechanisms.

The results reveal that submesoscale structures are mainly in the shallow coastal waters, the Bohai Strait, the regions near the islands and estuaries, and mostly tend to be parallel to the isobaths. These features agree well with the temperature gradient and frontal probability based on remote sensing data. Periodic variations of submesoscale motions are closely related to the periods or double of the periods of the main tidal constituents and spring-neap cycles in the Bohai Sea. The seasonal variations are also apparent, with more active submesoscale motions in summer.

One prominent feature of the submesoscale motions is that vertical vorticity is close to *f*. Through the vertical vorticity equation, it is found that the divergence and vertical mixing terms are primary sources for vertical vorticity. The curl of vertical mixing is large due to strong tidal velocity during spring tides in summer, resulting in more active submesoscale motions than neap tides. Despite of large curl of vertical mixing during spring tides in winter, the magnitudes of the divergence term are much smaller than that in summer. Based on the Lagrangian frontogenetic tendency equation, it is found that strong background horizontal and vertical density variance in summer provide more sources for inducing primary tendency terms, leading to more and stronger submesoscale fronts. The divergence and convergence near fronts enhance the magnitudes of vorticity. Therefore, compared to summer, submesoscale fronts are less active in winter.

Being different from the deep sea, tides and bottom friction are found to play important roles in the variability of submesoscale motions. The model horizontal resolution is 500 m, which is much larger than the water depth, so the hydrostatic approximation of the model is approximately valid for the submesoscale motions (Barkan et al., 2017). In future, it is of interest to explore the motions of finer spatial scales with nonhydrostatic models. With the increasing model resolutions, more detailed submesoscale processes are expected to be resolved. In this study, only the general characteristics and mechanisms of submesoscale motions in the Bohai Sea are investigated, while detailed analysis is not done for individual fronts or filaments. Further analysis will be conducted in the near future to show more detailed submesoscale dynamics in different local regions of the Bohai Sea.

Data availability statement

The raw data supporting the conclusions of this article will be made available by the authors, without undue reservation.

Author contributions

TW conceived the work. XS performed the model simulations. XS and TW conducted analyses and drafted the manuscript. YW gave input to the analysis process. All authors contributed to the article and approved the submitted version.

Funding

This study is supported by the National Natural Science Foundation of China (42076006) and the National Natural Science Foundation of China-Shandong Joint Fund (U2106204).

Acknowledgments

The authors thank Peng Zhao and Rui Li for providing the NEMO model outputs to build the open boundary conditions.

Conflict of interest

The authors declare that the research was conducted in the absence of any commercial or financial relationships that could be construed as a potential conflict of interest.

Publisher's note

References

Barkan, R., McWilliams, J. C., Molemaker, J., Choi, J., Srinivasan, K., Shchepetkin, A. F., et al. (2017). Submesoscale dynamics in the northern gulf of mexico. PartII: temperature-salinity relations and cross shelf transport processes. *J. Phys. Oceanogr.* 47, 2347–2361. doi: 10.1175/JPO-D-17-0040.1

Barkan, R., Molemaker, M. J., Srinivasan, K., McWilliams, J. C., and D'Asaro, E. (2019). The role of horizontal divergence in submesoscale frontogenesis. *J. Phys. Oceanogr.* 49, 1593–1618. doi: 10.1175/JPO-D-18-0162.1

Boccaletti, G., Ferrari, R., and Fox-Kemper, B. (2007). Mixed layer instabilities and restratification. *J. Phys. Oceanogr.* 37, 2228–2250. doi: 10.1175/JPO3101.1

Callies, J., Ferrari, R., Klymak, J. M., and Gula, J. (2015). Seasonality in submesoscale turbulence. *Nat. Commun.* 6, 1–8. doi: 10.1038/ncomms7862

Capet, X., McWilliams, J. C., Molemaker, M. J., and Shchepetkin, A. F. (2008). Mesoscale to submesoscale transition in the California current system. part III: Energy balance and flux. *J. Phys. Oceanogr.* 38, 2256–2269. doi: 10.1175/2008JPO3810.1

Castelao, R. M., and Wang, Y. (2014). Wind-driven variability in sea surface temperature front distribution in the California current system. *J. Geophys. Res. Oceans* 119, 1861–1875. doi: 10.1002/2013JC009531

Chen, D.Editorial Board for Marine Atlas (1993). *Marine atlas of bohai Sea, yellow Sea and East China Sea (Hydrology)* (Beijing: China Ocean Press).

Choi, B. H., Kim, K. O., and Eum, H. M. (2002). Digital bathymetric and topographic data for neighboring seas of Korea. *J. Korean Soc Coast. Ocean Eng.* 14, 41–50.

D'Asaro, E. A. (1988). Generation of submesoscale vortices: A new mechanism. *J. Geophys. Res.* 93, 6685–6693. doi: 10.1029/JC093iC06p06685

D'Asaro, E. A., Shcherbina, A. Y., Klymak, J. M., Molemaker, J., Novelli, G., Guigand, C. M., et al. (2018). Ocean convergence and the dispersion of flotsam. *Proc. Natl. Acad. Sci.* 115, 1162–1167. doi: 10.1073/pnas.1718453115

Dauhajre, D., and McWilliams, J. C. (2018). Diurnal evolution of submesoscale front and filament circulations. *J. Phys. Ocean.* 48, 2343–2361. doi: 10.1175/JPO-D-18-0143.1

Dauhajre, D. P., McWilliams, J. C., and Uchiyama, Y. (2017). Submesoscale coherent structures on the continental shelf. *J. Phys. Oceanogr.* 47, 2949–2976. doi: 10.1175/JPO-D-16-0270.1

Dong, J., Fox-Kemper, B., Zhang, H., and Dong, C. (2020). The seasonality of submesoscale energy production, content, and cascade. *Geophys. Res. Lett.* 47, 2020GL087388. doi: 10.1029/2020GL087388

Esposito, G., Berta, M., Centurioni, L., Johnston, H., Lodise, G., Özgökmen, T., et al. (2021). Submesoscale vorticity and divergence in the alboran Sea: Scale and depth dependence. *Front. Mar. Sci.* 8. doi: 10.3389/fmars.2021.678304

Fairall, C. W., Bradley, E. F., Rogers, D. P., Edson, J. B., and Young, G. S. (1996). Bulk parameterization of air-sea fluxes for tropical ocean-global atmosphere coupled-ocean atmosphere response experiment. *J. Geophys. Res. Oceans* 101, 3747–3764. doi: 10.1029/95JC03205

Fox-Kemper, B., Ferrari, R., and Hallberg, R. (2008). Parameterization of mixed layer eddies. part I: Theory and diagnosis. *J. Phys. Oceanogr.* 38, 1145–1165. doi: 10.1175/2007JPO3792.1

Gula, J., Molemaker, M. J., and McWilliams, J. C. (2014). Submesoscale cold filaments in the gulf stream. *J. Phys. Oceanogr.* 44, 2617–2643. doi: 10.1175/JPO-D-14-0029.1

Gula, J., Molemaker, M. J., and McWilliams, J. C. (2016). Topographic generation of submesoscale centrifugal instability and energy dissipation. *Nat. Commun.* 7, 12811. doi: 10.1038/ncomms12811

Hickox, R., Belkin, I., Cornilion, P., and Shan, Z. (2000). Climatology and seasonal variability of ocean fronts in the East China, yellow and bohai seas from satellite SST data. *Geophys. Res. Lett.* 27, 2945–2948. doi: 10.1029/1999GL011223

Hoskins, B. J. (1982). The mathematical theory of frontogenesis. *Annu. Rev. Fluid Mech.* 14, 131–151. doi: 10.1146/annurev.fl.14.010182.001023

Hu, C., Muller-Karger, F. E., Taylor, C., Carder, K. L., Kelble, C., Johns, E., et al. (2005). Red tide detection and tracing using MODIS fluorescence data: A regional example in SW Florida coastal waters. *Remote Sens. Environ.* 97, 311–321. doi: 10.1016/j.rse.2005.05.013

Large, W. G., McWilliams, J. C., and Doney, S. C. (1994). Oceanic vertical mixing: A review and a model with a nonlocal boundary layer parameterization. *Rev. Geophys.* 32, 363–403. doi: 10.1029/94RG01872

Lévy, M., Franks, P., and Smith, K. (2018). The role of submesoscale currents in structuring marine ecosystems. *Nat. Commun.* 9, 1–16. doi: 10.1038/s41467-018-07059-3

Lévy, M., Klein, P., and Treguier, A. (2001). Impact of sub-mesoscale physics on production and subduction of phytoplankton in an oligotrophic regime. *J. Mar. Res.* 59, 535–565. doi: 10.1357/002224001762842181

Li, X., Lorenz, M., Klingbeil, K., Chrysagi, E., Gräwe, U., Wu, J., et al. (2022). Salinity mixing and diahaline exchange flow in a large multi-outlet estuary with islands. *J. Phys. Oceanogr.* 52, 2111–2127. doi: 10.1175/JPO-D-21-0292.1

Li, R., Lu, Y., Hu, X., Guo, D., Zhao, P., Wang, N., et al. (2020). Space-time variations of sea ice in bohai Sea in the winter of 2009-2010 simulated with a coupled ocean and ice model. *J. Oceanogr.* 77, 243–258. doi: 10.1007/s10872-020-00566-2

Liu, G., Bracco, A., and Sitar, A. (2021). Submesoscale mixing across the mixed layer in the gulf of Mexico. *Front. Mar. Sci.* 8. doi: 10.3389/fmars.2021.615066

Li, X., Yuan, C., and Li, Y. (2013). Remote sensing monitoring and spatial-temporal variation of Bohai Bay coastal zone. *Remote Sens. Land Resour.* 25, 156–163. doi: 10.6046/gtzyyg.2013.02.26

Mahadevan, A. (2016). The impact of submesoscale physics on primary productivity of plankton. *Annu. Rev. Mar. Sci.* 8, 161–184. doi: 10.1146/annurev-marine-010814-015912

McWilliams, J. C. (2016). Submesoscale currents in the ocean. *Proc. R. Soc A: Math. Phys. Eng. Sci.* 472, 20160117. doi: 10.1098/rspa.2016.0117

McWilliams, J. C. (2021). Oceanic frontogenesis. *Annu. Rev. Mar. Sci.* 13, 227–253. doi: 10.1146/annurev-marine-032320-120725

McWilliams, J. C., Gula, J., Molemaker, M. J., Renault, L., and Shchepetkin, A. F. (2015). Filament frontogenesis by boundary layer turbulence. *J. Phys. Oceanogr.* 45, 1988–2005. doi: 10.1175/JPO-D-14-0211.1

McWilliams, J. C., Molemaker, M. J., and Olafsdottir, E. I. (2009). Linear fluctuation growth during frontogenesis. *J. Phys. Oceanogr.* 39, 3111–3129. doi: 10.1175/2009JPO4186.1

O'Donnell, J. (2010). "The dynamics of estuary plumes and fronts," in *Contemporary issues in estuarine physics*. Ed. A. V. Levinson (Cambridge, UK: Cambridge University Press), 186–246. doi: 10.1017/CBO9780511676567.009

Poje, A. C., Özgökmen, T. M., Lipphardt, B. L.Jr., Haus, B. K., Ryan, E. H., Haza, A. C., et al. (2014). Submesoscale dispersion in the vicinity of the deepwater horizon spill. *Proc. Natl. Acad. Sci.* 111, 12693–12698. doi: 10.1073/pnas.1402452111

Ralston, D. K., Geyer, W. R., and Lerczak, J. A. (2010). Structure, variability, and salt flux in a strongly forced salt wedge estuary. *J. Geophys. Res.* 115, C06005. doi: 10.1029/2009JC005806

Thomas, L. N., Tandon, A., and Mahadevan, A. (2008). Submesoscale processes and dynamics. *Ocean Model. Eddy. Reg.* 177, 17–38. doi: 10.1029/177GM04

Wang, T., Barkan, R., McWilliams, J. C., and Molemaker, M. J. (2021b). Structure of submesoscale fronts of the Mississippi river plume. *J. Phys. Oceanogr.* 51, 1113–1131. doi: 10.1175/JPO-D-20-0191.1

Wang, Y., Castelao, R. M., and Yuan, Y. (2015). Seasonal variability of alongshore winds and sea surface temperature fronts in Eastern boundary current systems. *J. Geophys. Res. Oceans* 120, 2385–2400. doi: 10.1002/2014JC010379

Wang, T., Chai, F., Xing, X., Ning, J., Jiang, W. S., and Riser, S. (2021a). Influence of multi-scale dynamic on the nitrate distribution around the kuroshio extension: An investigation based on BGC-argo and satellite data. *Prog. Oceanogr.* 193, 102543. doi: 10.1016/j.pocean.2021.102543

Wang, T., Zhao, S., Zhu, L., McWilliams, J. C., Galgani, L., Amin, R. M., et al. (2022). Accumulation, transformation and transport of microplastics in estuarine fronts. *Nat. Rev. Earth Environ* 3, 795-805. doi: 10.1038/s43017-022-00349-x

Warner, J. C., Geyer, W. R., and Lerczak, J. A. (2005). Numerical modeling of an estuary: A comprehensive skill assessment. *J. Geophys. Res. Oceans* 110, C05001. doi: 10.1029/2004JC002691

Wei, H., Hainbucher, D., Pohlmann, T., Feng, S., and Suendermann, J. (2004). Tidal-induced Lagrangian and eulerian mean circulation in the bohai Sea. *J. Mar. Syst.* 44, 141–151. doi: 10.1016/j.jmarsys.2003.09.007

Wei, H., Zhang, H., Yang, W., Feng, J., and Zhang, C. (2020). "The changing bohai and yellow seas: a physical view," in *Changing Asia-pacific marginal seas*. Eds. C.-T. A. Chen and X. Guo (Singapore: Springer Singapore), 105–120. doi: 10.1007/978-981-15-4886-4_7

Wilmott, C. J. (1981). On the validation of models. *Phys. Geogr.* 2, 184–194. doi: 10.1080/02723646.1981.10642213

Yu, X., Guo, X., and Takeoka, H. (2016). Fortnightly variation in the bottom thermal front and associated circulation in a semienclosed sea. *J. Phys. Oceanogr.* 46, 159–177. doi: 10.1175/JPO-D-15-0071.1

Yu, J., Zhang, X., Feng, Y., Jiang, W., and Deng, F. (2021). Analysis of tidal-induced connectivity among coastal regions in the bohai Sea using the complex network theory. *Estuar. Coast. Shelf Sci.* 260, 107506. doi: 10.1016/j.ecss.2021.107506

Zhan, P., Guo, D., Krokos, G., Dong, J., Duran, R., and Hoteit, I. (2022). Submesoscale processes in the upper red Sea. *J. Geophys. Res. Oceans* 127, e2021JC018015. doi: 10.1029/2021JC018015

Zhang, G., Wei, H., Xiao, J., Zhang, H., and Li, Z. (2020). Variation of tidal front position in liaodong bay during summer 2017. *Oceanol. Limnol. Sin.* 51, 1–12. doi: 10.11693/hyhz20190600110

Zhao, B., Cao, D., Li, W., and Wang, Q. (2001). Tidal mixing characters and tidal fronts phenomenons in the Bohai Sea. *Acta Oceanol. Sin.* 23, 113–120. doi: 10.3321/j.issn:0253-4193.2001.04.015

Zhao, L., and Wei, H. (2005). The influence of physical factors on the variation of phytoplankton and nutrients in the bohai Sea. *J. Oceanogr.* 6, 335–342. doi: 10.1007/s10872-005-0044-0

frontiers | Frontiers in Marine Science

TYPE Original Research
PUBLISHED 29 November 2022
DOI 10.3389/fmars.2022.1080314

OPEN ACCESS

EDITED BY
Shi-Di Huang,
Southern University of Science and Technology, China

REVIEWED BY
Shuang-Xi Guo,
South China Sea Institute of Oceanology, Chinese Academy of Sciences (CAS), China
Jin-Han Xie,
Peking University, China

*CORRESPONDENCE
Chan Joo Jang
cjjang@kiost.ac.kr
Fuad Azminuddin
fuad.azminuddin@gmail.com

SPECIALTY SECTION
This article was submitted to Physical Oceanography, a section of the journal Frontiers in Marine Science

RECEIVED 26 October 2022
ACCEPTED 16 November 2022
PUBLISHED 29 November 2022

CITATION
Azminuddin F, Jang CJ and Jeon D (2022) Destination of New Guinea Coastal Undercurrent in the western tropical Pacific: Variability and linkages.
Front. Mar. Sci. 9:1080314.
doi: 10.3389/fmars.2022.1080314

Destination of New Guinea Coastal Undercurrent in the western tropical Pacific: Variability and linkages

Fuad Azminuddin[1,2]*, Chan Joo Jang[1,2]* and Dongchull Jeon[2]

[1]Department of Oceanography, University of Science and Technology, Daejeon, South Korea, [2]Ocean Circulation Research Division, Korea Institute of Ocean Science and Technology, Busan, South Korea

The New Guinea Coastal Undercurrent (NGCUC) is considered a bottleneck in the western tropical Pacific (WTP), carrying upper-to-intermediate waters from the south to the northwestern Pacific, thereby playing a fundamen
tal role in the interhemispheric water mass exchange. However, how the NGCUC links to the circulation in the WTP was insufficiently studied. This work explores the destination of NGCUC waters, its spatiotemporal changes, and possible physical processes linked with the downstream NGCUC using ocean reanalysis for 22 years (1994 – 2015). Lagrangian particle tracking discloses eight major destinations of the NGCUC: The Equatorial Undercurrent (EUC, 35.26%), the North Equatorial Countercurrent (NECC, 12.3%), the North (13.33%) and South (8.85%) Subsurface Countercurrents, the Equatorial Deep Jet (11.49%), the Mindanao Undercurrent (13.24%), and the Indonesian (3.47%) and Halmahera (0.86%) Throughflows. The NGCUC waters are distributed mainly to the east (81.65%) and their dissemination varies markedly with depth. These destinations exhibit significant variations on seasonal and interannual time scales. The NGCUC strengthens (weakens) during summer (winter) and more NGCUC waters are distributed westward and northeastward (eastward). Interannually, the distribution of the NGCUC water is influenced by El Niño-Southern Oscillation, in which most of its eastward-distributed waters shift northward (equatorward) in El Niño (La Niña) phase joining the strengthened NECC (EUC). Changes in the NGCUC water destination can transform the water mass properties in the WTP. The findings of this study also emphasize the fundamental role of eddies in trapping and redistributing the NGCUC waters and linking the currents in the WTP.

KEYWORDS

New Guinea Coastal Undercurrent, seasonal variability, interannual variability, undercurrent linkage, Lagrangian particle tracking

1 Introduction

The western tropical Pacific (WTP) is the home of the largest area of permanent warm water (>28°C) in the world ocean, which is so-called western Pacific warm pool (Hu et al., 2020), and is characterized by the complex ocean circulation including the narrow alternating zonal flows and intense boundary current system, namely the Pacific western boundary currents (WBC) (Hu and Cui, 1991; Hu et al., 2020). The east coast of the Philippines and the north coast of New Guinea Island are two regions in the WTP with prominent boundary currents at both surface and subsurface layers. The Pacific WBC includes the Kuroshio Current (KC), Mindanao Current (MC), and New Guinea Coastal Current (NGCC) at the upper layer, and the Luzon Undercurrent, Mindanao Undercurrent (MUC), and New Guinea Coastal Undercurrent (NGCUC) below the thermocline (see Figure 1).

The WTP has also rich eddy activity. There are two prominent surface eddies, i.e., Mindanao Eddy (ME) and Halmahera Eddy (HE), in which nonlinearity on a β plane is previously suggested as the possible mechanism responsible for their establishment (Arruda and Nof, 2003). The ME and HE are thought to be quasi-stationary eddies with cyclonic and anticyclonic polarities, respectively, and are located at the retroflection points of the MC and NGCC/NGCUC, respectively, connecting these equatorward WBC with the eastward-flowing North Equatorial Countercurrent (NECC) (Kashino et al., 2013). Below the surface, there are, at least, two groups of subthermocline eddies (SEs): one is originated from the central Pacific and the other is originated from the New Guinea coast (e.g., Chiang and Qu, 2013; Chiang et al., 2015). In addition, a recent study has suggested that there is a distinct anticyclonic SE southeast of Mindanao Island (Azminuddin et al., 2022). Less is known about its characteristics and driving mechanism. While its presence remains uncertain, the establishment of this eddy feature is possibly due to the tilting of HE poleward with increasing depth (Qu et al., 1999; Kashino et al., 2013). In this study, the westward-propagating SEs, the anticyclonic SE southeast of Mindanao Island, and the northwestward-propagating SEs from the New Guinea Coast are then called SE(s)-1, SE-2, and SE(s)-3, respectively (see Figure 1).

It has been largely known that the WTP is a meeting place for intermediate waters. There are the northern, southern, and equatorial Pacific-sourced intermediate waters (Bingham and Lukas, 1994; Max et al., 2016). The NGCUC serves as the primary throughflow that transfers the South Pacific waters, e.g., South Pacific Tropical Water (SPTW) and Antarctic Intermediate Water (AAIW), into the northwestern tropical Pacific through the Vitiaz Strait, crossing the equator near 140°E and influencing the intermediate water properties and heat content in the North Pacific (e.g., Fine et al., 1994; Wang and Hu, 1998; Qu and Lindstrom, 2004; Kawabe et al., 2008; Hu et al., 2015). But the complexity of the current system in the WTP has made it challenging to accurately investigate how the South Pacific waters spread out over the northwestern Pacific.

Studies have confirmed that a large part of water masses carried by NGCUC are transported eastward mainly through Equatorial Undercurrent (EUC) and Northern Subsurface Countercurrent (NSCC), in which the NGCUC splits into some branches at different depths in the region between Mindanao and New Guinea (Wang et al., 2016b; Li et al., 2020; Zhang et al., 2020; Li et al., 2021). The eastward-flowing EUC centered around the equator over a depth range of 100 – 300 m, while NSCC lies just north of EUC and south of 4°N at the deeper layer around the depths of 200 – 600 m (Wang et al.,

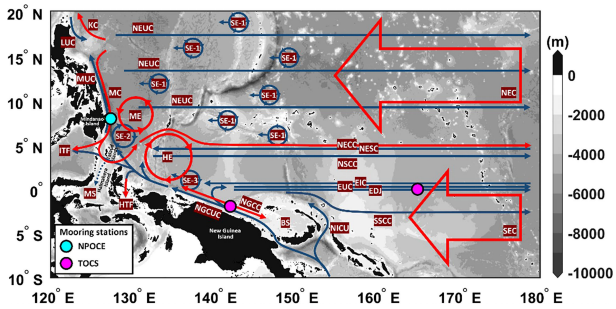

FIGURE 1
General pattern of the surface (red arrows) and subsurface (blue arrows) currents and eddies in the tropical western Pacific. The surface currents and eddies are the NEC (North Equatorial Current), the KC (Kuroshio Current), the MC (Mindanao Current), the NECC (North Equatorial Countercurrent), the SEC (South Equatorial Current), the NGCC (New Guinea Coastal Current), the ITF (Indonesian Throughflow), HTF (Halmahera Throughflow), the HE (Halmahera Eddy), and the ME (Mindanao Eddy). The subsurface currents and eddies are the NEUC (North Equatorial Undercurrent), the LUC (Luzon Undercurrent), the MUC (Mindanao Undercurrent), the NESC (North Equatorial Subsurface Current), the NSCC (North Subsurface Countercurrent), the EUC (Equatorial Undercurrent), EIC (Equatorial Intermediate Current), EDJ (Equatorial Deep Jets), the NGCUC (New Guinea Coastal Undercurrent), the NICU (New Ireland Coastal Undercurrent), the SE-1 (westward-propagating Subthermocline Eddy), the SE-2 (anticyclonic Subthermocline Eddy southeast of Mindanao Island), and the SE-3 (northwestward-propagating Subthermocline Eddy). The colored circles indicate the ADCPs mooring stations. The color shading indicates bathymetry (m).

2016b; Song et al., 2018). In addition, using Lagrangian trajectory computation Wang et al. (2019) suggested that the NGCUC water is also partly distributed into NECC at the shallower depth centered around 100 m.

While most of the NGCUC waters are transferred eastward, some portions are also distributed poleward through MUC. Some studies have made it evident that South Pacific water, i.e., AAIW, exists east of the Mindanao coast (e.g., Qu and Lindstrom, 2004). The NGCUC strengthening, topographic features, and SEs are hypothesized to facilitate their connection (Qu et al., 2012; Wang et al., 2016a). Although the poleward distribution of AAIW through MUC has been widely investigated, to date, the pathway and underlying process of AAIW into MUC have not been properly established presumably owing to a lack of direct measurements in the subsurface. Furthermore, mechanisms responsible for the NGCUC water allocation into several major destinations, i.e., EUC, NSCC, NECC, MUC, etc., and how they change over time have not been researched intensively. In the present study, ocean reanalysis data is analyzed for investigating the fate of NGCUC waters, its spatiotemporal changes, and how the NGCUC links to the currents in the WTP. We also consider the possible impacts of eddies on this circulation system that was previously suggested (e.g., Chiang and Qu, 2013; Wang et al., 2014).

The following sections of this paper are organized as follows: Section 2 briefly describes the data and methods used for the present study. The main results are described in Section 3, which presents the data validations, describes the mean structure of the currents that are possibly connected to the NGCUC, investigates the destination of the NGCUC, their spatiotemporal changes, and explores their implications on the characteristics and transformation of waters in the WTP. Section 4 discusses the potential roles of eddies and the possible currents' linkages. Section 5 summarizes the outcomes of the present study.

2 Data and methods

2.1 Data

In this study, 22 years (from 1994 to 2015) of velocity data from three widely-used global ocean reanalysis datasets are utilized. They are the daily Global Ocean Reanalysis and Simulation Version 4 (GLORYS2V4) produced by Mercator Ocean (http://marine.copernicus.eu) (Lellouche et al., 2013), 3-daily Oceanic General Circulation Model for the Earth Simulator (OFES) that driven by National Centers for Environmental Prediction winds (http://apdrc.soest.hawaii.edu/las_ofes) (Sasaki et al., 2008), and 3-hourly Hybrid Coordinate Ocean Model (HYCOM) version 2.2.99DH, which is the Global Ocean Forecasting System 3.1, (http://www.hycom.org) (Chassignet et al., 2009). The GLORYS2V4 has a horizontal resolution of 0.25° and 75 vertical layers, with a layer thickness that increases gradually from 1 m near the surface to approximately 200 m in the deep layer. The OFES has a horizontal resolution of 0.1°, 54 vertical layers, and a vertical resolution of 5 m near the surface to approximately 330 m in the deep layer. While the HYCOM has a horizontal resolution of 1/12°, 41 vertical layers, and a vertical resolution of 2 m near the surface to approximately 1,000 m in the deep layer. Detailed descriptions of these models are available in the above respective links and research papers.

Also included in this study are moored acoustic Doppler current profiler (ADCP) datasets from the Northwestern Pacific Ocean Circulation and Climate Experiment (NPOCE) (http://npoce.org.cn/) and the Tropical Ocean Climate Study (TOCS) (http://www.jamstec.go.jp/) programs (see Figure 1) to validate the model outputs. One mooring from NPOCE was deployed at the east of Mindanao Island (8°N, 127.3°E) from 1 December 2010 to 7 December 2012. The moored ADCPs have recorded velocities from the near-surface down to the depth deeper than 1,200 m by using an upward- and a downward-looking 75 kHz ADCPs manufactured by Teledyne RD Instruments (TRDI) that were mounted on the mooring line at about 400 m. More details of this mooring can be found in Zhang et al. (2014). Two moorings, which are provided by TOCS, were deployed at the north of New Guinea Island (2°S, 142°E) from 12 July 1995 to 5 September 1998 and at the equatorial pacific (165°E) from 31 January 1997 to 8 July 2001. Both recorded velocities of upper ~300 m by using upward-looking 150 kHz ADCPs manufactured by TRDI. Detailed information on these two moorings can be obtained in Kuroda (2000) and Kutsuwada and McPhaden (2002), respectively. These three mooring stations were selected to validate the reanalyses and to provide observational evidence for the MUC, NGCUC, and EUC, respectively.

2.2 Methods

2.2.1 Lagrangian particle tracking and experimental design

One possible way to understand the destination of NGCUC is by tracing its water parcels. In the present study, the Lagrangian particle tracking method (LPTM) is applied to track water parcels that originate from the NGCUC region, assuming that the water parcels are passive tracers. Following Seo et al. (2020) but without the wind drift (since subsurface water parcels rather than floating objects at the surface), the trajectories of each tracer can be calculated as follows:

$$\vec{X}_{t+\Delta t} = \vec{X}_t + \int_t^{t+\Delta t} \vec{V}(X_t, t)dt + R\sqrt{2K_h\Delta t} \qquad (1)$$

where $\vec{X}_t$ is the tracer's position (x,y) at time t, Δt is the time interval (daily), $\vec{V}$ is the velocity of ocean current. The last term in (1) is a random walk component to resolve sub-grid scale phenomenon, e.g., submesoscale turbulent flow (North et al., 2006). R is a normally distributed random number between -1 and 1, and K_h is a horizontal diffusion coefficient using the

Smagorinsky diffusivity scheme (Smagorinsky, 1963),

$$K_h = A\Delta x\Delta y\sqrt{\left(\frac{\partial u}{\partial x}-\frac{\partial v}{\partial y}\right)^2+\left(\frac{\partial v}{\partial x}+\frac{\partial u}{\partial y}\right)^2} \quad (2)$$

where A is an adjustment constant defined as 0.02, and Δx and Δy are the grid spacing (Choi et al., 2018).

This method allows us to trace the destination (forward integration) of water parcels from the given initial position. To accurately calculate the travel distance, we applied the Runge-Kutta 4th-order method for time integration (Dormand and Prince, 1980). The particle tracking was calculated by using the output of ocean reanalysis data, which is spatially discretized into a grid structure. To estimate the trajectories of each tracer, the velocities that are closest to the corresponding tracer are interpolated using bilinear interpolation, and then the tracer's position is updated daily. If a tracer reaches a land grid, it is set to be reflected to the nearest ocean grid since it cannot be beached. The reliability of the LPTM is further discussed in Section 3.1.

Tracing a water parcel below the surface, which consists of horizontal and vertical movements, is rather complicated. Nevertheless, it is much easier to move along isopycnals than across them (diapycnal). Therefore, the water flow typically tends to follow isopycnal layers, although diapycnal advection sometimes occurs due to mixing (Ledwell et al., 1993). To more reliably track the tracers, we applied the LPTM along the potential density (σ_θ) surface rather than the depth surface. We selected several isopycnal layers that cover most of the NGCUC's vertical range and are expected to represent the typical depth of the NGCUC destinations, i.e., 23, 25, 26, 26.75, 27, and 27.2 σ_θ. Detailed descriptions of these layers will be provided in Section 3.2.

For each isopycnal layer, we released 50 tracers from the NGCUC region (see Figure 2 for the tracers' initial position). The tracers were released every day from 1994 to 2013 with the travel time of two years, which is limited by computing resources. So, a total of 365,250 tracers were simulated at each layer. Preliminary experiments using GLORYS2V4 suggested that there are eight major destinations of NGCUC. Five destinations are the zonally eastward currents including the EUC, the NECC, the NSCC, the Southern Subsurface Countercurrent (SSCC), and the Equatorial Deep Jet (EDJ). The rest are the western route including the poleward MUC and the western (via Sulawesi Sea) and eastern (via Halmahera Sea) passages of the Indonesian throughflow (ITF). In this study, the main passage at the western is called the ITF, while that at the eastern is called the Halmahera throughflow (HTF).

To classify the tracers' destination, we defined a section at each designated current. We selected the section along 8°N (Mindanao coast – 130°N), 125°E (1.5° – 6°N), and 1°S (128° – 130.5°E) for MUC, ITF, and HTF, respectively. For the eastern route, we located the section along the longitude of 160°E. Placing the section too western may be difficult to distinguish the currents as some of them are typically found merging or are not even clearly formed yet far western (see Figure 1). On the other hand, placing the section farther east needs more time to arrive especially the tracers at the deeper layers (i.e., 27 and 27.2 σ_θ), which may lead to reducing the number of tracers that are successfully classified. Please notice that the horizontal range of the same section could be disparate at the different layers and not all sections are defined in each isopycnal layer. It certainly depends on the currents' vertical and horizontal ranges. The location and range of the sections that represent the tracer's destination are provided in Figure 2.

3 Results

3.1 Validations of datasets

The reliability of the model results was first assessed by comparing them to observations and suggested that, overall, the models reproduce reasonably well the ADCP's velocity profiles and their variability (see Figure 3). However, some notable discrepancies are clearly shown in OFES and HYCOM as compared to the observations, especially in simulating the weakening (strengthening) of the eastward-flowing EUC during the strong El Niño-Southern Oscillation (ENSO) event in 1997 (1998) (Figures 3I, O). Moreover, HYCOM seems to overestimate the northward-flowing MUC (Figure 3M). In comparison, the velocity profiles of GLORYS2V4 are in better agreement with the observed velocities in all regions.

To further test the validity of the model results in representing the undercurrents, we compared their time series with that of the observations (Figure 4). We used monthly mean velocity data and selected the depths of 650, 200, and 150 m for the moored ADCP's location deployed at the MUC, NGCUC, and EUC regions, respectively (see Figure 3). Based on the data used in these time series, we applied Taylor diagram analysis (Taylor, 2001) to examine how well each model matches the observation using three distinct statistics, i.e., centered RMSD, correlation coefficient, and STD. In the Taylor diagram, the closer the model is to the observation, which is represented by the RMSD, the better the model approximates the observation. This method determines the error (RMSD) that comes from the discrepancies in pattern similarity (correlation) or from the discrepancies in variance (STD). The results of the Taylor diagram clearly show that the GLORYS2V4 is closest to the observations at the MUC and EUC regions with the correlation coefficient of more than 0.6 and 0.8, respectively (see Figures 4B, F). In the NGCUC region, all models well approximate the observation with the correlation of more than 0.7. The GLORYS2V4 is slightly higher correlation than others. But, in terms of variance, HYCOM is closest to the observation. However, in this region, HYCOM seems to underestimate the eastward-flowing NGCC (see Figure 3N).

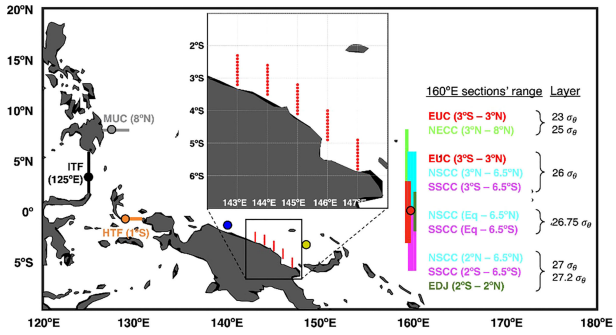

FIGURE 2
Experimental design of LPTM. The 50 red dots along the New Guinea coast are the locations where tracers were released. The color lines denote the location of the sections used to classify the tracers' major destinations. Color circles denote the locations that are selected to estimate θ -S diagrams.

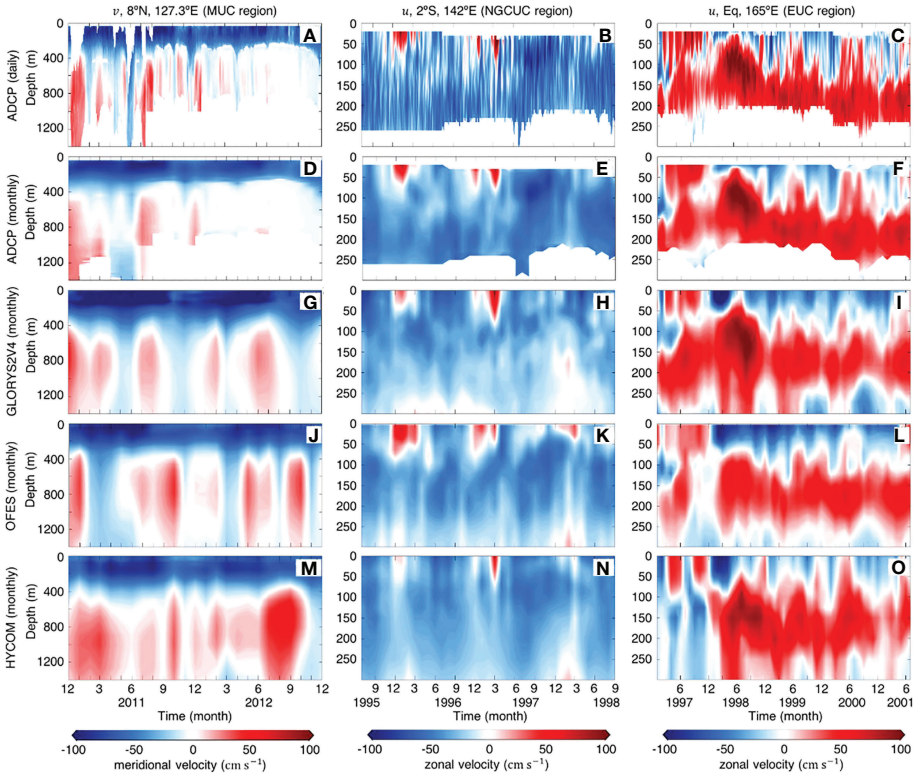

FIGURE 3
Time-depth sections of velocities (cm s^{-1}) from [first-row panels **(A-C)**] daily ADCPs, [second-row panels **(D-F)**] monthly ADCPs, [third-row panels **(G-I)**] monthly GLORYS2V4, [fourth-row panels **(J-L)**] monthly OFES, and [fifth-row panels **(M-O)**] monthly HYCOM at approximately (left panels) 8°N, 127.3°E, (middle panels) 2°S, 142°E, and (right panels) Equator, 165°E. The left, middle, and right panels are meridional, zonal, and zonal velocities, respectively.

While the OFES and HYCOM datasets have been extensively used in a number of earlier studies to investigate ocean circulation in the WP (e.g., Chiang and Qu, 2013; Wang et al., 2016b; Nan et al., 2019; Wang et al., 2019; Zhang et al., 2020; Zhang et al., 2021), the GLORYS2V4 is less utilized in this region. Nevertheless, our results have shown that among the models GLORYS2V4 best approximates the observations in three different regions and thereby reasonably well reproduces the regional circulation around the WP. Therefore, we believe that the results of this study can provide a better view of the

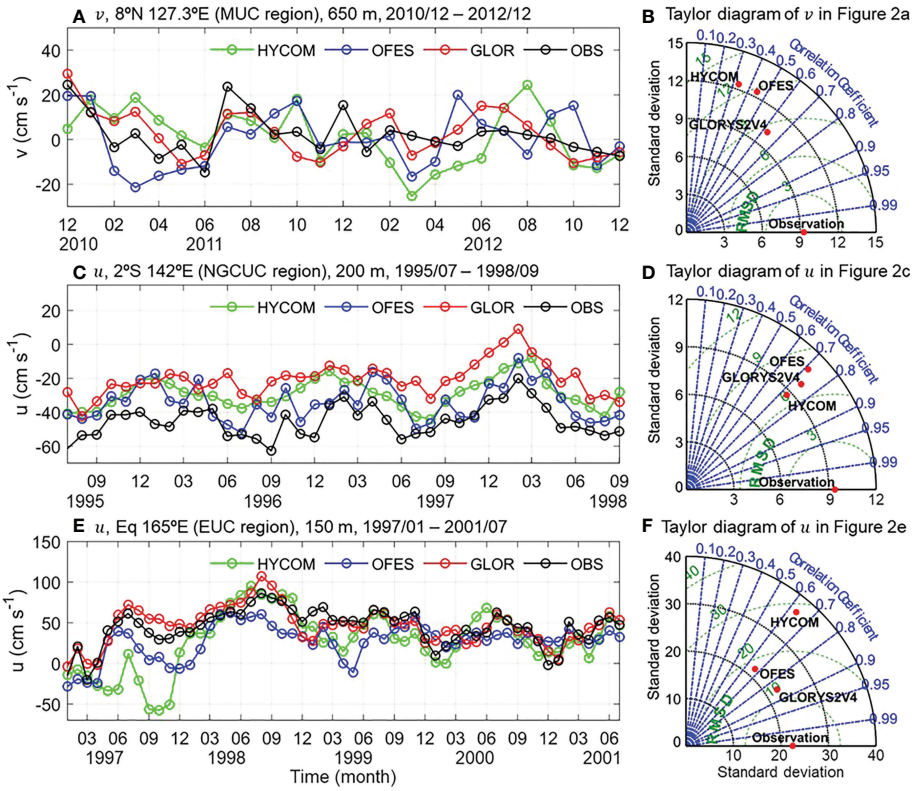

FIGURE 4
(A) Comparison of monthly meridional velocities (cm s^{-1}) from mooring observation (black line) and the model outputs from GLORYS2V4 (red line), OFES (blue line), and HYCOM (green line) from December 2010 to December 2012 at approximately 8°N, 127.3°E and at the depth of approximately 650 m. **(B)** The Taylor diagram compares the velocities from mooring observation to the model outputs in Figure 4A. **(C)** and **(D)** are same as **(A)** and **(B)**, respectively but monthly zonal velocities (cm s^{-1}) from July 1995 to September 1998 at approximately 2°S, 142°E and at the depth of approximately 200 m. **(E)** and **(F)** are same as **(A)** and **(B)**, respectively but monthly zonal velocities (cm s^{-1}) from January 1997 to July 2001 at approximately Equator, 165°E and at the depth of approximately 150 m.

physical processes in the WTP. As such, in the present study, we only utilize the reanalysis data from GLORYS2V4, including the temperature, salinity, and horizontal velocities.

To evaluate the reliability of GLORYS2V4-based LPTM, we applied this analysis to track the trajectory of surface drifting buoys, obtained by the Global Drifter Program (see Elipot et al., 2022 and https://www.aoml.noaa.gov/phod/gdp/hourly_data.php for details). We selected 5 drifters deployed in the WTP to validate the LPTM analysis. The detailed information of the drifters used in this simulation, e.g., initial location, initial date, and tracking time, is provided in Supplementary Table 1. The surface zonal and meridional velocities from GLORYS2V4 were utilized in this LPTM simulation. Figure 5 shows the trajectories of both drifters (red line) and tracer-tracking results (blue line). In general, the result of LPTM can reasonably approximate the trajectory of the drifters, in agreement with the background surface currents (see Figure 1). Therefore, this result confirms the reliability of the LPTM in tracing water parcels in the WTP. The slight discrepancies may result from unresolved submesoscale dynamics, which is beyond the scope of our study, possibly due to spatial and temporal discretization of the model. Nevertheless, we believe that the LPTM is still reliable and the above limitation will not significantly change the final destination of the tracer.

3.2 Mean structure

Before going into the results of the LPTM, it is beneficial to identify the mean structure of the currents that are possibly linked to the NGCUC. Figure 6 displays the vertical profiles of velocity overlaid with the contours of potential density at several sections. The results presented in this figure are based on model outputs from 1994 to 2015, where the first-, second-, and third-row panels are time average and composite during El Niño and La Niña phases, respectively. The sections were selected to show the typical structure of NGCUC and to preliminary identify its potential destinations. There are 180°E, 140°E, 125°E, 8°N, and

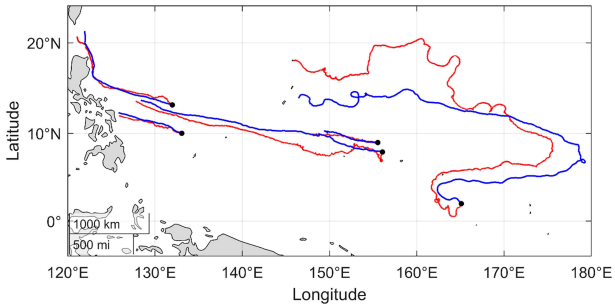

FIGURE 5
The trajectory of (red line) drifters and (blue line) LPTM results. The black dots denote the initial locations.

1°S sections to show the equatorial eastward currents (e.g., NECC, EUC, NSCC, SSCC, and EDJ), the NGCUC, the ITF, the MUC, and the HTF, respectively. In general, the vertical distribution of mean velocities from the model results shows consistency with previous studies (e.g., Qu et al., 2012; Wang et al., 2019; Delpech et al., 2020; Li et al., 2020; Zhang et al., 2020), displaying the typical formation of zonal or meridional velocities along each section.

The mean state of zonal velocity along 140°E shows that NGCUC ranges from nearly surface down to almost 800 m (or 27.2σ_θ) and extends almost 200 km from the coast (Figure 6B). Please note that the wider range of westward flow near the surface is due to merging with SEC, instead of the wider NGCUC (Wang et al., 2019). The maximum of the mean westward velocity of approximately 68 ± 16 cm s^{-1} is found around the depth of 163 m (~25σ_θ), which represents the NGCUC core.

In 180°E section (Figure 6A), a series of alternating zonal currents in the equatorial region is clearly shown, generally consistent with the results of previous studies (e.g., Delpech et al., 2020; Li et al., 2020). The result shows five eastward (i.e., NECC, EUC, NSCC, SSCC, and EDJ) and two westward (i.e., SEC and EIC) currents. The eastward currents shown in this figure are suspected to be the escape routes of the NGCUC waters into the central Pacific. Note that there might be some

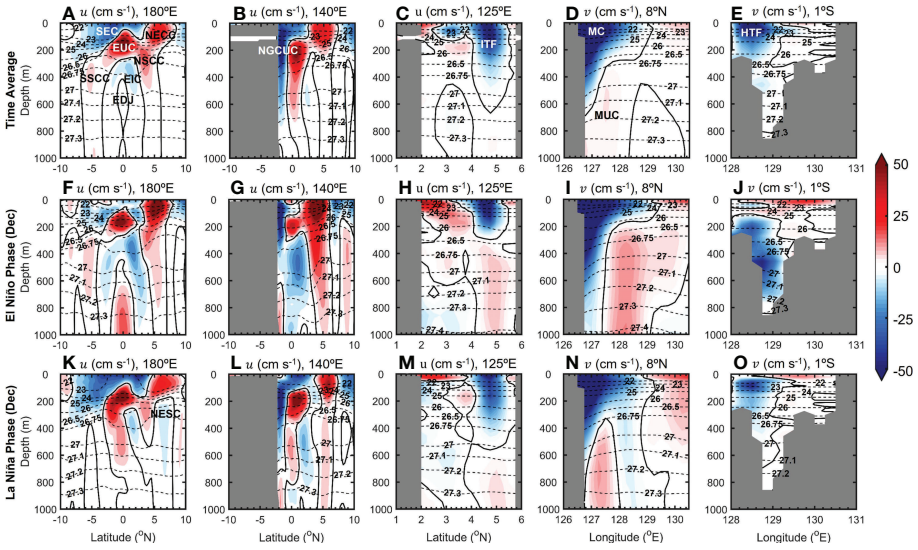

FIGURE 6
Latitude (longitude)-depth sections of zonal (meridional) velocities (cm s^{-1}) from GLORYS2V4 along [first-column panels, **(A, F, K)**] 180°E, [second-column panels, **(B, G, L)**] 140°E, [third-column panels, **(C, H, M)**] 125°E, [fourth-column panels, **(D, I, N)**] 8°N, and [fifth-column panels, **(E, J, O)**] 1°S. The first-, second-, and third-row panels are time average and composite during El Niño and La Niña phases, respectively, from January 1994 to December 2015. The black contours denote the zero velocity. The black dashed-contours denote the isopycnal layers ($\sigma\theta$), which are displayed for 22, 23, 24, 25, 26, 26.5, 26.75, 27, 27.1, 27.2, 27.3, and 27.4$_{\sigma\theta}$.

currents that do not appear in the mean state. For example, the westward core of EDJ (Delpech et al., 2020) and the westward-flowing NESC (Figure 6K, Li et al., 2020).

Multiple cores of ITF are shown along 125°E section (Figure 6C). The main core, which is centered at approximately 4.75°N, is a surface-intensified westward velocity (above $27\sigma_\theta$) with the maximum mean velocity reaching 60 cm s^{-1}. This core is mainly sourced from the MC that turns westward at the southern tip of Mindanao Island (Feng et al., 2018). Another core is much weaker (~3 cm s^{-1}) and is centered at approximately 3.25°N and $27.2\sigma_\theta$. The source of this core is unknown yet but could be from the equatorial Pacific *via* NESC (Li et al., 2021) or from the South Pacific *via* NGCUC. The lower core of ITF along 125°E section will be further investigated in Section 3.3.

Figure 6E shows the vertical profile of southward-flowing HTF. In the mean state, this flow is quite strong with the maximum mean velocity reaching 68 cm s^{-1} near the surface. Along 1°S section, the HTF core is mainly centered at the western part of the channel (~128.5°E) along the east coast of Halmahera Island. The result in Figure 6J suggests that the velocity core of the HTF is revealed deepening during El Niño phase. A detailed analysis of this event will be described in section 3.5.

Section 8°N shows a core of northward-flowing MUC with the maximum mean velocity reaching 4.5 cm s^{-1} at the depth of around 560 m (Figure 6D). This core extends approximately 120 km offshore and is found below 400 m (or below ~$26.75\sigma_\theta$). Previous studies have confirmed that this current is a quasi-permanent current with strong intraseasonal variability, which is closely related to SE-1 and SE-2 activities (Azminuddin et al., 2022).

3.3 Destination of NGCUC

The destination of NGCUC is deduced from the trajectories of tracers released from the NGCUC region using LPTM. Figures 7A–F display the resulting trajectories that represent the pathways of tracers in all selected density layers. The color shading denotes the mean probability distribution of NGCUC water parcels at each grid cell (0.25°×0.25°). The probability was estimated as the ratio between the number of tracers passing through grid cells and the total number of tracers released. The grid cells with higher probability are the region where the tracers pass more frequently. This interpretation can identify the destination of NGCUC including predicting its water mass distribution. The results show that the dissemination of NGCUC tracers varies markedly with depth, but in general, most tracers are distributed to the east, which is consistent with previous studies (Wang et al., 2016b; Li et al., 2020; Zhang et al., 2020; Li et al., 2021).

As described in Section 2.2, some predefined sections were selected to quantitatively classify the destination of each tracer (see Figure 2). The classification of the NGCUC tracers' fate from all isopycnal layers is summarized in Figures 7G-I. Within two years' travel time of tracer tracking, approximately 50.48%, 0.62%, and 30.84% of tracers are classified as major, minor, and transient destinations, respectively. Note that the total classified tracers into these destinations explain only 81.94% of the total tracers that were released daily from 1994 to 2013. The classified tracers are those that reach a predefined section, meaning the remaining unclassified portions (18.06%) do not pass through any predefined sections within the given travel time, possibly due to being slowed down by turbulence or the effect of a random-walk component in Eq. 1 that could suddenly change the direction of tracers' motion before reaching any destinations.

The tracers classified as the transient destinations are those that are trapped in the Pacific Western Boundary Eddies (hereafter called the WBE, defined here as the HE and SE-2 regions) or the Bismarck Sea (BS). The present study considers both WBE and BS as transient destinations (or transit locations) rather than major destinations of NGCUC, in which the tracers need more travel time to escape from there and be redistributed into one of the major or minor destinations. The results show that approximately 22.76% (8.08%) of total tracers are trapped in the WBE (BS).

To confirm this assumption and to further identify the fate of tracers trapped in those transient destinations, we released tracers in both WBE and BS and applied the same scenario of LPTM (see Figures 7G-II-III). It implies that the portion of NGCUC tracers trapped in the WBE and the BS will be distributed according to these respective ratios. The maps of mean probability distribution of tracers released at these regions can be seen in Supplementary Figures 1 and 2. The result reveals an overall decrease (increase) in the tracers distributed to the eastern destinations for the WBE (BS)-originated tracers as compared to the NGCUC-originated tracers. Notably, the tracers distributed to the MUC account for more than one-fourth of all tracers released from the WBE (Figure 7G-III) – a much bigger slice of the destination pie than the tracers directly released from the NGCUC region (i.e., 1.94%) (Figures 7G-I). Consequently, the total ratio of NGCUC's tracers distributed northward through the MUC increases up to 11.3% becoming 13.24% (Figure 7G-IV). A large portion of the WBE-originated tracers distributed to the MUC region is also clearly shown in Supplementary Figures 2D–F. This implies a critical role of eddy in trapping and transporting the NGCUC waters, and in connecting the NGCUC to the MUC, which is typically disconnected. A more detailed analysis of the WBE will be provided in Section 4.

By considering all NGCUC tracers directly originated from the NGCUC region, and the tracers temporarily trapped in the WBE and BS, the present study suggests the total destinations' ratio of the NGCUC tracers as summarized in Figure 7G-IV and Table 1. The results confirm that a large amount of the NGCUC waters is distributed to the central Pacific through the EUC,

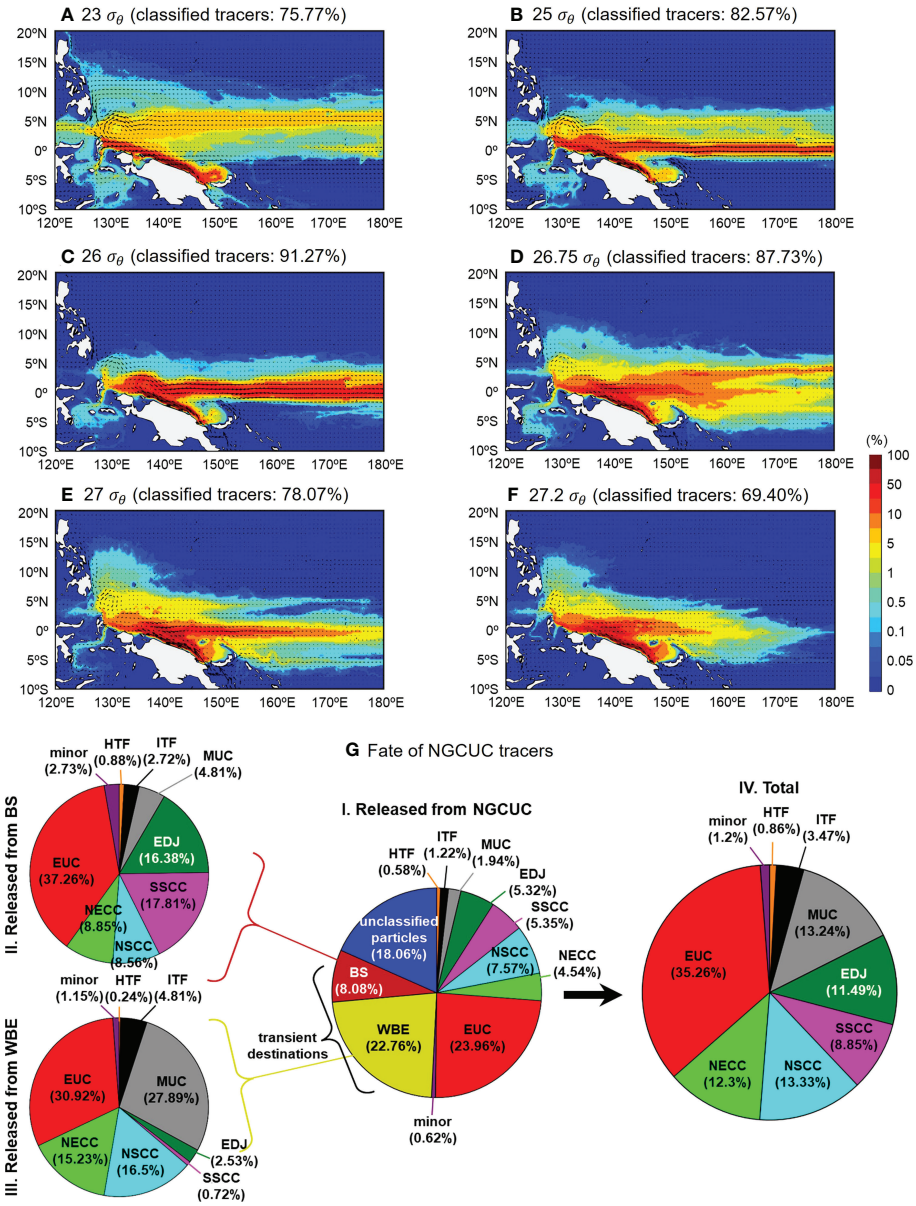

FIGURE 7
Mean probability distribution of tracers (%) released at the NGCUC region (see Figure 2 for the initial position of each tracer) at the isopycnal layers of **(A)** 23, **(B)** 25, **(C)** 26, **(D)** 26.75, **(E)** 27, and **(F)** 27.2 σ_θ . The tracers (50 tracers/layer) were released every day from 1994 to 2013 with the travel time of two years. The black arrows indicate current vectors. **(G)** Pie charts I, II, and III show the ratio of tracers' destinations released directly from the NGCUC, BS, and WBE regions. Pie chart IV shows the ratio of tracers' major and minor destinations from the total tracers released from the NGCUC region, including tracers that were temporarily trapped in the BS and WBE regions.

NECC, NSCC, SSCC, and EDJ. It accounts for 81.65% of all tracers released. Most of the remaining portions are distributed westward into the MUC, ITF, and HTF. This result may reflect the distribution's ratio of the total NGCUC transport.

By means of LPTM, various destinations of NGCUC are observed, but only eight major destinations are further analyzed in the present study. There are NECC (12.3%), EUC (35.26%), NSCC (13.33%), SSCC (8.85%), EDJ (11.49%), MUC (13.24%), ITF (3.47%), and HTF (0.86%). These are suggested as the major destinations considering the relatively high percentage (>0.5%) and the persistency of tracers passing through their territory or tracks. In addition, it is also observed that a few portions of tracers move toward the Maluku Sea (MS) (0.43%) and the Solomon Sea (SS) (0.42%), and the KC (0.34%). The tracers distributed into these minor destinations (i.e., SS, MS, and KC) explain approximately 1.2% of the total tracers released. The

10.3389/fmars.2022.1080314

TABLE 1 Classification of tracers that were released at the NGCUC region within two years' travel time, including the tracers that were temporarily trapped in the BS and WBE regions.

Layer (σ_θ)	Major destinations (%)								Minor destinations (%)				Classified tracers (%)	NGCUC transport's ratio (%)
	EUC	NECC	NSCC	SSCC	EDJ	MUC	ITF	HTF	Total	MS	SS	KC	Total		
23	14.22	48.39	–	–	–	–	7.95	0.67	71.23	0.99	2.18	1.37	4.54	75.77	14.68
25	67.75	12.51	–	–	–	–	1.34	0.5	82.1	0.13	–	0.38	0.47	82.57	19.28
26	87.17	–	2.91	0.14	–	–	0.41	0.52	91.15	0.12	–	–	0.12	91.27	17.47
26.75	–	–	47.76	26.71	–	10.08	1.77	1.14	87.46	0.27	–	–	0.27	87.73	21.66
27	–	–	2.4	7.53	39.5	25.11	2.51	0.78	77.83	0.24	–	–	0.24	78.07	14.68
27.2	–	–	3	4.6	23.09	34.22	3.58	0.49	68.97	0.43	–	–	0.43	69.4	12.23
Total	30.38	9.52	11.57	7.48	8.62	10.05	2.69	0.71	81.01	0.34	0.32	0.27	0.92	81.94	
Classified tracers' total ratio	35.26	12.3	13.33	8.85	11.49	13.24	3.47	0.86	98.8	0.43	0.42	0.34	1.2		

In this simulation, 50 tracers at each isopycnal layer were released daily from 1994 to 2013 (i.e., 365,250 tracers at each layer). The rightmost column is the ratio of NGCUC transport at each layer.

finding of these minor destinations, especially the KC and the SS, is surprising and beyond what we expected at the beginning of this study. Note that the upper NGCUC waters can be advected back to the SS by the southeastward-flowing NGCC. We suggest that some tracers, especially above $25\sigma_\theta$, can be advected northwestward to the KC after joining the NECC to the east and then the NEC to the west possibly due to the strong NEC phase (see Figures 5, 7A, B). This implies a possible connection between the NGCUC and the KC. However, further investigations with observational evidence are required to confirm this finding.

The results of LPTM show that different isopycnal layers can have disparate distributions of NGCUC waters. Along the isopycnal layers of 23 and $25\sigma_\theta$, only about 75.77 and 82.57% of total tracers, respectively, are successfully classified as major destinations. Most of the remaining portions are instead being trapped in the HE and the BS. A similar situation may also apply for the deeper layer, but being trapped in the SE-3 and the BS. Please note that the percentage of classified tracers is not only affected by the eddy's and the BS's trapping effects but also by the velocity of the flow itself. At the deeper layer, the current's velocity becomes slower and thus the tracers need more time to reach any destinations' section. For this reason, the total classified tracers are getting lower at the deeper layer (see Table 1). The percentage of classified tracers may increase with longer travel time, but we believe that it will not significantly change the ratio of the major destinations.

In the probability map (Figures 7A–F), the spreading of tracers is clear. The results show that the majority of NGCUC's water parcels turn eastward to the central Pacific through several eastward-flowing currents. However, their portions vary by isopycnal layers. Along the uppermost isopycnal surface (i.e., $23\sigma_\theta$), more than 67% (19%) of total classified tracers are distributed toward the east into NECC (EUC) around 5°N (equator). In comparison, at the isopycnal layers of 25 and $26\sigma_\theta$, most of the tracers (82.5% and 95.6%, respectively) turn eastward along the equator representing the core of EUC. At the deeper layer ($26.75\sigma_\theta$), this prominent eastward core disparts into northern and southern branches representing NSCC (54.6%) and SSCC (30.5%), respectively. The probability map shows that a core of equatorial eastward flow re-emerges at the isopycnal layer of $27\sigma_\theta$ representing EDJ (50.7%), while the NSCC and SSCC branches are vastly lessened. These three eastern destinations keep appearing at the deepest isopycnal layer ($27.2\sigma_\theta$) but with a shorter zonal extent and their cores seem to merge and are unclearly distinguished. Please notice that the vertical and latitudinal ranges of these eastern destinations are consistent with the result of the mean zonal velocity distribution shown in Figure 6A. Their cores are well represented by the tracer distribution, implying the reliability of the LPTM result.

The portions of tracers that are distributed to the western destinations (i.e., MUC, ITF, and HTF) also vary by isopycnal

layers. Up to 13.24% of total classified tracers are distributed poleward along the Philippine coast joining MUC. This portion is evident at the isopycnal layers below 26.75σ_θ (see Figures 7D–F) and the tracers may reach up to 15°N. This probability distribution is consistent with the poleward extent of AAIW (up to 15°N along the Philippine coast), which originates from the South Pacific *via* NGCUC, reported by Qu and Lindstrom (2004).

Around 3.47% of tracers are distributed to the ITF entrance (Celebes Sea) mainly through the south of Talaud Islands. These tracers are evident in most layers but mainly distributed at the uppermost (23σ_θ) and lowermost (27.2σ_θ) isopycnal layers which explain about 11.2% and 5.2% of total classified tracers, respectively. This result is consistent with the distribution of mean westward flow along 125°E section that also shows the westward cores around both 23σ_θ and 27.2σ_θ isopycnal layers (see Figure 6C). The LPTM results confirm that the southern westward flows (2.5° – 4°N) are mainly sourced from the NGCUC, while that at the northern (4° – 5.5°N) is obviously mainly sourced from the MC.

Other portions of NGCUC tracers also enter the Indonesian Sea, but through the eastern passage *via* Jailolo Strait (i.e., HTF). The number of tracers crossing HTF's section was only 0.86% from the total classified tracers. Although the percentage is relatively small, the results from LPTM confirm that the NGCUC tracers persistently pass through this route, especially at the upper layers. After entering the Jailolo Strait, the tracers flowed toward the eastern part of ITF route, including the Halmahera Sea, Seram Sea, Lifamatola Passage, and Banda Sea before finally arriving in the Indian Ocean through Ombai Strait or Timor Passage. South Pacific water advected into these Indonesian Seas through the HTF has been previously confirmed (e.g., Gordon et al., 2003), which is consistent with our results.

3.4 Spatiotemporal change of the destination

In Section 3.3, various destinations of the NGCUC have been identified. Nevertheless, the ratio of the destination may change over time. To identify the major signals that significantly control the spatiotemporal variation of the NGCUC destination, we applied the power spectral density function for the transport of the NGCUC and its major destinations. In most regions, the power spectrum results show peaks at seasonal and interannual periods (see Supplementary Figure 3). Further analyses using LPTM also confirm that the ratio of NGCUC destinations evidently changes with both timescales. Therefore, this study will focus mainly on seasonal and interannual variations.

3.4.1 Seasonal variation

Figure 8G shows the monthly climatology (1994 – 2015) of the volume transport anomaly of the NGCUC and its major destinations. The result confirms that there is seasonality in the NGCUC transport, in which the volume transport of NGCUC is greatest in August (boreal summer) and weakest in February (boreal winter), which is consistent with previous studies (e.g., Kuroda, 2000; Kawabe et al., 2008; Zhang et al., 2020). These studies have suggested that the seasonal variations of currents off the northern coast of New Guinea are closely related to the monsoon. In boreal summer (winter), the northwestward current is intensified (weakened) in response to the southeasterly (northwesterly) monsoonal winds. In this subsection, we mainly focus on how the destination of NGCUC waters changes seasonally.

To evaluate the seasonal change of the NGCUC destination, we applied the LPTM to track the NGCUC tracers released in boreal summer (July – September) and boreal winter (December – February) from 1994 to 2013. The composite maps of the mean probability distribution of the NGCUC tracers during both seasons are shown in Figure 9. The results display the seasonal change of the pathways of tracers in all selected density layers. In some regions, the number of tracers' distribution changes remarkably between summer and winter. Notably, along the 23 – 25σ_θ density layers (first- and second-row panels in Figure 9), the probability of tracers distributed to the NECC is higher in summer than in winter. At 26σ_θ density layer (third-row panel in Figure 9), where more than 87% of the NGCUC tracers are distributed to the EUC (Table 1), more tracers are distributed westward joining the HTF and the HE in summer than in winter. Below 26.75σ_θ (fourth-, fifth-, and sixth-row panels in Figure 9), the probability of tracers distributed poleward along the Philippine coast (i.e., MUC) is higher in summer than in winter.

To quantitatively analyze the seasonality of the NGCUC destination, we estimated the monthly climatology of the tracers' ratio that arrived at each destination (Figures 8A–F). Note that the monthly ratio represents the percentage of tracers at a month when the tracers were released at the NGCUC region, not when they arrived at the destination. The results exhibit significant seasonal variations in some destinations which further confirm the results shown in Figure 9. The ratio of NGCUC tracers distributed to the NECC is highest in late summer (September – October) and is lowest in spring (May) and late winter (February – March) at 23 and 25σ_θ density layers, respectively (Figures 8A, B). The result also confirms that along 23σ_θ the ratio of NGCUC tracers distributed to the ITF is highest (lowest) in late winter (late summer), which is the opposite seasonality to the NECC at 23σ_θ and the ITF below 26.75σ_θ (Figures 8D–F). This indicates that the upper and lower cores of the ITF have different seasonality. In addition, the upper HTF shows a higher (lower) tracers' ratio in early summer (winter). But that at the deeper layer doesn't clearly show the seasonal variation.

Along 25σ_θ density layer, the seasonal change of tracers' ratio distributed to the EUC and NECC reverse seasonally with a nearly opposite phase (Figure 8B). Although the tracers' ratio of EUC upper 25σ_θ shows quite different seasonality, that at the 26σ_θ layer, which is the main location of the EUC core, shows a

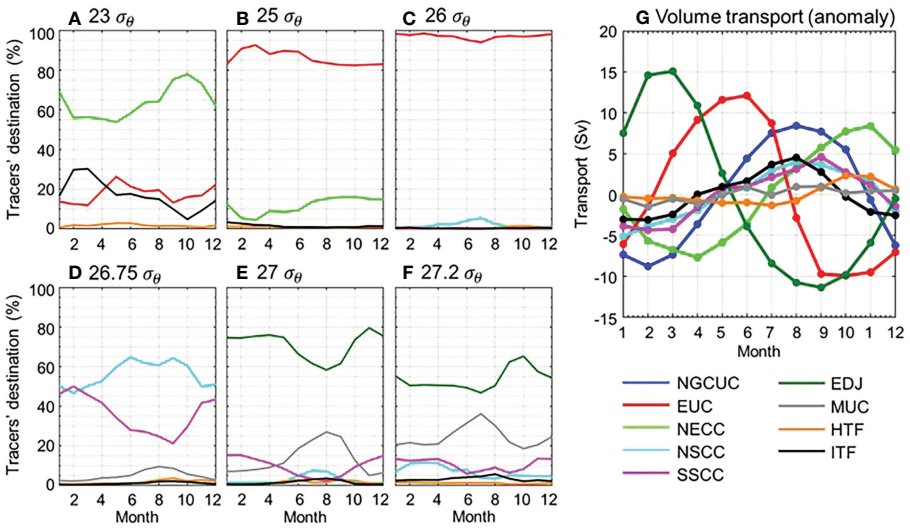

FIGURE 8
Monthly climatology (1994 – 2013) of the tracers' ratio that arrived at the predefined sections of destination (%) at the density layers of **(A)** 23, **(B)** 25, **(C)** 26, **(D)** 26.75, **(E)** 27, **(F)** 27.2σ_θ. **(G)** Monthly climatology (1994 – 2015) of volume transport's anomaly (Sverdrup) of NGCUC and its major destinations.

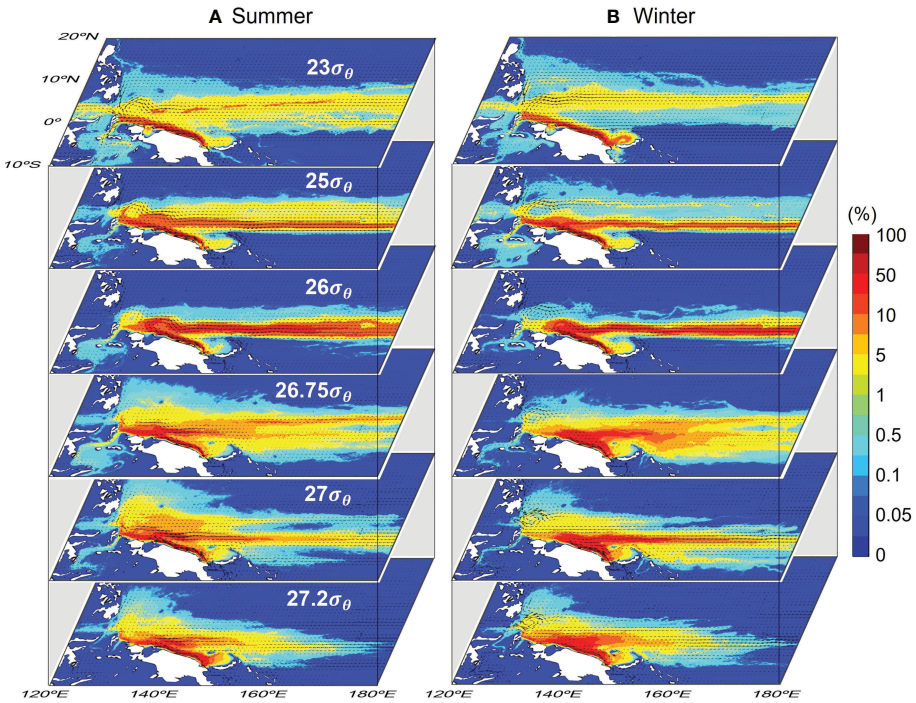

FIGURE 9
Composite map of mean probability distribution of NGCUC water parcels (%) at the isopycnal layers of 23, 25, 26, 26.75, 27, and 27.2 σ_θ. The probability at each layer was estimated from 50 tracers that were released around NGCUC region every day during **(A)** Summer and **(B)** Winter phases from 1994 to 2013 with the travel time of two years. The black arrows indicate current vectors.

lower (higher) tracers' ratio in summer (winter), which is the opposite seasonality to the NSCC at the same layer (Figure 8C). Along this isopycnal layer, the NSCC can also be considered as the lower part of the NECC (see Figure 6A). So, the tracers distributed northeastward after joining HE and becoming NECC at the upper layer can be represented by the tracers joining the NSCC at the lower layer and their seasonality is generally consistent with each other. Below $26\sigma_\theta$, the seasonal change of the NGCUC destinations can be clearly seen. The tracers' ratio of NSCC and MUC (SSCC and EDJ) is higher (lower) in summer and is the opposite in winter.

In summary, in summer more NGCUC tracers are distributed westward and northeastward increasing the ratio of NECC, NSCC, MUC, upper HTF, and lower ITF. While in winter more NGCUC tracers are distributed eastward increasing the ratio of EUC, SSCC, and EDJ. These results imply that the seasonality of the NGCUC strength may influence the seasonality of its water distribution. During summer, the strengthened NGCUC brings the more water further northwestward than the typical state. While during winter, when the NGCUC flow is weak, most waters turn clockwise to spread eastward decisively along the equator.

3.4.2 Interannual variation

Located in the equatorial WP, the interannual variability of the NGCUC destination is most likely related to the ENSO cycle. Zhang et al. (2020) confirmed that the NGCUC exhibits interannual variations associated with ENSO, in which its velocity core shoaling (deepening) during El Niño (La Niña), consistent with our results (see Figures 6G, L). In terms of volume transport, although weak, our result suggests that the NGCUC is negatively correlated with the ENSO cycle with the correlation coefficient of -0.36, estimated from 22 years monthly mean GLORYS2V4 outputs and Ocean Niño Index (ONI) 3.4.

To investigate how the spreading of the NGCUC waters varies interannually, we also applied the LPTM to track the NGCUC tracers released in El Niño and La Niña phases from 1994 to 2013. There were four El Niño (i.e., 1994/1995, 1997/1998, 2002/2003, and 2009/2010) and six La Niña (1995/1996, 1998/1999, 1999/2000, 2007/2008, 2010/2011, and 2011/2012) events during the whole time series from 1994 to 2013. The composite maps of mean probability distribution of the NGCUC tracers during El Niño and La Niña are shown in Figure 10. The results demonstrate the different pathways of tracers between El Niño and La Niña events in all selected isopycnal layers.

Note that in this LPTM simulation, the movement of tracers is fully controlled by ocean currents. This implies that the distribution of NGCUC tracers can reflect the strengthening or weakening of its destinated currents. For example, during El Niño, the NECC is strengthened (Figure 6F), at the same time the portion of NGCUC tracers into NECC is greater than that in La Niña phase (first-row panels in Figure 10). Along 25 – $26\sigma_\theta$ density layers (second- and third-row panels in Figure 10), the probability of tracers distributed to the EUC is much higher in the La Niña than that in El Niño, which coincides well with the strong eastward-flowing EUC during La Niña (Figure 6K). These results suggest that, interannually, the distribution of the NGCUC water is controlled by the strength of its destination currents associated with the ENSO cycle, in which more (less) NGCUC tracers are distributed to the strengthened (weakened) currents.

To quantitatively analyze the interannual change of the tracers' distribution, we estimated the daily time series of the ratio (%) of the tracers that arrived at the predefined sections from 1994 to 2013 and compared the results to the ONI 3.4 as shown in Figure 11. Note that the ratio represents the percentage of tracers on a day when the tracers were released at the NGCUC region, not when they arrived at the destination. The right panels denote the box plot of the time lag (days), which is the travel time from the NGCUC region to arrive at the predefined sections.

In general, the time series of tracers' ratio in most destinations exhibits no significant correlation with ENSO. But in some cases, the strong ENSO event may significantly change the distribution of the tracers. The 1997 – 1999 El Niño/La Niña phase is among the most remarkable ENSO event. A notable change in the tracers' distribution can be observed during this event. During the 1998/1999 La Niña event, most NGCUC tracers at the upper layer ($23\sigma_\theta$), which typically feed the NECC (see Figure 7A), shift equatorward becoming EUC, which is indicated by a significant increase in the tracers' ratio of EUC in 1998 (red line in Figure 11B), possibly due to the weakening of the NECC and strengthening of the EUC. It implies the vertical movement of the EUC core from $26\sigma_\theta$ to $23\sigma_\theta$, closing the surface. This remarkable event was evidently observed by a moored ADCP, which was also well reproduced by the GLORYS2V4 model, as shown in Figures 3C, F, I. A similar situation may also occur during the 2009 – 2011 El Niño/La Niña event that shows a shoaling core of the EUC in 2010, but not as strong as that in 1998.

The results shown in Figures 11B, C further confirm that the El Niño events do not significantly increase the number of NGCUC tracers going into the NECC, considering the increasing number of these tracers also occurred in other periods, e.g., in summer 2006 and 2012. But these results highlight the particular impact of La Niña in decreasing the tracers going into the NECC as clearly shown in all six La Niña events. On the other hand, Figures 11B–D also show that La Niña does not play a role in increasing the number of NGCUC tracers going into the EUC, but the ratio of the EUC decreases in El Niño events, especially clearly seen at the $26\sigma_\theta$ isopycnal layer. In summary, our results suggest that the ENSO cycle can meridionally shift the NGCUC waters that are distributed eastward, in which most of its eastward-distributed waters shift northward (equatorward) in El Niño (La Niña) phase joining the strengthened NECC (EUC).

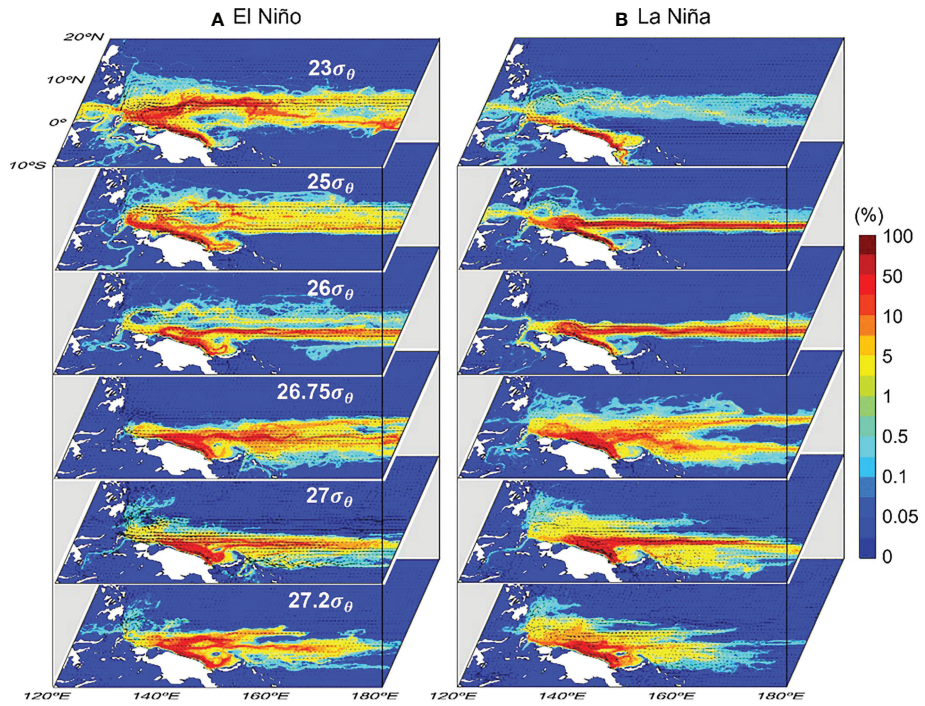

FIGURE 10
Same as Figure 8 except the tracers were released during **(A)** El Niño and **(B)** La Niña.

3.5 Water mass transformation

Although LPTM has been able to estimate the spatiotemporal change of NGCUC's destinations, the real distribution of NGCUC water mass at each destination has remained to be clarified. We then further analyze the water mass characteristics at each region by using θ -S diagram. Figures 12A, B display θ -S diagrams at the NGCUC region and its major destinations, which are estimated from model outputs and averaged from 1994 to 2015. To estimate the θ -S diagram, a point, where tracers pass more frequently, is selected as a proxy for each destination (i.e., 1.5°S, 140°E [NGCUC]; 8°N, 127.5°E [MC/MUC]; 1°S, 128.75°E [HTF]; 3.25°N, 125°E [ITF]; 3.5°S, 148.5°E [BS]; equator, 160°E [EUC/EDJ], see Figure 2).

Based on θ -S diagram analysis, the upper NGCUC water is characterized by a salinity maximum core (>35.1 psu) centered at 25σ_θ representing the SPTW that originates from the subtropical South Pacific (Fine et al., 1994; Qu et al., 1999). At the intermediate layer, NGCUC carries AAIW, which is characterized as salinity minimum water (34.55 psu) at 27.2σ_θ, originating from the Antarctic convergence zone (Qu and Lindstrom, 2004). The signatures of SPTW and AAIW, which are carried by NGCUC, can be found in most of the selected θ -S diagram points but with various transformations. Along 25σ_θ, the SPTW carried by the NGCUC is transformed into fresher water at BS and EUC regions. While at the other regions (i.e., HTF, ITF, and MC), the upper-layer water is mainly characterized by the fresher water NPTW, instead of the SPTW. It implies that upper-layer waters at the Pacific equatorial western boundary are mainly sourced from the MC that carries the NPTW.

At the MC/MUC region (8°N, 127.5°E), the θ -S diagram is characterized by the North Pacific waters, which is obvious, including the North Pacific Tropical Surface Water (NPTSW, a surface salinity minimum), the North Pacific Tropical Water (NPTW, a subsurface salinity maximum in the thermocline), and the North Pacific Intermediate Water (NPIW, a salinity minimum in the subthermocline) (Grey line in Figure 12B). However, below 27σ_θ the South Pacific water, i.e., AAIW, is confirmed, which is consistent with previous studies (e.g., Bingham and Lukas, 1994; Fine et al., 1994; Wang et al., 2016a). The results in Figures 6D and 12B suggest that in this region the fresher water NPIW is carried by the southward-flowing MC and the saltier water AAIW is transported by the northward-flowing MUC below 26.75σ_θ . The possible mechanism of how the South Pacific waters are transported to the Philippine coast has been suggested in our previous study (Azminuddin et al., 2022), which is carried by the NGCUC and the SE-2. This result is also well represented by the LPTM results in Section 3.3, implying the reliability of the particle tracking method.

Figures 12C–H show the θ -S diagrams with climatologically monthly mean (color θ -S diagrams) in all locations. The

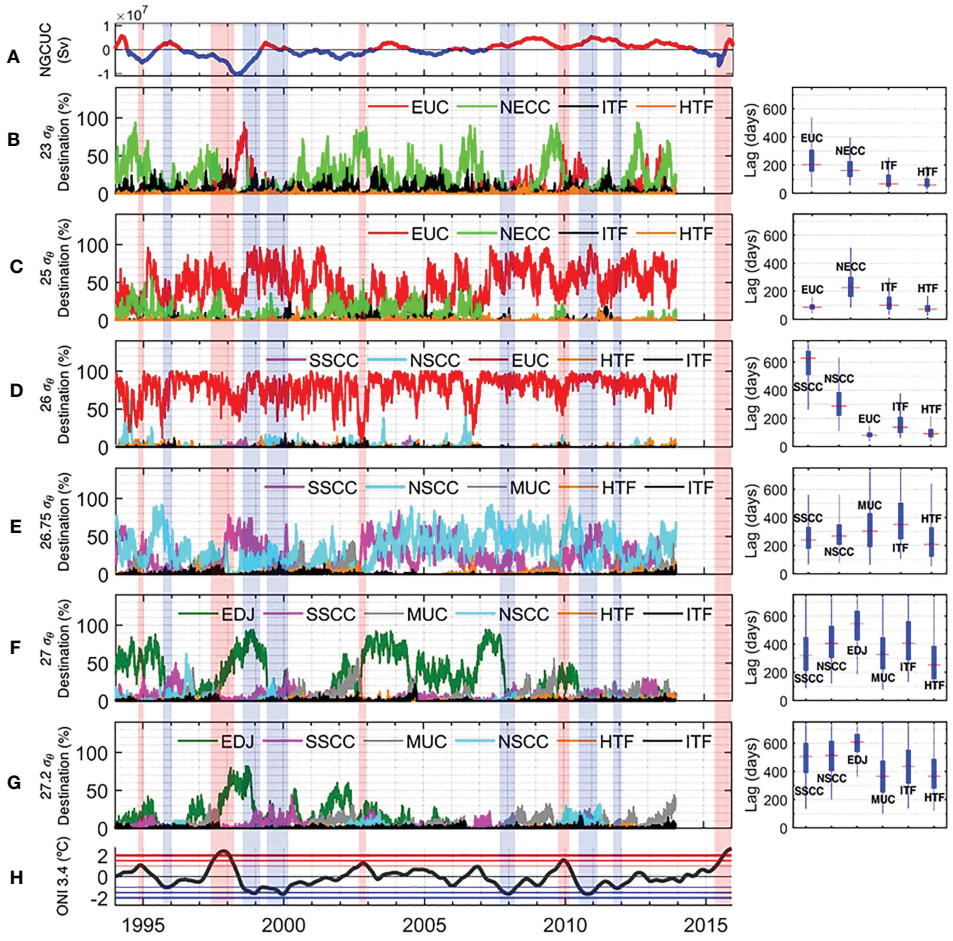

FIGURE 11
(A) The NGCUC transport's anomaly (Sverdrup) from 1994 to 2015. Percentage of the tracers released from the NGCUC region that arrived at the predefined sections of destination from 1994 to 2013 at the isopycnal layers of **(B)** 23, **(C)** 25, **(D)** 26, **(E)** 26.75, **(F)** 27, and **(G)** 27.2σ_θ. The right panels are box plot of the time lag (days), which is the travel time from the NGCUC region to arrive at the predefined sections. **(H)** Ocean Niño Index 3.4 (°C) from 1994 to 2015.

seasonal change of the water mass properties is clearly found in some regions, especially in the HTF region (Figure 12E). The results show that at the upper 24.5σ_θ, the HTF water transforms from relatively warm and salty water in summer to colder and fresher water in winter. This implies that during summer when the NGCUC is strengthened, the upper layer of HTF is transformed into saltier water possibly carrying the SPTW from NGCUC. While in winter, the upper layer of HTF is mainly sourced from the NPTW, which is characterized by relatively cold and fresh water. Note that this seasonal change is altered around the isopycnal layers of 25 – 25.7σ_θ. The results of LPTM further confirm that at the isopycnal layer of 23σ_θ the tracers are distributed more to the HTF in summer than in winter, but the case is reversed at the isopycnal layer of 25σ_θ (see first- and second-row panels in Figure 9). This result suggests that seasonal changes in the NGCUC strength can substantially magnify the seasonal water mass transformation of the HTF.

The interannual change of the θ-S diagrams at each region is also estimated as shown in Figures 12I–N. The black, red, and blue lines denote the time average and composite during El Niño, and La Niña, respectively, from 1994 to 2015. The AAIW at the MUC region is clearly defined in the La Niña phase. But the clarity is slightly lessened, which is fresher during El Niño years possibly mixing with the fresher water of NPIW. Figure 6I confirms that during El Niño the MC is strengthened and deepened, shifting the MUC further offshore. This event may transport more North Pacific waters to the MUC region and transform the intermediate water mass into becoming NPIW.

Figure 12K displays a noticeable water mass transformation of the HTF associated with the ENSO cycle, in which the upper HTF water is transformed into colder and fresher (warmer and saltier) water in the El Niño (La Niña) phase. This result implies that in addition to the NPTW and SPTW, the upper HTF can be sourced from another region. During La Niña (stronger

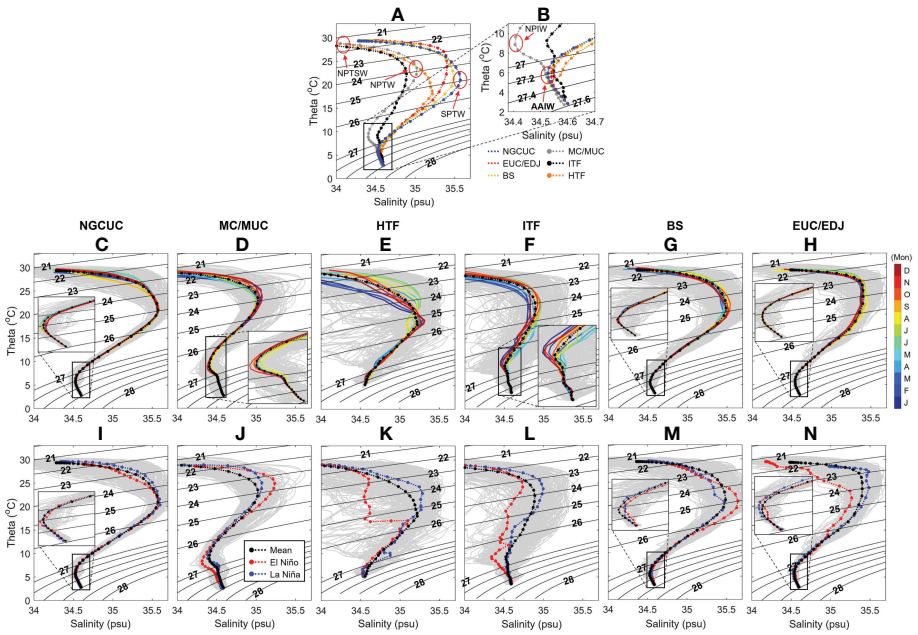

FIGURE 12
(A) θ -S diagrams at six locations (i.e., 1.5°S, 140°E [blue, NGCUC]; 8°N, 127.5°E [grey, MC/MUC]; 1°S, 128.75°E [orange, HTF]; 3.25°N, 125°E [black, ITF]; 3.5°S, 148.5°E [yellow, BS]; equator, 160°E [red, EUC/EDJ], see Figure 2) estimated from model outputs and averaged from 1994 to 2015. **(B)** Same as **(A)** but for the θ -S ranges of black rectangular that shown in **(A)**. Except **(A)** and **(B)**, the first- to sixth-column panels represent the θ -S diagrams at NGCUC **(C, I)**, MC/MUC **(D, J)**, HTF **(E, K)**, ITF **(F, L)**, BS **(G, M)**, and EUC/EDJ **(H, N)** regions, respectively. The second- (third-) row panels are θ -S diagrams with monthly climatology (ENSO) phases. In the second- and third-row panels, the daily (mean) θ -S diagrams along whole period are shown by grey (black) lines.

NGCUC), more SPTW waters enter the HTF resulting in warmer and saltier water. However, during El Niño the source of fresh and cold waters that lead to a unique water mass remains uncertain. It can be either from NPTW or Indonesian Seas (e.g., Banda Sea). Koch-Larrouy et al. (2006) confirmed that the Banda Sea is characterized by a relatively constant salinity (around 34.58 psu) below 20°C. This is consistent with the upper HTF water during El Niño phase (red line in Figure 12K). Moreover, the velocity core of the HTF is revealed deepening during El Niño phase (see Figure 6J), and its velocity upper $25.5\sigma_\theta$ reverses becoming a northward current, flowing from the Indonesian Sea to the Pacific Ocean. So, we suggest that during El Niño the upper HTF water mainly comes from the Banda Sea.

4 Discussion

The uncertainty of water masses' movement in the ocean is tightly linked to turbulence or eddy. Previous studies have confirmed various effects of mesoscale eddies on ocean circulation by, for example, influencing their strength (Azminuddin et al., 2022), transport (Lien et al., 2014), and generation (Qiu et al., 2013; Qiu et al., 2015). The eddies also act as an "underwater mixer" of intermediate waters (Nan et al., 2019). Unlike current that transports water masses continuously, eddy can trap fluid parcels within its core and transport them discretely (Zhang et al., 2014), thereby complicating the assessment of the spreading of NGCUC water mass.

To evaluate the contributions of eddies to the NGCUC's pathways, we released tracers at the core of the Pacific WBE at each density layer as shown in Supplementary Figure 2. In addition, we also estimated the travel time of the tracers (see Figure 13). These experimental approaches enable us to explore how long the NGCUC tracers are trapped in the Pacific WBE and how the trapped tracers are dispersed in the WTP. To identify the strength and core location of an eddy, we applied eddy kinetic energy (EKE) and Okubo-Weiss parameter (OWP) methods following Azminuddin et al. (2021). The OWP identifies eddy by quantifying the relative contribution of deformation and vorticity in the fluid flow. In this study, we selected the threshold value of 5×10^{-12} s^{-2} to define the eddy boundary.

The results of the mean probability distribution map show that the tracers released from the WBE are distributed to similar destinations to those released from the NGCUC (except the BS

and SS), but with different ratios (see Figure 7 and Supplementary Figure 2). It is obvious that no (or very rare) tracer is found in the New Guinea coast, BS, and SS regions, in which the tracers are blocked by the northwestward-flowing NGCUC. The ratio of the tracers' distribution has been detailed in Section 3.3. The result reveals an overall increase in the tracers distributed to the western destinations for the Pacific WBE-originated tracers as compared to the NGCUC-originated tracers. But still, most tracers released at the Pacific WBE are distributed eastward (> 66%). This implies that the presence of eddy enables the westward-distributed waters to return eastward, indicating the role of eddies in redistributing the NGCUC water.

The contribution of eddies to the NGCUC's pathways can be explained in part by estimating the transit time of tracers in the WBE that represents the trapping effect of the eddy. In this study, we define the transit time as the period (in days) of tracers to escape from the WBE. The results confirm that the transit time is getting longer at the deeper isopycnal layer (Figure 13), which is obvious as the water flow is getting slower in the deeper layer. The mean transit time of tracers in the WBE is approximately 34, 45, 49, 78, 102, and 107 days at the 23, 25, 26, 26.75, 27, and 27.2σ_θ isopycnal layers, respectively. In relation to the eddy strength, the results confirm that the tracers typically stay longer (shorter) in the WBE with lower (higher) EKE. So, the strengthened (weakened) WBE, which has faster (slower) water flow, traps the tracers shorter (longer).

Although the turbulence-driven dispersion of water parcels is not fully resolved in model outputs due to spatial and temporal discretization (Rühs et al., 2018), a random walk component ($R\sqrt{2K_h\Delta t}$) with the Smagorinsky diffusivity scheme was applied in the LPTM to approximate unresolved processes, e.g., sub-grid scale turbulent motion (North et al., 2006). Therefore, the results of LPTM can reasonably capture the path of tracers that were trapped and redistributed by the Pacific WBE. We believe that unresolved processes due to eddy (turbulent) diffusion do not significantly change the total ratio of the NGCUC destination, considering the dominance of eastern destination currents (i.e., EUC, NECC, NSCC, SSCC, and EDJ), which are robust. Nevertheless, future studies need to take this into account.

In addition, WBE also plays an important role in linking the currents. The HE has been widely known to link the NGCUC to the NECC (Arruda and Nof, 2003). The results further confirm that below the surface this prominent eddy partially connects the NGCUC to the EUC and the NSCC, in which some tracers

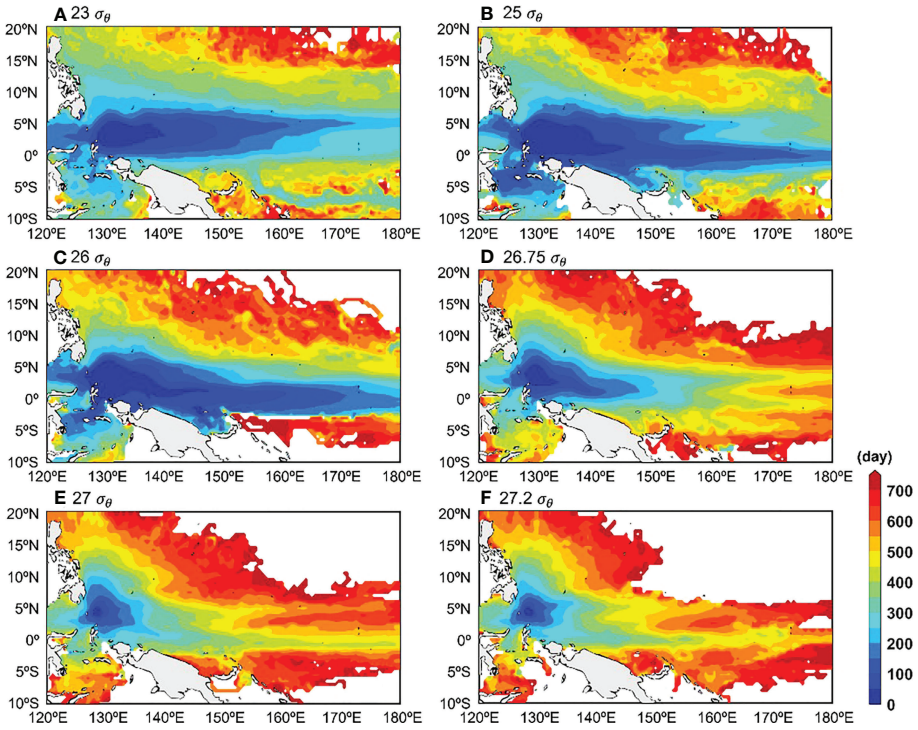

FIGURE 13
Mean travel time distribution of tracers (day) released at the WBE region at the isopycnal layers of **(A)** 23, **(B)** 25, **(C)** 26, **(D)** 26.75, **(E)** 27, and **(F)** 27.2 σ_θ . The tracers (50 tracers/layer) were released every day from 1994 to 2013 with the travel time of two years.

temporarily trapped in the HE were also distributed to these eastward flows. The present study suggests another fundamental linkage below the surface. The results confirm that the NGCUC can also be connected to the MUC by the SE-2. Unlike the HE, which continuously links the currents owing to its quasi-permanent nature and larger scale, this undercurrent linkage is intermittently connected, which highly depends on the NGCUC strength and behavior of the SE-2. Further analysis of these eddy-related current linkages is beyond the scope of the present study and is important as a subject for future studies.

5 Summary

The NGCUC spreads South Pacific water into the North Pacific, influencing the circulation and water mass characteristics. Therefore, it is important to investigate the geographical distribution of the NGCUC waters and its spatiotemporal changes to better understand the evolving circulation and water mass characteristics in the WTP.

The destination of NGCUC was deduced from the trajectories of tracers released from the NGCUC region daily from 1994 to 2013 with two years of travel time using forward LPTM. The lagrangian diagnostics allow us to document the lifecycle of NGCUC tracers before arriving at any destination including splitting, merging, and interacting with eddies. In general, the destinations of South Pacific waters carried by NGCUC into the NWP can be divided into two escape routes: the eastern and western routes. The western route is divided into the northwestern route and the Indonesian Seas route. Within these routes, we reveal eight major destinations of NGCUC: EUC (35.26%), NECC (12.3%), NSCC (13.33%), SSCC (8.85%), EDJ (11.49%), MUC (13.24%), ITF (3.47%), and HTF (0.86%). In addition, the particle tracking results suggest that a few portions of NGCUC waters are also distributed to three minor destinations, i.e., MS (0.43%), SS (0.42%), and KC (0.34%).

The ratio of NGCUC destinations exhibits pronounced seasonal variations closely associated with the seasonal change of the NGCUC strength. The NGCUC strengthens (weakens) during summer (winter) and more NGCUC waters are distributed westward and northeastward (eastward) into the MUC, lower ITF, upper HTF, NECC, and NSCC (EUC, SSCC, and EDJ). In addition, the results reveal that on interannual timescales the distribution of the NGCUC water is controlled by the ENSO cycle that modulates the strength of the currents linked with the downstream NGCUC. Most of its eastward-distributed waters shift northward (equatorward) in El Niño (La Niña) phase joining the strengthened NECC (EUC). These spatiotemporal changes of the NGCUC destination contribute to the water mass characteristics and their seasonal and interannual transformations. Detailed dynamic processes associated with the spatiotemporal changes of the NGCUC destination will be investigated in further studies.

Approximately 22.76% (8.08%) of tracers were temporarily trapped in the equatorial Pacific WBE (BS) before being redistributed. In the present study, the effects of eddies on the pathways of NGCUC's waters are evaluated. The results suggest that eddies could regionally affect water mass properties by trapping and redistributing the water mass. The presence of eddy enables the westward-distributed NGCUC waters to return eastward. Finally, the results suggest the fundamental role of the Pacific WBE in linking the currents in the equatorial WP, including the SE-2 that links the NGCUC to the MUC.

Data availability statement

The datasets presented in this study can be found in online repositories. The names of the repository/repositories and accession number(s) can be found below: The mooring data used in this study were provided by the Northwestern Pacific Ocean Circulation and Climate Experiment (NPOCE) (http://npoce.org.cn/dateAcc.aspx) and the Tropical Ocean Climate Study (TOCS) (https://www.jamstec.go.jp/e/database/ocean.html) programs. The GLORYS2V4 data are freely available from Mercator Ocean (https://doi.org/10.48670/moi-00024). The HYCOM data are freely available from the HYCOM consortium (http://www.hycom.org/dataserver/gofs-3pt1/reanalysis). The OFES data are freely available from APDRC Live Access Server (http://apdrc.soest.hawaii.edu/las_ofes). The drifter data are freely available from NOAA-AOML (https://www.aoml.noaa.gov/phod/gdp/hourly_data.php).

Author contributions

FA proposed the main ideas, collected the data, performed the data analysis, and wrote the original manuscript. CJ critically reviewed the data analysis results. All authors participated in the discussion, contributed to the improvement of the manuscript, and approved the submitted version.

Funding

This study was supported by the projects titled Korea-China Joint Ocean Research Center (20220407)" and "KIOS (Korea Indian Ocean Study): Korea-US Joint Observation Study of the Indian Ocean (20220548, PM63180)" funded by the Korean Ministry of Oceans and Fisheries, Korea, and the project titled "Projection and evaluation of ocean climate and extreme events based on AR6 scenarios (KMI2021-01511)" funded by the Korea Meteorological Administration.

Conflict of interest

The authors declare that the research was conducted in the absence of any commercial or financial relationships that could be construed as a potential conflict of interest.

Publisher's note

All claims expressed in this article are solely those of the authors and do not necessarily represent those of their affiliated organizations, or those of the publisher, the editors and the reviewers. Any product that may be evaluated in this article, or claim that may be made by its manufacturer, is not guaranteed or endorsed by the publisher.

Supplementary material

The Supplementary Material for this article can be found online at: https://www.frontiersin.org/articles/10.3389/fmars.2022.1080314/full#supplementary-material

References

Arruda, W. Z., and Nof, D. (2003). The Mindanao and halmahera eddies – twin eddies induced by nonlinearities. *J. Phys. Oceanogr.* 43, 2815–2830. doi: 10.1175/1520-0485(2003)033<2815:TMAHEE>2.0.CO;2

Azminuddin, F., Jeon, D., Kim, Y. H., Jang, C. J., and Park, J.-H. (2021). A newly observed deep countercurrent in the subtropical northwest pacific. *J. Geophys. Res. Oceans* 126, e2021JC017272. doi: 10.1029/2021JC017272

Azminuddin, F., Lee, J. H., Jeon, D., Shin, C.-W., Villanoy, C., Lee, S., et al. (2022). Effect of the intensified sub-thermocline eddy on strengthening the Mindanao undercurrent in 2019. *J. Geophys. Res. Oceans* 127, e2021JC017883. doi: 10.1029/2021JC017883

Bingham, F. M., and Lukas, R. (1994). The southward intrusion of north pacific intermediate water along the Mindanao coast. *J. Phys. Oceanogr* 24, 141–154. doi: 10.1175/1520-0485(1994)024%3C0141:TSIONP%3E2.0.CO;2

Chassignet, E. P., Hurlburt, H. E., Metzger, E. J., Smedstad, O. M., Cummings, J. A., Halliwell, G. R., et al. (2009). US GODAE: Global ocean prediction with the HYbrid coordinate ocean model (HYCOM). *Oceanography* 22 (2), 64–75. doi: 10.5670/oceanog.2009.39

Chiang, T.-L., and Qu, T. (2013). Subthermocline eddies in the Western equatorial pacific as shown by an eddy-resolving OGCM. *J. Phys. Oceanogr.* 43, 1241–1253. doi: 10.1175/JPO-D-12-0187.1

Chiang, T.-L., Wu, C.-R., Qu, T., and Hsin, Y.-C. (2015). Activities of 50–80 day subthermocline eddies near the Philippine coast. *J. Geophys. Res. Oceans* 120, 3606–3623. doi: 10.1002/2013JC009626

Choi, J.-G., Jo, Y.-H., Moon, I.-J., Park, J., Kim, D.-W., and Lippmann, T. C. (2018). Physical forces determine the annual bloom intensity of the giant jellyfish *Nemopilema nomurai* off the coast of Korea. *Reg. Stud. Mar. Sci.* 24, 55–65. doi: 10.1016/j.rsma.2018.07.003

Delpech, A., Cravatte, S., Marin, F., Morel, Y., Gronchi, E., and Kestenare, E. (2020). *J. Phys. Oceanogr* 50, 281–304. doi: 10.1175/JPO-D-19-0132.1

Dormand, J. R., and Prince, P. J. (1980). A family of embedded runge-kutta formulae. *J. Comput. Appl. Math.* 6 (1), 19–26. doi: 10.1016/0771-050X(80)90013-3

Elipot, S., Sykulski, A., Lumpkin, R., Centurioni, L., and Pazos, M. (2022) *Hourly location, current velocity, and temperature collected from global drifter program drifters world-wide. subset: The hourly dataset version 2.00* (NOAA National centers for Environmental Information) (Accessed 09-Nov-2022).

Feng, M., Zhang, N., Liu, Q., and Wijffels, S. (2018). The Indonesian throughflow, its variability and centennial change. *Geosci. Lett.* 5 (3), 1–10. doi: 10.1186/s40562-018-0102-2

Fine, R. A., Lukas, R., Bingham, F. M., Warner, M. J., and Gammon, R. H. (1994). The western equatorial pacific: A water mass crossroads. *J. Geophys. Res. Oceans* 99, 25063–25080. doi: 10.1029/94JC02277

Gordon, A. L., Giulivi, C. F., and Ilahude, A. G. (2003). Deep topographic barries within the Indonesian seas. *Deep Sea Res. II* 50, 2205–2228. doi: 10.1016/S0967-0645(03)00053-5

Hu, D., and Cui, M. (1991). The western boundary current of the pacific and its role in the climate. *Chin. J. Oceanol. Limnol.* 9 (1), 1–14. doi: 10.1007/BF02849784

Hu, D., Wang, F., Sprintall, J., Wu, L., Riser, S., Cravatte, S., et al. (2020). Review on observational studies of western tropical pacific ocean circulation and climate. *J. Oceanol. Limnol.* 38 (4), 906–929. doi: 10.1007/s00343-020-0240-1

Hu, D., Wu, L., Cai, W., Gupta, A. S., Ganachaud, A., Qiu, B., et al. (2015). Pacific western boundary currents and their roles in climate. *Nature* 522, 299–308. doi: 10.1038/nature14504

Kashino, Y., Atmadipoera, A., Kuroda, Y., and Lukijanto, (2013). Observed features of the halmahera and Mindanao eddies. *J. Geophys. Res. Oceans* 118, 6543–6560. doi: 10.1002/2013JC009207

Kawabe, M., Kashino, Y., and Kuroda, Y. (2008) Variability and linkages of new Guinea coastal undercurrent and lower equatorial intermediate current *J. Phys. Oceanogr.* 38, 8, 1780–1793. doi: 10.1175/2008JPO3916.1

Koch-Larrouy, A., Madec, G., Bouruet-Aubertot, P., Gerkema, T., Bessieres, L., and Molcard, R. (2006). On the transformation of pacific water into Indonesian throughflow water by internal tidal mixing. *Geophys. Res. Lett.* 34, L04604. doi: 10.1029/2006GL028405

Kuroda, Y. (2000). Variability of currents off the northern coast of New Guinea. *J. Oceanogr.* 56, 103–116. doi: 10.1023/A:1011122810354

Kutsuwada, K., and McPhaden, M. (2002). Intraseasonal variations in the upper equatorial pacific ocean prior to and during the 1997–98 El nino. *J. Phys. Oceanogr.* 32 (4), 1133–1149. doi: 10.1175/1520-0485(2002)032<1133:IVITUE>2.0.CO;2

Ledwell, J. R., Watson, A. J., and Law, C. S. (1993). Evidence for slow mixing across the pycnocline from an open-ocean tracer release experiment. *Nature* 364, 701–703. doi: 10.1038/364701a0

Lellouche, J.-M., Le Galloudec, O., Drevillon, M., Regnier, C., Greiner, E., Garric, G., et al. (2013). Evaluation of global monitoring and forecasting systems at Mercator ocean. *Ocean Sci.* 9, 57–81. doi: 10.5194/os-9-57-2013

Lien, R.-C., Ma, B., Cheng, Y.-H., Ho, C.-R., Qiu, B., Lee, C. M., et al. (2014). Modulation of kuroshio transport by mesoscale eddies at the Luzon strait entrance. *J. Geophys. Res. Oceans* 126, 2129–2142. doi: 10.1002/2013JC009548

Li, X., Yang, Y., Li, R., Zhang, L., and Yuan, D. (2020). Structure and dynamics of the pacific north equatorial subsurface current. *Sci. Rep.* 10, 11758. doi: 10.1038/s41598-020-68605-y

Li, M., Yuan, D., Gordon, A. L., Gruenburg, L. K., Li, X., Li, R., et al. (2021). A strong sub-thermocline intrusion of the north equatorial subsurface current into the makassar strait in 2016–2017. *Geophys. Res. Lett.* 48 (8), e2021GL092505. doi: 10.1029/2021GL092505

Max, L., Rippert, N., Lembke-Jene, L., Mackensen, A., Nurnberg, D., and Tiedemann, R. (2016). Evidence for enhanced convection of north pacific intermediate water to the low-latitude pacific under glacial conditions. *Paleoceanogr* 32, 41–55. doi: 10.1002/2016PA002994

Nan, F., Yu, F., Ren, Q., Wei, C., Liu, Y., and Sun, S. (2019). Isopycnal mixing of interhemispheric intermediate waters by subthermocline eddies east of the Philippines. *Sci. Rep.* 9, 2957. doi: 10.1038/s41598-019-39596-2

North, E. W., Hood, R. R., Chao, S. Y., and Sanford, L. P. (2006). Using a random displacement model to simulate turbulent particle motion in a baroclinic frontal zone: A new implementation scheme and model performance tests. *J. Mar. Syst.* 60 (3-4), 365–380. doi: 10.1016/j.jmarsys.2005.08.003

Qiu, B., Chen, S., Rudnick, D. L., and Kashino, Y. (2015). A new paradigm for the north pacific subthermocline low-latitude Western boundary current system. *J. Phys. Oceanogr.* 45, 2407–2423. doi: 10.1175/JPO-D-15-0035.1

Qiu, B., Chen, S., and Sasaki, H. (2013). Generation of the north equatorial undercurrent jets by triad baroclinic rossby wave interactions. *J. Phys. Oceanogr.* 43, 2682–2698. doi: 10.1175/JPO-D-13-099.1

Qu, T., Chiang, T.-L., Wu, C.-R., Dutrieux, P., and Hu, D. (2012). Mindanao Current/Undercurrent in an eddy-resolving GCM. *J. Geophys. Res.* 117, C06026. doi: 10.1029/2011JC007838

Qu, T., and Lindstrom, E. J. (2004). Northward intrusion of Antarctic intermediate water in the Western pacific. *J. Phys. Oceanogr.* 34 (9), 2104–2118. doi: 10.1175/1520-0485(2004)034<2104:NIOAIW>2.0.CO;2

Qu, T., Mitsudera, H., and Yamagata, T. (1999). A climatology of the circulation and water mass distribution near the Philippine coast. *J. Phys. Oceanogr.* 29, 1488–1505. doi: 10.1175/1520-0485(1999)029<1488:ACOTCA>2.0.CO;2

Rühs, S., Zhurbas, V., Koszalka, I., Durgadoo, J. V., and Biastoch, A. (2018). Eddy diffusivity estimates from Lagrangian trajectories simulated with ocean models and surface drifter data – a case study for the greater agulhas system. *J. Phys. Oceanogr.* 48 (1), 175–196. doi: 10.1175/JPO-D-17-0048.1

Sasaki, H., Nonaka, M., Masumoto, Y., Sasai, Y., Uehara, H., and Sakuma, H. (2008). "An eddy-resolving hindcast simulation of the quasiglobal ocean from 1950 to 2003 on the earth simulator," in *High resolution numerical modelling of the atmosphere and ocean*. Eds. K. Hamilton and W. Ohfuchi (New York, NY: Springer), 157–185. doi: 10.1007/978-0-387-49791-4_10

Seo, S., Park, Y.-G., and Kim, K. (2020). Tracking flood debris using satellite-derived ocean color and particle-tracking modeling. *Mar. Pollut. Bull.* 161, 111828. doi: 10.1016/j.marpolbul.2020.111828

Smagorinsky, J. (1963). General circulation experiments with the primitive equations. *Mon. Weather Rev.* 91 (3), 99–164. doi: 10.1175/1520-0493(1963)091<0099:GCEWTP>2.3.CO;2

Song, L., Li, Y., Wang, F., Wang, J., and Liu, C. (2018). Subsurface structure and variability of the zonal currents in the northwestern tropical pacific ocean. *Deep Sea Res. I* 141, 11–23. doi: 10.1016/j.dsr.2018.09.004

Taylor, K. E. (2001). Summarizing multiple aspects of model performances in a single diagram. *J. Geophys. Res.* 106, 7183–7192. doi: 10.1029/2000JD900719

Wang, F., and Hu, D. (1998). Dynamic and thermohaline properties of the Mindanao undercurrent, part II: Thermohaline structure. *Chin. J. Oceanol. Limnol.* 16, 206–213. doi: 10.1007/BF02845177

Wang, F., Song, L., Li, Y., Liu, C., Wang, J., Lin, P., et al. (2016a). Semiannually alternating exchange of intermediate waters east of the Philippines. *Geophys. Res. Lett.* 43, 7059–7065. doi: 10.1002/2016GL069323

Wang, Q., Wang, F., Feng, J., Hu, S., Zhang, L., Jia, F., et al. (2019). The equatorial undercurrent and its origin in the region between Mindanao and new Guinea. *J. Geophys. Res. Oceans* 124, 1–18. doi: 10.1029/2018JC014842

Wang, F., Wang, J., Guan, C., Ma, Q., and Zhang, D. (2016b). Mooring observations of equatorial currents in the upper 1000 m of the western pacific ocean during 2014. *J. Geophys. Res. Oceans* 121, 3730–3740. doi: 10.1002/2015JC011510

Wang, Q., Zhai, F., Wang, F., and Hu, D. (2014). Intraseasonal variability of the subthermocline current east of Mindanao. *J. Geophys. Res. Oceans* 119 (12), 8552–8566. doi: 10.1002/2014JC010343

Zhang, L., Hu, D., Hu, S., Wang, F., Wang, F., and Yuan, D. (2014). Mindanao Current/Undercurrent measured by a subsurface mooring. *J. Geophys. Res. Oceans* 119, 3617–3628. doi: 10.1002/2013JC009693

Zhang, L., Hui, Y., Qu, T., and Hu, D. (2021). Seasonal variability of subthermocline eddy kinetic energy east of the Philippines. *J. Phys. Oceanogr* 51 (3), 685–699. doi: 10.1175/JPO-D-20-0101.1

Zhang, L., Wu, J., Wang, F., Hu, S., Wang, Q., Jia, F., et al. (2020). Seasonal and interannual variability of the currents off the New Guinea coast from mooring measurements. *J. Geophys. Res. Oceans* 125, e2020JC016242. doi: 10.1029/2020JC016242

frontiers | Frontiers in Marine Science

TYPE Original Research
PUBLISHED 29 November 2022
DOI 10.3389/fmars.2022.1047690

OPEN ACCESS

EDITED BY
Shi-Di Huang,
Southern University of Science and Technology, China

REVIEWED BY
Junmin Meng,
Ministry of Natural Resources, China
Ru Chen,
Tianjin University, China

*CORRESPONDENCE
C. Yuan
yuanchunxin@ouc.edu.cn

SPECIALTY SECTION
This article was submitted to Physical Oceanography, a section of the journal Frontiers in Marine Science

RECEIVED 18 September 2022
ACCEPTED 08 November 2022
PUBLISHED 29 November 2022

CITATION
Wang W, Gong Y, Wang Z and Yuan C (2022) Numerical simulations of generation and propagation of internal tides in the Andaman Sea. *Front. Mar. Sci.* 9:1047690. doi: 10.3389/fmars.2022.1047690

Numerical simulations of generation and propagation of internal tides in the Andaman Sea

W. Wang[1], Y. Gong[2], Z. Wang[3,4] and C. Yuan[1]*

[1]School of Mathematical Sciences, Ocean University of China, Qingdao, China, [2]State Key Laboratory of Tropical Oceanography, South China Sea Institute of Oceanology, Chinese Academy of Sciences, Guangzhou, China, [3]Institute of Mechanics, Chinese Academy of Sciences, Beijing, China, [4]School of Engineering Science, University of Chinese Academy of Sciences, Beijing, China

The generation and propagation of internal tides in the Andaman Sea are investigated using a three-dimensional high-resolution numerical model. Three categories of experiments, including driving the model with four main semidiurnal tides (M2, S2, N2, and K2), four main diurnal tides (K1, O1, P1, and Q1), and eight main tides (M2, S2, N2, K2, K1, O1, P1, and Q1), are designed to examine the effects of barotropic tides. The results show that the semidiurnal internal tides are dominant in the Andaman Sea, and the inclusion of diurnal barotropic tides negligibly modulates this result. That is partly due to the strength of the diurnal barotropic tides is generally one order smaller than that of the semidiurnal barotropic tides in this region. The sensitivity experiments put this on a firmer footing. In terms of the internal tidal energy, the experiments driven by the diurnal barotropic tides are three orders and one order smaller than those driven by the semidiurnal barotropic tides, respectively, during the spring and neap tides. In addition, the experiments result in total barotropic-to-baroclinic energy conversion rates over the Andaman Sea 29.15 GW (driven by the eight tides), 29.24 GW (driven by the four semidiurnal tides), and 0.05 GW (driven by the fourdiurnal tides) in the spring tidal period and 3.08 GW, 2.56 GW, and 0.31 GW in the neap tidal period, respectively. Four potential generation regions of internal tides are found, three of which are in the Andaman and Nicobar Islands and one in the northeastern Andaman Sea.

KEYWORDS

internal tides, Andaman Sea, energy budget, generation regions, numerical simulations

1 Introduction

Oceanic internal waves are fluctuations occurring in the stratified water with the largest amplitudes in the interior, indicating that detecting internal waves is generally difficult. Internal waves possessing weak nonlinearity and tidal frequencies are usually called internal tides. Their wavelengths are typically tens of kilometers, and the energy travels along the rays. Internal tides were first observed in 1907 when the Swedish ship "Skagerak" obtained observational data with the semidiurnal tidal frequencies in the Great Belt. Petterson proposed the internal tides originated from the barotropic tides (Fang and Du, 2005). The dissipation, deformation, and wave breaking induced by internal tides can transfer energy between large-scale and small-scale motions. Therefore, internal tides play an essential role in the energy cascade process of the global ocean, thereby affecting climate change. The total energy of internal tides in the global ocean is about 1 TW (Egbert and Ray, 2000). The isopycnal fluctuations induced by internal tides can improve the primary productivity of the sea. Studying internal tides is of great value to understanding marine multi-scale energetics and marine ecological environment. Most internal tides generate at some specific bathymetries, e.g., continental slopes (Alford, 2003). Since the 1960s, the theory that internal tides are generated due to the interaction of barotropic tides and a steep ridge is gradually widely accepted (Rattray, 1960). Stably stratified seawater is disturbed when the barotropic tidal currents flow through the abrupt terrain, such as shelves, seamounts, and sills. The perturbation propagates outward, resulting in large vertical fluctuations consistent with tidal frequency. A portion of the barotropic energy is converted into baroclinic energy, resulting in the generation of internal tides, and the residual barotropic energy dissipates locally or continues to radiate away. The converted baroclinic energy dissipates near the internal tides generation sites or radiates away (Munk and Wunsch, 1998).

The Andaman Sea is the marginal sea of the Indian Ocean. It is located northeast of the Indian Ocean, bordering Myanmar and Thailand to the east, the Bay of Bengal to the west, and the Malacca Strait to the south. The Andaman Sea is characterized by rough bottom topography, which is deeper in the west and shallower in the east. The internal waves are very active in the southern Andaman Sea. On the west side are the thousand-kilometer-long Andaman and Nicobar Archipelago, where the abrupt bathymetry and strong tidal currents from the Bay of Bengal provide favorable conditions for the generation of internal waves. It indeed becomes one of the important sources of internal waves in the Andaman Sea (Mohanty et al., 2018; Jithin et al., 2019). Perry and Schimke (1965) pioneeringly studied internal waves in the Andaman Sea and identified them through temperature profiles. Both *in-situ* observations and satellite remote sensing images show the frequent emergence of intensive internal tides in the Andaman Sea (Osborne and Burch, 1980; Alpers et al., 1997; Hyder et al., 2005; Magalhaes et al., 2020; Yang et al., 2021). It has become one of the hot spots for investigating large internal tides.

The dynamic mechanism and energy budget of internal tides in the Andaman Sea have attracted much attention among oceanographers over the past decades, see, for example, (Mohanty et al., 2018; Magalhaes et al., 2020; Peng et al., 2021). Jithin et al. (2020) examined the semidiurnal internal tides in the Andaman Sea and found that the interaction between barotropic tides and bottom topography resulted in the conversion of one-third of M2 barotropic tidal energy into internal tides; this process mainly occurred in the Andaman and Nicobar Archipelago. Nevertheless, they estimated that 41% of the energy dissipates locally at the generation sites, almost double the estimation (20%) by Mohanty et al. (2018), which indicates that there needs further study to unravel this problem. Based on the MODIS true-color and SAR observations in the Andaman Sea, it is found that some potential generation regions of internal tides are mainly distributed in the Andaman and Nicobar Archipelago and the northeast Andaman Sea (Raju et al., 2019), as shown in Figure 1. To accurately identify these generation sites, the energy conversion from barotropic energy to baroclinic energy needs to be estimated, and Mohanty et al. (2018); Jithin et al. (2020) conducted numerical simulations to investigate this problem. They have found that the conversion occurred intensively near the Andaman and Nicobar Islands, however, note that the energy conversion between barotropic and baroclinic phenomena significantly depends on the model resolution. One question arises: is the grid size ~2km horizontally and ~40 layers vertically considered sufficiently fine to resolve the small scale motion and accurately estimate the energy conversion further? To answer this question, in this paper, we consider simulations using a higher resolution. Yadidya et al. (2022) investigated the seasonal variation of semidiurnal internal tides in the Andaman Sea using *in-situ* observational data and found the strong seasonal variability manifested itself as stronger in summer and autumn but weaker in spring and winter for semidiurnal internal tides, in contrast with the diurnal internal tides, stronger in summer and winter. Nonetheless, Sun et al. (2019) conducted statistics on the remote sensing images and concluded that most of the nonlinear internal waves occur from February to April. It is clear that there have been several pieces of the literature concentrated on the semidiurnalinternal tides in winter [Mohanty et al. (2018); Jithin et al. (2019)]; however, the dynamics of diurnal internal tides and their role on the entire energy budget in the Andaman Sea still needs to be examined, and the internal tides in a different season, for example, in spring, worth analysing as well. Overall, the energy budget of internal tides during the generation and propagation is worth exploring further, especially in the season different from winter. The comparisons of intensity and energy distributions between semidiurnal and diurnal tides also need to

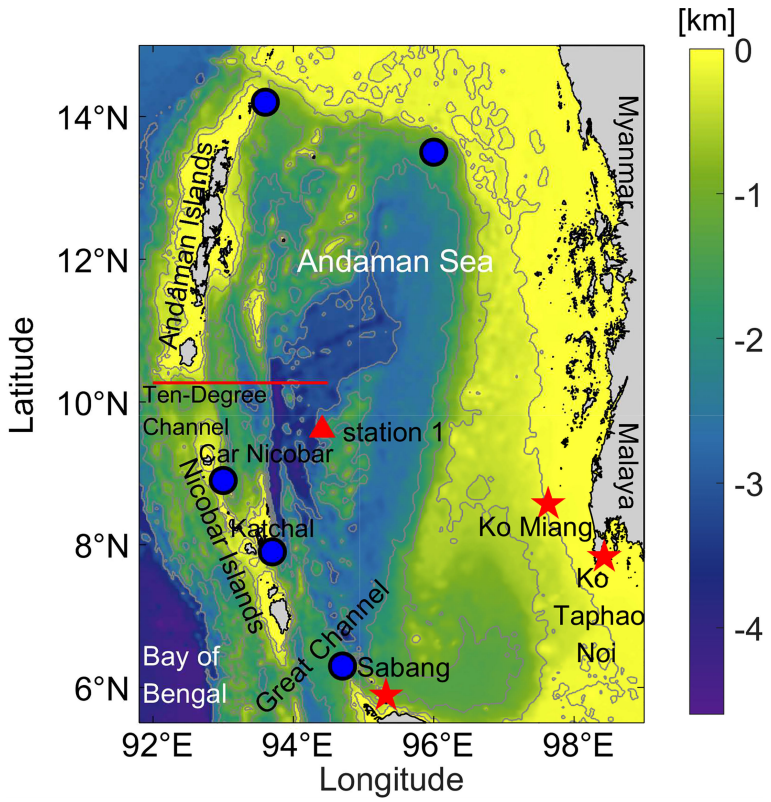

FIGURE 1
Bathymetry map of the model domain. Bathymetry contours are spaced at 100, 500, 1200, 2000, and 3000 m. The red stars represent the three observed stations in the Andaman Sea. The red line indicates one of the major paths of internal tides in the Andaman Sea. The red triangle illustrates the selected section to show the internal tidal form. The blue circles denote the potential generation regions of internal tides (Raju et al., 2019).

be further identified. This work is expected to provide a more comprehensive understanding and enrich the tidal energetics on the internal tides in the Andaman Sea.

The outline of this study is as follows: The numerical model setup and results' validations are described in Section 2. Tidal features in the Andaman Sea and theoretical frameworks are presented in Section 3. Section 4 is the results and discussion of the numerical model, including internal tidal form, generation sites, energy conversion and radiation, etc., in the generation and propagation processes. Conclusions and discussions are given in Section 5.

2 Numerical mode

2.1 Model setup

To examine the energy distribution and dynamical mechanism in the generation and propagation of internal tides in the Andaman Sea, we use the MITgcm (Massachusetts Institute of Technology General Circulation Model) model to conduct a high-resolution, three-dimensional, non-linear, hydrostatic approximation simulation. Orthogonal curvilinear coordinates are selected in the horizontal direction, and the classic z coordinate is selected in the vertical direction. The simulation domain is 5.5°–15°N to 91.8°–99°E. The bottom topography is derived from ETOPO1 dataset with the spatial resolution of (1′)×(1′) (Figure 1). Since the propagation of internal tides over the Andaman Sea is principally along the east-west direction, and the wavelengths are typically tens of kilometers, here the grid resolution is set to be (approximately) 500 m in the x direction and 1000 m in the y direction to achieve a balance between high resolution and accuracy. To capture the features of internal tides in the vertical column, we adopt more grids for the upper ocean than the lower ocean to achieve a balance between accuracy and efficiency. There are 150 layers with an entire depth of 4620 m, ranging from 1 m in each layer near the sea surface to 200 m near the bottom. The minimum depth of topography is set as 10 m to ensure the stability of the simulation, and the time step size is set as 10 s to satisfy the Courant–Friedrichs–Lewy (CFL) condition. An implicit free surface condition is implemented on the simulations, and the

diffusion of temperature and salinity are set to be zero; a similar configuration can be found in many other numerical simulations on internal waves, for example, (Wang et al., 2016; Mohanty et al., 2018; Jithin et al., 2020; Peng et al., 2021). The horizontal and vertical viscosity parameters are chosen homogeneously over the entire simulated area with $A_h = 10^{-3}$ m^2/s and $A_z = 10^{-6}$ m^2/s, and to resolve the energetics of the phenomena whose spatial scale is smaller than the grid size, the nonlocal K-Profile Parameterization scheme (Large et al., 1994) is invoked based on the sensitivity experiments we have conducted (not shown).

Based on MODIS images, Sun et al. (2019) conducted some statistical analyses, which suggested that internal waves occurred at the highest frequency in spring, especially in March, while at the lowest frequency in June and July. Therefore, we simulate the internal tides in the Andaman Sea in March, ranging from 1 March to 31 March 2006, including two complete spring and neap tidal cycles. The initial temperature and salinity (Figure 2) fields are set horizontally homogenous, and the data are extracted from the World Ocean Atlas 2018 (WOA18) dataset. In the upper 1500 m, we choose the monthly average in March, and below 1500 m, we choose the seasonal average. Buoyancy frequency $N = \sqrt{-\frac{g}{\bar{\rho}}\frac{d\rho}{dz}}$, where density ρ can be calculated according to the state equation of seawater EOS80 (UNESCO, 1981), $\bar{\rho}$ is the vertical average of density, z points upward, and g is the gravitational acceleration.

The barotropic tides are used at the four open boundaries, which are derived from the Oregon State University TOPEX/Poseidon Solution (TPXO8-atlas data) 1/30 degree (Egbert and Erofeeva, 2002). We set up 20 grids at the boundaries as the sponge layers, i.e., 10 km in the east-west direction and 20 km in the south-north direction. To compare the contribution of semidiurnal internal tides and diurnal internal tides in the Andaman Sea, we conducted three experiments. Specifically, theyare as follows: the experiments driven by the eight main tides (M2, S2, N2, K2, K1, O1, P1, and Q1), the experiments driven by the four main semidiurnal tides (M2, S2, N2, and K2), and the experiments driven by the four main diurnal tides (K1, O1, P1, and Q1). In all simulations, the salinity and temperature profile are set to be horizontally homogeneous, as in Zeng et al. (2019). To validate the model's accuracy, we also carry out barotropic experiments. The vertical layers decrease to 40 and thermohaline iteration is closed to reduce the computational resources. When the barotropic tidal experiments are conducted, the temperature and salinity are set to be equal throughout the simulated domain, respectively (temperature 7°C, salinity 35 PSU). The simulation duration is extended to 120 days, and other settings are the same as the experiments driven by the eight main tides. Note that detailed configurations of the four numerical experiments are listed in Table 1.

2.2 Model validation

2.2.1 Barotropic tidal validation

We select the results of barotropic sea surface elevation and zonal barotropic velocity from day 16 to day 120 in Experiment 0 and carry out harmonic analysis using the T-Tide toolkit (Pawlowicz et al., 2022) to obtain the amplitude and phase of thetidal constituent and compare them with TPXO8-atlas data. As the M2 and S2 components are the most powerful among all tidal constituents, we show the comparison of the barotropic sea surface elevation and zonal barotropic velocity of M2 and S2 componentsbetween the model results and TPXO8 data in Figure 3.

It is clear that, as shown in Figure 3, the model results are consistent with those of TPXO8 in terms of the co-tidal charts of sea surface elevation, especially in the Andaman and Nicobar Archipelago of the western Andaman Sea near the generation sites of the internal tides. The surface elevation distribution is

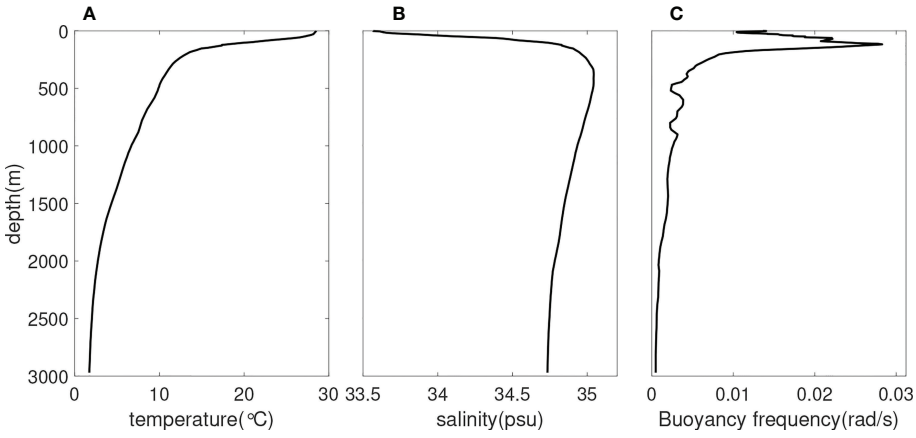

FIGURE 2
Vertical profiles of initial **(A)** temperature, **(B)** salinity, and **(C)** buoyancy frequency.

TABLE 1 The configurations of different numerical experiments.

Experiments number	Tidal forcing	Temperature and salinity distribution	Vertical layers	Simulation time
Barotropic experiment (Experiment 0)	M2, S2, N2, K2, K1, O1, P1, and Q1	Overall homogeneous	40 layers	120 days
The experiment driven by the eight main tides (Experiment 1)	M2, S2, N2, K2, K1, O1, P1, and Q1	horizontally homogeneous	150 layers	31 days
The experiment driven by the four main semidiurnal tides (Experiment 2)	M2, S2, N2, and K2	horizontally homogeneous	150 layers	31 days
The experiment driven by the four main diurnal tides (Experiment 3)	K1, O1, P1, and Q1	horizontally homogeneous	150 layers	31 days

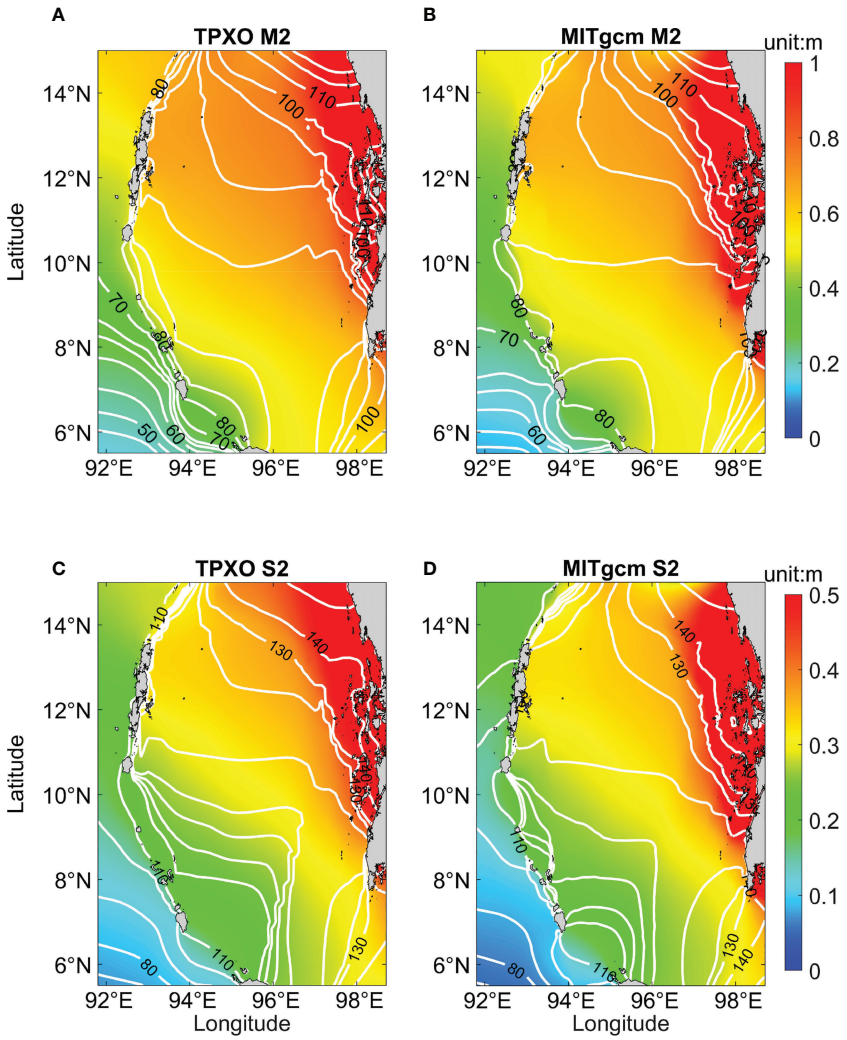

FIGURE 3
M2 and S2 cotidal charts for the barotropic tides based on the **(A, C)** TPXO and **(B, D)** simulation results. The colors indicate the amplitude, and the contours represent the phase. The color scale of M2 cotidal chart ranges from 0 to 1 m, and the color scale of S2 cotidal chart ranges from 0 to 0.5 m.

slightly different in the northern Andaman Sea, where the amplitudes of M2 and S2 tidal constituents obtained from the model results are smaller than those derived from TPXO8, likely due to the difference in bathymetry and the resolution between ETOPO1 and TPXO8. The absolute root-mean-square error (RMSE) can comprehensively evaluate the biases of amplitude and phase for each tidal harmonic (Cummins and Oey, 1997), which is given by

$$E_{ARMS} = \sqrt{\frac{1}{2}(A_0^2 + A_m^2) - A_0 A_m \cdot \cos\ (g_0 - g_m)}, \qquad (1)$$

where A_0 and A_m represent the velocity amplitude derived from TPXO8 and MITgcm, respectively, g_0 and g_m represent the corresponding phase. In Figure 4, the E_{ARMS} for most parts of the Andaman Sea are less than 0.1m/s, and the E_{ARMS} is larger in the east near-coastal area partly due to the bathymetry is abrupt. Overall, the model is adequate to simulate the barotropic tides of the Andaman Sea.

2.2.2 Comparison with observations

Additionally, the model-simulated barotropic sea surface elevations are compared with the field observations at three tide stations (see red stars in Figure 1) near Sumatra and Malay derived from the University of Hawaii Sea Level CENTER (UHSLC). Generally, the amplitude and phase of model-simulated barotropic sea level around spring tide agree well with tide gauge data and TPXO8 (see Figure 5). Specifically, the amplitude of simulated elevation around spring tide at Ko Taphao Noi is slightly higher than that of observations, but the phase matches well. TPXO8-atlas data does not contain the elevation information at Sabang due to its low resolution, so we only compare model-simulated elevation and tide gauge data from UHSLC at this station. The simulated elevation around neap tide at Sabang (at a water depth of 5 m) shows a slight discrepancy with the observational data, probably because there are differences between the bathymetry data and the real topography. In summary, the model-simulated results match well with the observations, suggesting the model is qualified to reproduce the tidal characteristics of the Andaman Sea.

3 Theoretical framework

To characterize barotropic tides in the Andaman Sea, we select Station 1, located in one of the main propagation paths of internal tides (see the red triangle in Figure 1). We present local zonal barotropic velocity and barotropic sea surface elevation. Figure 6 indicates the dominance of semidiurnal tidal constituents at the local site. The maximum zonal barotropic velocities of the eight main tides in Experiment 1 and the four main semidiurnal barotropic tides in Experiment 2 during the spring tide period are about 0.04 m/s. Whereas the velocity for the case of the four main diurnal barotropic tides in Experiment 3 is about 0.003 m/s, which is one order of magnitude smaller. This phenomenon is similar during the neaptide period. For the zonal barotropic velocity, the time series of the eight main tides match well with that of the four main semidiurnal barotropic tides during spring tide. However, the zonal barotropic velocity of the eight main tides is sometimes lower than that of the four main semidiurnal barotropic tides during neap tide. The

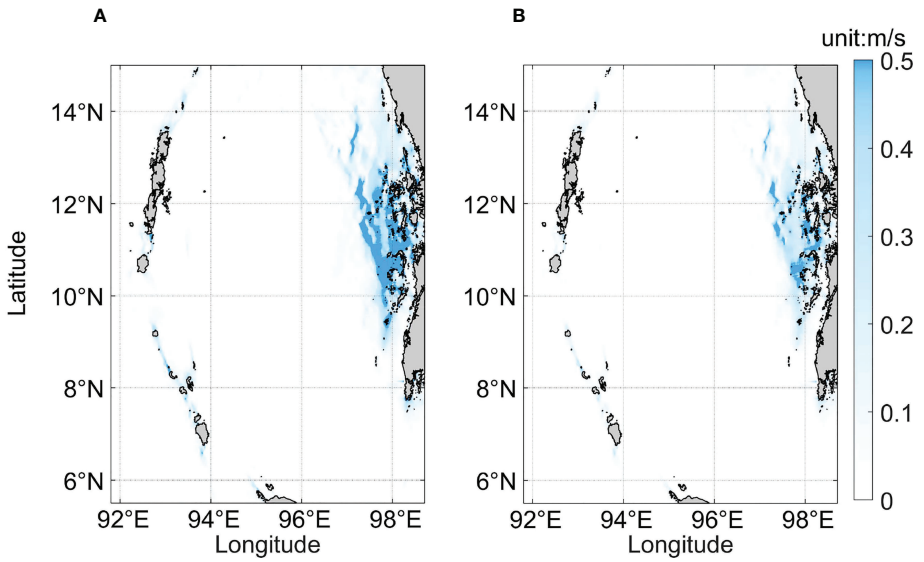

FIGURE 4
EARMS of zonal velocity of **(A)** M2 tidal constituent and **(B)** S2 tidal constituent.

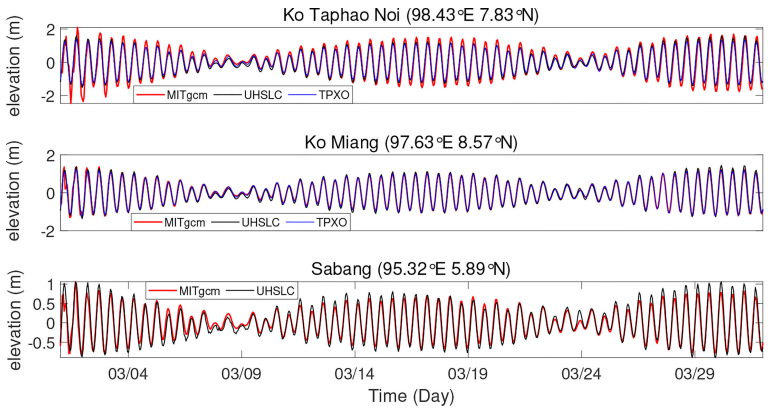

FIGURE 5
The comparisons of barotropic sea levels between model results and observations (locations are marked as red stars in Figure 1). The red line represents model-simulated elevation, the black line represents the tide gauge data from UHSLC, and the blue line represents the data of TPXO8 from 1 March to 31 March.

barotropic sea surface elevation shows similar circumstances at this station. It can be seen from the characteristics of barotropic tides that the semidiurnal tidal constituents are significantly stronger than the diurnal tidal constituents in the whole tidal cycle, and the gap between them is slightly smaller during neap tide. However, the baroclinic energy of internal tides excited by the two tidal constituents in the following calculation shows that the semidiurnal tidal energy is superior to diurnal tidal energy, and they can differ by order of magnitude even during neap tide.

In this paper, the tidally averaged baroclinic energy balance equation (Cummins and Oey, 1997; Kang and Fringer, 2012) is applied to analyze the generation and propagation processes of internal tides in the Andaman Sea, which is written as

$$\frac{\partial}{\partial t}(\langle KE\rangle + \langle APE\rangle) + \nabla\cdot\langle \boldsymbol{F}\rangle = \langle C\rangle - \langle D\rangle - \langle M\rangle, \quad (2)$$

where $\langle\rangle$ indicates depth integration. $KE = \frac{1}{2}\rho_0(u'^2 + v'^2 + w^2)$ denotes the baroclinic kinetic energy, where u' and v' are baroclinic horizontal zonal velocity and meridional velocity, respectively, which can be obtained by subtracting the barotropic components ($\boldsymbol{U}$) from the total velocity ($\boldsymbol{u}$). That is to say, $\mathbf{u}'=\boldsymbol{u}-\boldsymbol{U}$ and $\mathbf{U} = \frac{1}{H+\eta}\int_{-H}^{\eta}\boldsymbol{u}dz$, where η and H are the free surface elevation and bottom depth, respectively. w is

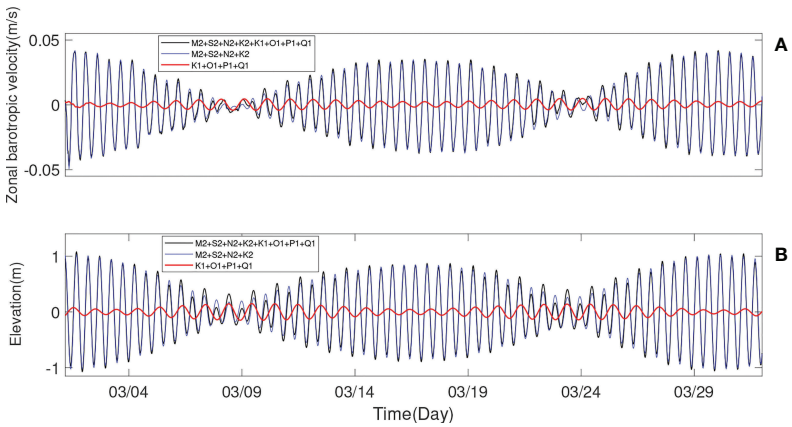

FIGURE 6
The time series of **(A)** model-simulated zonal barotropic velocity for Experiment 1 – 3 and **(B)** barotropic sea surface elevation derived from TPXO8 from 1 March to 31 March at Station 1 (see the red triangle in Figure 1), among which the black curve represents the eight main tides, the blue curve represents the four main semidiurnal tides, and the red curve represents the four main diurnal tides.

vertical velocity, and ρ_0 is reference density. $APE = g^2\ \rho'^2/(2\rho_0 N^2)$ denotes available potential energy, in which $\rho' = \rho(x, y, z, t) - \rho_b(z)$ is the perturbation density and $\rho_b(z)$ is the background density.

The third term of equation (2) represents the divergence of the baroclinic energy flux, which is calculated as follows

$$\langle \boldsymbol{F} \rangle = \langle \boldsymbol{u}'p' \rangle + \langle \boldsymbol{u}KE \rangle + \langle \boldsymbol{u}KE_0 \rangle + \langle \boldsymbol{u}APE \rangle - \langle K_h \nabla KE \rangle - \langle A_h \nabla APE \rangle . \quad (3)$$

p' is the perturbation pressure, which is given by

$$p' = \int_z^{\eta} \rho'(\hat{z}, t) g d\hat{z} - \frac{1}{H+\eta} \int_{-H}^{\eta} \int_z^{\eta} \rho'(\hat{z}, t) g d\hat{z}\, dz, \quad (4)$$

and $KE_0 = \rho_0(Uu' + Vv')$. K_h and A_h are the horizontal eddy diffusivity and viscosity parameters, respectively (Wang et al., 2018).

$C = \rho' g W$ is the barotropic-to-baroclinic energy conversion rate, the positive values of which are the sources of internal tidal energy. $W = -\nabla \cdot [(H+z)\boldsymbol{U}]$ is vertical barotropic velocity.

The following two parameters are calculated to evaluate whether the regions with high barotropic-to-baroclinic energy conversion rates are the internal tides generation sites

Slope criticality:

$$\alpha = \frac{\frac{dh}{dx}}{\sqrt{\frac{\omega^2 - f^2}{N^2 - \omega^2}}},$$

where $h(x)$ is the bathymetry, ω is the tidal frequency, and $f = 2\varpi \sin\varphi$ is the Coriolis parameter, with ϖ the Earth's rotational angular velocity and φ the corresponding latitude (Gilbert and Garrett, 1989; 206 Shaw et al., 2009). $\alpha > 1$, $\alpha = 1$, and $\alpha < 1$ represent supercritical, critical, and subcritical ridges, respectively. When $\alpha > 1$ internal tides are possibly generated (Hurley and Keady, 1997; Zhang et al., 2007).

Internal tide generating body force or Baines force:

$$F_{body} = \frac{\boldsymbol{Q} \cdot \nabla(1/h)}{\omega} \int_{-H}^{\eta} zN^2(z) dz,$$

in which $\boldsymbol{Q} = (Uh, Vh)$ is barotropic mass flux vector, and ∇ is the horizontal gradient operator. Internal tides are often generated where F_{body} is large ($F_{body} > 0.25 m^2/s^2$) (Lozovatsky et al., 2012; Raju et al., 2019).

4 Results and discussion

4.1 Internal tides form

The sections of modelled zonal baroclinic velocity and isotherms of semidiurnal internal tides and diurnal internal tides along 10.27°N are shown in Figure 7. There are evident internal tides beam of semidiurnal internal tides from 92.5°E to 94°E, while the diurnal internal tidal signals are relatively weak. In terms of isothermal displacements of 18°C, the amplitude of

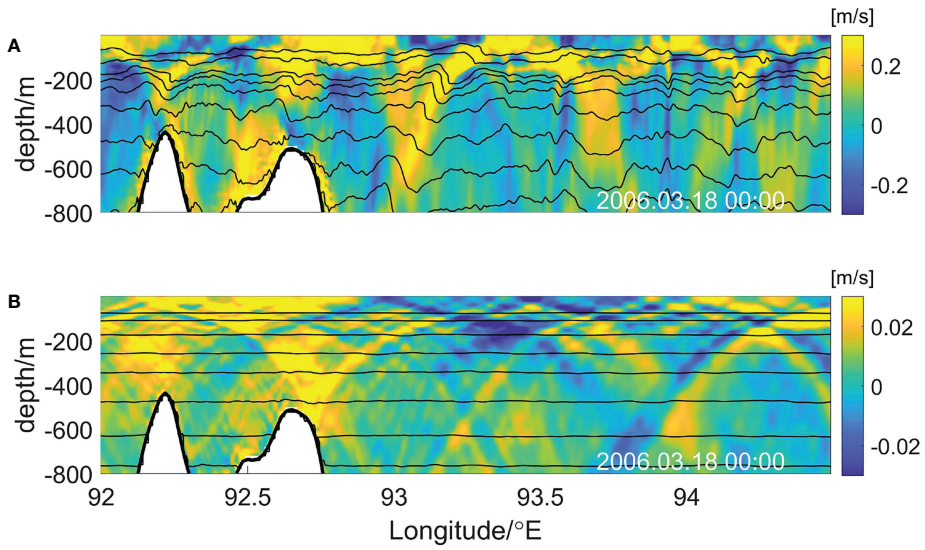

FIGURE 7
Selected section along 10.27°N (see the red line in Figure 1) of **(A)** semidiurnal internal tides and **(B)** diurnal internal tides showing modelled zonal baroclinic velocity (u ′, colour coded in m/s on the right-hand side) dated 18 March 2006 at 00:00. The solid black lines are isotherms. Note that the color scales in the two panels are different.

semidiurnal internal tides is about 40 m. In contrast, its counterpart, diurnal internal tides, is only about 4 m (see Figure 8). The two ridges located at 92.3°E and 92.7°E are capable of generating semidiurnal internal tides, which propagate east-westward (see Figure 8A). In Figure 8A, the distribution and propagation of semidiurnal internal tides can be clearly observed, characterized by east-west radiations in the entire model domain. The Andaman and Nicobar Archipelago are the main generation sites of semidiurnal internal tides. The fluctuation signals of the diurnal internal tides are not obvious (see Figure 8B), and there are no evident diurnal tidal generation sites.

4.2 Generation of internal tides

4.2.1 Energy distribution

To evaluate the different characteristics of internal tides during spring and neap tide, we select 15-16 March as the spring tide period and 23-24 March as the neap tide period, respectively, for calculation (see Figure 6). The generation of internal tides is accompanied by energy conversion from barotropic to baroclinic tides. Figure 9 shows spatial distributions of the time-averaged depth-integrated barotropic-to-baroclinic conversion rate during the spring and neap tide periods. The positive barotropic-to-baroclinic energy conversion rate represents the generation of internal tidal energy, and the negative means the reverse conversion from baroclinic to barotropic tides (e.g., Zilberman et al., 2009; Kerry et al., 2013; 233 Nagai and Hibiya, 2015). During the spring tide, the total barotropic-to-baroclinic energy conversion rate of the Andaman Sea is 29.15 GW in Experiment 1, 29.24 GW in Experiment 2, and 0.05 GW in Experiment 3, respectively. During the neap tide, the total barotropic-to-baroclinic energy conversion rate of the Andaman Sea is 3.08 GW in Experiment 1, 2.56 GW in Experiment 2, and 0.31 GW in Experiment 3, respectively. It can be seen that semidiurnal tidal energy is dominant since there is little difference between the energy conversion rate in Experiment 1 and Experiment 2. Four regions denoted as A, B, C, and D with high barotropic-to-baroclinic energy conversion rates are marked as black boxes in Figure 9. They are close to those found by Mohanty et al. (2018) and Raju et al. (2019), indicating the four main generation sites of internal tides in the Bay of Bengal. Note that in some regions, see Figures 9D, E, the conversion rate is negative, which can be generally attributed to the phase (greater than 90 degree) difference between the baroclinic pressure and vertical barotropic velocity. When the remotely-generated internal tides are dominant at the local site, the local pressure can be significantly influenced, thereby resulting in the negative conversion rate. It can be seen in Figure 9D, these negative conversions occured in domains B and C, where the remotely-generated internal tides are relatively strong. As the disturbance pressure of the remote internal tides and the local vertical

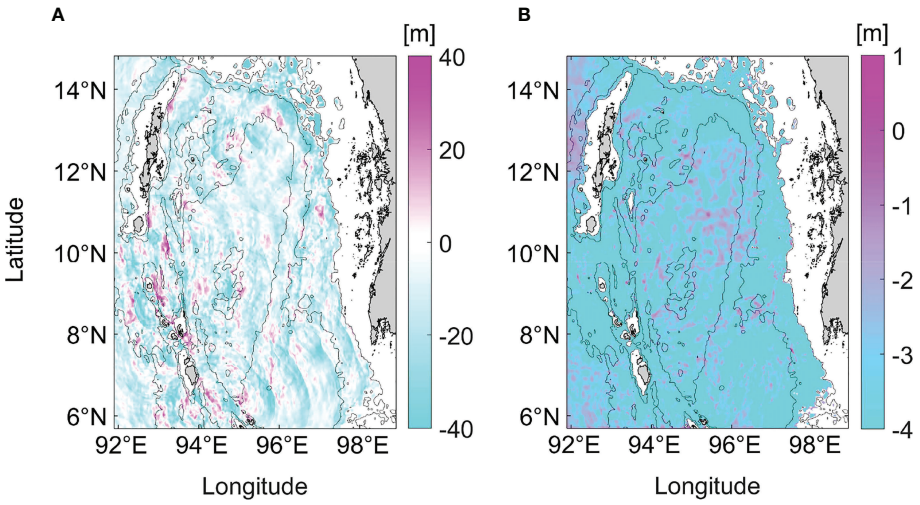

FIGURE 8
A snapshot of the model-predicted isothermal displacements of 18°C for **(A)** semidiurnal internal tides and **(B)** diurnal internal tides at 00:00 on 18 March 2006. Bathymetry contours are spaced at 100, 500, and 2000 m. The blank space represents the shelf. Note that the color scales in the two panels are different.

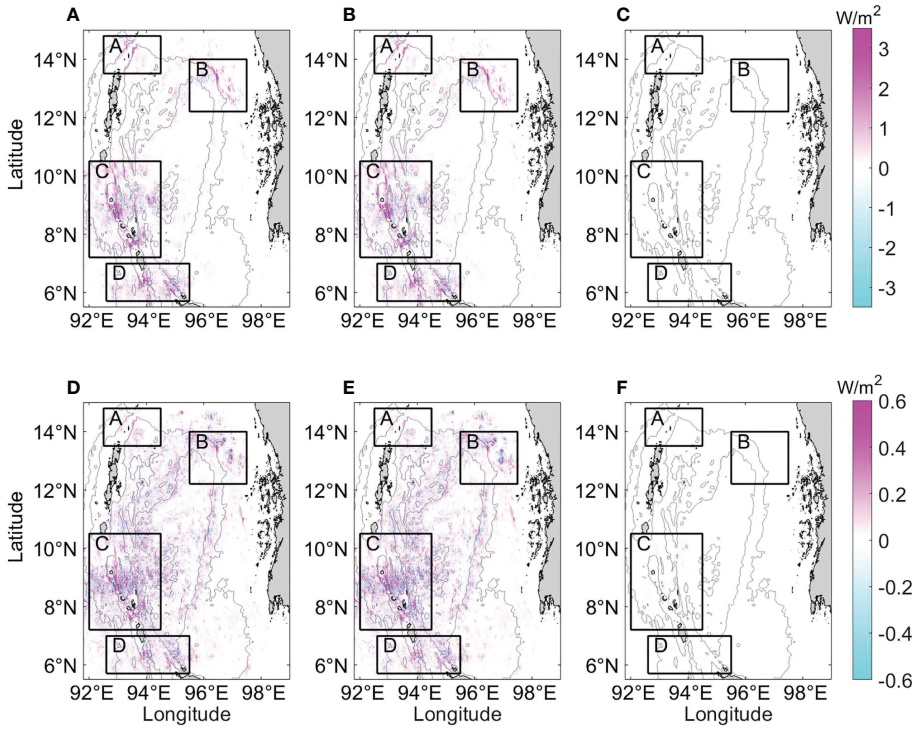

FIGURE 9
Spatial distributions of the time-averaged depth-integrated barotropic-to-baroclinic conversion rate in the **(A, D)** Experiment 1, **(B, E)** Experiment 2, and **(C, F)** Experiment 3. The period of **(A ~ C)** is spring tide, and the range of color scale is −3.5 ~ 3.5 W/m^2; the period of **(D ~ F)** is neap tide, and the range of color scale is −0.6 ~ 0.6 W/m^2. The four rectangles present the main generation subdomains of internal tides. Bathymetry contours are spaced at 500 and 2000 m.

barotropic velocity are out of phase, the conversion rate is negative, see Zilberman et al. (2011); Gong et al. (2019) for similar scenarios.

4.2.2 Generation regions

4.2.2.1 Slope criticality

Slope criticality is related to the period of tidal constituents. In the Andaman Sea, the M2 tidal constituent is the strongest among whole semidiurnal tidal constituents, and the K1 tidal constituent is the strongest among whole diurnal tidal constituents. The distribution of slope criticality greater than 1 of these two tidal constituents is shown in Figure 10. The high values of slope criticality of the M2 tidal constituent (in Figure 10) are mainly distributed in the Andaman and Nicobar Archipelago, northwest Sumatra, and the northeast Andaman Sea, close to the four regions with high barotropic-to-baroclinic energy conversion rate (Figure 9). For the K1 tidal constituent, the frequency of which is about half that of the M2 tidal constituent, and the angle between the internal tides beam and the horizontal direction excited by which is smaller than that excited by the M2 tidal constituent, so the distribution of high slope criticality is more extensive (Figure 10A).

4.2.2.2 Internal tide generating body force

The high body force regarding K1 and M2 tidal constituents is located in the vicinity of the Andaman and Nicobar Archipelago and northeastern Andaman Sea (Figure 11), which shows similar spatial patterns to slope criticality. It is noted that the body force of the M2 tidal constituent in the northeastern Andaman Sea is also high, as shown in Figure 11B, indicating that M2 internal tides can be generated here. However, the topography in these areas is shallow and abrupt, so the generated internal tides dissipate within a short distance (see Figure 8A). The body force of the K1 tidal constituent is smaller than that of the M2 tidal constituent, demonstrating that the formation of diurnal internal tides is limited. The areas with body force greater than 0.25m^2/s^2 regarding the M2 tidal constituent account for 33% of the model domain, and those regarding the K1 tidal constituent account for 17%. As internal tides are mainly generated where F_{body}>0.25m^2/s^2, the M2 internal tides are more likely to be generated in the Andaman Sea.

4.3 Propagation of internal tides

4.3.1. Energy distribution

To further determine the generation regions of internal tides, we calculate the internal tidal energy budget following equation (3).

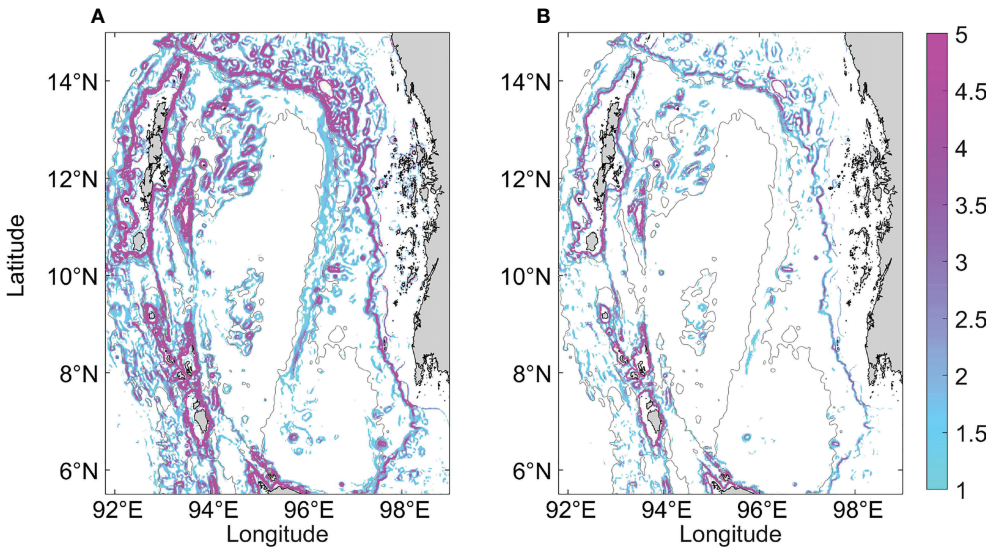

FIGURE 10
Slope criticality of **(A)** K1 tidal constituent and **(B)** M2 tidal constituent. Bathymetry contours are spaced at 500 and 2000 m.

we find that the magnitude of the first pressure term is much larger than the other five terms. Note that the following results are the comprehensive results of these six terms. The distribution of baroclinic energy flux in Experiment 2 (Figures 12B, E) is similar to that in Experiment 1 (Figures 12A, D), while that in Experiment 3 is indistinguishable (Figures 12C, F). The energy propagating direction of internal tides is mainly east-west, and the maximum value appears near the generation regions in Experiment 1.

In Figures 12A, B, the radiation sources of baroclinic energy are obvious during spring tides, mainly located in the Andaman and Nicobar Archipelago and the northeastern Andaman Sea, namely the four regions in Figure 9. The baroclinic energy flux in

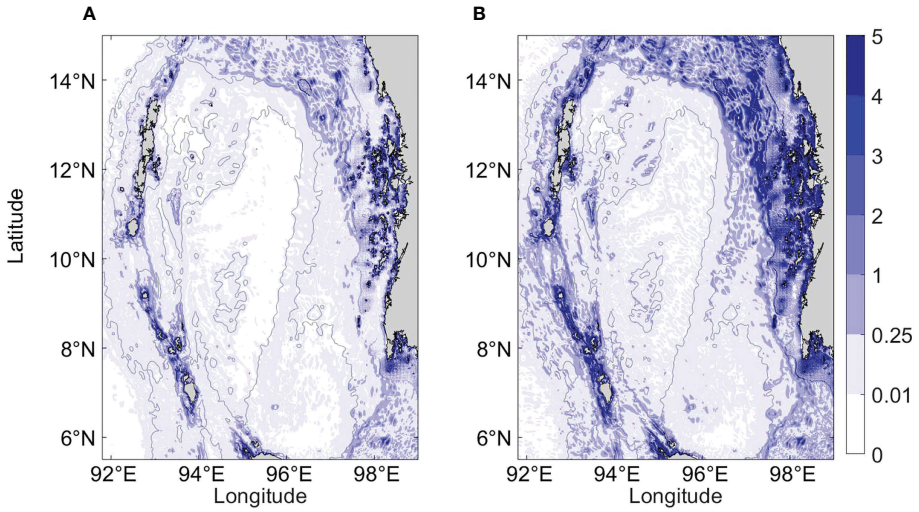

FIGURE 11
Maximum absolute value of depth-integrated internal tide generating body force of **(A)** K1 tidal constituent and **(B)** M2 tidal constituent in March. Bathymetry contours are spaced at 500 and 2000 m.

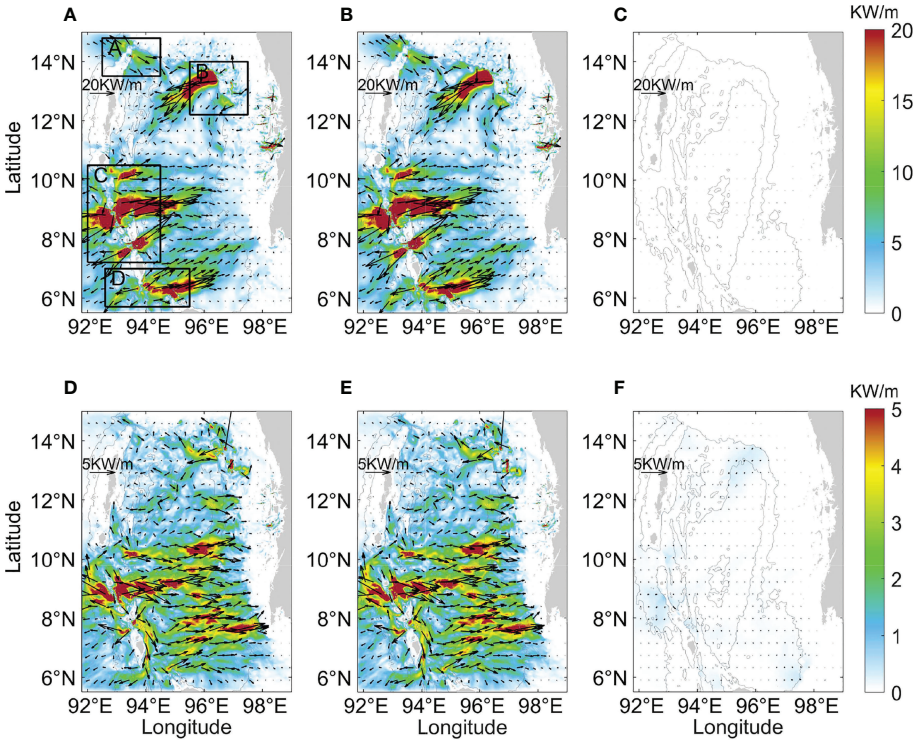

FIGURE 12
Spatial distribution of the time-averaged depth-integrated baroclinic energy flux in the **(A, D)** Experiment 1, **(B, E)** Experiment 2, and **(C, F)** Experiment 3. The period of **(A–C)** is spring tide, and the range of color scale is 0~20KW/m; the period of **(D–F)** is neap tide, and the range of color scale is 0~5KW/m. The color shade indicates the magnitude of the baroclinic energy flux, and the arrows indicate the direction of the baroclinic energy flux. The four rectangles in the panel **(A)** present the main generation subdomains of internal tides. Bathymetry contours are spaced at 500 and 2000 m.

Experiment 1 in subdomain C is significantly large (>20KW/m) and propagates at a relatively long distance (200 km). It can be seen that the energy flux can propagate both westward and eastward, butthe energy decreases rapidly when crossing 92°E and 95.5°E, respectively. There are three apparent energy sources in the vicinity of the ten-degree channel, Car Nicobar and Katchal. Among them, the south of Car Nicobar is the strongest site (see Figure 13A). Baroclinic energy flux around the northern Andaman Islands (subdomain A) is the smallest compared with the other three subdomains and mainly propagates northwestward and southeastward. The northwestward energy radiates into the northern Bay of Bengal and then interferes with local internal tides. The southeastward energy dissipates after propagating a distance of 20 km. The baroclinic energy in subdomain B mainly propagates southwestward, then interference with that from subdomain A near 94.8°E. In northwestern Sumatra (subdomain D), the propagation direction of baroclinic energy flux is also mainly east-westward, and the eastward energy issignificantly higher than the westward energy. The eastward baroclinic energy flux decreases sharply when crossing 95.7°E and gradually turns northeastward around 96°E. In the east of the Andaman Sea and west of Myanmar, the baroclinic energy can also be observed in the vicinity of 11~13°N, 98.2°E. Although baroclinic tides can be motivated over the complicated local topography,they only radiate away within a short distance and dissipate quickly.

The baroclinic energy flux during neap tide (Figures 12D, E) is smaller than that during spring tide (Figures 12A, B). The radiation sources of energy are scattered during the neap tides, and regions with high values of energy fluxes are mainly located in the southern Andaman Sea. The baroclinic energy flux in the southern Car Nicobar is still large, and the east-west propagation characteristics can also be seen. Still, the characteristics in the other three subdomains, especially in subdomain A, are not obvious.

The propagation of internal tides is accompanied by energy radiation and dissipation. By averaging over several tidal cycles, baroclinic energy is approximately equal to the sum of baroclinic energy flux divergence and baroclinic dissipation rate, namely $\langle \overline{C} \rangle = \langle \overline{\nabla \cdot F} \rangle + \langle \overline{D+M} \rangle$, where $\langle \overline{D+M} \rangle$ is the dissipation term and $\overline{(\ )}$ represents time average. In Figure 14, there is little difference between the baroclinic energy flux divergence in Experiment 1 and Experiment 2 compared with Experiment 3 during the spring and neap tide period. The baroclinic energy

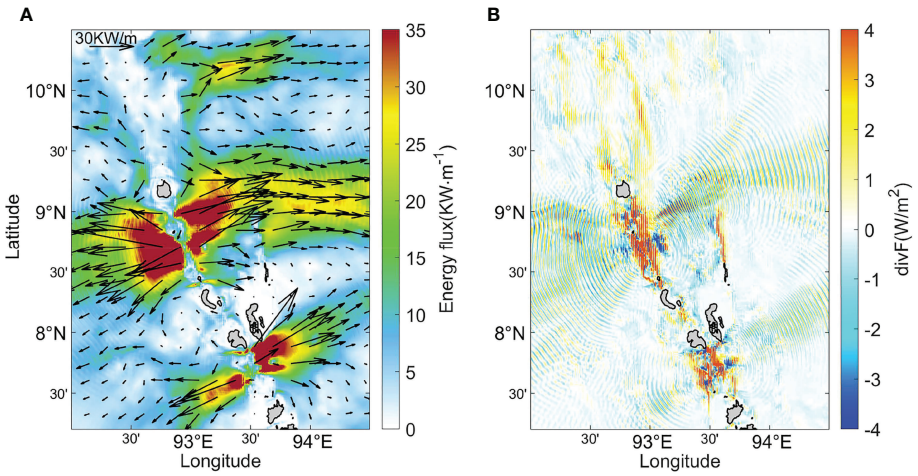

FIGURE 13
The distribution of **(A)** baroclinic energy flux and **(B)** the divergence during the spring tide period in the subdomain C in the Experiment 1.

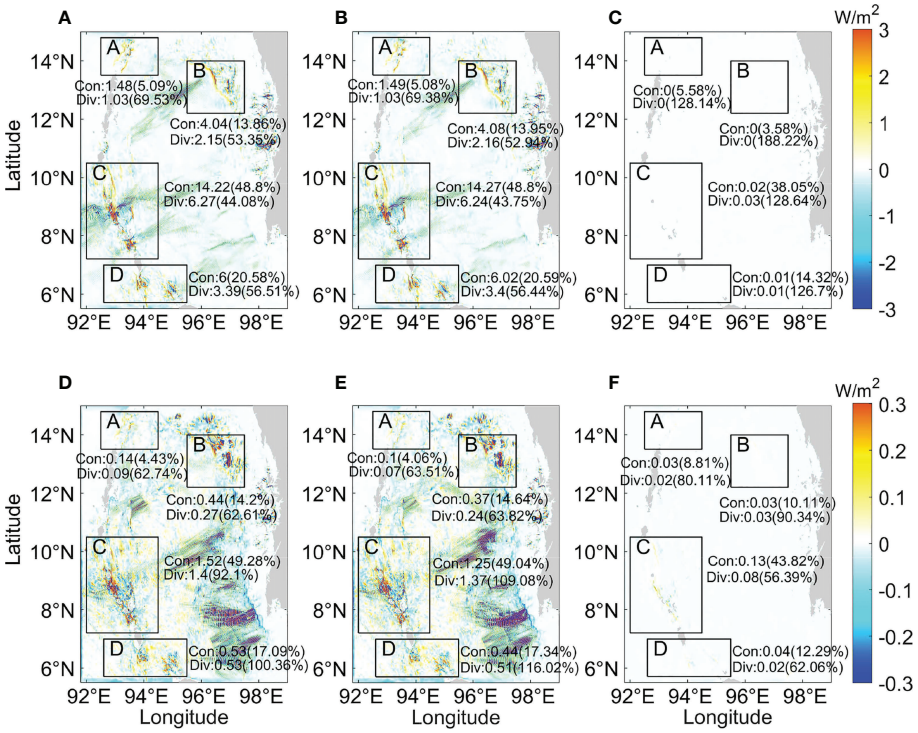

FIGURE 14
Spatial distribution of the time-averaged depth-integrated baroclinic energy flux divergence in the **(A, D)** Experiment 1, **(B, E)** Experiment 2, and **(C, F)** Experiment 3. The period of **(A–C)** is spring tide, and the range of color scale is −3~3W/m^2; the period of **(D–F)** is neap tide, and the range of color scale is −0.3~0.3W/m^2. The four rectangles present the main generation subdomains of internal tides. Con represents the barotropic-to-baroclinic energy conversion rate of the corresponding subdomain (unit: GW), and the percentage of that to the total barotropic-to-baroclinic energy conversion rate in the Andaman Sea is shown in brackets. Div represents the baroclinic energy flux divergence of the corresponding subdomain (unit: GW), and the percentage of that to the barotropic-to-baroclinic energy conversion rate of the corresponding subdomain is shown in brackets.

flux divergence of semidiurnal internal tides is three orders of magnitude larger than that of diurnal internal tides during the spring tides, while it is one order of magnitude larger than diurnal internal tides during the neap tides, similar to the barotropic-to-baroclinic energy conversion rate. The large values of divergence are mainly located at the generation sites of internal tides, and the distribution of which is similar to that of barotropic-to-baroclinic conversion rate, slope criticality, and body force. There is a lot of negative divergence during neap tide in the eastern Andaman Sea, corresponding to the local energy dissipation of internal tides in high modes. In Figures 14A, B, the largest baroclinic conversion rates occur in subdomain C during spring tide, and the percentage of energy flux divergence to the conversion rate (44%) is the smallest among the four subdomains, indicating that the relative dissipation is largest. The dissipation $\langle \overline{D+M} \rangle$ in subdomain C is about 56% during spring tide, demonstrating that half baroclinic energy of the rest will dissipate. The barotropic-to-baroclinic conversion rate and energy flux divergence in Experiment 2 are larger than in Experiment 1 in some regions, likely due to the out-phase of semidiurnal internal tides and diurnal internal tides. Moreover, the energy budget in the Andaman Sea is calculated during the entire tidal period (Figure 15), suggesting that the 14-day time-averaged energy flux divergence is always lower than the barotropic-to-baroclinic conversion rate in all three experiments. Nonetheless, the energy terms of diurnal internal tides are two orders of magnitude lower than that of semidiurnal internal tides.

4.3.2 Energy budget

In Figure 16, there are two peaks of barotropic-to-baroclinic energy conversion rate of both semidiurnal internal tides and diurnal internal tides during their tidal period (Figures 16C2, C3, D2, D3). For semidiurnal internal tides, the first (second) peak within 12 hours is bigger during the spring (neap) tide. For diurnal internal tides, there is no apparent difference between the two peaks within 24 hours. In fact, the generation of internal tides corresponds to the time when the second extreme appears. The two peaks of the barotropic-to-baroclinic energy conversion rate of the whole Andaman Sea are more evident than that of subdomain C (Figures 16A1, B1). In Figures 17C3 and D3, there are also two peaks of baroclinic energy flux divergence of both semidiurnal internal tides and diurnal internal tides within their tidal period during the neap tide. However, in Figure 17C2, there are multiple peaks of semidiurnal internal tides within 12 hours during spring tide. The baroclinic energy among subdomain C accounts for almost half of that among the whole Andaman Sea (Figures 16A1, 16B1, 17A1 and 17B1). Both the barotropic-to-baroclinic energy conversion rate and baroclinic energy divergence show that the energy variations in Experiment 1 are similar to those in Experiment 2.

5 Conclusions

In this study, a high-resolution three-dimensional MITgcm is configured to investigate the generation and propagation processes of internal tides in the Andaman Sea. The differences in spatial distributions and energy budgets between the semidiurnal and diurnal internal tides in the Andaman Sea are discussed. The semidiurnal internal tides are dominant in the Andaman Sea, and their intensity is not significantly different from that of the internal tides excited by eight main tides. Diurnal barotropic tides can independently reproduce internal tides, but the intensity of which is much weaker than that driven by semidiurnal components. The strength of diurnal barotropic tides (e.g., the maximum zonal barotropic velocity is 0.003 m/s at station 1 in Figure 1 during the spring tides period) is generally one order of magnitude smaller than that of the semidiurnal barotropic tides (e.g., the maximum zonal barotropic velocity is 0.04 m/s at station 1 in Figure 1 during the spring tides period).

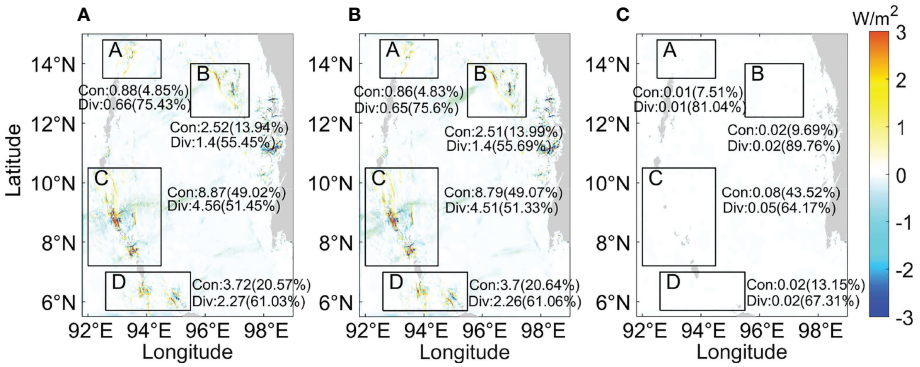

FIGURE 15
Same as Figures 14A–C, but during the entire tidal period (14 days).

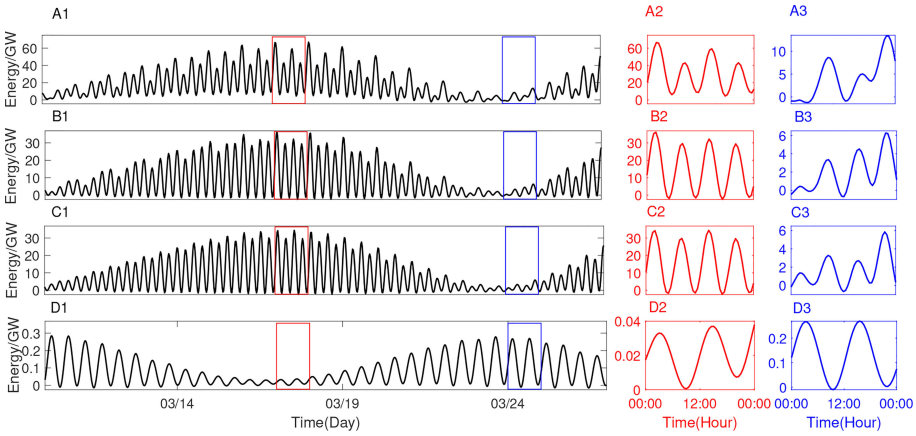

FIGURE 16
Time series of the barotropic-to-baroclinic energy conversion rate in the Andaman Sea, in which **(A1 ~ A3)** is in the whole Andaman Sea in Experiment 1, **(B1 ~ B3)** is in subdomain C in Experiment 1**, (C1 ~ C3)** is in subdomain C in Experiment 2, and **(D1 ~ D3)** is in subdomain C in Experiment 3. **A2 (A3)**, **B2 (B3)**, **C2 (C3)**, and **D2 (D3)** are on March 17 (24), corresponding to the red (blue) rectangle in **A1**, **B1**, **C1**, and **D1**.

However, the energy of diurnal internal tides (e.g., the total barotropic-to-baroclinic energy conversion rate in the Andaman Sea is 0.05 GW) is about three orders of magnitude lower than that of semidiurnal internal tides (e.g., the total barotropic-to-baroclinic energy conversion rate in the Andaman Sea is 29.24 GW) during the spring tides. The energy of diurnal internal tides (e.g., the total barotropic-to-baroclinic energy conversion rate in the Andaman Sea is 0.31 GW) is about one order of magnitude lower than that of semidiurnal internal tides (e.g., the total barotropic-to-baroclinic energy conversion rate in the Andaman Sea is 2.56 GW) during the neap tides. Calculations for the entire tide period in the Andaman Sea show that the diurnal tidal energy is two orders of magnitude lower than the semidiurnal tidal energy. There are evident semidiurnal internal tides beam, while the diurnal internal tidal signals are relatively weaker. The amplitude of diurnal internal tides reflected by the isothermal fluctuation is also one magnitude lower than that of semidiurnal internal tides. In addition, there are two peaks of barotropic-to-baroclinic energy conversion rate of both semidiurnal internal tides and diurnal internal tides during their tidal period, and the generation of internal tides corresponds to the second peak. For semidiurnal internal tides, the first peak within 12 hours is larger around spring tide, and the second peak is larger around the neap tide.

Four potential generation regions of internal tides are found, mainly distributed in the Andaman and Nicobar Archipelago and the northeastern Andaman Sea. These regions satisfy the generation conditions by calculating slope criticality and internal

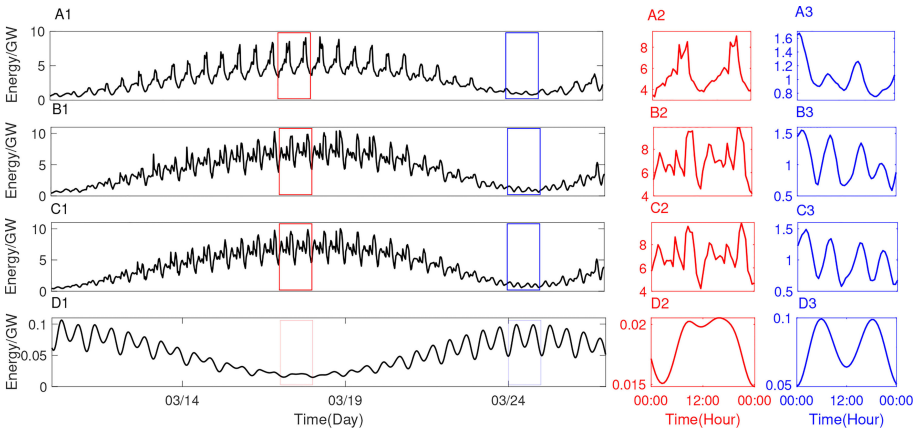

FIGURE 17
Same as Figure 16, but for baroclinic energy flux divergence.

tide generating body force. The distribution of baroclinic energy fluxes also shows that the internal tides are indeed generated in these subdomains and radiate outward. Among the four subdomains, the baroclinic energy in subdomain C accounts for about half of the whole Andaman Sea. Simultaneously, in the spring tides, most of the baroclinic energy is in the subdomain C, and more than half of the energy dissipates locally in this subdomain, contrasting to the subdomain A. Nevertheless, the baroclinic energy flux in subdomain C is significantly large (>20KW/m) and propagates over a relatively long distance (200 km). Inside subdomain C, we also find three obvious energy sources in the vicinity of the ten-degree channel, Car Nicobar and Katchal. In the neap tides, the baroclinic energy in region C is still large, and the generated internal tides propagate along the east-west direction; however, the energy contribution of the other three regions is much lower, especially region A. The internal tidal energy is mainly distributed in the southern Andaman Sea during this period. There are no evident diurnal internal tidal generation sites found, and the strength of the diurnal internal tides is also weak, which indicates that the inclusion of diurnal barotropic tides negligibly modulates the internal tides in the Andaman Sea.

In conclusion, this numerical study highlights the dominant semidiurnal internal tides in the Andaman Sea and the generation sites of internal tides. Moreover, understanding the generation mechanism of internal tides in the spring and neap tides and quantitatively identifying the tidal energy budget among the four regions in this study indeed give a complete story of internal tides during the generation, propagation, and dissipation processes in the Andaman Sea. Nonetheless, this work still leaves some questions which need to be further explored: the generation mechanism of the internal tides in the four subdomains identified; the radiating energy pathways after leaving the generation sites; the dynamical manner of the internal tides, especially its relationship with the large-amplitude nonlinear internal waves.

Data availability statement

Publicly available datasets were analyzed in this study. This data can be found here: https://www.tpxo.net/ https://ngdc.noaa.gov/mgg/global/global.html.

Author contributions

WW conducted the numerical simulations, performed the data analyses and wrote the manuscript. YG contributed significantly to the data analyses and manuscript preparation. ZW and CY conceived and designed the study, performed the data analyses and wrote the manuscript. All authors contributed to the article and approved the submitted version.

Funding

This work was supported by the National Natural Science Foundation of China (42006016, 12132018), the Fundamental Research Funds for the Central Universities (202265005), the Natural Science Foundation of Shandong Province (ZR2020QD063), the key program of the National Natural Science Foundation of China (91958206) and the National Natural Science Foundation of China (42206012).

Acknowledgments

The authors would like to thank the reviewers for their valuable suggestions on the manuscript.

Conflict of interest

The authors declare that the research was conducted in the absence of any commercial or financial relationships that could be construed as a potential conflict of interest.

Publisher's note

References

Alford, M. H. (2003). Redistribution of energy available for ocean mixing by long-range propagation of internal waves. *Nature* 423, 159–162. doi: 10.1038/nature01628

Alpers, W., Wang-Chen, H., and Hock, L. (1997). "Observation of internal waves in the Andaman Sea by ERS SAR," IGARSS'97. 1997 IEEE International Geoscience and Remote Sensing Symposium Proceedings. Remote Sensing - A Scientific Vision for Sustainable Development, 4, 1518–1520. doi: 10.1109/IGARSS.1997.608926

Cummins, P. F., and Oey, L.-Y. (1997). Simulation of barotropic and baroclinic tides off northern British Columbia. *J. Phys. Oceanogr.* 27, 762–781. doi: 10.1175/1520-0485(1997)027<0762:SOBABT>2.0.CO;2

Egbert, G. D., and Erofeeva, S. Y. (2002). Efficient inverse modeling of barotropic ocean tides. *J. Atmos. Oceanic Technol.* 19, 183–204. doi: 10.1175/1520-0426(2002)019<0183:EIMOBO>2.0.CO;2

Egbert, G. D., and Ray, R. D. (2000). Significant dissipation of tidal energy in the deep ocean inferred from satellite altimeter data. *Nature* 405, 775–778. doi: 10.1038/35015531

Fang, X., and Du, T. (2005). *Fundamentals of oceanic internal waves and internal waves in the China seas* (Qingdao: China Ocean University Press).

Gilbert, D., and Garrett, C. (1989). Implications for ocean mixing of internal wave scattering off irregular topography. *J. Phys. Oceanogr.* 19, 1716–1729. doi: 10.1175/1520-0485(1989)019<1716:IFOMOI>2.0.CO;2

Gong, Y., Rayson, M. D., Jones, N. L., and Ivey, G. N. (2019). The effects of remote internal tides on continental slope internal tide generation. *J. Phys. Oceanogr.* 49, 1651–1668. doi: 10.1175/JPO-D-18-0180.1

Hurley, D. G., and Keady, G. (1997). The generation of internal waves by vibrating elliptic cylinders. part 2. approximate viscous solution. *J. Fluid Mechanics* 351, 119–138. doi: 10.1017/S0022112097007039

Hyder, P., Jeans, D., Cauquil, E., and Nerzic, R. (2005). Observations and predictability of internal solitons in the northern Andaman Sea. *Appl. Ocean Res.* 27, 1–11. doi: 10.1016/j.apor.2005.07.001

Jithin, A., Francis, P., Unnikrishnan, A., and Ramakrishna, S. (2019). Modeling of internal tides in the western bay of Bengal: characteristics and energetics. *J. Geophys. Res.: Oceans* 124, 8720–8746. doi: 10.1029/2019JC015319

Jithin, A., Francis, P., Unnikrishnan, A., and Ramakrishna, S. (2020). Energetics and spatio-temporal variability of semidiurnal internal tides in the bay of Bengal and Andaman Sea. *Prog. Oceanography* 189, 102444. doi: 10.1016/j.pocean.2020.102444

Kang, D., and Fringer, O. (2012). Energetics of barotropic and baroclinic tides in the Monterey bay area. *J. Phys. Oceanogr.* 42, 272–290. doi: 10.1175/JPO-D-11-039.1

Kerry, C. G., Powell, B. S., and Carter, G. S. (2013). Effects of remote generation sites on model estimates of M_2 internal tides in the Philippine Sea. *J. Phys. Oceanogr.* 43, 187–204. doi: 10.1175/JPO-D-12-081.1

Large, W. G., McWilliams, J. C., and Doney, S. C. (1994). Oceanic vertical mixing: a review and a model with a nonlocal boundary layer parameterization. *Rev. Geophys.* 32, 363–403. doi: 10.1029/94RG01872

Lozovatsky, I., Liu, Z., Fernando, H., Armengol, J., and Roget, E. (2012). Shallow water tidal currents in close proximity to the seafloor and boundary-induced turbulence. *Ocean Dynamics* 62, 177–191. doi: 10.1007/s10236-011-0495-3

Magalhaes, J. M., da Silva, J. C. B., and Buijsman, M. C. (2020). Long lived second mode internal solitary waves in the Andaman Sea. *Sci. Rep.* 10, 1–10. doi: 10.1038/s41598-020-66335-9

Mohanty, S., Rao, A. D., and Latha, G. (2018). Energetics of semidiurnal internal tides in the Andaman Sea. *J. Geophys. Res.: Oceans* 123, 6224–6240. doi: 10.1029/2018JC013852

Munk, W., and Wunsch, C. (1998). Abyssal recipes II: energetics of tidal and wind mixing. *Deep Sea Res. Part I: Oceanogr. Res. Papers* 45, 1977–2010. doi: 10.1016/S0967-0637(98)00070-3

Nagai, T., and Hibiya, T. (2015). Internal tides and associated vertical mixing in the Indonesian archipelago. *J. Geophys. Res.: Oceans* 120, 3373–3390. doi: 10.1002/2014JC010592

Osborne, A. R., and Burch, T. L. (1980). Internal solitons in the Andaman Sea. *Science* 208, 451–460. doi: 10.1126/science.208.4443.451

Pawlowicz, R., Beardsley, B., and Lentz, S. (2002). Classical tidal harmonic analysis including error estimates in MATLAB using T_TIDE. *Comput. Geosci.* 28, 929–937. doi: 10.1016/S0098-3004(02)00013-4

Peng, S., Liao, J., Wang, X., Liu, Z., Liu, Y., Zhu, Y., et al. (2021). Energetics-based estimation of the diapycnal mixing induced by internal tides in the Andaman Sea. *J. Geophys. Res.: Oceans* 126, e2020JC016521. doi: 10.1029/2020JC016521

Perry, R. B., and Schimke, G. R. (1965). Large-Amplitude internal waves observed off the northwest coast of Sumatra. *J. Geophys. Res.* 70, 2319–2324. doi: 10.1029/JZ070i010p02319

Raju, N. J., Dash, M. K., Dey, S. P., and Bhaskaran, P. K. (2019). Potential generation sites of internal solitary waves and their propagation characteristics in the Andaman Sea–a study based on MODIS true-colour and SAR observations. *Environ. Monit. Assess.* 191, 1–10. doi: 10.1007/s10661-019-7705-8

Rattray, J. M. (1960). On the coastal generation of internal tides. *Tellus* 12, 54–62. doi: 10.3402/tellusa.v12i1.9344

Shaw, P.-T., Ko, D. S., and Chao, S.-Y. (2009). Internal solitary waves induced by flow over a ridge: with applications to the northern south China Sea. *J. Geophys. Res.: Oceans* 114, C02019. doi: 10.1029/2008JC005007

Sun, L., Zhang, J., and Meng, J. (2019). A study of the spatial-temporal distribution and propagation characteristics of internal waves in the Andaman Sea using MODIS. *Acta Oceanologica Sin.* 38, 121–128. doi: 10.1007/s13131-019-1449-8

UNESCO, I (1981). The practical salinity scale 1978 and the international equation of state of seawater 1980. In Tenth Report of the Joint Panel on Oceanographic Tables and Standards (JPOTS) *UNESCO Tech. Papers Mar. Sci.* 25.

Wang, X., Peng, S., Liu, Z., Huang, R. X., Qian, Y.-K., and Li, Y. (2016). Tidal mixing in the south China Sea: an estimate based on the internal tide energetics. *J. Phys. Oceanogr.* 46, 107–124. doi: 10.1175/JPO-D-15-0082.1

Wang, Y., Xu, Z., Yin, B., Hou, Y., and Chang, H. (2018). Long-range radiation and interference pattern of multisource M_2 internal tides in the Philippine Sea. *J. Geophys. Res.: Oceans* 123, 5091–5112. doi: 10.1029/2018JC013910

Yadidya, B., Rao, A. D., and Latha, G. (2022). Investigation of internal tides variability in the Andaman Sea: observations and simulations. *J. Geophys. Res.: Oceans* 127, e2021JC018321. doi: 10.1029/2021JC018321

Yang, Y., Huang, X., Zhao, W., Zhou, C., Huang, S., Zhang, Z., et al. (2021). Internal solitary waves in the Andaman Sea revealed by long-term mooring observations. *J. Phys. Oceanogr.* 51, 3609–3627. doi: 10.1175/JPO-D-20-0310.1

Zeng, Z., Chen, X., Yuan, C., Tang, S., and Chi, L. (2019). A numerical study of generation and propagation of type-a and type-b internal solitary waves in the northern south China Sea. *Acta Oceanologica Sin.* 38, 20–30. doi: 10.1007/s13131-019-1495-2

Zhang, H. P., King, B., and Swinney, H. L. (2007). Experimental study of internal gravity waves generated by supercritical topography. *Phys. Fluids* 19, 096602. doi: 10.1063/1.2766741

Zilberman, N. V., Becker, J. M., Merrifield, M. A., and Carter, G. S. (2009). Model estimates of M_2 internal tide generation over mid-Atlantic ridge topography. *J. Phys. Oceanogr.* 39, 2635–2651. doi: 10.1175/2008JPO4136.1

Zilberman, N. V., Merrifield, M. A., Carter, G. S., Luther, D. S., Levine, M. D., and Boyd, T. J. (2011). Incoherent nature of M2 internal tides at the Hawaiian ridge. *J. Phys. Oceanogr.* 41, 2021–2036. doi: 10.1175/JPO-D-10-05009.1

frontiers | Frontiers in Marine Science

TYPE Original Research
PUBLISHED 27 January 2023
DOI 10.3389/fmars.2023.1085679

OPEN ACCESS

EDITED BY
Shengqi Zhou,
South China Sea Institute of Oceanology (CAS), China

REVIEWED BY
Chenyue Xie,
Hong Kong University of Science and Technology, Hong Kong SAR, China
William Young,
University of California, San Diego, United States

*CORRESPONDENCE
Jin-Han Xie
jinhanxie@pku.edu.cn

SPECIALTY SECTION
This article was submitted to Physical Oceanography, a section of the journal Frontiers in Marine Science

RECEIVED 31 October 2022
ACCEPTED 12 January 2023
PUBLISHED 27 January 2023

CITATION
Zhang F and Xie J-H (2023) Scale dependence of near-inertial wave's concentration in anticyclones. *Front. Mar. Sci.* 10:1085679. doi: 10.3389/fmars.2023.1085679

Scale dependence of near-inertial wave's concentration in anticyclones

Furu Zhang[1] and Jin-Han Xie[1,2]*

[1]Department of Mechanics and Engineering Science at College of Engineering and State Key Laboratory for Turbulence and Complex Systems, Peking University, Beijing, China, [2]Joint Laboratory of Marine Hydrodynamics and Ocean Engineering, Pilot National Laboratory for Marine Science and Technology (Qingdao), Shandong, China

Near-inertial waves (NIWs), pervasive and dominating the mixing process in the upper ocean, are observed to concentrate in anticyclones. Based on the NIW amplitude equation derived by Young & Ben Jelloul, which captures dispersion and effects of vortical flow's advection and refraction, this work analytically and numerically studies the influence of scale on the concentration of NIWs. For a sinusoidal background shear flow, the exact solutions expressed as periodic Mathieu functions are approximated by a Gaussian envelope with Hermite polynomial oscillations to determine the distance to the anticyclones. Two dimensionless parameters control NIW's dynamics: (i) h/Ψ, where h is a constant capturing the strength of wave dispersion and Ψ is the magnitude of the background streamfunction capturing the ratio of dispersion to refraction; (ii) L_Ψ/L_M, the ratio between the spatial scales of background flow and NIWs, where L_Ψ and L_M, respectively, captures the relative strength between advection and refraction. The refraction by the background flow leads to the concentration in the regions with negative vorticity, dispersion controls the variance of the wave packet, and the advection shifts the center of NIWs away from the peak of negative vorticity, which is scale-dependent. When the refraction effect dominates, *i. e.*, small L_Ψ/L_M, NIWs concentrate in anticyclones, and this concentration becomes stronger as h/Ψ decreases; when the advection effect dominates, *i.e.*, large L_Ψ/L_M, the NIW's concentration is less obvious. Numerical simulations with backgrounds of sinusoidal shear, vortex quadrupoles and random vortices confirm these results. Considering the similarity between the NIW amplitude equation and the Schrödinger equation, we propose a new perspective that the combined effect of uncertainty relation and energy conservation leads to large-scale NIW's concentration in anticyclones.

KEYWORDS

near-internal waves, quasi-geostrophic flows, ocean processes, amplitude equation, uncertainty relation

1 Introduction

Near-inertial waves (NIWs) with frequency in the vicinity of the inertial frequency [Ferrari and Wunsch (2009); Alford et al. (2016)] are the energy-dominant high-frequency fluctuations in ocean waves with spatial scales up to 1000*km*. They lead to strong mixing in the upper ocean by inducing large vertical shear, and therefore contribute to the large-scale exchange of materials and energy [Alford (2001); Rimac et al. (2013)] and influence biological activities and climate processes in relevant regions [Granata et al. (1995); Jochum et al. (2013)]. NIWs are also believed to play an essential role in the energy transfer of mesoscale eddies and resolve the energy puzzle [Xie and Vanneste (2015); Rocha et al. (2018); Xie (2020)].

During propagation, NIWs change scales due to the influence of the large-scale planetary vorticities (the β-effect) and the mesoscale vorticities [van Meurs (1998)]. Evidence from ocean storm experiments suggests that the β-effect provides a global impact on the evolution of NIWs [D'Asaro et al. (1995)], resulting in a significant propagation perpendicular to the meridian. The local behavior of NIWs is more determined by the impact of relative vorticities [Weller (1982)], undergoing a scale decrease when encountering the background flows. An interesting phenomenon is that NIWs concentrate in anticyclones, which is justified by both numerical simulations [Lee and Niiler (1998); Zhai et al. (2005); Danioux et al. (2008)] and observations [Kunze and Sanford (1984); D'Asaro et al. (1995); Elipot et al. (2010); Joyce et al. (2013)].

Early studies on this phenomenon identified two regimes: the "trapping" regime and the "strong dispersion" regime [Kunze (1985); Wang (1991); Klein and Tréguier (1995); van Meurs (1998)], determined by the relative order of magnitude of the refraction and dispersion effects. In the "trapping" regime where the refraction dominants, using the Wentzel-Kramers-Brillouin (WKB) method, Kunze (1985) derived that the NIWs tend to move away from positive vorticities and towards negative ones. Here, the NIW frequency is modified by the background vorticity with a $\zeta/2$ shift where ζ is the relative vorticity, which is the so-called Kunze's effect. On the other hand, in the "strong dispersion" regime, NIWs are rapidly dispersed and less affected by the vorticity [Klein and Tréguier (1995)].

Subsequently, many new insights were proposed benefiting from the NIW model proposed by Young and Jelloul (1997), hereafter YBJ, which captures the effects of wave dispersion, vortical flow's advection and refraction. A crucial advantage of the YBJ model is that it does not rely on the assumption of horizontal scale separation between waves and background flows which is required by the WKB method. However, this scale separation is usually not valid for NIWs. Balmforth et al. (1998) explored the time scale and spatial modulation of decaying inertial oscillations influenced by the geostrophic flow. The demarcation line between the "trapping" regime and the "strong dispersion" regime in the YBJ model is determined by $\Psi/f_0R_n^2$, where Ψ is the magnitude of the background streamfunction, f_0 is the inertial frequency, R_n is the deformation radius of the nth vertical mode [Young and Jelloul (1997); Balmforth et al. (1998)]. As to a reduced-gravity shallow-water system, this parameter is reduced to Ψ/h where $h = g'H/f_0$ with g' and H the reduced gravity and horizontally averaged depth of the top layer. When $\Psi/h >>1$, the "trapping" dominants; in the opposite case, dispersion dominates. With a large-scale initial condition where the advection can be ignored compared with the refraction term, Klein and Smith (2001) investigated the spatial structure of inertial energy and suggested that the large-scale components contribute to the trapping regime in anticyclones. Introducing an extra short-time assumption, the temporal evolution of NIW energy is found to be proportional to the Laplacian of the vorticity field, *i.e.* $\Delta\zeta$ [Klein et al. (2004)]. So the inertial energy is concentrated in the structure where $\Delta\zeta$ is positive. Danioux et al. (2015) argued that the conservations in the YBJ equation lead to the concentration of NIWs in the anticyclone. With homogeneous initial conditions, they observed the long-time saturation scale of waves: in the "trapping" regime, the wave scale is much smaller than the vorticity scale, while in the "strong dispersion" regime, the wave scale is much larger than the vorticity scale. Nevertheless, this does not mean smaller-scale NIWs are easier concentrate in anticyclones for a given background flow. In this paper, we will show that for a fixed vorticity field, the larger the scale of the waves, the more favorable the concentration. However, then the concentration is suppressed by the increasing number of newly generated small-scale waves, eventually reaching saturation with an average scale shown by Danioux et al. (2015).

In this paper, we systematically study the scale dependence of NIW's concentration in anticyclones and interpret the reason behind the concentration from a perspective of uncertainty principle borrowed from quantum mechanics. The paper is structured as follows. In section 3, we discuss the dynamics and scaling characteristics of the YBJ equation. In section 4, we provide exact and approximate solutions for a sinusoidal background shear flow and indicate the scale effect of NIWs concentration in anticyclones. In sections 5-6, numerical simulations are performed to confirm the scale effect with vortex patches and random vortexes. Section 7 shows that the combined effect of uncertainty relation and energy conservation leads to the NIW's concentration in anticyclones. It is a new understanding of the concentration mechanism drawing on the basic concepts of quantum mechanics. Finally, we summarize and discuss our results in section 7.

2 The YBJ model

We study the evolution of NIWs in a background vorticity field by the shallow-water YBJ model (Young and Jelloul, 1997; Danioux et al., 2015):

$$\partial_t M + J(\psi, M) - i\frac{h}{2}\Delta M + i\frac{\Delta\psi}{2}M = 0, \tag{1}$$

where $M(x, y, t)$ is a complex amplitude of the horizontal velocity (u, v), $u+iv=Me^{-if_0t}$, describing the slow spatial and long-time modulation of the NIW field. f_0 is the local Coriolis frequency and $h=g'H/f_0$ is a dispersion parameter with g' and H the reduced gravity and horizontally averaged depth. ψ and $\Delta\psi$ are the barotropic geostrophic flow's streamfunction and vorticity field. For simplicity, we only focus on the barotropic case. The operator J is the horizontal Jacobian. In this paper, we are concerned with the long-time [more than 30 days, *e.g.*

Klein and Smith (2001); Danioux et al. (2015)] evolutionary nature of NIWs and assume that the background flow is steady.

The YBJ equation captures the advection, dispersion and refraction effects. The refraction term controls the capture of NIWs by the vorticity field, while the dispersion term promotes the escape of waves [Kunze (1985); Rocha et al. (2018)]. The relative strength of the dispersion and refraction can be measured by the dimensionless parameter h/Ψ (Young and Jelloul, 1997; Balmforth et al., 1998). Typical observation data from the North Atlantic imply that h/Ψ may range in (0.2, 8) (Danioux et al., 2015).

When the advection term is omitted, the YBJ equation is similar to the Schrödinger equation describing the motion of a single particle. In this analogy, $M(x,y)$ corresponds to the particle's complex wavefunction, h corresponds to the reduced Planck constant $\hbar$, and $h\Delta\psi/2$ corresponds to the potential field subjected by the particle. The particle prefers the lower potential region; accordingly, NIWs concentrate in negative relative vorticities. This concentration in anticyclone should still be valid when the advection term is non-zero but much smaller than the refraction. The ratio between the advection and refraction is only related to the spatial scales. So we can define L_ψ/L_M, where L_ψ and L_M are the spatial scale of the background streamfunction and wave amplitude, respectively, to capture this relative importance. However, the interpretation of the energy concentration *via* analogy to the Schrödinger equation fails when $L_\psi/L_M \gg 1$. In this paper, we will show that the advection prevents the NIW's concentration, which is weak for large-scale waves (small L_ψ/L_M).

By introducing the amplitude and phase of M, $M=M_0 e^{i\Theta}$ where M_0 and Θ are both real numbers, we define the local wavenumber

$$\boldsymbol{k}_{local} = \nabla\Theta, \tag{2}$$

or equivalently

$$\boldsymbol{k}_{local} = \mathrm{Im}(\nabla \ln M) = \mathrm{Im}\left(\frac{\nabla M}{M}\right), \tag{3}$$

which we practically use in analyzing our numerical results. We further define an averaged local wave-vector k_{ave}

$$k_{ave}(t) = \frac{\int\int \sqrt{k_{x,local}^2 + k_{y,local}^2}\,|M(x,y,t)|^2 dxdy}{\int\int |M(x,y,t)|^2 dxdy}, \tag{4}$$

with corresponding NIW's mean spatial scale $L_M = 2\pi/k_{ave}$.

3 Analytical solutions for a sinusoidal background shear flow

To reveal the scale dependence of NIW's concentration, we first study a simple case with a sinusoidal background shear flow, which can be solved analytically. Setting the core of negative vorticity as $y=0$, the stream function of the background shear flow reads $\psi = (\zeta_0/k_0^2)\cos k_0 y$, where $\zeta_0>0$ is the intensity of local relative vorticity, and the amplitude Ψ of ψ is defined as its root-mean-square that $\Psi = \zeta_0/\sqrt{2}k_0^2$. Because of the translational symmetry in the x-direction, we seek solutions with an ansatz that

$$M(x,y,t) = M(y)e^{i(k_x x-\omega t)}. \tag{5}$$

Substituting it into the YBJ (1) [Young and Jelloul (1997)] we obtain

$$\frac{h}{2}\partial_y^2 M(y) + \left(\omega - \frac{h}{2}k_x^2 - \frac{\zeta_0 k_x}{k_0}\sin\ k_0 y + \frac{\zeta_0}{2}\cos\ k_0 y\right)M(y) = 0. \tag{6}$$

Defining $A = \sqrt{(\zeta_0 k_x/k_0)^2 + (\zeta_0/2)^2}$ and $\varphi = arctan\ 2k_x/k_0$, we obtain

$$\frac{h}{2}\partial_y^2 M(y) + \left[\omega - \frac{h}{2}k_x^2 + A\cos\ (k_0 y + \varphi)\right]M(y) = 0, \tag{7}$$

which is the typical Mathieu equation, and the solutions are Mathieu functions of the first kind ([3]):

$$M(y) = C_1\ \ M_C(\omega', \xi, y') + C_2\ \ M_S(\omega', \xi, y'), \tag{8}$$

where $\omega' = 8(\omega - hk_x^2/2)/hk_0^2$, $\xi = -4A/hk_0^2$, $y' = (k_0 y+\varphi)/2$. M_C and M_S are even and odd functions of y', respectively. C_1 and C_2 are arbitrary constants. The period of background shear flow is $2\pi/k_0$, then the period of y' in Mathieu functions is π, which determines the value of the eigenvalues ω'. For the even functions $M_C(\omega',\xi,y')$, the eigenvalues ω' satisfy the relation in continued fractions that

$$\omega' = -\frac{2\xi^2}{2^2 - \omega' - \frac{\xi^2}{4^2-\omega'-\frac{\xi^2}{6^2-\omega'-\cdots}}}. \tag{9}$$

For the odd functions $M_S(\omega',\xi,y')$, the eigenvalues ω' satisfy

$$\omega' - 4 = -\frac{\xi^2}{4^2 - \omega' - \frac{\xi^2}{6^2-\omega'-\frac{\xi^2}{8^2-\omega'-\cdots}}}. \tag{10}$$

Interestingly, the centers of the waves, for both the eigenfunctions $M_C(\omega',\xi,y')$ and $M_S(\omega',\xi,y')$, are

$$\frac{y_c}{L_\psi} = -\frac{arctan\ (2k_x/k_0)}{2\pi}, \tag{11}$$

which is only scale-dependent and independent of the kinetic parameter h/Ψ. For the even functions M_C, y_c locates at the wave peaks, while for the odd functions M_S, y_c is the position of the nodes. Distributions of the first few modes of M_C and M_S are plotted in Figures 1–4. NIWs concentrate in the negative vorticity when L_ψ/L_M is small where $L_\psi = 2\pi/k_0$ and $L_M = 2\pi/k_x$. With the increase of L_ψ/L_M, the center of the waves gradually deviates from the core of the negative vorticity. For a large enough L_ψ/L_M, the waves tend to be localized at the boundary ($y/L_\psi = -sgn(k_x)/4$) between positive and negative vorticities.

If the original YBJ equation has no advection term, the sine term in Eq.(6) (or φ in Eq.(7)) would be zero, which would result in $y_c=0$. Therefore, the scale effect on the deviation from negative vorticity results from advection. The kinetic parameter h/Ψ controls the variance of the wave packet, with smaller $h/\Psi \ll 1$ corresponding to more compact wave packets; as h/Ψ increases, the wave packets widen. The oscillatory behavior of the waves grows when the order number of the eigenmodes increases, which would be seen visually by the approximate analytical solutions in the following subsection.

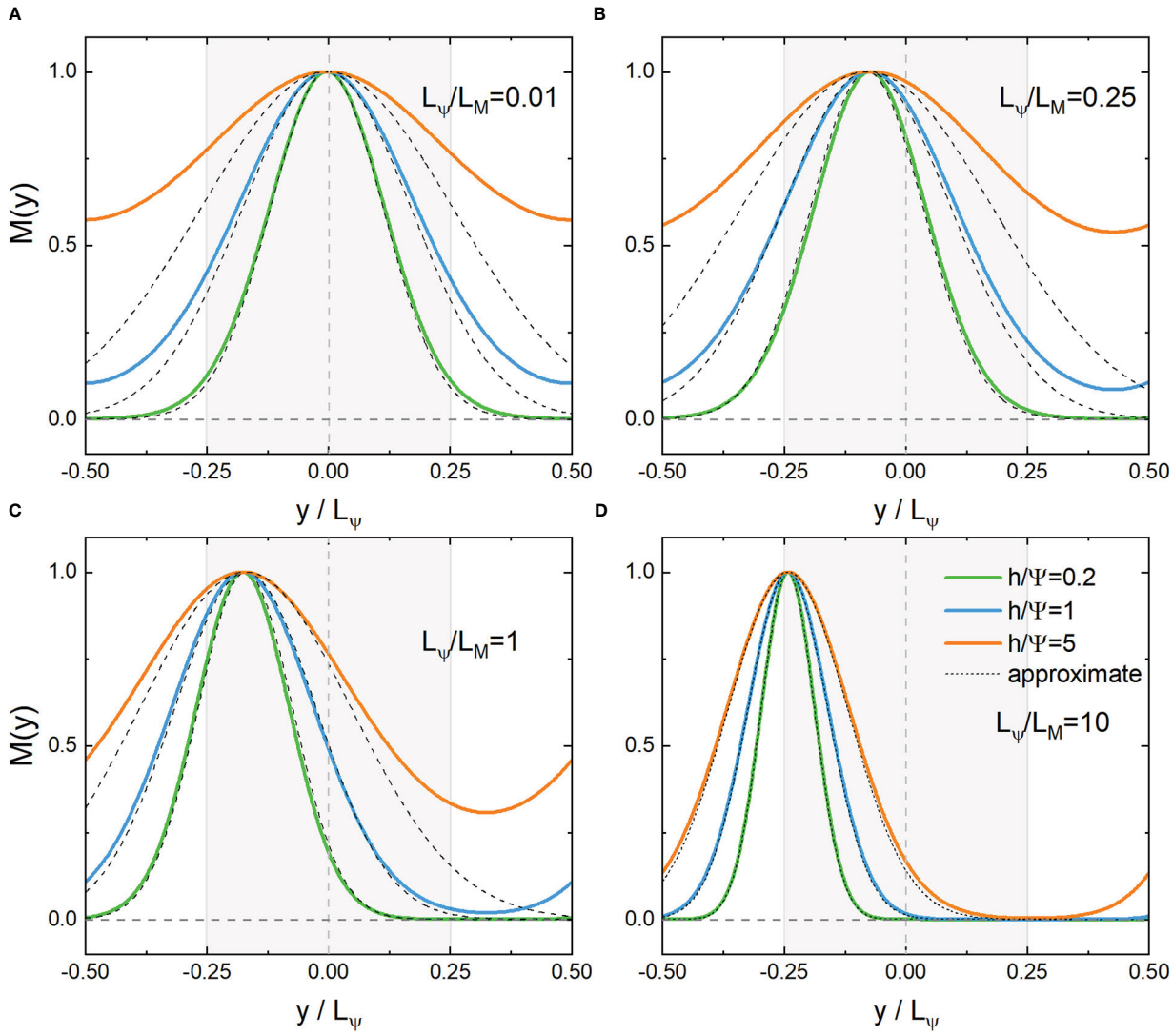

FIGURE 1
Distribution of the even eigenfunction $M_C(\omega',\xi,y')$ and its approximate solution near the core (y=0) **(A, B)** or boundary (y/L_Ψ=−1/4) **(C, D)** with the lowest eigenvalues. $L_\psi/L_M=k_x/k_0$=0.01,0.25,1,10, $h/\Psi = \sqrt{2}hk_0^2/\zeta_0$ = 0.2, 1, 5, respectively. Shaded areas indicate negative vorticities.

3.1 Approximate solutions near the core of vorticity (L_ψ / $L_M \ll 1$)

To see the behavior of the solutions more clearly, we consider approximate solutions near the core of the vorticity where $y\approx0$, and therefore $sin\ k_0y\approx k_0y$ and $\cos\ k_0y \approx 1 - k_0^2y^2/2$, then Eq.(6) becomes

$$\frac{h}{2}\partial_y^2 M(y) + \left(\omega' - ay^2 + by\right)M = 0, \tag{12}$$

Where

$$\omega' = \omega - \frac{h}{2}k_x^2 + \frac{\zeta_0}{2}, \quad a = \frac{\zeta_0 k_0^2}{4}, \quad b = -\zeta_0 k_x\,. \tag{13}$$

The general solutions with the boundary condition that M $(y\to\infty)\to0$ are the Parabolic cylinder functions $D_n(y)$ (the branch which is divergent at $y\to\infty$ is not shown):

$$M(y) = C_0\ \ D_n\left[\kappa\left(k_0y + \frac{2k_x}{k_0}\right)\right], \tag{14}$$

where C_0 is an arbitrary constant, n is a non-negative integer with

$$n = \frac{\sqrt{2}\left(b^2 + 4a\omega'\right)}{8\sqrt{a^3h}} - \frac{1}{2}, \quad \text{and} \quad \kappa = \left(2\frac{\zeta_0}{hk_0^2}\right)^{1/4}. \tag{15}$$

When n is even, $D_n(y)$ is an even function, while when n is odd, $D_n(y)$ is an odd function. The Parabolic cylinder functions can also be represented as:

$$D_n(y) = \frac{1}{2^{n/2}}e^{-y^2/4}H_n\left(\frac{y}{\sqrt{2}}\right), \tag{16}$$

where H_n (y) is the Hermite polynomial of the nth order (Matsuno, 1966). This form is useful because it consists of a Gaussian-type envelope and a fast oscillation. The order number n

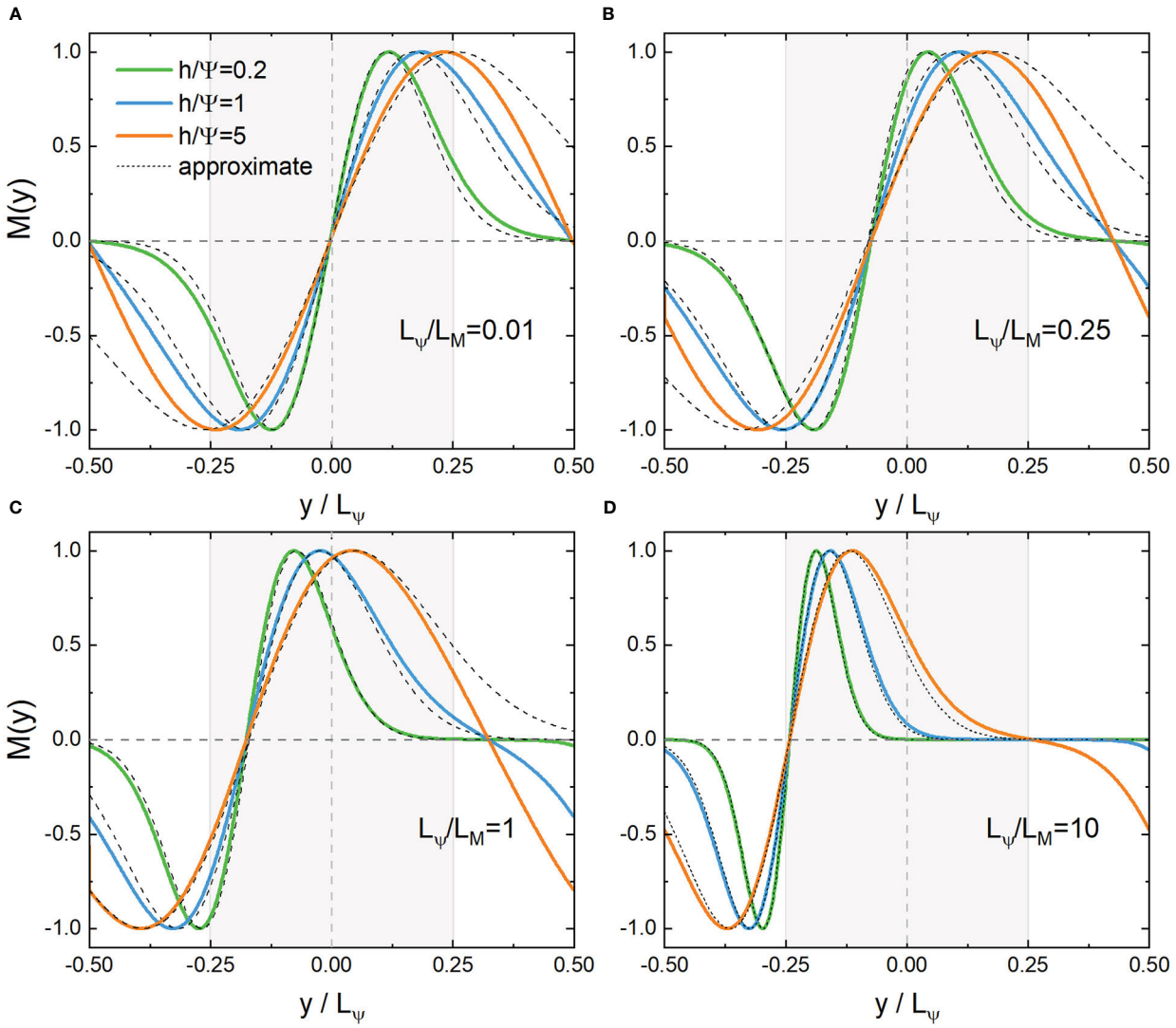

FIGURE 2
Distribution of the odd eigenfunction $M_S(\omega',\xi,y')$ and its approximate solution near the core (y=0) **(A, B)** or boundary (y/L_Ψ=−1/4) **(C, D)** with the lowest eigenvalues. $L_\psi/L_M=k_x/k_0$=0.01,0.25,1,10 , $h/\Psi=\sqrt{2}hk_0^2/\zeta_0$ = 0.2, 1, 5, respectively. Shaded areas indicate anticyclones.

of the modes appears only in the oscillation part, and the larger n is, the more pronounced the oscillation. The expression (16) gives us an image of the wave's shape. Since n is a non-negative integer, from Eq.(15) we get the frequency of M (x, y):

$$\omega = \left(\frac{h}{2} - \frac{\zeta_0}{k_0^2}\right)k_x^2 + \sqrt{\frac{h\zeta_0}{8}}(1+2n)k_0 - \frac{\zeta_0}{2}. \tag{17}$$

From Eq.(14) one can see that the distance between the center of M (y) and the core of negative vorticity, *i.e.* $k_0 y_c = -2k_x/k_0$, is proportional to the dimensionless scale factor $L_\psi/L_M=|k_x|/k_0$. When $L_\psi/L_M \ll 1$, the waves are trapped near the core of negative vorticities; but for large $L_\psi/L_M \gg 1$, the center of the wave leave the core of negative vorticity. The approximate behavior near the core of vorticity is shown in Figures 1–4 (A, B) which fits well with the exact solutions.

3.2 Approximate solutions near the boundary (for large L_ψ / $L_M \gg 1$)

Now we turn to the boundaries between the positive and negative vorticities, where the stream function of the background shear flow can be rewritten as $\psi = (\zeta_0/k_0^2)\sin\ k_0 y'$ with $y'=y+\pi/2k_0 \approx 0$. Performing a Taylor expansion on ψ and $\Delta\psi$ near the boundary, we get $\psi \approx (\zeta_0/k_0)y' - \zeta_0 k_0 y'^3/6$, $\psi_{y'} \approx \zeta_0/k_0 - \zeta_0 k_0 y'^2/2$ and $\Delta\psi \approx -\zeta_0 k_0 y'$. Under the ansatz $M(x,y',t)=M(y')e^{i(k_x x-\omega t)}$, the YBJ equation becomes

$$\frac{h}{2}\partial_{y'}^2 M + \left(\omega' - ay'^2 + by'\right)M = 0, \tag{18}$$

Where

$$\omega' = \omega - \frac{h}{2}k_x^2 + \frac{\zeta_0 k_x}{k_0},\ a = \frac{\zeta_0 k_0 k_x}{2},\ b = \frac{\zeta_0 k_0}{2}. \tag{19}$$

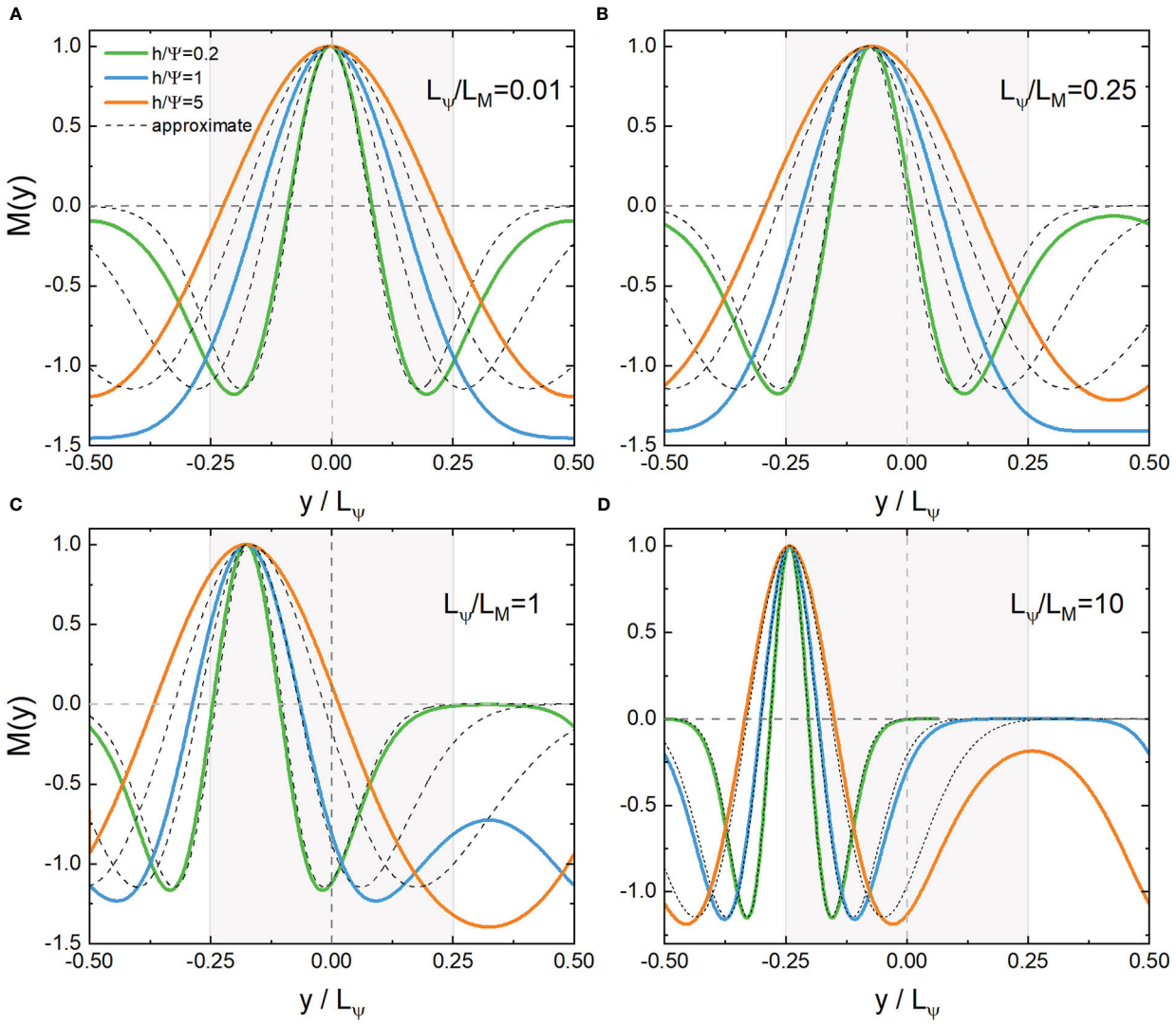

FIGURE 3
Distribution of the even eigenfunction $M_C(\omega',\xi,y')$ and its approximate solution near the core (y=0) **(A, B)** or boundary (y/L_Ψ=−1/4) **(C, D)** with the second lowest eigenvalues. $L_\psi/L_M=k_x/k_0$=0.01,0.25,1,10, $h/\Psi = \sqrt{2}hk_0^2/\zeta_0$ = 0.2, 1, 5, respectively. Shaded areas indicate negative vorticities.

The general solutions with the boundary condition $M(y'\to\infty)\to 0$ are (the branch which is divergent at $y'\to\infty$ is not shown)

$$M(y) = C_0\ D_n\left[\kappa\left(k_0 y' - \frac{k_0}{2k_x}\right)\right], \tag{20}$$

Where

$$n = \frac{8\omega' k_x + \zeta_0 k_0}{8\sqrt{\zeta_0 h k_0 k_x}k_x} - \frac{1}{2}, \quad \text{and} \quad \kappa = \sqrt{2}\left(\frac{\zeta_0 k_x}{hk_0^3}\right)^{1/4}. \tag{21}$$

There is a chiral selectivity between the wave number and the vorticity near the boundaries that $k_x\zeta_0>0$, while the opposite case $k_x\zeta_0<0$ corresponds to a branch which diverges at $y'\to\infty$. The approximate behavior near the boundary of vorticity is also shown in Figures 1–4 (C, D) which fits well with the exact solutions. Since n is a non-negative integer, from Eq.(21) we get the frequency of $M(x,y)$:

$$\omega = \frac{h}{2}k_x^2 - \frac{\zeta_0}{k_0}k_x + \frac{1+2n}{2}\sqrt{\zeta_0 h k_0 k_x} - \frac{\zeta_0 k_0}{8k_x}. \tag{22}$$

3.3 Scale effect emerging from the analytical solutions

In Figure 5, we plot the lowest eigenvalues of $M(x,y)$ from both the Mathieu functions and their approximations near the core and boundaries of the negative vorticity. When $k_x=k_0/2$, Eq.(17) and Eq.(22) provide the same result. The approximation near the core of vorticity works if $L_\psi/L_M=k_x/k_0\ll 1/2$, while when $L_\psi/L_M=k_x/k_0\gg 1/2$, the approximation near the boundary is more suitable. Moreover, when h/Ψ increases, the variance of the wave packet in Eqs. (14, 20) increases, and the dispersion term $hk_x^2/2$ in Eqs. (17, 22) plays a more important role, changing the convexity of the spectral curve in Figure 5. The frequencies obtained from the approximation near the core of the vorticity are not too accurate because the wave scale is large when $k_x\to 0$, which reduces the localization of the wave.

The difference in the approximate behavior at the vorticity core and the boundary is also manifested in the distance between the wave center and the vorticity core, y_c , whose dependence on L_ψ/L_M is

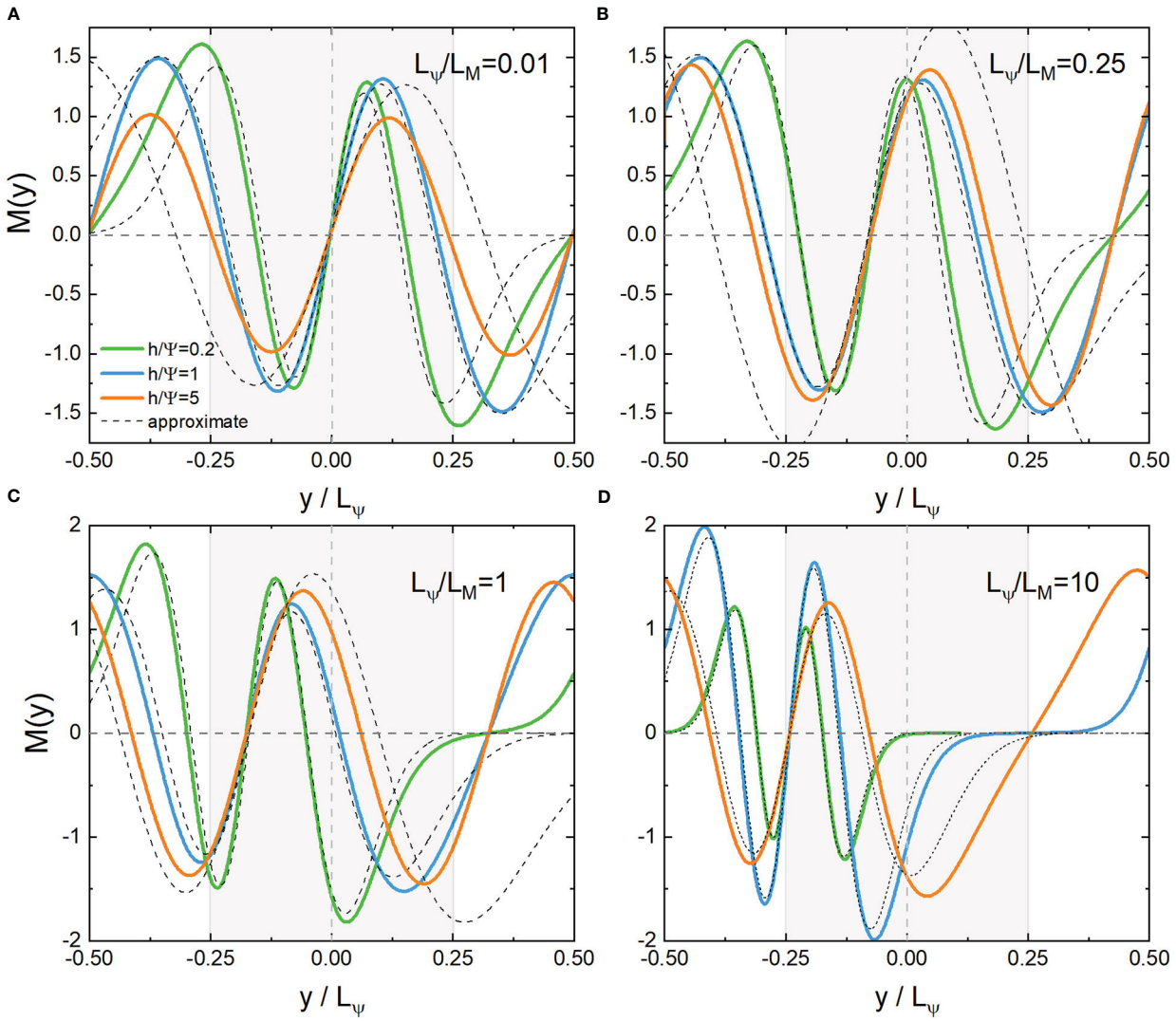

FIGURE 4
Distribution of the odd eigenfunction $M_S(\omega',\xi,y')$ and its approximate solution near the core (y=0) **(A, B)** or boundary (y/L_Ψ=−1/4) **(C, D)** with the second lowest eigenvalues. $L_\psi/L_M=k_x/k_0$=0.01,0.25,1,10 , $h/\Psi = \sqrt{2}hk_0^2/\zeta_0$ = 0.2, 1, 5, respectively. Shaded areas indicate anticyclones.

shown in Figure 6A. Near the core, y_c is proportional to L_ψ/L_M , while near the boundary, $(L_\psi/4-y_c)$ is inversely proportional to L_ψ/L_M . Thus, a large wave scale benefits the NIW's concentration.

We define a mean distance y_{ave} of the NIWs to the core of the negative vorticity y=0 as

$$y_{ave} = \frac{\int |y||M|^2 dy}{\int |M|^2 dy}, \tag{23}$$

with which the dimensionless ratio y_{ave}/L_ψ can be used to measure the concentration of NIWs, as shown in Figure 6B. y_{ave} increases as L_ψ/L_M increases, which is consistent with the behavior of y_c shown in Figure 6A. However, y_{ave} grows as h/Ψ increases, while the center of the eigenfunction y_c is independent of h/Ψ.

The scale effect can also be measured by the energy difference of NIWs between the positive and negative vorticities:

$$\sigma = \frac{e_P - e_N}{e_P + e_N}, \tag{24}$$

where e_P (e_N) is wave energy in the region with positive (negative) vorticity:

$$e_P = \int \int |M|^2 H(\triangle \psi) dxdy \quad \text{and} \quad e_N = \int \int |M|^2 H(-\triangle \psi) dxdy . \tag{25}$$

Here, H is the Heaviside function. When σ<0 (>0) , the NIWs concentrate in the negative (positive) vorticities. A plot of σ is presented in Figure 6C from the lowest eigenmodes of M_C and M_S , exhibiting the same positive correlation on L_ψ/L_M as in Figures 6 (A, B) Small h/Ψ and L_ψ/L_M refer to a "trapping" regime.

As L_ψ/L_M increases, the advection overtakes the refraction, weakening the capture. When in the "strong dispersion" regime, where $h/\Psi \gg 1$, the concentration becomes insignificant. Besides, the even function M_C has a stronger concentration than the odd M_S .

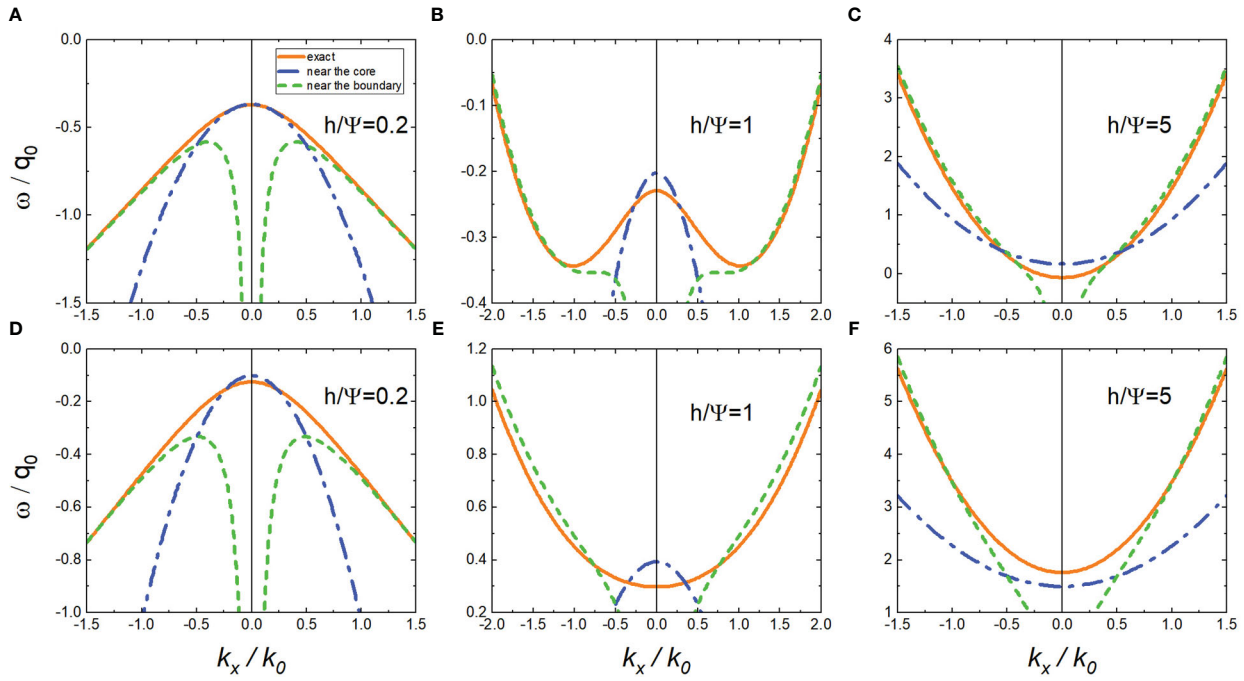

FIGURE 5
Dispersion relation of the lowest eigenvalues of $M_C(\omega',\xi,y')$ **(A–C)** and $M_S(\omega',\xi,y')$ **(D–F)** with $h/\Psi = \sqrt{2}hk_0^2/\zeta_0 = 0.2, 1, 5$, respectively.

4 Scale effect in a vortex quadrupole

With the help of the revelation from the above analytical solutions, we study the scale effect of NIWs further in a doubly sinusoidal vortex quadrupole whose streamfunction reads

$$\psi = -\left(\zeta_0/k_0^2\right) \sin\ k_0 x \sin\ k_0 y, \tag{26}$$

where $\zeta_0>0$. Thus, the spatial scale is $L_\psi=2\pi/k_0$.

For a given background field, we can obtain the eigenmodes of the system by a finite difference method, as shown in Figure 7. As can be seen from the figure, low-order modes concentrate near the core of anticyclones (Figures 7A, B), while high-order ones can concentrate near the boundaries or the saddle points (Figures 7C, D). For each eigenmode, we define the mean radius r_{ave} of NIWs concentrated in anticyclones as

$$r_{ave} = \frac{\int_{-L_\psi/2}^{0}\int_{0}^{L_\psi/2}\sqrt{(x-x_0)^2+(y-y_0)^2}|M|^2 dxdy}{\int_{-L_\psi/2}^{0}\int_{0}^{L_\psi/2}|M|^2 dxdy}, \tag{27}$$

in which the core of the anticyclone (x_0,y_0) locates at $(L_\psi/4,-L_\psi/4)$. We use the dimensionless ratio r_{ave}/L_ψ to measure the concentration of NIWs, and it depends on the parameter h/Ψ and the order number of the eigenmodes. In Figure 8A we plot r_{ave}/L_ψ of the eigenmodes with low frequency for different h/Ψ, and the corresponding spatial scale L_ψ/L_M is calculated according to Eq.(4). There is a clear positive correlation between r_{ave}/L_ψ and L_ψ/L_M , consistent with the trend of y_c and y_{ave} given by the analytical solutions shown in Figures 6 (A, B).

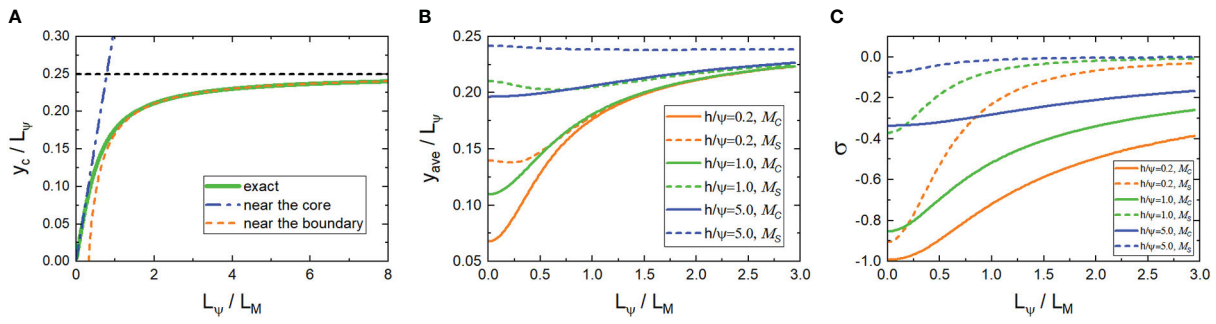

FIGURE 6
(A) The distance y_c between the center of the waves and the core of the negative vorticity as a function of L_ψ/L_M , which is caused by the advection term. **(B, C)** y_{ave}/L_ψ **(B)** and σ **(C)** vs L_ψ/L_M from the lowest eigenmodes of M_C and M_S with different h/Ψ=0.2,1,5, respectively.

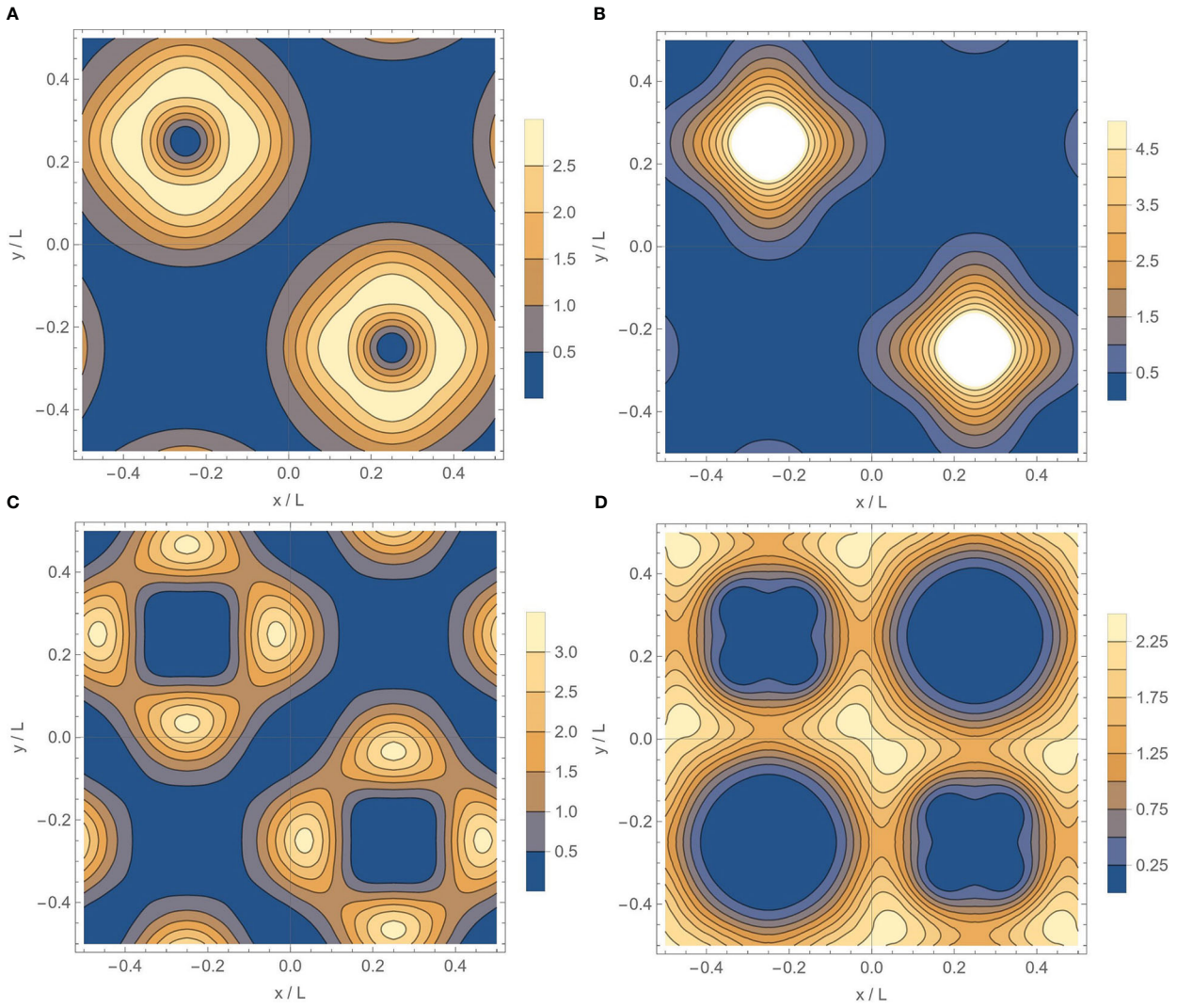

FIGURE 7
(A–D) Typical eigenmodes in the vortex quadrupole with order number n=1,4,8,9 , respectively. In **(A, B)**, the NIWs concentrate in anticyclones; in **(C)** they concentrate near the boundaries; while in **(D)**, they concentrate at the saddle points. h/Ψ=1 , L=L_ψ=$2\pi/k_0$.

Hence, a larger L_M is associated with a more concentrated NIW in anticyclone for a fixed background vortex quadrupole. It should be noted in Figure 8A that for each h/Ψ, a minimum value of L_ψ/L_M appears, which is inversely correlated with h/Ψ and determined by the most concentrated mode of the system.

Using Eq.(24), we can define the degree of energy concentration σ. Figure 8B also shows that a large wave scale facilitates the concentration. Moreover, a color map of σ as a function of h/Ψ and L_ψ/L_M is shown in Figure 9. With small h/Ψ and L_ψ/L_M, there is a "trapping" regime with a deep negative σ . When h/Ψ or L_ψ/L_M is large enough, the concentration of waves in anticyclones becomes insignificant.

With the initial state of the velocity field set as

$$M(x, y, t = 0) = (1 + i)\cos\ (nk_0x)\cos\ (nk_0y), \qquad (28)$$

where n is an adjustable parameter, we investigate the long-time (more than 30 days) behavior of NIWs. We plot the time average across the second half of the simulation (about 15-30 days) of r_{ave}/L_ψ and σ as a function of L_ψ/L_M in Figure 10. A similar scale effect emerges that the concentration of NIW favors larger wavelength L_M defined from Eq.(4). Typically, a larger initial wavelength gives a larger L_M, resulting in a greater concentration. When L_ψ/L_M is large enough, the NIWs are no longer concentrated in anticyclones but tend to the boundary, which leads to a saturation of r_{ave}/L_ψ and σ, which resembles the results shown by the analytical solutions presented in Figure 6. When h/Ψ increases, the dispersion is enhanced, weakening the concentration of the waves in anticyclones. Note that r_{ave}/L_ψ=0.25 is the vorticity boundary. Considering the dispersed distribution of M, r_{ave}/L_ψ can hardly reach the minimum value of 0 or the maximum value of 0.25.

5 Scale effect in random vortexes

To be more realistic, we explore the scale effect of NIWs in the random vortexes, with Gaussian covariance (cf. Danioux et al., 2015). The amplitude scale Ψ of the stream function ψ is defined as its root-mean-square. The numerical simulation of the YBJ equation is carried

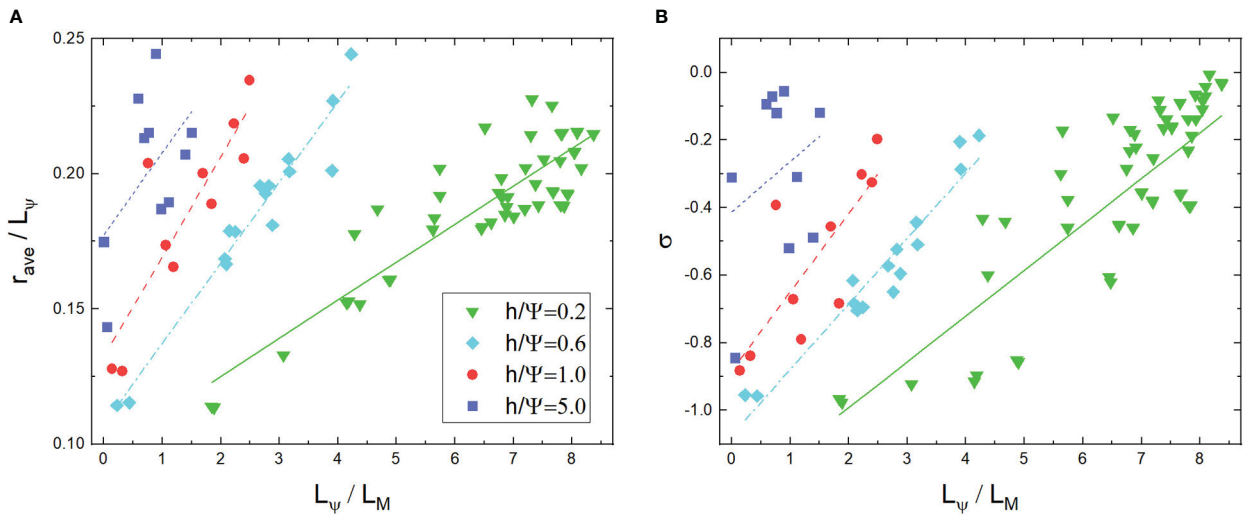

FIGURE 8
(A) r_{ave}/L_ψ vs L_ψ/L_M from the eigenmodes with low frequency whose σ<0. **(B)** σ vs L_ψ/L_M from the eigenmodes with lower frequency whose σ<0 . $\psi = -(\zeta_0/k_0^2)\sin k_0 x \sin k_0 y$. h/Ψ=0.2,0.6,1,5 , respectively. The lines are obtained by least-square fitting.

out on a doubly periodic 256×256 grid of a domain size $4\pi\times4\pi$ using the pseudo-spectrum method. In order to ensure numerical stability, a weak biharmonic dissipation $\nu=10^{-10}$ is introduced. Figures 11 (A, B) shows the streamfunction and the associated vorticity field.

Because it is not easy to directly get the spatial scale L_Ψ of the random streamfunction, we define the local wavenumber of ψ as

$$\boldsymbol{k}_\psi = \frac{\nabla\psi}{\psi}. \tag{29}$$

So an averaged local wavenumber $\overline{k_\psi}$ is then given as

$$\overline{\boldsymbol{k}_\psi} = \frac{\int\int |k_\psi||\psi|^2 dxdy}{\int\int |\psi|^2 dxdy}, \tag{30}$$

which corresponds to the spatial scale $L_\Psi = 2\pi/\overline{k_\psi}$.

With an initial wave field described by Eq.(28) and illustrated in Figure 11C, the long-time (more than 30 days) behaviors of NIWs are plotted in Figures 11 (D–F) for different h/Ψ . For a larger h/Ψ , the long-time evolution yields a larger saturation scale L_M on average, which is consistent with the result in Danioux et al. (2015) for a homogeneous initial condition $M(x,y,t=0)=C$ where C is a non-zero constant. When h/Ψ is fixed, *i.e.* for a steady background field, one can find the same positive correlation between the energy concentration σ and the scale factor L_ψ/L_M defined from Eq.(4), as shown in Figure 12. Danioux et al. (2015) argues that NIWs are most concentrated in anticyclones when $h/\Psi\sim1$. However, we point out that this depends on the wave scale in the initial condition and, therefore, on the saturation scale of the wave under long-time evolution. When h/Ψ=5 which belongs to the "strong dispersion" regime, the geostrophic flow has little effect on NIWs, and the concentration of NIWs in anticyclones is reduced. Correspondingly, the scale effect of concentration becomes less obvious. When h/Ψ=0.2 , the system enters the "strong advection" regime with a large $L_\psi/L_M\approx10$ and a weak concentration $\sigma\in(-0.1,0)$, which is not presented in the figure.

6 Conservation law and uncertainty relation of NIWs

By analogy with the Schrödinger equation, the YBJ equation can be rewritten as

$$ih\,\partial_t M = \hat{H}M, \tag{31}$$

where the Hamiltonian-like operator $\hat{H}$ reads

$$\hat{H} = \widehat{H_1} + \widehat{H_2} + \widehat{H_3}, \tag{32}$$

with

$$\widehat{H_1} = -\frac{h^2}{2}\nabla^2,\ \widehat{H_2} = \frac{h\Delta\psi}{2},\ \widehat{H_3} = -ih\left(\psi_x\nabla_y - \psi_y\nabla_x\right). \tag{33}$$

When $\hat{H}_3 = 0$, one obtains the Schrödinger equation that governs the complex wave function $M(x,y,t)$ for a single particle with unit mass and external potential $h\Delta\psi/2$. Similar to the conservation of energy for particles, *i.e.* $\partial_t\int\int M^*\hat{H}M dxdy = 0$, one can prove that the equation has the following conservation law using properties of the Jacobian and integrating by parts [Danioux et al. (2015)]:

$$\frac{d}{dt}(I_1 + I_2 + I_3) = 0, \tag{34}$$

Where

$$I_1 = \frac{h^2}{2}\int\int|\nabla M|^2 dxdy,\ I_2 = \frac{h}{2}\int\int\Delta\psi|M|^2 dxdy,\ I_3 = ih\int\int\psi J(M^*, M)dxdy. \tag{35}$$

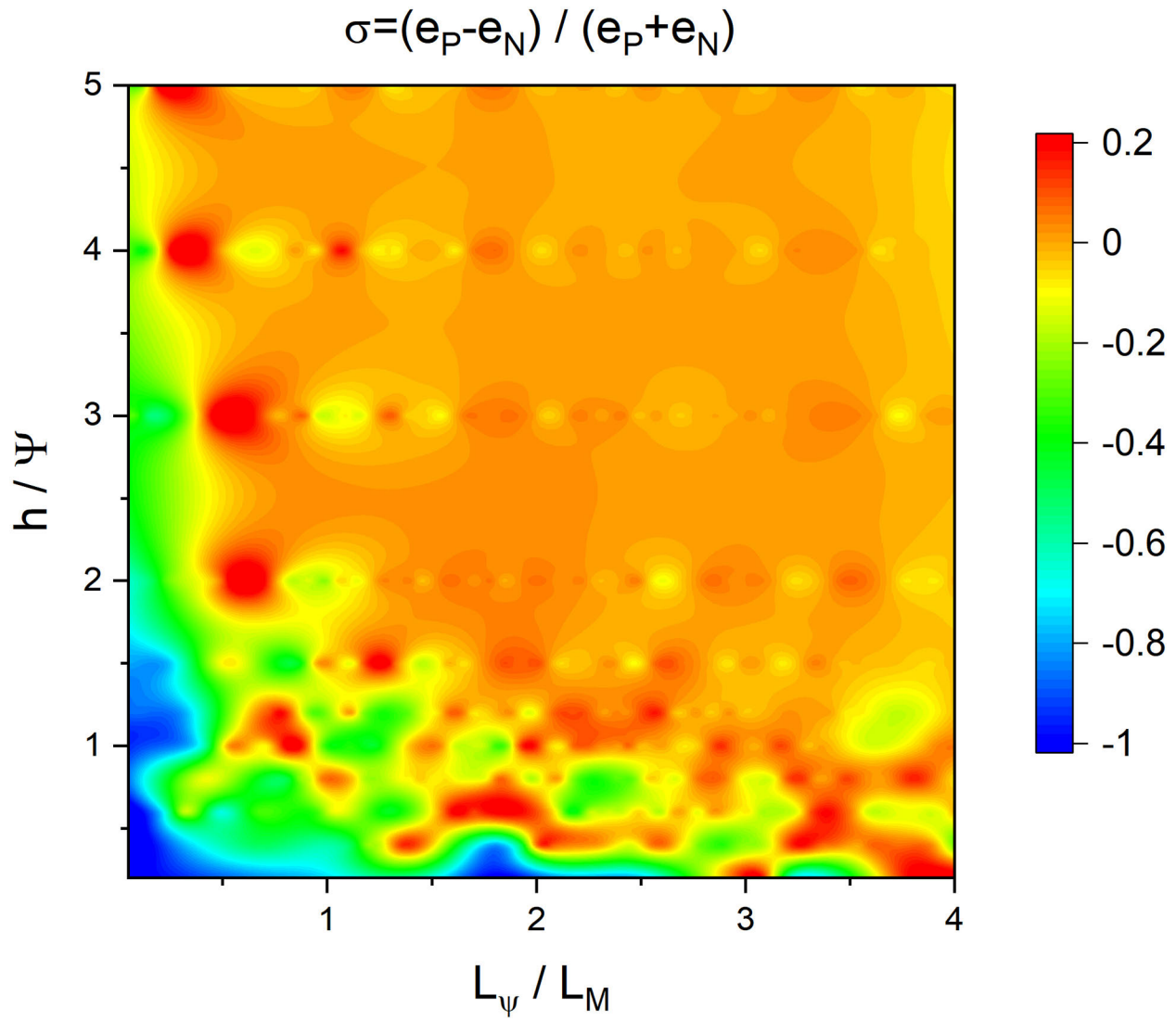

FIGURE 9
$\sigma=(e_P-e_N)/(e_P+e_N)$ from the first 120 eigenmodes as a map of h/Ψ and L_ψ/L_M.

Here, I_1 is non-negative, I_2 is the covariance between $\Delta\psi$ and $|M|^2$ reflecting the concentration of NIW energy, and I_3 is an effect of the advection.

In analogy to quantum mechanics, we define the position and momentum operators as

$$\hat{\boldsymbol{r}} = (x, y) \quad \text{and} \quad \hat{\boldsymbol{p}} = -ih\left(\nabla_x, \nabla_y\right). \tag{36}$$

Analogously to the uncertainty relation of matter waves, we obtain

$$\sqrt{\langle (\Delta\hat{\boldsymbol{r}})^2 \rangle \langle (\Delta\hat{\boldsymbol{p}})^2 \rangle} \geq \frac{h}{2}, \tag{37}$$

where $\hat{A}$ denotes the weighted average following $\int\int M^* \hat{A} M dxdy$, and $\Delta\hat{\boldsymbol{r}}$ and $\Delta\hat{\boldsymbol{p}}$ are defined as

$$\Delta\hat{\boldsymbol{r}} \equiv \hat{\boldsymbol{r}} - \langle \hat{\boldsymbol{r}} \rangle, \ \Delta\hat{\boldsymbol{p}} \equiv \hat{\boldsymbol{p}} - \langle \hat{\boldsymbol{p}} \rangle. \tag{38}$$

The weighted averages $\langle (\Delta\hat{\boldsymbol{r}})^2 \rangle$ and $\langle (\Delta\hat{\boldsymbol{p}})^2 \rangle$ are used to measure the uncertainty in position and momentum, acting like the variance of a data set. If $\langle (\Delta\hat{\boldsymbol{r}})^2 \rangle$ ($\langle (\Delta\hat{\boldsymbol{p}})^2 \rangle$) gets smaller, we learn that the waves become more concentrated in position (momentum) space. The uncertainty relation (37) tells us that the waves cannot be overly concentrated simultaneously in both position and momentum spaces, which is a natural consequence of the Fourier transform.

When the background field traps the waves, *i.e.* , small $\langle \hat{\boldsymbol{p}} \rangle$ guaranteeing that the waves do not tend to escape. Then the uncertainty in momentum becomes

$$\langle (\Delta\hat{\boldsymbol{p}})^2 \rangle \approx \langle \hat{\boldsymbol{p}}^2 \rangle = \langle 2\widehat{H_1} \rangle = 2I_1. \tag{39}$$

Supposing the NIWs are initially uniformly distributed, *i.e.* I_2=0 . Gradually, the waves become concentrated, corresponding to a decrease in the uncertainty in position $\langle (\Delta\hat{\boldsymbol{r}})^2 \rangle$, and then the uncertainty in momentum $\langle (\Delta\hat{\boldsymbol{p}})^2 \rangle$ increases according to Eq.(37).

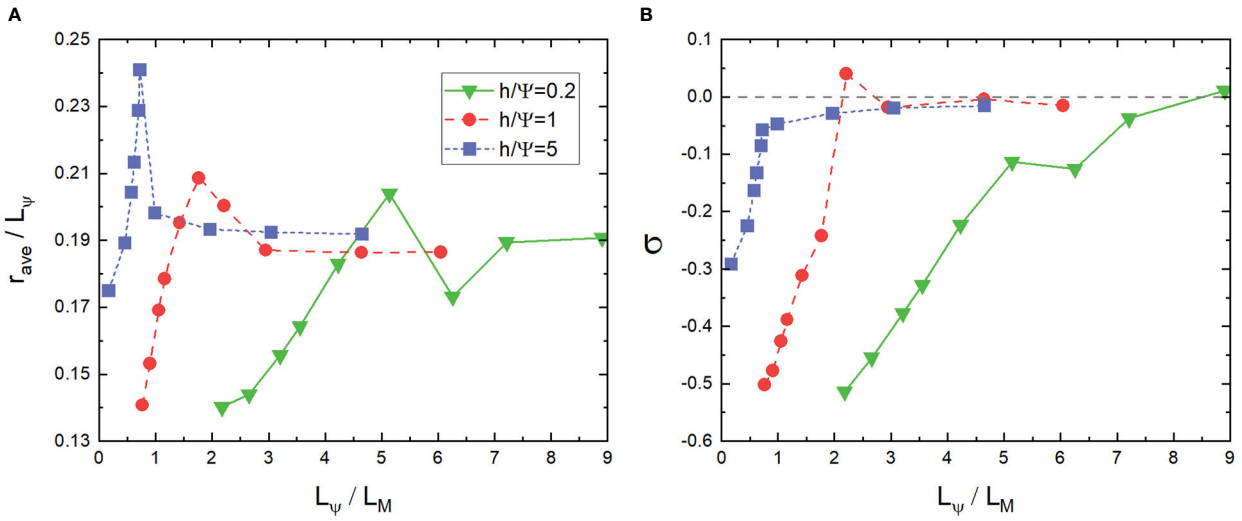

FIGURE 10
(A) r_{ave}/L_ψ vs L_ψ/L_M from the long-time average of $M(x,y,t)$. **(B)** σ vs L_ψ/L_M from the long-time average of $M(x,y,t)$. $\psi = -(\zeta_0/k_0^2)\sin k_0 x \sin k_0 y$. h/Ψ=0.2,1,5, respectively.

Thus, I_1 increases according to Eq.(39). When $L_\psi/L_M \gg 1$, one gets $I_3 \gg I_2$ according to a scaling analysis of Eq.(35). This corresponds to the "strong advection" regime where the NIW's concentration is insignificant. On the contrary, when $L_\psi/L_M \ll 1$, we have $I_2 \gg I_3$, and the conservation law implies that an increase in I_1 leads to negative I_2 . Thus, when large-scale NIWs are concentrated, the uncertainty relation guides them to concentration in anticyclones. This scale-dependent of NIW's concentration is inconsistent with our analytical and numerical results presented in Section 4–6.

7 Conclusion and discussion

Based on the YBJ equation, we analyze the scale effect of NIW's concentration by both analytical derivations and numerical simulations. We start from the exact and approximate solutions for a sinusoidal background shear flow and indicate that a larger wave scale facilitates the concentration. The particular forms of approximate solutions, consisting of envelopes and order-dependent oscillations, give us intuitions about the wave shapes and

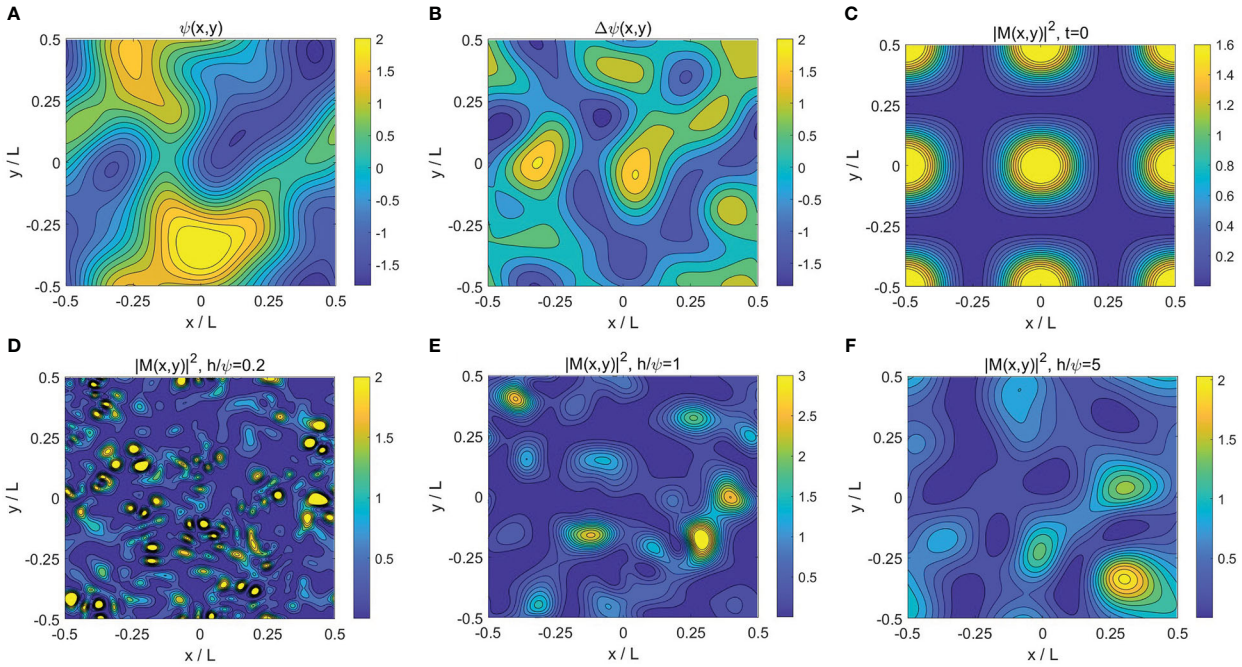

FIGURE 11
(A, B) Density plots of the random stream function **(A)** and associated vorticity field **(B)** with h/Ψ=1. **(C)** The initial condition for the velocity field, as set in Eq.(28) with n=1. **(D–F)** The long-time evolutionary behaviors of NIWs with different h/Ψ=0.2,1,5, respectively. The domain size is $L=4\pi$.

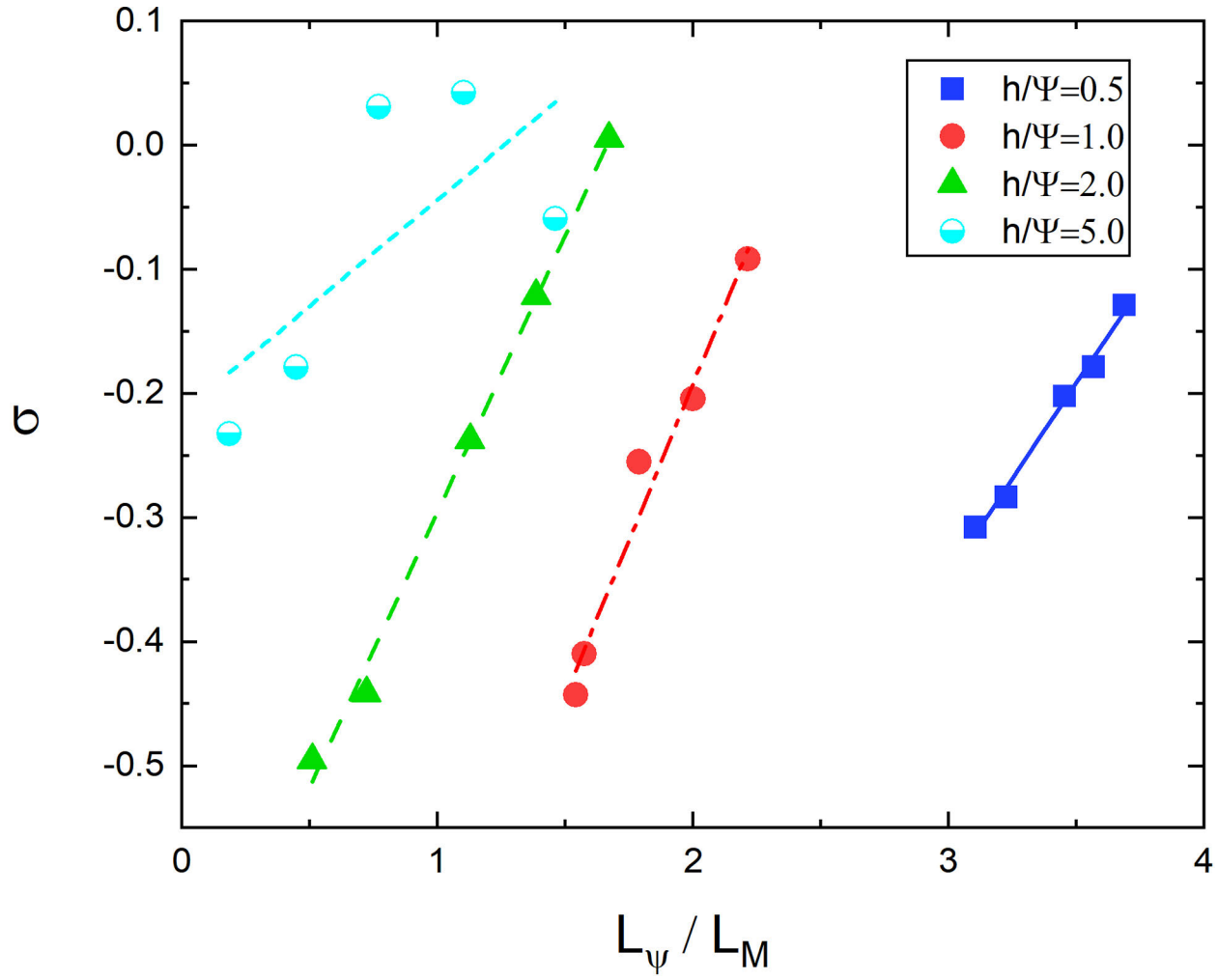

FIGURE 12
σ vs L_ψ/L_M from the long-time average of $M(x,y,t)$ with h/Ψ=0.5,1,2,5, respectively. The lines are obtained by least square fitting as references.

approximate frequency expressions. Numerical simulations with background vortex quadrupoles and random vortexes confirm the large scale's preference in enhancing the NIW's concentration.

Based on the two dimensionless parameters, h/Ψ and L_ψ/L_M , in the YBJ equation, we classify three dynamic regimes: a strong "dispersion" regime with $h/\Psi \gg 1$, a "trapping" regime with small h/Ψ and L_ψ/L_M, and an "advection" regime with a small h/Ψ and a large L_ψ/L_M . Figure 13 illustrates this classification. It is worth noting that for each h/Ψ , there exists a minimum value for L_ψ/L_M , which is determined by the scale of the most concentrated eigenmode of the system. Moreover, the smaller h/Ψ is, the larger the minimum will be. Unlike in Danioux et al. (2015), where with a homogeneous initial state, they attribute the energy concentration to the effect of only one parameter h/Ψ , we consider variable initial conditions and obtain a phase diagram about h/Ψ and L_ψ/L_M , which leads to a classification of "advection" regime.

The scale effect works mainly in the "trapping" regime. When NIWs concentrate in negative vorticities, their centers do not coincide precisely with the core of the vorticities, leaving a displacement originating from the advection. For strong "trapping", this displacement is proportional to the local wavenumber; However, when the advection effect becomes stronger, waves approach the boundaries between positive and negative vorticities, and the displacement is inversely proportional to the local wavenumber. Thus, the advection prevents the concentration of NIWs, and NIWs with large local wavenumbers (small scales) are more likely to appear at the boundaries. As small-scale structures continue to increase, the system enters a "strong advection" regime. In contrast to the two regimes mentioned above, in the "strong dispersion" regime, NIWs quickly disperse and are slightly influenced by the background vorticity. Therefore, the concentration of the NIWs is very weak in the "strong advection" and "strong dispersion" regimes (Llewellyn Smith, 1999).

Based on the similarity between the YBJ equation to the Schrödinger equation (Balmforth et al., 1998; Danioux et al., 2015), we present a new perspective for the NIW's concentration in the anticyclone using the uncertainty principle in quantum mechanics. Ignoring the advection term, these two equations are identical, so considering the higher probability of the particle being in the lower potential region, the NIWs prefer to concentrate in negative relative

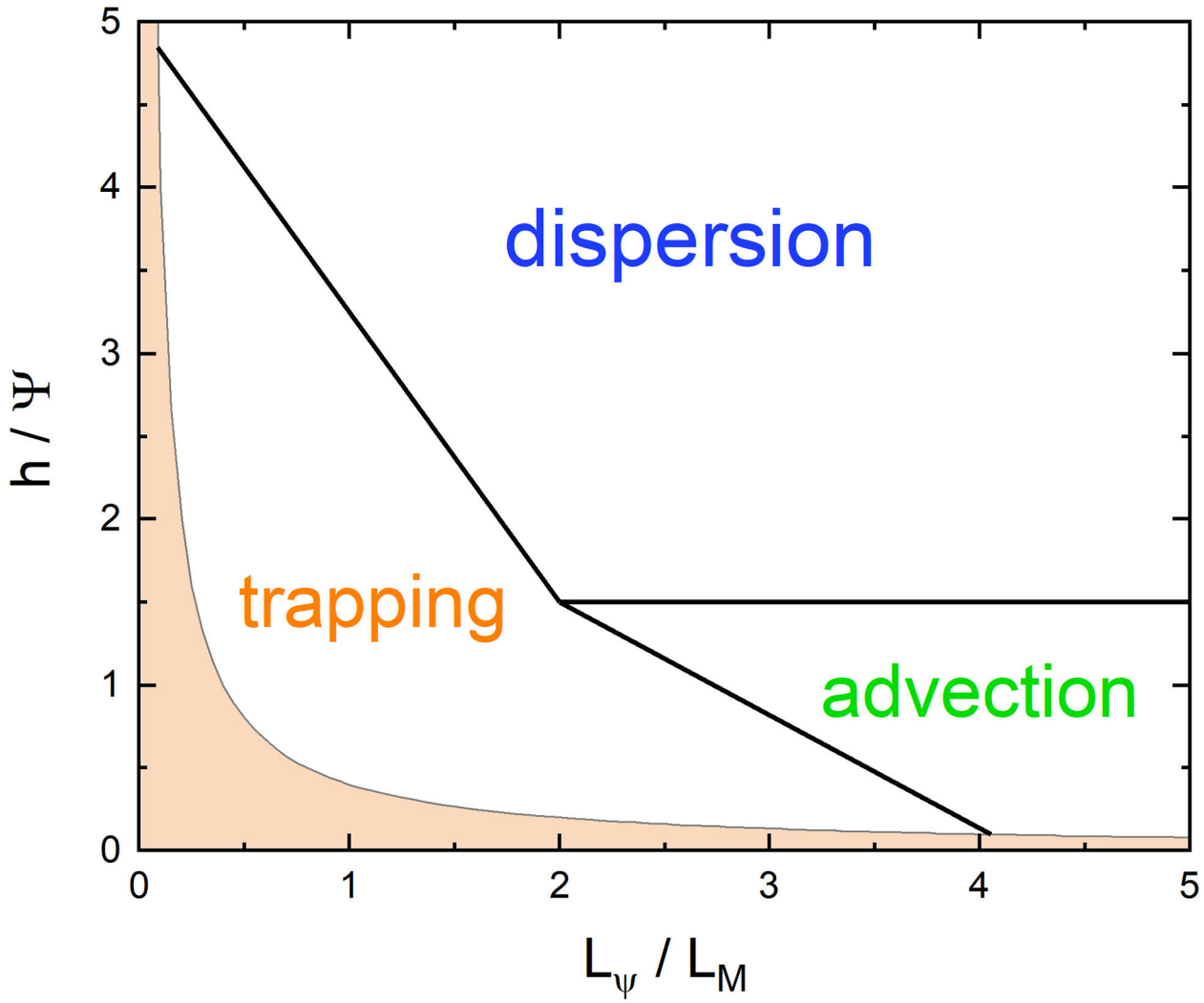

FIGURE 13
Schematic diagram of the regime classification. The shaded part is the forbidden area of the system, which is determined by the scale of the most concentrated eigenmode.

vorticities. Considering the advection's effect, which hinders NIW's concentration, this concentration trend could still be true if the change in the advection-related conservation, I_3 in Eq.35, is small enough. Based on the uncertainty relation, wave concentration means a decrease in the uncertainty of the wave's position, which leads to an increment in the uncertainty of its momentum. This will enhance the "particle" kinetic-like energy term, defined as I_1 in Eq.35. Then, due to the conservation of energy, it could reduce the vorticity-related energy term if $|\Delta I_3|<\Delta I_1$, leading the concentration towards negative vorticities. Thus, a link between the down-scale waves in space and the distribution of energy in anticyclones is naturally established.

We only consider some modes with low frequencies when studying eigenmodes in the sinusoidal shear flow and vortex quadrupole. This is reasonable because they contribute the most to the mode projection of a realistic initial condition (Balmforth et al. (1998)). For the low-frequency solutions, corresponding to small wavenumbers, the center of symmetry of the solutions can be regarded as the center of the energy distribution. While, for the modes with high frequencies, the Riemann-Lebesgue Lemma implies that the strong spatial oscillation induces only weak concentration if there is any. In addition, too high a frequency is already far from the near-inertial regime, which may make the YBJ equation invalid.

Data availability statement

The raw data supporting the conclusions of this article will be made available by the authors, without undue reservation.

Author contributions

FZ conducted the analytical derivations and numerical simulations, and wrote the first draft of the manuscript. J-HX conceived the idea and revised the manuscript. All authors contributed to the article and approved the submitted version.

Funding

This research was supported by the National Natural Science Foundation of China (NSFC) under grant no. 92052102 and 12272006, and the Joint Laboratory of Marine Hydrodynamics and Ocean Engineering, Pilot National Laboratory for Marine Science and Technology (Qingdao) under grant no. 2022QNLM010201.

Acknowledgments

The authors thank ShenHua Wang for his careful reading of the manuscript and his suggestions for revisions.

Conflict of interest

The authors declare that the research was conducted in the absence of any commercial or financial relationships that could be construed as a potential conflict of interest.

Publisher's note

All claims expressed in this article are solely those of the authors and do not necessarily represent those of their affiliated organizations, or those of the publisher, the editors and the reviewers. Any product that may be evaluated in this article, or claim that may be made by its manufacturer, is not guaranteed or endorsed by the publisher.

References

Alford, M. H. (2001). Internal swell generation: The spatial distribution of energy flux from the wind to mixed layer near-inertial motions. *J. Phys. Oceanography* 31, 2359–2368. doi: 10.1175/1520-0485(2001)031<2359:ISGTSD>2.0.CO;2

Alford, M. H., MacKinnon, J. A., Simmons, H. L., and Nash, J. D. (2016). Near-inertial internal gravity waves in the ocean. *Annu. Rev. Mar. Sci.* 8, 95–123. doi: 10.1146/annurev-marine-010814-015746

Balmforth, N. J., Smith, S. G. L., and Young, W. R. (1998). Enhanced dispersion of near-inertial waves in an idealized geostrophic flow. *J. Mar. Res.* 56, 1–40. doi: 10.1357/002224098321836091

Danioux, E., Klein, P., and Rivière, P. (2008). Propagation of wind energy into the deep ocean through a fully turbulent mesoscale eddy field. *J. Phys. Oceanography* 38, 2224–2241. doi: 10.1175/2008JPO3821.1

Danioux, E., Vanneste, J., and Bühler, O. (2015). On the concentration of near-inertial waves in anticyclones. *J. Fluid Mechanics* 773, R2. doi: 10.1017/jfm.2015.252

D'Asaro, E. A., Eriksen, C. C., Levine, M. D., Paulson, C. A., Niiler, P. P., and Meurs, P. V. (1995). Upper-ocean inertial currents forced by a strong storm. part i: Data and comparisons with linear theory. *J. Phys. Oceanography* 25, 2909–2936. doi: 10.1175/1520-0485(1995)025<2909:UOICFB>2.0.CO;2

Elipot, S., Lumpkin, R., and Prieto, G. (2010). Modification of inertial oscillations by the mesoscale eddy field. *J. Geophysical Research: Oceans* 115, (C9). doi: 10.1029/2009JC005679

Ferrari, R., and Wunsch, C. (2009). Ocean circulation kinetic energy: Reservoirs, sources, and sinks. *Annu. Rev. Fluid Mechanics* 41, 253–282. doi: 10.1146/annurev.fluid.40.111406.102139

Granata, T., Wiggert, J. D., and Dickey, T. D. (1995). Trapped, near-inertial waves and enhanced chlorophyll distributions. *J. Geophysical Res.* 100, 20793–20804. doi: 10.1029/95JC01665

Jochum, M., Briegleb, B. P., Danabasoglu, G., Large, W. G., Norton, N. J., Jayne, S. R., et al. (2013). The impact of oceanic near-inertial waves on climate. *J. Climate* 26, 2833–2844. doi: 10.1175/JCLI-D-12-00181.1

Joyce, T. M., Toole, J. M., Klein, P., and Thomas, L. N. (2013). A near-inertial mode observed within a gulf stream warm-core ring. *J. Geophysical Res.* 118, 1797–1806. doi: 10.1002/jgrc.20141

Klein, P., and Smith, S. G. L. (2001). Horizontal dispersion of near-inertial oscillations in a turbulent mesoscale eddy field. *J. Mar. Res.* 59, 697–723. doi: 10.1357/002224001762674908

Klein, P., Smith, S. L., and Lapeyre, G. (2004). Organization of near-inertial energy by an eddy field. *Q. J. R. Meteorological Soc.* 130, 1153–1166. doi: 10.1256/qj.02.231

Klein, P., and Tréguier, A. M. (1995). Dispersion of wind-induced inertial waves by a barotropic jet. *J. Mar. Res.* 53, 1–22. doi: 10.1357/0022240953213331

Kunze, E. (1985). Near-inertial wave propagation in geostrophic shear. *J. Phys. Oceanography* 15, 544–565. doi: 10.1175/1520-0485(1985)015<0544:NIWPIG>2.0.CO;2

Kunze, E., and Sanford, T. B. (1984). Observations of near-inertial waves in a front. *J. Phys. Oceanography* 14, 566–581. doi: 10.1175/1520-0485(1984)014<0566:OONIWI>2.0.CO;2

Lee, D.-K., and Niiler, P. P. (1998). The inertial chimney: The near-inertial energy drainage from the ocean surface to the deep layer. *J. Geophysical Research: Oceans* 103, 7579–7591. doi: 10.1029/97JC03200

Llewellyn Smith, S. G. (1999). Near-inertial oscillations of a barotropic vortex: trapped modes and time evolution. *J. Phys. oceanography* 29, 747–761. doi: 10.1175/1520-0485(1999)029<0747:NIOOAB>2.0.CO;2

Matsuno, T. (1966). Quasi-geostrophic motions in the equatorial area. *J. Meteorological Soc. Japan. Ser. II* 44, 25–43. doi: 10.2151/jmsj1965.44.125Matsuno1966

Rimac, A., von Storch, J.-S., Eden, C., and Haak, H. (2013). The influence of high-resolution wind stress field on the power input to near-inertial motions in the ocean. *Geophysical Res. Lett.* 40, 4882–4886. doi: 10.1002/grl.50929Rimac.et.al.2013

Rocha, C. B., Wagner, G. L., and Young, W. R. (2018). Stimulated generation: extraction of energy from balanced flow by near-inertial waves. *J. Fluid Mechanics* 847, 417–451. doi: 10.1017/jfm.2018.308Rocha.et.al.2018

van Meurs, P. (1998). Interactions between near-inertial mixed layer currents and the mesoscale: The importance of spatial variabilities in the vorticity field. *J. Phys. Oceanography* 28, 1363–1388. doi: 10.1175/1520-0485(1998)028<1363:IBNIML>2.0.CO;2

Wang, D.-P. (1991). Generation and propagation of inertial waves in the subtropical front. *J. Mar. Res.* 49, 619–633. doi: 10.1357/002224091784995747

Weller, R. A. (1982). The relation of near-inertial motions observed in the mixed layer during the jasin, (1978) experiment to the local wind stress and to the quasi-geostrophic flow field. *J. Phys. Oceanography* 12, 1122–1136. doi: 10.1175/1520-0485(1982)012<1122:TRONIM>2.0.CO;2

Xie, J.-H. (2020). Downscale transfer of quasigeostrophic energy catalyzed by near-inertial waves. *J. Fluid Mechanics* 904, A40. doi: 10.1017/jfm.2020.709Xie2020

Xie, J.-H., and Vanneste, J. (2015). A generalised-lagrangian-mean model of the interactions between near-inertial waves and mean flow. *J. Fluid Mechanics* 774, 143–169. doi: 10.1017/jfm.2015.251XieVanneste2015

Young, W. R., and Jelloul, M. B. (1997). Propagation of near-inertial oscillations through a geostrophic flow. *J. Mar. Res.* 55, 735–766. doi: 10.1357/0022240973224283

Zhai, X., Greatbatch, R. J., and Zhao, J. (2005). Enhanced vertical propagation of storm-induced near-inertial energy in an eddying ocean channel model. *Geophysical Res. Lett.* 32, (18). doi: 10.1029/2005GL023643

frontiers | Frontiers in Marine Science

TYPE Original Research
PUBLISHED 02 February 2023
DOI 10.3389/fmars.2022.995601

OPEN ACCESS

EDITED BY
Shengqi Zhou,
South China Sea Institute of Oceanology (CAS), China

REVIEWED BY
Zhiwu Chen,
State Key Laboratory of Tropical Oceanography (CAS), China
Hidekatsu Yamazaki,
Shanghai Ocean University, China
Yi-Chia Hsin,
Academia Sinica, Taiwan

*CORRESPONDENCE
Zengan Deng
dengzengan@163.com
Ru Chen
ruchen@tju.edu.cn

SPECIALTY SECTION
This article was submitted to Physical Oceanography, a section of the journal Frontiers in Marine Science

RECEIVED 16 July 2022
ACCEPTED 28 December 2022
PUBLISHED 02 February 2023

CITATION
Tang G, Deng Z, Chen R and Xiu F (2023) Effects of the Kuroshio on internal tides in the Luzon Strait: A model study. *Front. Mar. Sci.* 9:995601. doi: 10.3389/fmars.2022.995601

Effects of the Kuroshio on internal tides in the Luzon Strait: A model study

Guoqin Tang[1], Zengan Deng[1,2]*, Ru Chen[1]* and Fangrui Xiu[1]

[1]School of Marine Science and Technology, Tianjin University, Tianjin, China, [2]Guangxi Key Laboratory of Marine Environment Change and Disaster in Beibu Gulf, Beibu Gulf University, Qinzhou, China

Internal tides have a great impact on the meridional overturning circulation and climate variability through contributing to diapycnal mixing. The Luzon Strait (LS) is one of the most important sites of internal tide generation in the global ocean. In this study, we evaluate the effect of the Kuroshio on the M2 and K1 internal tides in both summer and winter seasons in the South China Sea (SCS), particularly within the LS. High-resolution ocean numerical simulations with the Kuroshio Current were compared with those without. We found that the Kuroshio has negligible impact on the generation site of internal tides. Compared to seasonal variability in the total barotropic to baroclinic conversion rate over the LS, the Kuroshio has relatively little influence. However, the Kuroshio flow strongly guides the propagating direction of the internal tides from the LS into the SCS. The Kuroshio also substantially decreases the southward energy fluxes going out of the LS. For both M2 and K1 tides, turning off the Kuroshio leads to a weaker energy exchange between the background shear and internal tides. Turning off the Kuroshio also weakens the divergence of internal tide energy due to the advection of background flow. Thus, our results reveal a non-negligible effect of the Kuroshio on the internal tides in the LS. If one aims to realistically simulate, or better understand, internal tides, these results indicate that one should include realistic oceanic circulation fields.

KEYWORDS

internal tide propagation, nonlinear interaction, energy conversion, Kuroshio, stratification

1 Introduction

Oceanic circulation can be greatly affected by internal tides, which often arise when barotropic tidal currents pass over topography in stratified oceans (Wang et al., 1991; Lamb, 1994; Munk and Wunsch, 1998; Simmons et al., 2004; Vlasenko et al., 2005). Although low-mode internal tides can propagate over thousands of kilometers, high-mode internal tides often break up and dissipate (Klymak et al., 2012). This break up of internal tides leads to strong turbulence and diapycnal mixing, and thus influences the abyssal stratification and global meridional overturning circulation (Munk and Wunsch, 1998; Egbert and Ray, 2000; St. Laurent, 2008). For example, Simmons et al. (2004) showed that internal tides contribute up to ~1 TW of energy to sustain global abyssal mixing.

The Luzon Strait (LS), connecting the South China Sea (SCS) to the Western Pacific, consists of double meridional submarine ridges (Hengchun and Lanyu ridges). Hereafter, for analyses, we will define the LS region as 120°E-123°E, 18°N-22°N. Strong internal tides with vertical isopycnal displacements of up to 150 m have been observed in this region (Duda et al., 2004; Ramp et al., 2004). In fact, the strong stratification and barotropic tidal action make the LS one of the world ocean's most important energy sources of internal tides and internal solitary waves (Guo and Chen, 2014; Alford et al., 2015). The large internal tide energy is also partly due to the double-ridge resonance mechanism (Zu et al., 2008; Alford et al., 2011; Buijsman et al., 2014). These locally generated internal tides can radiate both westward into the SCS and eastward into the Pacific Ocean. The observed time-averaged westward energy flux can reach 40 ± 8 kW m^{-1}, larger than other known estimates in the world (Alford et al., 2015). The low-mode internal tides can propagate more than 1000 km to the interior of the SCS and the Pacific Ocean (Zhao, 2014; Xu et al., 2016; Liu et al., 2017). During their propagation, these internal tides interact with other internal tides, such as those from the Mariana Island Arc and Ryukyu Ridge (Niwa and Hibiya, 2004; Kerry et al., 2013; Xu et al., 2016; Wang et al., 2018).

Internal tides in the LS region can be affected by the warm, salty Kuroshio. The Kuroshio is a western boundary current in the North Pacific, starting from the North Equatorial Current and flowing northward along the east coast of the Philippines. When the Kuroshio passes the SCS, part of the flow invades the SCS through the LS. Satellite observations reveal that, at any given time, the way that the Kuroshio invades can be one of three dominant types: the leaping path, the leaking path, or the looping path (Figure 1). The invasion path can change from one type to another within a few weeks (Nan et al., 2011). The strength of the Kuroshio invasion varies seasonally, being stronger in winter than in summer (Wyrtki, 1961; Shaw, 1991; Centurioni et al., 2004; Nan et al., 2015). The Kuroshio intrusion, which drives strong background subtidal currents, shifts the tilted thermocline to the west, thus changing the background stratification and affecting the generation, variability, and energy balance of internal tides in the LS (Varlamov et al., 2015; Li et al., 2016; Song and Chen, 2020). Using observations and numerical simulations, Ma et al. (2013) showed that the Kuroshio can influence the westward energy flux of internal tides in the LS by modifying the stratification and isopycnal slope. Besides internal tides in the LS, the Kuroshio also has significant impact on internal tides in other regions, such as northeast of Taiwan and the Izu-Ogasawara Ridge off the coast of Japan (Masunaga et al., 2018; Chang et al., 2019; Masunaga et al., 2019).

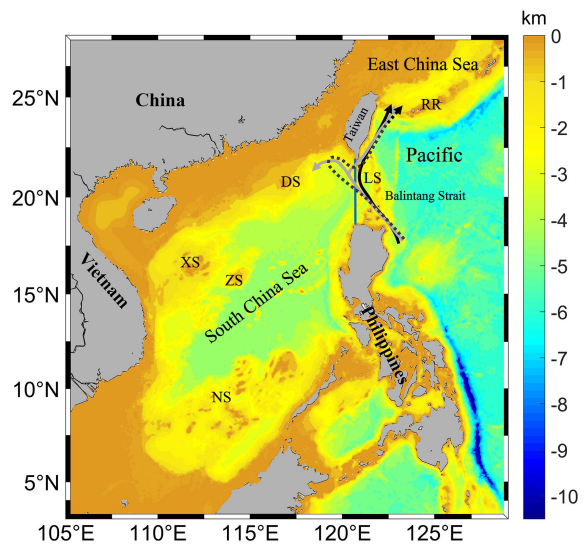

FIGURE 1
Bathymetry of the modelling domain. LS: Luzon Strait, DS: Dongsha Islands, XS: Xisha Islands, ZS: Zhongsha Islands, NS: Nansha Islands, RR: Ryukyu ridge. Arrows depict the type of Kuroshio invasion into the SCS (adapted from Nan et al., 2011): leaping path (solid black arrow), leaking path (solid gray arrow), and looping path (dashed black arrow). The blue line indicates the meridional section at 120.75°E, 18.5°N - 22°N, which is discussed in section 3.1.

Several numerical studies have examined the effects of the Kuroshio on internal tides in the LS (Jan et al., 2012; Varlamov et al., 2015; Song and Chen, 2020). A study using idealized topography found that both the location and magnitude of the Kuroshio can influence the generation and propagation of M_2 and K_1 internal tides (Jan et al., 2012). However, it is unclear whether their conclusions hold up for cases with realistic topography. Later, Varlamov et al. (2015) found that the M_2 tide variability in the LS can be modulated by the Kuroshio intrusion into the SCS. However, they used eight constituents of tidal forcing to force the model at the open boundary. Similarly, Song and Chen (2020) used simulations with all tidal constituents to examine the role of nonuniform stratification in modulating internal tides in the Northwest Pacific. However, M_2 and K_1 internal tides can respond to the Kuroshio in different ways. For example, Jan et al. (2012) found that the westward baroclinic energy flux of K_1 tides responds to the Kuroshio in an opposite way to that of M_2 tides. Therefore, it is important to consider each tidal constituent separately and evaluate whether the internal tide response to the Kuroshio is sensitive to the tidal constituents used for forcing. In addition, Song and Chen (2020) argued that nonlinearity in the baroclinic tide energy budget is important. Yet, the role of nonlinearity in the response of internal tides to the Kuroshio needs to be clarified and documented.

Inspired by these previous findings, we evaluate here the effects of the Kuroshio on the generation and propagation of internal tides in the SCS, particularly in the LS region. Specifically, we use the coastal and regional ocean community model (CROCO) to simulate the semidiurnal (M_2) or the diurnal (K_1) tidal forcing in summer and winter. The case with the Kuroshiois compared with the case without the Kuroshio for evaluating the energy conversion rate, the internal tide energy flux, as well as the baroclinic tide energy budget. We show that the Kuroshio greatly modulates the propagation direction of internal tides. The energy budget of internal tides is also sensitive to the existence of the Kuroshio.

This paper is organized as follows. Section 2 introduces the model configuration, data processing methods, and the energy diagnostic framework. Section 3 validates the model. Section 4 presents results about the effects of the Kuroshio on internal tides. Section 5 gives the summary and conclusion.

2 Method and diagnostic framework

2.1 Ocean model description

We use the CROCO model (version 1.0, https://www.croco-ocean.org), which has proved useful for simulating internal tides (Guo et al., 2020a; Guo et al., 2020b). It is a split-explicit, free-surface

ocean model based on the Boussinesq approximation. In our application, the wavelength of internal tides is much larger than the water depth (Vitousek and Fringer, 2011), and so following previous studies, we use the hydrostatic configuration (Jan et al., 2007; Jan et al., 2008; Rainville et al., 2010; Osborne et al., 2011; Powell et al., 2012; Kerry et al., 2013; Liu et al., 2019).

Our model has 40 vertical non-uniform sigma layers and a horizontal resolution of 1/30°. In our simulation domain (Figure 1), topography is complex, with multiple islands, ridges, continental slopes and deep-sea basins. The topography data is from GEBCO2019 (general bathymetric chart of the oceans, https://www.gebco.net/), then further smoothed to avoid the pressure-gradient errors arising from sigma coordinates (Niwa and Hibiya, 2004). The minimum and maximum depths are 20 and 6000 m. To represent vertical mixing, we use the K-profile parameterization (KPP) mixing scheme (Large et al., 1994). For horizontal mixing, we use the Laplacian method. The explicit lateral viscosity is set to be 10 m^2 s^{-1} and the bilaplacian background diffusivity is 20 m^2 s^{-1} in the implicit diffusion of advection scheme (Cambon et al., 2018).

Table 1 summarizes the setup of numerical experiments. All of the experiments exclude both wind forcing and heat flux. The model initial and boundary conditions for temperature, salinity, velocity and sea level, for all of the experiments are from the HYCOM 10-year (2002-2011) monthly-averaged reanalysis dataset at a horizontal resolution of 1/12° (GOFS 3.0, https://www.hycom.org/dataserver/gofs-3pt0/reanalysis). For the winter cases in Table 1, the 10-year monthly-averaged HYCOM outputs in January are used as the initial and boundary conditions; whereas for the summer cases, the July HYCOM outputs are used. In the control run (CtrlS and CtrlW in Table 1), tidal forcing is not specified at the open boundaries and thus the internal tides do not exist. For other experiments (cases with or without the Kuroshio in Table 1), they are driven by the barotropic semidiurnal tide (M_2) or the barotropic diurnal tide (K_1) at the open boundaries. The use of a single tide component here allows us to avoid the complex nonlinear interactions between internal tides of various components (Xie et al., 2010; Liu et al., 2015; Cao et al., 2018; Guo et al., 2020a; Song and Chen, 2020). The water levels and barotropic currents of each tidal component for the open boundary are obtained from the Oregon State University ocean topography experiment TOPEX/Poseidon Global Inverse Solution (TPXO9; Egbert and Erofeeva, 2002) tidal model with a horizontal resolution of 1/30°. The Flather condition (Flather and RA, 1976) is used for barotropic currents. Specifically, a 10-cell wide sponge layer is set at each lateral boundary to absorb the baroclinic energy and avoid energy reflection.

For the cases with the Kuroshio (M_2KS, M_2KW, K_1KS, K_1KW in Table 1), our model setup is the same as the control run, except that the tidal forcing is now included. As the initial and boundary conditions for temperature, salinity, velocity and sea level from the HYCOM outputs are realistic, the initial density and stratification are horizontally non-uniform, and the initial velocity field contains the Kuroshio information (Figure S1 in the supplementary material). In contrast, for the cases without the Kuroshio (M_2nKS, M_2nKW, K_1nKS, K_1nKW in Table 1), the initial and boundary conditions for temperature and salinity is obtained by spatial averaging the HYCOM outputs over the LS region. Therefore, both the density and stratification are horizontally uniform (Figure S1 in the supplementary material). Such uniform stratification has been used in previous studies on internal tides (e.g., Kerry et al., 2013; Xu et al., 2016; Wang et al., 2018; Chang et al., 2019). It is noted that the inflow/outflow boundary condition is specified in the with-Kuroshio cases and excluded in the without-Kuroshio cases. Based on the thermal-wind relation, a horizontally uniform hydrography corresponds to an absence of vertical shear, i.e, an absence of baroclinic flow. In addition, in these model runs (M_2nKS, M_2nKW, K_1nKS, K_1nKW in Table 1), the initial velocity is set to zero, so the Kuroshio flow is absent and thus its effects on internal tides are effectively removed.

Each case in Table 1 is run for 15 days for the following reasons. First, a 15-day period is long enough to allow internal tides to propagate through the model domain and this integration time was also used in previous studies involving the SCS or the LS (Jan et al., 2008; Xu et al., 2016; Guo et al., 2020b). Second, the domain-averaged sea surface height (SSH) and kinetic energy time series indicate that our model solution has reached equilibrium in 15 days (not shown). An even longer time of model integration may lead to large deviations between the simulation and the initial states, in particular, for the experiments without wind forcing and data assimilation. A relatively short model run can help our

TABLE 1 Setup for each experiment.

	Case	Season	Stratification	Tidal Component
Control run	CtrlS	Summer	Realistic	None
	CtrlW	Winter	Realistic	None
With-Kuroshio Cases	M_2KS	Summer	Realistic	M_2
	M_2KW	Winter	Realistic	M_2
	K_1KS	Summer	Realistic	K_1
	K_1KW	Winter	Realistic	K_1
Without-Kuroshio Cases	M_2nKS	Summer	Uniform	M_2
	M_2nKW	Winter	Uniform	M_2
	K_1nKS	Summer	Uniform	K_1
	K_1nKW	Winter	Uniform	K_1

The HYCOM outputs in January represent winter, July represent summer.

model solution maintain a climatological steady state that is close to that in the HYCOM reanalysis. Such a realistic Kuroshio is important for evaluating the Kuroshio's effect on the internal tides. Third, the Kuroshio intrusion into the SCS has different paths (Figure 1) and generally shows a seasonal pattern (Nan et al., 2011; Nan et al., 2015). However, the timescale of the dominant Kuroshio variability is $O(100)$ days, and thus much longer than the timescale of internal tides (Zhang et al., 2001; Johns et al., 2001; Yin et al., 2017; Chang et al., 2019). Therefore, for the with-Kuroshio cases, we assume that the Kuroshio is quasi-steady and include the Kuroshio information in only the initial and boundary conditions. Using the quasi-steady setup can help us focusing on fundamental dynamics, making it easier to interpret the Kuroshio's influence.

Our model setup has also been found useful in relevant previous studies. For example, to investigate the interaction between the M_2 internal tides and subtidal flow in Hawaii Ridge and the northeast of Taiwan, Zaron and Egbert (2014) and Chang et al. (2019) both used Simple Ocean Data Assimilation (SODA) ocean analysis data as the initial background field, and the models run for 14 and 30 days, respectively. Hsin et al. (2012) assessed the relative importance of open sea inflow/outflow, wind stress and surface heat flux in regulating Luzon Strait transport (LST) and its seasonality through several elimination model experiments. Their inflow/outflow at the open boundaries of the experiment NO was derived from the 10-year mean from North Pacific Ocean (NPO) model outputs, which is similar to our model settings of the with Kuroshio cases.

The change of Kuroshio invasion is related to the wind in the vicinity of the LS, such as the wind stress curl off southwest Taiwan (Wu and Hsin, 2012) and the East Asian monsoon (Hsin et al., 2012).But following Hsin et al. (2012); Jan et al. (2012) and Chang et al. (2019), wind forcing is not included in our experiments. The reasons are as follows. Winds can generate internal waves (Kitade and Matsuyama, 2000). Wind forcing can also influence the distribution and dissipation of internal tide energy (Hall and Davies, 2007; Masunaga et al., 2019). We avoid such added complexity here. Our current model setup without wind reduces the experiment to the simplest system, which allows us to focus on basic physics of the Kuroshio effect on internal tides. For the experiment NO in Hsin et al. (2012), the model runs are more stable in the absence of wind stress and heat flux forcing while fixing the open ocean inflows/outflows at the 10 year mean from NPO model.

2.2 Baroclinic tide energy equation

To assess the effects of background stratification, and thus the Kuroshio flow shear, on internal tides, we use the energy equation of the baroclinic tides from Song and Chen (2020). In this equation, the variable a is decomposed into a background mean state a^m and a perturbation component a':

$$a(x,y,z,t) = a^m(x,y,z) + a'(x,y,z,t)\,. \tag{1}$$

For example, a can represent pressure p, density ρ, or velocity vector $\boldsymbol{u}$. The perturbation component can be further decomposed into barotropic a^{bt} and baroclinic modes a^{bc},

$$a^{bt} = \frac{1}{\eta + H}\int_{-H}^{\eta} a'\,dz \quad , \qquad a^{bc} = a' - a^{bt}\,. \tag{2}$$

The variables η and H represent the ocean surface elevation and water depth, respectively. With this approach, the background field is described by the background mean-state variables (a^m) and assumed constant.

Using the above variable decomposition, one can obtain the time-and-depth-integrated nonlinear baroclinic tide energy equations as

$$Tran^{bc} + Conv - Div^{bc} = \epsilon^{bc}, \tag{3}$$

where $Tran^{bc}$ denotes the transfer of energy from the mean flow to the baroclinc tidal flow:

$$Tran^{bc} = -\int_{-H}^{\eta} (\rho_c \boldsymbol{u}_h^{bc} u') \cdot \nabla \boldsymbol{u}_h^{m}\,dz\,. \tag{4}$$

Here ρ_c is the constant density and u_h means horizontal velocity vector. The term $Tran^{bc}$ arises from the nonlinear interaction between the background shear and internal tides, and thus it is hereafter termed $I_{m\text{-}bc}$ (Song and Chen, 2020). The next term $Conv$ represents the total conversion rate of energy from barotropic to baroclinic tidal flow, hereafter called 'total conversion rate',

$$Conv = Conv\_linear \underbrace{-\rho_c \int_{-H}^{\eta} (u_h^{bc}\boldsymbol{u}_h)\cdot(\nabla_h \boldsymbol{u}_h^{bt})dz}_{I_{bt-bc}}, \tag{5}$$

where $I_{bt\text{-}bc}$ arises from the nonlinearity of the system and is zero in the linear case (Song and Chen, 2020). The term $Conv\_linear$ represents the linear conversion rate,

$$Conv\_linear = \frac{1}{2} p'_{\theta A}(-H) w_{bt\theta A}(-H)\cos(\theta_{p'} - \theta_{w_{bt}})\,. \tag{6}$$

$Conv\_linear$ has three factors: the amplitude of the pressure perturbation at the bottom $p'_{\theta A}(-H)$, the vertical component of the barotropic flow $w_{bt\theta A}(-H)$, and the Greenwich phase difference cos ($\theta p'$-θ_{Wbt})), where subscript A indicates amplitude. For the derivation of Eq. (6), see Zilberman et al. (2011), Kerry et al. (2013) and Kerry et al. (2014). The term Div^{bc} from Eq. (3) quantifies the divergence of the energy flux:

$$Div^{bc} = \nabla_h \cdot [\underbrace{\int_{-H}^{\eta} \boldsymbol{u}_h \cdot (ke^{bc} + ape)dz}_{F_{non}^{bc}} + \int_{-H}^{\eta} \boldsymbol{u}_h^{bc} p^{bc} dz], \tag{7}$$

where F_{non}^{bc} represents the horizontal advection of local mechanical energy of internal tides (ke^{bc} + ape) by the background circulation. Finally, ε^{bc} the right side of Eq. (3), denotes the dissipation rate of internal tides. Compared to the energy equations in the linear system, the nonlinear energy equations have three additional terms: $I_{m\text{-}bc}$ [Eq. (4)], $I_{bt\text{-}bc}$ [Eq. (5)], and the horizontal divergence of F_{non}^{bc} which is part of Div^{bc} [Eq. (7)]. For details of the derivation, see Song and Chen (2020).

To diagnose the above energy terms, the horizontal tidal velocity $\boldsymbol{u}'_h$, the density perturbation ρ', and the pressure perturbation ρ' are first filtered with a specific band to extract the semidiurnal (1.83-2.20 cpd) and diurnal (0.80-1.15 cpd) motions. Given the relatively low frequencies

of the background flow, we use a low-pass filter with a cutoff frequency of 0.3 cpd to extract subtidal motion. As Eqs. (3) - (7) are based on the assumption that the background flow is steady, we assume that the simulated background state is constant over three days, so we use the last three days of model outputs for the energy diagnosis.

3 Model validation

3.1 Background state

In the background state, the simulated Kuroshio flows northward along the eastern side of the Philippines, crossing the Balintang Strait and then entering the SCS (Figure 2, top row). It is about 120 km wide, with maximum speeds of ~1.2 m s^{-1} in winter and ~1.3 m s^{-1} in summer, averaged over the upper 100 m of the 121°E meridional section (Figure 2, the bottom row). Part of the Kuroshio flows out along the southern part of Taiwan and then travels northward along the eastern part of Taiwan. Overall, the modeled flow agrees well with that from the SODA reanalysis data. The RMSEs (root mean square error) of the current speed for cases CtrlS and CtrlW are 0.15 m s^{-1} and 0.16 m s^{-1} in the whole domain, respectively. The probability that the modeled current direction differs from SODA by less than 60° is ~70%, with less than 35° being about 50%, indicating good agreement.

Concerning SSH, we find the results in Figures 2C, D to closely agree with the altimeter data in Nan et al. (2011) (not shown in the figure). Moreover, the difference between the maximum and minimum SSH values, for both the simulation and SODA reanalysis data, exceed 0.50 m, which is much greater than the RMSE values (0.08-0.09 m). Also, the correlation coefficients are greater than 0.84. Thus, the SSH also agrees well with SODA.

Concerning the three main Kuroshio paths into the SCS, the leaking path dominates in winter, the leaping path dominates in summer, and the looping path instead appears just southwest of Taiwan more frequently in winter than in other seasons (Wu and Chiang, 2007; Nan et al., 2015). Similarly, our simulation generally has the leaking path in summer and the looping path in winter (Figures 2C, D). Overall, the simulated Kuroshio velocities and paths appear reasonable.

Our model also reasonably captures the background hydrographic fields. For example, the meridional cross-sections of temperature and salinity at 120.75°E agree well with those from WOA18 (Figure 3). The RMSEs of temperature for cases CtrlS and CtrlW are both less than 1, and the RMSEs of salt are both less than 0.2, with the correlation coefficients of temperature exceeding 99%. In addition, for both WOA18

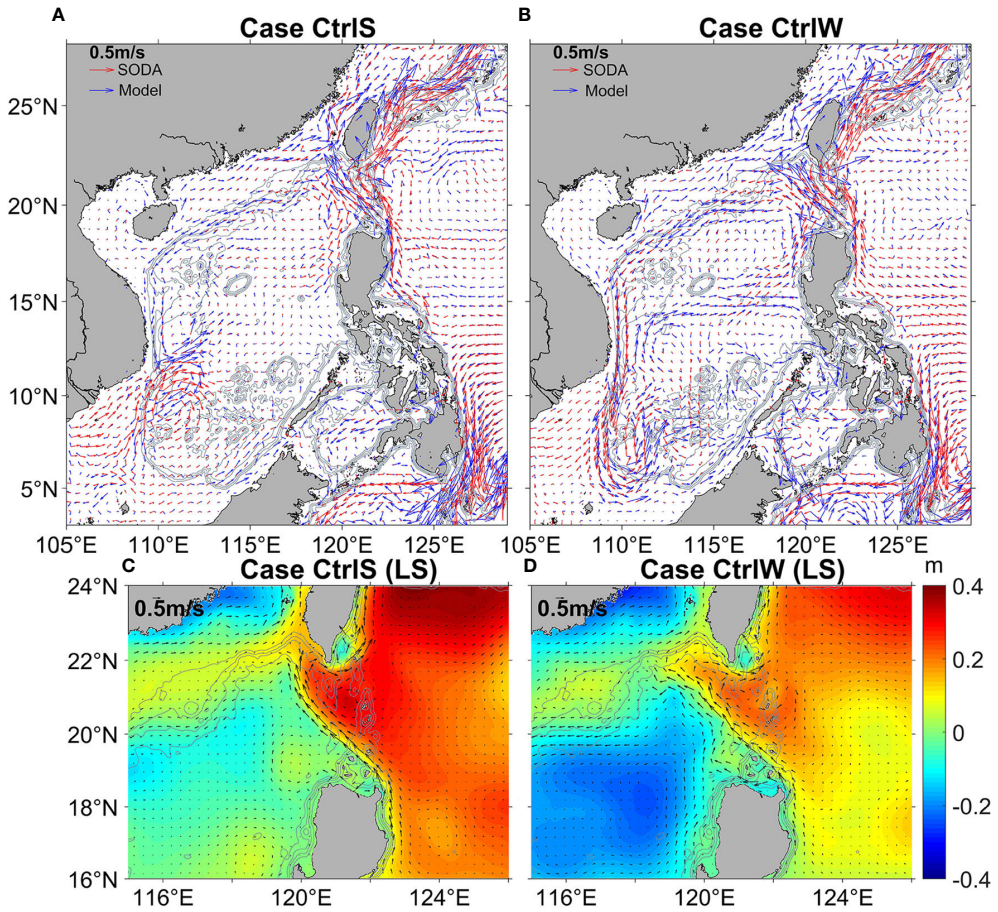

FIGURE 2
Mean flow vectors from the simulations and from the SODA (simple ocean data assimilation) reanalysis data. **(A)** Summer case CtrlS (blue), SODA (red). **(B)** Winter case CtrlW (blue), SODA (red). **(C, D)** show the mean velocity vector averaged over the upper 100 m and the sea surface height (color, m) from cases **(C)** CtrlS and **(D)** CtrlW in the LS region.

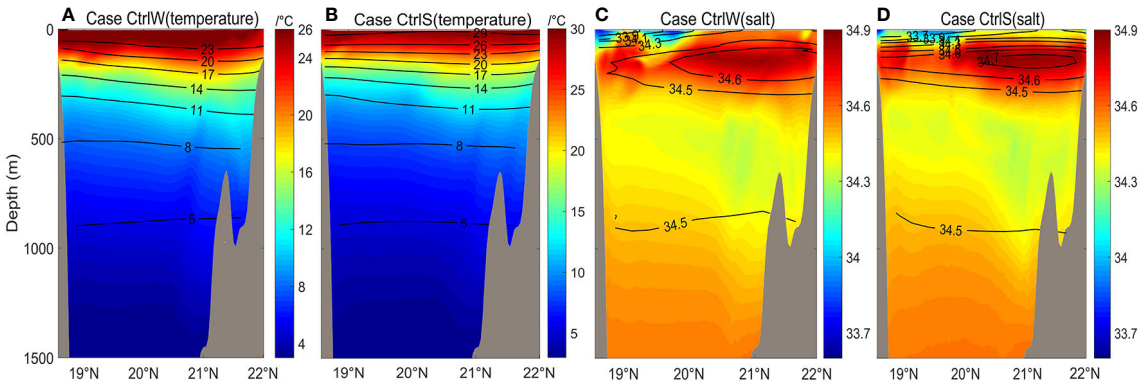

FIGURE 3
Simulated temperature and salinity profiles at 120.75°E, 18.5°N-22°N (blue line section in Figure 1) overlaid with WOA18 (world ocean database) annual mean data within the upper 1500 m. **(A)** Simulated temperature profile of winter case in color, with WOA18 temperatures as black contours. **(B)** Same as **(A)** except summer. **(C)** Same as **(A)** except salinity profile in winter. **(D)** Same as **(C)** except summer.

and our model solution, the isotherms in the LS region tilt toward the east (the Philippine Sea) (not shown).

3.2 Barotropic tides

Using the harmonic analysis method from Pawlowicz et al. (2002), we obtained the cotidal charts of M_2 and K_1 tides from the last three days of modelling outputs. In Figure 4, we compare the simulated results to the TPXO9 dataset. The distribution of simulated surface elevation and cophase lines are generally consistent with TPXO9, except that the simulated amplitude is slightly larger than TPXO9 near the shelf region. Small-scale fluctuations of the cophase lines occur in the LS and SCS regions, and these are mainly caused by the baroclinic tide signals (Niwa and Hibiya, 2004; Xu et al., 2016). Consistent with the altimetric estimates from Zhao (2014), the horizontal wavelength of M_2 and K_1 internal tides in our simulation, inferred from these fluctuations, are about 160 and 320 km, respectively. The RMSEs of the amplitudes are 11.70 and 6.95 cm, respectively for cases M_2KS and K_1KS, and the correlation coefficients of the amplitudes exceed 92% with a confidence level of 95%. Here, we further calculate a new RMSE specifically for tides in another way. Following Cummins and Oey (1997),

$$RMSE = \sqrt{\frac{1}{2}(A_o^2 + A_m^2) - A_o A_m \cos(\phi_o - \phi_m)}, \quad (8)$$

where A and ϕ represent the amplitudes and phases of the surface elevations. The subscripts o and m refer the results from TPXO9 and our model, respectively. The new mean RMSEs (calculated using Eq. 8) of the eight cases (M_2KS, M_2KW, M_2nKS, M_2nKW, K_1KS, K_1KW, K_1nKS and K_1nKW) are 4.50, 5.03, 4.58, 5.39, 4.34, 4.35, 4.37, and 4.38 cm, respectively.

3.3 Baroclinic tides

To assess our model fidelity on internal tides, we ran additional experiments that include semidiurnal tides (M_2 and S_2) and diurnal tides (K_1 and O_1) at the open boundaries. Results in Figures 4E, F show that the simulations well capture the propagation pattern of internal tides. For both diurnal and semidiurnal tides, the simulated energy-flux directions agree with observations from Alford et al. (2011). The energy-flux magnitudes also agree with observations, particularly in the region south of 20°N. We provide further statistics in Table 2. In the semidiurnal case, the simulated maximum energy flux is 55.2 kW m^{-1} in the LS region (120°E-122.5°E, 19°N-21.5°N), which is much greater than the energy flux RMSE of 9.1 kW m^{-1}, and the average energy flux is 15.3 kW m^{-1} (Table 2). The RMSE of the energy-flux direction is no more than 23.5°. In the diurnal case, the RMSE of energy flux is 7.1 kW m^{-1}, and that of the energy-flux direction is 32.5°. By including all semidiurnal tidal components in our simulation, smaller deviations would likely be obtained.

4 Effects of the Kuroshio on internal tides

4.1 Internal tides in the case with the Kuroshio

In the simulations with the Kuroshio, the internal tide energy flux and conversion rate are spatially heterogeneous. Figure 5 shows that the dominant generation site of internal tides is in the LS region. Here, the M_2 tide generates energy of ~17.1 GW (case M_2KS), whereas K_1 generates ~10.6 GW (case K_1KS). As marked by the light blue arrows in Figure 5A, there are three M_2 energy beams radiating from the LS: one points to the northeastern shelf of the SCS (northern beam), another directs southwest to the deep-sea basin (southern beam), and the third one east to the Pacific Ocean. This three-beam pattern is generally consistent with previous observational and modelling studies (Kerry et al., 2013; Zhao, 2014; Xu et al., 2016). The northern beam heads northwestward, converging near the Dongsha Islands, and then dissipating at the continental slope. The southern beam, much weaker than the northern beam, propagates southwestward, crossing the deep-sea basin, and then traveling for more than 1000 km to reach the Vietnam coast or the Nansha Islands due to its small dissipation rate. For the K_1 internal tides, two main beams radiate from the LS: one points southwest to the deep-sea basin

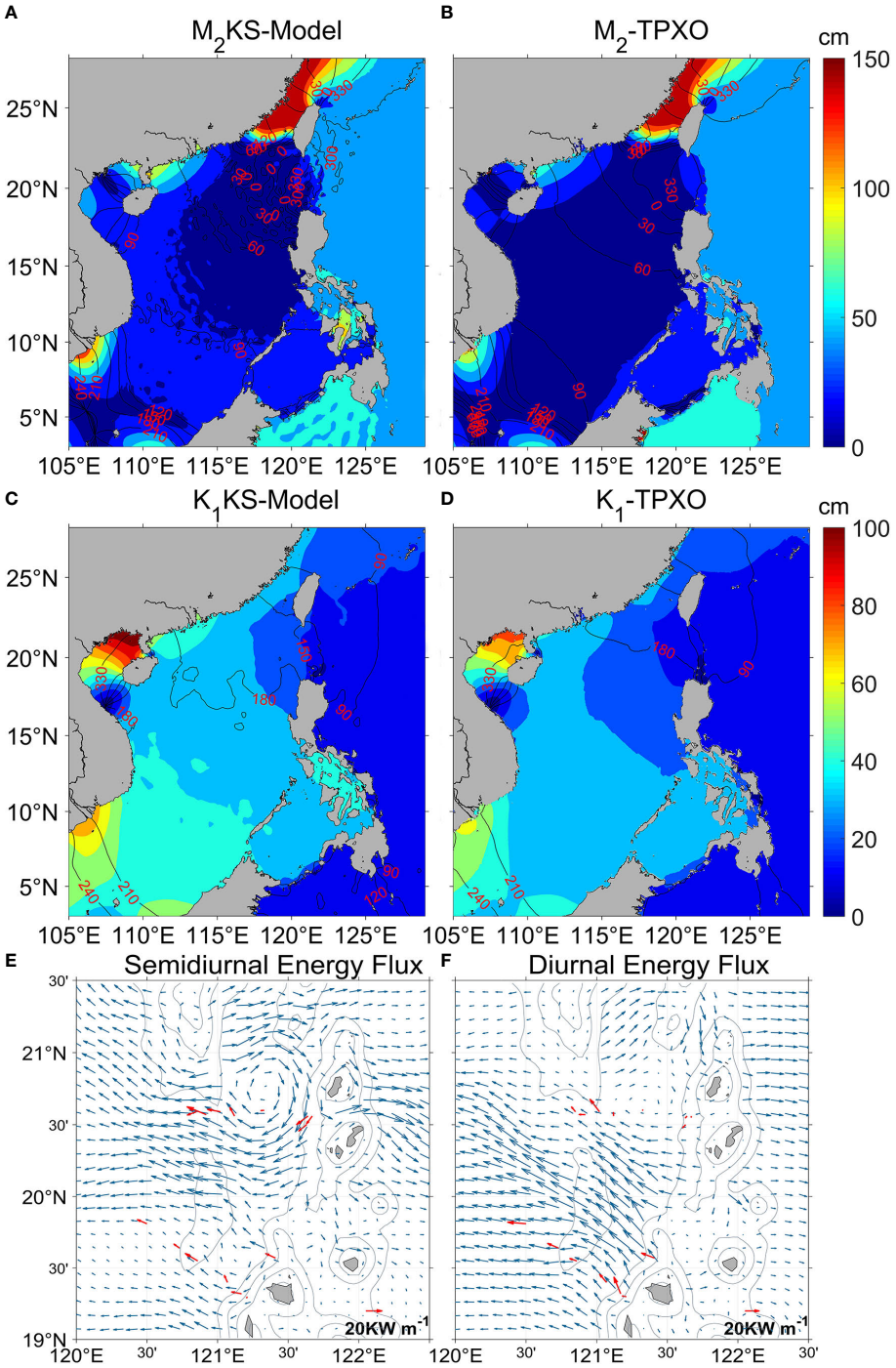

FIGURE 4
Modeled and observed cotidal chart and baroclinic energy flux. **(A)** Cotidal for case M_2KS. Color indicates amplitudes (cm) and black contours give the cophase lines (degree). **(B)** M_2 from TPXO9 observations. **(C)** Cotidal chart for case K_1KS. **(D)** K_1 of TPXO9. **(E)** Baroclinic energy flux from *in situ* observations (red, Alford et al., 2011) and our experiment forced by semidiurnal (M_2 and S_2) tide (blue). **(F)** The same as **(E)** but for diurnal (K_1 and O_1) tide.

TABLE 2 The RMSEs between internal tide energy flux of the simulations and that of the estimate from *in situ* observations (Alford et al., 2011).

	RMSE (energy flux, kW m^{-1})	RMSE(direction)	Maximum energy flux (kW m^{-1})	Average energy flux (kW m^{-1})
Semidiurnal case	9.1	23.5°	55.2	15.3
Diurnal case	7.1	32.5°	63.2	17.1

Maximum energy flux: The maximum energy flux in the LS region (120°E-122.5°E, 19°N-21.5°N, Figures 4E, F). Average energy flux: The average energy flux in the LS region.

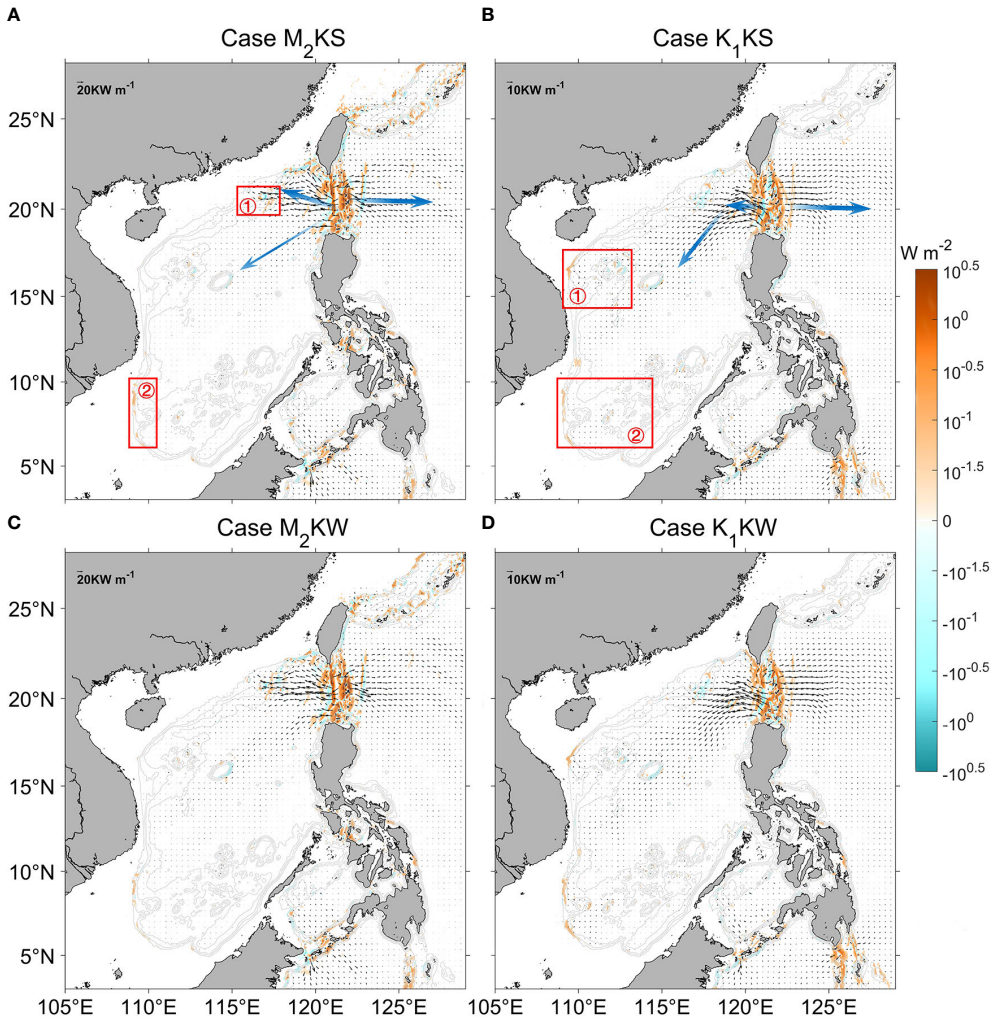

FIGURE 5
Modeled depth-integrated and period-averaged internal tide energy flux (black arrows, kW m^{-1}) and conversion rate (color, W m^{-2}) for with-Kuroshio cases. **(A)** Case M_2KS. Gray contours are isobaths. Blue arrows indicate energy beams. Red boxes marked ① and ② show the main areas of internal tide generation within the SCS. **(B)** Case K_1KS. **(C)** Case M_2KW. **(D)** Case K_1KW.

of the SCS and the other points east to the Pacific (Figure 5B). The complex wave forms and propagation paths of internal tides radiating from the LS into SCS may be due to the impact of rotation, complex topography, and the mutual interference with locally generated internal tides.

Besides the LS region, local generation sites of internal tides occur within the SCS. The strength of generation of these internal tides is controlled by both the topographic slope and the strength of barotropic tides. Also, the strength distribution of the K_1 barotropic tides differs from that of M_2 (Figure 4). Consequently, the generation sites of M_2 internal tides differ from those of K_1 within the SCS. In particular, the generation of M_2 lies mainly at the northeastern continental slope (box "1" in Figure 5A) and the southwestern continental slope (box "2"), whereas those for K_1 are similarly marked in Figure 5B, being around the Xisha Islands and the northwestern continental slope ("1"), and around the Nansha Islands and the southwestern continental slope ("2"). As shown in Zu et al. (2008), this difference is due to the fact that the energy flux intensities of the two barotropic tidal components vary in different regions within the SCS.

The seasonality of internal tides can be evaluated by comparing the summer cases in the top row of Figure 5 to the winter cases in the bottom row. In this realistic stratification scenario, the source and propagation direction of the tides in the SCS vary little from season to season. However, as shown in the next section, the energy magnitude undergoes a significant seasonal cycle.

4.2 Effects of the Kuroshio on conversion rates and baroclinic energy fluxes

4.2.1 M_2 internal tides

Results show that modulation of the double-ridge system complicate the generation and propagation of internal tides in the LS. For case M_2KS (with-Kuroshio, summer), Figure 6A shows the baroclinic energy flux and conversion rate. We examine the five main

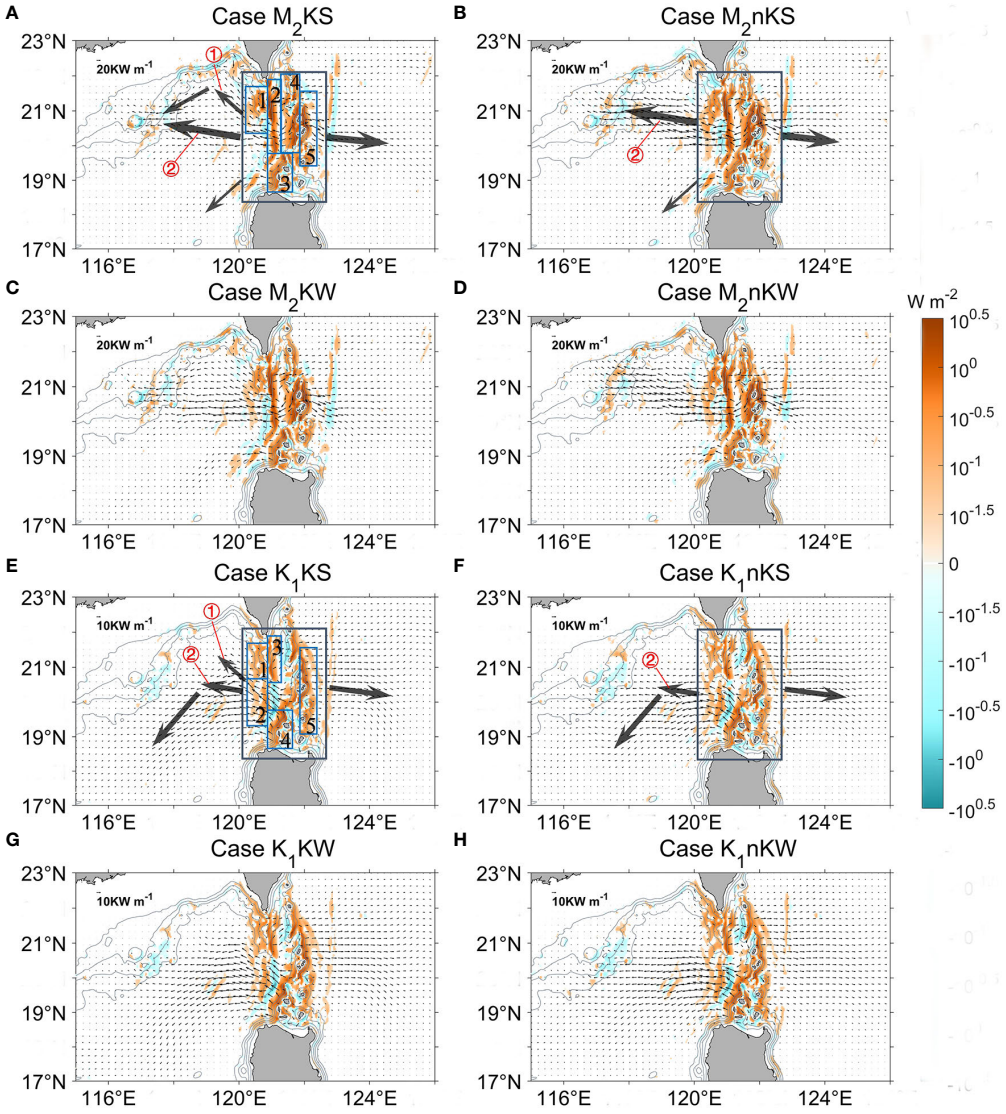

FIGURE 6
Modeled baroclinic energy flux (thin black arrows) and conversion rate (color) of the M_2 and K_1 internal tides in the LS and nearby regions. **(A–D)** For M_2 internal tides. Top row is summer, second row is winter. Left column is the with-Kuroshio cases, right is the without-Kuroshio cases. The gray boxes outline the LS region (120°E - 122.5°E, 18.3° N - 22° N). The blue boxes in the large gray boxes indicate the five M_2 subregions discussed in the main text. The thick black arrows show the main direction of internal tide energy from the source of the LS. Red circles ① and ② represent the northwestward and westward internal tide energy flux, respectively. **(E–H)** The same as **(A–D)**, but for K_1 internal tides.

M_2 internal tide-generating sites (labeled). Conversion rates at sites 2, 4, and 5 are significantly higher than those at 1 and 3 due to a larger topographic criticality there (Kerry et al., 2013). Sites 1 and 4 are the main sources of the 'northern beam', site 3 is the main source of the 'southern beam', and site 5 is the main generation site of internal tides propagating into the Pacific Ocean. The strongest energy flux is about 60 kW m^{-1}, propagating northwestward from just south of site 2. Despite the higher conversion rates at site 2, only a small portion of energy generated here crosses the high Lanyu ridge into the Pacific Ocean due to a topographic blocking effect.

West of the LS, the conversion rate near the Dongsha Islands (118°E, 20.75°N) is negative (Figure 6A). In general, negative values occur due to the phase differences between local- and remote-generated baroclinic tides, indicating the presence of multiple source sites (Zilberman et al., 2009; Hall and Carter, 2011; Carter et al., 2012). Here, the negative conversion rate indicates that remote signals from the LS modulate internal tides in the eastern part of the Dongsha Plateau. Therefore, the Dongsha Islands are an important convergence region for the M_2 internal tides.

For the with- and without-Kuroshio cases, the areas of the internal tide energy generation are similar in the LS, and the Kuroshio does not notably impact the source of the internal tides. However, the Kuroshio does affect the pattern of baroclinic energy fluxes. Specifically, the with-Kuroshio case shows a noticeable portion of internal tide energy from the LS that radiates northwestward onto the continental slope (Figure 6A, ①), whereas the without-Kuroshio case instead has a dominant energy radiation direction that is westward (Figure 6B, ②). Therefore, compared to case M_2nKS, the

with-Kuroshio case M_2KS shows much less far-distant propagating energy within the SCS. In case M_2nKS, the energy propagating to the Dongsha Plateau exceeds that of M_2KS, and most internal tides pass the north part of the Dongsha Islands. In case M_2KS, however, the Dongsha Islands is a region where internal tides converge.

In winter, for both the with-Kuroshio (Figure 6C) and without-Kuroshio (Figure 6D) cases, the dominant energy fluxes are zonally directed westward into the SCS. However, a northwestward radiation of energy from the LS occurs in the with-Kuroshio case, but not in the without-Kuroshio case. The width and direction of these northwestward-propagating tides resemble those of the Kuroshio flow, with both showing seasonal variations (Figures 2C, D). However, in the without-Kuroshio case, the dominant energy radiation directions, which are approximately zonal, are less affected by the seasons. Therefore, the with-Kuroshio case shows greater seasonal variations in the direction of tidal energy flux in the LS than in the without-Kuroshio case, especially for the northwestward internal tides under the influence of the Kuroshio.

4.2.2 K_1 internal tides

As was the case for the M_2 tides, the K_1 internal tides have five main generation sites in the with-Kuroshio case in summer. Figure 6E shows that sites 2 and 4 are the main generation areas of internal tides propagating westward into the SCS. The K_1 internal tides generated at site 3 propagate eastward, but are blocked by the northern part of the high Lanyu Ridge. As a result, site 5 is the most important source of eastward-propagating tides into the Pacific, showing relatively uniform radiation along the entire ridge. Similar to that of case M_2KS, the Dongsha Plateau is an important convergence area of K_1 internal tides, as revealed by the negative conversion rates there.

In summer, although their generation sites of internal tides are similar, the baroclinic energy flux directions without the Kuroshio differ from those with the Kuroshio (Figures 6E, F). On the SCS side, the with-Kuroshio case has both northwestward- (Figure 6E, ①) and westward-propagating (Figure 6E, ②) internal tides, whereas the without-Kuroshio case is dominated by westward internal tides (Figure 6F, ②). On the Pacific side, the dominant energy radiating direction is eastward for both the with- and without-Kuroshio cases. In winter, the effect of the Kuroshio on the energy radiation direction is similar to that in summer. However, the contrast between the two cases is less significant than that in summer (Figures 6G, H).

4.3 Effects of the Kuroshio on nonlinear energy terms

In the nonlinear case, there is energy exchange between the background shear and internal tides. The corresponding energy exchange rate $I_{m\text{-}bc}$ can be quantified using Eq. (4). Overall, the magnitude of $I_{m\text{-}bc}$ is only about 1-10% of the magnitude of the total conversion rate (*Conv*). Considering the spatial pattern of $I_{m\text{-}bc}$ in summer, both its peak magnitude and extent are larger in the with-Kuroshio case than those in the without-Kuroshio case (Figure 7). The tidal current can be generated by tidal forcing from the open boundary, which produces relatively weak background flow in the absence of Kuroshio. This weak background flow contributes a relatively small energy exchange rate between the background state and the internal tides (Figure S2 in the supplementary material).

Consider the horizontal shear $Shear_H$ and vertical shear $Shear_v$:

$$Shear_H = \sqrt{\left(\frac{du}{dx}\right)^2 + \left(\frac{du}{dy}\right)^2 + \left(\frac{dv}{dx}\right)^2 + \left(\frac{dv}{dy}\right)^2} \tag{9}$$

$$shear_V = \sqrt{\left(\frac{du}{dz}\right)^2 + \left(\frac{dv}{dz}\right)^2} \tag{10}$$

The distributions of $Shear_H$ and $Shear_V$ for cases M_2KS and M_2nKS are shown in Figure 8. In the with-Kuroshio case, the $Shear_H$ at 100 m depth along the Kuroshio path typically exceeds 1×10^{-5} s^{-1} (Figure 8A). In the without-Kuroshio case, the $Shear_H$ is generally less than 1×10^{-5} s^{-1} over the whole region (Figure 8B). For the $Shear_v$, the large values are also mainly distributed along the path of the Kuroshio, and the magnitude for the without-Kuroshio case is much smaller over the whole region (Figures 8C, D). In general, the notable background shear is mainly distributed along the Kuroshio path.

The energy exchange $I_{m\text{-}bc}$ in Figure 7 is large in the regions where both the background shear (Figure 8) and internal tide energy (Figure 5) are large. For the M_2KS case (Figure 7A), the magnitude of $I_{m\text{-}bc}$ in the LS region is about 10^{-2} - 10^{0} W m^{-2}, which is 1-2 orders of magnitude larger than that in the open ocean (about 10^{-2} W m^{-2}). Along the Kuroshio path (e.g., Hengchun Ridge and northeastern Taiwan), both the background shear and internal tide generation are intense, corresponding to a large $I_{m\text{-}bc}$. For case K_1KS (Figure 7C), elevated values of $I_{m\text{-}bc}$ mainly occur in the LS region. As the continental slope near northeast Taiwan is not the main generation region of the K_1 internal tides, the magnitude of $I_{m\text{-}bc}$ is small.

Besides the nonlinear interaction between the background shear and internal tides, there is also nonlinear interaction between barotropic and baroclinic tides (Section 2.2). The term $I_{bt\text{-}bc}$ from Eq. (5) represents the energy exchange rate between barotropic and baroclinic tides. Compared to $I_{m\text{-}bc}$, large values of $I_{bt\text{-}bc}$ cover a smaller area (Figures 9A-C). For case M_2KS, $I_{bt\text{-}bc}$is large in areas with prominent topography features, namely the East China Sea continental slope northeast of Taiwan and the two ridges of the LS (the Dongsha Plateau and the Ryukyu Ridge) (Figure 9A). In case M_2KS, $I_{bt\text{-}bc}$ is also large along the Kuroshio path, especially in the southern part of the Hengchun and Lanyu ridges. For case K_1KS, however, the area with elevated values of $I_{bt\text{-}bc}$ is smaller than that of case M_2KS, mainly along the two ridges of the LS (Figure 9C).

For case M_2KS, the magnitude of $I_{bt\text{-}bc}$ is only about 10^{-3}-10^{-1} W m^{-2} in the LS region, much smaller than the total conversion rate, and even much smaller than $I_{m\text{-}bc}$. Therefore, $I_{bt\text{-}bc}$ is a negligible nonlinear energy term in this case. Nevertheless, it can shed light on the source of internal tides and the Kuroshio effect. For both M_2 and K_1 internal tides, the magnitudes of $I_{bt\text{-}bc}$ in the without-Kuroshio case are much smaller than those in the with-Kuroshio case (Figure 9), indicating that the Kuroshio tends to promote the interaction between barotropic and baroclinic tides. This sensitivity of $I_{bt\text{-}bc}$ to the Kuroshio may be related to baroclinic tide generation. In particular, baroclinic internal tides can be generated when the background flow with temporal variability at tidal frequency passes a topography obstacle (e.g., a seamount or ridge). In the without-Kuroshio case, weak background flow shear probably corresponds to weak flow on

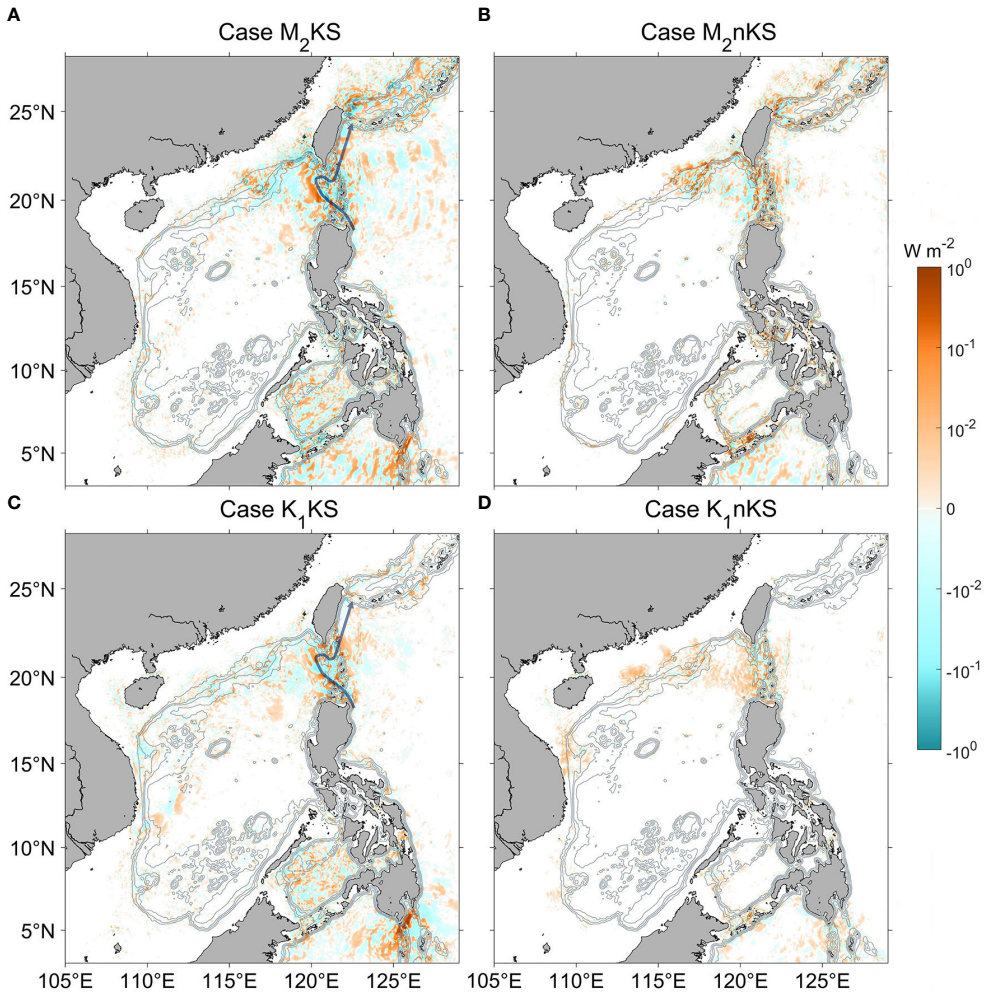

FIGURE 7
Distribution of $I_{m\text{-}bc}$ (color, W m^{-2}) for four summer cases. **(A)** M_2KS. Gray contours indicate isobaths. The blue line shows the Kuroshio path during the simulation period. **(B)** M_2nKS. **(C)** K_1KS. **(D)** K_1nKS. Left column is with-Kuroshio, right without.

topography. The weak flow decreases the energy exchange rate between barotropic and baroclinic tides and weakens the baroclinic internal tide.

In the baroclinic tide energy equation, the divergence of energy flux is induced by two processes: the advection of tide energy by background flow and the work done by pressure [Eq. (7)]. The contribution from advection is represented by the nonlinear term F_{non}^{bc} in Eq. (7). Representative results are shown in Figure 10. For the with-Kuroshio cases in summer (M_2KS and K_1KS, Figures 10A, B), the F_{non}^{bc} flux is largest in the LS, where it points northwestward and crosses the Hengchun Ridge to the SCS. Then, in winter (M_2KW), the F_{non}^{bc} flux is slightly stronger than in summer, directing northwestward and converging in the Dongsha Plateau (Figure 10C). The flux pattern here is similar to the leaking path of the Kuroshio (Figure 1), indicating that the contribution of the Kuroshio to F_{non}^{bc} is important for the with-Kuroshio case. For the M_2nKS case (Figure 10D), which does not include the Kuroshio, the maximum energy flux is only ~3 kW m^{-1}. It is much smaller than the maximum value of ~15 kW m^{-1} for the with-Kuroshio cases shown in Figures 10A-C. The direction of the F_{non}^{bc} flux seems random, with little resemblance to the Kuroshio path. The small value of energy flux in the without-Kuroshio case arises from weak background flow near the LS.

4.4 Energy budget in the Luzon Strait

4.4.1 Comparison with literature

We now consider the internal tide energy's total conversion rate in the LS. Seasonally, the total conversion rate within the LS varies significantly. Consistent with Guo et al. (2020b), the rate here in winter is larger than that in summer. Specifically, the total conversion rate from M_2KW is about 3.2% higher than M_2KS, whereas M_2nKW is 2.6% higher than M_2nKS (Table 3). Similarly, that from K_1KW is about 5.5% higher than K_1KS, and K_1nKW 5.7% higher than K_1nKS. Note that the total conversion rate of M_2 here is comparable to the estimate from Alford et al. (2015); Xu et al. (2016), and Guo et al. (2020b). However, it is larger than that from Niwa and Hibiya (2004); Jan et al. (2008), and Kerry et al. (2013). In all of experiments listed in Table 3, the ratio between the local dissipation rate and the total

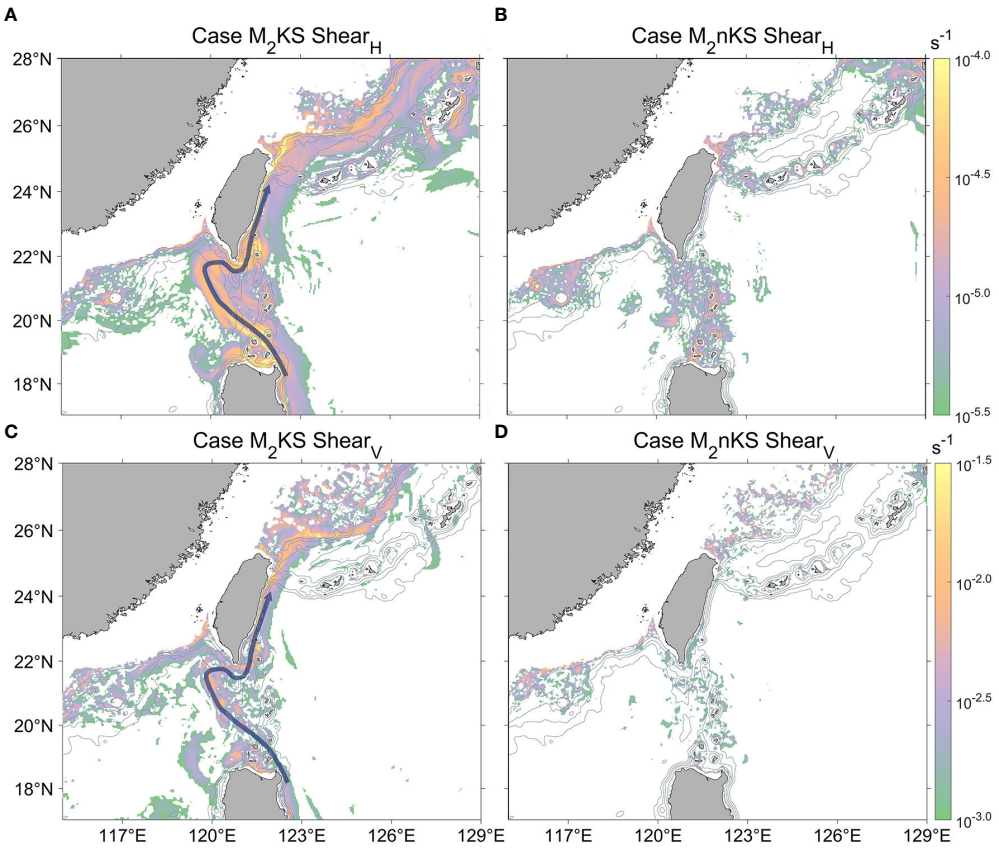

FIGURE 8
Distribution of $Shear_H$ and $Shear_V$ (color, s^{-1}) at 100 m depth for two summer cases (M_2KS and M_2nKS). The curved path represents the Kuroshio path. The top row **(A, B)** is $Shear_H$, and the bottom row **(C, D)** is $Shear_V$. The left column **(A, C)** gives the with-Kuroshio case (M_2KS), and the right column **(B, D)** shows the without-Kuroshio case (M_2nKS). Gray contours indicate the isobaths.

conversion rate is roughly 30%. This number is close to the estimate by Kerry et al. (2013) of 33%, but it is slightly lower than that from Alford et al. (2011). The disagreement may come from the stratification conditions, mesh resolution, terrain smoothing method, and the choice of subgrid parameterization schemes.

4.4.2 Energy fluxes

The content in Table 3 indicates that the response of the total conversion rate and local dissipation rate to the Kuroshio is small. However, the Kuroshio significantly affects the meridional energy fluxes radiating out of the LS. For example, the southward energy fluxes in M_2nKS is over twice that M_2KS, the same holding for M_2nKW over M_2KW as well as K_1KW over K_1nKW. Thus, removing the Kuroshio increases the southward energy fluxes in these cases. As to K_1KS and K_1nKS, removing the Kuroshio significantly decreases the northward energy fluxes going out of the LS. Compared to the K_1 experiments, both the westward and eastward energy fluxes in the M_2 experiments are larger (Table 3).

The internal tides propagating into the SCS are larger than that radiating into the Pacific Ocean. The energy flux patterns in Figure 6 show that the northward propagating internal tides are stronger in the with-Kuroshio case than those in the without-Kuroshio case. However, the direction of propagation to the Pacific differs little between the two cases. In other words, the propagation direction to the Pacific is less sensitive to the existence of the Kuroshio than that into the SCS.

4.4.3 Total conversion rate

We now consider how the Kuroshio influences the total energy conversion rate within the LS. Table 3 shows that the magnitude of $Tran^{bc}$ in the with-Kuroshio case exceeds that of the without-Kuroshio case. For the with-Kuroshio case, $Tran^{bc}$ accounts for about 2-6% of the total conversion rate, but only about 1-2% for the without-Kuroshio case. For the M_2 experiments, the total conversion rate for the with-Kuroshio case is smaller than that without the Kuroshio. For the K_1 experiments, however, the ratio of the total conversion rate between the with- and without-Kuroshio cases is nearly the same. This means that the K_1 case is less sensitive to the background condition than that for the M_2 case. For both with- and without-Kuroshio cases, the total conversion rate within the LS for the M_2 experiments are larger than those for the K_1 experiments. In general, the response of the total conversion rate to the Kuroshio is less than its seasonal variation.

We now examine the factors regulating the total conversion rate using Eqs. (5) and (6). As the nonlinear conversion rate from Eq. (5) is negligibly small, the total conversion rate *Conv* roughly equals *Conv_linear*. According Eq. (6), *Conv_linear* is determined by three factors: the bottom pressure perturbation $p'_{\theta A}(-H)$, the vertical component of the barotropic flow $w_{bt\theta A}(-H)$ or w_{bt} for short, and

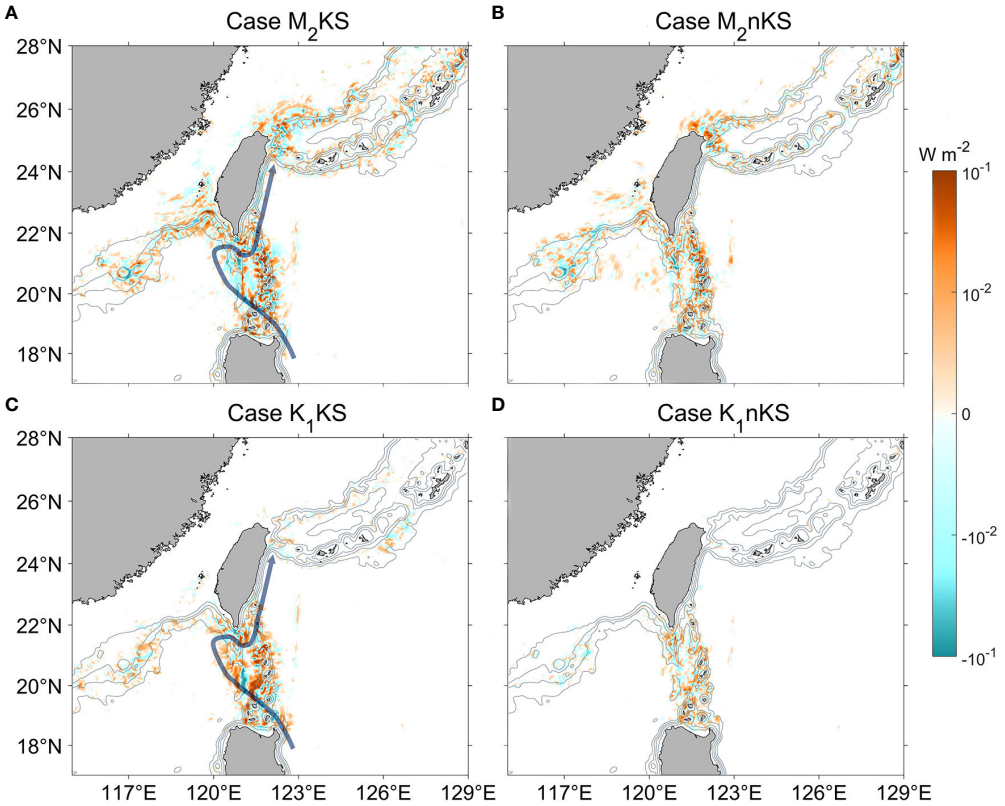

FIGURE 9
Distribution of Ibt-bc (color, W m-2) for four summer cases. **(A)** M2KS. Gray contours indicate isobaths. The blue line shows the Kuroshio path during the simulation period. **(B)** M2nKS. **(C)** K1KS. **(D)** K1nKS. Left column is with-Kuroshio, right without.

the phase difference $\cos(\theta_p'\text{-}\theta_{Wbt})$ between w_{bt} and the pressure perturbation, or just 'phase difference'. The role of these variables in regulating internal tides has been previously discussed. For example, Kelly and Nash (2010) showed that the remotely generated internal tides can increase or decrease the local generation of internal tides, depending on the phase of the barotropic tides and the bottom pressure perturbation induced by the internal tides. Kerry et al. (2013) later found that in the LS and

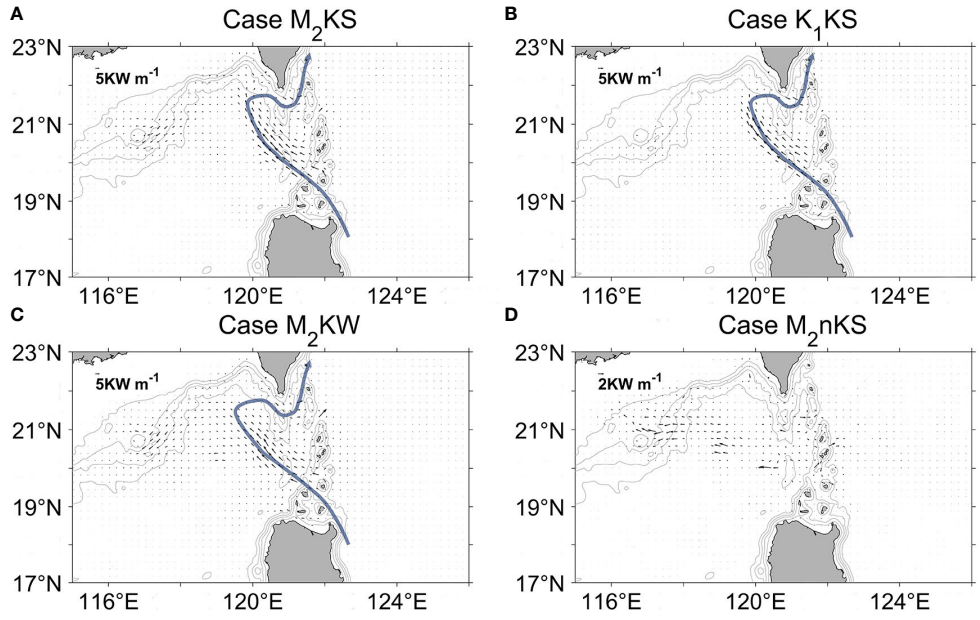

FIGURE 10
Spatial distribution of F_{non}^{bc} (vectors) in the LS for four cases. **(A)** M_2KS (summer, with-Kuroshio). Gray contours indicate isobaths. The curved path represents the Kuroshio path. **(B)** K_1KS (summer, with-Kuroshio). **(C)** M_2KW (winter, with-Kuroshio). **(D)** M_2nKS (summer, without-Kuroshio).

TABLE 3 The internal tide energy budget in the LS region (gray box, Figure 6A).

Case	$Tran^{bc}$ (GW)	Total conversion rate(GW)	Westward energy flux(GW)	Eastward energy flux (GW)	Northward energy flux(GW)	Southward energy flux(GW)	Percentage of local dissipation rate
M_2KS	-0.90	17.05	6.25	4.93	0.05	0.11	28.2%
M_2nKS	0.29	17.56	6.41	5.16	0.06	0.25	34.0%
M_2KW	0.71	17.59	7.30	5.30	0.15	0.08	31.1%
M_2nKW	0.24	18.02	6.82	5.50	0.14	0.21	31.0%
K_1KS	0.31	10.60	4.51	2.87	0.31	0.04	30.0%
K_1nKS	0.10	10.55	3.93	3.07	0.04	0.08	33.5%
K_1KW	-0.30	11.18	4.64	3.04	0.13	0.03	27.2%
K_1nKW	0.17	11.15	4.56	3.08	0.12	0.07	31.3%

Total conversion rate is that from barotropic to baroclinic tidal flow [Eq. (5)]. Westward, eastward, northward, and southward fluxes are energy fluxes going outward through the four boundaries of the LS region. The rightmost column shows the ration between the local dissipation rate and the total conversion rate.

Mariana Island Arc, distant internal tides affect the conversion between barotropic and baroclinic tides by varying the amplitude of the bottom pressure disturbances in a complex pattern of spatial variability.

To evaluate the relative importance of the three factors in regulating the conversion rate response to the Kuroshio, we first examine the ratio of the three factors for the with-to-without Kuroshio cases (e.g., K_1KS vs. K_1nKS, M_2KW vs. M_2nKW). In Table 4, we show the Pearson correlation coefficients between the conversion rate ratio and the pressure perturbation ratio (the second column). The same is shown for the other two factors in the next two columns.

In both winter and summer, and for both M_2 and K_1, the Pearson correlation coefficient between the conversion rate ratio and the bottom pressure perturbation ratio is approximately 0.7, whereas the correlation coefficient for the phase difference is smaller, at about 0.5. The correlation between the conversion rate ratio and w_{bt} is the smallest, ranging from 0.26 to 0.30. Nevertheless, all the correlation coefficients from Table 4 are significant at the 95% confidence level, indicating that the three factors from Eq. (6) jointly determine the conversion ratio between the with- and without-Kuroshio cases. However, the effect of both the phase difference and the term w_{bt} on the conversion rate ratio is smaller than that of the bottom pressure perturbation. This perturbation may result from tide-topography interactions (Simmons et al., 2004). In addition, the isopycnal displacement caused by the warmer and saltier Kuroshio flow is another factor impacting the pressure perturbation (Jan et al., 2012). Our results suggest that the Kuroshio significantly modulates the tide-topography interaction process at the ocean bottom.

5 Summary and conclusion

This study used high-resolution ocean numerical simulations to evaluate the effects of the Kuroshio on the generation, propagation, and energy budget of internal tides in the LS. To detect the Kuroshio effect, we compare model results between two stratification scenarios: one adopts realistic stratification as the initial condition, the other with uniform stratification. The uniform stratification case was introduced to effectively remove the background flow shear and thus remove the Kuroshio intrusion effect. Then, we considered winter and summer experiments separately. To avoid the nonlinear interaction between multiple tidal components, each simulation case shown in Table 1 is only driven by one of two tidal forcings (M_2 or K_1) at the open boundaries.

For cases with- or without-Kuroshio, the dominant generation site of internal tides was always the LS region. However, there were significant differences between the with- and without-Kuroshio cases in the energy flux pattern and thus the main propagating direction of internal tides. Specifically, with the Kuroshio, northwestward internal tides occurred for both M_2 and K_1 cases on the SCS side. The width and radiation direction of these tides resemble those of the Kuroshio flow. In the case without the Kuroshio, however, the dominant energy radiation direction on the SCS side was approximately zonal. In addition, for both M_2 and K_1 tides, the with-Kuroshio cases show greater seasonal variations in the direction of tidal energy flux in the LS than in the without-Kuroshio cases, especially for the northwestward internal tides under the influence of the Kuroshio. Besides the radiation direction of internal tides, the Kuroshio also greatly influenced the three nonlinear terms ($I_{m\text{-}bc}$, $I_{bt\text{-}bc}$, and F_{non}^{bc}), associated with the baroclinic tide energy budget. Among these

TABLE 4 Pearson correlation coefficients between the conversion rate ratio and the three factors listed in the column headings.

Case	Pressure perturbation	Phase difference	w_{bt}
M_2 summer (M_2KS/M_2nKS)	0.74 ± 0.02	0.51 ± 0.02	0.26 ± 0.02
M_2 winter (M_2KW/M_2nKW)	0.69 ± 0.01	0.52 ± 0.02	0.30 ± 0.02
K_1 summer (K_1KS/K_1nKS)	0.72 ± 0.02	0.54 ± 0.02	0.27 ± 0.03
K_1 winter (K_1KW/K_1nKW)	0.69 ± 0.01	0.49 ± 0.02	0.29 ± 0.03

Here 'ratio' means a proportion between the with- and without cases for a given factor. Error bars represent 95% confidence intervals.

terms, $I_{bt\text{-}bc}$ was negligible in the with-Kuroshio case. However, in the without-Kuroshio case, all three nonlinear terms were negligible, making the baroclinic tide energy equation roughly linear. Specifically, the magnitudes of $I_{m\text{-}bc}$ and $I_{bt\text{-}bc}$ in the with-Kuroshio case were larger than those in the without-Kuroshio case, especially in the southern part of the Hengchun and Lanyu ridges, where the Kuroshio passes. In the without-Kuroshio case, the background flow shear was weak, leading to a weak energy exchange rate between the background state and internal tides (small magnitude of $I_{m\text{-}bc}$). In addition, we argued that weak background flow shear in the without-Kuroshio case probably arises from a weak background flow passing the topography, which would lead to weak baroclinic internal tides and thus a small energy exchange rate between barotropic and baroclinic tides (small magnitude of $I_{bt\text{-}bc}$). The absence of the Kuroshio also weakens the energy flux due to the advection of internal tide energy by background circulation (F_{non}^{bc}). The radiation direction of F_{non}^{bc} in the with-Kuroshio case resembles the Kuroshio flow direction, indicating the important role of the Kuroshio in shaping F_{non}^{bc}. A detailed energy budget diagnosis within the LS further revealed that the Kuroshio greatly regulates the meridional energy fluxes radiating out of the LS.

Based on our experimental results and findings, this work can be a useful reference for future research about internal tides and circulation in the LS and SCS region. However, our study also has limitations. For example, the seasonal variation of the Kuroshio intrusion still has biases. Specifically, in summer and winter, the flow of the Kuroshio eastward out of the SCS is relatively small, while the flow northward to the Taiwan Strait is relatively large. At 120.75°E meridional section, the net LST in summer and winter are respectively -6.21 and -6.75 Sv. Among them, compared with previous models and observations (e.g., Lan et al., 2004 ; Wang et al., 2009; Hsin et al., 2012), our simulations show a much larger LST in summer and a slightly larger LST in winter. In particular, the Kuroshio intrusion variability can be influenced by the upstream Kuroshio and the wind forcing (Hsin et al., 2012; Wu and Hsin, 2012). Therefore, the intrusion biases might be reduced if one includes air-sea forcing or uses time-dependent boundary conditions instead of the 10-year monthly-mean ones used here. The biases might also be reduced if one uses an ultra-high-resolution model or improves the subgrid-scale mixing parameterization schemes. Nevertheless, even with more realistic Kuroshio intrusion runs, our key findings about the Kuroshio effect on internal tides should hold.

Challenges remain for future work. We used idealized experiments to focus on fundamental dynamics. For example, the initial and boundary conditions are based on the 10-year monthly-mean fields. Yet, the Kuroshio intrusions into the SCS have three types of paths: leaping, leaking, and looping. Further numerical studies are needed to assess how the internal tides respond to different Kuroshio intrusion paths. Future work should also consider more tidal constituents and interactions between tidal components. In addition, it would be worthwhile to revisit this problem with ultra-high-resolution models or improved subgrid-mixing parameterization schemes.

Data availability statement

The raw data supporting the conclusions of this article will be made available by the authors, without undue reservation.

Author contributions

ZD and RC conceived and designed the study. GT conducted the numerical experiments and wrote the original draft. All authors contributed to the article and approved the submitted version.

Funding

This work was supported by: Guangxi Key Laboratory of Marine Environment Change and Disaster in Beibu Gulf, Beibu Gulf University (No. 2021KF03); National Natural Science Foundation of China (No. 42176020 and No. 42076007); National Key Research and Development Program (2022YFC3105002).

Conflict of interest

The authors declare that the research was conducted in the absence of any commercial or financial relationships that could be construed as a potential conflict of interest.

Publisher's note

Supplementary material

The Supplementary Material for this article can be found online at: https://www.frontiersin.org/articles/10.3389/fmars.2022.995601/full#supplementary-material

References

Alford, M. H., MacKinnon, J. A., Nash, J. D., Simmons, H., Pickering, A., Klymak, J. M., et al. (2011). Energy flux and dissipation in Luzon strait: Two tales of two ridges. *J. Phys. Oceanography* 41, 2211–2222. doi: 10.1175/JPO-D-17-0209.1

Alford, M. H., Peacock, T., MacKinnon, J. A., Nash, J. D., Buijsman, M. C., Centurioni, L. R., et al. (2015). The formation and fate of internal waves in the south China Sea. *Nature* 521, 65–69. doi: 10.1038/nature14399

Buijsman, M. C., Klymak, J. M., Legg, S., Alford, M. H., Farmer, D., MacKinnon, J. A., et al. (2014). Three-dimensional double-ridge internal tide resonance in Luzon strait. *J. Phys. Oceanography* 44, 850–869. doi: 10.1175/JPO-D-13-024.1

Cambon, G., Marchesiello, P., Penven, P., Debreu, L., Benshila, R., and Jullien, S. (2018) *CROCO user guide*. Available at: http://www.croco-ocean.org/documentation/roms_agrif-user-guide/ (Accessed 9 March 2018).

Cao, A., Guo, Z., Song, J., Lv, X., He, H., and Fan, W. (2018). Near-inertial waves and their underlying mechanisms based on the south China Sea internal wave experiment 2010–2011). *J. Geophysical Research: Oceans* 123, 5026–5040. doi: 10.1029/2018JC013753

Carter, G. S., Fringer, O. B., and Zaron, E. D. (2012). Regional models of internal tides. *Oceanography* 25, 56–65. doi: 10.5670/oceanog.2012.42

Centurioni, L. R., Niiler, P. P., and Lee, D. K. (2004). Observations of inflow of Philippine Sea surface water into the south China Sea through the Luzon strait. *J. Phys. Oceanography* 34, 113–121. doi: 10.1175/1520-0485(2004)034<0113:OOIOPS>2.0.CO;2

Chang, H., Xu, Z., Yin, B., Hou, Y., Liu, Y., Li, D., et al. (2019). Generation and propagation of M2 internal tides modulated by the kuroshio northeast of Taiwan. *J. Geophysical Research: Oceans* 124, 2728–2749. doi: 10.1029/2018JC014228

Cummins, P. F., and Oey, L. Y. (1997). Simulation of barotropic and baroclinic tides off northern British Columbia. *J. Phys. oceanography* 27, 762–781. doi: 10.1175/1520-0485(1997)027<0762:SOBABT>2.0.CO;2

Duda, T. F., Lynch, J. F., Irish, J. D., Beardsley, R. C., Ramp, S. R., Chiu, C. S., et al. (2004). Internal tide and nonlinear internal wave behavior at the continental slope in the northern south China Sea. *IEEE J. Oceanic Eng.* 29, 1105–1130. doi: 10.1109/JOE.2004.836998

Egbert, G. D., and Erofeeva, S. Y. (2002). Efficient inverse modeling of barotropic ocean tides. *J. Atmospheric Oceanic Technol.* 19, 183–204. doi: 10.1175/1520-0426(2002)019<0183:EIMOBO>2.0.CO;2

Egbert, G. D., and Ray, R. D. (2000). Significant dissipation of tidal energy in the deep ocean inferred from satellite altimeter data. *Nature* 405, 775–778. doi: 10.1038/35015531

Flather, R. A., and RA, F. (1976). A tidal model of the north-west European continental shelf. *Mem. Soc R. Sci. Liege* 6, 141–164.

Guo, Z., Cao, A., Lv, X., and Song, J. (2020a). Impact of multiple tidal forcing on the simulation of the M2 internal tides in the northern south China Sea. *Ocean Dynamics* 70, 187–198. doi: 10.1007/s10236-019-01324-9

Guo, Z., Cao, A., Lv, X., and Song, J. (2020b). Impacts of stratification variation on the M2 internal tide generation in Luzon strait. *Atmosphere-Ocean* 58, 206–218. doi: 10.1080/07055900.2020.1767534

Guo, C., and Chen, X. (2014). A review of internal solitary wave dynamics in the northern south China Sea. *Prog. Oceanography* 121, 7–23. doi: 10.1016/j.pocean.2013.04.002

Hall, R. A., and Carter, G. S. (2011). Internal tides in Monterey submarine canyon. *J. Phys. Oceanography* 41, 186–204. doi: 10.1175/2010JPO4471.1

Hall, P., and Davies, A. M. (2007). A three-dimensional finite-element model of wind effects upon higher harmonics of the internal tide. *Ocean Dynamics* 57 (4), 305–323. doi: 10.1007/s10236-007-0117-2

Hsin, Y. C., Wu, C. R., and Chao, S. Y. (2012). An updated examination of the Luzon strait transport. *J. Geophysical Research: Oceans* 117, C03022. doi: 10.1029/2011JC007714

Jan, S., Chern, C. S., Wang, J., and Chao, S. Y. (2007). Generation of diurnal K1 internal tide in the Luzon strait and its influence on surface tide in the south China Sea. *J. Geophysical Research: Oceans* 112, C06019. doi: 10.1029/2006JC004003

Jan, S., Chern, C. S., Wang, J., and Chiou, M. D. (2012). Generation and propagation of baroclinic tides modified by the kuroshio in the Luzon strait. *J. Geophysical Research: Oceans* 117, C02019. doi: 10.1029/2011JC007229

Jan, S., Lien, R. C., and Ting, C. H. (2008). Numerical study of baroclinic tides in Luzon strait. *J. Oceanography* 64, 789–802. doi: 10.1007/s10872-008-0066-5

Johns, W. E., Lee, T. N., Zhang, D., Zantopp, R., Liu, C.-T., and Yang, Y. (2001). The kuroshio east of Taiwan: Moored transport observations from the WOCE PCM-1 array. *J. Phys. Oceanography* 31 (4), 1031–1053. doi: 10.1175/1520-0485(2001)031<1031:tkeotm>2.0.co;2

Kelly, S. M., and Nash, J. D. (2010). Internal-tide generation and destruction by shoaling internal tides. *Geophysical Res. Lett.* 37, L23611. doi: 10.1029/2010GL045598

Kerry, C. G., Powell, B. S., and Carter, G. S. (2013). Effects of remote generation sites on model estimates of M2 internal tides in the Philippine Sea. *J. Phys. Oceanography* 43, 187–204. doi: 10.1175/JPO-D-12-081.1

Kerry, C. G., Powell, B. S., and Carter, G. S. (2014). The impact of subtidal circulation on internal tide generation and propagation in the Philippine Sea. *J. Phys. oceanography* 44, 1386–1405. doi: 10.1175/JPO-D-13-0142.1

Kitade, Y., and Matsuyama, M. (2000). Coastal-trapped waves with several-day period caused by wind along the southeast coast of Honshu, Japan. *J. oceanography* 56 (6), 727–744. doi: 10.1023/A:1011186018956

Klymak, J. M., Legg, S., Alford, M. H., Buijsman, M., Pinkel, R., and Nash, J. D. (2012). The direct breaking of internal waves at steep topography. *Oceanography* 25, 150–159. doi: 10.5670/oceanog.2012.50

Lamb, K. G. (1994). Numerical experiments of internal wave generation by strong tidal flow across a finite amplitude bank edge. *J. Geophysical Research: Oceans* 99, 843–864. doi: 10.1029/93JC02514

Lan, J., Bao, X., and Gao, G. (2004). Optimal estimation of zonal velocity and transport through Luzon Strait using variational data assimilation technique. *Chin. J.Oceanology Limnology* 22, 335–339. doi: 10.1007/bf02843626

Large, W. G., McWilliams, J. C., and Doney, S. C. (1994). Oceanic vertical mixing: A review and a model with a nonlocal boundary layer parameterization. *Rev. geophysics* 32, 363–403. doi: 10.1029/94RG01872

Liu, J., He, Y., Wang, D., Liu, T., and Cai, S. (2015). Observed enhanced internal tides in winter near the Luzon strait. *J. Geophysical Research: Oceans* 120, 6637–6652. doi: 10.1002/2015JC011131

Liu, K., Sun, J., Guo, C., Yang, Y., Yu, W., and Wei, Z. (2019). Seasonal and spatial variations of the M2 internal tide in the yellow Sea. *J. Geophysical Research: Oceans* 124, 1115–1138. doi: 10.1029/2018JC014819

Liu, K., Xu, Z., and Yin, B. (2017). Three-dimensional numerical simulation of internal tides that radiated from the Luzon strait into the Western pacific. *Chin. J. Oceanology Limnology* 35, 1275–1286. doi: 10.1007/s00343-017-5376-2

Li, Q., Wang, B., Chen, X., Chen, X., and Park, J. H. (2016). Variability of nonlinear internal waves in the south China Sea affected by the kuroshio and mesoscale eddies. *J. Geophysical Research: Oceans* 121, 2098–2118. doi: 10.1002/2015JC011134

Ma, B. B., Lien, R. C., and Ko, D. S. (2013). The variability of internal tides in the northern south China Sea. *J. Oceanography* 69, 619–630. doi: 10.1007/s10872-013-0198-0

Masunaga, E., Uchiyama, Y., Suzue, Y., and Yamazaki, H. (2018). Dynamics of internal tides over a shallow ridge investigated with a high-resolution downscaling regional ocean model. *Geophysical Res. Lett.* 45, 3550–3558. doi: 10.1002/2017GL076916

Masunaga, E., Uchiyama, Y., and Yamazaki, H. (2019). Strong internal waves generated by the interaction of the kuroshio and tides over a shallow ridge. *J. Phys. Oceanography* 49, 2917–2934. doi: 10.1175/JPO-D-18-0238.1

Munk, W., and Wunsch, C. (1998). Abyssal recipes II: Energetics of tidal and wind mixing. *Deep Sea Res. Part I: Oceanographic Res. Papers* 45, 1977–2010. doi: 10.1016/S0967-0637(98)00070-3

Nan, F., Xue, H., Chai, F., Shi, L., Shi, M., and Guo, P. (2011). Identification of different types of kuroshio intrusion into the south China Sea. *Ocean Dynamics* 61, 1291–1304. doi: 10.1007/s10236-011-0426-3

Nan, F., Xue, H., and Yu, F. (2015). Kuroshio intrusion into the south China Sea: A review. *Prog. Oceanography* 137, 314–333. doi: 10.1016/j.pocean.2014.05.012

Niwa, Y., and Hibiya, T. (2004). Three-dimensional numerical simulation of M2 internal tides in the East China Sea. *J. Geophysical Research: Oceans* 109, C04027. doi: 10.1029/2003JC001923

Osborne, J. J., Kurapov, A. L., Egbert, G. D., and Kosro, P. M. (2011). Spatial and temporal variability of the M2 internal tide generation and propagation on the Oregon shelf. *J. Phys. Oceanography* 41, 2037–2062. doi: 10.1175/JPO-D-11-02.1

Pawlowicz, R., Beardsley, B., and Lentz, S. (2002). Classical tidal harmonic analysis including error estimates in MATLAB using T_TIDE. *Comput. Geosciences* 28, 929–937. doi: 10.1016/s0098-3004(02)00013-4

Powell, B. S., Janeković, I., Carter, G. S., and Merrifield, M. A. (2012). Sensitivity of internal tide generation in Hawaii. *Geophysical Res. Lett.* 39, L10606. doi: 10.1029/2012GL051724

Rainville, L., Johnston, T. S., Carter, G. S., Merrifield, M. A., Pinkel, R., Worcester, P. F., et al. (2010). Interference pattern and propagation of the M2 internal tide south of the Hawaiian ridge. *J. Phys. oceanography* 40, 311–325. doi: 10.1175/2009JPO4256.1

Ramp, S. R., Tang, T. Y., Duda, T. F., Lynch, J. F., Liu, A. K., Chiu, C. S., et al. (2004). Internal solitons in the northeastern south China sea. part I: Sources and deep water propagation. *IEEE J. Oceanic Eng.* 29, 1157–1181. doi: 10.1109/JOE.2004.840839

Shaw, P. T. (1991). The seasonal variation of the intrusion of the Philippine Sea water into the south China Sea. *J. Geophysical Research: Oceans* 96, 821–827. doi: 10.1029/90JC02367

Simmons, H. L., Jayne, S. R., Laurent, L. C. S., and Weaver, A. J. (2004). Tidally driven mixing in a numerical model of the ocean general circulation. *Ocean Model.* 6, 245–263. doi: 10.1016/S1463-5003(03)00011-8

Song, P., and Chen, X. (2020). Investigation of the internal tides in the Northwest pacific ocean considering the background circulation and stratification. *J. Phys. Oceanography* 50, 3165–3188. doi: 10.1175/JPO-D-19-0177.1

St. Laurent, L. (2008). Turbulent dissipation on the margins of the south China Sea. *Geophysical Res. Lett.* 35, L23615. doi: 10.1029/2008GL035520

Varlamov, S. M., Guo, X., Miyama, T., Ichikawa, K., Waseda, T., and Miyazawa, Y. (2015). M2 baroclinic tide variability modulated by the ocean circulation south of Japan. *J. Geophysical Research: Oceans* 120, 3681–3710. doi: 10.1002/2015JC010739

Vitousek, S., and Fringer, O. B. (2011). Physical vs. numerical dispersion in nonhydrostatic ocean modeling. *Ocean Model.* 40, 72–86. doi: 10.1016/j.ocemod.2011.07.002

Vlasenko, V., Stashchuk, N., and Hutter, K. (2005). *Baroclinic tides: theoretical modeling and observational evidence* (U. K.: Cambridge University Press).

Wang, Q., Cui, H., Zhang, S., and Hu, D. (2009). Water transports through the four main straits around the south China Sea. *Chin. J. Oceanology Limnology* 27 (2), 229–236. doi: 10.1007/s00343-009-9142-y

Wang, J., Ingram, R. G., and Mysak, L. A. (1991). Variability of internal tides in the laurentian channel. *J. Geophysical Research: Oceans* 96, 16859–16875. doi: 10.1029/91JC01580

Wang, Y., Xu, Z., Yin, B., Hou, Y., and Chang, H. (2018). Long-range radiation and interference pattern of multisource M2 internal tides in the Philippine Sea. *J. Geophysical Research: Oceans* 123, 5091–5112. doi: 10.1029/2018JC013910

Wu, C. R., and Chiang, T. L. (2007). Mesoscale eddies in the northern south China Sea. *Deep Sea Res. Part II: Topical Stud. Oceanography* 54, 1575–1588. doi: 10.1016/j.dsr2.2007.05.008

Wu, C. R., and Hsin, Y. C. (2012). The forcing mechanism leading to the kuroshio intrusion into the south China Sea. *J. Geophysical Research: Oceans* 117, C07015. doi: 10.1029/2012JC007968

Wyrtki, K. (1961). Scientific results of marine investigations of the south China Sea and the gulf of Thailand 1959-1961. *NAGA Rep.* 2, 195.

Xie, X., Shang, X., and Chen, G. (2010). Nonlinear interactions among internal tidal waves in the northeastern south China Sea. *Chin. J. Oceanology Limnology* 28, 996–1001. doi: 10.1007/s00343-010-9064-8

Xu, Z., Liu, K., Yin, B., Zhao, Z., Wang, Y., and Li, Q. (2016). Long-range propagation and associated variability of internal tides in the south China Sea. *J. Geophysical Research: Oceans* 121, 8268–8286. doi: 10.1002/2016JC012105

Yin, Y., Lin, X., He, R., and Hou, Y. (2017). Impact of mesoscale eddies on kuroshio intrusion variability northeast of Taiwan. *J. Geophysical Research: Oceans* 122, 3021–3040. doi: 10.1002/2016JC012263

Zaron, E. D., and Egbert, G. D. (2014). Time-variable refraction of the internal tide at the Hawaiian ridge. *J. Phys. oceanography* 44 (2), 538–557. doi: 10.1175/JPO-D-12-0238.1

Zhang, D., Lee, T. N., Johns, W. E., Liu, C. T., and Zantopp, R. (2001). The kuroshio east of Taiwan: Modes of variability and relationship to interior ocean mesoscale eddies. *J. Phys. Oceanography* 31 (4), 1054–1074. doi: 10.1175/1520-0485(2001)031<1054:TKEOTM>2.0.CO;2

Zhao, Z. (2014). Internal tide radiation from the Luzon strait. *J. Geophysical Research: Oceans* 119, 5434–5448. doi: 10.1002/2014JC010014

Zilberman, N. V., Becker, J. M., Merrifield, M. A., and Carter, G. S. (2009). Model estimates of M2 internal tide generation over mid-Atlantic ridge topography. *J. Phys. Oceanography* 39, 2635–2651. doi: 10.1175/2008JPO4136.1

Zilberman, N. V., Merrifield, M. A., Carter, G. S., Luther, D. S., Levine, M. D., and Boyd, T. J. (2011). Incoherent nature of M2 internal tides at the Hawaiian ridge. *J. Phys. Oceanography* 41, 2021–2036. doi: 10.1175/JPO-D-10-05009.1

Zu, T., Gan, J., and Erofeeva, S. Y. (2008). Numerical study of the tide and tidal dynamics in the South China Sea *Deep Sea Res.* Part I 55, 137–154. doi: 10.1016/j.dsr.2007.10.007

frontiers | Frontiers in Marine Science

TYPE Original Research
PUBLISHED 09 February 2023
DOI 10.3389/fmars.2022.1085340

OPEN ACCESS

EDITED BY
Shi-Di Huang,
Southern University of Science and Technology, China

REVIEWED BY
Lu Li,
Southern University of Science and Technology, China
Germán Rodríguez,
University of Las Palmas de Gran Canaria, Spain

*CORRESPONDENCE
Yongxiang Huang
yongxianghuang@gmail.com;
yongxianghuang@xmu.edu.cn

SPECIALTY SECTION
This article was submitted to Physical Oceanography, a section of the journal Frontiers in Marine Science

RECEIVED 31 October 2022
ACCEPTED 27 December 2022
PUBLISHED 09 February 2023

CITATION
Gao Y, Schmitt FG, Hu J and Huang Y (2023) Probability-based wind-wave relation.
Front. Mar. Sci. 9:1085340.
doi: 10.3389/fmars.2022.1085340

Probability-based wind-wave relation

Yang Gao[1,2], François G. Schmitt[2], Jianyu Hu[1] and Yongxiang Huang[1,3]*

[1]State Key Laboratory of Marine Environmental Science and College of Ocean and Earth Sciences, Xiamen University, Xiamen, China, [2]CNRS, Univ. Lille, Univ. Littoral Côte d'Opale, UMR 8187, LOG, Laboratoire d'Océanologie et de Géosciences, Wimereux, France, [3]Fujian Engineering Research Center for Ocean Remote Sensing Big Data, Xiamen University, Xiamen, China

In a fully developed sea, the significant wave height (*Hs*) and wind speed (U_{10}) are conventionally related to a pure quadratic equation. This relation is often violated, since in the field the measured local *Hs* is often contaminated by the swell, which is propagated from distant places. Therefore, a swell partition is required before the establishment of the wind-wave relation. The Spectra Energy Partition (SEP) is regarded as the best way to isolate the swell and the wind wave relation: it is based on the identification of a separation frequency in the ocean wave spectrum. However, for most field observations, the wave spectra information is unavailable, and thus the SEP is inapplicable. This work proposes a probability-based algorithm to identify the averaged swell without knowing the wave spectrum *a priori*. The local wind-wave relation is established by either a linear or an energy-conserved decomposition. We also find that the local wind-wave relation is a power-law when the wind speed U_{10} is above 4 m/s. The proposed method is first validated by applying the SEP method to buoy collected wave spectra data. The global pattern of the swell and the local wind waves is retrieved by applying the proposed method to a 17-year wind and wave database from the JASON satellite. Strong seasonal and spatial variations are obtained. Finally, a prediction model based on the empirical wind-wave relation is shown to successfully retrieve the wave field when the wind field is available.

KEYWORDS

wind-wave relation, swell separation, wave prediction, power-law scaling, spectra energy partition

1 Introduction

Ocean waves and the wind in the lower marine atmospheric boundary layer play crucial roles in the air-sea interactions and are both vital for the control of the weather and of the climate system. One of the most important topics in air-sea interactions is the relation between wind and waves, which dominates other processes, such as momentum and heat fluxes, or mass exchanges (Csanady, 2001; Holthuijsen, 2007; Babanin, 2011). Therefore, the relation between wind and waves has been extensively investigated (Cavaleri et al., 2018). For example, the first general relationship between wind and waves was quantified by Rossby and Montgomery (1935), i.e., $W_H = 0.3W_S^2 g^{-1}$, where W_H, g, and W_S are the wave height,

acceleration of gravity (e.g., 9.81N·kg^{-1}), and ocean surface wind speed, respectively. This relation was further studied by Bretschneider (1952). In the same year, Pierson and Marks (1952) performed a spectral analysis of the wave data, considering frequencies (or wavenumbers), the direction and height of the waves. After that, spectral analysis has been widely used to study the wind-wave relation, using data from field observations, remote sensing, laboratory, and numerical experiments (Wen, 1960; Pierson and Moskowitz, 1964; Wu, 1968; Hasselmann et al., 1973; Carter, 1982; Zhang et al., 2009; Rusu et al., 2014; Gao et al., 2021).

To establish the wind-wave relation, one often requires simultaneous observations of the wind speed (U_{10}) at 10-meter above the sea surface and the significant wave height (Hs). The latter quantity is traditionally defined as the mean wave height of the highest third of the waves. Conventionally, U_{10} can be locally recorded with an anemometer, or remotely sensed by light detection and ranging (LiDAR), sound detection and ranging (SoDAR), synthetic aperture radar (SAR), altimeter, or scatterometer, to name a few methods. On the contrary, there are only a very few observational approaches for Hs. Hs has been retrieved using buoy accelerometer wave gauges for a long time, which are not available in most open oceans. Nowadays, Hs is usually defined as four times the standard deviation of the ocean surface elevation, or equivalently as four times the root-mean-square of the zeroth-order moment of the wave spectrum (Holthuijsen, 2007). Based on this definition, Hs can also be retrieved using altimeters. However, only the nadir observation (downward-facing viewing by the satellite) can be used, which leads to sparse spatial sampling as compared to the U_{10} field observations performed by scatterometers (Hauser et al., 2020). Thus, the U_{10} field information is more accessible than the observation of Hs (Villas Bôas et al., 2019).

The wave information is important not only for the safety of coastal engineering systems (Faltinsen, 1990; Tucker and Pitt, 2001), but also in general for the knowledge of air-sea interactions (Cavaleri et al., 2018). With the establishment of a wind-wave relationship, Hs can be obtained empirically from U_{10}. In the pioneering work by Pierson and Moskowitz (1964), the so-called Pierson-Moskowitz spectrum (hereinafter PM64) was proposed based on 420 selected wave measurements in the northern Atlantic Ocean. Assuming that the wind blows steadily for a long time over a large area, the waves would be in an equilibrium state, called a fully developed sea (FDS). This results in a wave frequency spectra of the form $E(f) = C_0 g^2 (2\pi)^{-4} f^{-5} e^{-\frac{5}{4}(\frac{f_m}{f})^4}$, where C_0=8.1×10^{-3} is the Phillips constant (supposing C_0 is not affected by external circumstances), f is the frequency, and f_m is the frequency at the maximum of the spectrum, which can be deduced from U_{10} with the experimental relation f_m=0.855g/(2πU_{10}). Finally, the relationship between $\bar{Hs}$ and U_{10} is derived as,

$$\bar{Hs}(U_{10}) \simeq 0.0246 U_{10}^2 \tag{1}$$

Note that the notation $\bar{Hs}(U_{10})$ is used here to emphasize the fact that the significant wave height in this relation is considered as an average value at a given wind speed. Since then, this relation has been widely adopted and employed in the offshore engineering community (Goda, 1997; Liu et al., 2017). We note that PM64 is an idealized model, assuming that there is an FDS without the existence of swell waves. Swell waves are the so-called "old wind waves" that have been generated elsewhere, at distant places. They have a relatively long wave period and wavelength, and can travel thousands of kilometers (Jones and Toba 2001). As a consequence, the PM64 model might be less reliable in shallow waters, coastal regions, or weak wind areas (Cavaleri et al., 2018).

An improved WAve Model (WAM) for wind speed ranging from 0 to 30 m/s was proposed by the WAMDI Group (1988). According to this model, the wind-wave relation for the FDS can be expressed as (Pierson, 1991; Chen et al., 2002),

$$\bar{Hs}(U_{10}) = \begin{cases} 1.614 \times 10^{-2} U_{10}^2, 0 \le U_{10} \le 7.5\text{m/s} \\ 10^{-2} U_{10}^2 + 8.134 \times 10^{-4} U_{10}^3, 7.5 < U_{10} \le 30\text{m/s} \end{cases} \tag{2}$$

It is also known as the third generation wave model, in which the energy balance equation with the nonlinear wave-wave interactions is solved. However, differences between the WAM model and observations have been reported by several authors (Romeiser, 1993; Gulev et al., 1998; Heimbach et al., 1998; Cavaleri et al., 2018).

For predicting $\bar{Hs}(U_{10})$ more precisely, the water depth has also been taken into account by Andreas and Wang (2007). In their work, the data in the northeast coast of the United States observed by buoys were fitted with a parameterization as,

$$\bar{Hs}(U_{10}) = \begin{cases} C(D), U_{10} \le 4\text{m/s} \\ a(D) U_{10}^2 + b(D), U_{10} > 4\text{m/s}, \end{cases} \tag{3}$$

where D is the local water depth; C is a constant determined by averaging all the wave heights for U_{10}≤4 m/s; a and b are fitting parameters. For low wind speed conditions, the existence of $\bar{Hs}$ is due to the swell; for high wind speed conditions, a quadratic formula is adopted to describe the relation between U_{10} and $\bar{Hs}(U_{10})$, with two coefficients which are related to the water depth, and used to adjust the fitting curves to the in situ collected data.

Another attempt of using the quadratic function to extract the empirical relationship between $\bar{Hs}(U_{10})$ and U_{10} was performed by Sugianto et al. (2017) with the data collected in the Java Sea. Slightly different from the one used by Andreas and Wang (2007), a linear term is introduced in their formula, but without considering the existence of swell waves, which is written as, i.e., $\bar{Hs}(U_{10}) = cU_{10}^2 + dU_{10}$, where c and d are determined by fitting the collected data.

In all the aforementioned models, either the swell waves are not well-considered, or the scaling exponent is fixed as 2, where the FDS hypothesis is involved. It is worth mentioning that, in several works, the wave frequency spectrum scales in the form $f^{-\zeta}$, with values of ζ varying from 3 to 6 for different situations (Toba, 1972; Donelan et al., 1985; Young and Verhagen, 1996; Young, 1998). Namely, a non-negligible statistical variation in the value of ζ in the spectral equilibrium range should be noticed. This is partially due to the presence of swell, currents, water depth, length of wind fetch, and other factors. For example, in deep water conditions, the value of ζ could be 4 instead of the 5 adopted in the PM64 model. By setting the fitting ranges for the wave spectra from 0.1 to 0.5 Hz (e.g., with the wave periods from 2 to 10 s), the scaling exponents ζ for the wave spectra collected by an offshore buoy (46086) provided by National Data Buoy Center (NDBC, archived at www.ndbc.noaa.gov) are extracted. The mean wave spectra is shown in Figure 1A, power-law features can be identified in the fitting range, the corresponding scaling exponent ζ is found to 3.4 as indicated by the dashed line. The

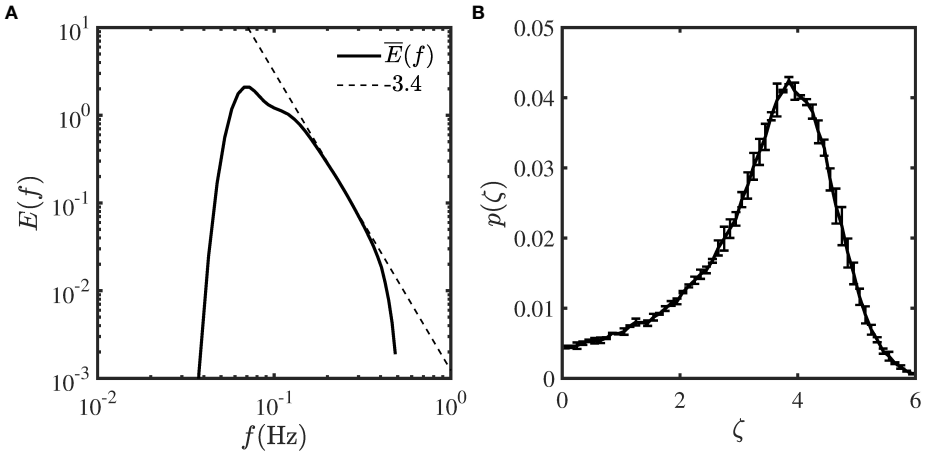

FIGURE 1
(A) Measured mean wave spectra collected by NDBC buoy 46086. **(B)** Measured PDF of scaling exponents in the wave spectra. The statistical difference between two subsets with equal sample size is indicated by error bar.

probability density function (PDF) for ζ is shown in Figure 1B, in which the statistical error (e.g., the statistical difference between two subsets with equal sample size) is also illustrated. It is clear that the values of ζ are mainly varying from 2 to 5, the most probable value is around 3.85, close to 4 mentioned above.

In such cases, the quadratic relation may not be valid (Resio et al., 1999). Indeed, if the f^{-5} spectrum in the PM64 theory is replaced by $f^{-\zeta}$, where the exponent ζ can take different values, one obtains,

$$E(f) = C_0 g^2 (2\pi)^{-4} f^{-\zeta} e^{-\frac{5}{4}(\frac{f_m}{f})^4} \tag{4}$$

According to the spectrum-based definition of *Hs*, *Hs* can be derived as,

$$Hs = 4\sqrt{\int_0^\infty E(f)df} \tag{5}$$

Note that f_m is also a cutoff frequency, e.g., $E(f)$ is vanishing small for $f \leq f_m$, thus,

$$Hs \simeq 4\sqrt{\int_{f_m}^\infty E(f)df} = \sqrt{\frac{C_0}{\zeta - 1}} \frac{g}{\pi^2} f_m^{-\frac{\zeta-1}{2}} \tag{6}$$

Finally, considering the relation between f_m and U_{10}, one obtains the wind wave relation as follows,

$$Hs(U_{10}) \simeq \sqrt{\frac{C_0}{\zeta - 1}} \frac{g}{\pi^2} \left(\frac{0.855g}{2\pi}\right)^{-\frac{\zeta-1}{2}} U_{10}^{\frac{\zeta-1}{2}} \tag{7}$$

Consequently, the scaling exponent β in the PM64-based wind-wave relation e.g.,

$$Hs(U_{10}) = \alpha U_{10}^{\beta} \tag{8}$$

can be related to ζ as $\beta=(\zeta-1)/2$. Using the observed range $3 \leq \zeta \leq 6$, one obtains β values in the range $1 \leq \beta \leq 2.5$, which corresponds to a generalization of the quadratic law.

The ocean surface gravity waves are mixed products of swell and wind waves. For a better understanding of the relation between wind and waves, a separation of the swell and wind-wave should be considered. There are few choices to make this identification, when additional information is available. For example, the swell can be distinguished by an observer's visual subjective criteria (Gulev et al., 1998; Gulev and Grigorieva, 2006), but the consistency and accuracy of such visual judgment results highly depend on the experience of the observer. Two objective approaches are also briefly discussed here. The first one is proposed in the framework of the wind-wave relation from the WAM model: Chen et al. (2002) defined the sea state of swell as the situations where the measured *Hs* is larger than the value predicted by this relation, while the wind waves correspond to the cases where the local measured *Hs* is smaller than the predicted value. However, as argued by Zheng et al. (2016), the "swell" defined by Chen et al. (2002) is still a sea state of mixed seas, thus the defined "swell" may be overestimated.

Another method which is supposed to be the best way to isolate swell from the wind-wave is the spectral partitioning (or Spectra Energy Partition, SEP) (Gerling, 1992; Hanson and Phillips, 2001; Wang and Hwang, 2001; Hanson and Jensen, 2004; Portilla et al., 2009; Hwang et al., 2012). As aforementioned, swell waves are conventionally thought as "old wind waves", while the properties of swell waves depend strongly on their propagation history, and a continuous evolution can be detected associated with the distance travelled, life stages such as young, mature, old, etc. Consequently, a progressively clearer frequency could be detected in the wave spectrum to separate wind waves and swell waves. The SEP analysis has strict requirements for the data observations to generate the high frequency directional wave energy spectrum $E(f,\theta)$, which is used to describe the distribution of sea surface elevation variance as a function of wave frequency and wave propagation direction (θ). Besides, the wind direction (φ) and the wave phase speed c_p are also needed for the decomposition process. Based on the fact that the wave ages for wind wave and swell are different, the two different wave components can be distinguished in the wave energy spectrum by identifying a separation frequency f_s. For the WAM model, this critical frequency is defined as the frequency corresponding to the wave phase speed $c=1.2\times28\times u_* \cos(\theta-\varphi)$, where the constant 1.2 is an

empirical tuning parameter, 28 corresponds to the peak phase speed c_p=28u_*, and u_* is the friction velocity. Finally, the wind wave and swell parts can be estimated by integrating over the high and low frequency parts of the spectrum, respectively. The 2D wave spectrum is not easily obtained; for instance it can be estimated using a High Frequency radar and a buoy equipped with a digital directional wave module. Thus, it is difficult to apply the SEP algorithm to large-scale field observations, due to the lack of wave spectrum information. Nevertheless, SEP is popularly used in wave model data analysis. For the sake of its simplicity, a 1D frequency wave spectrum was developed and can also be used to do the swell identification. There are different ways to define the separation frequency in a 1D wave spectrum (Portilla et al., 2009). For example, f_s can be derived from the peak frequency f_m of the PM64 spectrum as, f_s=0.8f_m (Earle, 1984 Quentin, 2002). Additionally, Wang and Gilhousen (1998) proposed the wave steepness algorithm to extract f_s with a 1D wave spectrum-based wave steepness function. It was further developed by Gilhousen and Hervey (2002) with the consideration of U_{10}. The SEP method has been used by many authors to study the regional or global view of swell and wind wave features (Semedo et al., 2015; Zheng et al., 2016; Portilla-Yandun, 2018). Portilla et al. (2009) compared the performances of various spectral partitioning techniques and methods on the identification of wind waves and swells: significant differences have been found using different partitioning methods, and it was found that the existing spectral partitioning methods may deliver inconsistent output for wave systems. Moreover, the typical number of detected partitions in a measured spectrum is of the order of tens, and associating neighbor wave components at different times becomes intricate. It is therefore difficult to determine a clear frequency to separate the families of wind wave and swell (Gerling, 1992; Portilla et al., 2009).

To take into account the swell wave and to relax the FDS assumption, we propose in the present work a generalized power-law relation between local wind and waves. In the following, we first present the data and methods. Long-term buoy collected wind and wave data are used to verify the new swell identification method, and the local wind wave relation. The method is then validated by the SEP analysis. Then, the global patterns of the swell wave and the wind-wave relations are reported by using a 17-year of JASON altimeter calibrated wind and wave data. Finally, discussions and conclusions are addressed in last two sections.

2 Data

The *in situ* U_{10} and *Hs* data from the NDBC are of high quality and have been extensively used for studying the wind wave interactions, validating model results and calibrating satellite systems (Ebuchi et al., 2002; Evans et al., 2003; Andreas and Wang, 2007; Zieger et al., 2015). Note that, the *Hs* is not directly estimated by sensors on board the buoys. The buoy-equipped accelerometers or inclinometers measure the heave acceleration or the vertical displacement of the buoy hull during the wave acquisition time. Then a fast Fourier transform is applied to the data to transform the temporal information into the frequency domain. After that, *Hs* is derived according to Equation (5) typically over the range from 0.0325 to 0.485 Hz.

The hourly averaged wind speed, significant wave height data provided by the NDBC buoy 46086 (located at 32.5°N and 118°W, with the water depth of 1844 m) for nearly 18 years (i.e., from 6 November 2003 to 31 December 2021) are used to illustrate the new swell identification method. The typical measurement accuracy for the NDBC buoy are 0.55 m/s and 0.2 m respectively for wind speed and significant wave height (Evans et al., 2003). Due to technical reasons, some data are missing, and there are a total of 149,089 valid pairs of wave height and wind speed values. The wind speed is measured by an anemometer located at z=4.1 m above the sea surface, a conversion from $U_{4.1}$ to U_{10} is required before further studying the relation between wind and waves. Assuming that the marine atmospheric boundary layer is in a neutral stability logarithmic state, the surface wind profile is,

$$U_z = \frac{u_\star}{\kappa} \ln \frac{z}{z_0} \tag{9}$$

where κ is the von Kármán constant and z_0 is the roughness length, which is usually set as 0.4 and 9.7 $\times 10^{-5}$ m, respectively; z is the height above the sea surface; u_* is the friction velocity which can be experimentally derived from U_{10} and the drag coefficient C_d (always set as 1.2 $\times 10^{-3}$) as follows,

$$u_\star = \sqrt{C_d} U_{10} \tag{10}$$

Combining the above two equations, U_z for z>0 can be re-expressed introducing U_{10}. By considering the measured wind speed at a height z_1 we finally have (Ribal and Young, 2019),

$$U_{10} = U_{z_1} \sqrt{\frac{\kappa^2}{C_d}} \frac{1}{\ln (z_1/z_0)} \tag{11}$$

Note that, to keep the self-consistency of this work, the parameters C_d and z_0 are the same as those in the second dataset (Ribal and Young, 2019). Finally, applying z_1=4.1 m in the above equation, the converted wind speed at 10 m can be expressed in a simplified way as U_{10}=1.084$U_{4.1}$. A further test shows that a variation of the height, e.g., 3$\lesssim z_1 \lesssim$5 m, will have less than 2% difference in the estimation of U_{10}. Figures 2A, B show the hourly U_{10} and *Hs* data collected by the NDBC buoy 46086, where annual cycles for wind speed and wave height are visible. Moreover, the corresponding hourly wave spectra with frequency on the range 0.02≤f≤0.485 Hz are also used to perform the SEP algorithm to retrieve the swell wave and wind waves: see the example of five days wave spectra during 27-31 December 2021 in Figure 2C. Two regimes are distinguished, the one with high frequency (e.g., f≥0.15 Hz) corresponds to the wind waves, and another one with low frequency (e.g., f≤0.15 Hz) indicates the swell waves.

Another dataset is a 17-year (from 2002 to 2018) calibrated JASON altimeters observed global measurements of U_{10} and *Hs* (Ribal and Young, 2019). Different pulses are received by the satellite altimeter, coming from reflections at the ocean's surface. These different backscattered echos are classically treated using a model of the ocean's rough surface (Brown, 1977), seen as the convolution of a point source, a flat sea surface, and an assumed probability density function of sea elevation. Based on the fitting of the Brown model echo to the recorded waveforms and the using of a maximum likelihood estimator, the *Hs* information could be

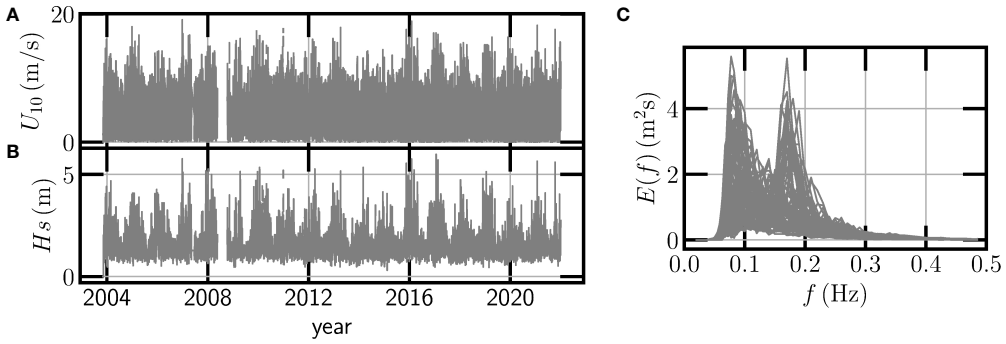

FIGURE 2
Illustration of the NDBC buoy 46086 collected hourly time series **(A)** U_{10} and **(B)** *Hs*. **(C)** The collected wave spectra during 27-31 December 2021.

retrieved. The U_{10} is then estimated by a mathematical relationship with the backscatter coefficient and the *Hs* using the Gourrion algorithm (Gourrion et al., 2002) and Collard table (Collard, 2005). This dataset was carefully quality controlled and calibrated to ensure long-term stability and cross-mission consistency. The wind and wave data were archived in 1°×1° bins in this dataset. It has been shown that this dataset agrees well with those provided by buoy and model reanalysis products (Young and Donelan, 2018; Takbash et al., 2019; Young and Ribal, 2019).

3 Method

3.1 Swell identification

As an example, here, we consider the empirical joint PDF $p(U_{10}, Hs)$ for the wind and wave data collected by NDBC buoy 46086. The measured joint PDF is shown in Figure 3A, where 10 points are considered in each order of magnitude on a logarithmic scale. The conditional PDF of *Hs* for a given U_{10} value possesses a well-defined maximum, which can be further confirmed by the individual normalized PDF curve for $U_{10}\lesssim 4$ m/s in Figure 3B, where the black solid curve is the average PDF. A well collapse of these PDFs is observed, indicating that in small wind conditions, the distribution of the measured $Hs(U_{10})$ are nearly independent of the local wind speed.

For a given U_{10} value, we denote as Hs_0 the value of *Hs* corresponding to this maximum. This defines a new continuous curve, which is denoted as $\hat{H}s_{sw}(U_{10})$ with the following formulation,

$$\hat{H}s_{sw}(U_{10}) = Hs_0; \qquad p(U_{10}, Hs_0) = \max_{Hs}\{p(Hs|U_{10})\} \tag{12}$$

This corresponds to a so-called skeleton of the joint PDF (Huang et al., 2008), illustrated as crosses in the figure. It is visible that $\hat{H}s_{sw}(U_{10})$ is nearly constant for light winds (e.g., $U_{10}\lesssim 4$ m/s), while increasing rapidly for strong winds (e.g., $U_{10}\gtrsim 4$ m/s). Thus, it is reasonable to assume that in small wind conditions, the wave height is independent or weakly dependent on the local wind speed, and the local wave is surpassed by regular swell waves that have been generated from distant weather systems. Therefore, we propose here that *Hs* with maximum probability of *Hs* at small wind speeds, as the swell significant wave

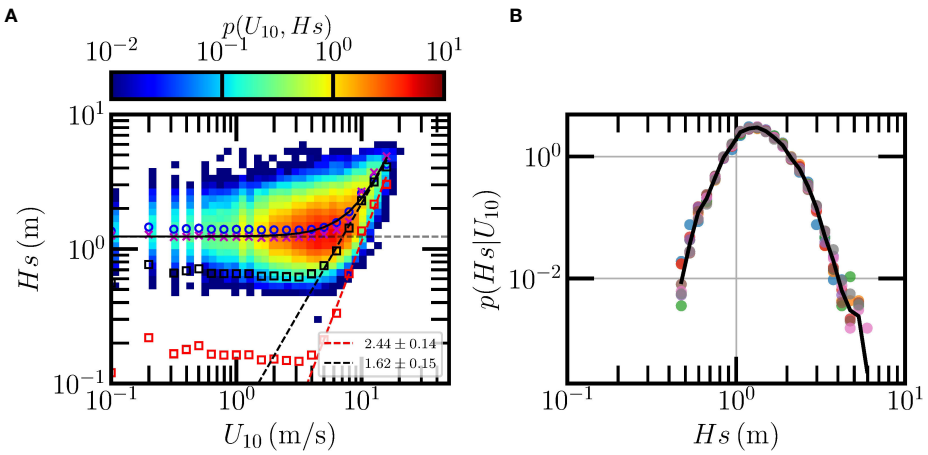

FIGURE 3
(A) Measured joint PDF of U_{10} and *Hs* collected by NDBC buoy 46086, where the open circles (O) are the conditional mean $\bar{H}s(U_{10})$; crosses (×) are the skeleton $Hs_0(U_{10})$ of the joint PDF; the red squares and black squares are the local significant wave height $\bar{H}s_{LI}(U_{10})$ and $\bar{H}s_{Le}(U_{10})$ derived via the linear decomposition and energy conservation approach, respectively. The dashed lines are the best fittings of the relation between $\bar{H}s_L(U_{10})$ and U_{10}. The black solid curve is a reconstruction of the $\bar{H}s(U_{10})$ based on Equation (16). **(B)** The conditional PDFs $p(Hs|U_{10})$ for *Hs* at small wind speeds, e.g., $U_{10}\lesssim 4$ m/s. The solid curve is the average PDF.

height. In the same figure, the conditional mean $\bar{H}s(U_{10}) = \int p(U_{10}, hs)hsdhs$ is also represented and illustrated as circles (e.g.), in the figure. As aforementioned, the maximum probability of $Hs(U_{10})$ at a given small wind speed is either a constant or weakly dependent on the local wind, one thus can further determine the overall swell significant wave height $\bar{H}s_{sw}$ by averaging the almost constant values for low wind speeds,

$$\bar{H}s_{sw} = \langle \hat{H}s_{sw}(U_{10}) \rangle_{U_{10} \leq U_{cr}} \tag{13}$$

where $\langle \cdot \rangle$ means average, U_{cr} is a critical wind speed (e.g., 4 m/s here), above which the local wind wave is then dominated. In this way, a constant swell value $\bar{H}s_{sw}$ is extracted from the data. For this case, $\bar{H}s_{sw}$ is found to be 1.24 m.

3.2 Wind-wave identification

Ideally, the collected significant wave height $Hs(U_{10})$ at a certain local wind speed U_{10} can be decomposed into two parts: i) the swell significant wave height Hs_{sw} that propagates from distant seas; ii) the local significant wave height $Hs_L(U_{10})$ generated by local winds. In the previous section, the average swell $\bar{H}s_{sw}$ is extracted by a probability-based approach, then two different wind-wave estimators are introduced here.

3.2.1 Linearly decomposed wind-wave

The first method to do the wind wave identification is based on the idea of linear decomposition. Let us assume that the collected waves are linearly composed by the swell and wind wave. Partially due to its simplicity, this assumption has been taken and used by many authors to construct the relation between wind and waves (Pandey et al., 1986; Chen et al., 2002; Andreas and Wang, 2007). In this way, the local significant wave height can be obtained by subtracting the swell value from the conditional mean as follows,

$$\bar{H}s_{Ll}(U_{10}) = \bar{H}s(U_{10}) - \bar{H}s_{sw} \tag{14}$$

Here the subscript l is used to indicate the linearly decomposed local wind-wave. This quantity is represented in Figure 3A as red squares, where a power-law relation with the wind speed above U_{cr} is evident,

$$\bar{H}s_{Ll}(U_{10}) = \alpha_l U_{10}^{\beta_l}; \qquad U_{10} > U_{cr} \tag{15}$$

where α_l=0.0044±0.0014 and β_l=2.44±0.14 are provided by the least square fit algorithm. Note that, as aforementioned, β_l can be different from the value of 2 for the FDS, see the red dashed line of the best fit curve in Figure 3A.

By doing so, that collected $\bar{H}s(U_{10})$ can be decomposed into $\bar{H}s_{sw}$ and $\bar{H}s_{Ll}(U_{10})$, the latter one can be related with U_{10} using a power-law relation. Consequently, $\bar{H}s(U_{10})$ is expressed as,

$$\bar{H}s(U_{10}) = \bar{H}s_{sw} + \alpha_l U_{10}^{\beta_l} \tag{16}$$

The composite curve, i.e., $\bar{H}s_{sw} + \alpha_l U_{10}^{\beta_l}$ is shown as a black solid line in Figure 3A. Visually, this curve agrees well with the measured $\bar{H}s(U_{10})$ when $U_{10} \lesssim 20$ m/s, with a relative error $\lessapprox 10\%$ or a standard deviation $\simeq 0.15$ m. A more careful check shows an average relative error of 5% or a mean absolute error $\simeq 0.1$ m when $4 \lesssim U_{10} \lesssim 20$ m/s. For $U_{10} \lesssim 4$ m/s, the reconstructed $\bar{H}s(U_{10})$ is overlapped with $\bar{H}s_0(U_{10})$. Moreover, it is interesting to see a sharp transition of the skeleton $\bar{H}s_0(U_{10})$ roughly at $U_{10} \simeq 8$ m/s, which confirms the above assumption that the swell wave dominates during the small winds.

3.2.2 Energy conserved wind-wave

As aforementioned, partially due to its simplicity, the measured significant wave height $\bar{H}s(U_{10})$ is linearly associated with the swell $\bar{H}s_{sw}$ and the so-called local wind-wave $\bar{H}s_{Ll}(U_{10})$, see Equation (14). According to ocean wave theory, in the meaning of the energy conservation, the total wave energy (i.e., $\bar{H}s^2(U_{10})$) is equal to the sum of swell energy (i.e., $\bar{H}s^2_{sw}$) and local wind-wave energy (i.e., $\bar{H}s^2_L(U_{10})$). This independence hypothesis might be violated by the above linear decomposition. To satisfy the energy conservation law, a strict analytical expression of the local significant wave height is written as,

$$\bar{H}s_{Le}(U_{10}) = \sqrt{\bar{H}s^2(U_{10}) - \bar{H}s^2_{sw}} \tag{17}$$

where the subscript e is adopted here to indicate the wind waves that follow the energy conservation law. The experimental $\bar{H}s_{Le}(U_{10})$ is shown as black squares in Figure 3A. A power-law behavior is observed in high winds as indicated by the black dashed line, which is expressed as,

$$\bar{H}s_{Le}(U_{10}) = \alpha_e U_{10}^{\beta_e}; \qquad U_{10} > U_{cr} \tag{18}$$

For this case, the fitted value of β_e=1.62±0.15, is smaller than the previous one. The values of $\bar{H}s_{Le}$ are larger than the ones extracted by the linear decomposition method. The overall significant wave height $\bar{H}s(U_{10})$ is then related with U_{10} as,

$$\bar{H}s(U_{10}) = \sqrt{\bar{H}s^2_{sw} + \left(\alpha_e U_{10}^{\beta_e}\right)^2} \tag{19}$$

Furthermore, it is easy to obtain from Equations (16) and (19) the following relation,

$$\bar{H}s_{Le}(U_{10}) \geq \bar{H}s_{Ll}(U_{10}) \tag{20}$$

Additionally for the high wind speed where the swell $\bar{H}s_{sw}$ can be ignored, the asymptotic behavior, i.e., $\bar{H}s(U_{10}) \simeq \bar{H}s_{Ll}(U_{10}) \simeq \bar{H}s_{Le}(U_{10})$ can be safely applied, and one has

$$\beta_l \geq \beta_e \tag{21}$$

This is partially due to the fact that for moderate wind speeds, the local wind wave $\bar{H}s_{Ll}(U_{10})$ provided by the linear decomposition is smaller than $\bar{H}s_{Le}(U_{10})$ provided by the energy conserved formula, see Equation (20). They should reach the same value of the significant wind wave height due to the asymptotic behavior. Therefore, the former one should grow faster than the latter one, indicated by the Equation (21), see an example in Figure 3.

3.3 Validation using the SEP algorithm

With the aforementioned probability analysis, a nominal swell $\bar{H}s_{sw}$ can be identified, thus the wind-wave $\bar{H}s_L(U_{10})$. To verify the extracted swell and wind-wave, the SEP analysis is also performed for the wave partitioning of the data collected by the NDBC buoy 46086. The PM64-

based algorithm (e.g., f_s=0.8f_m) is considered (Gilhousen and Hervey, 2002; Portilla et al., 2009). Note that when the wind speed is less than 2.1 m/s, the calculated f_s is then larger than 0.485 Hz. Therefore, in such cases no local wind-wave is extracted. The measured joint PDF of U_{10} and $Hs_{sw}(U_{10})$ derived by the PM64-based SEP approach is shown in Figure 4A, in which the solid red curve is the conditional mean $\bar{H}s_{sw}(U_{10})$, and the maximum statistical difference between two subsets with equal sample size is indicated by an error bar. It shows that there is roughly a constant value of $\bar{H}s_{sw}$ = 1.24 ± 0.12 m when $U_{10} \lesssim$ 13 m/s, confirming the above assumption that in small wind conditions, the swell wave is independent or weakly dependent on the local wind speed. Note that the SEP-based $\bar{H}s_{sw}$ is coincidentally the same as the value of 1.24 m derived from the probability-based approach for the wind speed U_{10}≤4 m/s. A higher value $\bar{H}s_{sw}$ = 1.35 m is obtained when U_{10}≤5 m/s.

Figure 4B shows the joint PDF of U_{10} and Hs_L, where the conditional mean wind wave $\bar{H}s_L(U_{10})$ is illustrated by a dashed curve. To emphasize the assumption mentioned above that in small wind conditions the local wind wave is surpassed by the regular swell wave, the ratio between extracted swell wave $\bar{H}s_{sw}(U_{10})$ and wind wave $\bar{H}s_L(U_{10})$ is shown in the inset of Figure 4B in a log-log plot. It suggests that the swell wave dominates the collected significant wave height when $U_{10} \ll$8 m/s. Moreover, a power-law decay for the ratio is found, in which an empirical exponent 2.07±0.01 is obtained. These results validate the assumption we made in the probability analysis, namely, that the measured $Hs(U_{10})$ is dominated by the swell wave for small wind conditions, and that the $\bar{H}s_{sw}(U_{10})$ is nearly independent of the local wind, which is confirmed also by analyzing the data provided by other buoys (not shown here).

For comparison, the $\bar{H}s_{sw}(U_{10})$ and $\bar{H}s_L(U_{10})$ retrieved by our new probability-based methods and the SEP algorithm are reproduced in Figure 5. It shows that the measured $\bar{H}s_{sw}(U_{10})$ (e.g., 1.35 m for U_{10}≤5 m) from the SEP is slightly larger than the one (e.g., 1.24 m) provided by the joint PDF in small winds. The above-mentioned two assumptions are well satisfied in small wind conditions. When U_{10}≥4 m/s, the SEP-based wind wave $\bar{H}s_L(U_{10})$ are collapsing well with the $\bar{H}s_{Le}(U_{10})$ provided by the energy-conserved decomposition. Power-law behavior is observed for the wind wave $\bar{H}s_L(U_{10})$ provided by all three methods when U_{10} exceeds 4 m/s with a scaling exponent β=1.69 for the SEP, a value β_l=2.44 is found for the linear decomposition approach, and β_e=1.62 for energy-conserved one.

With the proposed probability-based approach, the swell waves can be identified from the observed $Hs(U_{10})$ without the wave spectrum information. Consequently, the local wind-wave is defined by a linear decomposition or an energy conserved decomposition. After that, a power-law relation between the wind speed and the local wave is visible. One possible disadvantage of the probability-based method is that it requires a large number of data samples to construct the joint PDF $p(U_{10},Hs)$. The corresponding swell wave $\bar{H}s_{sw}$ is valid in an average sense. The main advantages of the current method are summarized as follows: i) only the overall significant wave height is needed when estimating the swell without knowing the wave spectrum *a priori*; ii) the influence of the anomalous values will be automatically excluded since they are in the tail of the PDFs; iii) the power-law relation between the local wind and waves is recovered for the high wind speeds for which the influence of the swell is nearly excluded.

4 Results

The buoy observations are often close to the coastal area, with few locations sampled over the global ocean, thus are spatially limited. To access global views of the swell and local wind-wave relation, satellite data are also used in this study. Here we combine the data collected by JASON-1 (from January 2002 to June 2013), JASON-2 (from July 2008 to July 2018), and JASON-3 (from February 2016 to July 2018) together (hereinafter referred to as JASON) to study the global distribution and seasonal variation of $\bar{H}s_{sw}$, and the relation between U_{10} and $\bar{H}s_L(U_{10})$. The calibrated data provided by

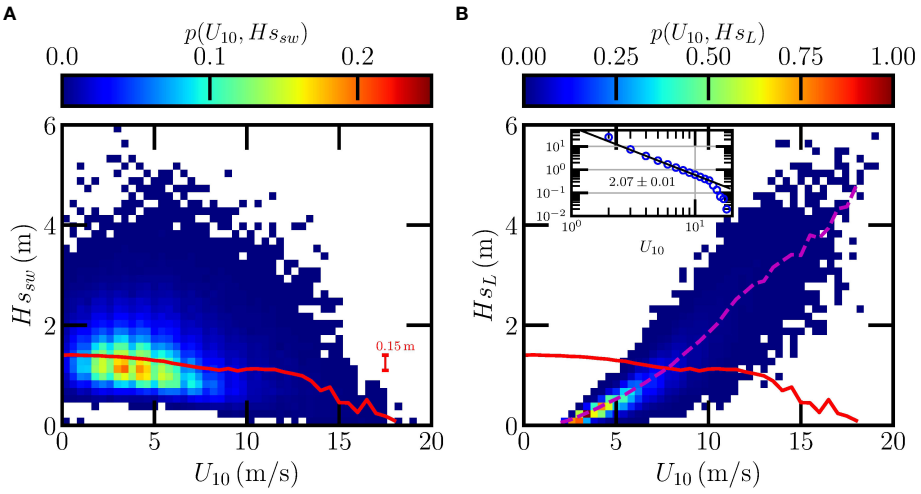

FIGURE 4
Measured joint PDFs of **(A)** U_{10} and Hs_{sw}, and **(B)** U_{10} and Hs_L extracted from the data provided by NDBC buoy 46086 with SEP analysis. The solid and dashed curves are the conditional average Hs_{sw} and Hs_L, respectively. The inset in **(B)** shows the ratio between $\bar{H}s_{sw}$ and $\bar{H}s_L$ at various wind speeds. The solid line indicates the best fit with the slope of −2.07. The maximum statistical difference between two subsets with equal sample size is indicated by an error bar in **(A)**.

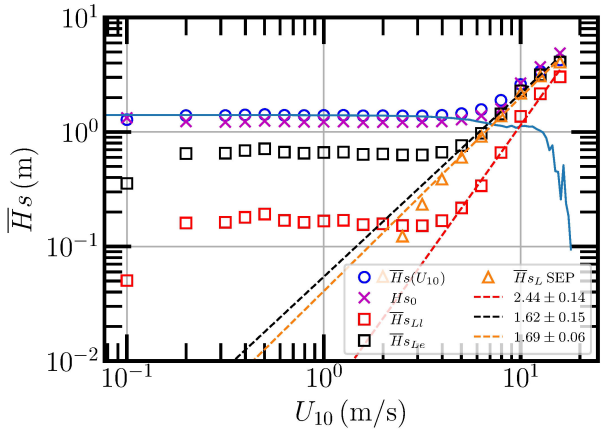

FIGURE 5
Comparison of the measured skeleton $\bar{H}s_0(U_{10})$ (×) for the joint PDF of U_{10} and Hs provided by the NDBC buoy 46086. The extracted local significant wave heights $\bar{H}s_{Ll}(U_{10})$ and $\bar{H}s_{Le}(U_{10})$ by the probability-based approach is illustrated as □. For comparison, the swell significant wave height $\bar{H}s_{sw}(U_{10})$ (horizontal solid line) and local significant wave height $\bar{H}s_L(U_{10})$ (△) extracted by the SEP approach are also shown. The dashed lines are the best fittings for the local significant wave height analysis.

Ribal and Young (2019) were archived in 1°×1° bins. For enhancing the accuracy of the swell wave and local wave decomposition, the data are reassigned in 2°×2° boxes. The data in the latitude coverage from 60°S to 60°N are considered for further analysis in this work.

4.1 Validation of JASON observations

Before processing the JASON data, the wind and wave data recorded by offshore NDBC buoys 41049 (located at 27.49°N, 62.94°W, with the water depth of 5,459 m) and 46006 (located at 40.77°N, 137.38°W, with the water depth of 4,323 m) are selected to perform comparisons with JASON observations, in order to examine the data quality. The joint PDFs for U_{10} and Hs data observed by JASON in the area close to the buoys are estimated, then the skeleton of the joint PDF for the data provided by buoy and JASON are extracted, see Figure 6. The skeleton is overlapped under $U_{10} \lesssim 6$ m/s for both cases, except for a deviation found at $U_{10} \simeq 0.75$ m/s for the second case: it might be induced by the uncertainty of satellite observations in extreme low wind conditions. According to the joint PDF, the $\bar{H}s_{sw}$ for NDBC buoy 41049, 46006 both equal to 1.25 m. The $\bar{H}s_{sw}$ extracted from JASON data which is close to the buoy 41049 is also 1.25 m, and the one corresponding to buoy 46006 is equal to 1.18 m.

The identified wind-wave is used to estimate the scaling exponents β for the local wind wave relation. Two decomposition methods are both used here, the results are illustrated in the insets in Figure 6, in which the squares and crosses are the wind-wave derived from the linear decomposition method and the energy conservation based approach, respectively. The colors green and black are used to

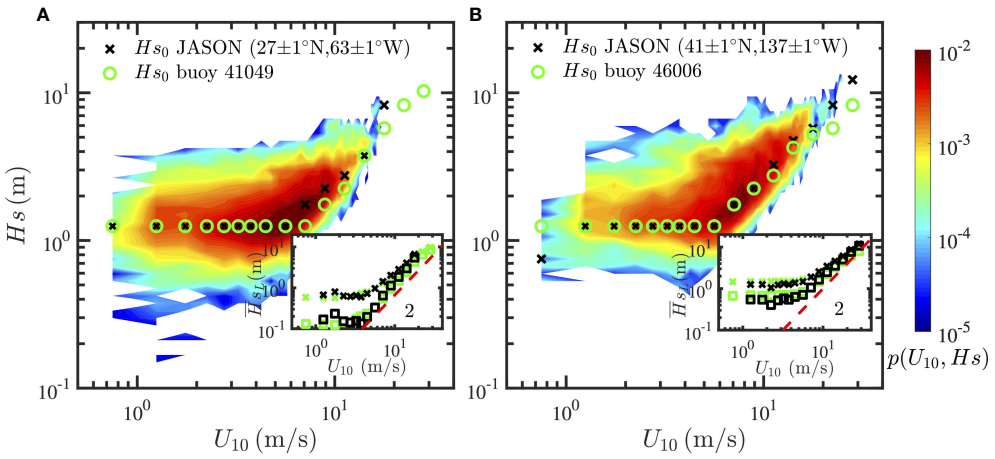

FIGURE 6
Measured joint PDFs of U_{10} and Hs recorded by JASON in the areas close to NDBC buoys **(A)** 41049 and **(B)** 46006. The black crosses and green circles are the skeletons of the joint PDFs for JASON and buoy data. The insets show the measured Hs_L, in which the squares and crosses indicate the $\bar{H}s_{Ll}$ from linear decomposition and the $\bar{H}s_{Le}$ from energy conserved decomposition, respectively. The colors green and black are used to indicate the results from buoy and satellite data. The dashed line is given as a reference with the slope of 2.

indicate the results from buoy and satellite data. Visually, the derived wind waves are in a good agreement between the buoy and satellite observed data, where a similar scaling feature is obtained. More precisely, for the linear decomposition, the measured β_l for the data recorded by the buoy 41049 and nearby JASON data are 2.03 and 2.11; the results for the buoy 46006 and JASON data are 1.71 and 1.53. On the other hand, for the energy conservation approach β_e for the buoy 41049 and JASON data are 1.37 and 1.49; β_e for the buoy 46006 and JASON data are 1.25 and 1.22. These results show that the JASON data have remarkable performances in the swell identification and the construction of a local wind-wave relation.

4.2 Identified swell wave

The probability-based wave decomposition procedure is performed at each geographic grid to derive $\bar{H}s_{sw}$ and $\bar{H}s_L(U_{10})$. To have a reasonable sampling size for each wind bin, we group the data into the four boreal seasons: Winter (DJF), Spring (MAM), Summer (JJA) and Autumn (SON). The derived swell is found on the range $0.5 \leq \bar{H}s_{sw} \leq 4$ m, with a mean value around 1.8 m and a strong seasonal variation, see Figure 7. More precisely, the retrieved swell is stronger in the boreal Winter than in Summer in the Northern Hemisphere. For instance, the average $\bar{H}s_{sw}$ around 50°N are equal to 2.3 m and 1.2 m in DJF and JJA, respectively. This is partially due to the fact that the swell is highly positively correlated with the wind speed at high latitudes, see Figure 8, in which the black and red curves are the longitudinal averaged $\bar{H}s_{sw}$ and U_{10}, respectively. Similar meridional variation trends of $\bar{H}s_{sw}$ and U_{10} are found, especially in high latitudes.

The spatial patterns illustrated in Figure 7 agree well with the ones reported by Semedo et al. (2011). For example, in DJF, large swells are seen in the extratropical areas of the Northern Hemisphere, small ones are found in several regions, e.g., the Gulf of Mexico, Indian monsoon area, South China Sea, north and east coast of Australia, to list a few. Additionally, the longitudinal averaged curve shows a nearly symmetric shape, see Figure 7A. In the Southern Hemisphere, high values are mainly found in the Antarctic Circumpolar Current (ACC) region, i.e., roughly from 48°S to 58°S, where there is almost no influence of the continents. In JJA, the swell is increasing from the north to the south, reaching its maximum value in the ACC region.

4.3 Local wind wave relation

The local wind wave relation is described by a power-law formula in this study, e.g., $\bar{H}s_L(U_{10}) = \alpha U_{10}^{\beta}$, while different definitions of $\bar{H}s_L(U_{10})$ correspond to distinct power-law features. In this section, the linear decomposition (i.e., Equation (14)) and energy conserved decomposition (i.e., Equation (17)) are both used to generate $\bar{H}s_L(U_{10})$ with JASON data. The prefactor α and the scaling exponent β in the power-law relation is then estimated by using an automatic search algorithm with a width of half order of the wind speed magnitude above 4 m/s. The choice of a half order is due to the limited range of wind speed values. The global distribution of measured α in DJF and JJA are shown in Figure 9, in which Figures 9A, B are the ones fitted with linearly decomposed $\bar{H}s_{Ll}$; Figures 9C, D are the results from the $\bar{H}s_{Le}(U_{10})$ estimated with energy conserved approach. The fitting algorithm fails on some geolocations due to the fact that the wind speed range is too short. This is observed in the small wind regions around the equator. The values of α_l extracted from $\bar{H}s_{Ll}(U_{10})$ are smaller than the ones derived from $\bar{H}s_{Le}(U_{10})$, the differences are around one order. However, as visible in the figures, the spatial patterns for α estimated from two defined $\bar{H}s_L(U_{10})$ are similar, with small values in the equator and large ones in mid-latitudes. Moreover, seasonal differences are observed, relatively large α are found in the boreal Winter for the Northern Hemisphere.

The corresponding measured β are shown in Figure 10. It is clear that the values of β_l derived from $\bar{H}s_{Ll}(U_{10})$ (Figures 10A, B) are larger than the ones fitted with $\bar{H}s_{Le}(U_{10})$ (Figures 10C, D), confirming the Equation (21). Linear decomposition based β_l are found close to the PM64 predicted value, e.g., 2 in the boreal winter for the Northern Hemisphere, where large winds are present. On the other hand, the values of β_e are close to 1.5 in DJF for the Northern Hemisphere. Moreover, seasonal variation and spatial differences for β are also found, large values of β are found mainly from 25°S to 25°N. The longitudinal averaged β is nearly symmetric in DJF, while is strongly asymmetric in JJA. Furthermore, opposite meridional variations for β are obtained as compared to the ones for α, large β values are found in low latitudes, corresponding to the areas with small winds.

With the extracted swell $\bar{H}s_{sw}$, and α and β for the local wind wave, $\bar{H}s_L(U_{10})$ can be predicted if the local wind U_{10} is available. Here, the seasonal average U_{10} is calculated for the JASON

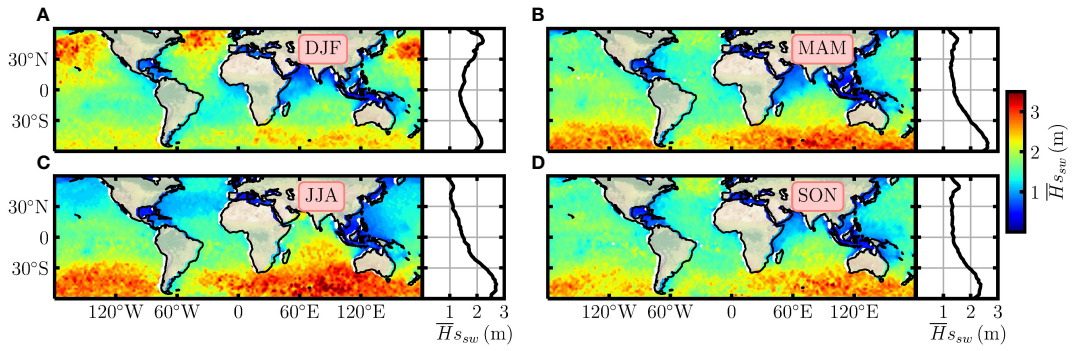

FIGURE 7
The global distributions of seasonal averaged $\bar{H}s_{sw}$ in **(A)** DJF, **(B)** MAM, **(C)** JJA, and **(D)** SON. The meridional variations are shown in the right panels.

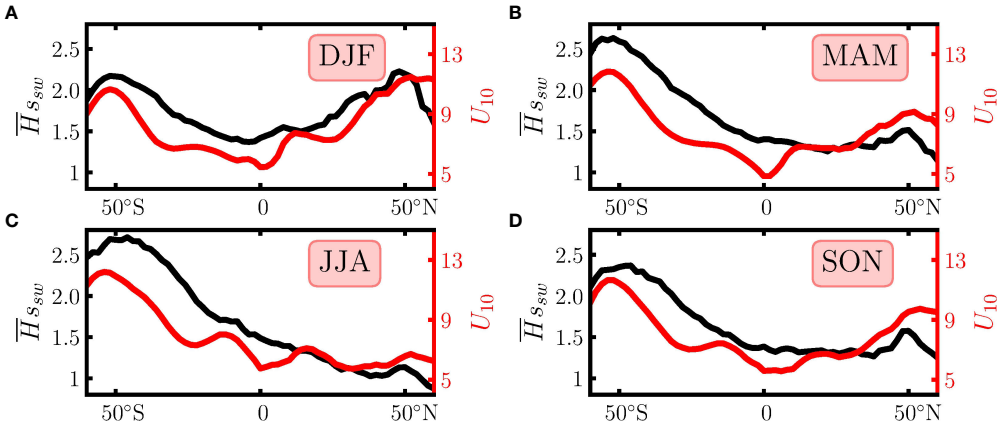

FIGURE 8
Meridional variations of $\bar{H}s_{sw}$ (black curve) and U_{10} (red curve) in **(A)** DJF, **(B)** MAM, **(C)** JJA, and **(D)** SON.

observation to predict $\bar{H}s_L$. The results in DJF and JJA are shown in Figure 11, in which Figures 11A, B are the ones derived with the power-law relations corresponding to the linear decomposed local wind waves, and Figures 11C, D are the ones estimated with the parameters from the energy conserved decomposition. The spatial and seasonal variation patterns are the same, with large $\bar{H}s_L$ occurring in mid-latitudes and in the boreal Winter for the Northern Hemisphere, except for the Somali coastal jet controlled region, where large $\bar{H}s_L$ are observed in JJA. The values of retrieved $\bar{H}s_{Ll}$ are smaller than $\bar{H}s_{Le}$. For instance, the measured $\bar{H}s_{Ll}$ in ACC are close to 1 m and 1.5 m in DJF and JJA, respectively. While the corresponding $\bar{H}s_{Le}$ in AAC are around 2.3 m and 3 m for the two seasons, respectively. Further comparison shows that the seasonal average $\bar{H}s_{Le}$ reproduced by the energy conservation-based theory are in good agreement with the ones reported by Semedo et al. (2011).

4.4 Relation between α and β

The empirical PDFs of α and β are shown in Figure 12, in which Figures 12A, C are the PDFs for α_l and β_l, and Figures 12B, D are the ones for α_e and β_e, respectively. For the linear decomposed results, the most probable values (corresponding to the maximum of the PDFs) are $\alpha_l \simeq 0.0065$ and $\beta_l \simeq 2.11$. The latter one agrees well with the FDS's prediction by Pierson and Moskowitz (1964), while the former value is found to be roughly one-fourth of their prediction. Globally, nearly one-third of the global ocean has values of β_l in the range of [1.8,2.2]. A longitudinal-averaged plot of the ratio for β_l values belonging to the range of [1.8,2.2] is shown in the inset of Figure 12C. Except for the boreal Summer, this ratio is nearly symmetric with large values in the high latitudes, and small values (e.g., less than 0.2) around the equator from 20°S to 20°N. A special case is observed for the Northern Hemisphere in JJA, for example, a mean value 0.18 is found from 20°N to 60°N, implying a strong influence of the monsoon. For the energy conserved decomposition, the most probable values for α_e and β_e are around 0.077 and 1.45, respectively, both significantly deviate from FDS's prediction. The ratio of β_e in the range of [1.8,2.2] is also measured and shown in the inset in Figure 12D. The maxima of the ratio are found close to the equator, with the value of 0.2. Due to the effect of monsoon, the JJA case shows relatively large ratios in the Northern Hemisphere.

To relate the derived α and β, phase diagrams α versus β are shown in Figures 13 in a semilog view, in which the PM64-based curve (see details in the discussion section) is also shown as a solid

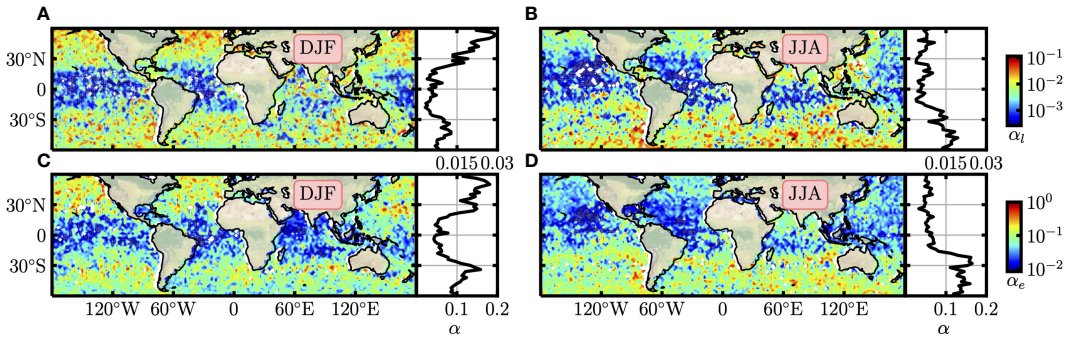

FIGURE 9
The global distributions of α_l measured with linearly decomposed $\bar{H}s_{Ll}$ in **(A)** DJF and **(B)** JJA. **(C, D)** are the α_e derived from the $\bar{H}s_{Le}$ decomposed by energy conservation theory. The meridional variations are shown in the right panels.

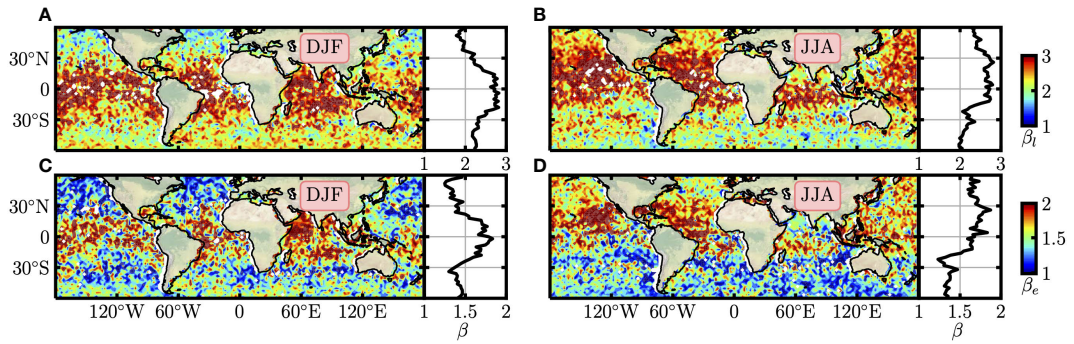

FIGURE 10
The global distributions of β_l measured with linearly decomposed $\bar{H}s_{Ll}$ in **(A)** DJF and **(B)** JJA. **(C, D)** are the β_e derived from the $\bar{H}s_{Le}$ decomposed by energy conserved approach. The meridional variations are shown in the right panels.

curve for comparison. It is interesting to see a nearly perfect exponential behavior, which is written as,

$$\alpha(\beta) = \omega e^{-\gamma\beta} \tag{22}$$

With the least square fitting algorithm, the exponential exponents are found to be ω_l=1.65 and γ_l=2.55. A further examination shows that the values of γ_l are latitude-dependent, e.g., a roughly linear decay is observed in the Southern Hemisphere from their maximum value of 3.0 to a minimum value of 2.25. It is then increasing linearly in the North Hemisphere. However, possibly due to the influence of the monsoon in the Northern Hemisphere, a strong seasonal variation is evident, e.g., a significant difference between the DJF and JJA cases is observed, a decreasing trend is found from 10°N to 60°N for measured γ_l in JJA. As for the energy conservation case, the fitted ω_e and γ_e are found with the values of 2.44 and 2.45, respectively. Hemispherical symmetric variations for γ_e are also found, with a linear decay from mid-latitudes to the equator, except for the one in the Northern Hemisphere in JJA.

5 Discussion

Without knowing the wave spectrum *a priori*, the proposed probability-based swell estimator relies on at least two closely related hypotheses: i) the observed significant wave height $Hs(U_{10})$ is dominated by the swell for the small wind condition and ii) the swell wave $\bar{H}s_{sw}(U_{10})$ is either weakly dependent or independent of the local wind. These two hypotheses are confirmed by applying the SEP algorithm to the data, see Figure 4. The idea is tested and verified with buoy collected data, then extended to altimeter data. Note that the *Hs* measured from the buoy and altimeter are in two different ways, namely, buoy-derived and satellite-derived *Hs* possess conceptual differences. The altimeter data used in this study have been calibrated and validated against NDBC buoy data, the detailed processes can be found in Ribal and Young (2019). Though the concepts for *Hs* are different, the magnitudes are close to each other. Thus, the extension of the proposed method from buoy data to altimeter data is reasonable.

One advantage of the current proposal is that the influence of anomalous values will be automatically excluded since the skeleton of the joint PDFs is considered. However, to accurately estimate the skeleton (i.e., the nominal swell), a minimum sample size is required. One consequence is that the analysis is performed on a coarse time period, e.g., seasons in this study. Note that both the atmospheric and oceanic movements are driven either directly or indirectly by solar radiations. Therefore, daily and annual cycles due to earth rotation and revolution are expected. The former one is hard to be detected using the current satellite database since it requires a much larger

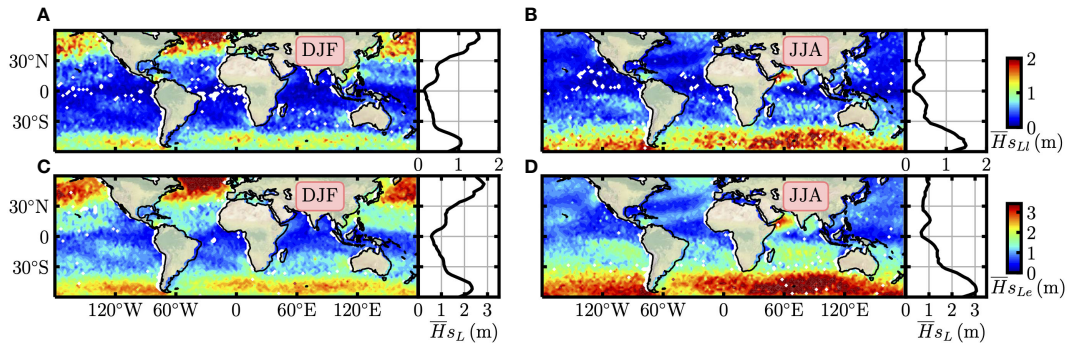

FIGURE 11
The global distributions $\bar{H}s_{Ll}$ predicted with the power-law models derived from linearly decomposed wind waves in **(A)** DJF and **(B)** JJA. **(C, D)** are the $\bar{H}s_{Le}$ estimated with the power-law models extracted from the wind waves decomposed by the energy conservation theory. The meridional variations are shown in the right panels. The model input U_{10} is the seasonal averaged JASON wind.

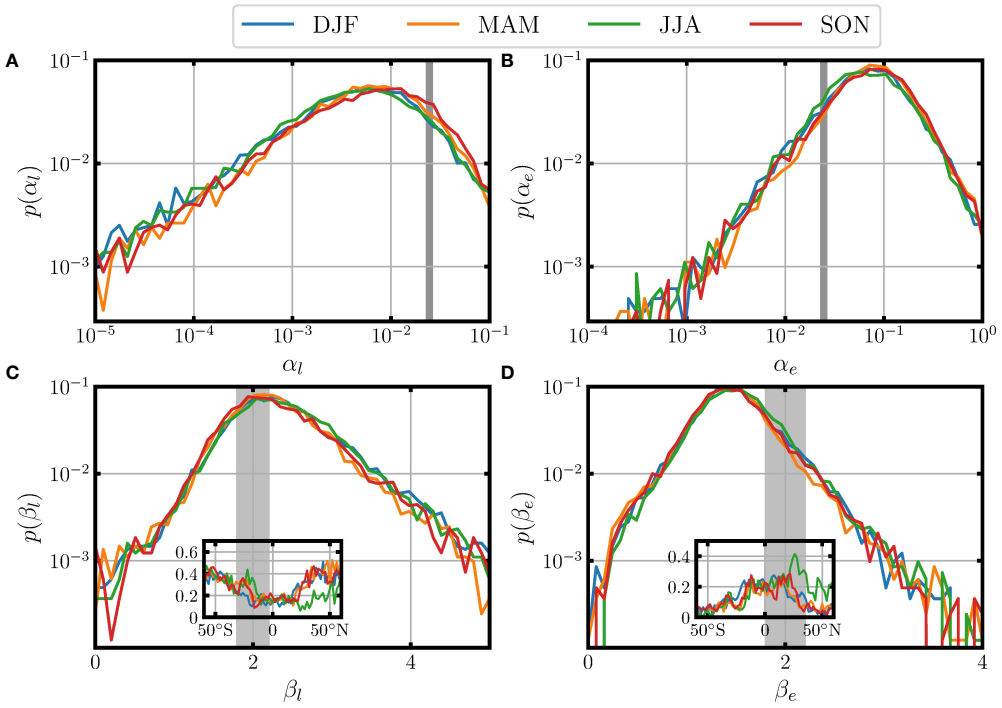

FIGURE 12
Measured PDFs for **(A)** α_l, **(B)** α_e, **(C)** β_l, and **(D)** β_e in four seasons. The insets in **(C, D)** are the ratios for β values in the range of [1.8,2.2] in various latitudes. The curves in different colors indicate different seasons.

dataset to capture the daily variation, while the latter one is confirmed by our results.

The swell $\bar{H}s_{sw}$ derived from the proposed probability-based method is validated against the SEP analysis, see the comparison between $\bar{H}s_0$ in small winds and $\bar{H}s_{sw}(U_{10})$ extracted from SEP approach in Figure 5. Thus, the introduced new method can be used to distinguish the swell $\bar{H}s_{sw}$ from collected $Hs(U_{10})$ without knowing the wave spectra information *a priori*. The global view of $\bar{H}s_{sw}$ was then extracted for the 17-year JASON data. The extracted seasonal variations and spatial distribution pattern for $\bar{H}s_{sw}$ are the same as the ones extracted by the SEP analysis of reanalysis data (Semedo et al., 2011). For instance, large $\bar{H}s_{sw}$ are found in mid-latitudes during the boreal winter time, and the values of $\bar{H}s_{sw}$ in ACC are larger than 2 m.

The local wind-wave $\bar{H}s_L(U_{10})$ are then identified by either the linear decomposition or energy conserved approach. The results show that the linearly decomposed $\bar{H}s_{Ll}(U_{10})$ are smaller than the ones extracted based on energy conserved approach, see the Equation (20) and the experimental comparison in Figure 5. The latter one is overlapped with the extracted $\bar{H}s_L(U_{10})$ from the SEP analysis in high winds since both of them are energy conserved. As illustrated by NDBC buoy data, the power-law relation of the local wind wave $\bar{H}s_L(U_{10})$ against the local wind speed is recovered for the high values of the wind speed, e.g., $U_{10}\gtrsim 4$ m/s, see Figure 3. To have the power-law behavior for at least half order range of wind speed, there should be enough data sample on the range $4\lesssim U_{10}\lesssim 25$ m/s. This condition might be not satisfied in small wind regions, e.g., the area around the equator, see Figures 9, 10. One possible solution is to fit the scaling exponent by using the fixed wind range, e.g., $U_{10}\geq 4$ m/s. Hopefully, with the accumulation of the observed products from the China France Oceanography SATellite (CFOSAT) data (Hauser et al., 2020), where the wind and waves are simultaneously collected, this difficulty will be overcome in the near future.

The fitted β_l for the linearly decomposed $\bar{H}s_{Ll}(U_{10})$ are closer to the PM64 prediction. For instance, β_l values lie in the range of [1.8,2.2] over one-third of the global ocean. On the contrary, the β_e extracted with energy conservation based $\bar{H}s_{Le}(U_{10})$ are relatively small, only a small portion have values close to 2. As for the prefactor α in the power-law relation, differences are also found between the two decomposed $\bar{H}s_L(U_{10})$. The most probable value for α_l is found to be around 0.0065, and the one for α_e is to be around 0.077, one order of magnitude larger.

Moreover, an exponential relation is found between the prefactor α and the scaling exponent β in the proposed wind wave relation, see Figure 13. If one ignores the existence of the swell wave, the relation between α and β could be derived from PM64-like theory. Using β to substitute $(\zeta-1)/2$ in the Equation (7), one obtains the following relation,

$$\alpha(\beta) = \sqrt{\frac{C_0}{2\beta}}\frac{g}{\pi^2}\left(\frac{0.855g}{2\pi}\right)^{-\beta} \tag{23}$$

The corresponding PM64-based prediction of the relation between α and β is illustrated as solid curves in Figure 13, where an exponential behavior is found when $\beta\gtrsim 2$. With the least square fit algorithm, the scaling exponent γ in the range $2\lesssim\beta\lesssim 5$ can be obtained with the value of 0.46, largely different from the measured ones. One possible reason is that the swell wave is excluded in this theoretical prediction. A more realistic model to take the swell into account is required in the future to explain this observed exponential relation.

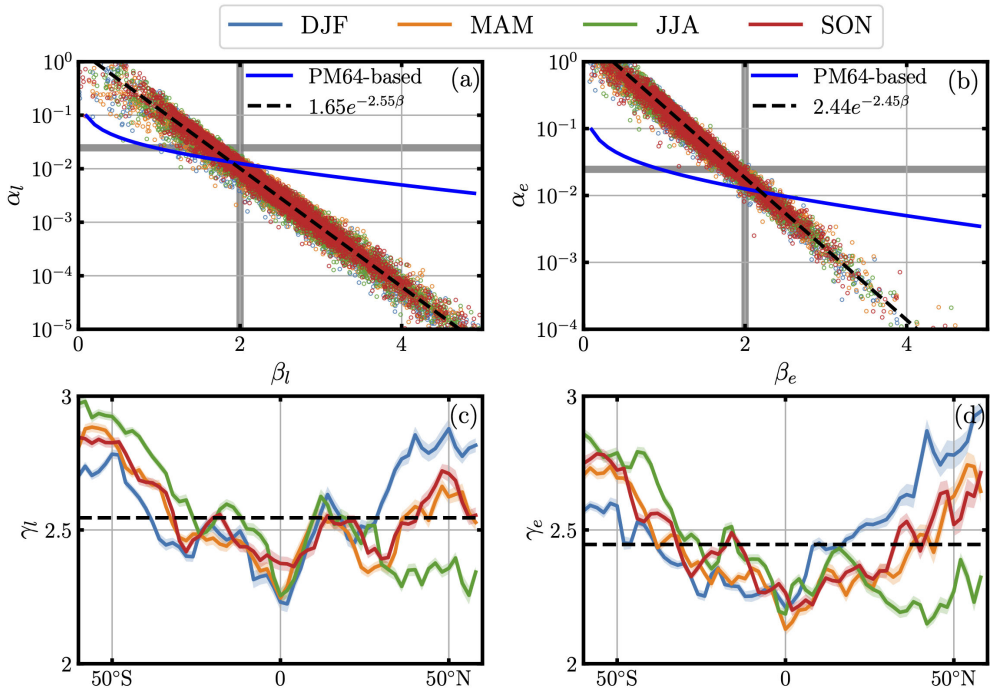

FIGURE 13
Relations between **(A)** α_l and β_l, **(B)** α_e and β_e. The dashed lines are the best fittings for the relation, the blue curve is the theoretical relation between α and β based on PM64 assumption. **(C, D)** are the meridional variations of the scaling exponents γ_l and γ_e, respectively, in which the dashed line is the average value.

With the above extracted wind wave power-law relation and the swell information, $\bar{Hs}(U_{10})$ can be predicted for a given U_{10} via the synthesizing Equation (16) or (19). By considering its simplicity, the linear synthesizing Equation (16) is recommended to reconstruct $\bar{Hs}$ here. For instance, using two years (from January 2020 to December 2021) annual average U_{10} provided by CFOSAT (Figure 14A), the $\bar{Hs}$ are calculated, see the global pattern of the model output in Figure 14C. The spatial pattern is very close to the CFOSAT observed one (Figure 14B): the differences between model output and observation are less than 0.3 m, see Figure 14D. More precisely, a relatively large discrepancy is found in mid-latitudes and a few nearshore regions around the equator. On the contrary, the differences are less than 0.3 m for most areas. More precisely, 88.1 % of the global oceans show differences within 0.25 m. Note that the accuracy for *Hs* measured by CFOSAT is 0.25-0.3 m or 5% of the mean value (Liu et al., 2020). Thus, the produced $\bar{Hs}$ by the wind-wave model is in good agreement with satellite observation in an average sense.

For other applications, such as marine shipping or offshore industries, the real-time wave information is a key parameter with strong potential implications. In such a framework, the proposed wind wave relation model in this work could be used to predict the instantaneous wave height with the knowledge of the wind field. Here we show an example of using CFOSAT observed wind field on January 16, 2022 with a spatial resolution of 12.5 km to estimate the corresponding *Hs*, see Figure 15, where Figure 15A is the wind scatterometer observed U_{10} (12.5 km spatial resolution, with the swath of 1000 km), Figure 15B the along-track *Hs* provided by the wave scatterometer with a spatial resolution of 1.5 km (Hauser et al., 2020) The model output significant wave height *Hs* is shown in Figure 15C. The spatial pattern for wave height is close to the one for wind speed. A comparison is made between CFOSAT observed along-track *Hs* (black dots) and the ones for model produced *Hs* (red dots) in Figure 15D. Similar meridional variations are found, the model results are close to the real observed ones for most latitudes, except for a small portion in low latitudes with a discrepancy around 0.5 m. The differences are acceptable for most regions when U_{10}≤12 m/s. Therefore, the model is suitable for moderate wind speeds to predict the instantaneous wave field. While the marine environment is complex, retrieved instantaneous wave height with the wind wave relation model may deviate systematically from the observations for the high-intensity wind speeds (figure not shown here). This systematical discrepancy is partially due to the underestimation of the high wind speed (Hauser et al., 2020). It might be corrected by either systematically checking the U_{10} dependent bias or using a machine learning based model when the accumulation of the CFOSAT data is enough in the future.

6 Conclusions

In summary, a probability-based swell and local wind-wave decomposition is proposed in this work, which does not require the knowledge of the wave spectrum information *a priori*. Its methodology is first illustrated by the joint probability analysis of a buoy collected wind and wave data, then validated by a comparison with the classical SEP analysis using wave spectra data. The new method is then applied to the 17-year JASON data to retrieve the spatial and seasonal patterns of the swell. Both spatial and temporal

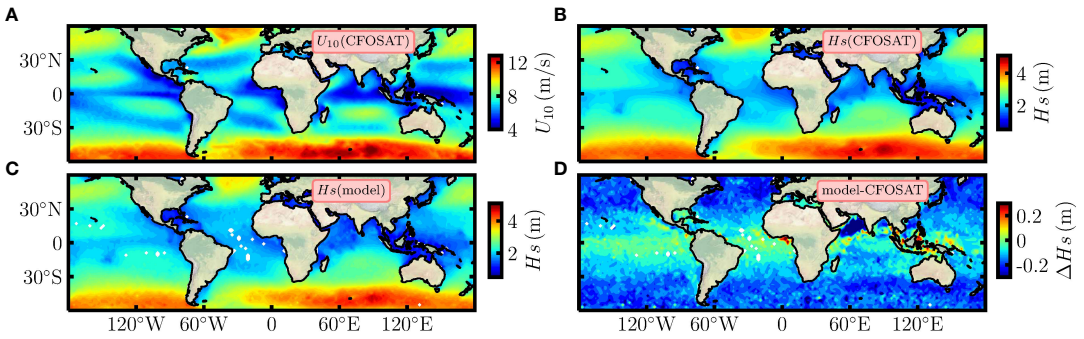

FIGURE 14
Annual average **(A)** U_{10} and **(B)** *Hs* from CFOSAT observation. **(C)** Wind-wave power-law model generated *Hs* based on annual average U_{10}. **(D)** The differences between model results and observations.

patterns agree well with the previous study by Semedo et al. (2011). In this work, two different local wind-wave decomposition approaches are proposed. The first one is a linear decomposition, and the other one is based on an energy conservation hypothesis. Comparisons of the identified wind-wave by the two methods are made. It is shown that the $\bar{H}s_{Le}(U_{10})$ extracted by the energy conservation based decomposition are close to the ones from SEP analysis, which can be explained by the fact that both are energy conserved approaches.

After the decomposition, a power-law formula of local significant wave height $\bar{H}s_L(U_{10})$ against the local wind speed U_{10}, e.g., $\bar{H}s_L(U_{10}) \propto U_{10}^{\beta}$, is advocated by relaxing the FDS hypothesis, where the scaling exponent β is treated as a free parameter. Global patterns of the derived β are presented for the first time. On average, the FDS hypothesis (with a scaling exponent equal to 2) might be satisfied in more than one-third of the oceans, according to the results derived by the linear decomposed $\bar{H}s_{Ll}(U_{10})$: mainly in the ACC region, and in the high latitude of the Northern Hemisphere in the boreal winter time, where a strong wind is present. The exponent is largely deviating from the FDS's prediction for the low latitude from 20°S to 20°N, where a weak wind is observed. On the contrary, the scaling exponents measured from the energy conserved approach $\bar{H}s_{Le}(U_{10}$ have relatively small values, with a most probable value of 1.45, which is not compatible with the FDS hypothesis.

Partially due to the influence of the monsoon and coverage of continents in the Northern Hemisphere, there is a strong seasonal variation for all parameters. For instance, in the Northern Hemisphere, the derived swell in JJA is much weaker than that in

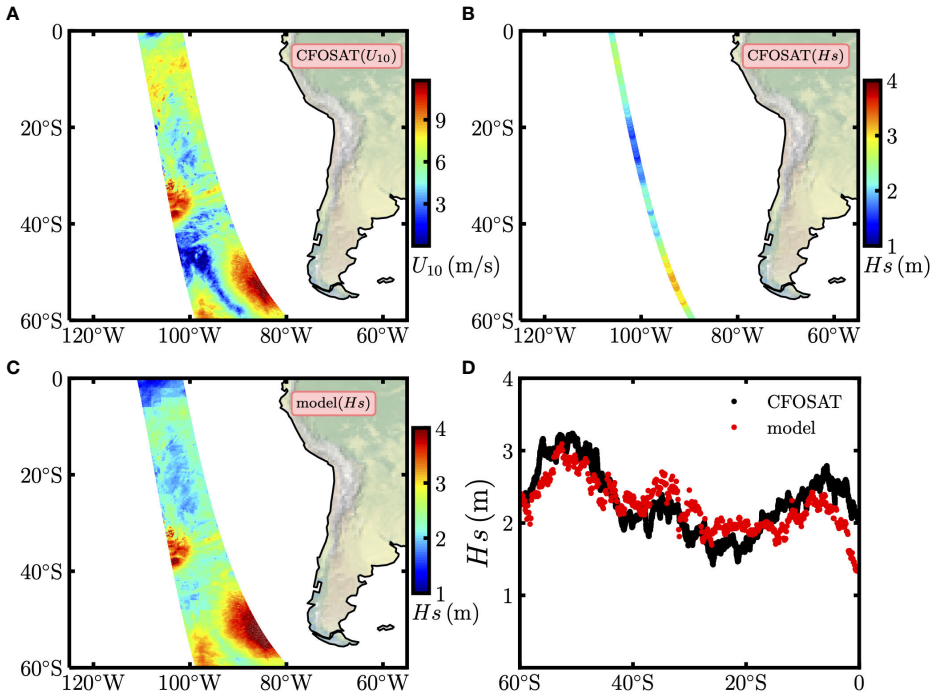

FIGURE 15
Simultaneously observed **(A)** U_{10} and **(B)** *Hs* by the CFOSAT on January 16, 2022. **(C)** Wind-wave power-law model predicted *Hs*. **(D)** The meridional variations for CFOSAT along-track *Hs* (black dots) and the corresponding model predicted *Hs* (red dots).

DJF (see Figure 7); the measured α in DJF is larger than the one in JJA (see Figure 9); the estimated β in JJA is larger than the one in DJF (see Figure 10). Furthermore, an exponential relation between the measured α and β is found, see Figure 13. A fine examination shows that the relation is latitudinal dependent, except for the boreal Summer case, and the exponent γ shows a linear decay from mid-latitudes to the equator, see Figure 13.

With the experimental wind wave relation in this work, a global view of $\bar{H}s$ can be obtained when only the wind speed is available. For example, with the annual average U_{10}, the corresponding global distribution of $\bar{H}s$ can be predicted, see Figure 14. The difference between the empirical model prediction and the so-called ground true value (e.g., the value provided by SWIM instrument of the CFOSAT satellite) is less than 0.3 m. Concerning instantaneous wave field prediction, the model output is quite accurate if the wind speed U_{10} is correctly measured. Therefore, it can be hoped that, in the near future, with the accumulation of the simultaneous collected wind and wave information by the CFOSAT project, wind and waves can be mutually corrected via a machine learning based approach.

This work provides an efficient approach to identify the swell and the local wind wave. With the accumulation of satellite data, the spatial and temporal features of swell will be more precise and the wind-wave relation will be further improved in the future. We would like to provide a comment on the physical mechanism associated with the wind-wave relation. As aforementioned, the exact mechanism is still a mystery (Pizzo et al., 2021): for instance, there is still no theoretical interpretation of the empirical relation by considering first-principles and the effect of swell. A fully convincing theoretical consideration of the swell and local wave is still to be found, and empirical results such as obtained here could be useful in a such framework.

Data availability statement

Publicly available datasets were analyzed in this study. This data can be found here: www.ndbc.noaa.gov, https://portal.aodn.org.au/.

Author contributions

FS, JH, and YH conceived and designed the experiments. YG and YH performed the experiments and data analysis. YG and YH drafted the original manuscript, and FS and YH revised and edited the manuscript. All authors contributed to the article and approved the submitted version.

Funding

This work was supported by the National Natural Science Foundation of China (91958203, U22A20579 and 11732010). This research has been performed in the frame of the MultiW2 project, funded by the CNES/TOSCA program. Funding of YG's Cotutella doctoral research project by Région Hauts-de-France and Xiamen University is acknowledged. YH is partially supported by State Key Laboratory of Ocean Engineering (Shanghai Jiao Tong University) (Grant No. 1910). A copy of Python codes to perform the analyses presented in this work can be found at https://github.com/lanlankai.

Conflict of interest

The authors declare that the research was conducted in the absence of any commercial or financial relationships that could be construed as a potential conflict of interest.

Publisher's note

All claims expressed in this article are solely those of the authors and do not necessarily represent those of their affiliated organizations, or those of the publisher, the editors and the reviewers. Any product that may be evaluated in this article, or claim that may be made by its manufacturer, is not guaranteed or endorsed by the publisher.

References

Andreas, E. L., and Wang, S. (2007). Predicting significant wave height off the northeast coast of the United States. *Ocean Eng.* 34, 1328–1335. doi: 10.1016/j.oceaneng.2006.08.004

Babanin, A. (2011). *Breaking and dissipation of ocean surface waves* (Cambridge, UK: Cambridge University Press).

Bretschneider, C. L. (1952). The generation and decay of wind waves in deep water. *EOS Trans. Am. Geophys. Union* 33, 381–389. doi: 10.1029/TR033i003p00381

Brown, G. (1977). The average impulse response of a rough surface and its applications. *IEEE Trans. Antennas Propagation* 25, 67–74. doi: 10.1109/TAP.1977.1141536

Carter, D. (1982). Prediction of wave height and period for a constant wind velocity using the JONSWAP results. *Ocean Eng.* 9, 17–33. doi: 10.1016/0029-8018(82)90042-7

Cavaleri, L., Abdalla, S., Benetazzo, A., Bertotti, L., Bidlot, J.-R., Breivik, ø., et al. (2018). Wave modelling in coastal and inner seas. *Prog. Oceanogr.* 167, 164–233. doi: 10.1016/j.pocean.2018.03.010

Chen, G., Chapron, B., Ezraty, R., and Vandemark, D. (2002). A global view of swell and wind sea climate in the ocean by satellite altimeter and scatterometer. *J. Atmos. Ocean. Technol.* 19, 1849–1859. doi: 10.1175/1520-0426(2002)019<1849:AGVOSA>2.0.CO;2

Collard, F. (2005). Algorithmes de vent et période moyenne des vagues JASON à base de réseaux de neurons. *Boost Technol.*

Csanady, G. T. (2001). *Air-sea interaction: laws and mechanisms* (Cambridge, UK: Cambridge University Press).

Donelan, M. A., Hamilton, J., and Hui, W. (1985). "Directional spectra of wind-generated ocean waves," *Philos. Trans. Roy. Soc. London* 315, 509–562. doi: 10.1098/rsta.1985.0054

Earle, M. (1984). *Development of algorithms for separation of sea and swell.* (Hancock County: National Data Buoy Center Tech Rep MEC-87-1) 53, 1–53.

Ebuchi, N., Graber, H. C., and Caruso, M. J. (2002). Evaluation of wind vectors observed by QuikSCAT/SeaWinds using ocean buoy data. *J. Atmos. Ocean. Technol.* 19, 2049–2062. doi: 10.1175/1520-0426(2002)019<2049:EOWVOB>2.0.CO;2

Evans, D., Conrad, C., and Paul, F. (2003). *Handbook of automated data quality control checks and procedures of the national data buoy center* (Stennis Space Center, USA: NOAA National Data Buoy Center Tech. Document, 03–02).

Faltinsen, O. (1990). Wave loads on offshore structures. *Annu. Rev. Fluid Mech.* 22, 35–56. doi: 10.1146/annurev.fl.22.010190.000343

Gao, Y., Schmitt, F. G., Hu, J. Y., and Huang, Y. X. (2021). Scaling analysis of the China France oceanography satellite along-track wind and wave data. *J. Geophys. Res. Oceans* 126, e2020JC017119. doi: 10.1029/2020JC017119

Gerling, T. W. (1992). Partitioning sequences and arrays of directional ocean wave spectra into component wave systems. *J. Atmos. Ocean. Technol.* 9, 444–458. doi: 10.1175/1520-0426(1992)009<0444:PSAAOD>2.0.CO;2

Gilhousen, D. B., and Hervey, R. (2002). "Improved estimates of swell from moored buoys," in *Ocean wave measurement and analysis 2001* (Alexandria, VA, ASCE), 387–393.

Goda, Y. (1997). Directional wave spectrum and its engineering applications. *Adv. Coast. Ocean Eng.* 3, 67–102. doi: 10.1142/9789812797568_0003

Gourrion, J., Vandemark, D., Bailey, S., Chapron, B., Gommenginger, G., Challenor, P., et al. (2002). A two-parameter wind speed algorithm for Ku-band altimeters. *J. Atmos. Ocean. Technol.* 19, 2030–2048. doi: 10.1175/1520-0426(2002)019<2030:ATPWSA>2.0.CO;2

Gulev, S. K., Cotton, D., and Sterl, A. (1998). Intercomparison of the north Atlantic wave climatology from voluntary observing ships, satellite data and modelling. *Phys. Chem. Earth* 23, 587–592. doi: 10.1016/S0079-1946(98)00075-5

Gulev, S. K., and Grigorieva, V. (2006). Variability of the winter wind waves and swell in the north Atlantic and north Pacific as revealed by the voluntary observing ship data. *J. Clim.* 19, 5667–5685. doi: 10.1175/JCLI3936.1

Hanson, J. L., and Jensen, R. E. (2004). "Wave system diagnostics for numerical wave models," in *8th international workshop on wave hindcasting and forecasting* (Oahu, Hawaii: Citeseer), 231–238.

Hanson, J. L., and Phillips, O. M. (2001). Automated analysis of ocean surface directional wave spectra. *J. Atmos. Ocean. Technol.* 18, 277–293. doi: 10.1175/1520-0426(2001)018<0277:AAOOSD>2.0.CO;2

Hasselmann, K., Barnett, T. P., Bouws, E., Carlson, H., Cartwright, D. E., Enke, K., et al. (1973). "Measurements of wind-wave growth and swell decay during the joint north Sea wave project (JONSWAP)," *Dtsch. Hydrog. Z. Suppl. A 8.95* (Hamburg, Germany), pp. 8–12.

Hauser, D., Tourain, C., Hermozo, L., Alraddawi, D., Aouf, L., Chapron, B., et al. (2020). "New observations from the SWIM radar on-board CFOSAT: Instrument validation and ocean wave measurement assessment," *IEEE Trans. Geosci. Remote Sens.* 59, 5-26. doi: 10.1109/TGRS.2020.2994372

Heimbach, P., Hasselmann, S., and Hasselmann, K. (1998). Statistical analysis and intercomparison of WAM model data with global ERS-1 SAR wave mode spectral retrievals over 3 years. *J. Geophys. Res. Oceans* 103, 7931–7977. doi: 10.1029/97JC03203

Holthuijsen, L. H. (2007). *Waves in oceanic and coastal waters* (Cambridge, UK: Cambridge University Press). doi: 10.1017/CBO9780511618536

Huang, Y., Schmitt, F., Lu, Z., and Liu, Y. (2008). An amplitude-frequency study of turbulent scaling intermittency using Hilbert spectral analysis. *Europhys. Lett.* 84, 40010. doi: 10.1209/0295-5075/84/40010

Hwang, P. A., Ocampo-Torres, F. J., and García-Nava, H. (2012). Wind sea and swell separation of 1D wave spectrum by a spectrum integration method. *J. Atmos. Ocean. Technol.* 29, 116–128. doi: 10.1175/JTECH-D-11-00075.1

Jones, I. S., and Toba, Y. (2001). *Wind stress over the ocean* (Cambridge, UK: Cambridge University Press).

Liu, J., Lin, W., Dong, X., Lang, S., Yun, R., Zhu, D., et al. (2020). First results from the rotating fan beam scatterometer onboard CFOSAT. *IEEE Trans. Geosci. Remote Sens.* 58, 8793–8806. doi: 10.1109/TGRS.2020.2990708

Liu, Y., Li, S., Yi, Q., and Chen, D. (2017). Wind profiles and wave spectra for potential wind farms in South China Sea. part II: Wave spectrum model. *Energies* 10, 127. doi: 10.3390/en10010127

Pandey, P., Gairola, R., and Gohil, B. (1986). Wind-wave relationship from SeaSat radar altimeter data. *Bound.-Layer Meteorol.* 37, 263–269. doi: 10.1007/BF00122988

Pierson, J. W.J. (1991). Comment on "Effects of sea maturity on satellite altimeter measurements" by Roman e. glazman and Stuart h. pilorz. *J. Geophys. Res. Oceans* 96, 4973–4977. doi: 10.1029/90JC02532

Pierson, W. J., and Marks, W. (1952). The power spectrum analysis of ocean-wave records. *EOS Trans. Am. Geophys. Union* 33, 834–844. doi: 10.1029/TR033i006p00834

Pierson, J. W.J., and Moskowitz, L. (1964). A proposed spectral form for fully developed wind seas based on the similarity theory of S.A. kitaigorodskii. *J. Geophys. Res.* 69, 5181–5190. doi: 10.1029/JZ069i024p05181

Pizzo, N., Deike, L., and Ayet, A. (2021). How does the wind generate waves? *Phys. Today* 74, 38–43. doi: 10.1063/PT.3.4880

Portilla, J., Ocampo-Torres, F. J., and Monbaliu, J. (2009). Spectral partitioning and identification of wind sea and swell. *J. Atmos. Ocean. Technol.* 26, 107–122. doi: 10.1175/2008JTECHO609.1

Portilla-Yandún, J. (2018). The global signature of ocean wave spectra. *Geophys. Res. Lett.* 45, 267–276. doi: 10.1002/2017GL076431

Quentin, C. G. (2002). Study of the ocean surface, its radar signature and its interactions with turbulent momentum fluxes within the framework of the FETCH experiment. Ph.D. thesis, université Pierre and Marie curie-Paris VI.

Resio, D., Swail, V. R., Jensen, R. E., and Cardone, V. J. (1999). Wind speed scaling in fully developed seas. *J. Phys. Oceanogr.* 29, 1801–1811. doi: 10.1175/1520-0485(1999)029<1801:WSSIFD>2.0.CO;2

Ribal, A., and Young, I. R. (2019). 33 years of globally calibrated wave height and wind speed data based on altimeter observations. *Sci. Data* 6, 1–15. doi: 10.1038/s41597-019-0083-9

Romeiser, R. (1993). Global validation of the wave model WAM over a one-year period using geosat wave height data. *J. Geophys. Res. Oceans* 98, 4713–4726. doi: 10.1029/92JC02258

Rossby, C.-G., and Montgomery, R. B. (1935). The layer of frictional influence in wind and ocean currents. *Pap. Phys. Oceanogr. Meteor.* 3, 1935-1904. doi: 10.1575/1912/1157

Rusu, L., Bernardino, M., and Guedes Soares, C. (2014). Wind and wave modelling in the Black Sea. *J. Oper. Oceanogr.* 7, 5–20. doi: 10.1080/1755876X.2014.11020149

Semedo, A., Sušelj, K., Rutgersson, A., and Sterl, A. (2011). A global view on the wind sea and swell climate and variability from ERA-40. *J. Clim.* 24, 1461–1479. doi: 10.1175/2010JCLI3718.1

Semedo, A., Vettor, R., Breivik, Ø., Sterl, A., Reistad, M., Soares, C. G., et al. (2015). The wind sea and swell waves climate in the Nordic Seas. *Ocean Dyn.* 65, 223–240. doi: 10.1007/s10236-014-0788-4semedo2015wind

Sugianto, D. N., Zainuri, M., Darari, A., Suripin, S., Darsono, S., and Yuwono, N. (2017). Wave height forecasting using measurement wind speed distribution equation in Java Sea, Indonesia. *Int. J. Civ. Eng. Technol.* Vol. 8, 604–619.

Takbash, A., Young, I. R., and Breivik, Ø. (2019). Global wind speed and wave height extremes derived from long-duration satellite records. *J. Clim.* 32, 109–126. doi: 10.1175/JCLI-D-18-0520.1

Toba, Y. (1972). Local balance in the air-sea boundary processes. *J. Oceanogr.* 28, 109–120. doi: 10.1007/BF02109772

Tucker, M. J., and Pitt, E. G. (2001). *Waves in ocean engineering* Vol. 5 (Amsterdam: Elsevier).

Villas Bôas, A. B., Ardhuin, F., Ayet, A., Bourassa, M. A., Brandt, P., Chapron, B., et al. (2019). Integrated observations of global surface winds, currents, and waves: Requirements and challenges for the next decade. *Front. Mar. Sci.* 6 425. doi: 10.3389/fmars.2019.00425

WAMDI Group (1988). The WAM model–a third generation ocean wave prediction model. *J. Phys. Oceanogr.* 18, 1775–1810. doi: 10.1175/1520-0485(1988)018<1775:TWMTGO>2.0.CO;2

Wang, D., and Gilhousen, D. (1998). "Separation of seas and swells from NDBC buoy wave data," in *Fifth int. workshop on wave hindcasting and forecasting* (Florida, FL, ASCE: Environment Canada Melbourne), 155–162.

Wang, D. W., and Hwang, P. A. (2001). An operational method for separating wind sea and swell from ocean wave spectra. *J. Atmos. Ocean. Technol.* 18, 2052–2062. doi: 10.1175/1520-0426(2001)018<2052:AOMFSW>2.0.CO;2

Wen, S. C. (1960). Generalized wind wave spectra and their applications. *Scientia Sin.* 9, 377–402. doi: 10.1360/ya1960-9-3-377wen1960generalized

Wu, J. (1968). Laboratory studies of wind–wave interactions. *J. Fluid Mech.* 34, 91–111. doi: 10.1017/S0022112068001783

Young, I. R. (1998). Observations of the spectra of hurricane generated waves. *Ocean Eng.* 25, 261–276. doi: 10.1016/S0029-8018(97)00011-5

Young, I. R., and Donelan, M. (2018). On the determination of global ocean wind and wave climate from satellite observations. *Remote Sens. Environ.* 215, 228–241. doi: 10.1016/j.rse.2018.06.006

Young, I. R., and Ribal, A. (2019). Multiplatform evaluation of global trends in wind speed and wave height. *Science* 364, 548–552. doi: 10.1126/science.aav9527

Young, I. R., and Verhagen, L. (1996). The growth of fetch limited waves in water of finite depth. part 2. Spectral evolution. *Coast. Eng.* 29, 79–99. doi: 10.1016/S0378-3839(96)00007-5

Zhang, F. W., Drennan, W. M., Haus, B. K., and Graber, H. C. (2009). On wind-wave-current interactions during the shoaling waves experiment. *J. Geophys. Res. Oceans*, 114. doi: 10.1029/2008JC004998

Zheng, K., Sun, J., Guan, C., and Shao, W. (2016). Analysis of the global swell and wind sea energy distribution using WAVEWATCH III. *Adv. Meteorol.* 2016, 8419580. doi: 10.1155/2016/8419580

Zieger, S., Babanin, A. V., Rogers, W. E., and Young, I. R. (2015). Observation-based source terms in the third-generation wave model WAVEWATCH. *Ocean Model.* 96, 2–25. doi: 10.1016/j.ocemod.2015.07.014

frontiers | Frontiers in Marine Science

TYPE Original Research
PUBLISHED 03 March 2023
DOI 10.3389/fmars.2023.1126088

OPEN ACCESS

EDITED BY
Zhiyu Liu,
Xiamen University, China

REVIEWED BY
Chunyan Li,
Louisiana State University, United States
Shuang-Xi Guo,
South China Sea Institute of Oceanology (CAS), China

*CORRESPONDENCE
Ying-Tien Lin
kevinlin@zju.edu.cn

SPECIALTY SECTION
This article was submitted to Physical Oceanography, a section of the journal Frontiers in Marine Science

RECEIVED 17 December 2022
ACCEPTED 21 February 2023
PUBLISHED 03 March 2023

CITATION
Yuan Y, Tan X and Lin Y-T (2023) Effect of sloping bottom on river plume dynamics on a laboratory-scale rotating table. *Front. Mar. Sci.* 10:1126088. doi: 10.3389/fmars.2023.1126088

Effect of sloping bottom on river plume dynamics on a laboratory-scale rotating table

Yeping Yuan, Xinyu Tan and Ying-Tien Lin*

Ocean College, Zhejiang University, Zhoushan, China

In nature, plumes usually enter the coastal ocean after they leave the estuary, and most of them interact with the continental shelf slope. To understand plume dynamics, laboratory experiments were carried out on a rotating table to simulate the evolution of plumes over a sloping bottom. We modified reduced gravity g', Coriolis parameter f, and shelf slope α to study their impacts on plume characteristics and freshwater fate, and used the optical thickness method to obtain the depth field. We found that with the increasing g' or decreasing f, plume maximum depth h_{max} decreases and plume maximum width W_{max} increases. We proposed a method to determine plume types based on their attachment to the shelf slope: when PCN (plume classification number) > 1.6, the plume is bottom-attached; when PCN< 1.6, the plume is surface-advected. In addition, we found the bulge will become unstable when BIN (bulge instability number)< 0.8. Our analysis shows that the sloping bottom is the most significant factor determining the ratio of freshwater accumulated in the bulge over transported with coastal currents. Generally, bottom-attached plume trapped near the coast inhibits offshore freshwater transport and promotes coastal current transport, while baroclinic instability tends to produce a large cyclonic vortex over a gentle slope which strongly enhances the offshore transport.

KEYWORDS

river plume, bottom attachment, bulge instability, plume classification, freshwater transport, laboratory experiments, rotating table

1 Introduction

Rivers issue into the coastal ocean as tidally modulated pulses of fresh water, which carry more than one-third of land-based precipitation to the ocean (Nash and Moum, 2005). They transport and transform the buoyant freshwater in the region around the river mouth as it merges with deeper, salty ocean waters, which makes terrigenous material carried by rivers affect coastal waters (Fasullo et al., 2007). The river plume is a low salinity water formed in the coastal area after the freshwater flows out of the estuary, generating recirculating bulge near the estuary, and then continuously propagating along the continental shelf as a buoyant coastal current (Dzwonkowski and Yan, 2005). In this process, the transport and mixing of plumes play an essential role in the vertical mixing of

water, sediment, temperature, and salinity (Lohan and Bruland, 2006). For example, the Yangtze River exports massive loadings of freshwater, sediments, and nutrients that significantly alter the hydrodynamics, turbidity, and nutrient composition in its area of influence (Chang and Isobe, 2003; Zhang et al., 2013). The massive nutrient brought from upstream of the Yangtze River causes severe eutrophication in the plume area, which seriously endangers the coastal ocean environment (Wang, 2006). Therefore, studying river plumes on their structure and freshwater transport has great ecological and social significance.

Under ideal conditions, a plume can be separated into two dynamically distinct regions: a bulge region near the river mouth and an alongshore coastal current propagating in the downstream direction (in the Kelvin wave sense) (O'Donnell, 1990; Chen, 2014). The plume expands in the direction of propagation of the coastally trapped waves after the freshwater release. The intrusion speed inside the estuary is consistently higher than that along the shelf. Energy is therefore accumulated near the estuary mouth, forming a bulge (Chao and Boicourt, 1986). In the bulge region, the plume forms an anticyclonic vortex (Northern Hemisphere) under the low wind and low ambient current condition, which has been confirmed in the observation of Columbia River (Horner-Devine et al., 2009) or Hudson River (Dzwonkowski and Yan, 2005). Many studies have been carried out on the geometric characteristic (Fong and Geyer, 2002), freshwater retention (Horner-Devine et al., 2006; Yuan et al., 2018), and stability (Avicola and Huq, 2003) of the bulge under different inflow conditions and environmental factors. They found that the bulge shape was related to the inflow condition, Coriolis force and ambient flow. And the bulge accumulated 60 – 70% of the freshwater discharge, and the baroclinic instability can increase freshwater accumulation (Avicola and Huq, 2003). In coastal currents, buoyant water forming a coastal current continues to propagate far from the mouth, such as Chesapeake Bay (Rennie et al., 1999) and Delaware Bay (Sanders and Garvine, 1996). Previous theoretical studies have found that coastal current transport is also related to inflow conditions, Coriolis force, and external forcing agents (Nof and Pichevin, 2001; Fong and Geyer, 2002). Some studies mentioned the spread of freshwater transport in coastal currents, which accounts for 27 – 77% of the river discharge (Nof and Pichevin, 2001; Chen, 2014). There are many previous studies on buoyancy flow transport on the sloping bottom, but these are less about both bulge and coastal current transport.

In nature, plumes usually enter the continental shelf after the estuary outflow and interact with the bottom shelf. According to the contact between the bottom and the front shown in the density field, Chapman and Lentz (1994) divided the plume into surface-advected (Figure 1A) and bottom-attached (Figure 1B). Surface-advected plume is characterized by shallow plume thickness and retention on the surface, generally associated with a strong vertical stratification (Garvine, 1974). Typically, surface-advected plumes are strongly affected by ambient flows, winds, and tides, while they are not appreciably influenced by the bottom topography. One classic example of surface-advected plume is the Mississippi River plume, where a vital stratification region leads to an anoxic lower layer, forming a famous "Dead Zone" (Rabalais et al., 2002). On the other hand, the bottom-attached plume creates a strong horizontal density gradient with a surface-to-bottom density front separating the freshwater from the shelf water (Blanton, 1981; Münchow and Garvine, 1993). These plumes generate the offshore flow of freshwater in the frictional bottom boundary layer, thereby altering the density and velocity fields. Terrestrial materials, including sediments, nutrients, and organic matter, are transported in both along-shelf and cross-shelf directions (Wu and Wu, 2018). One classic example of bottom-attached plume is the Niagara River plume, which is Lake Ontario's principal source of suspended and dissolved material (Mudroch, 1983). Examination

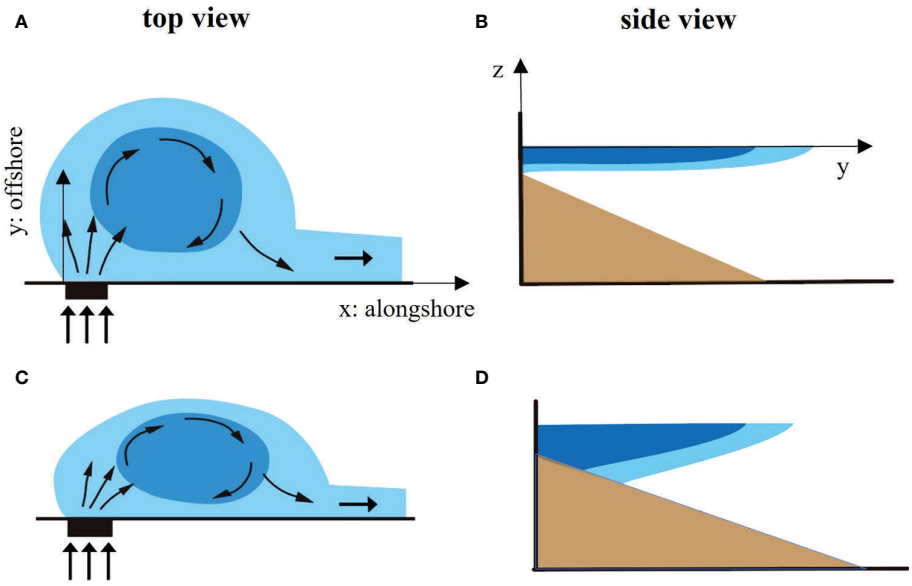

FIGURE 1
Schematic of a surface-advected plume (**A**: top view and **B**: side view) and a bottom-attached plume (**C**: top view and **D**: side view).

of bottom sediments in Lake Ontario has pinpointed the river as a major source of contaminants (Thomas, 1983). Bottom-attached plumes profoundly influence shelf circulation and coastal ecosystem health, so studying them is of great practical significance. According to field observations, plume types can change according to environmental factors. The Niagara plume changes into a surface-advected plume when the density difference between the plume and ambient water increases to 0.9 kg m^{-3} (Masse and Murthy, 1992). The Hudson River is a bottom-attached plume during spring tides but is surface-advected during neap tides (Hunter et al., 2010). The Delaware plume is bottom-attached and controlled by the continental slope during most of the year, while it becomes surfaced-advected during the spring freshet (Münchow and Garvine, 1993).

Extensive studies have proposed different non-dimensional parameters to distinguish among plume types. Yankovsky and Chapman (1997) classified the plume type by comparing the ratio of the buoyant inflow depth H_0 and the equilibrium depth h_g, and the ratio of the maximum seaward expansion of the surface-advected plume y_S and the offshore location of the bottom-attached plume y_b. The surface-advected plume forms when $h_g < H_0$, while the bottom-attached plume appears when $h_g > H_0$ and $y_b > y_S$. The intermediate plume is produced when $h_g > H_0$ and $0 < y_b < y_S$, which has features with both surface-advected and bottom-attached plumes. Yankovsky and Chapman (1997) defined whether a discharge is surface-advected or bottom-attached simply by the comparison between h_g and H_0. Lentz and Helfrich (2002) proposed a non-dimensional parameter c_w/c_α representing the response of buoyant flow to categorize plume type, where c_w is the propagation speed in limit of a steep bottom slope and c_α is the propagation speed in limit of a small bottom slope. The surface-advected plume forms when $c_w/c_\alpha << 1$, while the bottom-attached plume occurs when $c_w/c_\alpha >> 1$. Avicola and Huq (2001) suggested two non-dimensional parameters: the ambient depth parameter, h_g/H, where the ambient ocean depth H is defined as the depth of the fluid column at one Rossby radius L_b offshore, and the bottom slope parameter, L_b/y_b to distinguish the characteristics of coastal current (Avicola and Huq, 2001). Because of the different inflow conditions, Yankovsky and Chapman (1997) and Avicola and Huq (2001) mainly focused on the bulge region, and the method proposed by Lentz and Helfrich (2002) is mainly used to distinguish types of coastal currents. Based on their judgment criteria, we made modifications and proposed new criteria suitable for plume classification in our experiments, which will be discussed in detail in section 3.1.

Previous studies on surface-advected and bottom-attached plumes are mostly separated. For the surface-advected plume, previous researchers paid more attention to the bulge, studied the geometric characteristics, and proved that the bulge shape was related to the Rossby number Ro and Froude number Fr. Fong and Geyer (2002) suggested that the larger Ro and the offshore dimension relative to the alongshore scale cause the smaller quantity of fluid intercepted by the coastal current. Horner-Devine et al. (2006) concluded that coastal current transport will decrease for larger Fr and Ro. When they are large, the bulge forms a more complete circle and discharges less fluid into the coastal current. Yuan et al. (2018) observed high and low discharge plumes as circular and compressed plume structures by simulating the effects of periodically varying discharge on buoyant coastal plumes. For the bottom-attached plume, the continental shelf is usually simplified as a continuous sloping bottom in laboratory experiments under ideal conditions. Chapman and Lentz (1994) numerically studied the bottom-attached buoyancy flow. They found that due to the influence of bottom friction, the along-slope flow of the front drives an offshore transport in the bottom Ekman layer that widens the buoyancy flow until the vertically sheared, geostrophic flow at the density front separating the buoyant and ambient fluid is zero at the bottom. Based on the theory, buoyancy flow reaches a geostrophic equilibrium and stops spreading offshore, suppressing the circular bulge. Some experiments showed the effect of the sloping bottom on plume characteristics and offshore transport. Lentz and Helfrich (2002) found that there is no prominent bulge near the estuary for bottom-attached plumes. The buoyancy flow is weaker near the coast than the surface-advected plume and increases with distance offshore. Avicola and Huq (2001) found that coastal currents of the bottom-attached plume experience lateral compression because of the bottom friction and tend to be faster and narrower than the surface-advected plume. Some studies focus on the effect of slope on alongshore transport. Garvine (1999) found that the downshelf penetration decreases for increased slope due to the freshwater transport offshore through the numerical model. Garvine (1999) and Brasseale and MacCready (2021) both found that gentle slope promotes alongshore transport. In Brasseale and MacCready (2021), the shelf slope were set as 2×10^{-3} for steep slope case and 5×10^{-4} for gentle slope case. Due to the limitations of laboratory experiments, we cannot make such a gentle slope to simulate the real continental shelf. We also set two variations on the shelf slope [steep slope ($\alpha = 0.2$) and gentle slope ($\alpha = 0.1$)] to study the effect of changing the slope on the plume and provide a reference for future research.

In summary, the previous studies focused on the surface-advected plume and the bottom-attached plume respectively, but the formation mechanism, critical conditions and coastal current transport under different classifications of two plume types need to be systematically investigated, especially the influence of sloping bottom on freshwater transport needs further study. In this study, we aim to investigate the effect of sloping bottom on plumes and analyze the impact of the reduced gravity g', Coriolis parameter f, and shelf slope α on plume types and freshwater transport, and laboratory experiments on a rotating platform were carried out. We set up cameras on the top and side of the platform to obtain images and used the optical thickness method to estimate the depth field, which was used to calculate the width and depth of bulge, bulge volume and coastal current transport. The remainder of this paper is organized as follows. In section 2, we describe the experimental device, detailed conditions and data processing methods. The results and a discussion are given in section 3 and section 4, and concluding remarks are presented in section 5.

2 Method

2.1 Experimental setup

The experiments were carried out on a rotating table with a size of 3m × 3m × 0.5m in the Geophysical Fluid Dynamics Laboratory

of Zhejiang University (Figure 2A). The experimental tank forms a circular experimental area, and a wall across one side forms the coastal wall. The bottom with a triangular section is used to simulate a continental shelf, and its top is attached to the estuary gate (Figure 2B).

The freshwater of density ρ_0 is used to simulate river injection in the estuary, which is marked using small concentrations of dye to facilitate flow visualization. At the preparation stage, the tank filled with salt water of density ρ_a to simulate seawater was rotated for at least 4 hours to achieve solid body rotation. During the experiments, the freshwater was pumped into the estuary with discharge Q, and the gate was opened simultaneously to produce the plume. During the whole process, the CCD camera installed atop was used to capture the top-view image (Figure 2C), and the Gopro was set up on the side to acquire side-view images (Figure 2D).

2.2 Experiment procedure

Before the experiments, the empty calibration tank was fixed on the coastal wall and filled with dyed freshwater (Figures 3A, B). Then the top-view camera took an image for calibration. Finally, we obtained the relationship between normalized image intensity and depth (Figure 3C), so that the depth field can be calculated using the exponential relationship: $I/I_0=Ae^{-hB}+C$, where constants A, B and C will be determined in the calibration program (Yuan et al., 2010). The background intensity I_0 is the reference image captured just before the dyed freshwater is injected into the tank. Image intensity is the gray value of the image at each pixel obtained by MATLAB program.

The video recorded by CCD camera (Figure 2C) was converted into sequence pictures, and the color pictures were transformed into gray images. The side-view images taken by the Gopro were used to determine if the plume contacts the bottom in real-time, which can be compared with the depth field taken by the overhead camera for verification (Figure 2D).

The bulge structure and coastal current transport of the plume are mainly controlled by two parameters: Rossby number Ro and Froude number Fr (Horner-Devine et al., 2006). We maintained the width (W_0 = 8 cm) and height (H_0 = 2 cm) of the estuary constant and changed the rotation period T, reduced gravity g' and shelf slope α (Table 1). We use non-dimensional parameters:

$$\mathbf{Ro} = U/fW \tag{1}$$

$$\mathbf{Fr} = U/(g' H_0)^{1/2} \tag{2}$$

where U is the inflow velocity, H_0 is the initial inflow depth, W_0 is the estuary width, $g'=g(\rho_a-\rho_0)/\rho_0$ is the reduced gravity, ρ_a is the ambient fluid density, ρ_0 is the inflow freshwater density.

3 Results

3.1 Plume classification

In our experiments, we focused on the influence of the sloping bottom. According to the contact between the bottom and the plume, we divided plumes into three types: surface-advected plumes, bottom-attached plumes, and transitional plumes. Figures 4A–F show the section at the maximum depth of the

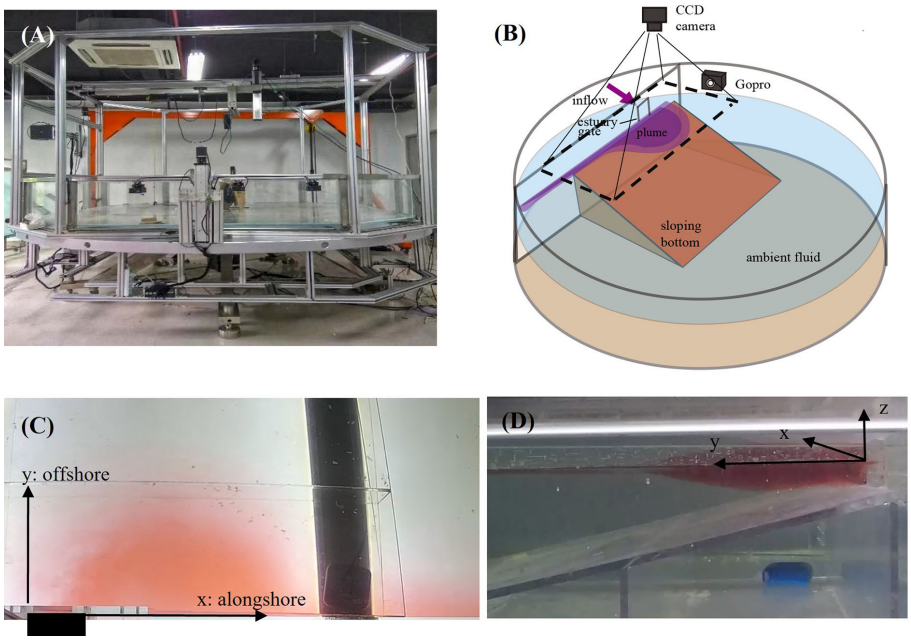

FIGURE 2
Schematic of the experimental setup. **(A)** Photo of the rotating table. **(B)** The setup of the cameras and bottom slope over the circular flume, **(C)** and **(D)** show the field of view captured by the top-mounted CCD camera and the side-mounted Gopro, respectively.

10.3389/fmars.2023.1126088

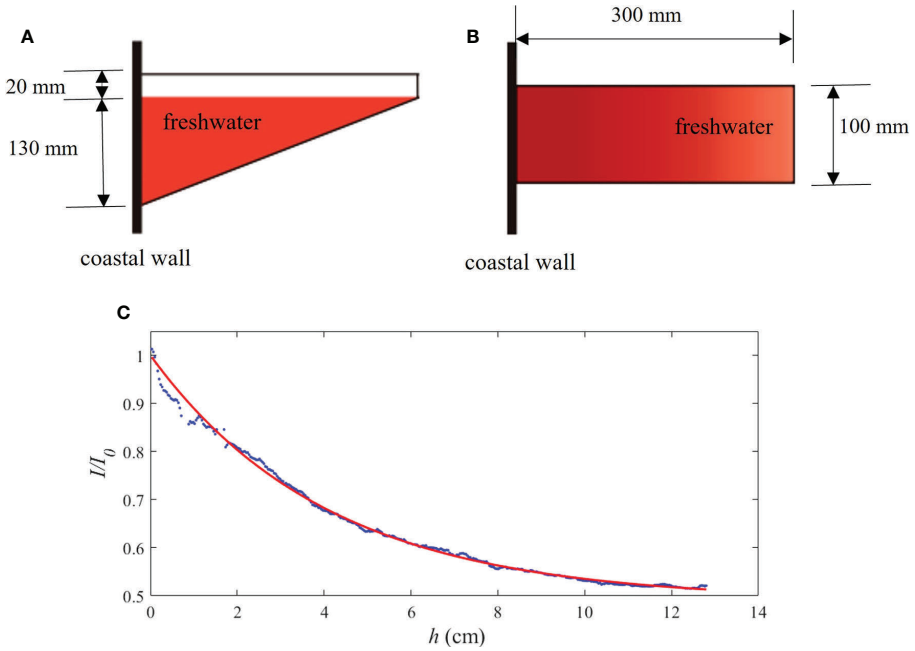

FIGURE 3
The calibration tank and normalized intensity-depth relationship. **(A)** Schematic of the calibration tank viewed from the side. **(B)** Schematic of the calibration tank viewed from above. **(C)** Relationship curve between normalized image intensity I/I_0 and depth h. Blue circles indicate data points; the solid red line is the fitted curve.

TABLE 1 Experimental conditions and parameters.

Run	α	Q (cm^3/s)	ρ_a (g/cm^3)	ρ_0 (g/cm^3)	g' (cm/s^2)	T (s)	W_0 (cm)	H_0 (cm)	Ro	Fr
1	–	50	1.003860	0.999701	4.06	20	8	2	0.62	1.10
2	–	50	1.003630	0.999531	4.00	30	8	2	0.93	1.10
3	–	50	1.003579	0.999510	3.97	40	8	2	1.24	1.11
4	–	50	1.003617	0.999503	4.02	50	8	2	1.56	1.10
5	–	50	1.003696	0.999596	4.00	60	8	2	1.87	1.10
6	0.2	50	1.004178	1.000021	4.06	20	8	2	0.62	1.10
7	0.2	50	1.003665	0.999524	4.04	30	8	2	0.93	1.10
8	0.2	50	1.003650	0.999535	4.02	40	8	2	1.24	1.10
9	0.2	50	1.003560	0.999535	3.93	50	8	2	1.56	1.11
10	0.2	50	1.003522	0.999456	3.97	60	8	2	1.87	1.11
11	0.2	50	1.004211	0.998638	5.44	20	8	2	0.62	0.95
12	0.2	50	1.004400	0.998733	5.53	30	8	2	0.93	0.94
13	0.2	50	1.004208	0.998668	5.41	40	8	2	1.24	0.95
14	0.2	50	1.004243	0.998568	5.54	50	8	2	1.56	0.94
15	0.2	50	1.004149	0.998509	5.50	60	8	2	1.87	0.94
16	0.2	50	1.005655	0.998444	7.03	20	8	2	0.62	0.83
17	0.2	50	1.005664	0.998484	7.00	30	8	2	0.93	0.84

(Continued)

TABLE 1 Continued

Run	α	Q (cm^3/s)	ρ_a (g/cm^3)	ρ_0 (g/cm^3)	g' (cm/s^2)	T (s)	W_0 (cm)	H_0 (cm)	Ro	Fr
18	0.2	50	1.004660	0.997494	7.00	40	8	2	1.24	0.84
19	0.2	50	1.004498	0.997422	6.90	50	8	2	1.56	0.84
20	0.2	50	1.004631	0.997439	7.02	60	8	2	1.87	0.83
21	0.2	50	1.007647	0.997293	10.07	20	8	2	0.62	0.70
22	0.2	50	1.007514	0.997167	10.06	30	8	2	0.93	0.70
23	0.2	50	1.007220	0.997100	9.85	40	8	2	1.24	0.70
24	0.2	50	1.007376	0.997105	10.00	50	8	2	1.56	0.70
25	0.2	50	1.007531	0.997182	10.07	60	8	2	1.87	0.70
26	0.1	50	1.004858	1.000820	3.94	20	8	2	0.62	1.11
27	0.1	50	1.004929	1.000872	3.96	30	8	2	0.93	1.11
28	0.1	50	1.004858	1.000751	4.01	40	8	2	1.24	1.10
29	0.1	50	1.004891	1.000782	4.01	50	8	2	1.56	1.10
30	0.1	50	1.004977	1.000937	3.94	60	8	2	1.87	1.11
31	0.1	50	1.007353	1.001635	5.56	20	8	2	0.62	0.94
32	0.1	50	1.007236	1.001590	5.49	30	8	2	0.93	0.94
33	0.1	50	1.007150	1.001550	5.45	40	8	2	1.24	0.95
34	0.1	50	1.007187	1.001537	5.50	50	8	2	1.56	0.94
35	0.1	50	1.007317	1.001686	5.48	60	8	2	1.87	0.94
36	0.1	50	1.005252	0.998047	7.02	20	8	2	0.62	0.83
37	0.1	50	1.005242	0.998095	6.97	30	8	2	0.93	0.84
38	0.1	50	1.004917	0.997900	6.84	40	8	2	1.24	0.84
39	0.1	50	1.005001	0.998010	6.82	50	8	2	1.56	0.85
40	0.1	50	1.005184	0.998067	6.94	60	8	2	1.87	0.84
41	0.1	50	1.011089	1.000667	10.10	20	8	2	0.62	0.70
42	0.1	50	1.010825	1.000545	9.97	30	8	2	0.93	0.70
43	0.1	50	1.010704	1.000474	9.92	40	8	2	1.24	0.70
44	0.1	50	1.011370	1.000956	10.09	50	8	2	1.56	0.70
45	0.1	50	1.010950	1.000643	9.99	60	8	2	1.87	0.70

bulge, from which we can see the obvious boundary between freshwater and ambient water, similar to the plume front observed in the field (O'Donnell et al., 1998). We determined the plume type depending on whether the plume is in contact with the bottom.

Surface-advected plumes spread far offshore and have no contact with the bottom. In this case, a buoyant inflow primarily remains on top of the shelf water forming a thin layer with the ambient denser water beneath (Figures 4A–C). On the other hand, bottom-attached plumes have been in contact with the bottom during the whole process. In this case, the plume occupies the entire water column into depths much greater than the depth of the inflow (Figures 4D–F). Transitional plumes contact with the bottom at the beginning but eventually do not touch the bottom over time. Thus, the plume has properties like the bottom-attached plume at the beginning but eventually behaves more like a surface-advected plume. This plume is different from the intermediate plume proposed by Yankovsky and Chapman (1997), which is in contact with the bottom during the whole process. Transitional plumes are not the focus of our study.

As shown in Figures 4G–L, we can clearly distinguish the two main components of a typical plume from the depth field: the bulge region and the coastal current region (Horner-Devine et al., 2006; Yuan et al., 2018). The central vortex structure is established at t = 3T, and the coastal current begins to form along the wall by the end of the third period (Figures 4G, J). From 3T to 6T, the coastal current proceeds further along the shore, and both the bulge and the coastal current grow in the offshore direction (Figures 4H, K). From

10.3389/fmars.2023.1126088

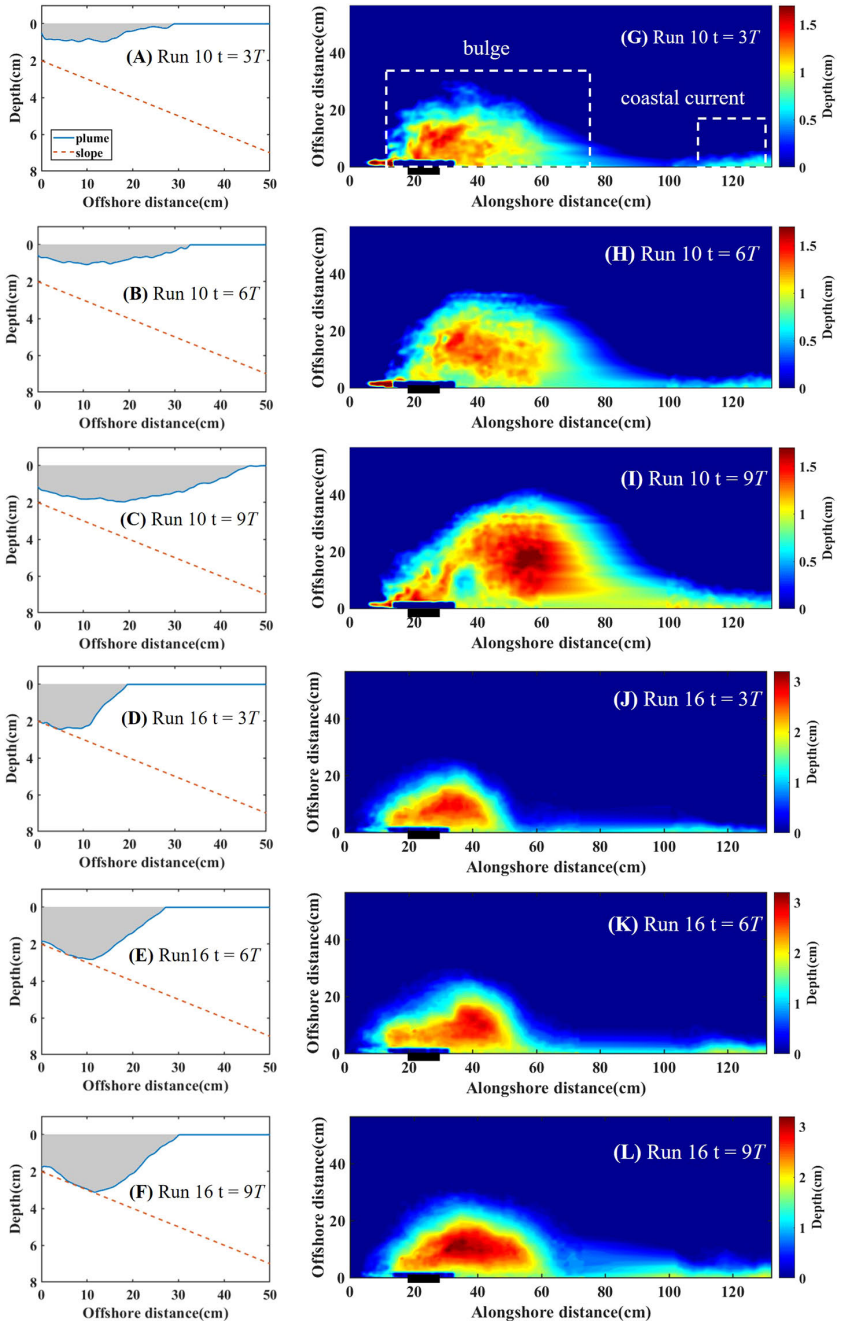

FIGURE 4
(A–F) Side-view of the interaction of plume and the bottom slope. The blue line and red dash line indicate plume contour and the sloping bottom. **(G–L)** Plume thickness field. The white dash boxes indicate bulge region and coastal current region. The top six panels are the example of surface-advected plume (run 10) with t = 3*T* **(A, G)**, 6*T* **(B, H)**, and 9*T* **(C, I)**, while the bottom six panels are the example of bottom-attached plume (run 16) with t = 3*T* **(D, J)**, 6*T* **(E, K)**, and 9*T* **(F, L)**.

7*T* to 9*T*, the bulge continues to grow offshore, and more freshwater accumulates in the bulge region, causing an increase in the bulge surface width and area. Compared with the earlier period, the width of the coastal current increases significantly because of more downstream freshwater transport (Figures 4I, L).

In most no-slope runs, the bulge grows unstable after 10*T* so that we limited our analysis to the first 10 rotation periods (Chapman and Lentz, 1994). In our experiments, we also observed the unstable plume within 10*T* in α = 0.1 cases. As shown in Figure 5, the unstable plume shows that a new cyclonic vortex develops in the bulge, which makes its shape quite different from the stable plume. The phenomenon of instability we found is manifested by the continuous separation of the cyclonic vortex from the bulge, making the bulge shape fluctuate periodically. Specifically, the bulge is no longer a circle or semicircle, and the bulge offshore distance is larger. According to whether the bulge generates the cyclonic vortex, we divided plumes into two types: stable plumes and unstable plumes.

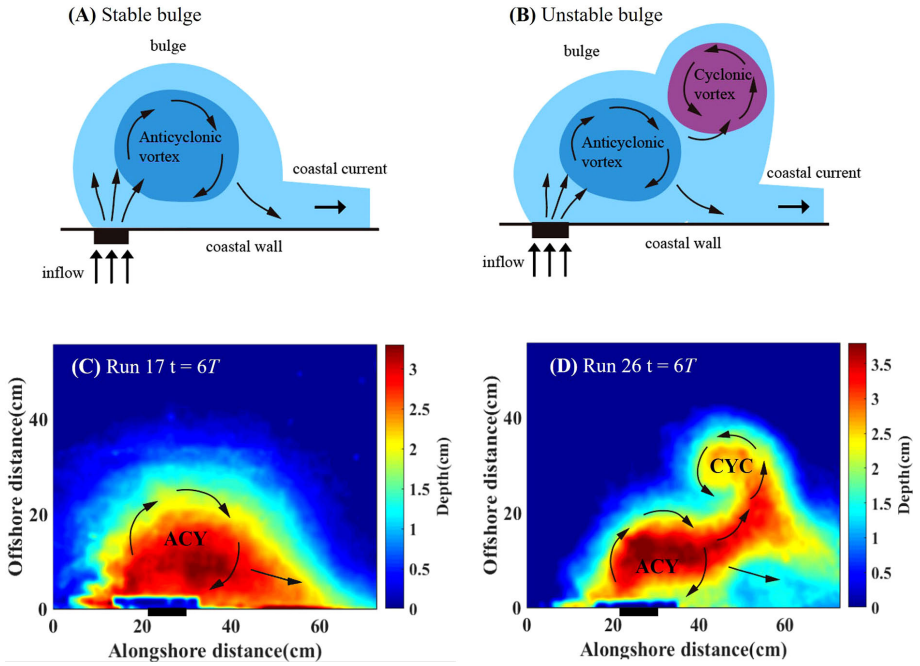

FIGURE 5
Schematics (top) and typical depth field (bottom) of stable plumes (left) and unstable plumes (right). **(A, B)** are schematic representations of the bulge. **(C, D)** are depth fields of the bulge at t = 6*T*. Black arrows in each panel indicate flow direction, while ACY and CYC represent anticyclonic vortex and cyclonic vortex, respectively.

Table 2 shows the plume types for all experimental conditions. Surface-advected plumes will generate with larger α, T and g'. Unstable plumes only occur in $\alpha = 0.1$ case, so we conclude that shelf slope is the main parameter to control the bulge stability. We then try to quantify the plume type using non-dimensional parameters h_g/H_0 (depth), $\alpha L_b/h_g$ (shelf slope), and θ (instability).

3.1.1 Bottom-attached versus surface-advected plumes

Assuming that the plume front is in geostrophic balance (Avicola and Huq, 2001), Eqs. (3), (4) and (5) are used to normalize the depth, width, and velocity, respectively, which can be used to characterize the evolution of the bulge.

$$h_g = \left(\frac{2Qf}{g'}\right)^{1/2} \tag{3}$$

$$L_b = \frac{\sqrt{g' h_g}}{f} = \left(\frac{2Qg'}{f^3}\right)^{1/4} \tag{4}$$

$$c = \sqrt{g' h_g} \tag{5}$$

Chapman and Lentz (1994) assumed that the offshore buoyancy flux of a buoyant coastal current interacting with the bottom occurs in a thin bottom Ekman layer. They obtained the offshore extent y_b of this bottom-trapped layer:

$$y_b = \frac{f\rho_0}{\alpha g}\frac{u_{max}}{\partial\rho/\partial y} \tag{6}$$

We scaled y and u_{max} in Eq. (6) by L_b and c given in Eqs. (4) and (5), respectively. We will have:

$$y_b \sim \frac{f\rho_0}{\alpha g}\frac{\sqrt{g' h_g}\sqrt{g' h_g}/f}{\Delta\rho} = \frac{h_g}{\alpha} \tag{7}$$

Finally, based on the theory of Avicola and Huq (2001), we calculate the bottom-slope parameter suitable for our experiments, using the ratio between the bulge Rossby radius L_b and the bottom-trapped width y_b:

$$\frac{L_b}{y_b} = \frac{\alpha L_b}{h_g} \tag{8}$$

For $h_g<H_0$ case, the bottom boundary layer does not influence plume dynamics (Yankovsky and Chapman, 1997). Therefore, the depth parameter (h_g/H_0) can be used to predict the offshore spreading and types of buoyant inflow. We combined the above two non-dimensional parameters and the non-dimensional parameter space (h_g/H_0, $\alpha L_b<h_g$) that comprises the depth and bottom-slope parameters as shown graphically in Figure 6A.

The small values of $h_g<H_0$ indicate that the plume is isolated from the bottom (surface-advected plume), while the large values of $h_g<H_0$ mean that the plume is interacting with the bottom (bottom-attached plume). Values on the left edge of Figure 6A characterize coastal currents that are forced to grow wider than the buoyant scale, but values on the right edge of Figure 6A show that the current is compressed in width. $\alpha L_b<h_g > 1$ implies that the scale width is larger than the trapped width so that the bulge experiences horizontal "compression" at its base. On the other hand, if $\alpha L_b<h_g<1$, the bulge undergoes lateral expansion at its base beyond its scale

TABLE 2 The plume types of experimental conditions.

α	T (s) g′ (cm/s^2)	20	30	40	50	60
0.1	4	BA Unstable	BA Unstable	BA Unstable	BA Unstable	BA Unstable
	5.5	BA Unstable	BA Unstable	BA Unstable	SA Unstable	SA Unstable
	7	BA Unstable	BA Unstable	SA Unstable	SA Unstable	SA Unstable
	10	BA Unstable	SA Unstable	SA Unstable	SA Stable	SA Stable
0.2	4	BA Stable	BA Stable	BA Stable	TP Stable	SA Stable
	5.5	BA Stable	BA Stable	TP Stable	SA Stable	SA Stable
	7	BA Stable	TP Stable	SA Stable	SA Stable	SA Stable
	10	BA Stable	SA Stable	SA Stable	SA Stable	SA Stable
No shelf	4	SA Stable	SA Stable	SA Stable	SA Stable	SA Stable

BA, SA and TP represent bottom-attached, surface-advected and transitional plumes, respectively.

width (Avicola and Huq, 2003). We defined the threshold of surface-advected and bottom-attached plumes as plume classification number (PCN), PCN = $\frac{h_g}{H_0}/\frac{\alpha L_b}{h_g}$, using least-square method to calculate the criterion between two plumes. As shown in Figure 6A (dash line), when PCN > 1.6, the plume is bottom-attached; when PCN< 1.6, the plume is surface-advected.

Yankovsky and Chapman (1997) proposed that a surface-advected plume forms when the predicted equilibrium depth for the bottom-attached plume is shallower than the depth of the buoyant inflow (h_g<H_0). They distinguished whether the plume contacts with the bottom only by comparing h_g and H_0. However, in our experiment, there are also surface-advected plumes when h_g>H_0. Avicola and Huq (2001) proposed the bottom-slope parameter L_b<y_b, the ratio of the internal Rossby radius to the bottom-trapped width, which describes the effect of the slope on the dynamics of the coastal current. We used the above methods to verify the plume type in our experiment and found that it is not completely consistent with them, possibly due to laboratory experiments or different working conditions. Therefore, we proposed non-dimensional parameters suitable for plume classification in laboratory experiments according to specific conditions.

3.1.2 Stable versus unstable plumes

Saunders (1973) studied the baroclinic instability of vortex, which is controlled by the normalized instability parameter θ (the ratio of buoyancy force to the Coriolis force):

$$\theta = \frac{g' H}{r^2 f^2} \tag{9}$$

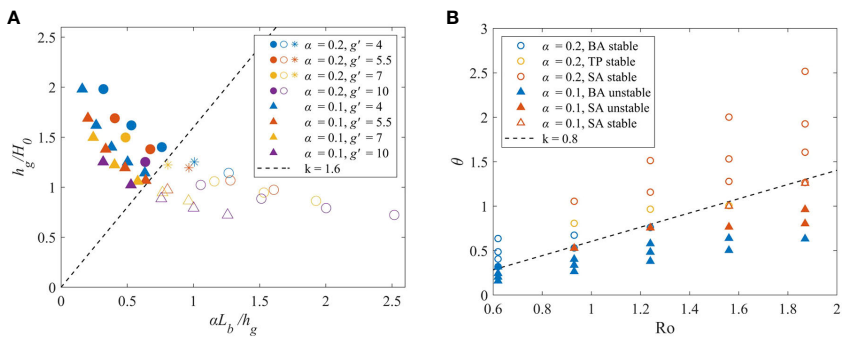

FIGURE 6
Plume types according to the bottom attachment **(A)** or bulge stability **(B)**. In panel **(A)**, the solid, asterisk and hollow symbols represent bottom-attached plumes, transitional plumes, and surface-advected plumes, respectively. The dash line denotes the boundary of surface-advected and bottom-attached plume, which is PCN = 1.6. In panel **(B)**, the solid and the hollow symbols represent unstable and stable plumes, respectively. The dash line stands for the boundary of stable and unstable plume, which is BIN = 0.8.

where r is the offshore radius and H is the environmental ocean depth, which is defined by Avicola and Huq (2003) as the depth at a Rossby radius. Therefore, in our experiments:

$$H = H_0 + \alpha L_b \tag{10}$$

Plugging Eq. (10) into Eq. (9) and using the Rossby radius L_b to represent the offshore radius, we obtain the instability parameter θ as:

$$\theta \sim \frac{g'\alpha}{L_b f^2} \tag{11}$$

The instability parameter θ is a ratio of the available potential energy in a baroclinic vortex to the rotational kinetic energy (Avicola and Huq, 2003). When θ is small, the plume is prone to baroclinic instability. The bulge stability is closely related in θ and Ro (Figure 6B), where θ/Ro is the ratio of buoyancy to inertial force. The two types are roughly separated by a straight line with a gradient of 0.8 (k = 0.8). We defined the threshold of stable and unstable plumes as bulge instability number (BIN), BIN = θ/Ro. When BIN > 0.8, buoyancy is the dominant factor, the transport is strong, and the plume is less affected by the slope, so it is relatively stable. And surface-advected plumes appear more often when BIN > 0.8, which verifies the conclusion that buoyancy dominates in this case. When BIN< 0.8, there are all unstable plumes. The rotational kinetic energy is dominant, and the plume develops a cyclonic vortex. And bottom-attached plumes appear more often when BIN< 0.8, which verifies that the buoyancy effect is relatively small in this case.

3.2 Fate of freshwater

3.2.1 Bulge characteristics

In this section, we will calculate the maximum depth h_{max} (Figure 7A) and maximum width W_{max} (Figure 7B) of the bulge region. Based on the depth field, the top 5% depth value was selected as the maximum depth (h_{max}) of the plume. Based on h_{max}, we choose 20% h_{max} as the threshold to determine plume boundary, so that the maximum width (W_{max}) can be determined. Then, the bulge volume (V_b) is calculated by summing the depth of each point in the plume profile according to the depth field (Figure 7C).

In the exponential phase (0 – 3T), h_{max} and W_{max} increase dramatically. Due to the effect of bottom friction, the plume flows offshore until the vertical shear geostrophic flow at the density front separating the buoyancy fluid from the ambient fluid is zero at the bottom (Chapman and Lentz, 1994). And then h_{max} and W_{max} gradually become stable during 3 – 10T. In our experiments, we found that when $\alpha = 0.1$, unstable plumes cause fluctuations of h_{max} and W_{max}values (Figures 7A, B), showing that the cyclonic vortex continuously separates from the bulge and transports downstream as time proceeds, which lead to the periodic changes of the bulge width and depth. The fluctuations of depth and width correspond to each other, but their phases are opposite, so V_b does not fluctuate (Figure 7).

We plotted the mean value of non-dimensional plume depth and width during the stationary phase (8 – 9T) versus the bottom-slope parameter ($\alpha L_b/h_g$) in Figure 8. $\alpha L_b/h_g$ larger than 1 indicates most plumes are surface-advected, while it smaller than 1 indicates most plumes are bottom-attached. Obviously, h_{max} of the bottom-attached plume is greater than that of the surface-advected plume (Figure 8A). W_{max} of the bottom-attached plume is smaller than that of the surface-advected plume (Figure 8B). Because of the conservation of freshwater, the depth and width are corresponding, that is, when the plume depth is small, it will develop farther offshore.

We found that h_{max} decreases and W_{max} increases with the increase of g', which is consistent with the laboratory study of Thomas and Linden (2007). This is because the density difference between buoyant water and ambient fluid increases, and the effect of buoyancy increases, easily producing the surface-advected plumes. As g' is larger, buoyancy drives the offshore transport further. Shelf slope has little effect on the depth, that is, h_{max} is approximately same in different α and the same f and g' cases (Figure 8A), indicating h_{max} is mainly related to f and g'. Shelf slope has a great impact on W_{max} (Figure 8B). According to the fitting curves, h_{max} decreases and W_{max} increases rapidly with $\alpha L_b/h_g$ in gentle slope case (α = 0.1), which mean that depth and width are more sensitive to the change of plume attachment type in gentle slope case. And in this case, W_{max} is larger than steep slope case. Avicola and Huq (2003) revealed that baroclinic instability in the bulge might account for its relatively large radial growth but weak vertical growth. The cyclonic vortex caused by the instability increases the

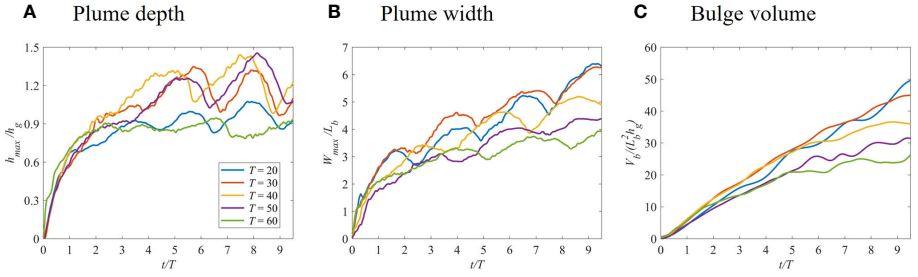

FIGURE 7
Time series of plume featured parameters normalized maximum plume depth **(A)**, maximum plume width **(B)** and bulge volume **(C)** for different rotation rates in runs 36 – 40 (α = 0.1, g' = 7 case).

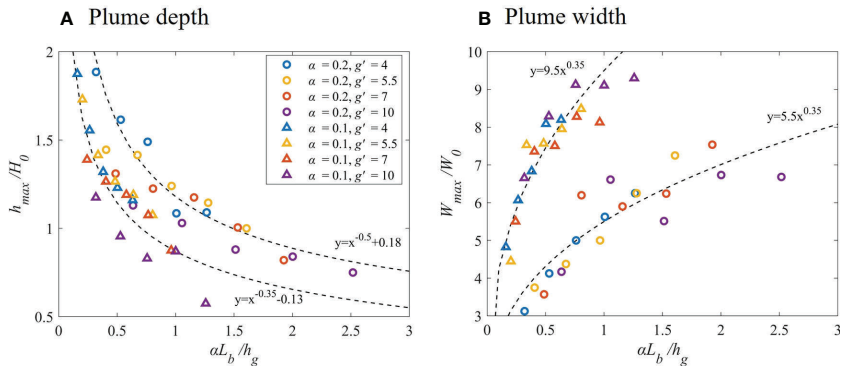

FIGURE 8
Normalized mean maximum plume depth **(A)**, maximum plume width **(B)**. Black dash lines are the best fitting curves of two different slope cases.

offshore distance in the bulge region, which can explain why W_{max} is much larger in gentle slope case.

3.2.2 Freshwater accumulated in the bulge

Here, we calculated time series of bulge volume (V_b) to characterize the freshwater accumulated in the bulge and to study the shelf slope impact (Figure 9). V_b increases with time during the exponential stage (0 – 3T), and then the growth rate gradually slows down. After 3T, the V_b difference of each case increases. We found that for the larger f, the rotation effect is greater; hence, the growth rate of V_b increases, representing more freshwater accssssssumulates in the bulge. In gentle slope case ($\alpha = 0.1$), the growth rate is greater than steep slope case (α = 0.2) after 3T, which means that freshwater keeps accumulating in the bulge region, possibly caused by the baroclinic instability. The instability forms the cyclonic vortex to recirculate freshwater to the bulge region, and thus freshwater is continuously accumulated.

We plotted stationary phase mean $V_b/(L_b^2 h_g)$ against Rossby number Ro (Figure 10). For a smaller g', the buoyancy effect is small, which inhibits the diffusion of freshwater to the downstream, causing more freshwater accumulates in the bulge. In steep slope case (α = 0.2), V_b is relatively consistent compared with no-slope case (Figure 10A). In gentle slope case (α = 0.1), V_b is larger than no-slope case (Figure 10B). Baroclinic instability was observed in α = 0.1 cases, which is reported in previous experiments. Avicola and Huq (2003) found that the instability leads to the increase of

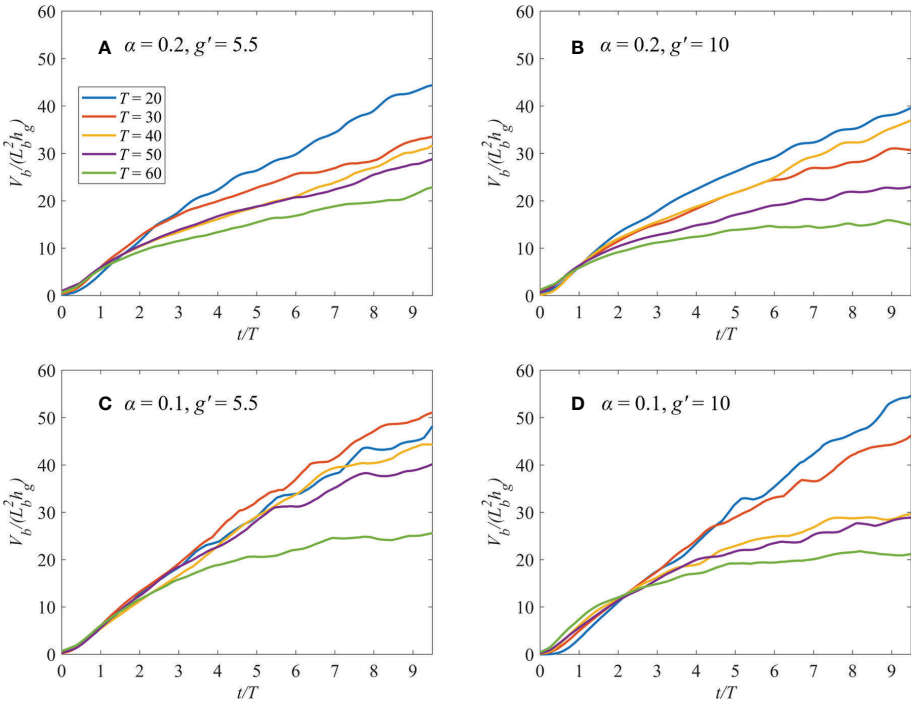

FIGURE 9
Time series of normalized bulge volume for different rotation rates. **(A)** Runs 11 – 15 (α = 0.2, g' = 5.5 case). **(B)** Runs 21 – 25 (α = 0.2, g' = 10 case). **(C)** Runs 31 – 35 (α = 0.1, g' = 5.5 case). **(D)** Runs 41 – 45 (α = 0.1, g' = 10 case).

bulge volume, and about 60% of source volume and density anomaly flux are stored in the bulge area. There are multiple rotating cores within the larger anticyclonic vortex, causing freshwater to accumulate in the bulge and inhibiting the transport to the downstream.

3.2.3 Freshwater transported alongshore with coastal currents

Most alongshore transport occurs in the coastal current region, which is typically in geostrophic balance (Avicola and Huq, 2001). In the absence of significant external forcing, the transport is driven primarily by the plume's buoyancy and strongly mediated by Earth's rotation (Horner-Devine et al., 2015). In addition, shelf slope will influence the structure and transport in the coastal current (Chapman and Lentz, 1994; Yankovsky and Chapman, 1997; Avicola and Huq, 2001).

In this section, we calculated the normalized coastal current transport Q_{cc}/Q_{in} to study the influence of various factors (f, g' and α) on the freshwater transport in coastal current. Freshwater transport Q_{cc} is equal to inflow discharge rate Q_{in} minus bulge charge rate Q_b as shown below:

$$Q_{cc} = Q_{in} - \ Q_b \tag{12}$$

where $Q_b = \frac{V_b(i+1)-V_b(i)}{\Delta t}$.

Figure 11 shows that the coastal current is generally monitored after 1T, and it grows rapidly in exponential phase and then reaches a stationary phase with a slow growth rate. We plotted stationary phase mean Q_{cc}/Q_{in} against Rossby number Ro (Figure 12). The trend of Q_{cc}/Q_{in} with increasing Ro corresponds to Figure 10, i.e., the larger g' and smaller f cause more freshwater transport to the downstream.

We found that Q_{cc}/Q_{in} is most significantly affected by shelf slope. On the one hand, it affects the growth trend of Q_{cc}/Q_{in}. In steep slope case (α = 0.2), Q_{cc}/Q_{in} reaches stability after 3 – 4 T (Figures 11A, B). In gentle slope case (α = 0.1), Q_{cc}/Q_{in} increases significantly after 3 – 4 T, and then there is still a slight increase trend and strong fluctuation (Figures 11C, D). And Q_{cc}/Q_{in} increases with the increasing Ro (Figure 12). The result is different from previous no-slope experiments of Fong and Geyer (2002), which showed that Q_{cc}/Q_{in} drops from 0.65 to 0.4 as Ro increases from 0.1 to 1.

On the other hand, the gentle slope promotes baroclinic instability. As shown in Figure 11, the most notable cases are unstable plumes. For example, the occurrence of coastal current is delayed to 4 – 5T with periodic oscillation (Figure 11C). Compared stable BA (Figure 11C, T = 20, 30) with unstable BA (Figure 11D, T = 20, 30), Q_{cc}/Q_{in} decreases by about 50%. When α is reduced from 0.2 (Figure 12A) to 0.1 (Figure 12B), Q_{cc}/Q_{in} changes from 40% – 80% to 20% – 80%. The lower limit is greatly reduced, and the freshwater transport is significantly reduced, especially under baroclinic instability conditions. In previous no-slope experiments, Avicola and Huq (2003) found that only approximately 1/3 of the outflow incorporates to the coastal current, with the rest going into bulge formation in the laboratory. According to Figure 12, Q_{cc}/Q_{in} is larger than the no-slope case except for T = 20 case, in which baroclinic instability and strong Coriolis force produce a large cyclonic vortex, which inhibits freshwater transport. We can conclude that the sloping bottom promotes freshwater transport.

4 Discussion

In nature, the plume is a very complex marine physical phenomenon because it is affected by the estuary and coastal areas, and the mixing between freshwater and saltwater is continuously changing. Therefore, in addition to the bottom topography, plumes are also affected by many factors, such as inflow conditions, Coriolis force, wind, ambient flow field, and so on (Nash and Moum, 2005). Horner-Devine et al. (2006) found that Ro reflects inflow rate and estuary size. When Ro is large, the bulge is nearly circular in shape, and most of the freshwater is trapped in the bulge region. When Ro is small, more freshwater forms coastal currents. Garvine (1999) found that as the Coriolis force decreases, more and more freshwater accumulates in the bulge region, inhibiting the formation of coastal currents in downstream. In addition, Narayanan and Garvine (2002) discovered that when

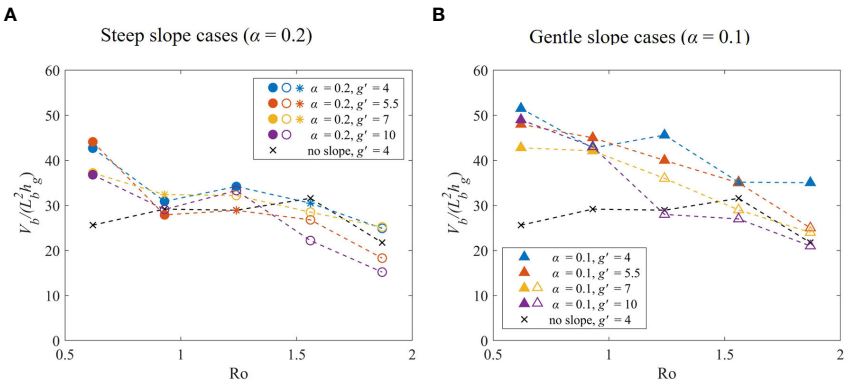

FIGURE 10
Normalized mean bulge volume in stationary phase (8 – 9T). Circle and triangle symbols represent steep (α = 0.2) and gentle slope (α = 0.1) cases, respectively. The solid, asterisk and hollow symbols represent bottom-attached, transitional and surface-advected plumes, respectively. Black dash lines with cross symbols are the no-slope case for comparison. The dash line represents the trend of V_b/(L_b^2h_g) changing with Ro.

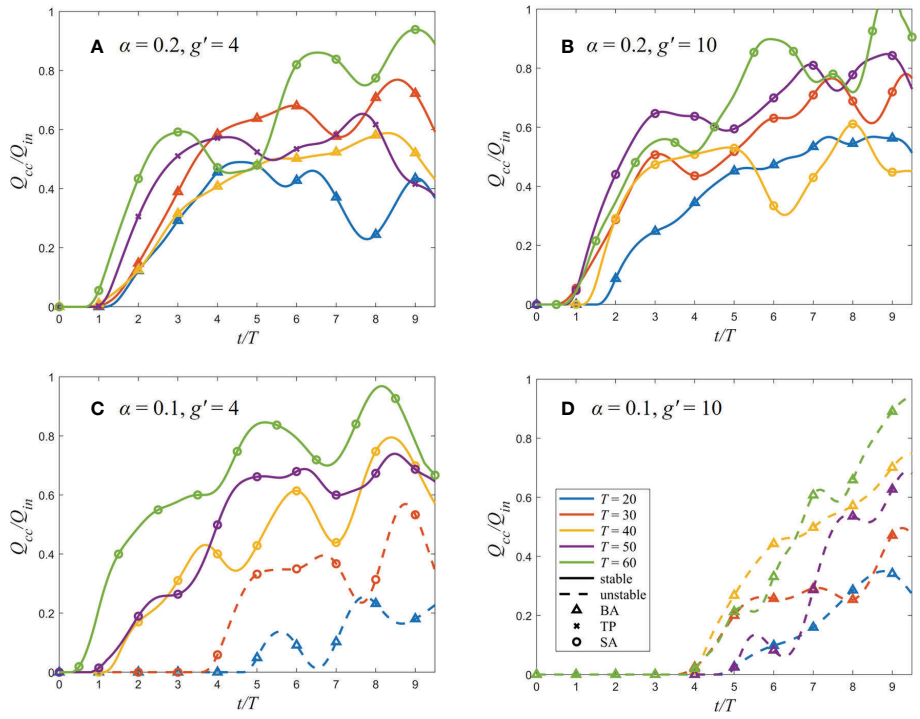

FIGURE 11
Time series of normalized coastal current transport of different rotation rates. **(A, B)** are steep slope cases, while **(C, D)** are gentle slope cases. For each line, solid and dash line represent the bulge as stable and unstable, respectively. The triangle, cross and circle symbols mean the plume is bottom-attached, transitional and surface-advected, respectively.

other conditions remain unchanged, the inflow increase will intensify the offshore plume diffusion. External forcing agents, such as wind and ambient flows, may also influence plume behavior. Walker (1996) showed that river flow and wind are the main factors affecting the Mississippi River plume using NOAA satellite data. Fong and Geyer (2002) found that ambient flows can significantly change plume structure and freshwater transport characteristics.

In the present study, we classify plume types according to bottom attachment and bulge stability. Plume types are determined by g', f and α, which represent the buoyancy, Coriolis force, and topography factors, respectively. Freshwater accumulation in the bulge is a way to recycle the outflow from the estuary as the inflow, which requires a large Fr (Chant et al., 2008). As g' increases, buoyancy increases, driving plume transport and thereby promoting coastal current formation. Fong and Geyer (2002) found that the larger Ro reduces the coastal current transport in no-slope experiments. The Coriolis deflection strengthens the anticyclonic eddy, which enhances the near-field anticyclonic bulge and weakens the development of the far-field coastal jet (Chao, 1990). As f increases Coriolis force is strong, promoting freshwater accumulation in the bulge. Compared with

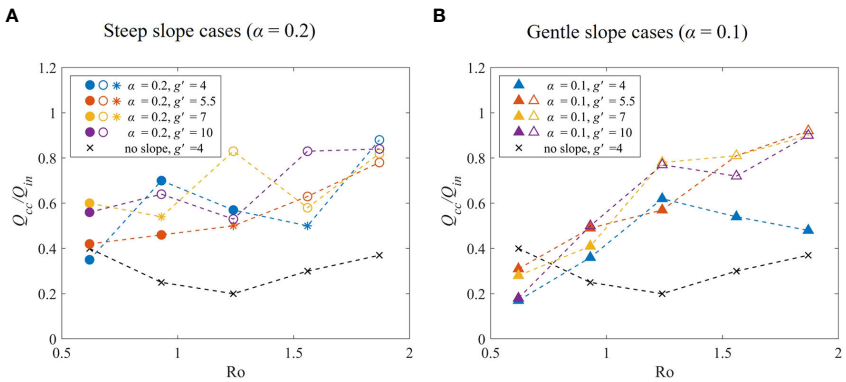

FIGURE 12
Normalized mean coastal current transport in stationary phase (8 – 97). Circle and triangle symbols represent steep (α = 0.2) and gentle slope (α = 0.1) cases, respectively. The solid, asterisk and hollow symbols represent bottom-attached, transitional and surface-advected plumes, respectively. Black dash lines with cross symbols are the no-slope case for comparison. The dash line represents the trend of Q_cc/Q_in changing with Ro.

the no-slope experiment, bottom attachment and bulge instability are two new features in our experiments. We find that sloping bottom is the most critical factor affecting plume shape and freshwater transport. Therefore, in this section, we will first discuss how the bottom attachment affects freshwater transport and their relationship with other factors.

In section 3.1, we use the bottom-slope parameter $\alpha L_b/h_g$ to classify plume types: when PCN > 1.6, the plume is bottom-attached; when PCN< 1.6, the plume is surface-advected. The transitional plume is located at the boundary, which is not the main content of this paper. For the bottom-attached plume, the freshwater, thick in bulge is trapped near the coastal wall (Figure 4), which inhibits offshore transport, resulting in a smaller bulge (Figure 1). Due to the conservation of total freshwater discharge, the alongshore coastal current transport increases. As shown in Hudson's outflow (Chant et al., 2008), bulge formation tends to limit freshwater transport in coastal currents and enhance offshore transport. Even during a period of downwelling favorable winds, the freshwater transport in the coastal current is less than 1/2 of the estuarine freshwater outflow. Brasseale and MacCready (2021) found that the gentle slope promoted the downstream transport, while the upstream transport on the steep slope disappeared, which is consistent with our results. Therefore, we can conclude that bottom attachment promotes alongshore transport. However, in Figure 12A (stable plumes), the transport is stronger under larger Ro (T = 50) conditions of surface-advected plumes. This is because the Coriolis force is weak, possibly, and the bulge spreads very far and is close to the calculation position of the coastal current. Therefore, we may calculate some eddies as the coastal current.

It is noteworthy that the slope is far less than 0.1 in reality, but it is difficult to make a such gentle slope in our experiment. Therefore, we use the bottom-slope parameter $\alpha L_b/h_g$ instead of just α to compare with the real field work, which includes inflow discharge, slope, Coriolis force, reduced gravity, estuarine conditions and other factors. In addition, when slope is gentle, while $\alpha L_b/h_g$ becomes smaller. The data will be on the left side of the boundary shown as a bottom-attached plume. In future research, we will further discuss the application of the parameters to the real field work.

We use the instability parameter θ to classify plume types: when BIN > 0.8, the plume is stable; when BIN< 0.8, the plume is unstable. The plume instability in our experiments only occurs in α = 0.1 case, and it will occur regardless of whether the plume is in contact with the bottom. This is consistent with the study of Mississippi–Atchafalaya River plume by Hetland (2017), where they found that shelf slope determines the evolution of baroclinic instability. As shown in Figure 5, the phenomenon of baroclinic instability is that freshwater separates from the bulge and returns in the form of a cyclonic vortex, which leads to the fluctuation of Q_{cc}/Q_{in} (Figure 11) and Q_{cc}/Q_{in} decreases greatly in unstable cases (Figure 12). We can conclude that the instability inhibits freshwater transport in coastal currents. Figure 12B shows that Q_{cc}/Q_{in} increases with the increasing Ro in unstable plumes, which is different from the conclusion of Fong and Geyer (2002). This is because the inhibition effect of freshwater transport caused by the instability is stronger than the promotion effect caused by Coriolis force reduction and the promotion effect caused by bottom attachment in small T (large f) case. And when Ro increases, the instability is weaker, and the role of the bottom, g' and f is gradually enhanced.

To sum up, we divide the four quadrants according to attachment and bulge instability to classify the four plume types (Figure 13). According to our experiment results, the stable surface-advected plume has the maximum alongshore freshwater transport, which occurs in the larger T (smaller f) and g' cases, while stable bottom-attached plume has smaller alongshore freshwater transport, found in the smaller T (larger f) and g' cases. For stable bottom-attached plumes, the bulge is elongated because it is trapped by the bottom, leading to the minimum offshore freshwater transport. In the limit of small vertical mixing and vanishing bottom drag, the difference in intrusion speeds in and out of the estuary is reduced. The seaward expansion of the bulge decreases, and the undercurrent leaks out of the bulge and propagates as the coastal current (Chao and Boicourt, 1986). The bulge area is small in steep slope case (Garvine, 1999; Avicola and Huq, 2003). A typical stable surface-advected example is the Columbia River plume, which consists of a well-pronounced anticyclonic bulge and a narrower coastal current (Jia and Yankovsky, 2012). A typical stable bottom-attached example is the Delaware plume, forming a narrow but unstable coastal jet instead of a wide and diffuse plume region (Münchow and Garvine, 1993). Shelf slope contributes to the effective diffusivity over different shelf regions, which also proves that the bottom promotes coastal current transport (Masse, 1990). For unstable plumes, the bulge shape becomes irregular. The bottom-attached cyclonic vortex generated at the bulge boundary is even larger than the anticyclonic vortex. In this case, because the plume is trapped near the coast by the bottom, it has the maximum offshore freshwater transport and minimum alongshore freshwater transport, consistent with previous observations (Yankovsky, 2004; Karageorgis et al., 2009). They found that the Danube River plume comprises several mesoscale eddies but without a coherent structure of the river plume similar to the Columbia River. The rapid growth of the cyclonic vortex contains a large amount of freshwater, which substantially (up to 35%) reduces the alongshore freshwater flux farther downstream (Jia and Yankovsky, 2012).

5 Conclusion

A series of laboratory experiments were carried out on a rotating table to simulate the evolution of plumes over the sloping bottom. During the experiment, we changed the reduced gravity g', Coriolis parameter f, and shelf slope α to study their effects on plume characteristics, focusing on the analysis of plume types and corresponding freshwater transport.

We classify plumes according to observed phenomena and quantified parameters. According to bottom attachment of the bulge, we divide plumes into three types: bottom-attached plumes, surface-advected plumes, and transitional plumes. On the other hand, according to the bulge stability, we divide plumes into

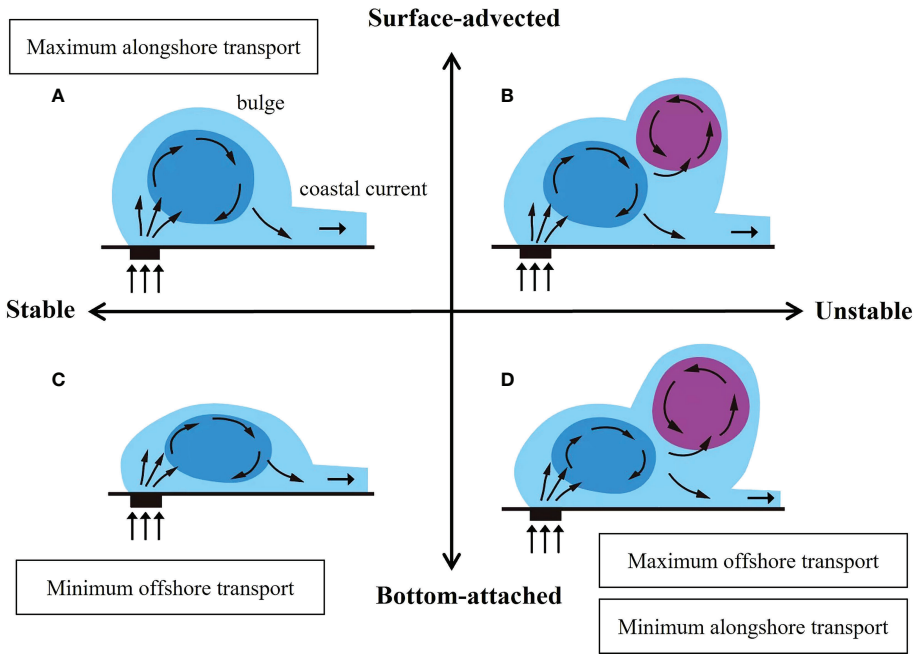

FIGURE 13
Schematic diagram to show the effects of bottom attachment and bulge instability on freshwater transport in the alongshore and offshore direction. **(A–D)** show stable surface-advected, unstable surface-advected, stable bottom-attached, and unstable bottom-attached plumes, respectively.

two types: stable plumes and unstable plumes. Based on our analysis, parameters PCN and BIN can be used to predict the plume types. When PCN > 1.6, the plume tends to be bottom-attached; when PCN< 1.6, the plume tends to be surface-advected. When BIN > 0.8, the plume is stable, while the plume is unstable when BIN< 0.8. These thresholds are calculated by the least-square method.

To further quantitatively study the plume characteristics, we estimated the maximum depth (h_{max}) and maximum width (W_{max}) through the depth field. The study shows that shelf slope has little effect on the depth but a great influence on the width. h_{max} decreases and W_{max} increases with the increasing g' and decreasing f. For unstable cases, the width and depth fluctuate, and the width increases significantly.

We calculated the bulge volume (V_b) and the coastal current transport (Q_{cc}/Q_{in}) to understand freshwater transport. Due to the conservation of total freshwater discharge, the conclusions of bulge and coastal current are consistent. Bottom attachment and bulge instability are the main differences on the plume evolution over a sloping bottom. Compared with the no-slope case, the bottom traps the freshwater near the coastal wall, inhibiting offshore transport and promoting the coastal current transport. The cyclonic vortex caused by baroclinic instability strongly restricts the coastal current transport.

In summary, the plume type and freshwater transport are results of the coupling effect of g', f and α. For stable plumes, bottom attachment promotes freshwater transport, but when the Coriolis force is very weak (small f), the surface-advected plumes will further promote transport. For unstable plumes, when f is large, the cyclonic vortex plays a dominant role in the suppression of the transport. When f is small, bottom attachment and buoyancy play a dominant role in promoting the transport. Baroclinic instability is a critical factor restraining freshwater transport, mainly caused by the gentle slope (small α) and enhanced by strong Coriolis force (large f).

There are still some limitations in our experiments. On the one hand, the sloping bottom in laboratory experiments cannot be made at a similar slope as the actual continental shelf. It is impossible to make the slope as gentle as 0.01 (or even 0.001) in the numerical models (Yankovsky and Chapman, 1997; Brasseale and MacCready, 2021), so the bottom-attached plume we observed still has a noticeable bulge. Although we cannot simulate the phenomenon in reality, our conclusion is still applicable when the slope is very gentle. For example, inserting smaller slope values into Figures 6 and 8 still yields a similar conclusion. Moreover, if we consider the slope Burger number $S = Nf^{-1}\alpha$ discussed in Hetland (2017), the ratio of bottom slope over Coriolis force is on the same range between our experiments and realistic model simulations. Based on the observation of Delaware coastal current, the bottom slope parameter $\alpha L_b/h_g$ is 0.51 (Münchow and Garvine, 1993), which is the same order of magnitude as the bottom slope parameter calculated in our experiment. Therefore, our experiments can deepen our understanding on plume evolution and be used to verify numerical models and field observations. In future research, we will change α and H_0 to be closer to the real situation by numerical model. In addition, we will further discuss the application of the parameters to the real field work. On the other hand, baroclinic instability only occurs in a few conditions with $\alpha =$ 0.1 and small Ro. However, baroclinic instabilities may be generated or enhanced by external forces in nature, such as wind (Hetland,

2017), ambient stratification (Jia and Yankovsky, 2012), etc., which will be the direction of our further research.

Data availability statement

The raw data supporting the conclusions of this article will be made available by the authors, without undue reservation.

Author contributions

YY and Y-TL conceived the work. XT performed the experiment. YY and XT conducted analyses and drafted the manuscript. All authors contributed to the article and approved the submitted version.

Funding

This research was funded by the National Natural Science Foundation of China (Grant no. 41876089); the Science Foundation of Donghai Laboratory (Grant No. DH-2022KF01016); Zhejiang Provincial Natural Science Foundation of China (Grant no. LY20A020009).

Acknowledgments

The authors thank Professor Xu Chen, Yujun Yu and Guofeng Fu from Ocean University of China for their help to build the rotating table, and thank Haocheng Song and Ling Liu for their assistance during the experiments.

Conflict of interest

The authors declare that the research was conducted in the absence of any commercial or financial relationships that could be construed as a potential conflict of interest.

Publisher's note

References

Avicola, G., and Huq, P. (2001). Scaling analysis for the interaction between a buoyant coastal current and the continental shelf: experiments and observations. *J. Phys. Oceanogr.* 32 (11), 3233–3248. doi: 10.1175/1520-0485(2002)0322.0.CO;2

Avicola, G., and Huq, P. (2003). The characteristics of the recirculating bulge region in coastal buoyant outflows. *J. Mar. Res.* 61 (4), 435–463. doi: 10.1357/002224003322384889

Blanton, J. O. (1981). Ocean currents along a nearshore frontal zone on the continental shelf of the southeastern united states. *J. Phys. Oceanogr.* 11 (12), 1627–1637. doi: 10.1175/1520-0485(1981)011<1627:OCAANF>2.0.CO;2

Brasseale, E., and MacCready, P. (2021). The shelf sources of estuarine inflow. *J. Phys. Oceanogr.* 51 (7), 2407–2421. doi: 10.1175/jpo-d-20-0080.1

Chang, P. H., and Isobe, A. (2003). A numerical study on the changjiang diluted water in the yellow and East China seas. *J. Geophys. Res. Oceans* 108 (C9), 1–17. doi: 10.1029/2002jc001749

Chant, R. J., Glenn, S. M., Hunter, E., Kohut, J., Chen, R. F., Houghton, R. W., et al. (2008). Bulge formation of a buoyant river outflow. *J. Geophys. Res.* 113 (C1), C01017. doi: 10.1029/2007jc004100

Chao, S. Y. (1990). Tidal modulation of estuarine plumes. *J. Phys. Oceanogr.* 20 (7), 1115–1123. doi: 10.1175/1520-0485(1990)0202.0.CO;2

Chao, S. Y., and Boicourt, W. C. (1986). Onset of estuarine plumes. *J. Phys. Oceanogr.* 16 (12), 2137–2149. doi: 10.1175/1520-0485(1986)016<2137:OOEP>2.0.CO;2

Chapman, D. C., and Lentz, S. J. (1994). Trapping of a coastal density front by the bottom boundary layer. *J. Phys. Oceanogr.* 24 (7), 1464–1479. doi: 10.1175/1520-0485(1994)0242.0.CO;2

Chen, S.-N. (2014). Enhancement of alongshore freshwater transport in surface-advected river plumes by tides. *J. Phys. Oceanogr.* 44 (11), 2951–2971. doi: 10.1175/jpo-d-14-0008.1

Dzwonkowski, B., and Yan, X. H. (2005). Tracking of a Chesapeake bay estuarine outflow plume with satellite-based ocean color data. *Cont. Shelf Res.* 25 (16), 1942–1958. doi: 10.1016/j.csr.2005.06.011

Fasullo, J., Dai, A., Qian, T., Smith, L., and Trenberth, K. E. (2007). Estimates of the global water budget and its annual cycle using observational and model data. *J. Hydrometeorol.* 8 (4), 758–769. doi: 10.1175/jhm600.1

Fong, D. A., and Geyer, W. R. (2002). The alongshore transport of freshwater in a surface-trapped river plume*. *J. Phys. Oceanogr.* 32 (3), 957–972. doi: 10.1175/1520-0485(2002)0322.0.CO;2

Garvine, R. W. (1974). Physical features of the Connecticut river outflow during high discharge. *J. Geophys. Res.* 79 (6), 831–846. doi: 10.1029/JC079i006p00831

Garvine, R. W. (1999). Penetration of buoyant coastal discharge onto the continental shelf: A numerical model experiment. *J. Phys. Oceanogr.* 29 (8), 1892–1909. doi: 10.1175/1520-0485(1999)029<1892:Pobcdo>2.0.Co;2

Hetland, R. D. (2017). Suppression of baroclinic instabilities in buoyancy-driven flow over sloping bathymetry. *J. Phys. Oceanogr.* 47 (1), 49–68. doi: 10.1175/jpo-d-15-0240.1

Horner-Devine, A. R., Fong, D. A., Monismith, S. G., and Maxworthy, T. (2006). Laboratory experiments simulating a coastal river inflow. *J. Fluid Mech.* 555, 203–232. doi: 10.1017/s0022112006008937

Horner-Devine, A. R., Hetland, R. D., and MacDonald, D. G. (2015). Mixing and transport in coastal river plumes. *Annu. Rev. Fluid Mech.* 47 (1), 569–594. doi: 10.1146/annurev-fluid-010313-141408

Horner-Devine, A. R., Jay, D. A., Orton, P. M., and Spahn, E. Y. (2009). A conceptual model of the strongly tidal Columbia river plume. *J. Mar. Syst.* 78 (3), 460–475. doi: 10.1016/j.jmarsys.2008.11.025

Hunter, E. J., Chant, R. J., Wilkin, J. L., and Kohut, J. (2010). High-frequency forcing and subtidal response of the Hudson river plume. *J. Geophys. Res. Oceans* 115, C07012. doi: 10.1029/2009JC005620

Jia, Y., and Yankovsky, A. (2012). The impact of ambient stratification on freshwater transport in a river plume. *J. Mar. Res.* 70 (1), 69–92. doi: 10.1357/002224012800502408

Karageorgis, A. P., Kourafalou, V. H., Anagnostou, C., Tsiaras, K. P., Raitsos, D. E., Papadopoulos, V., et al. (2009). River-induced particle distribution in the northwestern black Sea (September 2002 and 2004). *J. Geophys. Res. Oceans* 114. doi: 10.1029/2009jc005460

Lentz, S. J., and Helfrich, K. R. (2002). Buoyant gravity currents along a sloping bottom in a rotating fluid. *J. Fluid Mech.* 464, 251–278. doi: 10.1017/S0022112002008868

Lohan, M. C., and Bruland, K. W. (2006). Importance of vertical mixing for additional sources of nitrate and iron to surface waters of the Columbia river plume: Implications for biology. *Mar. Chem.* 98 (2-4), 260–273. doi: 10.1016/j.marchem.2005.10.003

Masse, A. K. (1990). Withdrawal of shelf water into an estuary: A barotropic model. *J. Geophys. Res. Oceans* 95 (C9), 16085–16096. doi: 10.1029/JC095iC09p16085

Masse, A. K., and Murthy, C. R. (1992). Analysis of the Niagara river plume dynamics. *J. Geophys. Res. Oceans* 97 (C2), 2403-2420. doi: 10.1029/91JC02726

Mudroch, A. (1983). Distribution of major elements and metals in sediment cores from the western basin of lake Ontario. *J. Gt. Lakes Res.* 9 (2), 125–133. doi: 10.1016/S0380-1330(83)71883-6

Münchow, A., and Garvine, R. W. (1993). Dynamical properties of a buoyancy-driven coastal current. *J. Geophys. Res.* 98 (C11), 20063-20077. doi: 10.1029/93jc02112

Narayanan, C., and Garvine, R. W. (2002). Large Scale buoyancy driven circulation on the continental shelf. *Dyn. Atmos. Oceans* 36 (1-3), 125–152. doi: 10.1016/S0377-0265(02)00028-3

Nash, J. D., and Moum, J. N. (2005). River plumes as a source of large-amplitude internal waves in the coastal ocean. *Nature* 437 (7057), 400–403. doi: 10.1038/nature03936

Nof, D., and Pichevin, T. (2001). The ballooning of outflows. *J. Phys. Oceanogr.* 31 (10), 3045–3058. doi: 10.1175/1520-0485(2001)031<3045:Tboo>2.0.Co;2

O'Donnell, J. (1990). The formation and fate of a river plume: A numerical model. *J. Phys. Oceanogr.* 20 (4), 551–569. doi: 10.1175/1520-0485(1990)020<0551:TFAFOA>2.0.CO;2

O'Donnell, J., Marmorino, G. O., and Trump, C. L. (1998). Convergence and downwelling at a river plume front. *J. Phys. Oceanogr.* 28 (7), 1481–1495. doi: 10.1175/1520-0485(1998)028<1481:CADAAR>2.0.CO;2

Rabalais, N. N., Turner, R. E., and Wiseman, W. J. (2002). Gulf of Mexico hypoxia, A.K.A. "The dead zone". *Annu. Rev. Ecol. Syst.* 33, 235–263. doi: 10.1146/annurev.ecolsys.33.010802.150513

Rennie, S. E., Largier, J. L., and Lentz, S. J. (1999). Observations of a pulsed buoyancy current downstream of Chesapeake bay. *J. Geophys. Res. Oceans* 104 (C8), 18227–18240. doi: 10.1029/1999jc900153

Sanders, T. M., and Garvine, R. W. (1996). Frontal observations of the Delaware coastal current source region. *Cont. Shelf Res.* 16 (8), 1009–1021. doi: 10.1016/0278-4343(95)00043-7

Saunders, P. M. (1973). The instability of a baroclinic vortex. *J. Phys. Oceanogr.* 3, 61–65. doi: 10.1175/1520-0485(1973)003<0061:TIOABV>2.0.CO;2

Thomas, R. L. (1983). Lake-Ontario sediments as indicators of the Niagara river as a primary source of contaminants. *J. Gt. Lakes Res.* 9 (2), 118–124. doi: 10.1016/s0380-1330(83)71882-4

Thomas, P. J., and Linden, P. F. (2007). Rotating gravity currents: small-scale and large-scale laboratory experiments and a geostrophic model. *J. Fluid Mech.* 578, 35–65. doi: 10.1017/S0022112007004739

Walker, N. D. (1996). Satellite assessment of Mississippi river plume variability: Causes and predictability. *Remote Sens. Environ.* 58 (1), 21–35. doi: 10.1016/0034-4257(95)00259-6

Wang, B. (2006). Cultural eutrophication in the changjiang (Yangtze river) plume: History and perspective. *Estuar. Coast. Shelf Sci.* 69 (3-4), 471–477. doi: 10.1016/j.ecss.2006.05.010

Wu, T., and Wu, H. (2018). Tidal mixing sustains a bottom-trapped river plume and buoyant coastal current on an energetic continental shelf. *J. Geophys. Res. Oceans* 123 (11), 8026–8051. doi: 10.1029/2018JC014105

Yankovsky, A. E. (2004). Interaction of transient shelf currents with a buoyancy-driven coastal current. *J. Mar. Res.* 62 (4), 545–563. doi: 10.1357/0022240041850066

Yankovsky, A. E., and Chapman, D. C. (1997). A simple theory for the fate of buoyant coastal discharges*. *J. Phys. Oceanogr.* 27 (7), 1386–1401. doi: 10.1175/1520-0485(1997)027<1386:Astftf>2.0.Co;2

Yuan, Y., Avener, M. E., and Horner-Devine, A. R. (2010). A two-color optical method for determining layer thickness in two interacting buoyant plumes. *Exp. Fluids* 50 (5), 1235–1245. doi: 10.1007/s00348-010-0969-y

Yuan, Y., Horner-Devine, A. R., Avener, M., and Bevan, S. (2018). The role of periodically varying discharge on river plume structure and transport. *Cont. Shelf Res.* 158, 15–25. doi: 10.1016/j.csr.2018.02.009

Zhang, J., Zhu, J., Shen, F., Gu, J., Hu, J., Yuan, R., et al. (2013). Detiding measurement on transport of the changjiang-derived buoyant coastal current. *J. Phys. Oceanogr.* 43 (11), 2388–2399. doi: 10.1175/jpo-d-12-0158.1

frontiers | Frontiers in Marine Science

TYPE Original Research
PUBLISHED 24 March 2023
DOI 10.3389/fmars.2023.1147292

OPEN ACCESS

EDITED BY
Yeping Yuan,
Zhejiang University, China

REVIEWED BY
Yongxiang Huang,
Xiamen University, China
Shuang-Xi Guo,
South China Sea Institute of Oceanology (CAS), China

*CORRESPONDENCE
Huan Mei
hmei@just.edu.cn
Qian Liu
liuqian@just.edu.cn

SPECIALTY SECTION
This article was submitted to Physical Oceanography, a section of the journal Frontiers in Marine Science

RECEIVED 18 January 2023
ACCEPTED 10 March 2023
PUBLISHED 24 March 2023

CITATION
Li K, Mei H, Wu X, Dong J and Liu Q (2023) Influence of multiple islands on the hysteresis and dynamics of a western boundary current perturbed by a mesoscale eddy at a gap.
Front. Mar. Sci. 10:1147292.
doi: 10.3389/fmars.2023.1147292

Influence of multiple islands on the hysteresis and dynamics of a western boundary current perturbed by a mesoscale eddy at a gap

Kunshan Li, Huan Mei*, Xiangbai Wu, Jianxin Dong and Qian Liu*

School of Naval Architecture and Ocean Engineering, Jiangsu University of Science and Technology, Zhenjiang, China

The hysteresis of a western boundary current (WBC) flowing across a gap and the dynamics of the mesoscale eddy–WBC interaction with the presence of two islands in the gap are studied using a 1.5-layer ocean model. The hysteresis of the WBC suggests that the two islands in the gap facilitate the WBC to intrude into the western basin by shedding eddies compared with the no-island case, but they promote the WBC to leap across the gap compared with the one-island case. The mesoscale eddies from the east of the gap can induce the critical-state WBC shifting from penetration to leap and vice versa. The dynamics revealed by the vorticity balance analysis shows that the increased (decreased) meridional advection of the WBC perturbed by the eddy forces the WBC to leap across (intrude into the western basin through) the gap. We also present the parameter space of the critical strength of the eddy with variable north–south locations inducing the critical WBC transition. For the WBC critical from the eddy-shedding to leaping regime, the regime shift is most sensitive to the anticyclonic eddy from the gap center and to the cyclonic eddy from the southern gap. It is least sensitive to the eddy downstream of the WBC. For the WBC critical from the leaping to eddy-shedding regime, the regime shift is most sensitive to the anticyclonic eddy upstream of the WBC and to the cyclonic eddy from the southern gap. The least sensitive eddy is from the northern gap.

KEYWORDS

South China Sea, mesoscale eddy, western boundary current, dynamics, island

1 Introduction

The South China Sea (SCS) is a semi-enclosed marginal sea in the northwestern Pacific Ocean and extends from the equator to 23°N and from 99° to 121°E. The SCS connects the Indian Ocean through the Malacca Strait and the Northwest Pacific Ocean through the Luzon Strait. The Luzon Strait is a wide gap between Taiwan of China and Luzon of

the Philippines, with a meridional width of ~340 km and a maximum depth of more than 2,500 m. The Luzon Strait is the most important channel of mass, momentum, and energy exchanges between the SCS and the Pacific Ocean (Nitani, 1972; Qu et al., 2000; Qu et al., 2004; Caruso et al., 2006; Nan et al., 2015; Shen et al., 2022). The Kuroshio, a strong western boundary current (WBC) in the northwestern Pacific, originates from the northern branch of the North Equatorial Current east of Luzon Island and flows northward along the eastern Philippine coast. The Kuroshio either intrudes into the SCS through the gap or leaps across the gap as it passes by the Luzon Strait (treated as a gap in this study) (Nitani, 1972; Yuan et al., 2006; Song et al., 2018; Song et al., 2019; Yuan et al., 2019). The Kuroshio intrusion has been confirmed to exhibit different intruding paths southwest of Taiwan (Metzger and Hurlburt, 2001; Sheremet, 2001; Caruso et al., 2006; Yuan et al., 2006; Sheremet and Kuehl, 2007; Kuehl & Sheremet, 2009). Caruso et al. (2006) identified five types of Kuroshio paths, including the Kuroshio SCS branch, the Kuroshio loop, the detached anticyclonic eddy, the cyclonic intrusion, and the leaping path. The integral of geostrophic vorticity was also used to identify three typical Kuroshio paths: the looping path, the leaking path, and the leaping path (Nan et al., 2011; Nan et al., 2015). The hysteresis is considered to be one of the most important dynamic mechanisms to explain the Kuroshio intrusion. Sheremet (2001) studied the hysteresis of a WBC using a quasi-geostrophic model and summarized the gap-leaping problem in the balance between the beta effect (promoting the penetration) and the inertia (promoting the leap). Next, the presence of the multiple states and hysteresis of the WBC in a gap-leaping system was verified in laboratory experiments (Sheremet and Kuehl, 2007; Kuehl and Sheremet, 2009; Kuehl and Sheremet, 2014; McMahon et al., 2021). Moreover, the external factors, i.e., meridional wind (Wang et al., 2010), island in the gap (Mei et al., 2019), mesoscale eddy (Yuan and Li, 2008; Yuan and Wang, 2011; Mei et al., 2022), and large-scale circulation in the SCS (Mei et al., 2023), are also proved to be crucial to affect the WBC path in a gap-leaping system. As for the other aspects, Wang and Yuan (2012); Wang and Yuan (2014) studied the collision of two opposite WBCs with equal or unequal transport at a gap, and Song et al. (2019) and McMahon et al. (2021) studied the effect of throughflow on the WBC transition. In addition to the Kuroshio, the Gulf of Mexico Loop Current is another example of the application of hysteresis and multiple equilibrium states of the WBC to the gap-leaping problem (Kuehl and Sheremet, 2022; Sheremet et al., 2022).

In the vicinity of the Luzon Strait, the westward-moving mesoscale eddies from the northwestern Pacific interact with the WBC and frequently induce the variation of the WBC path (Yuan et al., 2006; Yuan and Li, 2008; Sheu et al., 2010; Yuan and Wang, 2011; Zhong et al., 2016; Yang et al., 2020; Mei et al., 2022). A reduced-gravity model was used to study the interaction of an eddy with a WBC by Chern and Wang (2005) and Kuo and Chern (2011); however, a gappy western boundary was not considered in their idealized model. In a gap-leaping system, on the one hand, the interactions of a mesoscale eddy with a WBC far away from the critical state and a critical-state WBC in the vicinity of the gap were studied by Song et al. (2018) and Yuan et al. (2019), respectively. They focused on the evolution and development of the eddy rather than those of the WBC transition. On the other hand, Yuan and Wang (2011) focused on the WBC transition perturbed by a mesoscale eddy in a gap-leaping system and found that both cyclonic and anticyclonic eddies could induce the critical-state WBC shifting regimes from penetration to leap, while only cyclonic eddies could induce the WBC transition from leap to penetration. Mei et al. (2022) considered the effect of an island with variable meridional sizes on the eddy–WBC interaction. They found that both anticyclonic and cyclonic eddies could shift regimes of the critical-state WBC from penetration to leap, and vice versa. Figure 1 shows a Kuroshio Loop current eddy-shedding event using the AVISO altimeter data (http://www.aviso.oceanobs.com/). The Kuroshio leaped across the Luzon Strait initially (Figures 1A, B). Meanwhile, an anticyclonic eddy from the northwestern Pacific moved westward to impinge and interact with the Kuroshio near the southeastern location of the Luzon Strait, and then it moved northward along with the Kuroshio. As the eddy interacted fully with the Kuroshio, a loop current was gradually formed in the vicinity of the Luzon Strait (Figure 1C). Lastly, an anticyclonic eddy was shed from the Kuroshio, and the main stream of the Kuroshio leaped across the gap again (Figure 1D). In this case, it seems that the perturbation of the eddy from the east induces the Kuroshio transition between penetration and leap and will be explored in this study.

In fact, there are two island chains in the Luzon Strait, including the southern Babuyan Island chain composed of the Camiguin, Calayan, Fuga, and Dalupiri Islands, and the central Batanes Island chain composed of the Sabtang, Batanes, and Itbayat Islands, as shown in Figure 1 (Liang et al., 2008; Huang et al., 2017). Intuitively, these island chains may influence the WBC intrusion into the SCS to some extent. Metzger and Hurlburt (2001) found that the Calayan Bank and a shoal north of the Calayan Island within the Luzon Strait reduce the westward intrusion of the Kuroshio into the SCS by using the NRE Layered Ocean Model. Mei et al. (2019); Mei et al. (2022) investigated the influence of an island on the WBC regime and found that the presence of an island promotes the WBC shedding eddies compared with the no-island case in the gap. Previous numerical studies focus on the effect of one island in the gap (resembling the central Batanes Island), which facilitates the WBC intrusion usually. However, the southern Babuyan Island may conversely prevent the Kuroshio from intruding into the SCS to some extent because the WBC leaps across the gap more easily as the southern gap width decreases, as examined by Mei et al. (2019). To what extent the combined quantitative impacts the southern and central islands on the WBC hysteresis and the critical-state WBC transition is worth studying. This paper is a continuation of Mei et al. (2019); Mei et al. (2022) and further considers the eddy–WBC interaction in the vicinity of a gap between two islands, which resemble the central Batanes Island and the southern Babuyan Island in the Luzon Strait.

In this study, we use a non-linear 1.5-layer ocean model to study the hysteresis of the WBC with two islands in the gap and the dynamics of the critical-state WBC transition impinged by a mesoscale eddy from the east. The model is described in Section 2. The hysteresis of the WBC with two islands in the gap and the

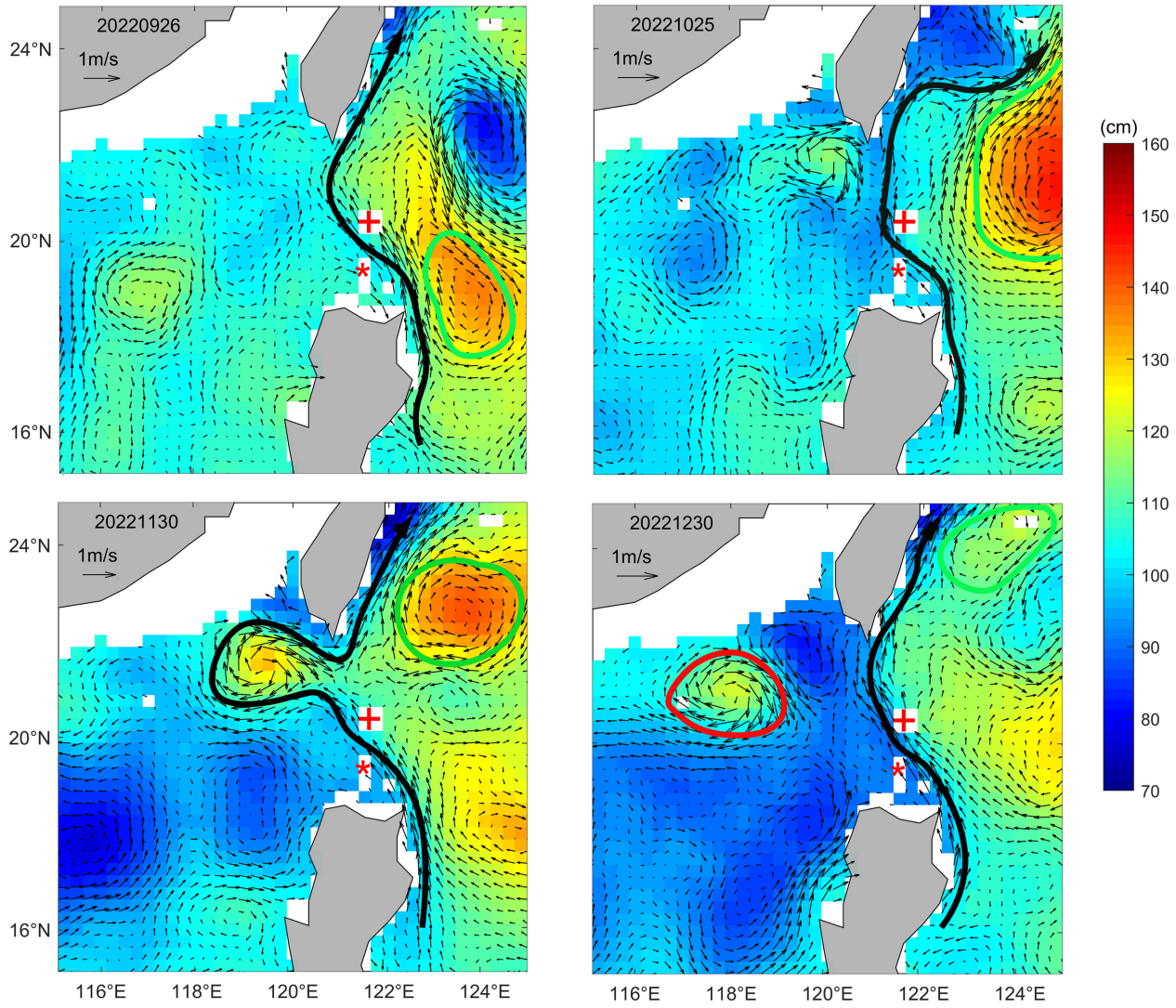

FIGURE 1
Absolute dynamical topography (cm; shading) and geostrophic currents (m/s; vector) in the northeastern SCS showing an anticyclonic eddy shed from the Kuroshio in 2022. A westward-moving anticyclonic eddy from the northwestern Pacific interacted with the Kuroshio in the Luzon Strait area inducing the Kuroshio transition. Regions with water shallower than 100 m are in white. The Batanes Island Chain and Babuyan Island Chain are marked by red plus and asterisk, respectively. The black, red, and green bold curves represent the Kuroshio axis, the anticyclonic eddy shed from the Kuroshio, and the westward-moving anticyclonic eddy from the northwestern Pacific, respectively. SCS, South China Sea.

dynamics of the eddy–WBC interaction are studied in Section 3. The conclusion and discussion are given in Section 4.

2 The model

In this study, a non-linear 1.5-layer reduced gravity model is adopted for simulation. The application of the model to the western Pacific Ocean, the Luzon Strait, and the SCS has been proven to be reasonable (Yuan et al., 2019; Mei et al., 2023), and the methodology has been well validated to the gap-leaping problem (Mei et al., 2019; Mei et al., 2022; Mei et al., 2023). The governing equations are as follows:

$$\boldsymbol{u}_t + \xi \boldsymbol{k} \times \boldsymbol{u} = -\nabla E + A_h \nabla^2 \boldsymbol{u} - R\boldsymbol{u} + \frac{\boldsymbol{\tau}}{\rho_0 h}, \quad (1)$$

$$h_t + \nabla \cdot (h\boldsymbol{u}) = 0, \quad (2)$$

where $u = (\boldsymbol{u}, v)$ is the horizontal velocity vector in the x and y directions, $\xi = f + \boldsymbol{k} \cdot \nabla \times \boldsymbol{u}$ is the absolute vorticity, and $f = f_0 + \beta y$ is the Coriolis parameter on the β-plane with constant Rossby parameter $\beta = 2 \times 10^{-11}$ m^{-1} s^{-1}, where the southern boundary of the model is set as the equator with $f_0 = 0$; $\mathbf{k}$ is the unit vector in the vertical direction, and h is the upper-layer thickness with the initial resting thickness of 300 m, which is close to the thermocline depth of approximately 300–500 m in the western Pacific Ocean; $E = g'h + (u^2 + v^2)/2$ is the total energy, $\boldsymbol{\tau} = (\tau_x, \tau_y)$ is the surface wind stress vector in the x and y directions, $A_h = 300\ m^2\ s^{-1}$ is the horizontal eddy viscosity coefficient, $R = 5 \times 10^{-8}\ s^{-1}$ is the Rayleigh friction coefficient, $\rho_0 = 1024\ kg\ m^{-3}$ is the reference density, and

$g' = 0.031\ \mathrm{m\ s^{-2}}$ is the reduced gravity. Moreover, the model set is similar to that in Qiu and Chen (2012), and the choices of the lateral viscosity and the Rayleigh friction coefficient are similar to those in Jiang et al. (1995).

The vorticity equation is derived from the cross-differentiation forms of the momentum equations in Equation 1 for vorticity balance analysis first, as follows:

$$\zeta_t + J(\psi, \zeta) + \beta\psi_x = A_h \nabla^2 \zeta - R\zeta + \nabla \times \left(\frac{\tau}{\rho_0 h}\right), \tag{3}$$

where $\zeta = \nabla^2\psi$ is the relative vorticity, ψ is the stream function, and J is the Jacobian operator. The effect of the lower-layer circulation is neglected in the hysteresis characteristics of the WBC in the gap-leaping system, and an additional term $-[fh_E/2h]\zeta$ is added to the vorticity equation to estimate the insignificance of the lower-layer circulation, where $h_E = \sqrt{2\nu/f}$ is the Ekman layer depth and $\nu = 0.01\ \mathrm{m^2\ s^{-1}}$ is the molecular viscosity (estimating the vertical Ekman layer depth) (Zavala Sanson and Van Heijst, 2002; Cushman-Roisin and Beckers, 2011; Kuehl and Sheremet, 2014; McMahon et al., 2020; McMahon et al., 2021; Mei et al., 2022; Mei et al., 2023). In fact, the horizontal spatial scale is four orders of magnitude larger than the vertical spatial scale in this study. Therefore, the molecular viscosity of about four orders of magnitude lower than the horizontal eddy viscosity coefficient (A_h) is reasonable (Cushman-Roisin and Beckers, 2011).

An idealized rectangular domain separated by a thin meridional barrier into two rectangular basins is adopted, and a thin gap is inserted into the middle of the meridional barrier. The western basin covers 100°–120°E, and the eastern basin, 120°–150°E; both extend from 0° to 30°N. The thin meridional barrier is placed along 120°E with a gap of $2a$ (~290 km) in width from 13.8°N to 16.4°N. Two meridional islands are inserted into the gap. The Munk layer width $L_M = (A_h/\beta)^{1/3}$ is 24.7 km. Then, the ratio of the half width of the gap to the Munk layer width ($\gamma = a/L_M$) is 5.87, which guarantees the existence of WBC hysteresis (Sheremet, 2001). The inertial boundary layer thickness ($L_I = \sqrt{U_0/\beta}$) is used to estimate the balance between the relative vorticity advection and β effect, where $U_0 (= Q/L)$ is the Sverdrup interior velocity scale, Q is the transport per unit depth of the WBC, and L is the basin length scale (McMahon et al., 2021; Mei et al., 2022; Mei et al., 2023).

The WBC is driven by an idealized zonal wind in the eastern basin, and the transport of the WBC depends on the wind stress strength parameter α_τ, which is controlled by the following equation:

$$\tau_x = -\alpha_\tau \tau_0 \cos\left(\frac{\pi\phi}{D_{N-S}}\right), \tag{4}$$

where $\tau_0 = 0.1\ N\ m^{-2}$, ϕ is the latitude, and $D_{N\text{-}S}$ is the latitude interval between the northern and southern boundaries. In the numerical experiments, the integration time of the controlling equation should be long enough for each α_τ for the WBC to reach a steady solution. Then, the transport per unit depth of the WBC (Q) is calculated from the steady solution on the zonal section from 120°E to 121°E at 13.8°N, and the Reynolds number is defined and calculated as $\mathrm{Re} = Q/A_h$. The partial differential equations in Equations 1 and 2 are solved using the finite difference method. The spatial resolution of the model is 0.1°, and the grid convergence has been validated in the numerical experiments (not shown).

In the numerical experiments, the mesoscale eddy of a Gaussian stream function distribution is added to the critical-state WBC as a perturbation. The zonal (u_{eddy}) and meridional (v_{eddy}) velocity components of the eddy are given as follows (Yuan and Li, 2008; Yuan and Wang, 2011; Mei et al., 2022):

$$u_{\mathrm{eddy}} = \psi_0 \frac{y}{r^2} \exp\left(-\frac{x^2+y^2}{2r^2}\right), \tag{5}$$

$$v_{\mathrm{eddy}} = -\psi_0 \frac{x}{r^2} \exp\left(-\frac{x^2+y^2}{2r^2}\right), \tag{6}$$

where ψ_0 is the maximum stream function value of the mesoscale eddy at the center, with positive (negative) ψ_0 representing an anticyclonic (a cyclonic) eddy, and r is the distance of the maximum azimuthal velocity of the eddy at 80 km from the eddy center.

3 Results

3.1 Hysteresis of WBC with two islands in the gap

In order to study the hysteresis of the WBC with two islands in the gap, numerous numerical experiments are designed, and the results are compared with those of Mei et al. (2019); Mei et al. (2022). We place two islands of ~22 km in meridional width on the gap, where the position of the northern island is from 15° to 15.2°N, and that of the southern island is from 14° to 14.2°N, resembling the central Batanes Island and the southern Babuyan Island in the Luzon Strait. Figure 2 shows the hysteresis curves of the WBC in the no-island, one-island, and two-island cases, where X_P represents the farthest distance to the west of the $\psi = Q/2$ streamline of the WBC main stream into the western basin from the gap. In the numerical experiments, α_τ is first increased with an interval of 0.01 from 0.18 to 0.83 [the wind stress increasing stage, as in Mei et al. (2019)], and then, it gradually decreased from a supercritical value of more than 0.83 to 0.18 [the wind stress decreasing stage, as in Mei et al. (2019)]. Note that the steady-state solution of the earlier integration is used as the initial condition of the later integration to retain the historical WBC status, as in Mei et al. (2019); Mei et al. (2022). For each α_τ, the Re is calculated for both the cases in the wind stress increasing and decreasing stages.

During the wind stress increasing stage, Figure 2 shows that the WBC flow state experiences three types of regimes as Re is increased, including the penetrating, periodic eddy-shedding, and leaping regimes. First, the WBC intrudes into the western basin as an anticyclonic loop current near the gap at low Re. Then, the WBC path experiences a first transition from the penetrating to the periodic eddy-shedding regime at $\mathrm{Re}_{C\text{-}2} = 31$ (the lower Hopf bifurcation) for the two-island case, corresponding to the multivalued hysteresis curves, which indicates the distances of the farthest and closest WBC intrusion into the western basin between the two adjacent half periods during one eddy-shedding process. At

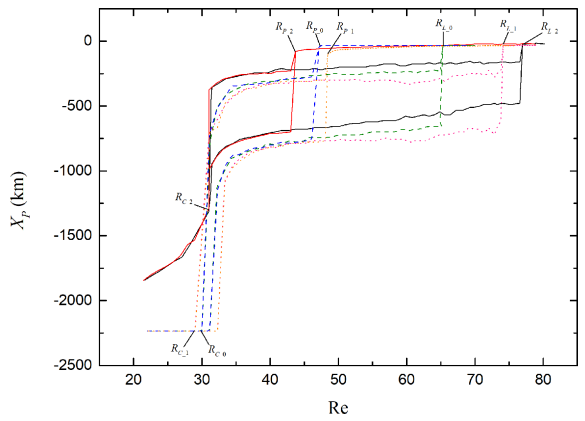

FIGURE 2
Hysteresis curves of the WBC with no island, one island, and two islands in the gap, where X_P is the westernmost position of the $\psi = Q/2$ streamline of the WBC, with 0 standing for the position of the barrier; the Reynolds number is defined as $Re = Q/A_h$; $Re_{C\text{-}2}$ ($Re_{C\text{-}0}$, $Re_{C\text{-}1}$) is the critical value of the WBC in the gap with two islands (no island, one island) shifting from the penetrating to the eddy-shedding regime. $Re_{L\text{-}2}$ ($Re_{L\text{-}0}$, $Re_{L\text{-}1}$) is the critical value of the WBC in the gap with two islands (no island, one island) shifting from the eddy-shedding to leaping regime. $Re_{P\text{-}2}$ ($Re_{P\text{-}0}$, $Re_{P\text{-}1}$) is the critical value of the WBC in the gap with two islands (no island, one island) shifting from the leaping to eddy-shedding regime. The double curves indicate the WBC in the periodic eddy-shedding regime. WBC, western boundary current.

that moment, the WBC begins to intrude into the western basin as a periodic eddy-shedding path. It can be seen in Figure 2 that the lower Hopf bifurcation is almost unchanged for the three cases regardless of the island's presence in the gap, where the corresponding Re of the no-island and one-island cases are $Re_{C\text{-}0} = 30$ and $Re_{C\text{-}1} = 29$, respectively. When the Re is increased to be more than another critical value Re_L, the WBC experiences a second transition from the periodic eddy-shedding to leaping regimes at $Re_{L\text{-}2} = 77$ (the upper Hopf bifurcation). Then, the WBC leaps across the gap, and the hysteresis curve changes to be a single-value curve again. As a result, the hysteresis curves suggest that the presence of the two islands in the gap facilitates the WBC intrusion into the western basin in the eddy-shedding regime compared with the no-island case ($Re_{L\text{-}0} = 65$) and one-island case ($Re_{L\text{-}1} = 74$) in the wind stress increasing stage, because the difference of Re (defined as $\Delta Re_{IN} = Re_L\text{-}Re_C$ in the wind stress increasing stage) between the upper and lower Hopf bifurcations is $\Delta Re_{2,IN} > \Delta Re_{1,IN} > \Delta Re_{0,IN}$.

During the wind stress decreasing stage, the hysteresis curves indicate that the WBC also experiences the above-mentioned three flow regimes as Re is decreased. When Re is reduced from a supercritical value to $Re_{P\text{-}0} = 46$, $Re_{P\text{-}1} = 48$, and $Re_{P\text{-}2} = 43$, respectively, the WBC shifts regimes from the leaping path to the periodic eddy-shedding path for the no-island case, one-island case, and two-island case. The results suggest that the WBC hysteresis occurs in a specific interval of Re in this situation, i.e., the eddy-shedding regime and leaping regime of the WBC coexist at the same Re in the range of (Re_P, Re_L). As Re is further reduced to Re_C, the transition of the WBC path from the periodic eddy-shedding to penetrating (an anticyclonic loop current) regime occurs. In this case, however, the presence of two islands in the gap is unfavorable to the WBC to intrude into the western basin by shedding eddies compared with the no-island and one-island cases, because the difference of Re (defined as $\Delta Re_{DE} = Re_P - Re_C$ in the wind stress decreasing stage) is $\Delta Re_{1,DE} > \Delta Re_{0,DE} > \Delta Re_{2,DE}$.

From the above results, on the one hand, it can be concluded that the presence of two islands in the gap facilitates the WBC intrusion compared with the no-island case, but it is unfavorable to the WBC intrusion compared with the one-island case, by shedding eddies into the western basin. This is evidenced by the comparison of the parameter space of the WBC in the eddy-shedding regime, i.e., $(\Delta Re_{1,IN} + \Delta Re_{1,DE}) > (\Delta Re_{2,IN} + \Delta Re_{2,DE}) > (\Delta Re_{0,IN} + \Delta Re_{0,DE})$. On the other hand, the farthest intrusive distance (corresponding to the maximum value X_P) of approximately 1,700 km for the two-island case is smaller than that of approximately 2,200 km for both the no-island and one-island cases in Figure 2. This indicates that the presence of the southern island hinders the intrusive distance of the WBC into the western basin to some extent, and the result is in accord with the realistic model result in Metzger and Hurlburt (2001).

The time evolution of the WBC pattern in the vicinity of the gap with two islands under different Re is shown in Figure 3. In the wind stress increasing stage, the WBC begins to intrude into the western basin as a loop current at Re = 24 (Figure 3A). Then, the WBC starts to the shed eddies at Re = 31, and it retains the eddy-shedding path until at Re = 75, as shown in Figure 3B. Note that the WBC mainly flows into the western basin through the gap between the northern and southern islands, with a little of WBC water leaking into the western basin through the narrow gap between the southern island and the southern barrier. As Re is increased to $Re_{L\text{-}2} = 77$ (Figure 3C), the WBC transforms to leap across the gap. In the wind stress decreasing stage, the WBC stays in the leaping regime until Re is reduced to $Re_{P\text{-}2} = 43$, where the WBC path is transited to the eddy-shedding pattern (Figure 3E). It can be seen that the eddy-shedding and leaping patterns of the WBC coexist at the same Re (=75) in Figures 3B, D, which indicates that WBC hysteresis occurs at that moment. When Re is further decreased to Re = 24, the WBC intrudes into the western basin as a loop current again (Figure 3F). According to the above experiments, the inertial boundary layer thickness L_I changes from approximately 9.5 to 19.6 km, which is smaller than the Munk boundary layer thickness (24.7 km). This indicates that horizontal friction dominated the advection and Rayleigh friction (McMahon et al., 2021; Mei et al., 2022; Mei et al., 2023).

3.2 Impact of mesoscale eddy on the WBC regime shifts with two islands in the gap

In this section, the impact of two islands in the gap on the critical-state WBC transition during the WBC–eddy interaction is studied and compared with that of the no-island case (Yuan and Wang, 2011) and the one-island case (Mei et al., 2022). The impact of north–south locations of the mesoscale eddy on the critical-state WBC path is also studied. As shown in Figure 2, the WBC begins to shift regimes from the eddy-shedding path to the leaping path at

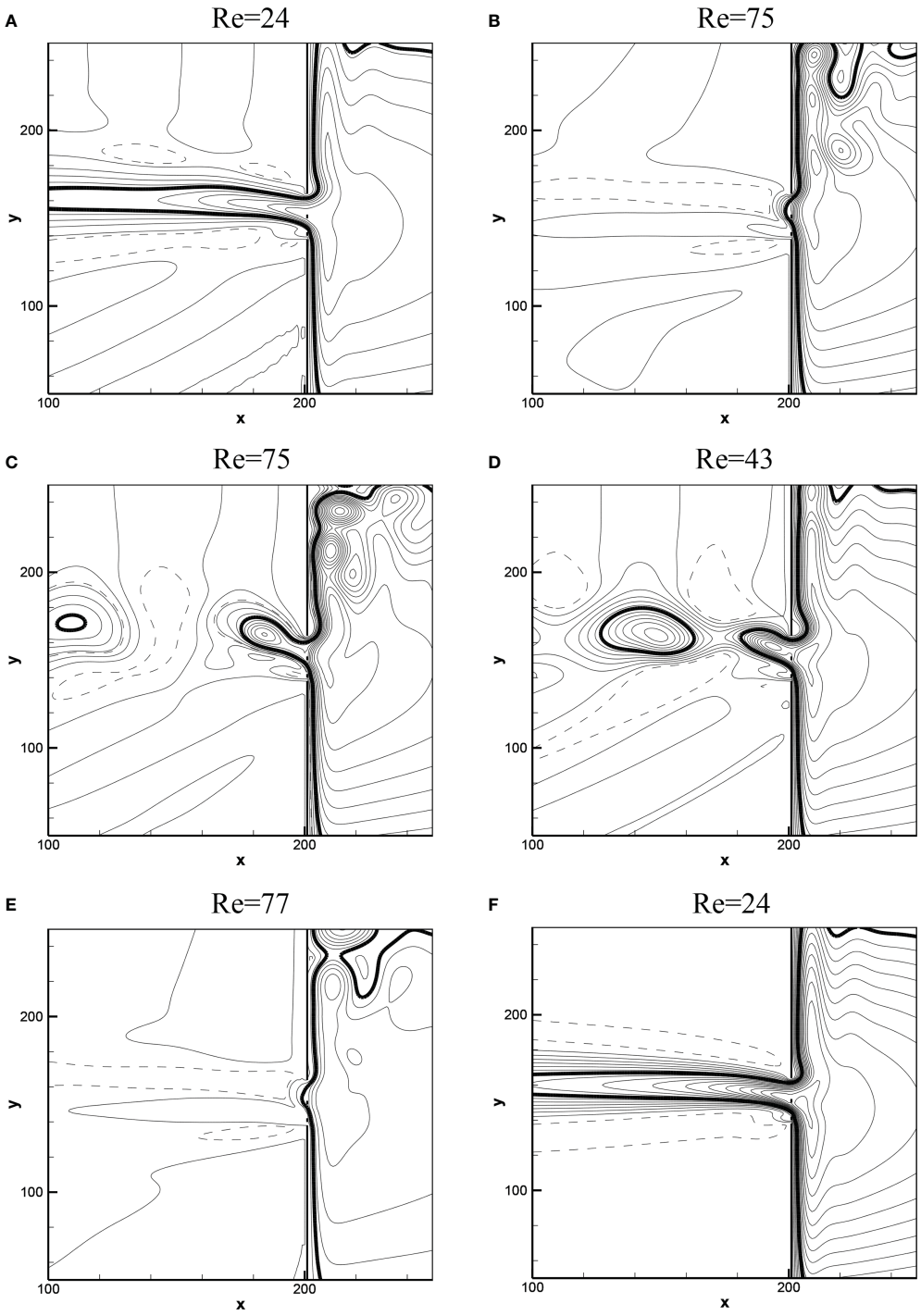

FIGURE 3
Time evolution of the WBC in the vicinity of the gap with two islands under different Re. **(A–C)** The WBC pattern in the wind stress increasing stage and **(D, F)** that in the wind stress decreasing stage. **(C, E)** The $Re_{L\text{-}2}$ and $Re_{P\text{-}2}$ positions in Figure 1. The bold curve represents the $\psi = Q/2$ streamline of the WBC and shed eddy. WBC, western boundary current.

$Re_{L\text{-}2}$ = 77 and from the leaping path to the eddy-shedding path at $Re_{P\text{-}2}$ = 43. Then, the steady solution of the critical-state WBC at Re = 76 (Re = 44) in the wind stress increasing (decreasing) stage is used as the background flow. A mesoscale eddy is inserted 300 km east of the gap into the critical-state WBC solution as the initial condition (Yuan and Li, 2008; Yuan and Wang, 2011; Mei et al., 2022).

3.2.1 From penetration to leap

First, when the WBC is critical from the eddy-shedding to leaping regime, an anticyclonic eddy is released due east of the gap center, and then it moves westward on the β plane. The time evolution of the WBC flow pattern in the vicinity of the gap is shown in Figure 4. In this case, the critical strength of the eddy that can induce the WBC transition from penetration to leap is ψ_c =

26,000 m^2 s^{-1}. As the anticyclonic eddy moves to the gap and interacts with the WBC, the critical WBC gradually stops at the shed eddies and begins to leap across the gap at approximately 700 days. Then, the WBC remains in the leaping regime permanently. The left fling of the anticyclonic eddy enhances the WBC speed as well as the meridional advection at the entrance of the gap, and then it induces the WBC transition, similar as in Yuan and Wang (2011) and Mei et al. (2022).

The dynamics of the WBC transition is analyzed by extracting each vorticity term from Equation 3 at a grid point nearest to X_P, as shown in Figure 5. At the initial stage of the numerical experiment, all the vorticity balance terms are oscillatory. As the anticyclonic eddy interacts fully with the WBC at approximately day 700, the vorticity balance shows that the meridional advection term increases by one order of magnitude, and the vorticity balance is mainly between the beta term and the other terms. Then, the WBC transition from the eddy-shedding regime to leaping regime occurs. In the above experiment, the lower-layer circulation estimated by the additional term $-[fh_E/2h]\zeta$ is at least one order of magnitude smaller than the meridional advection and β terms (not shown). Further, the observations and model results show that the barotropic component of full-depth current and the lower-layer circulation in the SCS are both one order of magnitude smaller than the velocity of the upper-layer circulation, as mentioned in Mei et al. (2023). This illustrates the lower-layer circulation is negligible.

We also examine the impact of a central cyclonic eddy on the regime shifts of the WBC critical from the eddy-shedding to leaping regime. The critical strength of the cyclonic eddy inducing the WBC transition is ψ_c = 28,000 m^2 s^{-1}. Figure 6 shows the time evolution of the critical WBC impinged by the cyclonic eddy near the gap. When the westward-moving cyclonic eddy approaches the gap and impinges on the WBC, the eddy shape is squeezed and distorted,

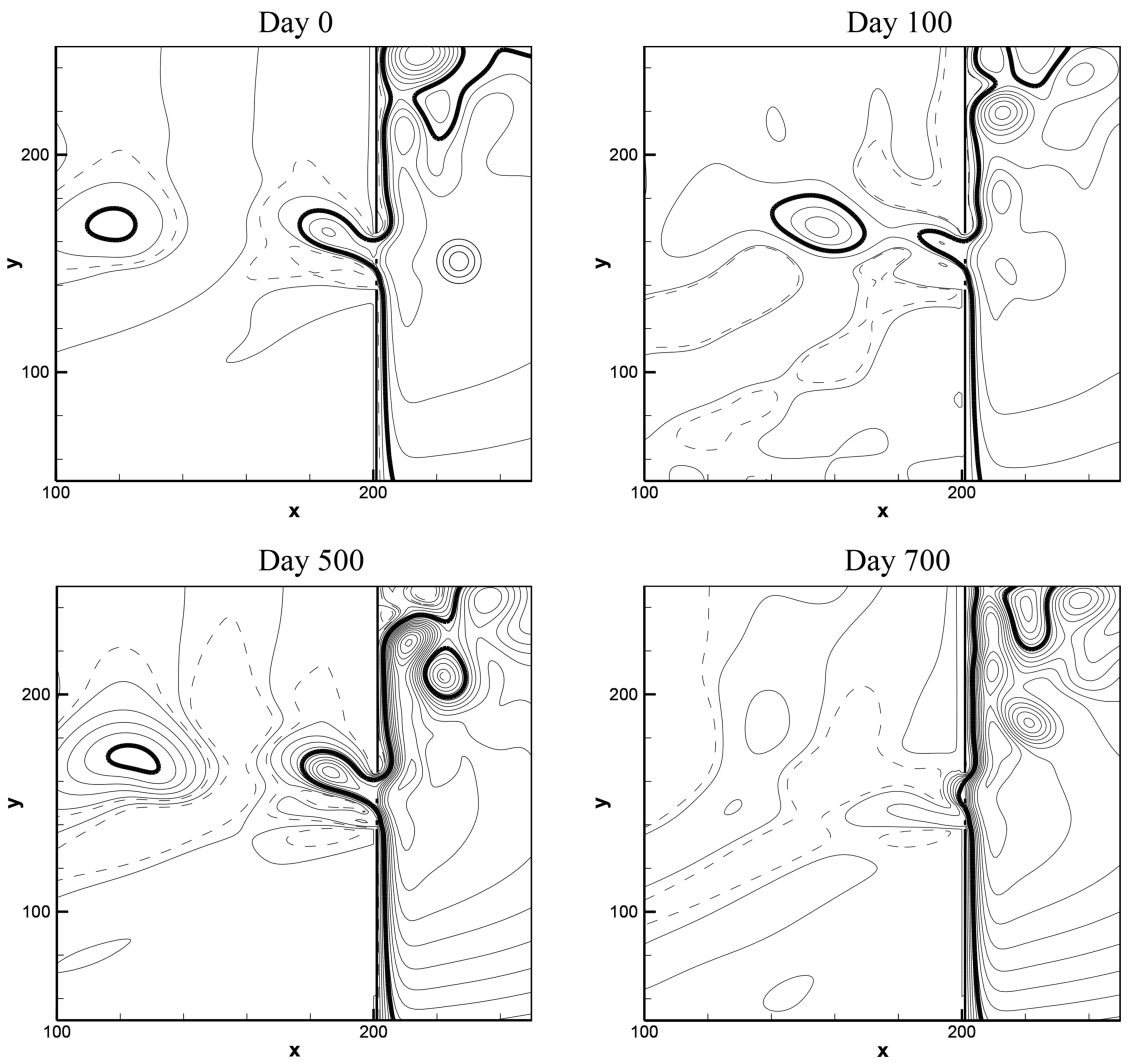

FIGURE 4
Time evolution of the WBC critical from the eddy-shedding to leaping regime at Re = 76 impinged by an anticyclonic eddy in the vicinity of the gap with two islands. An initial anticyclonic eddy with a radius of approximately 80 km is inserted 300 km east of the gap into the background flow, and it propagates toward the gap. The critical strength of the eddy (ψ_c = 26,000 m^2 s^{-1}) is the minimum value that can induce the critical WBC transition from penetration to leap. WBC, western boundary current.

and then the eddy energy is almost absorbed by the WBC to transport westward and northward. As the right fling of the eddy approaches the gap area, the WBC speed at the entrance of the gap is enhanced by the northward current of the eddy, and then the WBC turns to leap across the gap at approximately day 900.

Figure 7 shows the vorticity balance analysis of the cyclonic eddy–WBC interaction near X_P. All the vorticity balance terms start to oscillate until at approximately day 900 when the beta and meridional advection terms increase by one order of magnitude. Then, the vorticity balance is mainly the increased beta term balances the increased meridional advection and viscosity terms. As the WBC transition occurs, the WBC maintains the leaping path over time. Note that the cyclonic eddy takes more time to induce the WBC regime shift than that in Figure 5. This is because the right fling of the cyclonic eddy takes more time to reach the gap than that of the left fling of the anticyclonic eddy.

Next, the impact of variable north–south locations of the mesoscale eddy on the critical-state WBC transition is studied with the presence of two islands in the gap-leaping system. In the following numerical experiments, the eddies are specified unchangeably 300 km east of the gap in the zonal direction, but their north–south locations are changed continuously in the meridional direction. The critical strength of the eddy (ψ_c) that is able to induce the WBC transition is normalized by the critical WBC strength, i.e., $\gamma = \psi_c/Q_c$. The dimensionless parameter $\lambda(=L_i/L_g)$ is defined to indicate the location of the initial eddy, where L_i is the meridional distance between the latitude of the eddy center and that of the northern tip of the southern barrier, and L_g is the gap width. The critical strength of the eddy inducing the critical WBC transition from the periodic eddy-shedding to leaping regime as a function of λ for the two-island case is shown in Figure 8. First, the WBC regime shift is most sensitive to the anticyclonic eddy due east of the gap center, and it is least sensitive to the anticyclonic eddy approaching the gap downstream of the WBC (Figure 8A). The least sensitive location of the anticyclonic eddy is in accord with the no-island case in Yuan and Wang (2011) and one-island case in Mei et al. (2022), where the northern anticyclonic eddy can induce the critical-state WBC transition more difficultly than from the center and south of the gap. Second, the regime shift of the WBC is most sensitive to the cyclonic eddy from the south of the gap and least sensitive to the cyclonic eddy downstream of the WBC (Figure 8B). The most sensitive location of the cyclonic eddy is in accord with the no-island case in Yuan and Wang (2011) but is opposite to the one-island case in Mei et al. (2022).

3.2.2 From leap to penetration

In this subsection, we examine the influence of a mesoscale eddy on the regime shifts of the WBC critical from the leaping to eddy-shedding path. When a cyclonic eddy is inserted 300 km due east of the gap center as the initial condition, the critical eddy strength that can induce the WBC transition from leap to penetration is ψ_c = 28,000 $m^2\ s^{-1}$. Figure 9 shows the time evolution of the critical WBC pattern at Re = 44 impinged by the cyclonic eddy in the vicinity of the gap with two islands. At approximately day 700, the cyclonic eddy is eventually absorbed by the WBC, and the southward current of the left fling of the eddy reduces the northward speed of the WBC at the entrance of the gap, which induces the WBC regime shifts. Then, the WBC pattern is permanently shifted from the leaping regime to the penetrating regime.

The vorticity balance of the cyclonic eddy–WBC interaction is analyzed in Figure 10. As the cyclonic eddy moves westward and eventually approaches the gap area, it reduces the meridional advection term of the WBC during the interactional process, and then the decreased beta term is mainly balanced by the decreased meridional advection and viscosity terms when the WBC pattern translates to the eddy-shedding path. At last, all the vorticity balance terms appear to be periodic.

Then, the impact of an anticyclonic eddy on the critical WBC path is studied as well. In this case, the critical strength of the anticyclonic eddy is ψ_c = 41,000 $m^2\ s^{-1}$. Figure 11 shows the time evolution of the critical WBC pattern impinged by the anticyclonic eddy in the vicinity of the gap between the two islands. It can be seen that the WBC shifts regimes under the perturbation of the eddy. It is the right fling of the anticyclonic eddy that reduces the

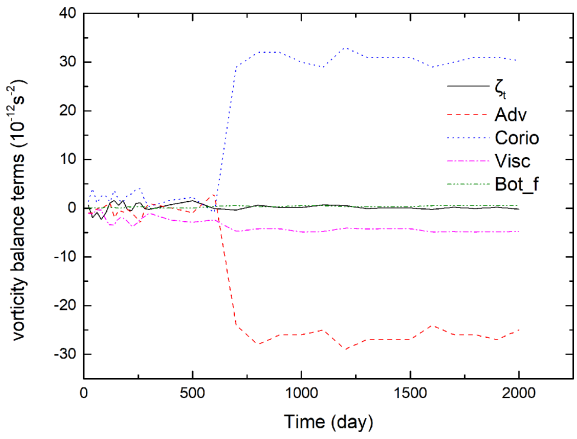

FIGURE 5
Time evolution of the vorticity balance terms near X_P during the interaction of the anticyclonic eddy and the WBC critical from penetration to leap at Re = 76 in the vicinity of the gap with two islands. WBC, western boundary current.

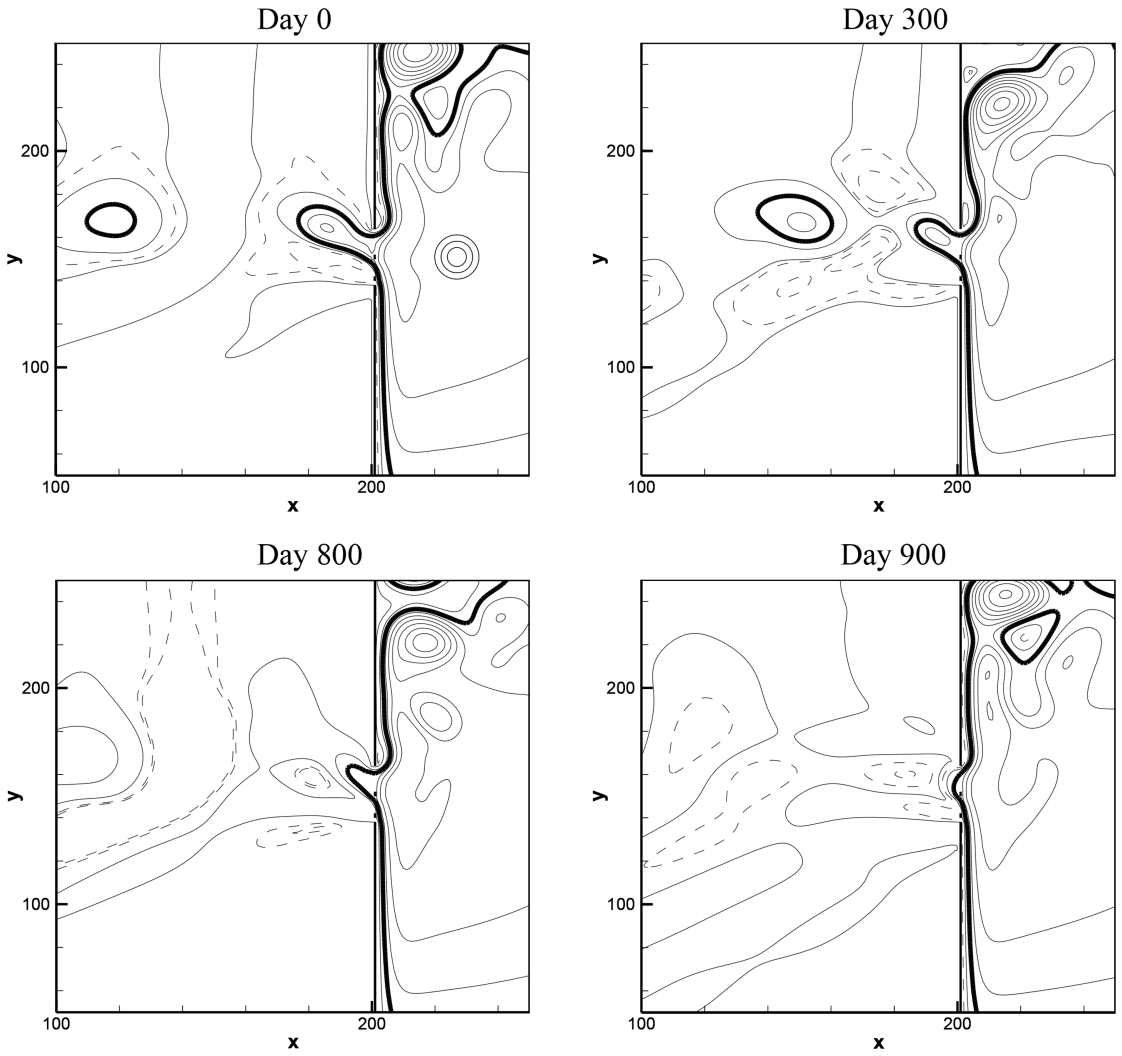

FIGURE 6
Same as Figure 4, except for the critical WBC pattern impinged by a cyclonic eddy. The critical strength of the eddy is ψ_c = 28,000 m^2 s^{-1}. WBC, western boundary current.

northward current of the WBC as well as the meridional advection at the entrance of the gap, so as to promote the WBC intrusion into the western basin and induce the WBC transition. The result is similar to that in Mei et al. (2022), where the anticyclonic eddies from the east were able to induce the critical WBC regime shifts from the leaping to eddy-shedding regime when one island is present in the gap. However, it is opposite to Yuan and Wang (2011), who concluded that the anticyclonic eddies could not induce the WBC transition from the leap to penetration.

Figure 12 shows the vorticity balance analysis of the anticyclonic eddy–WBC interaction and indicates that the decreased beta term is balanced by both the decreased meridional advection and viscosity terms when the WBC path shifts from the leaping regime to the eddy-shedding regime. Then, the WBC keeps the penetrating path, and all vorticity terms appear to be periodic as time elapses.

At last, we examine the critical-state WBC regime shifts from leap to penetration perturbed by the mesoscale eddy of variable north–south locations. The critical strength of the eddy inducing the WBC transition as a function of λ for the two-island case is shown in Figure 13. It can be seen that the critical strength of the cyclonic eddy from the south of the gap is almost unchanged (Figure 13A). The WBC transition is most sensitive to the southern cyclonic eddies and least sensitive to the northern cyclonic eddies, which is in accord with the one-island case in Mei et al. (2022). Moreover, the most sensitive location of the cyclonic eddy is in accord with the no-island case in Yuan and Wang (2011). However, the northern cyclonic eddy cannot induce the WBC transition from leap to penetration in their study. However, the critical strength of the anticyclonic eddy increases as λ increases (Figure 13B). The regime shift of the WBC is most sensitive to the anticyclonic eddy upstream of the WBC and least

10.3389/fmars.2023.1147292

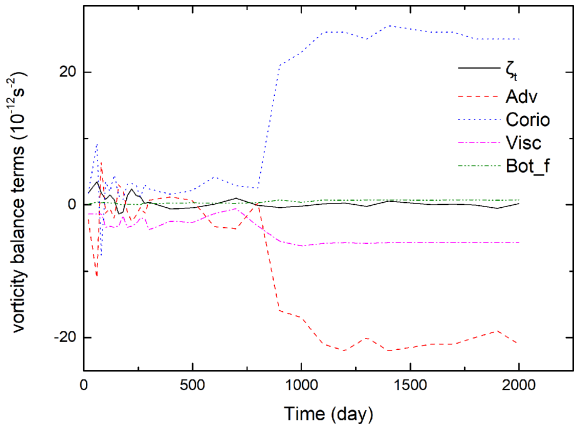

FIGURE 7
Same as Figure 5, except for the cyclonic eddy–WBC interaction. WBC, western boundary current.

sensitive to that from the northern gap, which is opposite to the one-island case in Mei et al. (2022).

4 Conclusions and discussion

In this paper, the hysteresis of the WBC flowing across the gap with two islands and the dynamics of the mesoscale eddy–WBC interaction affected by the two islands are studied using the nonlinear 1.5-layer ocean model. The hysteresis curves show that the lower Hopf bifurcation of the WBC transition exhibits no differences in the two-island case compared with the existing results in the no-island and one-island cases. The critical Re of the upper Hopf bifurcation for the two-island case is larger than that of the no-island and one-island cases. However, the critical Re of the WBC transiting from the leaping to eddy-shedding regime is

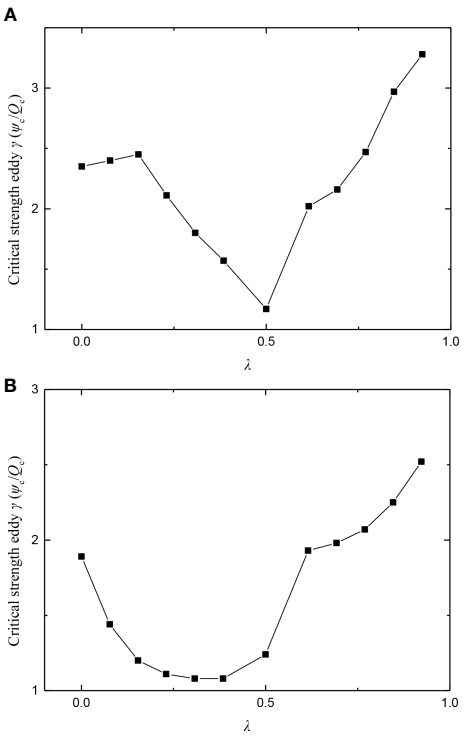

FIGURE 8
The dimensionless critical strength (γ) of the anticyclonic eddy **(A)** and the cyclonic eddy **(B)** inducing the critical WBC transition from the penetrating to leaping regime as a function of λ ($=L_i/L_g$), where $\gamma = \psi_c/Q_c$ represents the critical strength of the eddy (ψ_c) normalized by the critical WBC strength (Q_c), L_i is the meridional distance between the latitude of the eddy center and the latitude of the northern tip of the southern barrier, and L_g is the gap width. WBC, western boundary current.

10.3389/fmars.2023.1147292

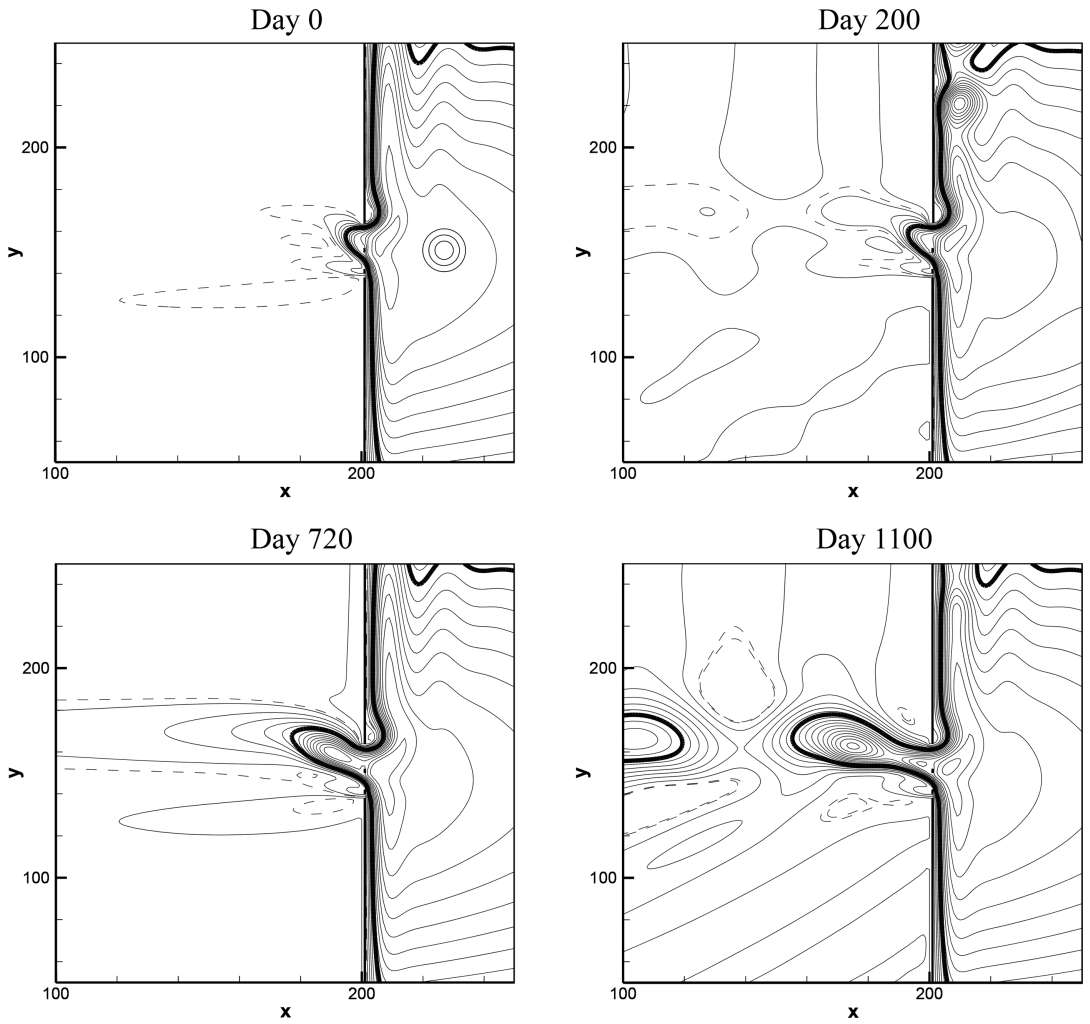

FIGURE 9
Time evolution of the WBC critical from the leaping to eddy-shedding regime at Re = 44 impinged by a cyclonic eddy in the vicinity of the gap with two islands. The cyclonic eddy with a radius of 80 km is inserted 300 km east of the gap into background flow and propagates toward the gap. The critical strength of the eddy is ψ_c = 28,000 m^2 s^{-1} to induce the critical WBC transition from leap to penetration. WBC, western boundary current.

smaller than that of the no-island and one-island cases. Considering the parameter space of the WBC in the eddy-shedding regime, it is found that the presence of two islands in the gap is favorable to the WBC intrusion by shedding eddies compared with the no-island case, but it is unfavorable to the WBC intrusion compared with the one-island case because the size of order of the parameter is $(\Delta Re_{1,IN} + \Delta Re_{1,DE}) > (\Delta Re_{2,IN} + \Delta Re_{2,DE}) > (\Delta Re_{0,IN} + \Delta Re_{0,DE})$.

The westward-moving mesoscale eddies from the east of the gap are able to induce the critical WBC transition with the two islands' presence in the gap. Both the anticyclonic and cyclonic eddies can induce the critical WBC shifting from the eddy-shedding regime to leaping regime and vice versa. The dynamics revealed by the vorticity balance show all the vorticity terms oscillate periodically for the WBC in the eddy-shedding regime, and then the meridional advection and viscosity terms are increased to balance the increased beta term perturbed by the eddy, which induces the WBC transition from penetration to leap. Conversely, the decreased meridional advection and viscosity terms are balanced by the decreased beta term perturbed by the eddy, which is responsible for the WBC transition from leap to penetration.

The model results suggest that the mesoscale eddy with variable north–south locations has a significant impact on the critical-state WBC transition with the presence of two islands in the gap-leaping system. When the critical WBC is shifted from the eddy-shedding to leaping regime, the WBC transition is most sensitive to the

10.3389/fmars.2023.1147292

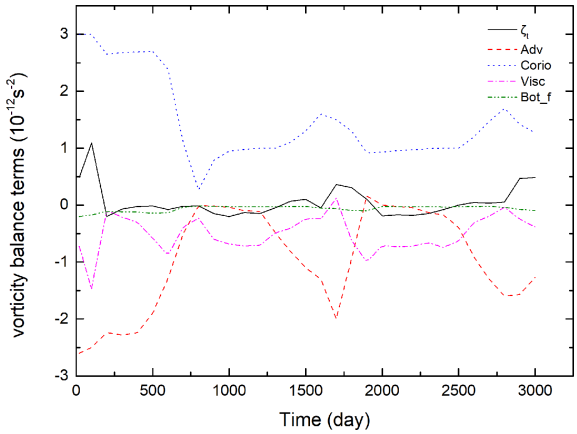

FIGURE 10
Time evolution of the vorticity balance terms near X_P during the interaction between a cyclonic eddy with the WBC critical from leap to penetration at Re = 44 in the vicinity of the gap with two islands. WBC, western boundary current.

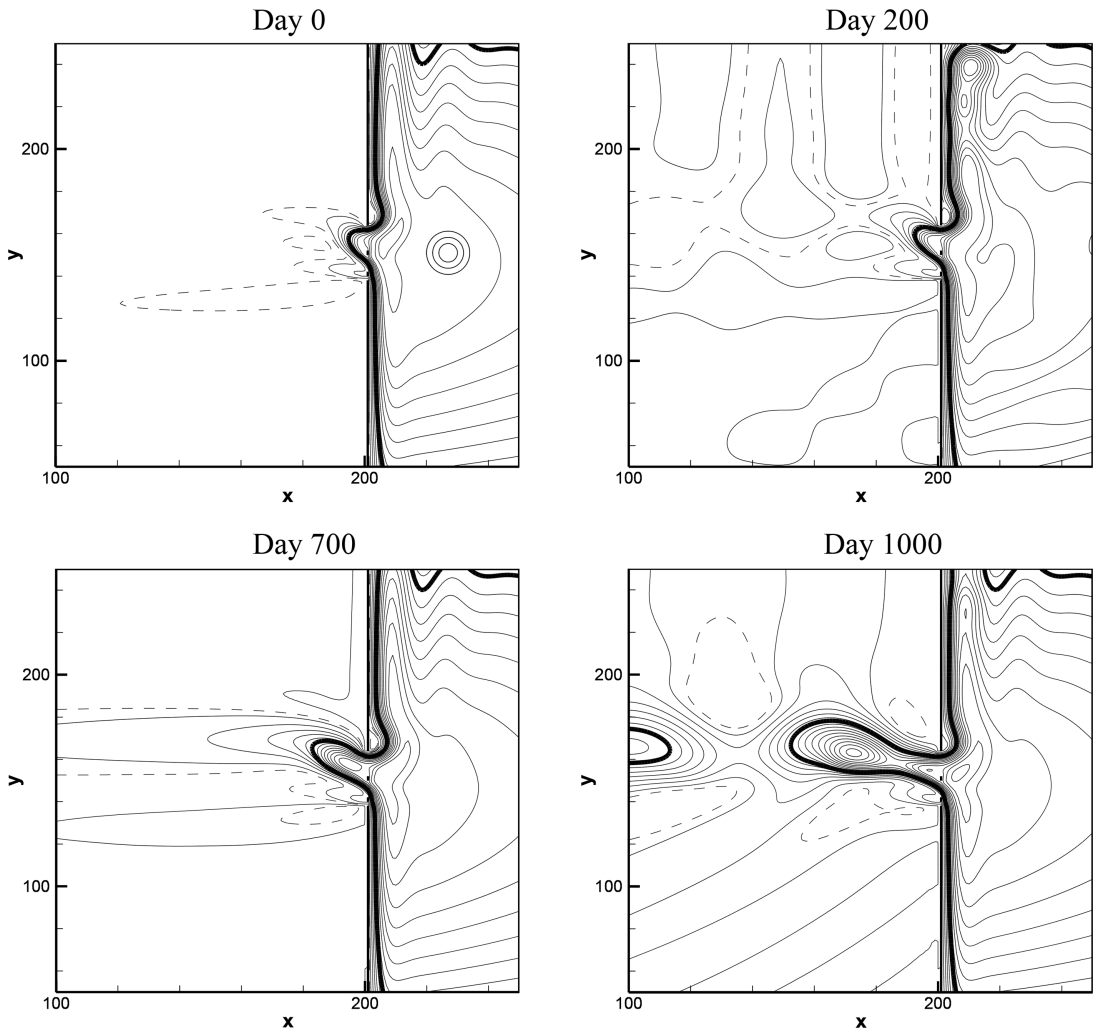

FIGURE 11
Same as Figure 9, except for the critical WBC path impinged by an anticyclonic eddy. The critical strength of the eddy is ψ_c = 41,000 m^2 s^{-1}. WBC, western boundary current.

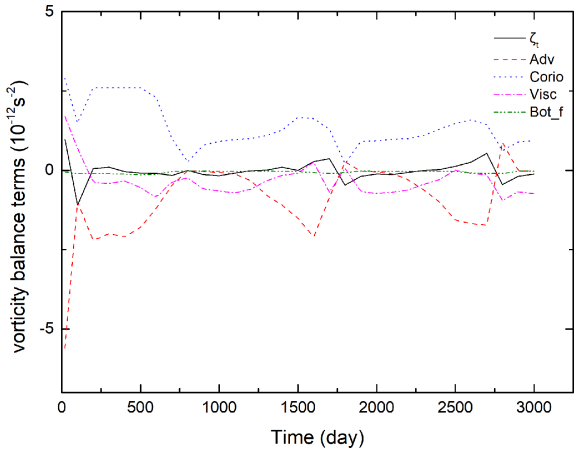

FIGURE 12
Same as Figure 10, except for the anticyclonic eddy–WBC interaction. WBC, western boundary current.

anticyclonic eddy due east of the gap center and is most sensitive to the cyclonic eddy from the south of the gap. It is least sensitive to the anticyclonic and cyclonic eddies downstream of the WBC. When the critical WBC is shifted from the leaping to eddy-shedding regime, the cyclonic eddies from the southern part of the gap exhibit no obvious difference in the critical eddy strength in inducing the critical WBC transition. In this case, the critical WBC regime shifts are most sensitive to the southern cyclonic eddies and least sensitive to the northern cyclonic eddies. The regime shift of the WBC is most sensitive to the anticyclonic eddy upstream of the WBC and least sensitive to that from the northern gap.

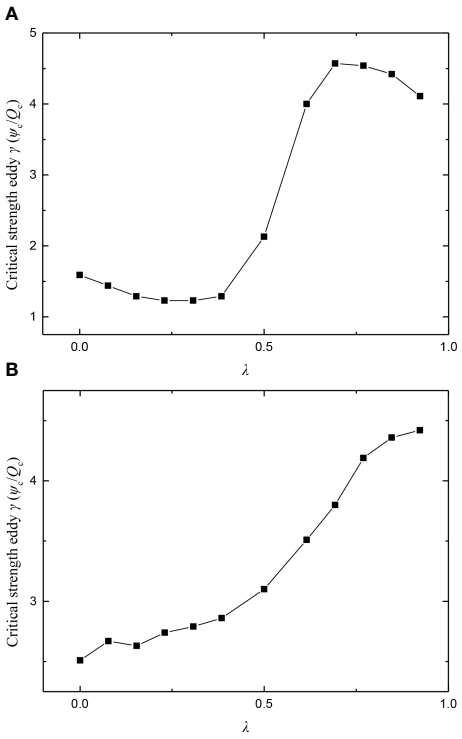

FIGURE 13
The dimensionless critical strength (γ) of the cyclonic eddy **(A)** and the anticyclonic eddy **(B)** inducing the critical WBC transition from the leaping to penetrating regime as a function of λ. WBC, western boundary current.

This study improves our understanding of the dynamics in the regional ocean that the Kuroshio passes by the Luzon Strait in the leaping or penetrating regime. Mei et al. (2022) suggested that the chance of the WBC in the leaping regime is equal to that in the eddy-shedding regime as one island presents in the gap, which overestimates the observation that the time of the Kuroshio in the leaping regime was about twice of that in the penetrating regime in the real world, as summarized in Yuan et al. (2006). Meanwhile, Mei et al. (2022) suspected that the southern Babuyan Island may prevent the Kuroshio from intruding into the SCS to some extent, which was confirmed by the model results in Mei et al. (2019), where only a southern island presents in the gap. The present results with two islands in the gap support that the southern island facilitates the WBC to leap across the gap compared with the one-island case in Mei et al. (2022), despite the chance of the WBC in the leaping or penetrating regime perturbed by the mesoscale eddy is not changed. This may force the WBC to remain in the leaping regime for a longer time than that in the one-island case and should be confirmed in reality in the future. Moreover, the impact of the meridional location of the mesoscale eddy approaching the gap with two islands exhibits an obvious difference in comparison with the no-island case (Yuan and Wang, 2011) and the one-island case (Mei et al., 2022). This indicates that the southern island in the gap affects the eddy–WBC interaction to some extent. In fact, the two-island model is closer to the reality in the Luzon Strait in this study. Obviously, further study using realistic models or observations on the interactions of the mesoscale eddy and the Kuroshio needs to be carried out in the future.

Data availability statement

The original contributions presented in the study are included in the article/supplementary material. Further inquiries can be directed to the corresponding authors.

Author contributions

KL performed the numerical simulation and data analysis and wrote the first draft of the manuscript. HM and QL proposed the work ideas and contributed to the numerical simulation, data analysis, and writing. XW and JD contributed to the data analysis. All authors contributed to the article and approved the submitted version.

Funding

This research is supported by the National Natural Science Foundation of China (Nos. 42076005 and 41706003) and the Natural Science Foundation of Jiangsu Province (No. BK20210885).

Conflict of interest

The authors declare that the research was conducted in the absence of any commercial or financial relationships that could be construed as a potential conflict of interest.

Publisher's note

References

Caruso, M. J., Gawarkiewicz, G. G., and Beardsley, R. C. (2006). Interannual variability of the kuroshio intrusion in the south China Sea. *J. Oceanogr.* 62, 559–575. doi: 10.1007/s10872-006-0076-0

Chern, C. S., and Wang, J. (2005). Interactions of mesoscale eddy and western boundary current: A reduced-gravity numerical model study. *J. Oceanogr.* 61 (2), 271–282. doi: 10.1007/s10872-005-0037-z

Cushman-Roisin, B., and Beckers, J. M. (2011). *Introduction to geophysical fluid dynamics: physical and numerical aspects* (New York: Academic press), 223–224.

Huang, Z., Liu, H., Lin, P., and Hu, J. (2017). Influence of island chains on the kuroshio intrusion in the Luzon strait. *Adv. Atmos. Sci.* 34 (3), 397–410. doi: 10.1007/s00376-016-6159-y

Jiang, S., Jin, F., and Ghil, M. (1995). Multiple equilibria, periodic, and aperiodic solutions in a wind-driven, double-gyre, shallow water model. *J. Phys. Oceanogr.* 25 (5), 764–786. doi: 10.1175/1520-0485(1995)025<0764:MEPAAS>2.0.CO;2

Kuehl, J. J., and Sheremet, V. A. (2009). Identification of a cusp catastrophe in a gap-leaping western boundary current. *J. Mar. Res.* 67 (1), 25–42. doi: 10.1357/002224009788597908

Kuehl, J. J., and Sheremet, V. A. (2014). Two-layer gap-leaping oceanic boundary currents: experimental investigation. *J. fluid Mech.* 740, 97–113. doi: 10.1017/jfm.2013.645

Kuehl, J. J., and Sheremet, V. A. (2022). Effect of the coastline geometry on the boundary currents intruding through the gap. *Fluids* 7 (2), 71. doi: 10.3390/fluids7020071

Kuo, Y. C., and Chern, C. S. (2011). Numerical study on the interactions between a mesoscale eddy and a western boundary current. *J. oceanogr.* 67 (3), 263–272. doi: 10.1007/s10872-011-0026-3

Liang, W. D., Yang, Y. J., Tang, T. Y., and Chuang, W. S. (2008). Kuroshio in the Luzon strait. *J. Geophys. Res.: Oceans* 113 (C08048). doi: 10.1029/2007JC004609

McMahon, C. W., Kuehl, J. J., and Sheremet, V. A. (2020). A viscous, two-layer western boundary current structure function. *Fluids* 5 (2), 63. doi: 10.3390/fluids5020063

McMahon, C. W., Kuehl, J. J., and Sheremet, V. A. (2021). Dynamics of gap-leaping Western boundary currents with throughflow forcing. *J. Phys. Oceanogr.* 51 (7), 2243–2256. doi: 10.1175/JPO-D-20-0216.1

Mei, H., Li, K., Liu, Q., Wang, B., and Wu, X. (2023). Interaction of a hysteresis western boundary current with a large-scale marginal sea circulation in a gap-leaping system. *J. Phys. Oceanogr.* 53 (3), 943–957 doi: 10.1175/JPO-D-22-0194.1

Mei, H., Qi, Y., Cheng, X., Wu, X., and Wang, Q. (2022). Nonlinear dynamics of a hysteresis Western boundary current perturbed by a mesoscale eddy at a gap with an island. *J. Phys. Oceanogr.* 52, 1992–2007. doi: 10.1175/JPO-D-22-0016.1

Mei, H., Qi, Y., Qiu, B., Cheng, X., and Wu, X. (2019). Influence of an island on hysteresis of a western boundary current flowing across a gap. *J. Phys. Oceanogr.* 49 (5), 1353–1366. doi: 10.1175/JPO-D-18-0116.1

Metzger, E. J., and Hurlburt, H. E. (2001). The importance of high horizontal resolution and accurate coastline geometry in modeling south China Sea inflow. *Geophys. Res. Lett.* 28 (6), 1059–1062. doi: 10.1029/2000GL012396

Nan, F., He, Z., Zhou, H., and Wang, D. (2011). Three long-lived anticyclonic eddies in the northern south China Sea. *J. Geophys. Res.: Oceans* 116 (C05002). doi: 10.1029/2010JC006790

Nan, F., Xue, H., and Yu, F. (2015). Kuroshio intrusion into the south China Sea: A review. *Prog. Oceanogra.* 137, 314–333. doi: 10.1016/j.pocean.2014.05.012

Nitani, H. (1972). Beginning of the kuroshio. *Kuroshio Phys. Aspect Japan Current*. H. Stommel, K. Yashida, Eds. (University of Tokyo Press) 129–63.

Qiu, B., and Chen, S. (2012). Multidecadal sea level and gyre circulation variability in the northwestern tropical pacific ocean. *J. Phys. Oceanogr.* 42 (1), 193–206. doi: 10.1175/jpo-d-11-061.1

Qu, T., Kim, Y. Y., Yaremchuk, M., Tozuka, T., Ishida, A., and Yamagata, T. (2004). Can Luzon strait transport play a role in conveying the impact of ENSO to the south China Sea? *J. Climate* 17 (18), 3644–3657. doi: 10.1175/1520-0442(2004)017<3644:CLSTPA>2.0.CO;2

Qu, T., Mitsudera, H., and Yamagata, T. (2000). Intrusion of the north pacific waters into the south China Sea. *J. Geophys. Res.* 105 (C3), 6415–6424. doi: 10.1029/1999JC900323

Shen, J. Q., Fang, W. D., Li, L., Qiu, Y., Xiao, Z., Zhang, J. P., et al. (2022). Slope undercurrent in the northwestern south China Sea beneath the winter western boundary current. *Front. Mar. Sci.* 9. doi: 10.3389/fmars.2022.918077

Sheremet, V. A. (2001). Hysteresis of a western boundary current leaping across a gap. *J. Phys. Oceanogr.* 31 (5), 1247–1259. doi: 10.1175/1520-0485(2001)031<1247:HOAWBC>2.0.CO;2

Sheremet, V. A., Khan, A. A., and Kuehl, J. (2022). Multiple equilibrium states of the gulf of Mexico loop current. *Ocean Dynamics* 72 (11), 731–740. doi: 10.1007/s10236-022-01534-8

Sheremet, V. A., and Kuehl, J. (2007). Gap-leaping western boundary current in a circular tank model. *J. Phys. Oceanogr.* 37 (6), 1488–1495. doi: 10.1175/JPO3069.1

Sheu, W. J., Wu, C. R., and Oey, L. Y. (2010). Blocking and westward passage of eddies in the Luzon Strait. *Deep Sea Res. Part II: Topical Stud. Oceanogr.* 57 (19–20), 1783–1791. doi: 10.1016/j.dsr2.2010.04.004

Song, X., Yuan, D., and Li, R. (2018). Migration of mesoscale eddies across a leaping or penetrating western boundary current in the vicinity of a gap. *J. Ocean. Limnol.* 36, 2098–2109. doi: 10.1007/s00343-019-7296-9

Song, X., Yuan, D., and Wang, Z. (2019). Hysteresis of a periodic or leaking western boundary current flowing by a gap. *Acta Oceanol. Sin.* 38, 90–96. doi: 10.1007/s13131-018-1251-z

Wang, Z., and Yuan, D. (2012). Nonlinear dynamics of two western boundary currents colliding at a gap. *J. Phys. Oceanogr.* 42 (11), 2030–2040. doi: 10.1175/JPO-D-12-05.1

Wang, Z., and Yuan, D. (2014). Multiple equilibria and hysteresis of two unequal-transport western boundary currents colliding at a gap. *J. Phys. Oceanogr.* 44 (7), 1873–1885. doi: 10.1175/JPO-D-13-0234.1

Wang, Z., Yuan, D., and Hou, Y. (2010). Effect of meridional wind on gap-leaping western boundary current. *Chin. J. Oceanology Limnol.* 28 (2), 354–358. doi: 10.1007/s00343-010-9281-1

Yang, Q., Liu, H., and Lin, P. (2020). The effect of oceanic mesoscale eddies on the looping path of the kuroshio intrusion in the Luzon strait. *Sci. Rep.* 10 (1), 1–10. doi: 10.1038/s41598-020-57487-9

Yuan, D., Han, W., and Hu, D. (2006). Surface kuroshio path in the Luzon strait area derived from satellite remote sensing data. *J. Geophys. Res.* 111, C11007. doi: 10.1029/2005JC003412

Yuan, D., and Li, R. X. (2008). Dynamics of eddy-induced kuroshio variability in Luzon strait (in Chinese with English abstract). *J. Trop. Oceanogr.* 27 (4), 1–9.

Yuan, D., Song, X., Yang, Y., and Dewar, W. K. (2019). Dynamics of mesoscale eddies interacting with a western boundary current flowing by a gap. *J. Geophys. Res. Oceans* 124 (6), 4117–4132. doi: 10.1029/2019JC014949

Yuan, D., and Wang, Z. (2011). Hysteresis and dynamics of a western boundary current flowing by a gap forced by impingement of mesoscale eddies. *J. Phys. Oceanogr.* 41 (5), 878–888. doi: 10.1175/2010JPO4489.1

Zavala Sanson, L., and Van Heijst, G. J. F. (2002). Ekman effects in a rotating flow over bottom topography. *J. Fluid Mech.* 471, 239–255. doi: 10.1017/S0022112002002239

Zhong, L., Hua, L., and Luo, D. (2016). The eddy–mean flow interaction and the intrusion of western boundary current into the south China Sea–type basin in an idealized model. *J. Phys. Oceanogr.* 46 (8), 2493–2527. doi: 10.1175/JPO-D-15-0220.1

frontiers | Frontiers in Marine Science

TYPE Brief Research Report
PUBLISHED 16 May 2023
DOI 10.3389/fmars.2023.1176226

OPEN ACCESS

EDITED BY
Shi-Di Huang,
Southern University of Science and Technology, China

REVIEWED BY
Xian-Rong Cen,
Foshan University, China
Guang-Yu Ding,
Southern University of Science and Technology, China

*CORRESPONDENCE
Devang Falor
devangfalor@iisc.ac.in

RECEIVED 28 February 2023
ACCEPTED 20 April 2023
PUBLISHED 16 May 2023

CITATION
Falor D, Gayen B, Sengupta D and Ivey GN (2023) Evaporation induced convection enhances mixing in the upper ocean. *Front. Mar. Sci.* 10:1176226. doi: 10.3389/fmars.2023.1176226

Evaporation induced convection enhances mixing in the upper ocean

Devang Falor[1]*, Bishakhdatta Gayen[1,2], Debasis Sengupta[1,3] and Gregory N. Ivey[4]

[1]Centre for Atmospheric and Oceanic Sciences, Indian Institute of Science, Bengaluru, India, [2]Department of Mechanical Engineering, University of Melbourne, Melbourne, VIC, Australia, [3]Divecha Centre for Climate Change, Indian Institute of Science, Bengauru, India, [4]Oceans Graduate School and Oceans Institute, University of Western Australia, Crawley, WA, Australia

The upper ocean surface layer is directly affected by the air-sea fluxes. The diurnal variations in these fluxes also cause the upper ocean mixed layer turbulence and mixing to diurnally vary. The underlying thermohaline structure also varies accordingly throughout the day. Here we use large-eddy simulation to quantify the role of surface evaporation in modulating the diurnal mixed layer turbulence and mixing in the presence of wind forcing. During daytime, the upper ocean boundary layer becomes thermally stratified, and a salinity inversion layer is formed in the upper 10m, leading to double diffusive salt-fingering instability. During nighttime, the mixed layer undergoes convective deepening due to surface buoyancy loss redfrom both surface cooling and evaporation. We find that salinity makes a major contribution to the convective instability during both transitions between day and night. Overall surface evaporation increases the mixed layer depth and irreversible mixing through convection, both during nighttime and daytime, and leads to better prediction of the dynamical variables as sea surface salinity (SSS) and sea surface temperature (SST). Our findings can help improve the ocean parameterizations to improve the forecasts on a diurnal timescale.

KEYWORDS

convection, turbulence, upper ocean mixed layer, irreversible mixing, salt-fingering, turbulence modelling

1 Introduction

The ocean mixed layer (OML) is highly turbulent with nearly uniform vertical distribution of temperature, salinity and density. The mixed layer mediates the exchange of mass, momentum, heat and freshwater between the atmosphere and the ocean. The time-varying surface fluxes and the depth of the OML are both important determinants of sea surface temperature (SST), sea surface salinity (SSS) and ocean heat content. Thus it is

imperative to understand the mixed layer dynamics, turbulence and the associated irreversible mixing under various external conditions in a rapidly changing climate.

The fluxes of momentum, heat and freshwater at the ocean surface vary on all time scales, the diurnal scale being one of the most prominent. The net surface heat flux is the sum of shortwave radiation, net longwave radiation, latent heat flux and sensible heat flux. Shortwave (solar) radiation incident at the ocean surface, as well as net surface heat flux, have well-marked diurnal variability, tending to heat the ocean in the daytime and cooling the ocean at night. The other components of heat flux also have diurnal variations. For example, latent heat flux varies due to diurnal changes in surface winds (Wallace and Hartranft, 1969; Stull, 1988; de Szoeke et al., 2021).

The ocean responds to the boundary forcing and changes some of the key variables that define the ocean state. The solar radiation is absorbed by the water column during daytime, in a volumetric sense (Paulson and Simpson, 1977), while the combined effect of non solar components cool the air-sea interface at almost all the times, also called as the cool skin effect (Fairall et al., 1996). As a result, the OML generally deepens during the nighttime cooling, when this convective turbulence tends to dominate, while the near surface generally gets stratified in the daytime, leaving behind a remnant mixed layer (Brainerd and Gregg, 1993). The SST also varies during this time, due to this net heating during the daytime and cooling in nighttime. These processes are interdependent as the daytime's stratification is dictated by how deep the OML was during nighttime, and consequently the nighttime deepening depends on the strength of the daytime stratification. Wind shear transfers momentum flux into the ocean. Under weak winds, the turbulent mixing is suppressed (Hughes et al., 2020b) leading to strong diurnal SST variations (Flament et al., 1994; Soloviev and Lukas, 1997; Sui et al., 1997) and vice versa under strong winds (Yan et al., 2021). Evaporation happens at all times in the ocean, increasing the sea surface salinity (SSS) but precipitation occurs only during wet spells. The combined effect of this saltier and cooler skin makes it always statically unstable (Saunders, 1967; Yu, 2010). The upper ocean thus experiences diurnal variations in both momentum and buoyancy (heat) fluxes and undergoes a diurnal cycle of turbulence and mixing (Lombardo and Gregg, 1989; Brainerd and Gregg, 1993; Moulin et al., 2018).

Several previous studies have focussed on the response of the upper ocean to diurnally varying surface forcing using observations and model experiments. Lombardo and Gregg (1989) took microstructure measurements at 34°N, made during the PATCHEX experiment (1986) and gave a similarity scaling for the turbulence occurring during nighttime convection. The kinetic energy dissipation was normalized by the sum of scalings obtained from wind stress driven and convectively driven turbulence. Using the same dataset, the restratification processes and the daily cycle of turbulence within the OML were analyzed (Brainerd and Gregg, 1993). Price et al. (1986) used field observations from 30.9°N to analyze the diurnal response and to further develop the widely used one-dimensional Price-Weller-Pinkel model (PWP). This is a slab model, integrating and balancing quantities over the entire OML. In the equatorial Pacific, a linear stability analysis was used to show that the enhanced near-surface shear that forms in the daytime, descends in the evening, leaving the nighttime mixing layer above it (Smyth et al., 2013). This layer merged with the deeper Equatorial Undercurrent, triggering deep cycle turbulence. This study was supplemented with ship-based measurements of velocity, stratification and turbulent dissipation (Moum et al., 2009). Large-eddy simulations using temperature as a single scalar were conducted (Pham et al., 2013; Pham et al., 2017) to study the dynamic processes leading to deep cycle turbulence and its seasonality. In the equatorial Atlantic, using PIRATA mooring data, Wenegrat and McPhaden (2015) explored diurnal stratification, shear and SST. They also hinted at the possibility of deep cycle turbulence, owing to the presence of marginal instability between the OML and the thermocline. In the Indian Ocean, the surface diurnal warm layer was studied during the DYNAMO experiment (Matthews et al., 2014). From the DYNAMO measurements, de Szoeke et al. (2021) demonstrated that convective turbulence in the atmosphere is caused by diurnal ocean warming. The Bay of Bengal is known for a shallow salinity -stratified layer due to copious freshwater input from rivers and rainfall during summer monsoon season. Idealized turbulence-resolving simulations for the Bay of Bengal were conducted to explore the diurnal OML turbulence by Sarkar and Pham (2019), who concluded that the mixed layer salinity changed solely due to the entrainment of saltier subsurface water. The effects of haline forcing were studied by Drushka et al. (2016; 2014), who examined the diurnal salinity cycle in the tropics, and the dynamics of the upper ocean after rain events using the General Ocean Turbulence Model (GOTM). The diurnal amplitude of salinity anomalies, with major contributions from diurnal entrainment and precipitation, were found to be around ~ 0.005 PSU. Yu (2010) tried to study the effect of evaporation on the salty skin. However to the best of our knowledge, none of the above mentioned studies focused on the role of evaporative fluxes and resulting changes in SSS in modifying and quantifying the irreversible turbulent mixing in the OML.

We conduct large-eddy simulations of the ocean, representative of the Bay of Bengal, using both temperature and salinity as active scalars, with diurnally varying forcing to quantify the upper ocean turbulence and mixing. The results provide new insights into the spatio-temporal character of diurnal turbulence and mixing. We show that the evaporation can play a major role on diurnal timescales for controlling the SSS and hence enhancing the mixing in the surface layer. We also show the existence of a salinity inversion layer and the presence of salt-fingering instability, during daytime, for the case of weak winds, due to evaporation.

2 Methodology

To perform the convection resolving simulations, we take a cuboidal domain at centered around the Bay of Bengal mooring (Weller et al., 2016) at 18°N, 89.5°E of dimensions 100m × 100m × 250m. Periodic boundary conditions are imposed in the horizontal directions so as to remove the effect of any lateral density gradients. The domain is bounded at the top by a flat air-sea interface, where

we prescribe the boundary conditions of momentum, heat and evaporative haline (salt) fluxes. These boundary conditions are based on smoothed air-sea fluxes (Figure 1A) taken from the mooring observations during wintertime in the Bay (Weller et al., 2019). The evaporation rate E (m/s) is calculated from the latent heat flux Q_L as:

$$E = \frac{Q_L}{\rho_0 L_v} \tag{1}$$

where ρ_0 is the reference density and. is the latent heat of vaporization. We also include the effects of shortwave penetration by putting it as a source term in the governing equations. Here we have also put diurnally oscillating wind stress to give unsteadiness to the system. We also add a sponge layer of height 50m, extending up to 200m so as to damp any reflections coming from the bottom boundary thus mimicking open ocean conditions. Note that this study does not include the effects of precipitation, as it has been well documented in an earlier study (Drushka et al., 2016).

Large-eddy simulations are used to evaluate the velocity and scalar fields (temperature and salinity) from the incompressible, non-hydrostatic Navier-Stokes equation, with Boussinesq and f-plane approximation. Additional model details can be found in the Supplementary Document. We employ a linear equation of state for calculating the density field. The LES domain uses a grid of $N_x = N_y = 128$ and $N_z = 417$ which is uniform in both the x and y directions and stretched in the z direction to achieve higher resolution near the top boundary in order to resolve the $\sim \mathcal{O}(1mm)$ thick laminar diffusive layer. The required resolution criteria is discussed in Rosevear et al. (2021). Model runs are initialized with temperature and salinity profiles, fitted from the mooring observations prior to the event (Figures 1, S1). The water has a molecular viscosity of $\nu = 10^{-5}$ m^2/s, thermal diffusivity $\kappa_T = 1.4 \times 10^{-6}$ m^2/s and salt diffusivity $\kappa_S = 1.2 \times 10^{-8}$ m^2/s. Variable

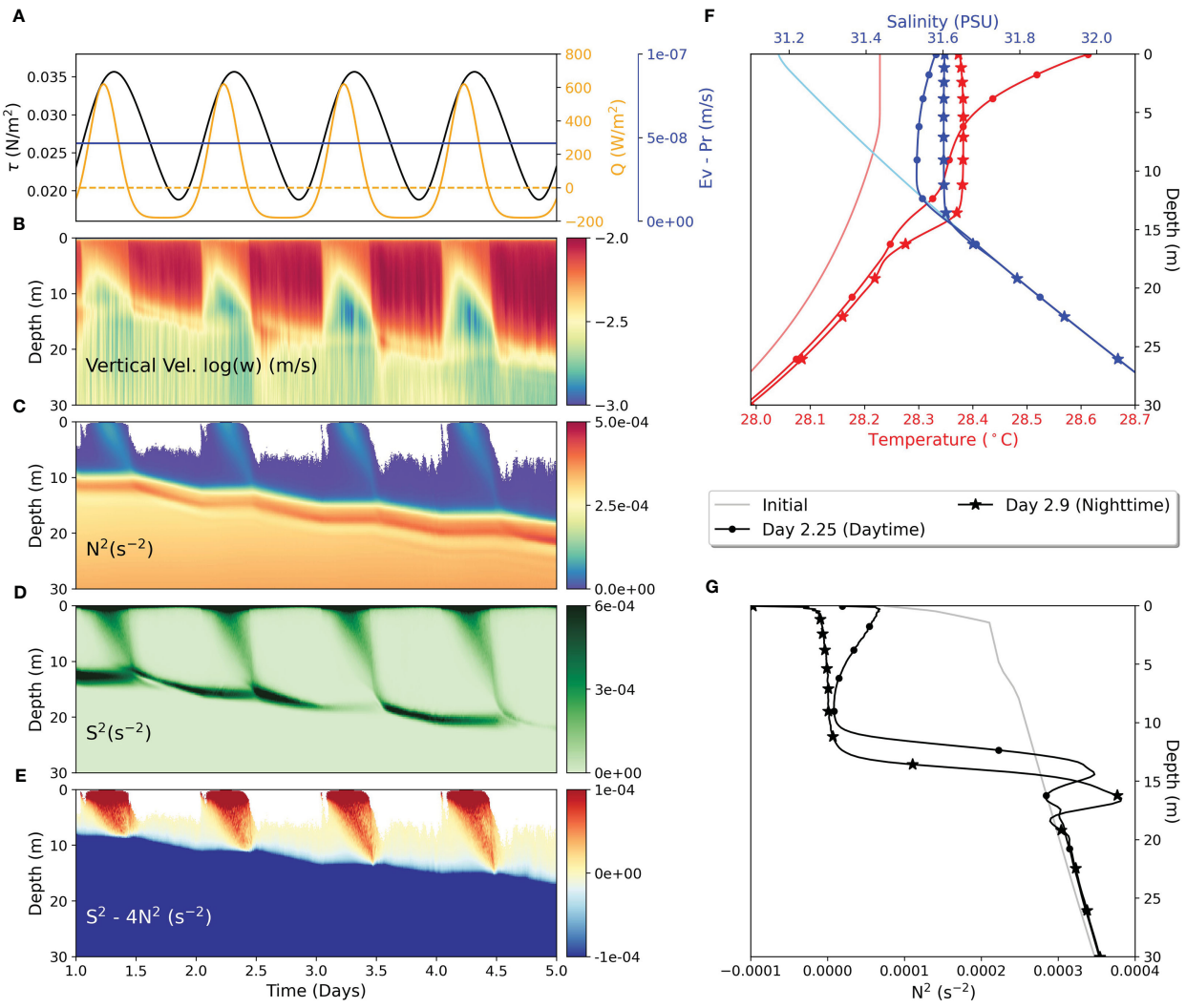

FIGURE 1
(Left) Upper ocean response to diurnal forcing. **(A)** Surface boundary conditions of net heat flux Q (W/m^2) (orange), wind stress magnitude τ (N/m^2) (black) and evaporation minus precipitation E-P (m/s) (blue). **(B)** Horizontally averaged root mean squared fluctuating vertical velocity w (m/s). **(C)** Brunt Vaisala Frequency squared N^2 (s $^{-2}$), where white patches indicate $N^2 < 0$. **(D)** Shear squared S^2 (s $^{-2}$). **(E)** Reduced shear or Modified Richardson number S^2 - 4 N^2 (s $^{-2}$). **(F, G)** Initial profiles of T, S and N^2 (solid), at day 2.25 (dotted) and day 2.9 (star marked).

time stepping with a fixed Courant–Friedrichs–Lewy (CFL) number of 1.2 and typical time steps of the order $\mathcal{O}(1s)$ is used. To quantify the role of evaporation, two sets of simulations have been performed: a) complete forcing with momentum, heat and haline fluxes, and b) forcing with momentum and heat fluxes only. Note that we also performed simulations with constant wind stress, but it didn't have much effect on the resulting dynamics (Figure S4). All the further analysis has been done from the second diurnal cycle onward, as the model spin-up time was about one day.

3 Results

3.1 Overview of diurnal turbulence

The diurnal nature of the surface fluxes cause the upper ocean to cyclically stir and restratify. During the nighttime, the negative net heat flux cools the surface of the ocean (Figure 1A), and results in unstable stratification (Figures 1C, G) and convective deepening of the OML. Convective plumes penetrate into the subsurface depths reaching the diurnal pycnocline, as can be seen from the horizontally averaged root mean squared fluctuating vertical velocity, which varies over an order of magnitude, and the Brunt-Väisäla frequency squared (N2)

$$N^2 = \frac{-g}{\rho_0}\frac{d\langle\rho\rangle}{dz} \tag{2}$$

where g is the acceleration due to gravity, ρ_0 is the reference density and $\langle\rho\rangle$ is the total horizontally averaged density, (Figures 1B, C) which peaks at around 4×10^{-4} s $^{-2}$ within the pycnocline (Figure 1G). As the daytime begins and the shortwave is absorbed by up the ocean bulk, most of the turbulence is suppressed and thermal stratification begins to build and the OML shallows (Figures 1F, G). The increased stratification traps horizontal momentum within a very thin layer, called the diurnal warm layer, enhancing the near-surface shear. The squared shear S^2 (Figure 1D) is calculated as:

$$S^2 = \left(\frac{d\langle u\rangle}{dz}\right)^2 + \left(\frac{d\langle v\rangle}{dz}\right)^2 \tag{3}$$

where $\langle u\rangle$ and $\langle v\rangle$ are the plane averaged zonal and meridional velocities respectively. This shear layer descends towards the pycnocline, as the net heat flux begins to decrease after reaching its peak value. Note that, at all times the oscillating surface wind stress also continues to produce shear turbulence, but it is enhanced near the surface during daytime and near the pycnocline during the nighttime. This phenomena has also been documented in previous studies (Moulin et al., 2018; Hughes et al., 2020a). Figure 1E shows the reduced squared shear S^2 - $4N^2$, where positive values indicate that the water column is unstable to KH-like shear instability. The competition between this diurnal jet and stratification makes the near-surface unstable to shear instabilities. In addition, we also see the subsurface depths getting unstable as this shear layer descends (Moulin et al., 2018; Wijesekera et al., 2020). Evaporation leads to a persistent unstable gradient of near surface salinity (Figure 1F), which is present even during daytime. This enhances the convective instability during nighttime and also compensates for the increase in the overall stratification during daytime due to thermal heating alone. This also causes enhanced mixing, especially during daytime, as will be discussed further.

3.2 Salt-fingering instability in the diurnal mixed layer

Surface evaporation tends to increase the SSS (Asher et al., 2014; Drushka et al., 2014; Boutin et al., 2016). The accumulation of heat and excess salinity in the top layer over colder and fresher deeper waters are the conditions favorable for double diffusive salt-fingering instability (Soloviev and Lukas, 1997). This is quantified using the density ratio R and *Turner angle* Tu defined as:

$$R = \frac{\alpha T_z}{\beta S_z} = -\tan\,(Tu + 45^\circ) \tag{4}$$

where α and β are the thermal expansion and haline contraction coefficients, and T_z and S_z denote the plane averaged vertical temperature and salinity gradients (Ruddick, 1983). For warm/salty waters over cold/fresh, $-45° < Tu < 45°$, indicating salt-fingering (SF) instability is likely, whereas $-45^\circ < Tu < 90^\circ$ indicates absolute stability. However $Tu < -90^\circ$ or $Tu > 90^\circ$ denotes static instability ($N^2 < 0$). The former is caused due to the overwhelming effect of destabilizing thermal gradient and the latter vice versa. Figure 2B shows the temporal evolution of Tu for two consecutive diurnal cycles. During the daytime, the entire water column down to the pycnocline is susceptible to salt-fingering instability. L424 This can also be verified from the T/S profiles in Figure 2D during daytime. Figure 2E shows the contribution of both scalar gradients to the overall stratification. They are defined as:

$$N_T^2 = g\alpha\frac{\langle\partial T\rangle}{\partial z} \quad \text{and} \quad N_S^2 = -g\beta\frac{\langle\partial S\rangle}{\partial z} \tag{5}$$

The salinity gradient compensates the temperature gradient in the daytime, however keeping the overall stratification stable. When the surface heat flux changes sign from positive to negative, indicating a shift from daytime to nighttime, both the scalars contribute negatively to the stratification, causing convective static instability. This implies that both $N_T^2, N_S^2 < 0$. However, since the boundary condition of temperature changed from heating to cooling, it takes some time to adjust. Hence initially, even if both $N_T^2, N_S^2 < 0$, but $|N_T^2| < |N_S^2|$, making the contribution of salinity gradient the dominant effect in destabilizing the density gradient. This can also be seen through Turner angle, where the near surface values are more than 90° just as the heat flux changes sign from positive to negative. After some time however, the values of Turner angle become less than -90° indicating that surface cooling dominates the convective mixing. The convection almost homogenizes both the T/S profiles, leaving almost negligible gradient, except near the top, where the localized effects of both surface cooling and evaporation persist (Figures 2D, E). As soon as the shortwave begins however, even when the heat fluxis still negative, the turbulence begins to decrease due to the build up of

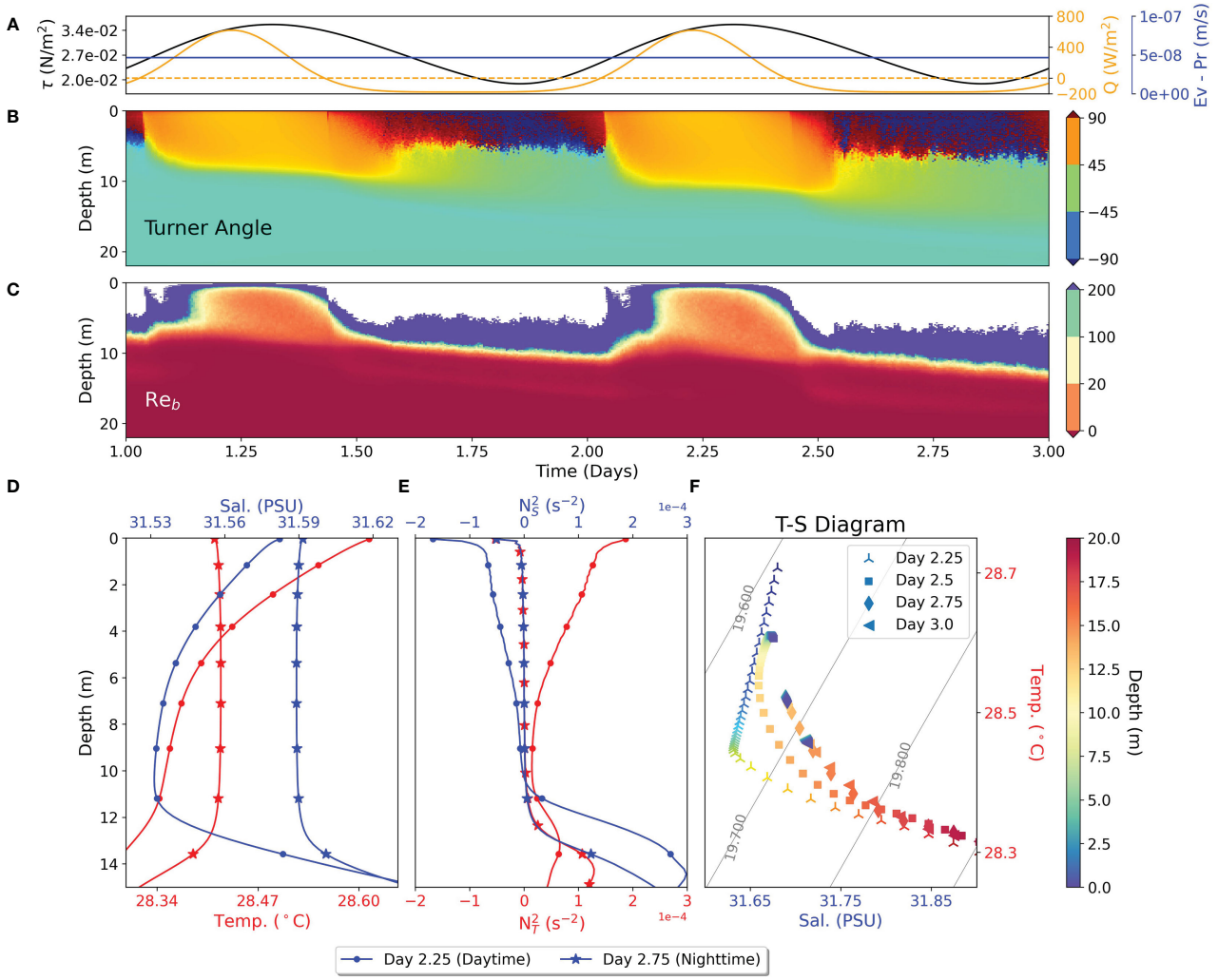

FIGURE 2
(A) Wind stress magnitude τ (N/m^2) (black), net heat flux Q (W/m^2) (orange) and evaporation minus precipitation E-P (m/s) (blue). **(B)** Turner angle *Tu* from LES simulations. **(C)** Buoyancy Reynolds number Re_b contour from LES simulations, where white patches indicate $N^2 < 0$. **(D, E)** Depthwise profiles of temperature T, salinity S and N_T^2, N_S^2 plotted at day 2.25 (dotted) and day 2.75 (star marked). **(F)** TS diagram plotted at day 2.25, 2.5, 2.75, 3.0 till 20m depth.

thermal stratification and increased potential energy. At that instant, the convection switches back to being salinity dominated and the whole cycle repeats the next day.

To supplement the findings above, we also plot the buoyancy Reynolds number, calculated as:

$$Re_b = \frac{\epsilon}{\nu N^2} \tag{6}$$

where ϵ is the turbulent kinetic dissipation (defined in the next section) and N^2 is the squared Brunt Vaisala frequency. This quantity can be interpreted as the ratio of Ozmidov to Kolmogorov length scales. For $Re_b < 20$, there is weak buoyancy controlled turbulence, while for $Re_b > 100$ the turbulence is energetic (Bouffard and Boegman, 2013). Previous studies have indicated that salt-fingering can enhance mixing for $Re_b < 200$ (Nagai et al., 2015). Figure 2C shows that during daytime, $Re_b < 200$ almost throughout the diurnal thermocline, which further supports that salt-fingering is the major contributor to turbulent mixing. The TS diagram (Figure 2F) provides another description of these dynamics. It has been plotted every 6 hours, for the whole of day 2 (after initialization). By day 2.25, when the neat heat flux is positive, in the top 7m or so the presence of warm and salty waters over cold and fresh waters and indication of salt-fingering can be seen here as well. Soon after nighttime begins (day 2.5), a small inversion can be seen in both the scalars due to the net surface destabilizing buoyancy flux. During peak night times, the profiles have been almost homogenized down to the pycnocline, which can be seen by both day 2.5 and 3. Note that the changes in these T/S properties only occur for depths less than about 15m, as the OML itself is about 13m. These changes in time have profound consequences on irreversible turbulent mixing, discussed in the next section.

3.3 Turbulence statistics and mixing

Figure 3 shows the evolution of horizontally averaged turbulence statistics from the ocean's response. The small scale

turbulent kinetic energy (Figure 3B) is defined as:

$$TKE = \frac{1}{2} \langle u_i' u_i' \rangle \tag{7}$$

where, u_i' , the fluctuating velocity, is calculated from the horizontally averaged mean field as $u_i' = u_i - \langle u_i \rangle$ ($\langle . \rangle$ denotes horizonatlly averaged quantity). During nighttime, TKE is enhanced within the whole mixed layer due to convection, while it is restricted to the near-surface during daytime. The mixed layer depth (MLD) for both the test cases, calculated using a density threshold criteria of 0.01 kg/m^3 is also plotted. It varies diurnally for both the cases, however the combined case has greater MLD than the case without evaporation. Using higher thresholds may cause MLD to not shallow much during daytime. A continued increase over time of MLD for the combined case, can be observed as the net surface buoyancy flux integrated over a day is non-zero (and positive) and the surface wind stress also continues to provide a source of mechanical turbulence all the time. There is some leakage of TKE below the mixed layer as well, which is likely due to the downward propagation of internal waves from the pycnocline. The shear production P (Figure 3C) shows the variability of mechanically generated turbulence, given by

$$P = -\langle u_i' u_j' \rangle \frac{\partial \langle u_i \rangle}{\partial x_j} \tag{8}$$

The enhanced values near the surface are the direct result of the stress applied, while the descent of the shear layer causes shear instability and turbulence, as discussed before (Figure 1E). The subsurface enhancement of shear production within the pycnocline can be seen during nighttime, producing internal waves. The turbulent buoyancy flux.

$$B = -\frac{g}{\rho_0} \langle \rho' w' \rangle \tag{9}$$

represents the conversion of energy from TKE to available potential energy (APE) and vice versa (Figure 3E). This includes contributions from both the scalars respectively. Positive values indicate APE being converted to TKE, through convection, while negative values show the energy spent in destroying stable stratification (conversion from TKE to APE). During nighttime, the turbulence is mostly convective in nature, while during the daytime, the shear-induced turbulence has to work against the stable stratification. The turbulent kinetic dissipation ϵ is the sink of TKE, denoting how much energy is spent in overcoming the viscous stresses.

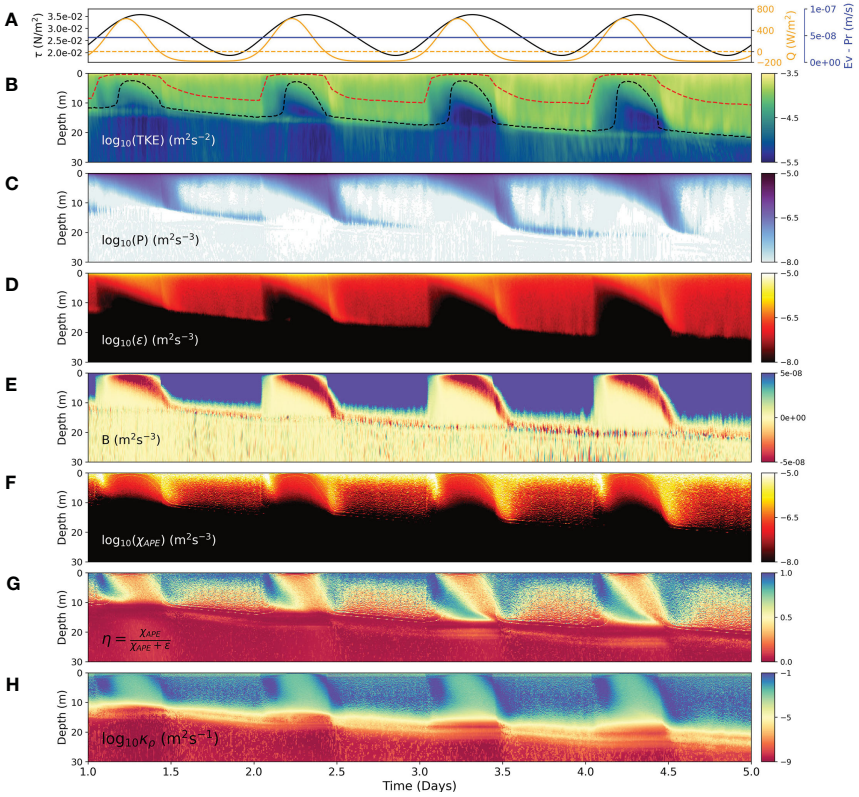

FIGURE 3
Turbulence and mixing statistics for the upper ocean. **(A)** Wind stress magnitude τ (N/m^2) (black), net heat flux Q (W/m^2) (orange) and evaporation minus precipitation E-P (m/s) (blue). **(B)** Turbulent Kinetic Energy (TKE) with the mixed layer depth for case with evaporation (black) and without evaporation (red). **(C)** Shear Production P . **(D)** Total kinetic dissipation ϵ. **(E)** Turbulent Buoyancy Flux B. **(F)** Mixing χ_{APE} defined as the sink of APE. **(G)** Mixing efficiency η. **(H)** Diapycnal Diffusivity κ_ρ calculated following (Osborn and Cox, 1972). Panels **(B–D, F, H)** show the logarithm of respective quantities.

$$\epsilon = \nu \left\langle \frac{\partial u_i'}{\partial x_j} \frac{\partial u_i'}{\partial x_j} \right\rangle \tag{10}$$

As discussed before, depending on the time of the day, the turbulence could be either mechanical or convective in nature. The dissipation also follows this variability (Figure 3D). During the daytime, the values of ϵ and P are comparable near the surface and during descent of the shear layer. However, in the convective regime, the buoyancy flux tries to balance ϵ, throughout the mixed layer. This has also been reported in previous studies (Shay and Gregg, 1986; Lombardo and Gregg, 1989; Ivey and Imberger, 1991; 214 Imberger, 1985).

The irreversible mixing, defined as the sink of APE, is calculated following Gregg (2021) (Figure 3F).

$$\chi_{APE} = \frac{g^2}{\rho_0^2 N_*^2} \chi_\rho \tag{11}$$

where χ_ρ is the rate of destruction of density variance or scalar dissipation.

$$\chi_\rho = 2\kappa_\rho \left\langle \frac{\partial \rho'}{\partial x_i} \frac{\partial \rho'}{\partial x_i} \right\rangle \approx 2\rho_0^2 \left[\alpha^2 \kappa_T \left\langle \frac{\partial T'}{\partial x_i} \frac{\partial T'}{\partial x_i} \right\rangle + \beta^2 \kappa_S \left\langle \frac{\partial S'}{\partial x_i} \frac{\partial S'}{\partial x_i} \right\rangle \right] \tag{12}$$

Here $\kappa_{T,S}$ are the sum of the molecular and eddy diffusivity of the scalars evaluated from the subgrid scale model and N_*^2 is the buoyancy frequency squared calculated from the sorted density profile (Arthur et al., 2017). The irreversible mixing also follows a diurnal cycle, where we observe high values during nighttime, as convective turbulence is an efficient mixing mechanism. During the daytime, most of the energy produced by the shear goes into dissipation, rather than mixing, however, the opposite happens during nighttime. With the change of sign of net heat flux, different peaks in mixing can also be seen. The first peak occurs during the transition from daytime to nighttime due to the fact that now both the scalars are destabilizing the density gradient. It is here that the Tu also shifts from showing salt-fingering to salinity dominated convective static instability (Figure 2B). The second peak is again just when the shortwave heating begins and the convection shifts from being cooling dominated to salinity dominated. Similar behavior can also be seen in mixing efficiency η (Figure 3G), which is defined as the ratio of sink of APE to the sum total of sink of APE and sink of TKE. In other words, it provides the relative amount of energy going into irreversible mixing, as compared to viscous dissipation. Here as well, high values of more than 0.5 can be seen during nighttime, when convective turbulence dominates. Such high values are also found in previous studies (Gayen et al., 2013; Wykes et al., 2015; Sohail et al., 2018; Ivey et al., 2021). We also calculate the turbulent eddy diffusivity following Osborn and Cox (1972).

$$\kappa_{\rho,eddy} = \frac{\chi_\rho}{2\left(\frac{d\langle\rho\rangle}{dz}\right)^2} \tag{13}$$

Within the OML, during nighttime, the eddy diffusivity (Figures 3H, S2) reaches values around 10^{-1} m^2/s, while in the daytime, it remains about 10^{-3} m^2/s, due to less mixing by shear-driven turbulence. Note that the presence of evaporation increases both mixing and diapycnal diffusivity and has a deeper MLD, as compared to the case without it (Figures 3B, S3). The peaks in both $\kappa_{\rho,eddy}$ and η during the transition times are a result of the shifting nature of convection, as discussed above. These varying regimes of high and low mixing has consequences on SSS and SST as discussed in the next section.

3.4 Evolution of SST and SSS: role of evaporation

Figure 4 shows the comparison between the two cases: with and without evaporation. Vertically integrated mixing (Figure 4B) shows that the case with evaporation has about two orders of magnitude greater mixing than the case without evaporation especially during daytime. During nighttime, the difference is not so much although, as nighttime convection is predominantly

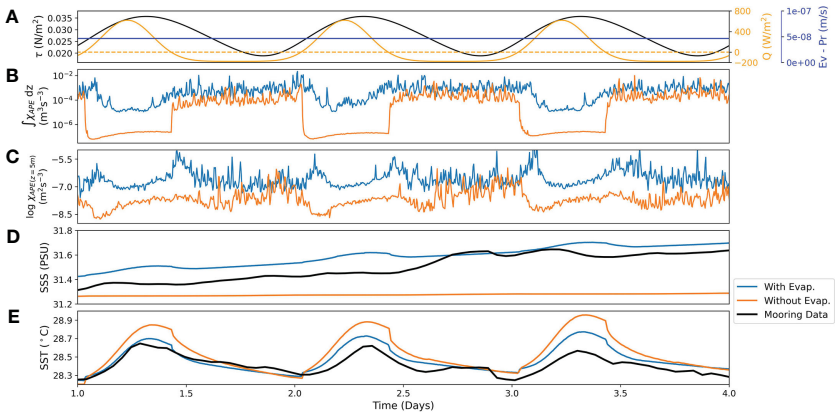

FIGURE 4
(A) Wind stress magnitude τ (N/m^2) (black), net heat flux Q (W/m^2) (orange) and evaporation minus precipitation E-P (m/s) (blue). **(B)** Vertically integrated mixing till 250m for both the cases. **(C)** Logarithm of mixing plotted for both cases. **(D)** SSS comparison and **(E)** SST comparison of both the cases with mooring data.

controlled by the surface cooling, especially in the later hours. This can also be seen in the magnitude of mixing, plotted at 5m depth (Figure 4C). The difference is very evident during daytime, and we also see the two peaks during transition times, which are missing for the case without evaporation. But during late nighttime, the difference decreases as the surface cooling begins to dominate evaporative flux, for nighttime convection. During transition from daytime to nighttime and vice versa, peaks in mixing can also be observed in the case with evaporation (Figures 4C, 3F). These peaks correspond to the changing nature of convection (from being salinity dominated to temperature dominated, and vice versa) during these transition periods, as discussed before. Throughout the day, evaporation continues to enhance mixing throughout the water column, which also leads to better prediction of the other variables. SST and SSS are compared for both the cases with the available mooring data (Figures 4D, E). Note that the salinity at 0.6m depth is used as a proxy for mooring SSS. It can be clearly seen that the case with evaporation better predicts SSS than the case without it. This is due to the enhanced mixing caused by double diffusive salt-fingering, especially during daytime, which leads to increase in SSS. The other mechanism of entrainment of saltier subsurface waters is not efficient so as to increase the SSS. This mechanism is responsible for SSS evolution for the case without evaporation, and has been discussed in previous studies (Sarkar and Pham, 2019). Similarly, the case with evaporation gives a much better match with the mooring SST. The reduced amplitude of the diurnal SST in the case with evaporation, especially during daytime is due to the enhanced mixing caused by the salt-fingering. However, in the case without evaporation, we are not providing any salt flux, and hence the mixing is also reduced, causing higher amplitude of diurnal SST.

4 Discussion

Convection resolving large-eddy simulations have been employed to study the upper ocean turbulence and mixing in response to a diurnal forcing of surface fluxes including evaporation, having both temperature and salinity as scalars. Quantifying the associated turbulence and mixing, we have especially focused on the role of evaporation in controlling the SSS and increasing mixing. We present the first evidence for evaporatively caused salt-fingering instability in the near surface layer during daytime. The surface evaporation enhances mixing by almost order of magnitude as compared to the case without evaporation, during daytime. In addition to above, we also show that the changing nature of convection when surface cooling during nighttime is the major contributor towards mixing, while evaporation plays a secondary role. The overall increase in mixing also causes deeper OML, as compared to the case without evaporation. Our simulation results agree well with the mooring observations. The balance between the evaporative flux and the interior mixing dictates the evolution of SSS, and the increased mixing also helps to better predict the SST. The diapycnal diffusivity differs by almost couple of orders of magnitudes during daytime and nighttime, and peaks around 10^{-1} m^2/s during nighttime. Similarly, the irreversible mixing χ_{APE} and its efficiency η are also enhanced during nighttime, reaching values close to 1, which are previously reported in convection dominated systems. Future work concerns including the effects of surface waves, Langmuir turbulence and developing appropriate convective parameterizations for including the evaporative effects on turbulence and mixing within the existing ocean models.

Data availability statement

The datasets presented in this study can be found in online repositories. The names of the repository/repositories and accession number(s) can be found in the article/Supplementary Material.

Author contributions

DF, BG, and DS designed the research problem. DF performed the numerical simulations and analyzed the data. DF, BG, DS, GI wrote the paper. All authors contributed to the article and approved the submitted version.

Funding

DF acknowledges the Prime Minister's Research Fellows (PMRF) scheme and BG is supported by Australian Research Council Future Fellowship Grant FT180100037. Numerical simulations were conducted on the Australian National Computational Infrastructure, the Australian National University, which is supported by the Commonwealth of Australia. This work is supported by the Ministry of Earth Sciences under India's National Monsoon Mission.

Conflict of interest

The authors declare that the research was conducted in the absence of any commercial or financial relationships that could be construed as a potential conflict of interest.

Publisher's note

Supplementary material

The Supplementary Material for this article can be found online at: https://www.frontiersin.org/articles/10.3389/fmars.2023.1176226/full#supplementary-material

References

Arthur, R. S., Venayagamoorthy, S. K., Koseff, J. R., and Fringer, O. B. (2017). How we compute n matters to estimates of mixing in stratified flows. *J. Fluid Mechanics* 831, R2. doi: 10.1017/jfm.2017.679

Asher, W. E., Jessup, A. T., and Clark, D. (2014). Stable near-surface ocean salinity stratifications due to evaporation observed during strasse. *J. Geophysical Research: Oceans* 119, 3219–3233. doi: 10.1002/2014JC009808

Bouffard, D., and Boegman, L. (2013). A diapycnal diffusivity model for stratified environmental flows. *Dynamics Atmospheres Oceans* 61, 14–34. doi: 10.1016/j.dynatmoce.2013.02.002

Boutin, J., Chao, Y., Asher, W. E., Delcroix, T., Drucker, R., Drushka, K., et al. (2016). Satellite and *in situ* salinity: understanding near-surface stratification and subfootprint variability. *Bull. Am. Meteorological Soc.* 97, 1391–1407. doi: 10.1175/BAMS-D-15-00032.1

Brainerd, K., and Gregg, M. (1993). Diurnal restratification and turbulence in the oceanic surface mixed layer: 1. *observations. J. Geophysical Research: Oceans* 98, 22645–22656. doi: 10.1029/93JC02297

de Szoeke, S. P., Marke, T., and Brewer, W. A. (2021). Diurnal ocean surface warming drives convective turbulence and clouds in the atmosphere. *Geophysical Res. Lett.* 48, e2020GL091299. doi: 10.1029/2020GL091299

Drushka, K., Asher, W. E., Ward, B., and Walesby, K. (2016). Understanding the formation and evolution of rain-formed fresh lenses at the ocean surface. *J. Geophysical Research: Oceans* 121, 2673–2689. doi: 10.1002/2015JC011527

Drushka, K., Gille, S. T., and Sprintall, J. (2014). The diurnal salinity cycle in the tropics. *J. Geophysical Research: Oceans* 119, 5874–5890. doi: 10.1002/2014JC009924

Fairall, C., Bradley, E. F., Godfrey, J., Wick, G., Edson, J. B., and Young, G. (1996). Cool-skin and warm-layer effects on sea surface temperature. *J. Geophysical Research: Oceans* 101, 1295–1308. doi: 10.1029/95JC03190

Flament, P., Firing, J., Sawyer, M., and Trefois, C. (1994). Amplitude and horizontal structure of a large diurnal sea surface warming event during the coastal ocean dynamics experiment. *J. Phys. oceanography* 24, 124–139. doi: 10.1175/1520-0485(1994)024<0124:AAHSOA>2.0.CO;2

Gayen, B., Hughes, G. O., and Griffiths, R. W. (2013). Completing the mechanical energy pathways in turbulent rayleigh-bénard convection. *Phys. Rev. Lett.* 111, 124301. doi: 10.1103/PhysRevLett.111.124301

Gregg, M. C. (2021). *Ocean mixing* (Cambridge University Press). 78–79.

Hughes, K. G., Moum, J. N., and Shroyer, E. L. (2020a). Evolution of the velocity structure in the diurnal warm layer. *J. Phys. Oceanography* 50, 615–631. doi: 10.1175/JPO-D-19-0207.1

Hughes, K. G., Moum, J. N., and Shroyer, E. L. (2020b). Heat transport through diurnal warm layers. *J. Phys. Oceanography* 50, 2885–2905. doi: 10.1175/JPO-D-20-0079.1

Imberger, J. (1985). The diurnal mixed layer 1. *Limnology oceanography* 30, 737–770. doi: 10.4319/lo.1985.30.4.0737

Ivey, G. N., Bluteau, C. E., Gayen, B., Jones, N. L., and Sohail, T. (2021). Roles of shear and convection in driving mixing in the ocean. *Geophysical Res. Lett.* 48, e2020GL089455. doi: 10.1029/2020GL089455

Ivey, G., and Imberger, J. (1991). On the nature of turbulence in a stratified fluid. part i: the energetics of mixing. *J. Phys. Oceanography* 21, 650–658. doi: 10.1175/1520-0485(1991)021<0650:OTNOTI>2.0.CO;2

Lombardo, C., and Gregg, M. (1989). Similarity scaling of viscous and thermal dissipation in a convecting surface boundary layer. *J. Geophysical Research: Oceans* 94, 6273–6284. doi: 10.1029/JC094iC05p06273

Matthews, A. J., Baranowski, D. B., Heywood, K. J., Flatau, P. J., and Schmidtko, S. (2014). The surface diurnal warm layer in the indian ocean during cindy/dynamo. *J. Climate* 27, 9101–9122. doi: 10.1175/JCLI-D-14-00222.1

Moulin, A. J., Moum, J. N., and Shroyer, E. L. (2018). Evolution of turbulence in the diurnal warm layer. *J. Phys. Oceanography* 48, 383–396. doi: 10.1175/JPO-D-17-0170.1

Moum, J., Lien, R.-C., Perlin, A., Nash, J., Gregg, M., and Wiles, P. (2009). Sea Surface cooling at the equator by subsurface mixing in tropical instability waves. *Nat. Geosci.* 2, 761–765. doi: 10.1038/ngeo657

Nagai, T., Inoue, R., Tandon, A., and Yamazaki, H. (2015). Evidence of enhanced double-diffusive convection below the main stream of the k uroshio e xtension. *J. Geophysical Research: Oceans* 120, 8402–8421. doi: 10.1002/2015JC011288

Osborn, T. R., and Cox, C. S. (1972). Oceanic fine structure. *Geophysical Fluid Dynamics* 3, 321–345. doi: 10.1080/03091927208236085

Paulson, C. A., and Simpson, J. J. (1977). Irradiance measurements in the upper ocean. *J. Phys. Oceanography* 7, 952–956. doi: 10.1175/1520-0485(1977)007<0952:IMITUO>2.0.CO;2

Pham, H. T., Sarkar, S., and Winters, K. B. (2013). Large-Eddy simulation of deep-cycle turbulence in an equatorial undercurrent model. *J. Phys. Oceanography* 43, 2490–2502. doi: 10.1175/JPO-D-13-016.1

Pham, H. T., Smyth, W. D., Sarkar, S., and Moum, J. N. (2017). Seasonality of deep cycle turbulence in the eastern equatorial pacific. *J. Phys. Oceanography* 47, 2189–2209. doi: 10.1175/JPO-D-17-0008.1

Price, J. F., Weller, R. A., and Pinkel, R. (1986). Diurnal cycling: observations and models of the upper ocean response to diurnal heating, cooling, and wind mixing. *J. Geophysical Research: Oceans* 91, 8411–8427. doi: 10.1029/JC091iC07p08411

Rosevear, M. G., Gayen, B., and Galton-Fenzi, B. K. (2021). The role of double-diffusive convection in basal melting of antarctic ice shelves. *Proc. Natl. Acad. Sci.* 118, e2007541118. doi: 10.1073/pnas.2007541118

Ruddick, B. (1983). A practical indicator of the stability of the water column to double-diffusive activity. *Deep Sea Res. Part A. Oceanographic Res. Papers* 30, 1105–1107. doi: 10.1016/0198-0149(83)90063-8

Sarkar, S., and Pham, H. T. (2019). Turbulence and thermal structure in the upper ocean: turbulence-resolving simulations. *Flow Turbulence Combustion* 103, 985–1009. doi: 10.1007/s10494-019-00065-5

Saunders, P. M. (1967). The temperature at the ocean-air interface. *J. Atmospheric Sci.* 24, 269–273. doi: 10.1175/1520-0469(1967)024<0269:TTATOA>2.0.CO;2

Shay, T. J., and Gregg, M. (1986). Convectively driven turbulent mixing in the upper ocean. *J. Phys. Oceanography* 16, 1777–1798. doi: 10.1175/1520-0485(1986)016<1777:CDTMIT>2.0.CO;2

Smyth, W., Moum, J., Li, L., and Thorpe, S. (2013). Diurnal shear instability, the descent of the surface shear layer, and the deep cycle of equatorial turbulence. *J. Phys. Oceanography* 43, 2432–2455. doi: 10.1175/JPO-D-13-089.1

Sohail, T., Gayen, B., and Hogg, A. M. (2018). Convection enhances mixing in the southern ocean. *Geophysical Res. Lett.* 45, 4198–4207. doi: 10.1029/2018GL077711

Soloviev, A., and Lukas, R. (1997). Observation of large diurnal warming events in the near-surface layer of the western equatorial pacific warm pool. *Deep Sea Res. Part I: Oceanographic Res. Papers* 44, 1055–1076. doi: 10.1016/S0967-0637(96)00124-0

Stull, R. B. (1988). *An introduction to boundary layer meteorology* Vol. vol. 13 (Springer Science & Business Media). 255.

Sui, C., Li, X., Lau, K., and Adamec, D. (1997). Multiscale air–sea interactions during toga coare. *Monthly weather Rev.* 125, 448–462. doi: 10.1175/1520-0493(1997)125<0448:MASIDT>2.0.CO;2

Wallace, J., and Hartranft, F. (1969). Diurnal wind variations, surface to 30 kilometers. *Monthly Weather Rev.* 97, 446–455. doi: 10.1175/1520-0493(1969)097<0446:DWVSTK>2.3.CO;2

Weller, R. A., Farrar, J. T., Buckley, J., Mathew, S., Venkatesan, R., Lekha, J. S., et al. (2016). Air-sea interaction in the bay of bengal. *Oceanography* 29, 28–37. doi: 10.5670/oceanog.2016.36

Weller, R., Farrar, J., Seo, H., Prend, C., Sengupta, D., Lekha, J. S., et al. (2019). Moored observations of the surface meteorology and air–sea fluxes in the northern bay of bengal in 2015. *J. Climate* 32, 549–573. doi: 10.1175/JCLI-D-18-0413.1

Wenegrat, J. O., and McPhaden, M. J. (2015). Dynamics of the surface layer diurnal cycle in the equatorial atlantic ocean (0, 23 w). *J. Geophysical Research: Oceans* 120, 563–581. doi: 10.1002/2014JC010504

Wijesekera, H. W., Wang, D. W., and Jarosz, E. (2020). Dynamics of the diurnal warm layer: surface jet, high-frequency internal waves, and mixing. *J. Phys. Oceanography* 50, 2053–2070. doi: 10.1175/JPO-D-19-0285.1

Wykes, M. S. D., Hughes, G. O., and Dalziel, S. B. (2015). On the meaning of mixing efficiency for buoyancy-driven mixing in stratified turbulent flows. *J. Fluid Mechanics* 781, 261–275. doi: 10.1017/jfm.2015.462

Yan, Y., Zhang, L., Yu, Y., Chen, C., Xi, J., and Chai, F. (2021). Rectification of the intraseasonal sst variability by the diurnal cycle of sst revealed by the global tropical moored buoy array. *Geophysical Res. Lett.* 48, e2020GL090913. doi: 10.1029/2020GL090913

Yu, L. (2010). On sea surface salinity skin effect induced by evaporation and implications for remote sensing of ocean salinity. *J. Phys. oceanography* 40, 85–102(. doi: 10.1175/2009JPO4168.1

frontiers | Frontiers in Marine Science

TYPE Original Research
PUBLISHED 07 July 2023
DOI 10.3389/fmars.2023.1173163

OPEN ACCESS

EDITED BY
Shengqi Zhou,
Chinese Academy of Sciences (CAS), China

REVIEWED BY
William Smyth,
Oregon State University, United States
Takanori Horii,
Japan Agency for Marine-Earth Science and Technology (JAMSTEC), Japan

*CORRESPONDENCE
Zengan Deng
dengzengan@163.com
Ting Yu
julia_yu_nmdis@163.com

RECEIVED 24 February 2023
ACCEPTED 12 June 2023
PUBLISHED 07 July 2023

CITATION
Chu Y, Deng Z and Yu T (2023) Effects of tropical storm on equatorial Kelvin waves: a study based on both observation and modeling.
Front. Mar. Sci. 10:1173163.
doi: 10.3389/fmars.2023.1173163

Effects of tropical storm on equatorial Kelvin waves: a study based on both observation and modeling

Yubin Chu[1], Zengan Deng[1*] and Ting Yu[2,3*]

[1]School of Marine Science and Technology, Tianjin University, Tianjin, China, [2]National Marine Data and Information Service, Tianjin, China, [3]Key Laboratory of Marine Environmental Information Technology, Ministry of Natural Resources, Tianjin, China

Tropical cyclones (TCs) play an important role in sea-air interactions and cross-scale impacts on of El Niño–Southern Oscillation events by influencing the turbulent mixing and heat distribution in the upper ocean. Utilizing the observational data and simulations from a numerical model with modified surface wind forcing, this study systematically investigates the effects of a tropical storm (TS) on equatorial Kelvin waves based on TS Dujuan, which is a low-intensity TC. Observations of anomalies combine with the equatorial wave decomposition method are used to confirm the passage of a downwelling Kelvin wave during the same period with properties similar to those of the modeled wave. Modeling results indicate that the TS amplifies the equatorial Kelvin wave, raising the sea surface height by ~2.1 cm and the upper ocean temperature by ~0.34°C and accelerating the eastward zonal current. These signals propagate eastward with the wave and decrease rapidly, and finally decrease to approximately 3-35% of their original strength, particularly the temperature decrease is greatest. Our findings reveal that, in the region close to the equator, even low-intensity cyclones like TS Dujuan can significantly impact the dynamics and propagation of Kelvin waves. TS Dujuan is capable of altering the thermal structure of the equatorial Pacific by amplifying the Kelvin waves. As TS Dujuan occurred during a La Niña event, we infer from our specific study that the forcing effects of TS on equatorial Kelvin waves may reduce the duration of La Niña events.

KEYWORDS

tropical storm, equatorial Kelvin wave, La Niña, ocean modeling, upper ocean

1 Introduction

A tropical cyclone (TC) is an intense cyclonic vortex with a warm core structure, originating from warm tropical or subtropical oceans. TCs play an important role in sea-air coupling interactions. On one hand, they can drive mesoscale ocean circulation and intensify the turbulent mixing within specific regions, resulting in alterations to the temperature and salinity structure of the upper ocean. The passage of TCs involves the input of a large amount of mechanical energy into the ocean, leading to the loss of local sea surface water vapor and heat due to the high wind stress and the associated wave action. Furthermore, TCs can induce Ekman pumping and heat pumping, causing the cooling of the surface's warm water, and the heating of the subsurface's cold water. With the passing of TCs, the surface water returns to the normal thermal condition of the Pre-TCs, and the subsurface water remains warm (Emanuel, 2001). Additionally, strong turbulent mixing and upwelling can be caused in the subsurface water due to the entrainment of TCs (Greatbatch, 1984; Monaldo et al., 1997; Gierach and Subrahmanyam, 2008; Hung et al., 2013; Chang et al., 2014). On the other hand, the energy input to the ocean from TCs propagates as near-inertial internal waves and interacts nonlinearly with local internal waves and near-inertial oscillations in the ocean, ultimately affecting energy distribution in the ocean basin and even globally (Quanan et al., 2006; Furuichi et al., 2008; Elipot et al., 2010). Since temperature anomalies of surface and subsurface seawater are closely related to global climate (Wyrtki, 1985; Zebiak and Cane, 1987), TCs exert significant impacts on climate-scale events.

TCs commonly occur in the equatorial Pacific, particularly in the northwestern region of the western equatorial Pacific, which accounts for approximately one-third of the global total (Wang and Chan, 2002; Chan, 2005). Additionally, almost all equatorial Kelvin waves originate in the western equatorial Pacific. Previous studies (Sriver et al., 2008; Fedorov et al., 2010; Sriver and Huber, 2010) indicated that TCs can affect equatorial Kelvin waves and thereby influence ocean dynamics. Therefore, examining the potential relationship between TCs and equatorial ocean dynamics can further deepen our understanding of TC generation and climate processes.

Previous studies have explored the forcing effect of cross-equatorial TCs and TC pairs on equatorial Pacific dynamics based on buoy data and found that individual synoptic events may influence the entire El Niño–Southern Oscillation (ENSO) cycle (Keen, 1982; Nitta, 1989). Based on a statistical analysis of observations of multiple TC events at an interannual timescale, Gao et al. (1988) found that the near-equatorial tropical cyclones developed equatorward of 10°N can intensify the equatorial westerlies and produce the Kelvin waves, which propagate to the South American coasts in about 2-3 months, inducing the rise of Sea Surface Temperature (SST) there. Chen and Gao (1994) pointed out that the durations of TCs (in days) in the near-equatorial and tropical areas of the Northwest Pacific are significantly higher in El Niño than in non-El Niño years, and concluded that the development of TCs in the near-equatorial and tropical areas of the Northwest Pacific strengthens the equatorial westerly wind pulse and excites the Kelvin waves, contributing to the development and maintenance of El Niño. Sriver et al. (2013) used the Community Climate System Model to prove that three successive TC events may excite equatorial Kelvin and Yanai waves, and they found the wave amplitude is directly proportional to TCs wind speed. They also suggested that the wind forcing of TCs would affect the period and amplitude of ENSO events. Wang et al. (2019) proposed that TC events in the Western Pacific could significantly affect the development of ENSO events, mediated by Walker circulation and equatorial Kelvin waves. Previous modeling studies on the effects of TCs on Kelvin waves mainly focused on multiple TC events at interannual scales. However, the response of equatorial Kelvin waves to an individual TC remains unknown. To our knowledge, the forcing effect of a tropical storm (TS), which is a low-intensity TC, on Kelvin waves has never been studied.

In this study, we concentrate on TS Dujuan, which lasted for approximately 10 days (from the tropical disturbance stage) in the western equatorial Pacific in February 2021. The primary reason we select it is that it was active near the equator for a very long time (Figure 1A). TS Dujuan occurred when the Eastern Pacific was transitioning from a La Niña to a neutral state (Figure 1B), which is more conducive to the development of Kelvin waves (McPhaden, 1999). For the first time, the forcing effect of individual TS on the equatorial Kelvin wave and the associated ocean dynamics are investigated in this study.

The data and the anomalous ocean signals during TS Dujuan are described and discussed in Section 2. The configuration of the global ocean circulation model and the model verification are given in Section 3. The diagnostic modeling results are analyzed in Section 4, and the discussion and conclusions are presented in Section 5.

2 Analysis based on the observational data

Based on the analysis of the anomalous ocean signals, the existence of a Kelvin wave in the equatorial Pacific between February 1 and April 30, 2021 is inferred. Although easterly anomalies dominate over the Pacific during La Niña events, more than 50% of the tropical cyclones in the western Pacific reverse the direction of local trade winds by enhancing the equatorial westerly anomalies (Lian et al., 2019) (Figure 2A), which is conducive to the generation of downwelling Kelvin waves.

2.1 Data

The coupled forecast system model version 2 (CFSv2, https://cfs.ncep.noaa.gov/) hourly wind data product, developed at the Environmental Modeling Center at the National Center for Environmental Prediction (NCEP), is adopted to calculate the wind stress anomaly (Figure 2A) from 1990 to 2022. We calculated the wind stress based on the bulk formula by Large

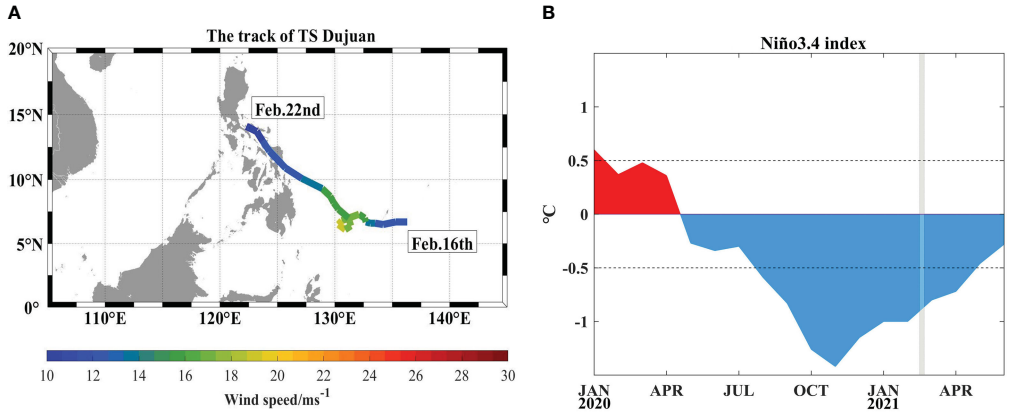

FIGURE 1
(A) The track of TS Dujuan during its entire activity. Colors denote the maximum central wind speed. The information on typhoon path and intensity used in this study comes from the China Meteorological Administration (CMA) Best Track dataset (https://www.typhoon.org.cn/) collected and compiled by the Shanghai Typhoon Research Institute. **(B)** Monthly average Niño3.4 index from January 2020 to July 2021, the shadow area is the TS Dujuan activity duration. Six consecutive months of temperature anomalies exceeding + (-) 0.5°C as El Niño (La Niña) events, derived from NOAA/NCEP CPC sea surface temperature data based on ERSSTv5.

and Pond (1981). We use data from Copernicus Marine Environment Monitoring Service (CMEMS) to draw the longitude-time plots of sea-level anomalies (SLAs, https://marine.copernicus.eu/) for the study area from February 1 to April 30, 2021 (Figures 2B, C). The SLA product is calculated once a day, and the method of multi-satellite data integration used in the product has been proven to improve the ability to capture large-scale or mesoscale variabilities (Pujol et al., 2016). The SLA data is validated using upper ocean heat content and thermocline depth (D20) anomalies from the Tropical Atmosphere Ocean (TAO, https://www.pmel.noaa.gov/) buoy array. The TAO buoys are located between the latitudes of 10°S–10°N, and the spatial resolution of data in the meridional direction is much higher than that in the zonal direction. The asymmetrical design of this buoy array helps to effectively capture the information of equatorial Kelvin waves. The observational range of the buoys in the vertical extends from the surface to a depth of ~500 m, precisely including the tropical thermocline. Data from this buoy array has contributed greatly to the theoretical study of several ENSO events, including the "Delayed Oscillator" (McPhaden et al., 2010).

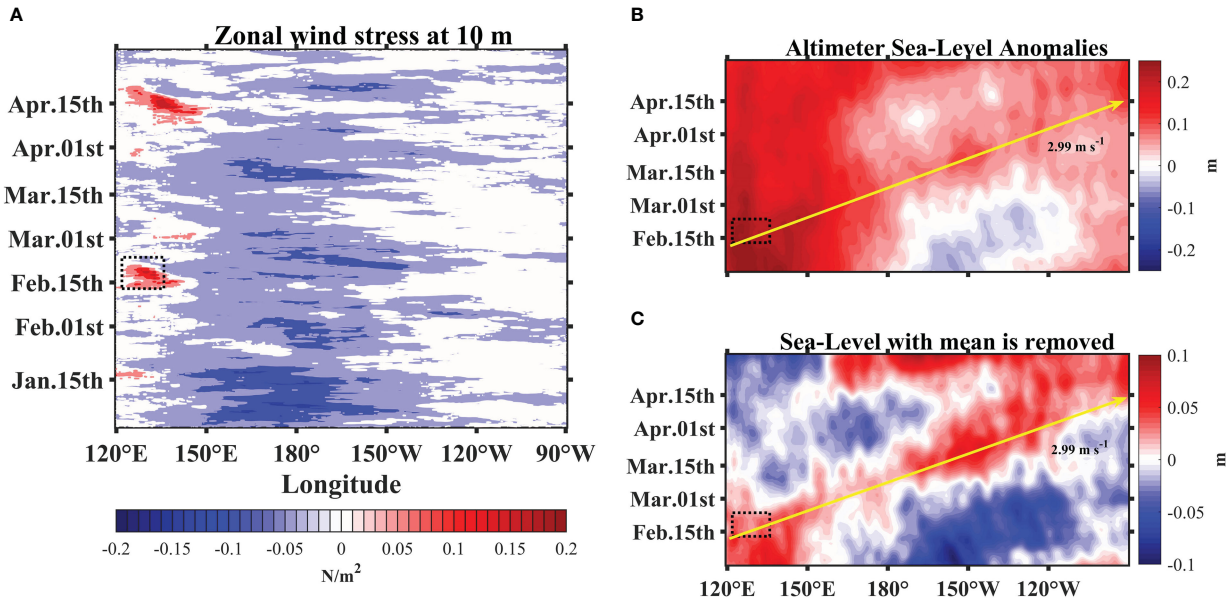

FIGURE 2
Longitude-time plots of daily anomalous **(A)** zonal wind stress at 10m, **(B)** sea surface height, **(C)** sea surface height with the mean is removed. Wind stress anomalies are averaged between 5°S and 5°N. Sea surface height anomalies are averaged between 2°S and 2°N and filtered using the mean filter. The dashed area denotes the TS Dujuan activity region. The solid yellow arrow denotes the estimated observed Kelvin wave speed.

2.2 Responses of anomalous signals in the equatorial Pacific Ocean to TS Dujuan

Generally, the influence of zonal wind stress anomalies on equatorial Kelvin waves can be categorized into two types. The first is that the zonal wind stress anomaly shows low-frequency variations. The second is that the action time of the wind stress anomaly is very short, i.e., the wind stress anomaly can be regarded as a wind "pulse" at the initial moment of occurrence, and the wind stress anomaly quickly approaches zero within a short time. The wind stress anomaly of TS Dujuan during the La Niña event belongs to the second type (Figure 2A).

The features of anomalous signals in the equatorial Pacific are shown in Figures 2B, C. A clear positive SLA can be observed in the TS Dujuan-forcing area around February 15, 2021, because TS Dujuan induces local wind stress curl in the northern part of the western equatorial Pacific (~6°N), which produces Ekman upwelling and divergence in the range of 135°E–140°E (Figure S1). Under the effects of negative wind stress curl and the Coriolis force, seawater converged to the equatorial region, resulting in a sea level rise within the 5°S–5°N region. Meanwhile, as the influencing of the La Niña event, the southeast trade winds blew the seawater to the west of the Pacific, and the seawater converged on the west coast, generating a positive SLA higher than 20 cm. The spatio-temporal variation of this SLA is characterized by a clear eastward movement. TS Dujuan is active near both the location and time of onset of the eastward propagation of SLA, according to Figure 2B. The eastward propagation of the positive anomaly is more pronounced in Figure 2C. The eastward propagation of the anomaly starts from the western Pacific near 130° E and reaches the eastern coast of the Pacific after ~62 days, resulting in a positive SLA in the eastern Pacific. Using satellite-derived SLA data, we also estimate the zonal and meridional geostrophic velocity anomalies (GVAs) (See Supplementary Material 1). Zonal GVAs (Figure 3A) are generally consistent with the spatial and temporal features of the SLAs shown in Figures 2B, C. However, as shown in Figure 3B, the meridional GVAs do not show an obvious eastward-propagation response. This suggests that TS-forced eastward propagation brings about the redistribution of zonal geostrophic velocities, and thus leads to the zonal transport, but has little effect on the meridional transport (Delcroix et al., 1991; Sriver et al., 2013). The distribution of zonal GVAs is relatively scattered to the west of the International Date Line, which may be due to deviations from the calculation method or the altimeter data.

Variations in the heat content and D20 anomalies in the upper ocean also agree with the main characteristics of equatorial Kelvin waves, therefore it is useful to analyze the upper ocean heat anomaly. To further determine the nature of the eastward propagation of the SLA and its effect on the upper ocean, we analyze the heat content anomaly and D20 anomaly based on TAO observations (Figure 4) for the same period as that used for the validation of the SLA. As shown in Figure 4A, compared to the climatological state, the entire east-central Pacific exhibits a cold anomaly in early February, whereas the eastern part of the western Pacific presents a warm anomaly. These zonal depth differences in the equatorial Pacific thermocline, i.e., an increase in the east-west

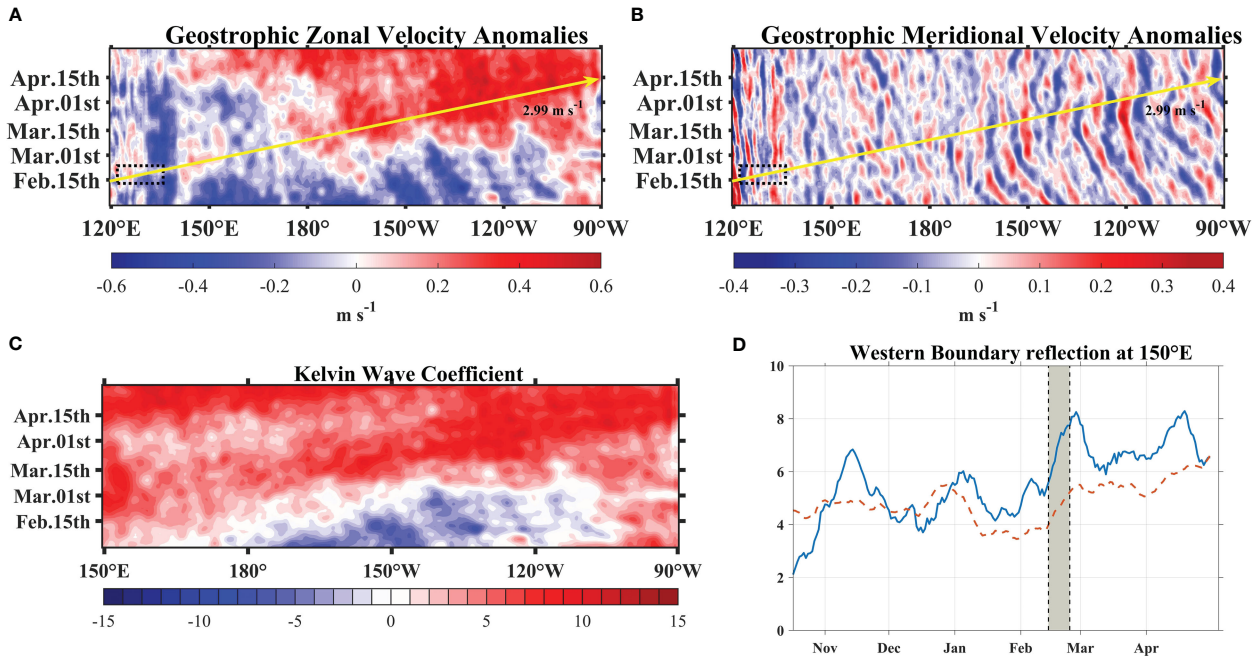

FIGURE 3
Longitude-time plots of anomalous daily **(A)** geostrophic zonal velocity (eastward positive, within 2°S-2°N), **(B)** geostrophic meridional velocity (northward positive, within 5°S-5°N), **(C)** Kelvin coefficient and **(D)** Kelvin coefficients (solid line) and Rossby coefficients (dash line) at 150°E, The positive value represents downwelling, the negative value represents upwelling. For instance, a coefficient of 10 units would yield an equatorial sea surface height amplitude of 5cm and an equatorial zonal current amplitude of 16 cm s^{-1}. The dashed area denotes the TS Dujuan activity region. The solid yellow arrow denotes the estimated observed Kelvin wave speed.

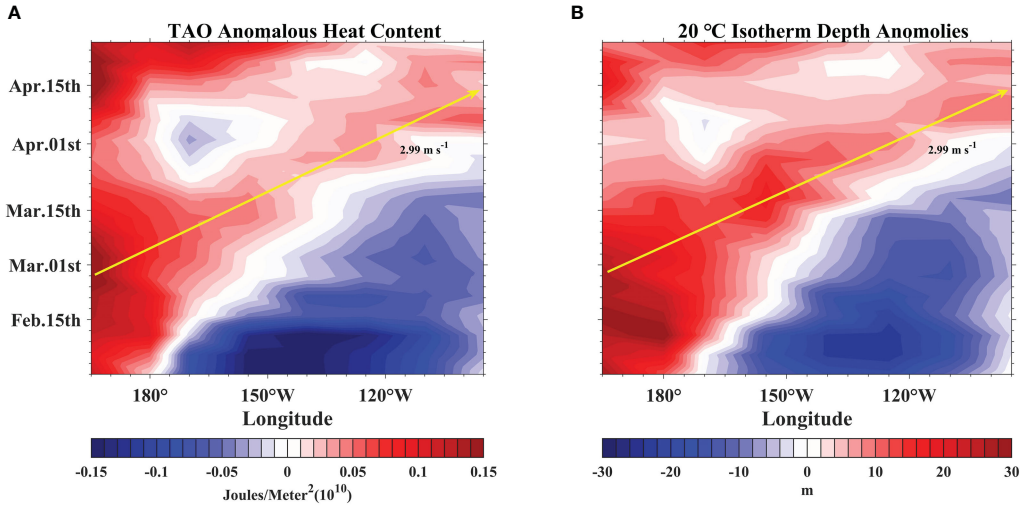

FIGURE 4
Longitude-time plots of observed anomalies **(A)** the upper ocean heat content, and **(B)** D20, derived from TAO buoy array. Heat content anomalies were based on existing buoy locations, and integrated to 300m depth. All quantities are compared to climatology and interpolated by Akima to 165° E-95°W, averaged at 2°S-2°N. The solid yellow arrow denotes the estimated observed Kelvin wave speed.

Pacific thermocline gradient, are consistent with the characteristics observed in the equatorial Pacific during La Niña events. By mid-February, TS Dujuan causes anomalous forcing of the westerly wind, and the cold phase of the ENSO gradually returns to the neutral state as the heat anomaly moving eastward across the equatorial Pacific (Figure 1B). Moreover, the thermocline in the Western Pacific is depressed by 20–30 m, and the heat also accumulates in the same location. Both the heat content anomaly and D20 anomaly show an extremely strong correlation with SLA (also shown in Rebert et al., 1985). The D20 and positive heat content anomalies in the upper ocean of the western Pacific propagate eastward to the eastern Pacific with time in the form of waves. This eastward-propagation process redistributes the upper ocean heat anomalies, which is consistent with the effect of nonlinear equatorial Kelvin waves in the equatorial Pacific (Sommer and Zeitlin, 2005). At the same time, the eastward-propagating wave transfers thermocline anomalies to the eastern Pacific, affecting surface temperature anomalies (Chao and Xu, 2001). One part of the thermocline anomalies is transported poleward, and the other is deflected westward in the form of downwelling Rossby waves. Finally, the heat content of the entire equatorial Pacific increases, depressing the thermocline and attenuating the large zonal gradient of equatorial Pacific heat during the La Niña event. The combination of the spatial and temporal features of sea-level, upper ocean heat, and D20 anomalies indicate that a downwelling equatorial Kelvin wave is forced by TS Dujuan during this period. To directly represent the activity of the downwelling Kelvin wave, we calculate the Kelvin coefficient and first Rossby wave coefficient using the equatorial wave decomposition method (Boulanger and Menkes, 1995) based on the SLAs and zonal GVAs. As shown in Figures 3C, D, a downwelling Kelvin wave travels within the equatorial Pacific from February to May.

We have also examined the contribution of Rossby wave reflections at the western boundary to the Kelvin waves. Considering the low-frequency reflection, even-order Rossby waves make a minor contribution to the total reflection Kelvin wave coefficient. The reflection coefficient of even-order Rossby waves decreases with the increasing frequency of incident waves. According to the findings of Yuan and Han (2006), the Rossby waves that make the primary contribution to the linearly reflected Kelvin wave can be represented by the first baroclinic mode of the first-order Rossby wave, shown by the dashed line in Figure 3D. The consistency between the solid and dashed lines indicates that the linearly reflected Kelvin wave is mainly derived from the reflection of the first baroclinic mode Rossby wave. The difference between the solid and dashed lines may be attributed to the influence of nonlinearity. In addition, simulations of the equatorial Pacific from February 01 to April 30 using the Hybrid Coordinate Ocean Model (HYCOM) are employed to calculate the mean wave speed through the vertical mode function. Model simulations yielded a Kelvin wave speed of 3.09 m s^{-1}, which agrees with the first baroclinic Kelvin wave speed (Boulanger and Menkes, 1995). Furthermore, the observed Kelvin wave speed is estimated to be 2.99 m s^{-1} based on the propagation distance and time of the heat content anomalies and D20 anomalies. Both the modeled and observed wave speeds agree well with the wave observations recorded by the TAO buoy array (Shinoda et al., 2008).

3 Modeling configurations and validations

Kelvin wave has been identified above, but the effects of TS Dujuan on the Kelvin wave during the La Niña event remain unclear. Therefore, here we perform diagnostic experiments to systematically

identify the specific effects of TS Dujuan forcing on the equatorial Kelvin wave.

3.1 Modeling configurations

The ocean general circulation model used in this study is HYCOM 2.3, which is based on the Miami Isopycnic-Coordinate Ocean Model and has proved useful for simulating equatorial Kelvin waves (Shinoda et al., 2008). HYCOM uses hybrid coordinates in the vertical, which is the salient feature of this model. HYCOM retains isopycnal coordinates in the open, stratified ocean, and the isopycnal vertical coordinates smoothly transition to z-coordinates in the weakly stratified upper mixed layer. In the shallow water region, the vertical coordinates become terrain-following (sigma) coordinates; in the very shallow water near the shore, the coordinates become z-level coordinates again.

K-Profile Parameterization (Large et al., 1994) was selected in our simulation to calculate vertical mixing. The modeling domain covers the region from 0° to 360° and from 70°N to 65°S, with a uniform horizontal grid that had a resolution of 0.5° at the equator (Philander, 1990), at which resolution the equatorial Rossby radius can be well resolved (Hsieh et al., 1983). There are total of 32 levels in the vertical with 12 layers in the upper 300m. We use global bathymetric grid data with a spatial grid size of 30″ × 30″ from the General Bathymetric Chart of the Oceans (GEBCO, https://www.gebco.net/) that released in December 2014 (GEBCO_2014) to represent the model topography.

The model is first spun up using climatological forcings and initial conditions. The initial temperature and salinity data are adopted from World Ocean Atlas 2018 (WOA18, https://odv.awi.de/data/ocean/world-ocean-atlas-2018/) and the climatological forcings are from Coordinated Ocean-Ice Reference Experiments (CORE II, https://data1.gfdl.noaa.gov/nomads/forms/core/COREv2/). After the model reaches an equilibrium state, the diagnostic experiments are run for the whole year of 2021 using hourly forcings of wind stress and heat fluxes from NCEP reanalysis data.

To examine the forcing effect of TS Dujuan on the Kelvin wave in the equatorial Pacific, we reconstructed two sets of wind forcing to drive two numerical experiments referring to the method of Wang et al. (2014). Initially, we eliminated the winds within a distance equals to 25 times the radius of maximum wind from the center of the tropical cyclone (Willoughby and Rahn, 2004). This TC center was provided by the CMA. In effect, we removed the original winds within this specified region. Subsequently, we employed a traditional recursive filter (Xie et al., 2005; Xie et al., 2011) to supplement the data. The smoothing parameter α was set to a range between 0.5 and 0.9, a value contingent on the wind speed. Using the filter, the high winds of TS Dujuan is excluded within a certain spatial range (Figure 5). Two experiments were designed: one forced by the original winds including the information of TS Dujuan (hereafter referred to as TSF) and the other forced by winds excluding TS Dujuan information (hereafter referred to as NONTSF).

3.2 Model validations

A complete validation of the model is beyond the scope of this study. In this work, we mainly focus on the sea surface height (SSH), temperature, and zonal current. The simulations are compared with *in-situ* and reanalysis data to evaluate the modeling skill.

3.2.1 Sea surface height

Figure 6 shows the simulated SSH and the comparison with HYCOM+NCODA (Hybrid Coordinate Ocean Model and Navy Coupled Ocean Data Assimilation) Global 1/12° Reanalysis data (https://hycom.org/data/). We also provide some statistics in Figure 7, including mean error (ME), root-mean-square error (RMSE), and correlation coefficient (CC). The maximum ME is 1.73 cm, and the minimum is -2.27 cm. The RMSE is lower than 1.68 cm and the CCs all exceed 88%. The simulated SSH is lower than the reanalysis data in the western Pacific, which may be due to the parameterization scheme and viscosity terms of the model, however, the deviation is generally acceptable.

3.2.2 Temperature

Figure 8 shows the vertical profiles of temperature from February to April. The temperature is verified using Argo data (ftp://ftp.argo.org.cn/pub/ARGO/global/). The vertical depths of both the simulations and buoy observations are interpolated to 43 layers using the Akima interpolation method. The simulated temperature in the upper ocean is slightly lower than the temperature given by the Argo data, the maximum deviation within 0-300 m is ~2.2°C. Since data assimilation is not performed in our model, deviations are mainly accumulated during the time of integration. In general, there is a good agreement between the simulations and Argo observations, with the correlation coefficient exceeding 99% (Figure 9, for further details regarding the Argo buoy, please refer to Table S1).

3.2.3 Zonal currents

The equatorial undercurrent, an important part of the ocean circulation in the tropical Pacific, is a stable eastward flow existing in the upper equatorial ocean. The currents from February to April are presented in Figure 10, showing the monthly variability and the comparison with reanalysis data from the Nucleus for European Modeling of the Ocean (NEMO, downloaded from CMEMS). The equatorial undercurrent is weak in February and stronger in March and April, which is related to the eastward propagation of the anomalous temperature signals in the upper ocean and further reflects the potential activity of the Kelvin wave. The simulated maximum zonal current is between 1 and 1.6 m s^{-1}, consistent with the results of Firing et al. (1983). It is indicated that our model is capable of reproducing the prominent features of the equatorial undercurrent.

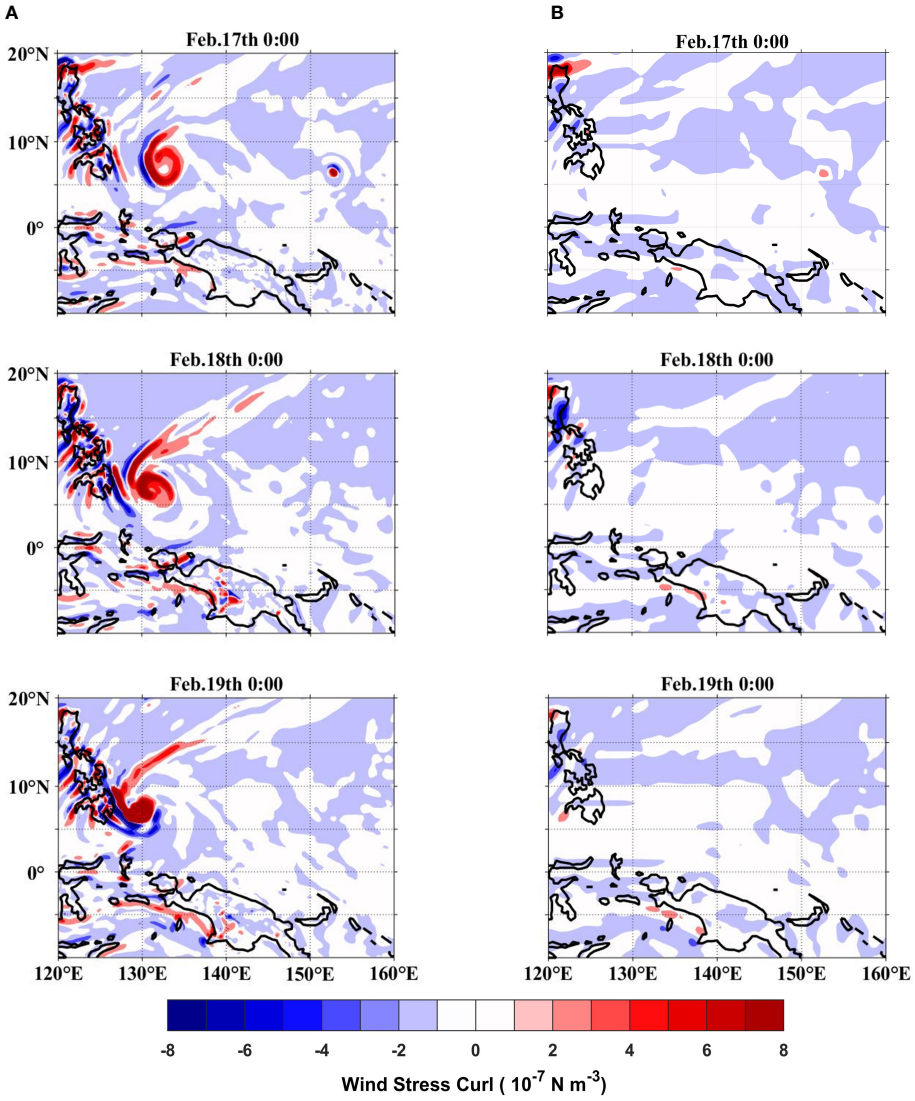

FIGURE 5
Wind stress curl from February 17th to 19th **(A)** the original data, **(B)** the filtered data.

4 Analysis based on the modeling results

Here we compare the differences in detail between the simulations of the TSF and NONTSF experiments. The oceanic responses, including SSH, temperature, and zonal current, to the forcing of TS Dujuan are analyzed and discussed in the following.

The longitude-time plots for the results of TSF and NONTSF from February to May 2021 are shown in Figure 11. The locations of the alternating positive and negative differences in the western equatorial Pacific correspond to those of the zonal wind stress anomalies in late February (Figure 2A), indicating that TS Dujuan causes the change in SSH in the western Pacific. The intensity of TS Dujuan is low, and consequently so is the accumulated cyclone energy (ACE; only 0.54×10^4 m^2 s^{-2}). Therefore, the SSH characteristics in the TSF experiment do not differ considerably from those in the NONTSF experiment, which is depicted visually in Figures 11A, B. Compared to the NONTSF case, TS Dujuan winds raise the SSH on the east side of the forcing region (by more than 2.1 cm) and lower it on the west side. The differences between the positive and negative increase with proximity to the TS track (Sun et al., 2014). In the Northern Hemisphere, the asymmetrical nature of the SSH (i.e., raised on the east side of the TS track and lowered on the west side) is probably due to the local winds. The direction of the local winds on the east side of the TS track is consistent with that of the Ekman drift. For a slow-moving TS, the wind enhances Ekman pumping and induces stronger upwelling on the east side of the TS than that on the west side, driving sea surface water masses away from the center of the TS. As a result, the water accumulates on the east side of the TS, and the SSH rises. In addition to local differences, the eastward propagation phenomenon also occurs. The negative SSH difference between the TSF and NONTSF in the Western Pacific caused by TS Dujuan propagates westward in the form of Rossby waves and remains in the Western Pacific. Over the next ~60 days, the positive SSH

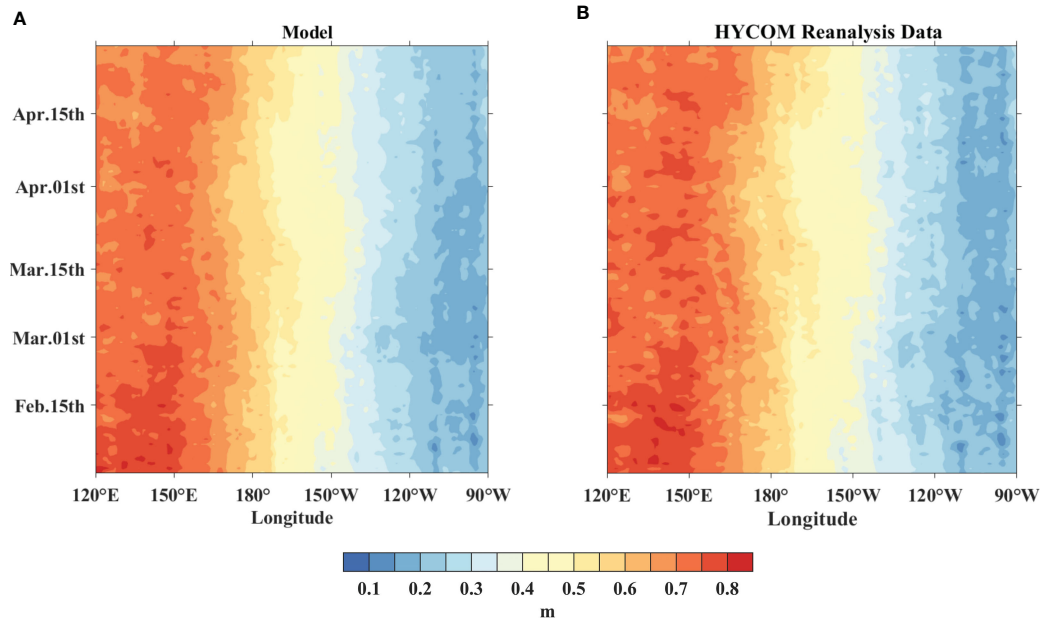

FIGURE 6
Longitude-time plots of daily SSH (within 5°S-5°N), for **(A)** the model simulation, **(B)** the HYCOM+NCODA Global 1/12° Reanalysis Data.

difference propagates eastward at a speed consistent with Kelvin waves (Figure 11C, yellow dashed line). The signal raises the SSH in the eastern equatorial Pacific and ultimately reaches the eastern boundary.

Compared to the NONTSF, the TSF has positive temperature differences; the maximum value is about 0.34°C between 130°E and 135°E on February 21. The characteristics of the temperature differences between the TSF and NONTSF experiments are also consistent with those of the SSH differences between the two experiments (Figure 11F).

The characteristics of the temperature differences between the TSF and NONTSF experiments along the TS track could also be explained by the fact that the direction of wind stress on the east side of the TS is aligned with that of the Ekman drift. As the TS moves from south to north, the energy input to the ocean on the east side of its track will be greater than that on the west side. The vertical mixing, entrainment, and Ekman pumping that occur on the east side can be more intensive and more likely to transport the subsurface low-temperature seawater up to the sea surface. Due to the heat-pumping effect of TS, more warm water masses at the surface can be transported downward by entrainment and mixing, warming the subsurface seawater. Moreover, the negative wind stress curl is input by the TS on the left side of the track (Figure 5), causing the equator-ward Sverdrup transport. The subsurface seawater is conveyed to the equator and accumulated, resulting in a change in the equatorial D20. The temperature differences in the upper ocean then propagate eastward with Kelvin waves. Since the temperature differences between the TSF and NONTSF experiments are small and the upper ocean temperature difference can only reach ~120°E, we speculate that the effect of TS Dujuan on the equatorial Kelvin wave is an amplification rather than an excitation. The differences between the TSF and NONTSF

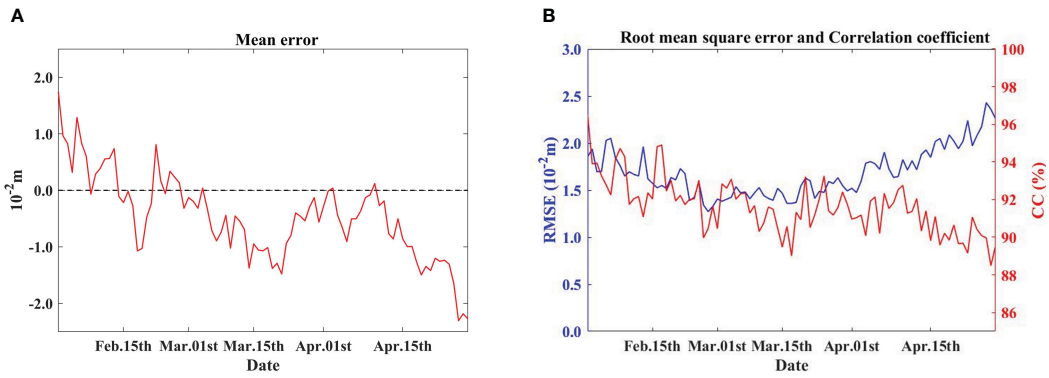

FIGURE 7
The evaluation indices of daily sea surface height, for **(A)** the mean error, **(B)** the root mean squared error, and correlation coefficient.

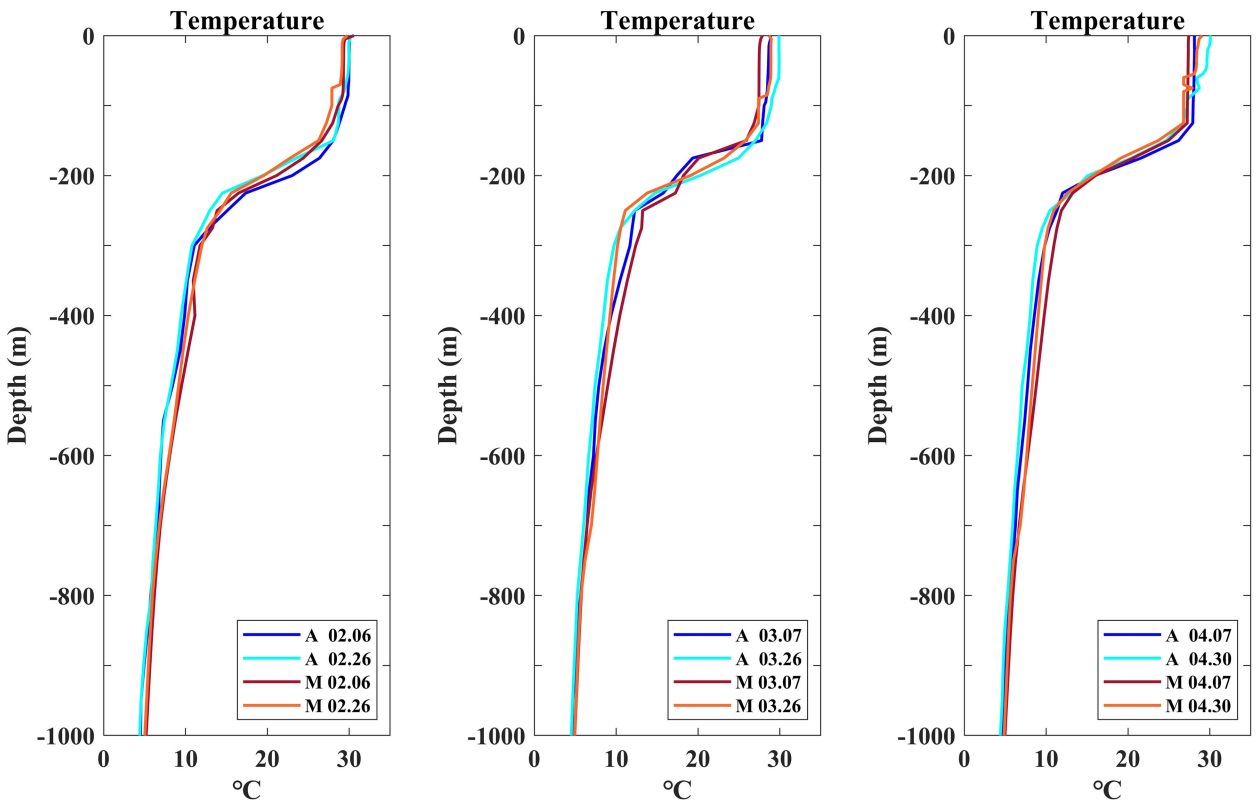

FIGURE 8
Vertical temperature profiles. M is the model simulation result, and A is the Argo buoy data.

highlight the fact that the temperature change in the upper ocean of the western Pacific is caused by TS Dujuan rather than the climatological winds (Figures 11C, F, I). The TS winds induce the vertical mixing and intensify the air-sea heat exchange, causing the decrease of the temperature in the upper ocean on the west side of the forcing area, whereas the increase on the east side. The negative temperature differences on the west side present in the western Pacific, whereas the positive temperature difference on the east side moves eastward to a certain extent. TS Dujuan causes much more local changes than remote changes in SST (Figure S2A). In order to verify the negative feedback of Dujuan on La Niña events, the Niño3.4 index is calculated. The ENSO cycle in TSF enters the neutral state 1 to 2 days before that in the NONTSF (Figure S2B), and the difference between the two is slight due to low ACE, reflecting the contribution of TS-forced Kelvin waves in the La Niña event. However, for a significant impact on a La Niña event to be observed, the interactions and actions of multiple tropical cyclones are necessary (Sriver et al., 2013; Wang et al., 2019; Chen and Lian, 2020; Tong et al., 2023).

The effects of TS Dujuan on zonal currents in the upper ocean are analyzed based on our model simulations as well as a conceptual model (See Supplementary Material 2). A westward current is presented in both the TSF and NONTSF experiments (Figures 11G, H), which is in good agreement with the results shown in Figure 12A, further verifying the reliability of the model results. The distribution pattern of the speed differences between the TSF and NONTSF is similar to that of the SSH and temperature differences. TS Dujuan causes the zonal current in the equatorial region to produce the extreme value of the speed difference between TSF and NONTSF. The zonal current on the western side of the extreme value accelerates westward, and that on the eastern side accelerates eastward. The equatorial wind pulse induced by TS Dujuan produces the same acceleration characteristics in $\bar{u}$ and τ^x (Figures 12A–C, E), and also results in alternating positive and negative changes in the zonal pressure gradient (Figure 12F), causing the Kelvin wave pulse during this period. Meanwhile, it is found that the TS-induced extreme values shown in Figures 11C, F, I lag behind the TS Dujuan activity. The cross-correlation analysis of $\Delta u'$ and τ^x indicates that the shear current lags behind the pulsing wind for ~6 days. Based on this, we calculate the vertical eddy viscosity coefficients using the e-folding scale and regression fitting and estimate the values to be 132 $cm^2\ s^{-1}$ and 64 $cm^2\ s^{-1}$ (Figure 12D), respectively. The latter is roughly half of the former, similar to the relation obtained by McPhaden et al. (1988). However, the estimated value is lower than that in previous studies. Because the selected point is placed at the edge of TS Dujuan and the duration of the wind pulse is relatively short, and the wind intensity is relatively low.

In TSF, TS Dujuan induces the increases in local SSH, upper ocean temperature, and zonal current speed. Those signals propagate eastward as Kelvin waves. Nevertheless, as seen in Figure 13, the difference between TSF and NONTSF declines rapidly. The SSH, temperature, and zonal current speed are decreased to 33%, 30%, and 53% of their maximum values at the

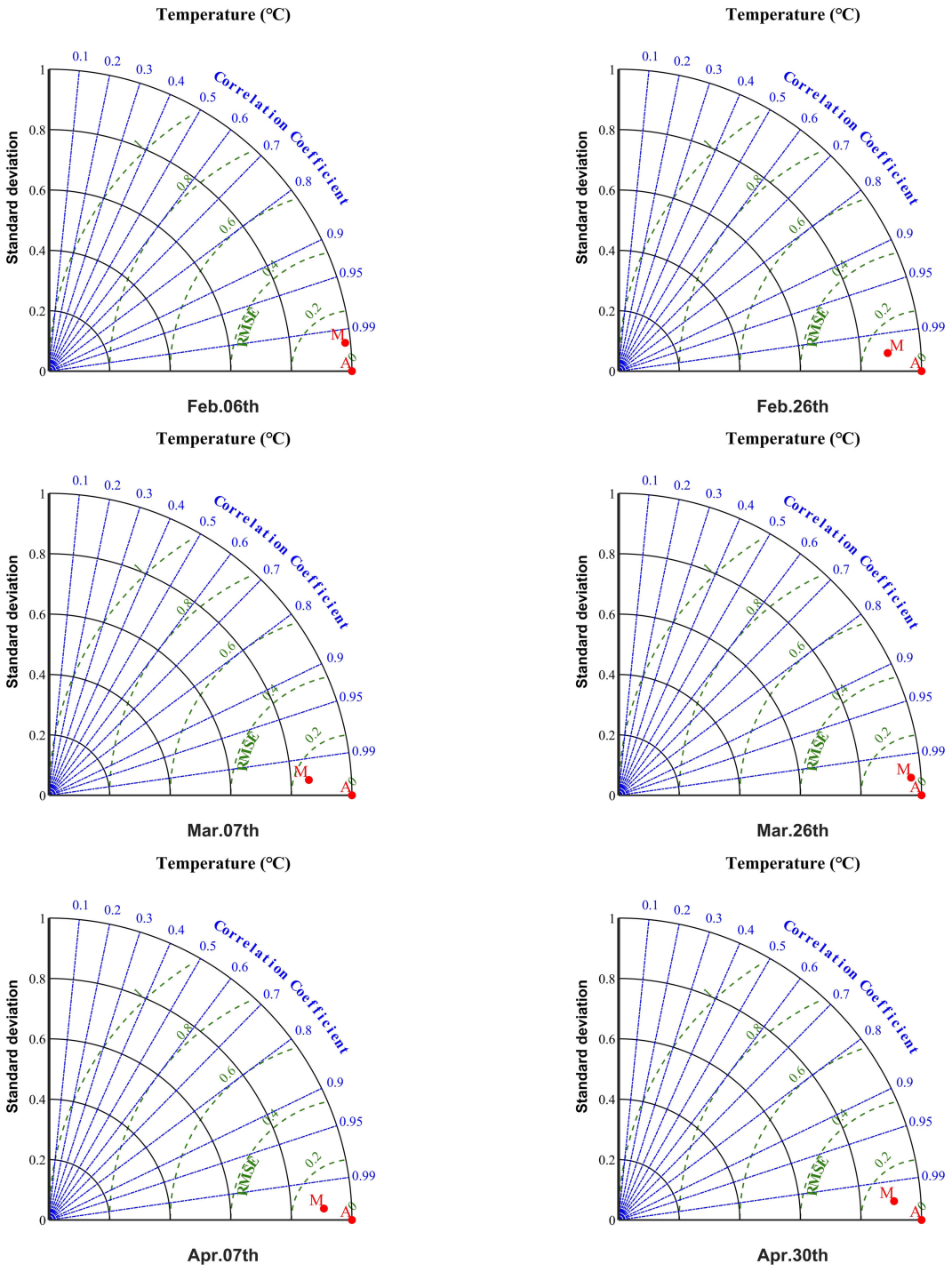

FIGURE 9
Taylor plots of 0-300 m vertical temperature distribution. Point M represents the index calculated from the model data compared to the Argo buoy data (point A). Standard deviation and root mean square error were normalized.

start of eastward-propagation, and then to only 11%, 3%, and 35% in the eastern Pacific. We speculate that the weak propagation of the temperature gradient to the eastern boundary is due to the strength of TS Dujuan and thermal damping. Consequently, we suggest that TS Dujuan is not the primary source of the Kelvin waves activity shown in Figures 2–4, given the fact that the amplitude of SSH in NONTSF is lower than that in TSF by<4%.

In this study, the equatorial Kelvin waves are primarily excited by the reflection of Rossby waves at the western boundary of the Pacific Ocean. The diagnostic experiments allow us to detect the forcing effect of Dujuan on the equatorial Kelvin waves. Since the difference between the TSF and NONTSF rapidly decays during the eastward-propagation process, the temperature difference between the TSF and NONTSF does not propagate to the eastern boundary

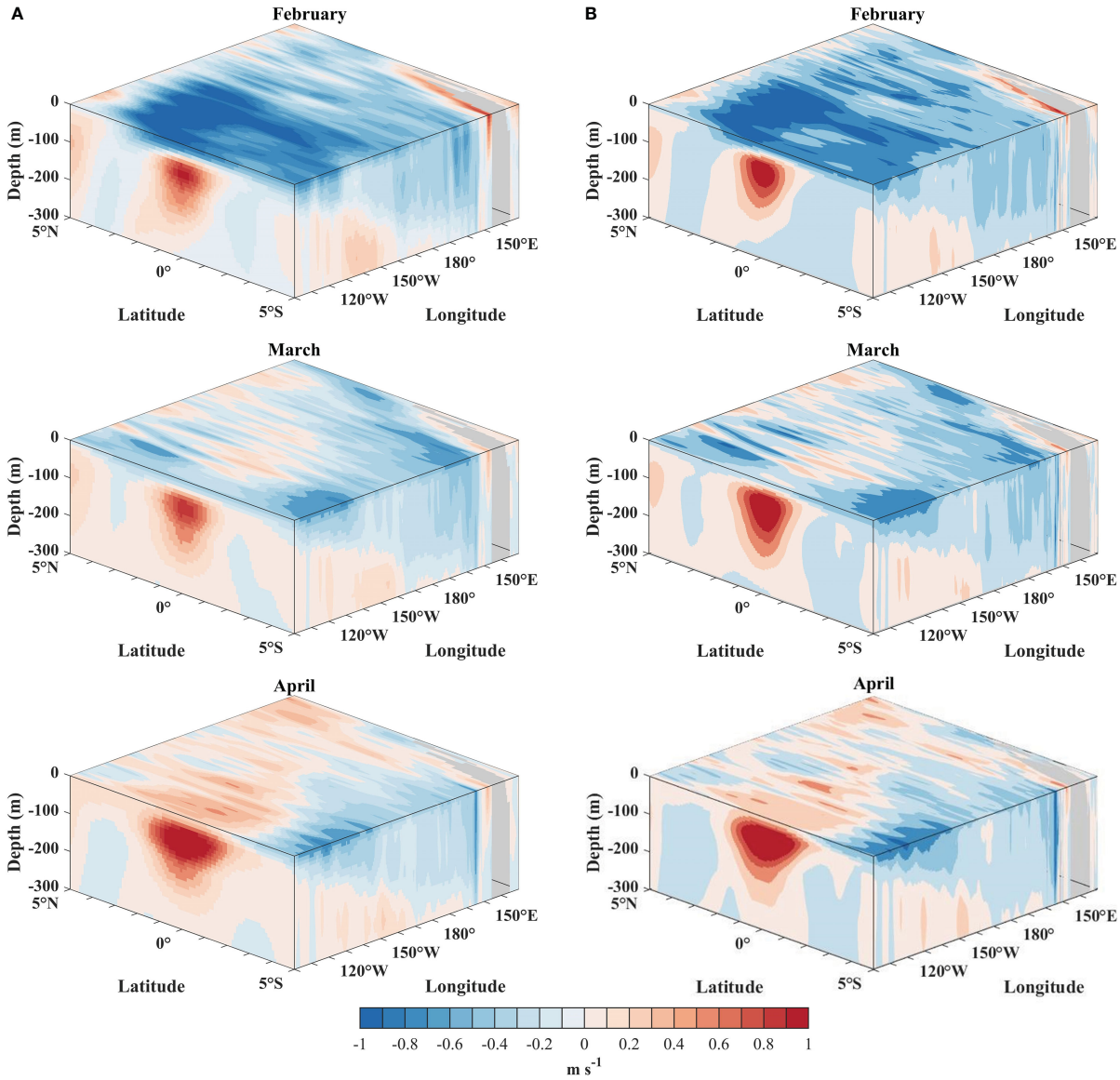

FIGURE 10
The 3D plots of the monthly mean zonal velocity between 0 to 300 m, for **(A)** the model simulation, and **(B)** the NEMO Reanalysis Data.

of the equatorial Pacific (Figures 11F, 13B). Moreover, the difference between the TSF and NONTSF experiments is much smaller than the change from the long-term average (anomalous signals), so we infer that TS Dujuan amplifies the Kelvin waves.

5 Summary and conclusion

The 2020/2021 La Niña event began in August 2020 and ended in May 2021. TS Dujuan, which was active in the northwest Pacific in mid-February 2021, caused significant changes in the upper ocean in the equatorial Pacific, and the timing of the eastward propagation of the TS-forced wave coincided with the transition from the La Niña to a neutral state, which provided negative feedback to the development of La Niña.

In this study, the responses of the ocean to TS Dujuan are quantified and the effects of TS Dujuan on the equatorial oceanic Kelvin wave are analyzed and discussed based on satellite data, TAO buoy observations, and model simulations. According to both the satellite observations and simulations, the strong zonal wind anomaly which links to TS Dujuan elevates the local sea level, and pushes warm water from the sea surface into the subsurface, thereby deepening the D20, and accelerating zonal currents. These anomalies propagate eastward along the equator as Kelvin waves, the equatorial wave decomposition method is adopted to detect the wave. In addition to the zonal redistribution of heat, the spatial-temporal patterns of the surface GVAs reveal that the TS-forced Kelvin waves also redistribute the zonal current at the surface. We assume that there might be a connection between the TS Dujuan and the Kelvin wave because TS Dujuan happened near both the

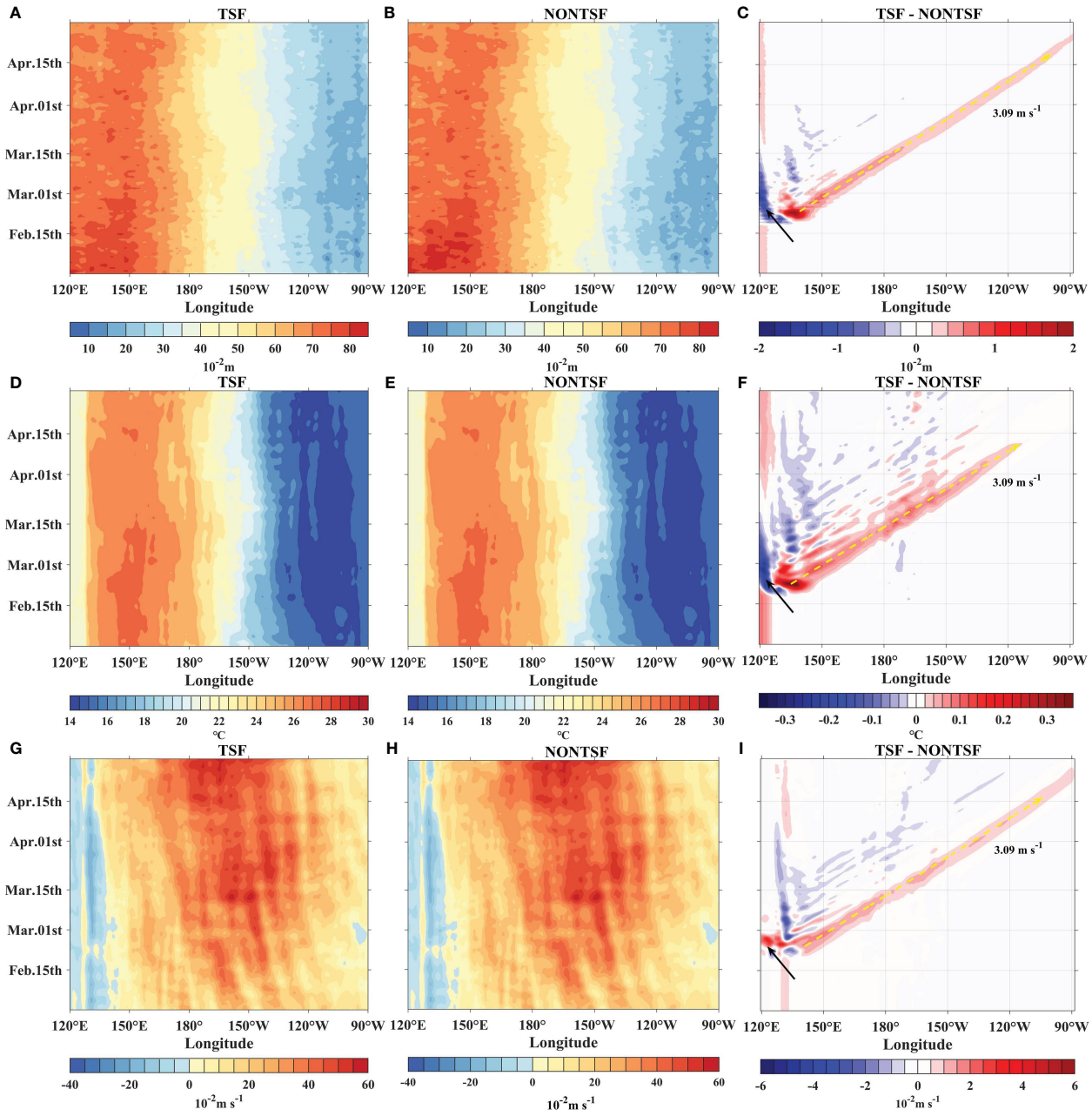

FIGURE 11
Longitude-time plots of daily TSF, NONTSF and their differences of **(A–C)** sea surface height, **(D–F)** 100-200 m upper ocean temperature, **(G–I)** 100-200 m upper ocean zonal velocity. **(A)** Same as Figure 6A, sea surface high anomalies data are all averaged at 5°S-5°N, and the upper layer temperature and zonal flow are averaged at 0°-5°N and are processed by 2D mean filter. The black arrow represents the projection of the TS Dujuan track on the equator. The yellow dashed arrow denotes the estimated modeled Kelvin wave speed and the value is 3.09 m s^{-1}.

location and time of the onset of the equatorial Kelvin wave. To elucidate the forcing effect of TS Dujuan, we designed the diagnostic experiments using recursive filters to modify the surface wind forcing. The simulated SSH, upper ocean temperature, and zonal current are generally consistent with the observations, indicating that the modeling results are reliable.

Our simulation results suggest that even low-intensity cyclones like TS Dujuan can have a significant effect on the dynamics and propagation of Kelvin waves. The modeled Kelvin wave propagates faster than the observed one. Compared with the case in which the wind forcing of TS Dujuan is removed, TS Dujuan wind forcing induces a rise in the local SSH by ~2.1 cm and an increase in the upper ocean temperature by ~0.34°C, exhibiting a strong positive correlation. The simulation results also show that TS Dujuan promotes the acceleration of the zonal current. This acceleration lags behind the TS winds, and the acceleration effect spreads to the eastern Pacific. The equatorial upper ocean is impacted by TS Dujuan, causing Ekman suction to cool the surface seawater and

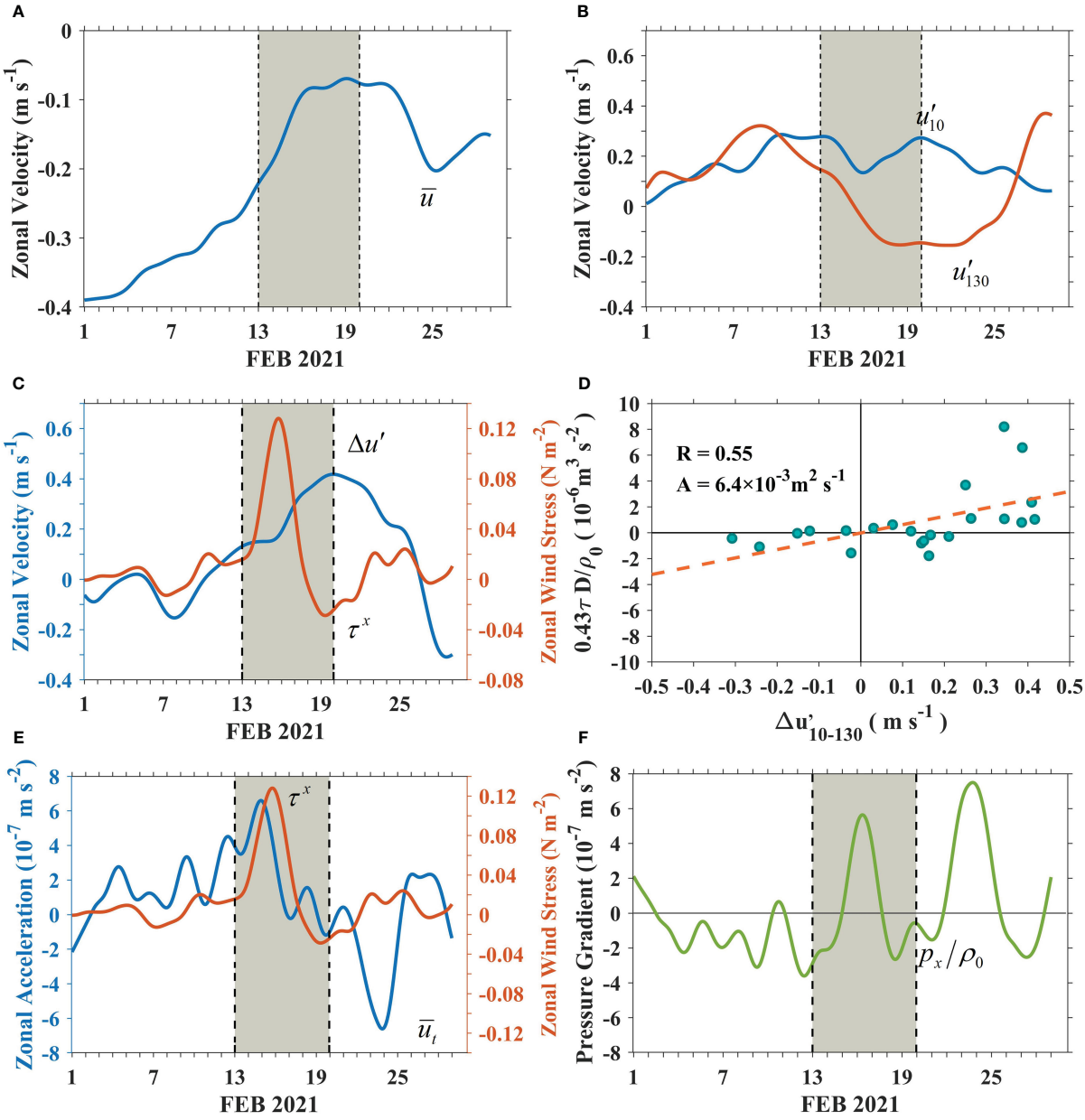

FIGURE 12
Time series of hourly data smoothed using the 5-day Hanning filter at 0°, 140°E, for **(A)** the zonal velocity, averaged over 0-150 m ($\bar{u}$), **(B)** current at 10 m and 130 m relative to the average ($u'_{10} - u'_{130}$), **(C)** the wind stress (τ^x) and the velocity difference $\Delta u' = u'_{10}$, u'_{130}, **(D)** regression of advanced by 6 days for daily data estimates of $0.43\tau^x/\rho_0$ and $\Delta u'$. The slope is the eddy viscosity A, **(E)** the zonal acceleration ($\bar{u}_t$) and wind stress (τ^x), **(F)** the zonal pressure gradient (p_x) (eastward direction is positive).

heat the subsurface seawater (Emanuel, 2001). Combined with the negative wind stress curl input by TS Dujuan on the left side of its track, the warm water in the upper ocean is transported to the equator and further propagates eastward. Our results demonstrate that the transient wind forcing of TS Dujuan can redistribute the zonal heat and current of the upper ocean in the equatorial Pacific through the equatorial Kelvin waves. The outcomes of our model bear a striking resemblance to those derived from prior research (Sriver et al., 2013). However, a noteworthy deviation from other studies is observed in that the positive discrepancy rapidly descends to 30-53% of its peak. Additionally, the difference in the upper ocean temperature fails to extend to the eastern boundary of the equatorial Pacific. Also, the signal of SSH difference is significantly smaller than the SLA signal. Therefore, we infer that the forcing effect of TS Dujuan on the equatorial Kelvin wave is an amplification. In conclusion, the enhanced equatorial Kelvin wave propagates to the eastern Pacific, deepening the thermocline and inducing warm temperature anomalies, thus reducing the zonal

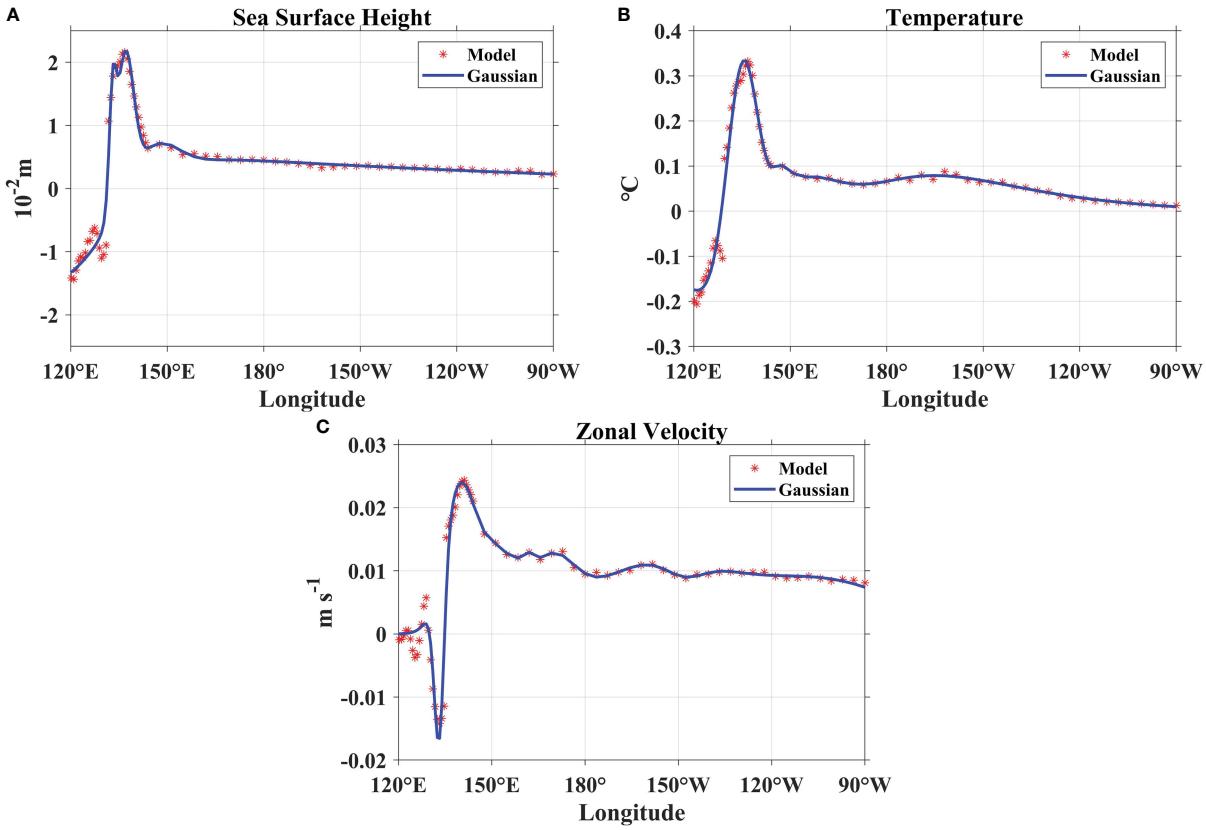

FIGURE 13
The differences of **(A)** sea surface height, **(B)** 100-200 m upper ocean temperature, **(C)** 100-200 m upper ocean zonal velocity. The solid line is obtained from the model data by Gaussian fitting. The data is selected along the yellow arrow in Figures 11C, G, I.

thermal gradient of the equatorial Pacific during the La Niña phase and to a small extent accelerating the transition from the cold phase of ENSO to a neutral state in May 2021.

As the global warming, more strong tropical cyclones can be generated in the near-equatorial Pacific. It is estimated that before 2100 the continuous SST rise in the low-latitude area of the northwest Pacific will increase the intensity of tropical cyclones by ~14% (Emanuel, 2005; Webster et al., 2005; Mei et al., 2015). Further understanding of the forcing effects of near-equatorial TCs on equatorial Kelvin waves would help improving the predictions of ENSO events. Different from the previous researches that focused on asymmetric multi-TC forcing and symmetric twin-TC forcing (Keen, 1982; McPhaden et al., 1988; Nitta, 1989; Sriver et al., 2013), our study for the first time concentrated on the effect of a single TS. Based on the simulated results, we validly confirm the amplification effect of an individual TS on equatorial Kelvin waves from the perspectives of SSH, temperature, and zonal current. Owing to the limit of the TS wind stress intensity, the forcing effect is not very great. However, it can still be used as a reference for the study of the cross-scale influence of TCs on ENSO events. In addition, this study only investigated the forcing effect of the atmosphere on the ocean, without the coupling interactions between the ocean and the atmosphere (Boucharel et al., 2016). The impacts of ocean variability on the generation and development of TS Dujuan have not been considered.

Data availability statement

The raw data supporting the conclusions of this article will be made available by the authors, without undue reservation.

Author contributions

ZD conceived and designed the study. YC conducted the numerical experiments and wrote the original draft. TY carried out the data analysis and language review. All authors contributed to the manuscript and agreed to the submitted version of the manuscript.

Funding

This work was supported by the National Natural Science Foundation of China (No. 42176020), the National Key Research and Development Program (2022YFC3105002), and the CAE Advisory Project (2022-XBZD-11).

Acknowledgments

We thank Prof. Xuefeng Zhang for providing the recursive filter code and for his helpful suggestions. We also appreciate NCEP, NOAA, CMEMS, and CMA for providing the observational and reanalysis data.

Conflict of interest

The authors declare that the research was conducted in the absence of any commercial or financial relationships that could be construed as a potential conflict of interest.

Publisher's note

All claims expressed in this article are solely those of the authors and do not necessarily represent those of their affiliated organizations, or those of the publisher, the editors and the reviewers. Any product that may be evaluated in this article, or claim that may be made by its manufacturer, is not guaranteed or endorsed by the publisher.

Supplementary material

The Supplementary Material for this article can be found online at: https://www.frontiersin.org/articles/10.3389/fmars.2023.1173163/full#supplementary-material

References

Boucharel, J., Jin, F. F., England, M. H., Dewitte, B., Lin, I. I., Huang, H. C., et al. (2016). Influence of oceanic intraseasonal kelvin waves on eastern pacific hurricane activity. *J. Clim.* 29 (22), 7941–7955. doi: 10.1175/JCLI-D-16-0112.1

Boulanger, J. P., and Menkes, C. (1995). Propagation and reflection of long equatorial waves in the pacific ocean during the 1992–1993 El nino. *J. Geophys. Res. Oceans.* 100, 25041–25059. doi: 10.1029/95JC02956

Chan, J. C. (2005). Interannual and interdecadal variations of tropical cyclone activity over the western north pacific. *Meteor. Atmos. Phys.* 89, 143–152. doi: 10.1007/s00703-005-0126-y

Chang, Y. C., Chu, P. C., Centurioni, L. R., and Tseng, R. S. (2014). Observed near-surface currents under four super typhoons. *J. Mar. Syst.* 139, 311–319. doi: 10.1016/j.jmarsys.2014.07.011

Chao, J., and Xu, X. (2001). The dynamic theory of shelf waves and its effect in the propagation of El niño signal. *Acta Meteor. Sin.* 59 (5), 515–523. doi: 10.3321/j.issn:0577-6619.2001.05.002

Chen, D., and Lian, T. (2020). Frontier of El Niño-Southern Oscillation research. *Chin. Sci. Bull.* 65 (35), 4001–4003. doi: 10.1360/TB-2020-1219

Chen, X., and Gao, S. (1994). The typhoon activity in the north-west pacific in el nino year. *Marin. Forec.* 11, 47–54. doi: 10.11737/j.issn.1003-0239.1994.03.009

Delcroix, T., Picaut, J., and Eldin, G. (1991). Equatorial kelvin and rossby waves evidenced in the pacific ocean through geosat sea level and surface current anomalies. *J. Geophys. Res. Oceans.* 96, 3249–3262. doi: 10.1029/90JC01758

Elipot, S., Lumpkin, R., and Prieto, G. (2010). Modification of inertial oscillations by the mesoscale eddy field. *J. Geophys. Res. Oceans.* 115 (C9), C09010. doi: 10.1029/2009JC005679

Emanuel, K. A. (2001). Contribution of tropical cyclones to meridional heat transport by the oceans. *J. Geophys. Res.* 106, 14771–14781. doi: 10.1029/2000JD900641

Emanuel, K. A. (2005). Increasing destructiveness of tropical cyclones over the past 30 years. *Nature* 436 (7051), 686–688. doi: 10.1038/nature03906

Fedorov, A. V., Brierley, C. M., and Emanuel, K. (2010). Tropical cyclones and permanent El niño in the early pliocene epoch. *Nature* 463, 1066–1070. doi: 10.1038/nature08831

Firing, E., Lukas, R., Sadler, J., and Wyrtki, K. (1983). Equatorial undercurrent disappears during 1982-1983 El niño. *Sci* 222, 1121–1123. doi: 10.1126/science.222.4628.1121

Furuichi, N., Hibiya, T., and Niwa, Y. (2008). Model-predicted distribution of wind-induced internal wave energy in the world's oceans. *J. Geophys. Res. Oceans.* 113, C09034. doi: 10.1029/2008JC004768

Gao, S., Wang, J., and Ding, Y. (1988). The triggering effect of near-equatorial cyclones on El niño. *Adv. Atmos. Sci.* 5 (1), 87–95. doi: 10.1007/BF02657349

Gierach, M. M., and Subrahmanyam, B. (2008). Biophysical responses of the upper ocean to major gulf of Mexico hurricanes in 2005. *J. Geophys. Res. Oceans.* 113, C04029. doi: 10.1029/2007JC004419

Greatbatch, R. J. (1984). On the response of the ocean to a moving storm: parameters and scales. *J. Phys. Oceanogr.* 14, 59–78. doi: 10.1175/1520-0485(1984)014<0059:OTROTO>2.0.CO;2

Hsieh, W. W., Davey, M. K., and Wajsowicz, R. C. (1983). The free kelvin wave in finite-difference numerical models. *J. Phys. Oceanogr.* 13, 1383–1397. doi: 10.1175/1520-0485(1983)013<1383:TFKWIF>2.0.CO;2

Hung, C. C., Chung, C. C., Gong, G. C., Jan, S., Tsai, Y., Chen, K. S., et al. (2013). Nutrient supply in the southern East China Sea after typhoon morakot. *J. Mar. Res.* 71, 133–149. doi: 10.1357/002224013807343425

Keen, R. A. (1982). The role of cross-equatorial tropical cyclone pairs in the southern oscillation. *Mon. Wea. Rev.* 110, 1405–1416. doi: 10.1175/1520-0493(1982)110<1405:TROCET>2.0.CO;2

Large, W. G., McWilliams, J. C., and Doney., S. C. (1994). Oceanic vertical mixing: review and a model with a nonlocal boundary layer parameterization. *Rev. Geophys.* 32, 363–403. doi: 10.1029/94RG01872

Large, W. G., and Pond, S. (1981). Open ocean momentum flux measurements in moderate to strong winds. *J. Phys. Oceanogr.* 11, 324–336. doi: 10.1175/1520-0485(1981)011<0324:OOMFMI>2.0.CO;2

Lian, T., Ying, J., Ren, H. L., Zhang, C., Liu, T., and Tan, X. X. (2019). Effects of tropical cyclones on ENSO. *J. Climate.* 32, 6423–6443. doi: 10.1175/JCLI-D-18-0821.1

McPhaden, M. J. (1999). Genesis and evolution of the 1997-98 El niño. *Sci* 283 (5404), 950–954. doi: 10.1126/science.283.5404.950

McPhaden, M. J., Ando, K., Bourles, B., Freitag, H. P., Lumpkin, R., Masumoto, Y., et al. (2010). The global tropical moored buoy array. *Proc. OceanObs.* 9, 668–682. doi: 10.5270/OceanObs09.cwp.61

McPhaden, M. J., Freitag, H. P., Hayes, S. P., Taft, B. A., Chen, Z., and Wyrtki, K. (1988). The response of the equatorial pacific ocean to a westerly wind burst in may 1986. *J. Geophys. Res. Oceans.* 93, 10589–10603. doi: 10.1029/JC093iC09p10589

Mei, W., Xie, S. P., Primeau, F., McWilliams, J. C., and Pasquero, C. (2015). Northwestern pacific typhoon intensity controlled by changes in ocean temperatures. *Sci. Adv.* 1 (4), e1500014. doi: 10.1126/sciadv.1500014

Monaldo, F. M., Sikora, T. D., Babin, S. M., and Sterner, R. E. (1997). Satellite imagery of sea surface temperature cooling in the wake of hurricane Edouard(1996). *Mon. Wea. Rev.* 125, 2716–2721. doi: 10.1175/1520-0493(1997)125<2716:SIOSST>2.0.CO;2

Nitta, T. (1989). Development of a twin cyclone and westerly bursts during the initial phase of the 1986-87 El niño. *J. Meteor. Soc Jpn. Ser. II.* 67, 677–681. doi: 10.2151/jmsj1965.67.4_677

Philander, S. G. H. (1990). *El Niño, la niña, and the southern oscillation* (San Diego: Academic Press), 1–299.

Pujol, M. I., Faugère, Y., Taburet, G., Dupuy, S., Pelloquin, C., Ablain, M., et al. (2016). DUACS DT2014: the new multi-mission altimeter data set reprocessed over 20 years. *Ocean. Sci.* 12, (5), 1–48. doi: 10.5194/os-12-1067-2016

Quanan, Z., Jiayi, P. A. N., and Timothy, L. W. (2006). Observation of ocean current response to 1998 hurricane georges in the gulf of Mexico. *Acta Oceanol. Sin.* 25, 1–14. doi: 10.1016/S0090-6980(01)00146-0

Rebert, J. P., Donguy, J. R., Eldin, G., and Wyrtki, K. (1985). Relations between sea level, thermocline depth, heat content, and dynamic height in the tropical pacific ocean. *J. Geophys. Res. Oceans.* 90, 11719–11725. doi: 10.1029/JC090iC06p11719

Shinoda, T., Roundy, P. E., and Kiladis, G. N. (2008). Variability of intraseasonal kelvin waves in the equatorial pacific ocean. *J. Phys. Oceanogr.* 38, 921–944. doi: 10.1175/2007JPO3815.1

Sommer, J. L., and Zeitlin, V. (2005). Tracer transport during the geostrophic adjustment in the equatorial ocean, in Chaotic Dynamics and Transport in Classical and Quantum Systems. *NATO Advanced Study Institute on International, School on Chaotic Dynamics and Transport in Classical and Quantum Systems*, 413–429. doi: 10.1007/1-4020-2947-0_19

Sriver, R. L., and Huber, M. (2010). Modeled sensitivity of upper thermocline properties to tropical cyclone winds and possible feedbacks on the Hadley circulation. *Geophys. Res. Lett.* 37 (8), L08704. doi: 10.1029/2010GL042836

Sriver, R. L., Huber, M., and Chafik, L. (2013). Excitation of equatorial kelvin and yanai waves by tropical cyclones in an ocean general circulation model. *Earth. Syst. Dynam.* 4, 1–10. doi: 10.5194/esd-4-1-2013

Sriver, R. L., Huber, M., and Nusbaumer, J. (2008). Investigating tropical cyclone-climate feedbacks using the TRMM microwave imager and the quick scatterometer. *Geochem. Geophy. Geosy.* 9, Q09V11. doi: 10.1029/2007GC001842

Sun, L., Li, Y. X., Yang, Y. J., Wu, Q., Chen, X. T., Li, Q. Y., et al. (2014). Effects of super typhoons on cyclonic ocean eddies in the western north pacific: a satellite data-based evaluation between 2000 and 2008. *J. Geophys. Res. Oceans.* 119, 5585–5598. doi: 10.1002/2013JC009575

Tong, B., Wang, X., Wang, D., and Zhou, W. (2023). A novel mechanism for extreme El niño events: interactions between tropical cyclones in the Western north pacific and Sea surface warming in the Eastern tropical pacific. *J. Clim.* 36 (8), 2585–2601. doi: 10.1175/JCLI-D-21-1014.1

Wang, B., and Chan, J. C. (2002). How strong ENSO events affect tropical storm activity over the western north pacific. *J. Climate* 15, 1643–1658. doi: 10.1175/1520-0442(2002)015<1643:HSEEAT>2.0.CO;2

Wang, Q., Li, J., Jin, F. F., Chan, J. C., Wang, C., Ding, R., et al. (2019). Tropical cyclones act to intensify El niño. *Nat. Commun.* 10, 1–13. doi: 10.1038/s41467-019-11720-w

Wang, X., Wang, C., Han, G., Li, W., and Wu, X. (2014). Effects of tropical cyclones on large-scale circulation and ocean heat transport in the south China Sea. *Clim. Dyn.* 43, 3351–3366. doi: 10.1007/s00382-014-2109-5

Webster, P. J., Holland, G. J., Curry, J. A., and Chang, H. R. (2005). Changes in tropical cyclone number, duration, and intensity in a warming environment. *Sci* 309 (5742), 1844–1846. doi: 10.1126/science.1116448

Willoughby, H. E., and Rahn, M. E. (2004). Parametric representation of the primary hurricane vortex. part I: observations and evaluation of the Holland, (1980) model. *Monthly. Weather. Rev.* 132 (12), 3033–3048. doi: 10.1175/MWR2831.1

Wyrtki, K. (1985). Water displacements in the pacific and the genesis of El niño cycles. *J. Geophys. Res. Oceans.* 90, 7129–7132. doi: 10.1029/JC090iC04p07129

Xie, Y., Koch, S., McGinley, J., Albers, S., Bieringer, P. E., Wolfson, M., et al. (2011). A space-time multiscale analysis system: a sequential variational analysis approach. *Mon. Wea. Rev.* 139, 1224–1240. doi: 10.1175/2010MWR3338.1

Xie, Y., Koch, S. E., McGinley, J. A., Albers, S., and Wang, N. (2005). "July: A sequential variational analysis approach for mesoscale data assimilation. in preprints, 21st conf. on weather analysis and Forecasting/17th conf," in *Numerical weather prediction*, vol. 15. (Washington, DC, Amer: Meteor. Soc. B).

Yuan, D., and Han, W. (2006). Roles of equatorial waves and western boundary reflection in the seasonal circulation of the equatorial Indian ocean. *J. Phys. Oceanogr.* 36 (5), 930–944. doi: 10.1175/JPO2905.1

Zebiak, S. E., and Cane, M. A. (1987). A model El nino-southern oscillation. *Mon. Wea. Rev.* 115, 2262–2278. doi: 10.1175/1520-0493(1987)115<2262:AMENO>2.0.CO;2

frontiers | Frontiers in Marine Science

TYPE Original Research
PUBLISHED 20 July 2023
DOI 10.3389/fmars.2023.1213470

OPEN ACCESS

EDITED BY
Shi-Di Huang,
Southern University of Science and Technology, China

REVIEWED BY
Gao Xiaoqian,
Shandong University of Science and Technology, China
Junhong Liang,
Louisiana State University, United States
Daniela Di Iorio,
University of Georgia, United States

*CORRESPONDENCE
Guangyu Xu
guangyux@uw.edu

RECEIVED 28 April 2023
ACCEPTED 30 June 2023
PUBLISHED 20 July 2023

CITATION
Xu G and German CR (2023) Dispersion of deep-sea hydrothermal plumes at the Endeavour Segment of the Juan de Fuca Ridge: a multiscale numerical study. *Front. Mar. Sci.* 10:1213470. doi: 10.3389/fmars.2023.1213470

Dispersion of deep-sea hydrothermal plumes at the Endeavour Segment of the Juan de Fuca Ridge: a multiscale numerical study

Guangyu Xu[1]* and Christopher R. German[2]

[1]Applied Physics Laboratory, University of Washington, Seattle, WA, United States, [2]Geology & Geophysics, Woods Hole Oceanographic Institution, Woods Hole, MA, United States

A multiscale numerical framework has been developed to investigate the dispersion of deep-sea hydrothermal plumes that originate from the Endeavour Segment of the Juan de Fuca Ridge located in the Northeast Pacific. The analysis of simulation outputs presented in this study provides insights into the influences of tidal forcing and the buoyancy flux associated with hydrothermal venting on ocean circulation and plume dispersion in the presence of pronounced seafloor topography. The results indicate that tidal forcing drives anti-cyclonic circulation near the ridge-axis, while hydrothermal venting induces cyclonic circulation around vent fields within the axial rift valley. Tidal forcing has a notable impact on plume dispersion, particularly near the large topographic features to the north of the Endeavour Segment. Furthermore, plume dispersion exhibits notable inter-annual variability, with a northbound trajectory in 2016 and a southbound trajectory in 2021. The study also reveals that both buoyancy fluxes and tidal forcing enhance the mixing of hydrothermal plumes with ambient seawater.

KEYWORDS

numerical model, hydrothermal vent, plume dispersion, tidal forcing, buoyancy, mixing

1 Introduction

Hydrothermal discharge from volcanically hosted submarine vents plays a crucial role in the transfer of heat from the Earth's interior and the release of essential chemicals that impact ocean and atmospheric biogeochemistry (German and Seyfried, 2014). These vents are also home to unique ecosystems that are fuelled mainly by geothermal and geochemical energy, decoupled from the photosynthesis that sustains the majority of life on the planet. Because of their remote locations, however, such vents remain chronically under-investigated and new and profound discoveries about their significance on a global scale continue apace. Only in the past decade, for example, has sustained exploration revealed the

significance of hydrothermal vents as sources of iron (Fe) that can stimulate primary productivity and draw-down of CO_2 from the atmosphere (Resing et al., 2015; Jenkins et al., 2020). These recent discoveries – that hydrothermal plumes enriched in Fe and Mn can persist for thousands of kilometres away from ridge-axis sources (Gartman and Findlay, 2020) – challenge the long-standing view that these trace metals are mostly removed from hydrothermal solution through oxidation near their vent sources (German et al., 1991; Field and Sherrell, 2000). Despite ongoing deep-sea explorations, our understanding of the dispersion of hydrothermal materials from their sources into the ocean remains limited. This is largely due to the difficulty in directly observing the dispersion and evolution of hydrothermal plumes with sufficient spatial coverage and resolution.

The physical structure of a deep-sea hydrothermal plume can be divided into two parts: the buoyant stem and the non-buoyant cap (Lupton, 1995). The former refers to the portion of the plume that has positive buoyancy compared to ambient seawater. This buoyant stem of the plume originates from the source vent and expands outward, akin to an inverted cone, as it rises. On the other hand, the plume's non-buoyant cap is in density equilibrium with the surrounding water column; therefore, instead of continuing to rise, the non-buoyant hydrothermal fluid spreads laterally along isopycnic surface and can travel far from the source vent while maintaining distinct geochemical signatures. The dynamics and transition between the buoyant stem and non-buoyant cap occur over a broad range of spatial and temporal scales. For example, turbulence within the buoyant stem can range from a few centimetres close to the vent orifice to tens of meters when the rising fluid reaches density equilibrium with the surrounding water column, hundreds of meters above the seafloor (e.g., Speer and Marshall, 1995). This process of fluid ascent in the buoyant stem typically takes no longer than 1 hour regardless of ocean stratification (Lupton, 1995). In contrast, the dispersion of the non-buoyant cap, which begins at its juncture with the buoyant stem and continues until its geochemical signature is indistinguishable from the ambient seawater, occurs on much larger spatial scales (e.g., thousands of kilometres) and over extended periods of time (e.g., years to decades). Additionally, the flow within the buoyant stem of a hydrothermal plume is primarily determined by the source heat flux and the ambient stratification. In comparison, the dynamics inside the non-buoyant cap are dominated by the ambient ocean circulation. A comprehensive investigation of these multi-scale, multi-disciplinary processes with direct field measurements is technically challenging and requires a combination of ship- and AUV-based surveys. Within the on-going US GEOTRACES program, ship-based surveys have been used to investigate the geochemical impacts of hydrothermal venting through the study of hydrothermal plumes' dispersing non-buoyant caps at length scales of 100 km to 1000 km away from source vents (Resing et al., 2015; Jenkins et al., 2020). By contrast, AUV-based surveys offer the opportunity to study plume dispersion over 1 to 10 to 100km length scales (German et al., 2008; German et al., 2010). Even so, the implementation time for a coordinated AUV-based survey strategy may be long compared to the timescales of variability in plume dispersion close to a vent-source.

Consequently, achieving the spatial resolution required to reveal the complex (physical and biogeochemical) structures of such plumes remains challenging.

Numerical modelling has proven to be a valuable tool for investigating the physical evolution of hydrothermal discharge and the dispersal of vent larvae and chemicals near ocean ridges. Previous studies, such as those by Thomson et al. (2005); Thomson et al. (2009); Lavelle et al. (2010); Lavelle et al. (2013); Xu et al. (2018), and Vic et al. (2018), have demonstrated the effectiveness of numerical models in providing synoptic realizations of the dispersion of hydrothermally sourced materials in dynamic ocean-ridge environments. One notable example is the numerical study of the dispersal of hydrothermal Fe from the Mid-Atlantic Ridge (MAR) (Tagliabue et al., 2022). That study highlights the importance of incorporating sufficient spatial resolution to accurately represent dispersal processes over pronounced and variable ridge topography. Here, we investigate the dispersion of hydrothermal plumes from active vent sites on the Endeavour Segment of the Juan de Fuca Ridge (JDFR) through three-dimensional (3-D), multi-scale hydrodynamical simulations. In Section 2, we provide an overview of previous observations and modelling efforts related to ocean circulation and hydrothermal discharge at the Endeavour Segment. Section 3 details the configuration of our multi-scale modelling framework, and in Section 4 we present validation of our modelling approach in the form of a comparison with concurrent measurements of near-bottom flow velocity and observations from previous ship-based plume surveys. In Section 5, we describe the main simulation results and discuss the impact of various ocean processes on plume dispersion. Finally, we summarize our findings in Section 6.

2 Endeavour Segment, Juan de Fuca Ridge: hydrothermal vents, hydrography, and circulation

The Endeavour Segment of the Juan de Fuca Ridge (JDFR) is an intermediate rate spreading center located approximately 300 km offshore of British Columbia, Canada and Washington State, USA. The central portion of the 90 km long segment is a volcanic high dissected by a rift valley that is 100 – 200 m deep and 1 – 2 km wide. The axis of the valley is oriented along a heading of 020°T (relative to True North). Within the rift valley, there are at least five major hydrothermal vent fields, situated along the ridge axis, as well as multiple low-temperature discharge (i.e., diffuse flow) sites. The five major vent fields are: Mothra, Main Endeavour Field (MEF), High Rise (HR), Salty Dawg, and Sasquatch, listed from south to north (Figure 1). According to Kellogg and McDuff (2010), who conducted systematic hydrographic surveys using an AUV, the total hydrothermal heat flux from the axial valley is up to 900 MW, which makes Endeavour one of the most active second-order ridge segments known, worldwide (Kelley et al., 2012). The relative heat contributions from the five major hydrothermal fields are: Mothra (15%), MEF (34%), HR (43%), Salty Dawg (8%), and Sasquatch

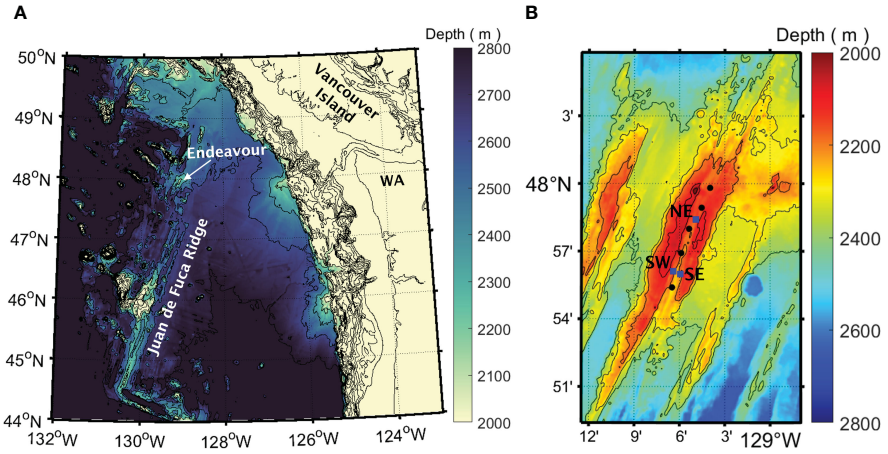

FIGURE 1
(A) Bathymetric maps of the JDFR in the Northeast Pacific, offshore Vancouver Island and Washington State (WA). The Endeavour Segment is located at the northern end of the ridge. **(B)** An expanded view of the Endeavour Segment, showing the rift valley that divides the central portion of the segment and the locations of the five major hydrothermal vent fields (black dots). From south to north, these vent fields are Mothra, MEF, HR, Salty Dawg, and Sasquatch. Three cabled current-meter moorings (RCM-NE, RCM-SW, RCM-SE) are denoted by blue squares and labeled NE, SW, and SE, respectively. Bathymetric data are from the Global Multi-Resolution Topography (GMRT) Synthesis of the Marine Geoscience Data System (Ryan et al., 2009).

(<1%) (Kellogg, 2011). Seismic imaging has revealed magma bodies under all five major hydrothermal fields, suggesting that the vigorous venting at Endeavour is primarily driven by the heat output from the underlying magma chamber (Van Ark et al., 2007; Carbotte et al., 2012).

Observations from ship-based water-column surveys have revealed the presence of a non-buoyant plume cap at ~2000-2100 m depth, i.e., approximately 100 – 200 m above the source vent fields on the Endeavour Segment. This non-buoyant plume cap disperses along the 27.7 kg/m^3 potential density anomaly (σ_θ) surface, and its thermal and particulate signatures have been traced for more than 15 km away from the ridge-crest vents, downstream along the prevailing southwest current flow direction (Baker and Massoth, 1987; Thomson et al., 1992). Previous studies reported a southwestward mean flow along the ridge axis immediately above the axial valley (Baker and Massoth, 1987; Thomson et al., 2003). Current-meter moorings deployed along the Endeavour Segment, however, have recorded a more complex, time-varying pattern of circulation close to the ridge axis, characterized by distinct vertical and horizontal structures generated from interactions between large-scale abyssal flow, oscillatory currents, and the topography of the ridge axis (Thomson et al., 2003). Circulation within the axial valley is further influenced by dynamics driven by the buoyancy fluxes associated with hydrothermal venting. Close to the valley floor, the flow is directed into the valley from its northern and southern ends. The strength of this inflow is skewed towards the south, resulting in persistent northward flow from the southern end well past the middle of the valley (Thomson et al., 2003). Hydrothermal venting is thought to be the mechanism that draws flow into the valley through turbulent entrainment into rising buoyant plumes (Thomson et al., 2003). This hypothesis is supported by the findings of numerical simulations (Thomson et al., 2005; Thomson et al., 2009). Superimposed on this mean circulation pattern are oscillatory currents at a range of frequencies, including the semidiurnal (~12 hr), diurnal (~24 hr), near-inertial (~16 hr), and a low-frequency 'weather' band with a broad spectral peak around 4 to 6-day periods (e.g., Cannon and Thomson, 1996; Thomson et al., 2003). These currents are amplified near the ridge crest but damped within the axial valley; their orientations also vary markedly from above the ridge crest down to the valley floor (e.g., Allen and Thomson, 1993; Mihaly et al., 1998; Lavelle and Cannon, 2001; Thomson et al., 2003; Berdeal et al., 2006).

3 Materials and methods

3.1 Model domain and bathymetry

The multi-scale modelling framework developed for this study utilizes a nested construct of the Regional Ocean Modelling System (ROMS). ROMS is a free-surface, terrain-following primitive equation model widely used to study ocean dynamics in diverse environments, from the sea surface to deep ocean ridges (e.g., Shchepetkin and McWilliams, 2005; Warner et al., 2010; Vic et al., 2018). ROMS implements efficient nesting schemes to transfer data between different grids in a multi-resolution simulation. The nesting can either be one-way, where a coarse grid provides the lateral boundary conditions for the embedded finer grid(s), or two-way, where the fine grid(s) also provide(s) feedback to update the coarse-grid solutions. For this study, we adopt two-way nesting to ensure a smooth transition of model fields and energy cascades between nested grids.

The multi-resolution domain of our modelling framework (Figure 2) consists of two layers of nested grids having spatial resolutions that increase from 360 m (fine) in the outer layer (Figure 2B) to 72 m (ultra-fine) in the inner layer (Figure 2C).

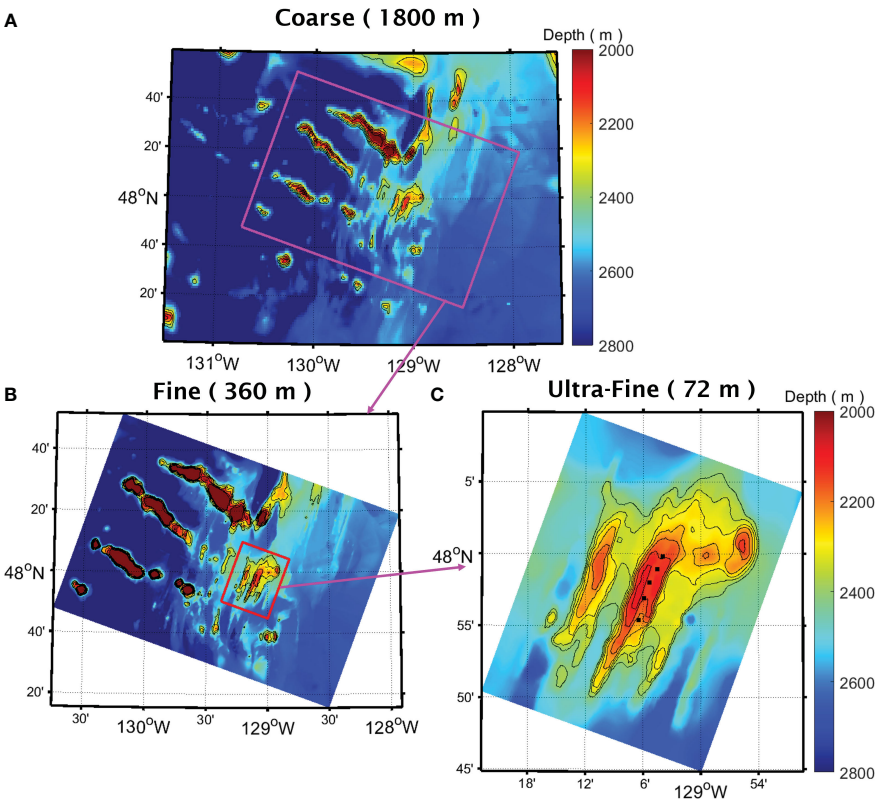

FIGURE 2
(A) Bathymetry within the coarse domain of the intermediate simulation. The box outlines the lateral boundaries of the fine domain of the nested multiscale simulations. **(B)** Bathymetry within the fine domain. The box outlines the nesting interface between the fine and ultra-fine grids. **(C)** Bathymetry within the ultra-fine domain. The black dots mark the locations of the five major hydrothermal vent fields within the axial valley of the Endeavour Segment.

Both grids are rotated to align with the ridge axis (20° from true north). The computational cells in each grid are uniform in the horizontal direction and each grid consists of 32 vertically stretched layers designed to enhance the resolution near the ocean surface and the seafloor, yielding a vertical resolution of approximately 15 m at the crest of the Endeavour Segment. The dynamics within the model domain are driven at the lateral boundaries of the fine grid and at the surface of both grids. The model relies upon lateral boundary conditions that are derived from the daily averaged output from a stand-alone pilot simulation, which covers a larger domain (Figure 2A) and has a lower horizontal resolution of approximately 1800 m (coarse). The lateral boundary forcing for the pilot simulation is constructed from the daily averaged product of the Copernicus Marine Environment Monitoring Service (CMEMS) global ocean eddy-resolving (1/12°) reanalysis (Fernandez and Lellouche, 2021). The surface forcing used in the pilot simulation is derived from the 3-hourly winds, atmospheric pressure, and fluxes from the fifth generation European Centre for Medium-Range Weather Forecasts atmospheric reanalysis of the global climate (ERA5, Copernicus Climate Change Service (C3S), 2017).

The pilot simulation serves as a transition between the global reanalysis and our regional simulations, maintaining a grid refinement factor (i.e., the ratio of spatial resolutions between two consecutive grids) of approximately five. To account for tidal forcing, which is absent in the global reanalysis and the pilot simulation, we have added tidal elevation and barotropic currents acquired from the TPXO global tidal solution (Egbert and Erofeeva, 2002) to the lateral boundary forcing for the fine domain. We derive the surface forcings for both fine and ultra-fine domains from the same ERA5 3-hourly dataset used in the pilot simulation. The initial model fields used for the pilot simulation are constructed from the CMEMS global reanalysis data. The initial fields for the nested simulations are interpolated from the pilot simulation output onto the fine and ultra-fine grids. The computational time increments are 150 sec, 30 sec, and 6 sec on the coarse (pilot), fine, and ultra-fine grids, respectively.

The seafloor topography in our model is constructed from the Global Multi-Resolution Topography (GMRT) Synthesis of the Marine Geoscience Data System (Ryan et al., 2009). The original GMRT bathymetry has a spatial resolution of 250 m. Before interpolating on our model grids, we first apply a spatial median filter to smooth out features with length scales smaller than twice the size of a computational cell (i.e., the smallest resolvable wavelength). To further enhance numerical stability, we then apply the smoothing techniques described in Sikirić et al. (2009)

to reduce the maximum stiffness ratio (Shchepetkin and McWilliams, 2005).

3.2 Hydrothermal venting and model parameters

The model incorporates the buoyancy generated by hydrothermal venting as bottom heat flux originating from the five major vent fields located within the axial valley. Specifically, each of the vent fields is represented as a 216 m by 216 m (3 by 3 cells) heat source in the ultra-fine domain. The corresponding heat flux is obtained from ship-based hydrographic surveys conducted in September 2004 (Kellogg and McDuff, 2010; Kellogg, 2011) and are prescribed as follows: 135 MW for Mothra, 306 MW for MEF, 387 MW for HR, 67.5 MW for Salty Dawg, and 4.5 MW for Sasquatch. In the model, the sources are treated as having no explicit volume flux. Consequently, the hydrothermal discharge is represented as thermally driven plumes. This simplified treatment of the plume sources is reasonable, considering that hydrothermal plumes are typically characterized as 'lazy' plumes (Hunt and Kaye, 2005). In such cases, the volume flux of the source has negligible influence on the plume's behaviour and dynamics downstream. The vertical eddy viscosity and diffusivity in the model are determined using the Mellor-Yamada 2.5 level turbulent closure scheme (Mellor and Yamada, 1982), which has been shown in previous studies to enable simulation of vertical motions of plume fluid and the associated entrainment of ambient seawater into the plume, despite the use of the hydrostatic approximation (Thomson et al., 2005; Thomson et al., 2009).

3.3 Simulation timeframe and settings

In this study, we have conducted simulations covering two calendar-year periods: 2016 and 2021. We selected these years primarily due to the availability of concurrent observational data, which can be used for model validation. Those observations include the time series of flow velocity measured by current meters on cabled moorings deployed within the axial valley of Endeavour as part of the NEPTUNE seafloor observatory infrastructure by Ocean Networks Canada (Kelley et al., 2012) (Figure 1B). Additionally, comparing the model outputs between these two one-year periods enables us to investigate the interannual variability in ocean circulation and plume dispersion near the ridge segment.

To investigate how ocean tides and buoyancy from seafloor venting impact plume dispersion and ocean circulation near the ridge segment, we have conducted three runs for the 2016 simulation. The primary simulation output for model validation and interpretation was obtained from the first run, referred to as 'baseline' hereafter, which utilized the full set of forcings described in Sections 3.1 and 3.2. The remaining two runs employed a similar model configuration, but with a reduced set of forcings. Specifically, the second run, referred to as 'no tide' hereafter, included buoyancy from venting but not ocean tides, while the third run, referred to as 'no vent', included ocean tides but not buoyancy from venting. Additionally, we have conducted one run of the 2021 simulation using the full set of forcings (2021 baseline).

4 Model-observation comparison

4.1 Flow velocity time series

Our evaluation of the accuracy of simulated flow velocities utilizes concurrent, collocated comparisons with measurements obtained from the three current-meter moorings (RCM-NE, RCM-SE, RCM-SW) deployed within the axial valley of the Endeavour Segment (Figure 1B). Specifically, we utilized the current-meter time series from all three moorings to assess model skill during the 2016 simulation period. On the other hand, for the 2021 simulation period, we only used data from the two southern moorings (RCM-SW and RCM-SE) since no data was available from RCM-NE for most of the simulation period. We quantify the statistical agreement between the model and the observations using the Willmott Skill Score (*WSS*), which measures the normalized mean squared error in the forms of

$$WSS_U = 1 - \frac{|U_m - U_d|^2}{(|U_m - U_m| + |U_d - U_d|)^2} \quad (1)$$

and

$$WSS_V = 1 - \frac{|V_m - V_d|^2}{(|V_m - V_m| + |V_d - V_d|)^2} \quad (2)$$

for the zonal (U) and meridional (V) flow velocities, respectively. In equations (1) and (2), the subscript 'm' denotes model output, while 'd' indicates observed data. The angled brackets (e.g., $|U_m - U_d|^2$) represent time averaging of the quantity enclosed within the brackets. The score is a measure of the similarity between the model output and the observed data. The score ranges from 0 to 1, with higher values indicating better model performance (Willmott, 1981). The *WSS* listed in Table 1 suggest that the model performs better at simulating the meridional velocity (V) than the zonal velocity (U).

A one-to-one comparison between the simulated flow velocities and measurements for all three moorings demonstrates an encouraging level of agreement. Considering flow at RCM-SW in 2021 for illustration (Figure 3), the observed currents predominantly flow in directions that are roughly aligned with the orientation of the ridge-axis at RCM-SW. This alignment is likely caused by the steering of flow within the topographic confinement of the axial rift valley. At a depth of 2162 m, just 1 m above the seafloor (Figure 3G), the direction of the observed currents oscillated between south-southwest (SSW) and north-northeast (NNE). This included an episode of intensified southwestward flow around Oct 27th, 2021. During that episode, the magnitude of the 2-day averaged flow velocity reached a maximum of 7.4 cm/s, compared with a median magnitude of 0.8 cm/s over the measurement period. At a shallower level, at 2117 m depth (Figure 3E), the direction of the observed currents was primarily SSW and only occasionally switched to north-northwest

TABLE 1 Willmott Skill Scores (WSS) calculated from the measured and simulated flow velocity during July – Oct 2016 and Jul – Dec 2021.

Mooring (2016)	Depth (m)	Altitude (m)	WSS_U	WSS_V
RCM-NE	1956	200	0.49	0.76
RCM-NE	2030	125	0.54	0.69
RCM-NE	2106	50	0.52	0.71
RCM-SW	2049	125	0.49	0.67
RCM-SW	2123	50	0.54	0.79
RCM-SE	2027	200	0.43	0.71
RCM-SE	2100	125	0.47	0.71
RCM-SE	2175	50	0.39	0.72
Mean			0.48	0.72
Mooring (2021)	Depth (m)	Altitude (m)	WSS_U	WSS_V
RCM-SW	1967	200	0.55	0.72
RCM-SW	2042	125	0.51	0.69
RCM-SW	2117	50	0.51	0.71
RCM-SW	2162	5	0.50	0.66
RCM-SE	2093	125	0.51	0.71
RCM-SE	2167	50	0.47	0.73
Mean			0.51	0.70

(NNW). Higher in the water column, at 2042 m and 1967 m depths which are shallower than the confining depths of the axial rift valley (Figure 3A, C), the westward component of the observed flow velocity was more prominent and the predominant flow direction was rotated toward the west-southwest (WSW), likely indicating a weakening of topographic steering effects at these higher altitudes. Encouragingly, the magnitude and direction of the simulated velocities (Figure 3B, D, F, H) are largely consistent with the observations at all depths at RCM-SW. There are two notable exceptions to this general case, 1) at 2042 m depth, the change of flow direction from SW to NW that occurred around Oct 16, 2021 is much less pronounced in the model velocity (Figure 3C vs 3D); 2) at 2162 m depth, the episode of intensified currents around Oct 27th, 2021 is absent in the simulated velocity (Figure 3G vs 3H).

At mooring RCM-SE, (Supplementary Figure 1) the observed currents at 2093 m and 2167 m depths are not as well aligned with the ridge segment as they are at similar depths at RCM-SW, despite the proximity of the two moorings (Figure 1B, Supplementary Figure 1). In particular, the observed currents at 2167 m depth predominantly flow in the NNW direction (Supplementary Figure 1C), differing from the currents observed at approximately the same depth at RCM-SW that oscillated between SSW and NNE (Figure 3G). In comparison, at 2093 m depth, the observed flow direction at RCM-SE is primarily SSW, occasionally shifting to NNW (Supplementary Figure 1A). This vertically sheared flow structure between 2167 m and 2093 m depths at RCM-SE is not observed at RCM-SW. However, the simulated flow velocity for RCM-SE does faithfully reproduce a similar vertical sheared structure, with currents predominantly flowing in the NNW and SSW directions at 2167 m and 2093 m depths, respectively. One notable discrepancy between measured and simulated flows at the RCM-SE locale is that the simulated SSW flow at 2093 m depth is more uniformly consistent than the observations (Supplementary Figure 1a vs 1b). The differences in observed currents between RCM-SW and RCM-SE reveal evidence for a complex flow pattern that exhibits both horizontal and vertical shear along the ridge segment, especially within the axial valley. Overall, these features are reproduced, at least qualitatively, by the model.

For the 2016 simulation period, the flow velocities obtained from the simulation generally match the measurements taken at the RCM-NE (Supplementary Figure 2), RCM-SE (Supplementary Figure 3), and RCM-SW (Supplementary Figure 4) moorings. However, one notable distinction is evident for the current meter situated at a depth of 1956 m on RCM-NE, where the observed currents (Supplementary Figure 2A) predominantly flow southward throughout most of the simulation period. In comparison, the simulated flow velocity (Supplementary Figure 2B) primarily exhibits a westward direction, transitioning from NNW to SSW during the initial few months of the simulation period, and subsequently shifting towards a southward direction for the remainder of the simulation period. At the RCM-SE mooring for the same period, both the observed and simulated currents at 2027m predominantly flow southward, but the observed flow velocity exhibits a larger magnitude compared to the simulated flow velocity, which also has a stronger westward component (Supplementary Figure 3A,B).

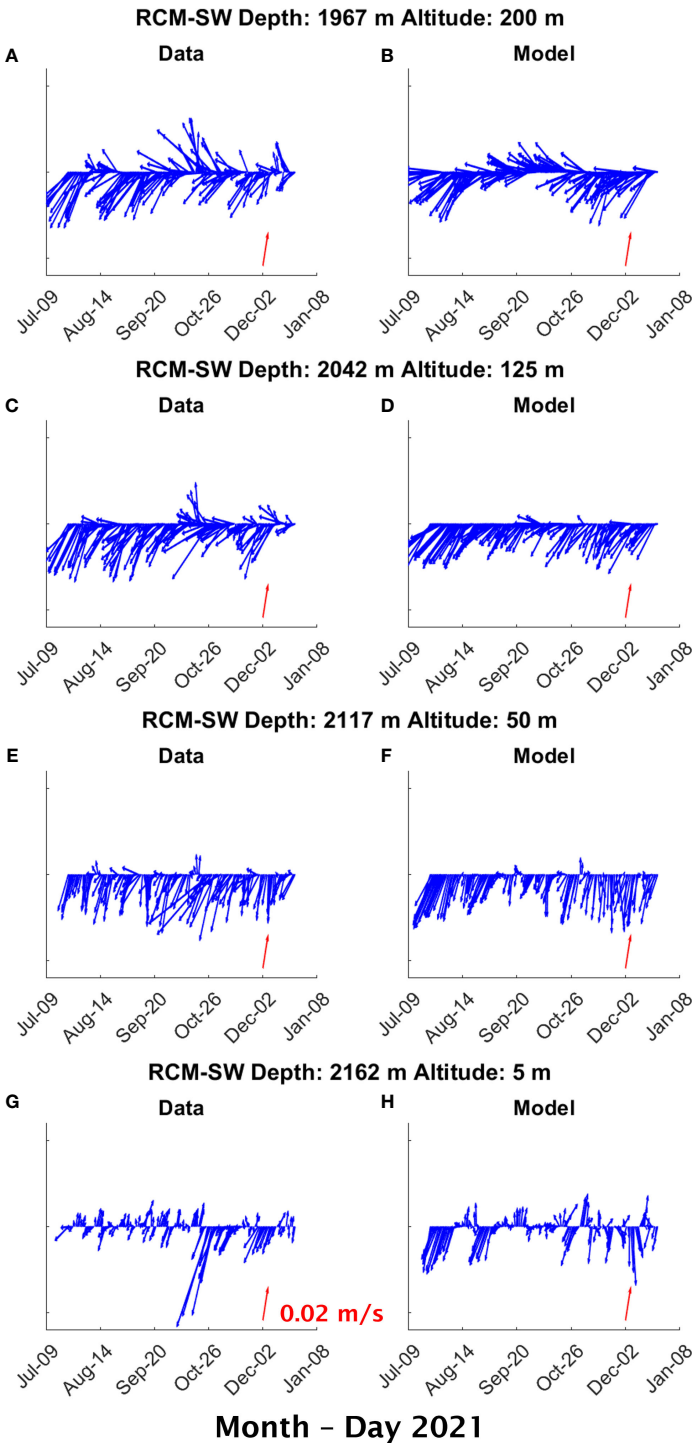

FIGURE 3
Comparison between measured (left) and simulated (right) 2-day averaged flow velocity at 1967 m **(A, B)**, 2042 m **(C, D)**, 2117 m **(E, F)**, and 2162 m **(G, H)** depths at current-meter mooring RCM-SW during Jul – Dec 2021. The red arrow denotes velocity of 0.02 m/s with a heading of 20° relative to true north, which corresponds to the orientation of the ridge segment.

4.2 Flow velocity spectrum

To assess the model's proficiency in reproducing the oscillations in flow velocity at various frequencies, we have computed the power spectra for both observed and simulated velocity time series at RCM-SW (Figure 4) for the 2021 simulation period and at RMC-NE (Supplementary Figure 5) for the 2016 simulation period. The spectrum of the measured flow velocity exhibits prominent peaks at semi-diurnal (S, ~2 cycles/day) and diurnal (D, ~1 cycle/day) tidal frequencies, as well as near the local inertial frequency (f, ~1.48 cycles/day) at the mooring sites. Moreover, the flow velocity measured at all but the lowest current meter (5 m above bottom)

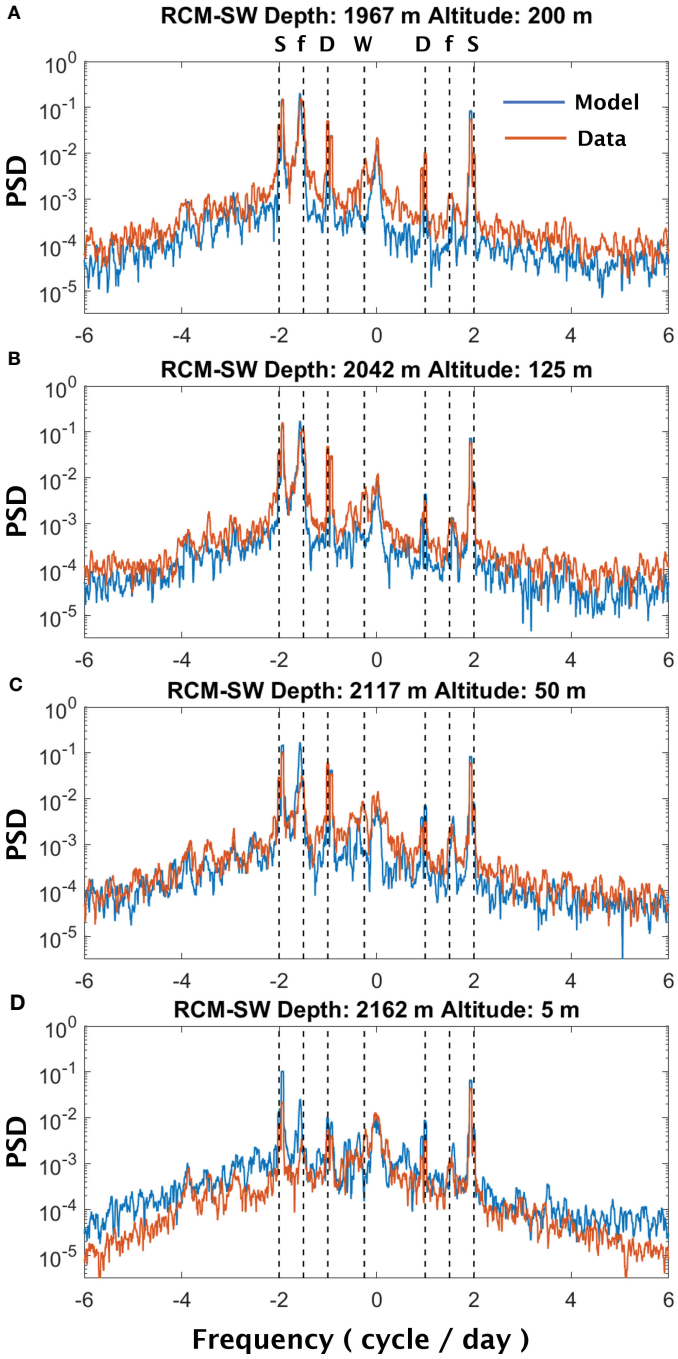

FIGURE 4
Power spectral density (PSD) computed from the measured (red) and simulated (blue) 4-hr averaged flow velocity at 1967 m **(A)**, 2042 m **(B)**, 2117 m **(C)**, and 2162 m **(D)** depths at current-meter mooring RCM-SW during Jul – Dec 2021. The negative frequencies correspond to the clockwise (CW) rotatory component of the spectrum, while the positive frequencies correspond to the counterclockwise (CCW) rotary components of the spectrum. The vertical dashed lines denote spectral peaks corresponding to the semi-diurnal tidal (S) (~2 cycle/day), inertial (f) (~1.48 cycle/day), diurnal tidal (D) (~1 cycle/day), and the 4-day 'weather' band (W) (~0.25 cycle/day) oscillations.

on RCM-SW in 2021 (Figure 4) displays significant oscillations in the observational data within the 'weather' band previously noted, with a peak near a period of 4 days in the clockwise component of the spectrum (Cannon and Thomson, 1996; Thomson et al., 2003).

In comparison, the spectra derived from simulated flow velocity time series demonstrate overall agreement with the observations, with a few noticeable discrepancies. Firstly, the simulated flow velocity lacks the 4-day 'weather' band oscillations present in the observations. Secondly, the model appears to overestimate the near-inertial oscillations (f) at the current meters located close to the seafloor, specifically at altitudes of 50 m and 5 m (Figures 4C, D and Supplementary Figure 5C). As indicated by Thomson et al. (2003), the near-inertial oscillations experience significant attenuation within the rift valley of the Endeavour Segment. This previous

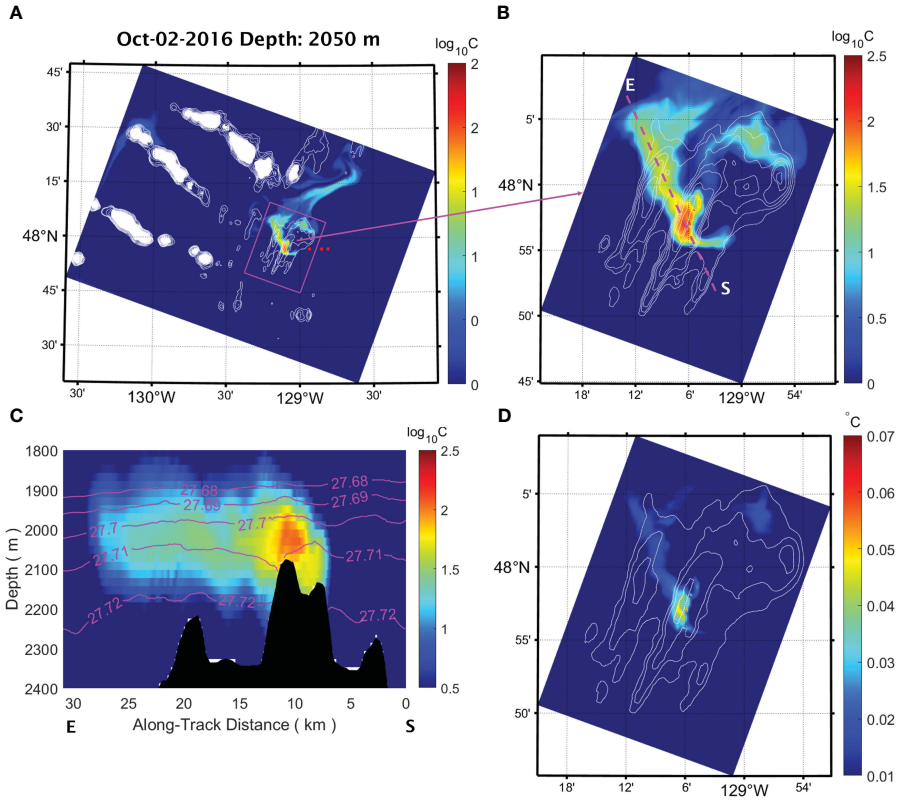

FIGURE 5
Concentration of a passive tracer released from the vent sources within the axial valley of the Endeavour Segment on Oct 2nd, 2016, shown in horizontal cross-sections across the interiors of the fine **(A)** and the ultra-fine **(B)** domains at 2050 m depth. The red dots in **(A)** mark the locations of the three background hydrographic stations. **(C)** a cross-section of the same tracer concentrations as in **(B)** along the transect indicated from start (S) to end (E). Contours denote isopycnic surfaces. **(D)** A horizontal cross-section of potential temperature anomaly at 2050 m depth within the same ultra-fine domain and as tracer concentration plot shown at **(B)**.

finding is consistent with our current observations, which demonstrate a decrease in the magnitude of the near-inertial spectral peak as depth increases (Figure 4 and Supplementary Figure 5). On the other hand, the simulated flow velocity shows less prominent attenuation of near-inertial oscillations within the axial valley. This discrepancy can likely be attributed to the smoothing of the bathymetry used in the simulations, which is done to enhance computational stability and reduce numerical errors. The bathymetric smoothing process within the model potentially suppresses the ruggedness of the axial valley, thus reducing its damping effect on near-inertial oscillations. The reason behind the absence of 4-day oscillations in simulated flow velocity remains unclear. Cannon and Thomson (1996) attributed the occurrence of these oscillations observed along the Juan de Fuca Ridge to local storms. Therefore, the lack of such oscillations in our simulations may indicate an inadequate representation of local storm events in the surface forcing used by the model (Section 3.1).

4.3 Plume distribution

To evaluate the model skill in simulating plume dispersion, we compare the characteristics of the non-buoyant cap of the plume generated by the model with observations from previous studies (Baker and Massoth, 1987; Thomson et al., 1992; Kellogg and McDuff, 2010). Specifically, we focus on three key properties of the plume's non-buoyant cap: height, core potential temperature anomaly, and core density. Our analysis shows that in the two instances demonstrated in Figures 5, 6, the buoyant plumes rising from the five major vent fields coalesce and reach neutral buoyancy at a height of 100 – 200 m above the floor of the axial valley. In the interior of the ultra-fine domain, within tens of kilometers of the ridge segment (Figures 5B, 6B), the non-buoyant plume cap disperses as a cohesive band in the NW and SW direction on Oct 2, 2016 and Aug 16, 2021, respectively. In comparison, as the plume cap spreads farther away from the ridge segment, it becomes more diffuse and displays meandering patterns (Figures 5A, 6A). In both cases, the core of the plume's non-buoyant cap is situated at depths between 2000 m and 2050 m, between the 27.7 and 27.71 kg/m^3 isopycnic surfaces (Figures 5C, 6C). We calculate the isohaline potential temperature anomaly ($\Delta\theta_S$) using the method described in Kellogg and McDuff (2010) as the deviation of absolute potential temperature (θ) from a reference for a given salinity (S). To obtain the reference temperature, we fit a second-order polynomial to the model θ/S data between 1700 m and 2300 m depths at three background stations (Figures 5B, 6B). These stations are located east of the MEF at (47.95°N, 128.94°W), (47.95°N, 128.85°W), and (47.95°N, 128.81°W), respectively. The resulting $\Delta\theta_S$ at the core of

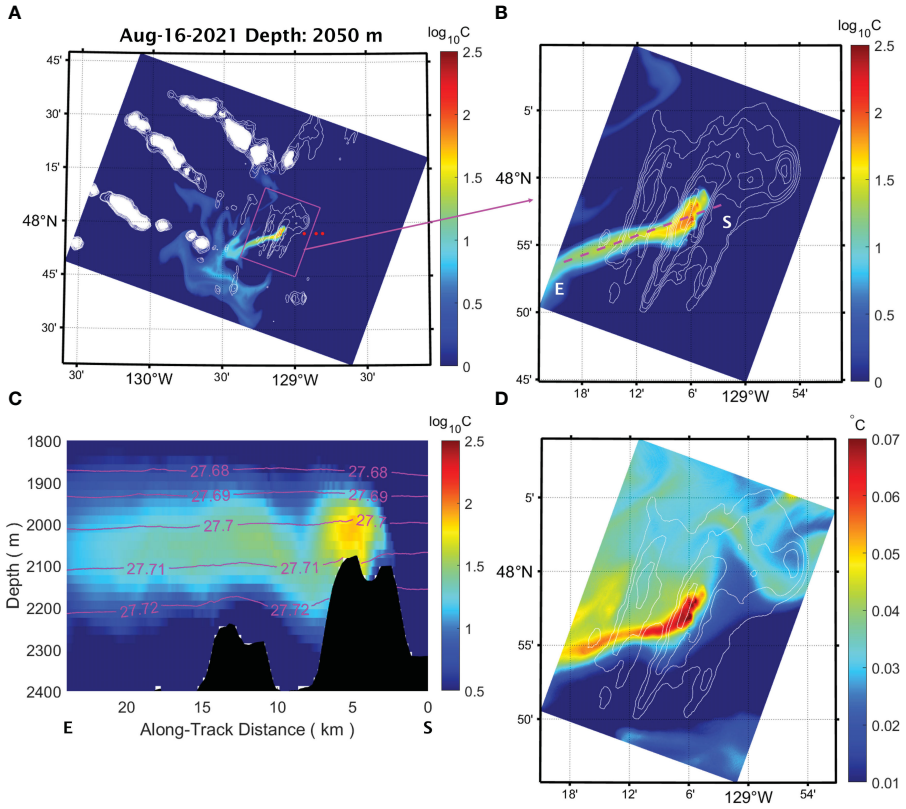

FIGURE 6
Concentration of a passive tracer released from the vent sources within the axial valley of the Endeavour Segment on Aug 16th, 2021, shown in horizontal cross-sections across the interiors of the fine **(A)** and the ultra-fine **(B)** domains at 2050 m depth. The red dots in **(A)** mark the locations of the three background hydrographic stations. **(C)** a vertical cross-section of the same tracer concentrations as in **(B)** along the transect indicated from start (S) to end (E). Contours denote isopycnic surfaces. **(D)** A horizontal cross-section of potential temperature anomaly at 2050 m depth within the same ultra-fine domain and as tracer concentration plot shown at **(B)**.

the non-buoyant plume exhibited a maximum, at a depth of 2050 m, of approximately 0.08°C and 0.10°C on Oct 2, 2016 and Aug 16, 2021, respectively (Figures 5D, 6D). In comparison, a hydrographic survey conducted along the axial valley in June 2004 showed hydrothermally influenced water with $\Delta\theta_S \approx 0.10$°C at the same depth (Kellog and McDuff, 2010).

5 Results and discussion

5.1 Near-ridge ocean circulation

The analysis of the 2016 baseline solution (Figure 7A) shows that the flow field, when averaged over a five-month period from July to November 2016, exhibits an anti-cyclonic circulation (clockwise in the northern hemisphere) that is centered around the high point on the western side of the ridge segment. Specifically, there is a poleward along-ridge flow over the western flank of the ridge, while an equatorward along-ridge flow is present over the eastern flank (Figure 8A). At the core of these ridge flank jets, the velocity reaches a maximum of approximately 0.04 m/s at a depth about 2050 m. A similar anti-cyclonic circulation has been observed around the North Cleft Segment of the southern JDFR and was attributed to two potential generation mechanisms: hydrothermal forcing and tidal rectification (Cannon and Pashinski, 1997). More specially, the entrainment of ambient seawater into buoyant hydrothermal discharge can drive an anti-cyclonic circulation at the spreading level of the non-buoyant plume cap (Speer, 1989). Additionally, tidal rectification has been shown to generate anti-cyclonic residual currents around pronounced topographic features such as Georges Bank (Chen and Beardsley, 1995) and Axial Seamount (Xu and Lavelle, 2017).

A comparison between the baseline solution and the results of the no-tide run indicates that the anti-cyclonically sheared mean flow across the ridge segment substantially weakens after the removal of the tidal forcing (Figure 7A vs 7B, Figure 8A vs 8B). Furthermore, a comparison between the baseline solution and the results of the no-vent run also shows a reduction in the strength of the anti-cyclonic flank jets along the ridge-axis, albeit to a lesser extent (Figure 7A vs 7C, Figure 8A vs 8C). Taken together, these comparisons suggest that tidal forcing is likely the primary driver of the anti-cyclonic circulation around the ridge segment, with hydrothermal venting playing a secondary role. This finding is consistent with Cannon and Pashinski (1997)'s conclusion that tidal forcing is the dominant generation mechanism for the anti-cyclonic circulation around the North Cleft Segment.

The buoyant hydrothermal plumes that rise from the axial valley draw in surrounding water and drive an inflow, which is most

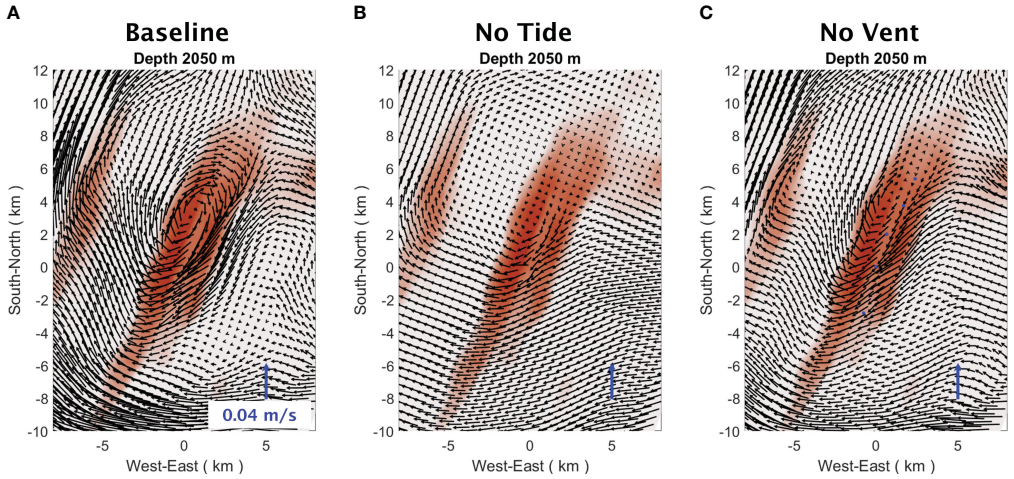

FIGURE 7
Flow velocity averaged over a five-month period from Jul 1st to Nov 30th, 2016, at 2050 m from **(A)** the baseline solution of the 2016 simulation, **(B)** the no-tide run, and **(C)** the no-vent run. The blue arrow denotes a northward flow of 0.04 m/s.

pronounced around the HR vent field with which exhibit the highest heat outputs (Figures 9A, C). This inflow alters the near-bottom mean flow within the axial valley, which is primarily directed along the ridge axis in the SSW direction in the absence of venting (Figure 9B). In comparison, the venting-induced local circulation causes the mean flow to become cyclonically sheared within the valley, with an equatorward current on the western side and poleward current on the eastern side (Figures 8A, 9A, B). This cyclonically sheared flow pattern is also evident in current-meter measurements from the RCM-SW and RCM-SE moorings in 2016. At approximately 50 m above the seafloor, the current at RCM-SW on the western side of the valley primarily flowed in an equatorward direction along the ridge axis, while the current measured at RCM-SE on the eastern side of the valley was primarily poleward along the ridge axis (Supplementary Figure 3E vs Supplementary Figure 4C). The model currents sampled at the same locations as these two moorings show reasonable agreement with the measurements (Supplementary Figures 3, 4). Previously, current velocity measurements within the axial valley had been interpreted in such a way as to suggest that venting drives a steady near-bottom flow into the valley from its northern and southern ends (Thomson et al., 2003). However, the long-term current-meter measurements and concurrent simulation results presented here reveal a more complex venting-induced flow structure that is cyclonically sheared

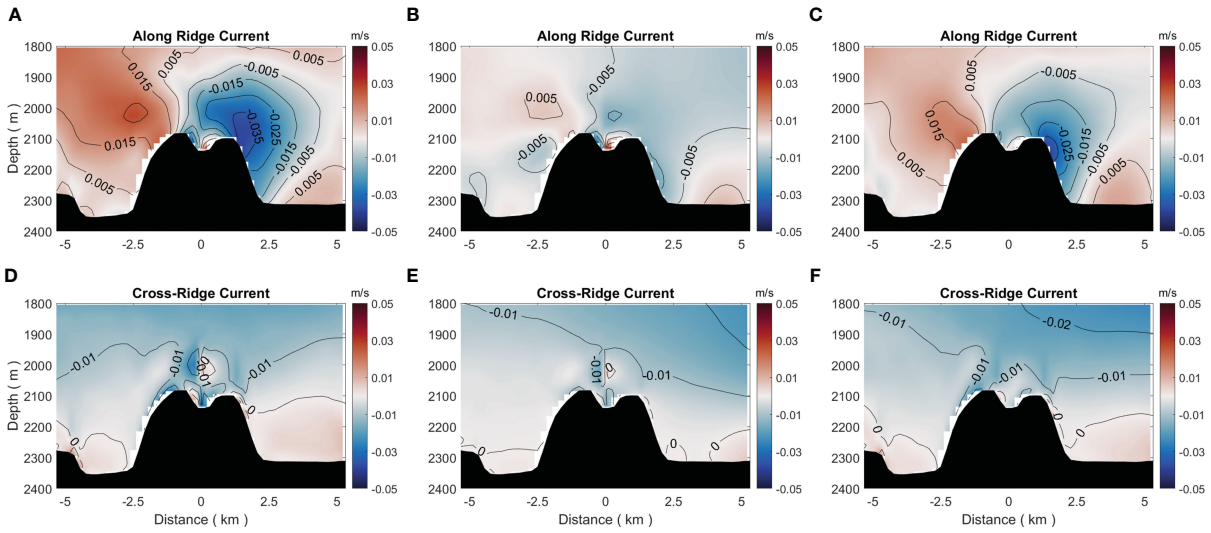

FIGURE 8
Velocity sections in the along-ridge **(A–C)** and cross-ridge directions **(D–F)** averaged over a 5-month period, from Jul 1st to Nov 30th, 2016, plotted in vertical cross-sections along a 10 km long transect that runs perpendicular to the ridge axis and passes through HR at the center of the transect. The panels in the left column **(A, D)** show the results of the baseline solution of the 2016 simulation, while the panels in the middle **(B, E)** and right **(C, F)** columns display the results of the no-tide and no-vent runs, respectively. A positive along-ridge velocity is oriented 20 from true north, and a positive cross-ridge velocity is oriented 110 from true north.

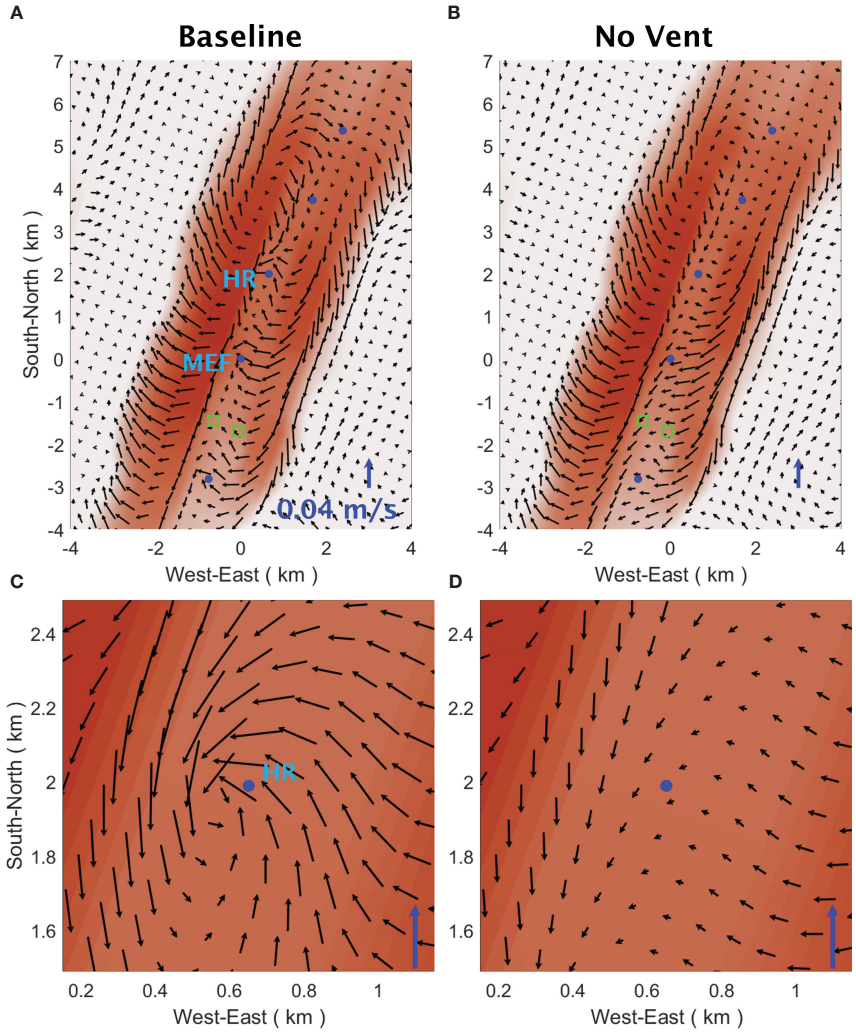

FIGURE 9
Near bottom flow velocity within the axial valley and surrounding areas, averaged over a five-month period (Jul 1st to Nov 30th, 2016). The velocity data is taken from the second terrain-following layer above the seafloor. **(A)** shows the results of the baseline solution of the 2016 simulation, while **(B)** depicts the results of the no-vent run. The blue dots mark the locations of the five major hydrothermal vent fields within the axial valley. The green squares denote the locations of the current-meter moorings RCM-SW (on the western side of the valley) and RCM-SE (on the eastern side of the valley). **(C, D)** show the flow velocity within the immediate vicinity of the High Rise (HR) vent field. The blue arrow in each panel denotes a northward flow of 0.04 m/s.

across the valley. Our findings are consistent with those from a previous numerical study, which showed a similar cyclonically sheared near-bottom flow within the axial valley, using realistic ridge topography, a near-steady cross-ridge flow and hydrothermal venting as forcing (Thomson et al., 2009). Based on previous laboratory and numerical studies (e.g., Speer, 1989; Helfrich and Battisti, 1991; Speer and Marshall, 1995; Fabregat Tomàs et al., 2016), it has been observed that the influx of surrounding water into a turbulent buoyant plume drives a local circulation that is anti-cyclonic near the spreading level of the non-buoyant plume cap and cyclonic around the plume stem below. In our simulations that account for realistic ridge topography, the deeper forced circulation, driven by the convergent flow towards the plume within the confinement of the axial valley, leads to the formation of the cyclonically sheared mean flow within the valley (Figures 8A, 9A, C). Meanwhile, the divergent flow out of the non-buoyant plume cap contributes to the formation of the anti-cyclonically sheared mean flow at depths overlying the axial valley floor (Figure 7A).

5.2 Dispersion of hydrothermal plumes

The 2016 baseline solution shows that, within the ultra-fine domain, the non-buoyant plume cap disperses primarily towards the north within a few tens of kilometres from the Endeavour Segment (Figures 10A, C, E). As the plume travels further away (Figures 11A, C, E), it splits into two branches near the Endeavour Seamount (ESM) and the southern end of the West Valley Segment (WVS) of the JDFR, which lies immediately to the north of the Endeavour Segment. One of those branches continues its northward movement, to the east of Endeavour Segment, while the other turns westward flowing south of the Heck Seamount chain (Figures 11A,

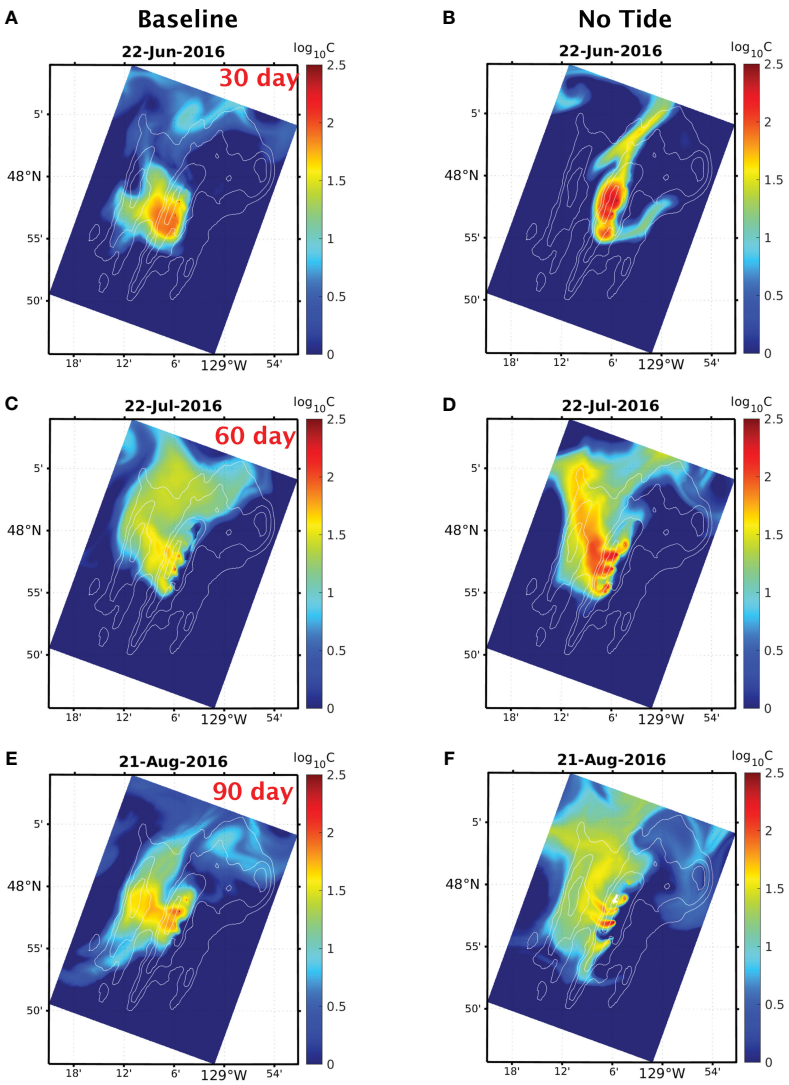

FIGURE 10
Comparison of the dispersion of a passive tracer released from the vent sources within the axial valley of the Endeavour Segment across the interior of the ultra-fine domain from the baseline solution (left column) and the no-tide run of the 2016 simulation. The tracer concentration is plotted across the interior of the fine domain on: **(A, B)** Jun 22nd (30 days after the onset of venting), **(C, D)** Jul 22nd (60 days after), and **(E, F)** Aug 21st (90 days after). The colorbar indicates the range of maximum tracer concentration between 26.69 kg/m^3 and 27.71 kg/m^3 isopycnal surfaces on a logarithmic scale.

C, E). In comparison, the no-tide run shows a similar northward dispersion within the vicinity of the Endeavour Segment (Figures 10B, D, F). Farther afield, however, instead of bifurcating into northward and westward moving branches as in the baseline solution, the plume veers to the northeast past Endeavour Seamount (Figures 11B, D, F). This disparity in plume dispersion patterns can be attributed to the existence of tidally rectified anti-cyclonic circulation in the baseline solution around Endeavour Seamount, the West Valley Segment, and the Heck Seamount (HSM) chain (Supplementary Figure 6A). In particular, the baseline solution shows a strong northwestward current flowing along the south-facing flanks of these topographic structures, which drives the westward moving branch of the plume fluid. This current is significantly weaker in the no-tide run, explaining the observed deviation in plume dispersion (Supplementary Figure 6B).

To investigate the interannual variability of plume dispersion patterns, we have calculated the plume occupancy rates for both the 2016 baseline and 2021 baseline simulation results. These rates represent the proportion of time that a given location is occupied by a hydrothermal anomaly at the depth of the non-buoyant plume cap (Figure 12). The results reveal a shift in dispersion direction between 2016 and 2021. Specifically, the 2016 simulation results show that the non-buoyant plume cap primarily dispersed towards the north of the Endeavour Segment before splitting into two branches that continued northward and westward, respectively. In contrast, the 2021 simulation results demonstrate that the plume cap primarily dispersed towards the southwest of the Endeavour Segment then southward farther away from the ridge segment. This southwest dispersal direction is more consistent with previous field observations of the non-buoyant plume cap by Baker and Massoth (1987). Meanwhile, the north-to-south change of

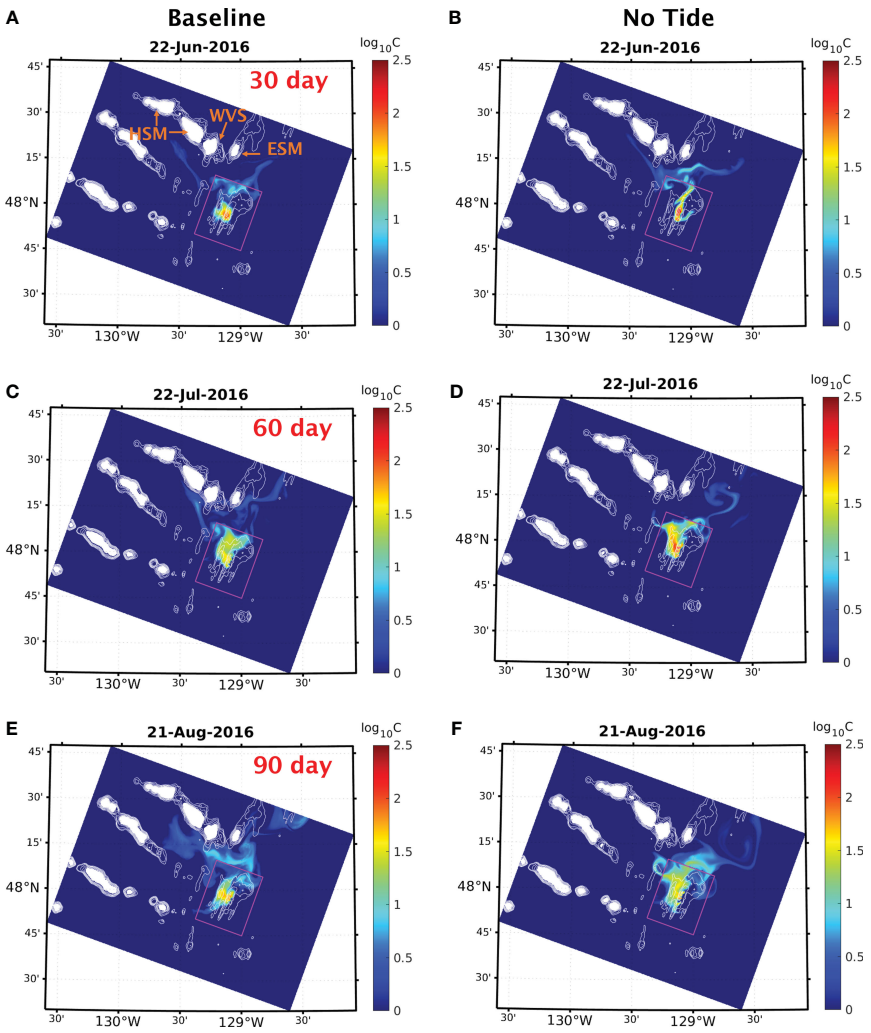

FIGURE 11
Comparison of the dispersion of a passive tracer released from the vent sources within the axial valley of the Endeavour Segment across the interior of the fine domain from the baseline solution (left column) and the no-tide run of the 2016 simulation. The tracer concentration is plotted across the interior of the fine domain on: **(A, B)** Jun 22nd (30 days after the onset of venting), **(C, D)** Jul 22nd (60 days after), and **(E, F)** Aug 21st (90 days after). The colorbar indicates the range of maximum tracer concentration between 26.69 kg/m3 and 27.71 kg/m3 isopycnal surfaces on a logarithmic scale. The box outlines the boundaries of the ultra-fine domain. The arrows in **(A)** mark the locations of Endeavour Seamount (ESM), the West Valley Segment (WVS), and the Heck Seamount chain (HSM).

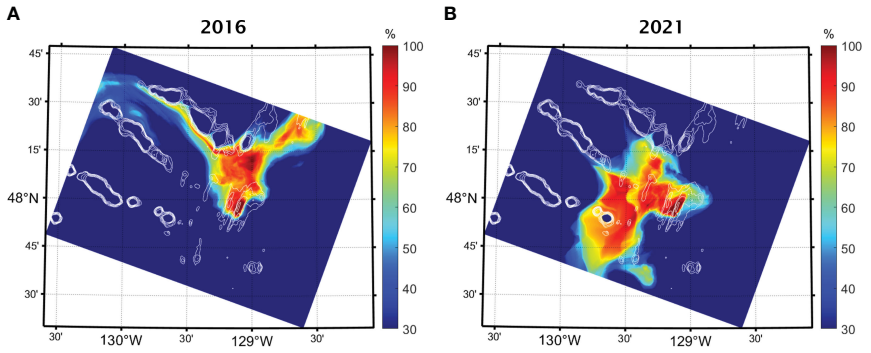

FIGURE 12
Plume occupancy rates calculated from **(A)** the 2016 baseline solution and **(B)** the results of the 2021 simulation.

dispersion direction between 2016 and 2021 suggests that the trajectory of the plume can vary significantly on interannual time scales.

What might be the cause of such pronounced inter-annual variability? Large-scale abyssal flow plays a critical role in driving the dispersion of hydrothermal plumes, particularly in off-axis regions. Consequently, a plausible explanation for the change in dispersion direction between 2016 and 2021 could be a shift in the direction of abyssal flow near the depth of the non-buoyant plume cap, around 2100 m (Figures 5C, 6C). To investigate this proposed explanation, we have examined the flow field at a depth of 2100 m from the CMEMS global reanalysis (Fernandez and Lellouche, 2021) for July to September of 2016 and 2021, respectively (Figure 13). The results exhibit a noticeable alteration in the flow direction within the regions surrounding the Endeavour Segment. Specifically, in 2016, currents flowed northward across the ultra-fine domain (Figure 13A), whereas in 2021, the predominant flow was southwestward over and to the east of the ridge axis, and westward over the western flank (Figure 13B). These flow directions are largely consistent with the plume dispersion directions observed in our simulations for both 2016 and 2021.

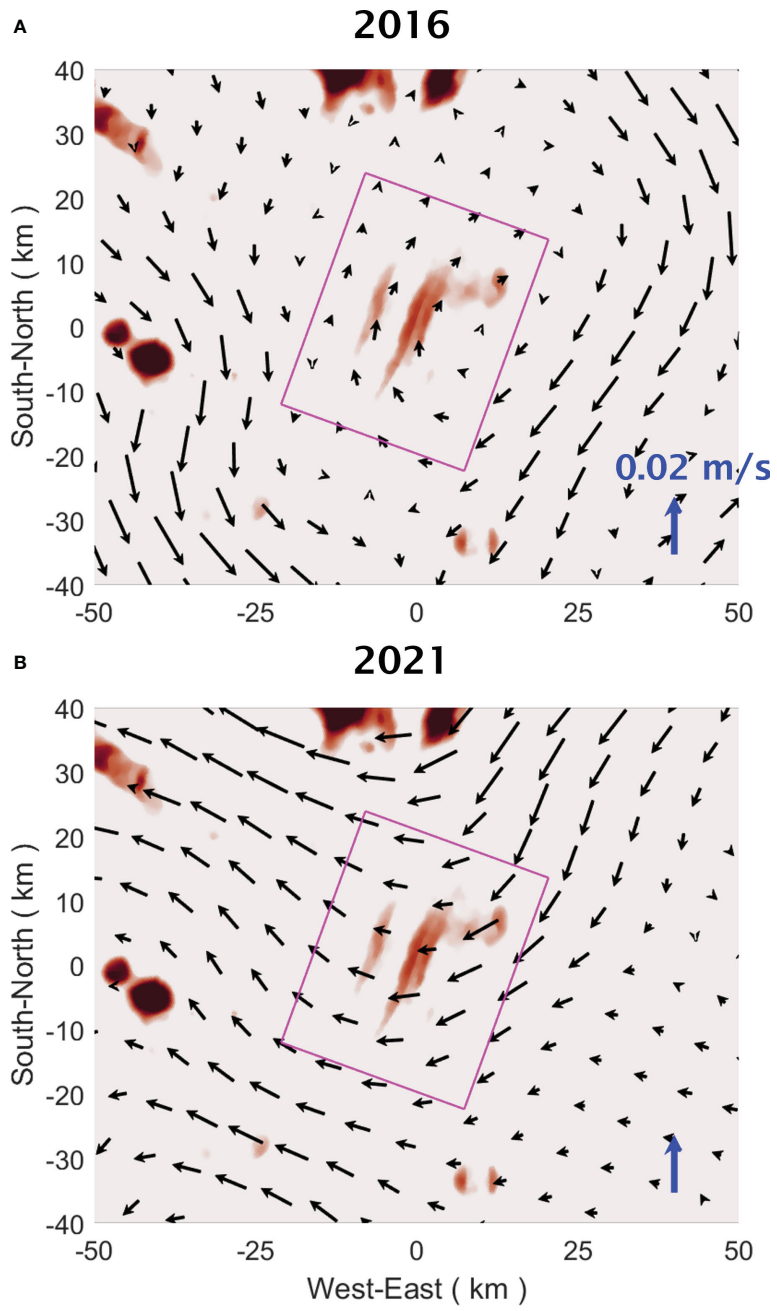

FIGURE 13
Flow velocity at 2100 m depth from the CMEMS global reanalysis averaged over a three-month period of July to September in 2016 **(A)** and 2021 **(B)**.

5.3 Mixing of hydrothermal plumes

The hydrothermal anomaly, which is quantified by the concentration of the passive tracer released from the source vent sites, exhibits higher values in the non-buoyant plume cap in our no-tide simulation results when compared to the baseline solution results (Figures 10, 11). Generally, a larger hydrothermal anomaly indicates a lower degree of plume fluid dilution and thus less entrainment of ambient seawater. Previous laboratory and numerical studies have demonstrated that the presence of a cross-flow enhances the entrainment of ambient water into a buoyancy-driven plume, yielding increased dilution factors (e.g., Xu and Di Iorio, 2012). To quantify the mixing of plume fluid with ambient seawater, we calculate the volume integrated variance of the concentration of the passive tracer (C) released from the source vents as

$$Var(C) = \int_V C'^2 dV \tag{3}$$

In equation (3), $C' = C - C_m$, C_m being the tracer concentration averaged over the integration volume (V), which encloses the interior of the final domain, bounded by the seafloor and the sea-surface. The loss of variance of a conservative tracer is a well-established approach for defining mixing in studies of ocean turbulence (e.g., Burchard and Rennau, 2008; Wang and Geyer, 2018). More recently, destruction of salinity variance has been used to quantify mixing in estuaries (e.g., MacCready et al., 2018; Broatch and MacCready, 2022).

In our simulations, during the time between when the tracer is released and when it reaches the lateral boundaries of the integration volume, tracer variance is produced at the source vents on the seafloor and destroyed within the volume of the plume due to mixing of plume fluid with ambient seawater. A comparison among the four simulation runs demonstrates that: $Var(C)$ computed from the 2016 no-vent simulation results has the highest overall value over a 70-day period starting from the onset of tracer release; $Var(C)$ computed from the 2016 no-tide run has the second highest overall value; $Var(C)$ computed from the 2016 baseline solution and the 2021 baseline solution have the lowest overall values (Figure 14). This suggests that the buoyancy flux from venting and tidal forcing both enhance mixing of hydrothermal plumes with ambient seawater, but that the buoyancy flux effect has the larger impact.

5.4 Limitations and future research implications

The preceding simulation results demonstrate the model's proficiency in capturing the dispersion of hydrothermal plumes within a complex flow field that arises from the dynamic interaction between abyssal flow, ocean tides, and the topography of the ridge segment. Nonetheless, the comparison of the simulated flow velocity with direct measurements has revealed certain discrepancies, which may affect the accuracy of simulated plume distributions and trajectories with implications for future research efforts. The most apparent discrepancy is the absence of the 4-day 'weather' band oscillations in the simulated flow velocity (Figure 4). Previous observations by Cannon and Thomson (1996) have indicated that these oscillations could have a significant impact on the dispersion of hydrothermal plumes near the ridge axis. Therefore, the absence or misrepresentation of these oscillations in our simulations has the potential to undermine their overall accuracy, particularly concerning the dispersion of hydrothermal plumes in close proximity to the ridge segment.

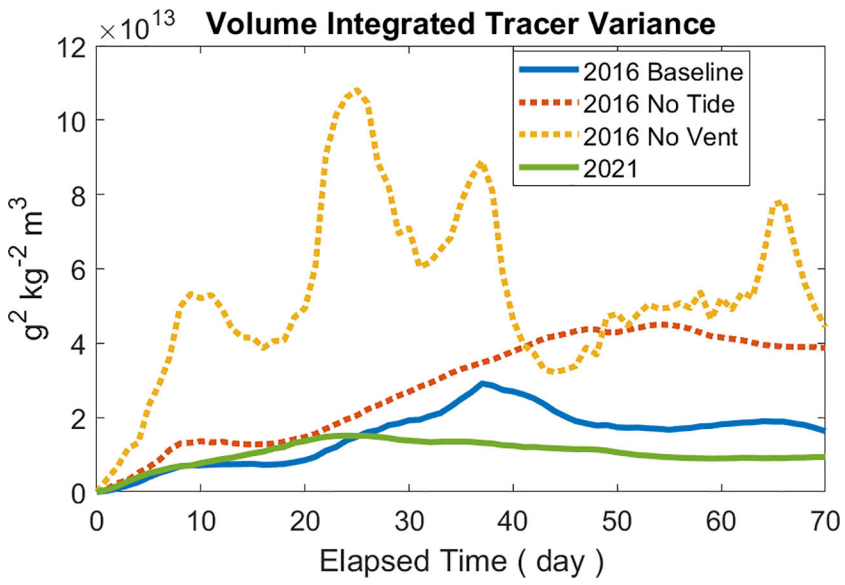

FIGURE 14
Volume integrated tracer variance over a 70-day period following when the tracer is released from the 2016 baseline solution (solid blue), no-tide run (dotted red), no-vent run (dotted yellow), and the 2021 simulation results (solid green).

As mentioned in Section 4.2, the lack of 4-day oscillations in the simulated flow velocity could potentially be attributed to inaccuracies in the surface atmospheric forcing, such as wind stress, employed in the model. While a definitive understanding of the generation mechanism for the 4-day oscillations remains elusive, previous studies have indicated that these oscillations are associated with local storms (Cannon et al., 1991; Cannon and Thomson, 1996) and could be characterized as ridge-trapped subinertial waves (Allen and Thomson, 1993). In order to gain further insights into the generation of the 4-day oscillations along the Endeavour Segment and other regions of the JDFR, a potentially effective approach would involve diagnosing the factors contributing to the absence of these oscillations in our simulations. By making adjustments to the surface forcing and other model parameters, we can strive for an improved representation of these oscillations in future numerical studies. This approach holds promise for enhancing our understanding of the mechanisms underlying the 4-day oscillations and their behavior along the JDFR, making an important avenue for future research.

Additionally, we can achieve a more robust and comprehensive validation of our modeling framework by leveraging the continuously advancing capabilities of deep-diving autonomous underwater vehicles (AUVs). A carefully designed field program, employing an AUV equipped with dedicated *in-situ* instruments, would be able to provide direct observations of plume-specific tracers across a wide spatial area. Such future AUV-based plume surveys would be able to complement the use of the data collected by stationary instruments, such as the current-meter mooring data employed here, enhancing our assessment of model performance by enabling us to compare simulated plume distributions and trajectories with field observations.

6 Summary

The multiscale simulations conducted in this study have yielded valuable insights into flow dynamics and hydrothermal plume dispersion near the Endeavour Segment of the JDFR:

- The time-averaged flow field exhibits an anti-cyclonic circulation around the ridge segment, with a northward flow over the western side of the ridge and a southward flow over the eastern side. Tidal forcing is identified as the primary driver of this anti-cyclonic circulation, while hydrothermal venting is a secondary contributing mechanism. Within the axial rift valley, hydrothermal venting induces cyclonic circulation around vent sites through entrainment by buoyant plumes. This cyclonic circulation is most evident around High Rise, which has the highest heat flux among the five major vent fields in the axial valley.
- Tidal forcing has a significant impact on plume dispersion, particularly near the large topographic features to the north of the Endeavour Segment.
- A comparison between the 2016 and 2021 baseline solutions has revealed significant inter-annual variability in hydrothermal plume dispersion, with the plume dispersing primarily north of the Endeavour Segment in 2016 and to the south of the segment in 2021.
- Both hydrothermal buoyancy flux and tidal forcing enhance the mixing of hydrothermal plumes with ambient seawater, with the buoyancy flux effect having a larger impact.
- In addition to elucidating the physical dispersion of heat and tracers away from the Juan de Fuca Ridge ridge-axis, we anticipate that this study may also prove valuable for informing future studies of biogeochemical processes that may be active within Endeavour segment hydrothermal plumes.

We have also identified two important avenues for future research:

- Investigating methods to enhance the performance of the model, with a specific focus on the accurate representation of the 4-day 'weather' band oscillations in flow velocity near the ridge segment.
- Exploring innovative approaches, such as the utilization of AUVs equipped with appropriate *in situ* sensors to augment field observations for comprehensive model validation.

Data availability statement

Publicly available datasets were analyzed in this study. This data can be found here: Ocean Networks Canada https://data.oceannetworks.ca/DataSearch.

Author contributions

This manuscript is the outcome of a collaborative effort between GX and CG, where GX took the lead in numerical modeling and data analysis, while CG contributed to data interpretation and presentation.

Funding

This study is funded by the National Science Foundation (award numbers: OCE-1851199 and OCE-1851007).

Acknowledgments

The authors would like to thank the NCAR Computational and Information System Lab (CISL) for providing the high-performance computing (HPC) platform and resources used for this work.

Conflict of interest

The authors declare that the research was conducted in the absence of any commercial or financial relationships that could be construed as a potential conflict of interest.

Publisher's note

All claims expressed in this article are solely those of the authors and do not necessarily represent those of their affiliated organizations, or those of the publisher, the editors and the reviewers. Any product that may be evaluated in this article, or claim that may be made by its manufacturer, is not guaranteed or endorsed by the publisher.

Supplementary material

The Supplementary Material for this article can be found online at: https://www.frontiersin.org/articles/10.3389/fmars.2023.1213470/full#supplementary-material

References

Allen, S. E., and Thomson, R. E. (1993). Bottom-trapped subinertial motions over midocean ridges in a stratified rotating fluid. *J. Phys. oceanogr.* 23 (3), 566–581. doi: 10.1175/1520-0485(1993)023<0566:BTSMOM>2.0.CO;2

Baker, E. T., and Massoth, G. J. (1987). Characteristics of hydrothermal plumes from two vent fields on the Juan de Fuca Ridge, northeast Pacific Ocean. *Earth Planetary Sci. Lett.* 85 (1-3), 59–73. doi: 10.1016/0012-821X(87)90021-5

Berdeal, I. G., Hautala, S. L., Thomas, L. N., and Johnson, H. P. (2006). Vertical structure of time-dependent currents in a mid-ocean ridge axial valley. *Deep Sea Res. Part I: Oceanographic Res. Pap.* 53 (2), 367–386. doi: 10.1016/j.dsr.2005.10.004

Broatch, E. M., and MacCready, P. (2022). Mixing in a salinity variance budget of the Salish Sea is controlled by river flow. *J. Phys. Oceanogr.* 52 (10), 2305–2323. doi: 10.1175/JPO-D-21-0227.1

Burchard, H., and Rennau, H. (2008). Comparative quantification of physically and numerically induced mixing in ocean models. *Ocean Model.* 20 (3), 293–311. doi: 10.1016/j.ocemod.2007.10.003

Cannon, G. A., and Pashinski, D. J. (1997). Variations in mean currents affecting hydrothermal plumes on the Juan de Fuca Ridge. *J. Geophys. Res.: Oceans* 102 (C11), 24965–24976. doi: 10.1029/97JC01910

Cannon, G. A., Pashinski, D. J., and Lemon, M. R. (1991). Middepth flow near hydrothermal venting sites on the southern Juan de Fuca Ridge. *J. Geophys. Res.: Oceans* 96 (C7), 12815–12831. doi: 10.1029/91JC01023

Cannon, G. A., and Thomson, R. E. (1996). Characteristics of 4-day oscillations trapped by the Juan de Fuca Ridge. *Geophys. Res. Lett.* 23 (13), 1613–1616. doi: 10.1029/96GL01370

Carbotte, S. M., Canales, J. P., Nedimović, M. R., Carton, H., and Mutter, J. C. (2012). Recent seismic studies at the East Pacific Rise 8 20'–10 10'N and Endeavour Segment: Insights into mid-ocean ridge hydrothermal and magmatic processes. *Oceanography* 25 (1), 100–112. doi: 10.5670/oceanog.2012.08

Chen, C., and Beardsley, R. C. (1995). A numerical study of stratified tidal rectification over finite-amplitude banks. Part I: Symmetric banks. *J. Phys. Oceanogr.* 25 (9), 2090–2110. doi: 10.1175/1520-0485(1995)025<2090:ANSOST>2.0.CO;2

Egbert, G. D., and Erofeeva, S. Y. (2002). Efficient inverse modelling of barotropic ocean tides. *J. Atmospheric Oceanic Technol.* 19 (2), 183–204. doi: 10.1175/1520-0426(2002)019<0183:EIMOBO>2.0.CO;2

Fabregat Tomàs, A., Poje, A. C., Özgökmen, T. M., and Dewar, W. K. (2016). Effects of rotation on turbulent buoyant plumes in stratified environments. *J. Geophys. Res.: Oceans* 121 (8), 5397–5417. doi: 10.1002/2016JC011737

Fernandez, E., and Lellouche, J. M. (2021) *Product User Manual: For the Global Ocean Physical Reanalysis product*. Available at: https://cmems-resources.cls.fr/documents/PUM/CMEMS-GLO-PUM-001-030.pdf.

Field, M. P., and Sherrell, R. M. (2000). Dissolved and particulate Fe in a hydrothermal plume at 9 45′ N, East Pacific Rise:: Slow Fe (II) oxidation kinetics in Pacific plumes. *Geochimica Cosmochimica Acta* 64 (4), 619–628. doi: 10.1016/S0016-7037(99)00333-6

Gartman, A., and Findlay, A. J. (2020). Impacts of hydrothermal plume processes on oceanic metal cycles and transport. *Nat. Geosci.* 13 (6), 396–402. doi: 10.1038/s41561-020-0579-0

German, C. R., Bennett, S. A., Connelly, D. P., Evans, A. J., Murton, B. J., Parson, L. M., et al. (2008). Hydrothermal activity on the southern Mid-Atlantic Ridge: tectonically-and volcanically-controlled venting at 4–5 S. *Earth Planetary Sci. Lett.* 273 (3-4), 332–344. doi: 10.1016/j.epsl.2008.06.048

German, C. R., Bowen, A., Coleman, M. L., Honig, D. L., Huber, J. A., Jakuba, M. V., et al. (2010). Diverse styles of submarine venting on the ultraslow spreading Mid-Cayman Rise. *Proc. Natl. Acad. Sci.* 107 (32), 14020–14025. doi: 10.1073/pnas.1009205107

German, C. R., Campbell, A. C., and Edmond, J. M. (1991). Hydrothermal scavenging at the Mid-Atlantic Ridge: Modification of trace element dissolved fluxes. *Earth Planetary Sci. Lett.* 107 (1), 101–114. doi: 10.1016/0012-821X(91)90047-L

German, C. R., and Seyfried, W. E.Jr. (2014). "Hydrothermal processes," in *Treatise on geochemistry, 2nd Edition*. Amsterdam, Netherlands: Elsevier Ltd. vol. 8, 191–233.

Helfrich, K. R., and Battisti, T. M. (1991). Experiments on baroclinic vortex shedding from hydrothermal plumes. *J. Geophys. Res.: Oceans* 96 (C7), 12511–12518. doi: 10.1029/90JC02643

Hunt, G. R., and Kaye, N. B. (2005). Lazy plumes. *J. Fluid Mechanics* 533, 329–338. doi: 10.1017/S002211200500457X

Jenkins, W. J., Hatta, M., Fitzsimmons, J. N., Schlitzer, R., Lanning, N. T., Shiller, A., et al. (2020). An intermediate-depth source of hydrothermal 3He and dissolved iron in the North Pacific. *Earth Planetary Sci. Lett.* 539, 116223. doi: 10.1016/j.epsl.2020.116223

Kelley, D. S., Carbotte, S. M., Caress, D. W., Clague, D. A., Delaney, J. R., Gill, J. B., et al. (2012). Endeavour Segment of the Juan de Fuca Ridge: One of the most remarkable places on Earth. *Oceanography* 25 (1), 44–61. doi: 10.5670/oceanog.2012.03

Kellogg, J. P. (2011). Temporal and spatial variability of hydrothermal fluxes within a mid-ocean ridge segment. Ph.D. thesis. University of Washington.

Kellogg, J. P., and McDuff, R. E. (2010). A hydrographic transient above the Salty Dawg hydrothermal field, Endeavour segment, Juan de Fuca Ridge. *Geochem. Geophys. Geosys.* 11 (12). doi: 10.1029/2010GC003299

Lavelle, J. W., and Cannon, G. A. (2001). On subinertial oscillations trapped by the Juan de Fuca Ridge, northeast Pacific. *J. Geophys. Res.: Oceans* 106 (C12), 31099–31116. doi: 10.1029/2001JC000865

Lavelle, J. W., Di Iorio, D., and Rona, P. (2013). A turbulent convection model with an observational context for a deep-sea hydrothermal plume in a time-variable cross flow. *J. Geophys. Res.: Oceans* 118 (11), 6145–6160. doi: 10.1002/2013JC009165

Lavelle, J. W., Thurnherr, A. M., Ledwell, J. R., McGillicuddy, D. J. Jr., and Mullineaux, L. S. (2010). Deep ocean circulation and transport where the East Pacific Rise at 9–10 N meets the Lamont seamount chain. *J. Geophys. Res.: Oceans* 115 (C12). doi: 10.1029/2010JC006426

Lupton, J. E. (1995). Hydrothermal plumes: near and far field. *Washington DC Am. Geophys. Union Geophys. Monograph Ser.* 91, 317–346.

MacCready, P., Geyer, W. R., and Burchard, H. (2018). Estuarine exchange flow is related to mixing through the salinity variance budget. *J. Phys. Oceanogr.* 48 (6), 1375–1384. doi: 10.1175/JPO-D-17-0266.1

Mellor, G. L., and Yamada, T. (1982). Development of a turbulence closure model for geophysical fluid problems. *Rev. Geophys.* 20 (4), 851–875. doi: 10.1029/RG020i004p00851

Mihaly, S. F., Thomson, R. E., and Rabinovich, A. B. (1998). Evidence for nonlinear interaction between internal waves of inertial and semidiurnal frequency. *Geophys. Res. Lett.* 25 (8), 1205–1208. doi: 10.1029/98GL00722

Resing, J. A., Sedwick, P. N., German, C. R., Jenkins, W. J., Moffett, J. W., Sohst, B. M., et al. (2015). Basin-scale transport of hydrothermal dissolved metals across the South Pacific Ocean. *Nature* 523 (7559), 200–203. doi: 10.1038/nature14577

Ryan, W. B., Carbotte, S. M., Coplan, J. O., O'Hara, S., Melkonian, A., Arko, R., et al. (2009). Global multi-resolution topography synthesis. *Geochem. Geophys. Geosys.* 10 (3). doi: 10.1029/2008GC002332

Shchepetkin, A. F., and McWilliams, J. C. (2005). The regional oceanic modelling system (ROMS): a split-explicit, free-surface, topography-following-coordinate oceanic model. *Ocean Model.* 9 (4), 347–404. doi: 10.1016/j.ocemod.2004.08.002

Sikirić, M. D., Janeković, I., and Kuzmić, M. (2009). A new approach to bathymetry smoothing in sigma-coordinate ocean models. *Ocean Model.* 29 (2), 128–136. doi: 10.1016/j.ocemod.2009.03.009

Speer, K. G. (1989). A forced baroclinic vortex around a hydrothermal plume. *Geophys. Res. Lett.* 16 (5), 461–464. doi: 10.1029/GL016i005p00461

Speer, K. G., and Marshall, J. (1995). The growth of convective plumes at seafloor hot springs. *J. Mar. Res.* 53 (6), 1025–1057. doi: 10.1357/0022240953212972

Tagliabue, A., Lough, A. J., Vic, C., Roussenov, V., Gula, J., Lohan, M. C., et al. (2022). Mechanisms driving the dispersal of hydrothermal iron from the northern Mid Atlantic Ridge. *Geophys. Res. Lett.* 49 (22), e2022GL100615. doi: 10.1029/2022GL100615

Thomson, R. E., Delaney, J. R., McDuff, R. E., Janecky, D. R., and McClain, J. S. (1992). Physical characteristics of the Endeavour Ridge hydrothermal plume during July 1988. *Earth Planetary Sci. Lett.* 111 (1), 141–154. doi: 10.1016/0012-821X(92)90175-U

Thomson, R. E., Mihály, S. F., Rabinovich, A. B., McDuff, R. E., Veirs, S. R., and Stahr, F. R. (2003). Constrained circulation at Endeavour ridge facilitates colonization by vent larvae. *Nature* 424 (6948), 545–549. doi: 10.1038/nature01824

Thomson, R. E., Subbotina, M. M., and Anisimov, M. V. (2005). Numerical simulation of hydrothermal vent-induced circulation at Endeavour Ridge. *J. Geophys. Res.: Oceans* 110 (C1). doi: 10.1029/2004JC002337"10.1029/2004JC002337

Thomson, R. E., Subbotina, M. M., and Anisimov, M. V. (2009). Numerical simulation of mean currents and water property anomalies at Endeavour Ridge: Hydrothermal versus topographic forcing. *J. Geophys. Res.: Oceans* 114 (C9). doi: 10.1029/2008JC005249"10.1029/2008JC005249

Van Ark, E. M., Detrick, R. S., Canales, J. P., Carbotte, S. M., Harding, A. J., Kent, G. M., et al. (2007). Seismic structure of the Endeavour Segment, Juan de Fuca Ridge: Correlations with seismicity and hydrothermal activity. *J. Geophys. Res.: Solid Earth* 112 (B2). doi: 10.1029/2005JB004210

Vic, C., Gula, J., Roullet, G., and Pradillon, F. (2018). Dispersion of deep-sea hydrothermal vent effluents and larvae by submesoscale and tidal currents. *Deep Sea Res. Part I: Oceanographic Res. Pap.* 133, 1–18.

Wang, T., and Geyer, W. R. (2018). The balance of salinity variance in a partially stratified estuary: Implications for exchange flow, mixing, and stratification. *J. Phys. Oceanogr.* 48 (12), 2887–2899. doi: 10.1175/JPO-D-18-0032.1

Warner, J. C., Geyer, W. R., and Arango, H. G. (2010). Using a composite grid approach in a complex coastal domain to estimate estuarine residence time. *Comput. geosci.* 36 (7), 921–935. doi: 10.1016/j.cageo.2009.11.008

Willmott, C. J. (1981). On the validation of models. *Phys. Geogr.* 2 (2), 184–194. doi: 10.1080/02723646.1981.10642213

Xu, G., and Di Iorio, D. (2012). Deep sea hydrothermal plumes and their interaction with oscillatory flows. *Geochem. Geophys. Geosys.* 13 (9). doi: 10.1029/2012GC004188

Xu, G., and Lavelle, J. W. (2017). Circulation, hydrography, and transport over the summit of Axial Seamount, a deep volcano in the Northeast Pacific. *J. Geophys. Res.: Oceans* 122 (7), 5404–5422. doi: 10.1002/2016JC012464

Xu, G., McGillicuddy, D. J. Jr., Mills, S. W., and Mullineaux, L. S. (2018). Dispersal of hydrothermal vent larvae at East Pacific Rise 9–10 N segment. *J. Geophys. Res.: Oceans* 123 (11), 7877–7895. doi: 10.1029/2018JC014290

frontiers | Frontiers in Marine Science

TYPE Original Research
PUBLISHED 15 August 2023
DOI 10.3389/fmars.2023.1192056

OPEN ACCESS

EDITED BY
Yeping Yuan,
Zhejiang University, China

REVIEWED BY
Yongxiang Huang,
Xiamen University, China
Ru Chen,
Tianjin University, China

*CORRESPONDENCE
Jordyn E. Moscoso
jmoscoso@ucsc.edu

RECEIVED 22 March 2023
ACCEPTED 09 May 2023
PUBLISHED 15 August 2023

CITATION
Moscoso JE, Tripoli RE, Chen S, Church WJ, Gonzalez H, Hill SA, Khoo N, Lonner TL and Aurnou JM (2023) Low-cost table-top experiments for teaching multi-scale geophysical fluid dynamics. *Front. Mar. Sci.* 10:1192056. doi: 10.3389/fmars.2023.1192056

Low-cost table-top experiments for teaching multi-scale geophysical fluid dynamics

Jordyn E. Moscoso[1,2,3]*, Rachel E. Tripoli[4], Shizhe Chen[4,5], William J. Church[6,7], Henry Gonzalez[4], Spencer A. Hill[8,9], Norris Khoo[4], Taylor L. Lonner[4,10] and Jonathan M. Aurnou[4]

[1]Department of Atmospheric and Oceanic Sciences, University of California, Los Angeles, Los Angeles, CA, United States, [2]Ocean Sciences Department, University of California, Santa Cruz, Santa Cruz, CA, United States, [3]Department of Biological Sciences, University of Southern California, Los Angeles, CA, United States, [4]Department of Earth, Planetary, and Space Sciences, University of California, Los Angeles, Los Angeles, CA, United States, [5]Computer Science Department, University of California, Los Angeles, Los Angeles, CA, United States, [6]White Mountain Science, Inc., Littleton, NH, United States, [7]Communicating Research in Climate STEM, Littleton, NH, United States, [8]Lamont-Doherty Earth Observatory, Columbia University, Palisades, NY, United States, [9]Program in Atmospheric and Oceanic Sciences, Princeton University, Princeton, NJ, United States, [10]Aerospace Engineering Sciences, University of Colorado, Boulder, CO, United States

Multi-scale instabilities are ubiquitous in atmospheric and oceanic flows and are essential topics in teaching geophysical fluid dynamics. Yet these topics are often difficult to teach and counter-intuitive to new learners. In this paper, we introduce our state-of-the-art Do-It Yourself Dynamics (DIYnamics) LEGO® robotics kit that allows users to create table-top models of geophysical flows. Deep ocean convection processes are simulated via three experiments – upright convection, thermal wind flows, and baroclinic instability – in order to demonstrate the robust multi-scale modeling capabilities of our kit. Detailed recipes are provided to allow users to reproduce these experiments. Further, dye-visualization measurements show that the table-top experimental results adequately agree with theory. In sum, our DIYnamics setup provides students and educators with an accessible table-top framework by which to model the multi-scale behaviors, inherent in canonical geophysical flows, such as deep ocean convection.

KEYWORDS

geophysical fluid dynamics, deep ocean convection, experiments, teaching, multi-scale instabilities

1 Introduction

Oceanic and atmospheric flows have instabilities occurring over a vast range of length and time scales (e.g., Vallis, 2017). The need to understand multi-scale processes is inherent to any careful consideration of geophysical fluid systems. In this paper, we present a suite of easily built, analog desktop experiments that provide concrete demonstrations of multi-scale ocean dynamics.

Deep ocean convection is an optimal geophysical fluid dynamics (GFD) system because it encapsulates the core concepts taught in undergraduate (Mackin et al., 2012; Marshall and Plumb, 2016) and graduate level courses in oceanography and geophysical fluid dynamics (McWilliams et al., 2006; Cushman-Roisin and Beckers, 2011; Lappa, 2012; Kundu et al., 2015; Vallis, 2017). The three main phases of flow all occur on different length and time scales, and thus provide an excellent example of multi-scale oceanic dynamics in which to focus our experiments. Although we are going to focus here on ocean dynamics, these same table-top experiments can be used to model aspects of large-scale atmospheric dynamics as well (Nadiga and Aurnou, 2008; Illari et al., 2009; Cushman-Roisin and Beckers, 2011; Marshall and Plumb, 2016; Illari et al., 2017; Hill et al., 2018).

We focus on the main processes of deep ocean convection events (Marshall and Schott, 1999), which occur primarily in the Labrador Sea, the Weddell Sea, and the Gulf of Lyon in the Mediterranean Sea (Killworth, 1983). Figure 1 contains a schematicized evolution of a deep ocean convection event. First, local cooling becomes sufficiently strong to drive top-down vertical convective instabilities –also called upright convection– that can penetrate all the way to the seafloor (Figure 1A). The convective downwelling cells produce a cooled chimney of fluid that extends across the entire fluid layer. This cold chimney geostrophically adjusts to a large-scale thermal wind flow (Rossby, 1937; Jones and Marshall, 1993; Stone and Nemet, 1996), as shown in Figure 1B. The thermal wind field is then subject to baroclinic instabilities (Pedlosky, 1964; Orlanski and Cox, 1973; Robinson and McWilliams, 1974; Pierrehumbert and Swanson, 1995; Flór et al., 2002), which acts to restratify the ocean and laterally disperse the cooled chimney in the form of eddies (Jones and Marshall, 1993; Maxworthy and Narimousa, 1994; Jacobs and Ivey, 1998), shown in the Figure 1C sketch. Deep ocean convection sets the residence time scale for fluid in the deep ocean. Since the deep ocean has the largest thermal capacity of any component of the atmosphere-ocean climate system, deep ocean convection comprises a key component of deep ocean thermal storage and cycling. Deep ocean convection additionally provides a substantial sink for carbon sequestration and, thus, is crucial to our understanding of long-term climate dynamics.

With deep ocean convection as our canonical multi-scale ocean dynamics problem, we present here three separate table-top experiments each representing one of the main dynamical stages of deep ocean convection (Figure 1). It is possible to generate all three of these flows in a single, long experiment (cf. Maxworthy and Narimousa, 1994; Jacobs and Ivey, 1998; Aurnou et al., 2003; Aujogue et al., 2018). However, such experiments require carefully controlled buoyancy fluxes and thermal boundary conditions, both of which are hard to maintain using low-cost table-top devices. Instead we will model each dynamical stage of deep ocean convection via a separate experiment, each with moderately good control of the single phenomenon at hand.

Figure 1 shows illustrations of the experimental configurations used. The first experiment simulates the downwelling vertical convection phase of deep ocean convection (e.g., Haine and Marshall, 1998). This is accomplished by spraying dense dye atop the fluid surface in the center of a rotating tank of water (Figure 1A). The dye forms a gravitationally unstable top boundary layer, from which rotating convective plumes descend into the fluid bulk, similar to upright convective flows modeled in the literature (cf. Nakagawa and Frenzen, 1955; Hide and Ibbetson, 1966; Boubnov and Golitsyn, 1986; Aurnou et al., 2015; Zhang and Afanasyev, 2021). In the second and third experiments, the dye is replaced with a cold, ice-filled central cylinder (Figure 1B). The cold cylinder maintains a relatively strong, quasi-steady buoyancy flux across the fluid annulus. In slowly rotating experiments, this lateral buoyancy flux drives large-scale axisymmetric thermal winds. In more rapidly rotating experiments, the axisymmetric thermal wind flow breaks apart baroclinically to form eddies (cf. Maxworthy and Narimousa, 1994; Jacobs and Ivey, 1998; Read, 2001; Aurnou et al., 2003). See Figure 1C. In all three configurations presented here, the results match well with those of more complex experimental studies carried out in the geophysical fluids community (e.g., Matulka et al., 2016; Rodda et al., 2018).

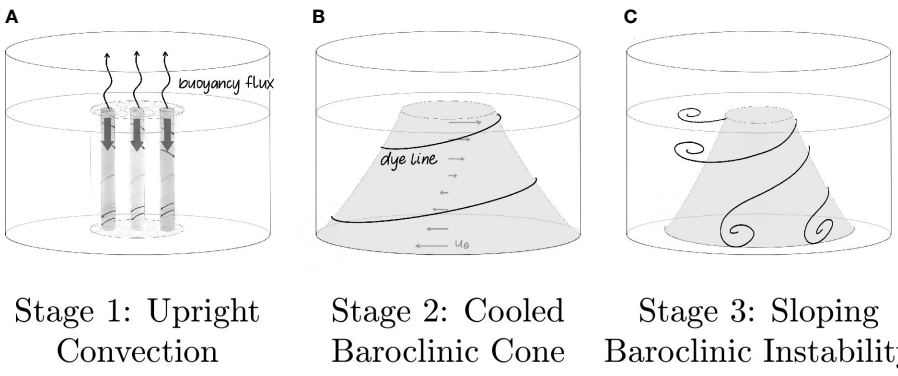

FIGURE 1
Schematic adapted from Marshall and Schott (1999) showing the main stages of deep ocean convection. **(A)** Evaporation at the ocean surface, driving convective downwelling and creating a cold column of water. **(B)** Vertical column of cold water becomes a cooled baroclinic cone through geostrophic adjustment; thermal wind flows develop about the baroclinic cone. **(C)** Thermal winds become unstable and form eddies.

2 The *DIY*namics framework

Our team has developed a broad suite of GFD experimental hardware kits, starting first with the LEGO-based kit presented in Hill et al. (2018). They allow users to study key aspects of geophysical (and many astrophysical) fluid flows: rotating dynamics of low viscosity fluids (Cushman-Roisin and Beckers, 2011). Our DIYnamics kits can all be built from the ground-up by students or teachers alike. They are similar in scientific capability to the MIT 'Weather in a Tank' system (Illari et al., 2009; Marshall and Plumb, 2016). Our LEGO-based do-it-yourself (DIY) kits differ in that their parts are purchasable online with no need for custom machining or custom fabrication of the essential hardware. Additionally, the DJ table can be easily adapted from many basic record players, and does not require any machining. While the HT3 table requires some custom machining, users are able to acquire the parts from any machine shops and acrylic manufacturers. We note, however, that our favorite configurations of these kits make use of custom-built acrylic containers.

Our low-cost, do-it-yourself approach also differs significantly from the fabrication of traditional GFD experiments, which are often found only at R1 universities in GFD-focused laboratories and typically cost in the tens of thousands of dollars at the low end. The goal of the *DIY*namics project is to flip that model on its head by developing less expensive, easily scalable devices that can be built and used across a wide range of educational environments.

We have developed three main series of *DIY*namics hardware kits to date: The LEGO series, the DJ series, and the HT series. The kits in the LEGO series make use of an OXO rotary table. The outer rim of the rotary table is directly coupled to a drive wheel powered by a LEGO motor (Figure 2A; https://diynamics.github.io/pages/lego.html). These LEGO-based drive systems have been built by 10 year olds at outreach reach fairs in under 20 minutes. The rotation rate of the rotary table can be controlled by driving the standard LEGO motor with a variable power supply. The most recent generations of LEGO motors are programmable, and their rotation speeds can be controlled via Bluetooth connection, as will be described in the following section.

Figure 2B shows an example from the DJ series (https://diynamics.github.io/pages/dj.html). It is comprised of a disk jockey (DJ) quality record player with a cylindrical tank centered upon it. DJ turntables, such as the Numark TTX shown, have rotation rates that can range from 17 to 117 revolutions per minute (RPM), which maintain rotational stability to within 1 part in 10^4. By placing the turntable on a rolling cart, this system can be easily rolled in and out of classrooms. Including a portable battery on the cart allows the system to be self-contained, with no power chords for students to trip over.

Figure 2C shows the HT3, the latest member of the HT series of DIYnamics rotating tables (https://diynamics.github.io/pages/ht3.html). The HT3 is currently the largest *DIY*namics kit, with its 80 cm tank. This tank sits upon a brushless servo-driven pedestal with rotation rates from 0.16 up to 13.33 RPM. It has an upper deck that can be used for holding cameras and cell phones as well as other possible measurement equipment. In addition, we designed a dedicated cart for it with sturdy, large-diameter, lockable wheels, which makes it ideal for rolling outside over uneven pavement, as is often necessary at public outreach events and the like.

2.1 The LEGO SPIKE set up

The three desktop experiments carried out here are made using the LEGO SPIKE Kit (Figure 3), which is the newest LEGO series kit, built around LEGO's SPIKE Prime robotics kit. While the DJ and HT3 kits have better rotational stability and finer rotational

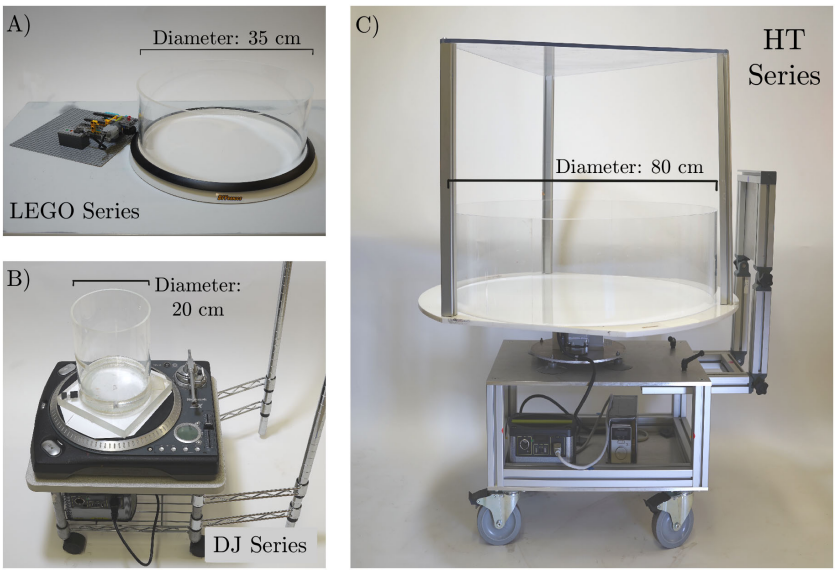

FIGURE 2
Images of **(A)** LEGO series, **(B)** DJ series and **(C)** HT3 series *DIY*namics kits.

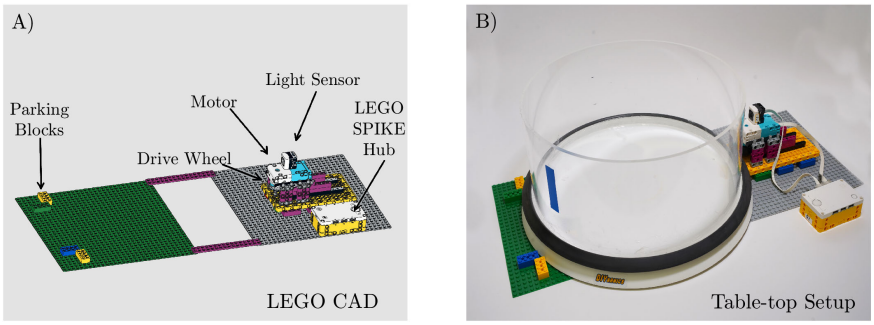

FIGURE 3
(A) Rendering of the LEGO SPIKE kit made using the Brick Studio LEGO CAD software. **(B)** Image of the SPIKE set up, including OXO turntable on a table-top.

control, we use the LEGO kit to show that it is possible to generate all three deep ocean convection flows using one of the LEGO series kits, which are the simplest and most 'DIY' of our different systems.

The LEGO-based kits provide students the broadest range of learning and engagement opportunities. First, students can build the LEGO kits from the ground up, using, for example, the detailed BrickStudio build instructions given here in the Supplementary Materials (Figure 3A). Second, the SPIKE motor can be programmed using the LEGO SPIKE app, providing an opportunity for students to program a real-world, physical experimental system using either the graphical language Scratch or the structured language microPython. The LEGO SPIKE Kit allows students to build up a range of hands-on engineering and coding skills. Students can additionally take data directly via the SPIKE's Hub microcontroller. By placing the SPIKE's light sensor atop the motor in conjunction with a piece of colored tape on the tank sidewall (see Figure 3B), it is possible to program the SPIKE to acquire measurements of the tank's rotation period. Example Scratch and microPython codes that rotate the tank and acquire rotation period data can be found at https://github.com/rachtrip/DIYnamics-LEGO-SPIKE.git.

Any container that fits on the OXO can be used, but for our experiment, we maximize space by installing an acrylic sidewall that is nearly equal to the OXO's inner diameter. The LEGO system that we present here requires the acrylic sidewalls are secured onto the OXO turntable using silicone or epoxy (e.g., https://youtu.be/sN1ahWml17w). Note that it takes one to two days for most silicones or epoxies to fully cure, so this step should be done before students follow the supplementary BrickStudio instructions to build the LEGO SPIKE kits in the classroom.

All the images and videos shown in this paper have been acquired using cameras situated in the non-rotating lab frame. However, we have ways to view the experiments in the rotating frame. For instance, a gooseneck clamp can be used to hold a camera in the rotating frame. Placing a sheet of paper on the outside of the tank, opposite of the location of the camera removes the apparent spinning of the background (e.g., https://youtu.be/jX5ppPQaea4). Side views are most useful in thermal wind experiments, allowing students to see the thermal wind shear clearly.

To view the experiment in top view, place a camera above the rotating tank's axis of rotation. This top view camera can be situated in the rotating frame using a gooseneck clamp or it may be situated in the lab frame. Since it is typically simpler and faster to set up the camera in the lab frame, we have developed an associated web-served app, *DIY*rotate, that digitally transforms the axial rotation rate in a given top view digital movie (https://DIYnamics.github.io/pages/diyrotate.html). Using *DIY*rotate, it is possible to transform lab frame camera footage into the tank's rotating frame (e.g., https://youtu.be/u6OoYdrYZ0o). When carrying out experiments, experimenters can measure the tank's rotation period using the SPIKE light sensor or by using a stopwatch to measure it by hand and supply that as input to *DIY*rotate.

Leveling the tank will minimize the amplitude of surface waves that that are not being simulated here. The tank can be leveled incrementally by using shims (e.g., playing cards) and a bubble level. Alternatively, the tank can left unleveled, which can facilitate discussion of waves and inertial modes in rotating systems.

Before actually adding dye to the fluid, it is essential that all the water in the tank is rotating at the same angular velocity as the tank. This state of the fluid is called solid body rotation. If the water is not in solid body rotation, the ensuing experiments rarely work correctly. Spin-up in these experiments occurs via an approximately exponential response that occurs on the time scale (Warn-Varnas et al., 1978; Duck and Foster, 2001):

$$\tau_{su} \simeq \frac{H}{(\nu\Omega)^{1/2}} = \frac{3.1H}{(\nu\mathcal{N}_{RPM})^{1/2}}, \tag{1}$$

where H is the depth of the fluid layer, ν is the kinematic viscosity of the working fluid (10^{-6} m^2/s for room temperature water), $\mathbf{\Omega} = 2\pi/\tau_{\Omega}$ is the tank's angular rotation velocity that can be recast in terms of revolutions per minute as

$$\mathcal{N}_{RPM} = \frac{60}{\tau_{\Omega}} = 60\frac{\Omega}{2\pi},$$

with τ_{Ω} being the tank's rotation period in seconds. Based on our experience, the fluid is adequately spun-up when the system rotates for $5\tau_{su}$ before starting a given experimental case. Figure 4 shows this wait time plotted as a function of $\mathcal{N}_{RPM}$ for H = 5 and 10 cm fluid layer depths.

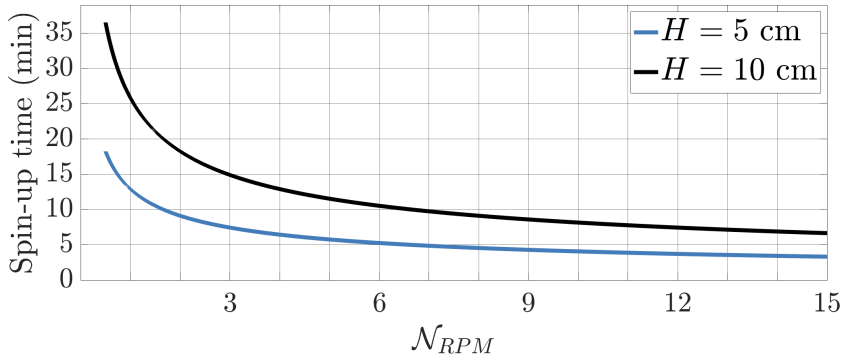

FIGURE 4
Estimated spin-up equilibration time,$5\tau_{su}$, plotted as a function of tank rotation rate, $\mathcal{N}_{RPM}$, for H = 5 and 10cm fluid layer depths.

The reader is directed to the 'Tips' page on the DIYnamics site for further ideas on how best to optimize the experiments (https://diynamics.github.io/pages/tips.html).

3 Desktop models of deep ocean convective flows

3.1 Experiment 1: downwelling dye-driven convection

Desktop simulations of the upright convection phase of deep ocean convection are made by filling the OXO tank with 10 cm of water and rotating the SPIKE motor at its maximum rate, which corresponds to a rotation period of $\tau_\Omega = 5.36$ seconds for the drive wheel employed here. Thus, the tank spins at

$$\mathcal{N}_{\rm RPM} = 10.26 \quad \text{RPM}, \tag{2}$$

corresponding to an angular velocity of

$$\Omega = \frac{\pi \mathcal{N}_{\rm RPM}}{30} = 1.07 \quad \text{rad/s}. \tag{3}$$

In order to create a controllable localized central dye patch, we place a 6.4 mm thick acrylic sheet over the top of the tank, with an 11 cm centered thru hole cut out of it see Figure S1B. Once the fluid has spun-up, we spray dense food dye through the hole in the sheet. The sheet is then removed and we image the subsequent evolution of the ≈ 15cm diameter dye patch.

The food dye acts as a proxy for the cold, dense surface waters that become convectively unstable in deep ocean convection events. The convective forcing is often described by the non-dimensional Rayleigh number,

$$Ra = (\delta\rho/\rho) g H^3/(\nu\kappa) \simeq 2 \times 10^9, \tag{4}$$

which estimates the ratio of buoyancy versus diffusional effects. Here, $g = 9.8\text{m/s}^2$ is gravity, $\delta\rho/\rho = (\rho_{dye} - \rho)/\rho = 0.007$is the density of anomaly of the food dye relative to pure water, where our dye density is measured to be $\rho_{dye} = 1.007$ g/cm^3 and we take $\rho = 1$ g/cm^3 as the density of water. The axial depth of the fluid layer is $H = 10$cm, $\nu = 10^{-6}\text{m}^2/\text{s}$ is the kinematic viscosity of water, and $\kappa \sim 3 \times 10^{-8}$ m^2/s is estimated to be the chemical diffusivity of the food dye. The strength of rotational effects is characterized by the non-dimensional Ekman number,

$$Ek = \nu/(2\Omega H^2) = 15\nu/(\pi \mathcal{N}_{RPM} H^2) = 4.7 \times 10^{-5}, \tag{5}$$

which estimates the ratio of viscous and Coriolis forces. The working fluid's material properties are cast in terms of the Prandtl number,

$$Pr = \nu/\kappa \simeq 30. \tag{6}$$

The regime of rotating convection is often characterized in terms of the so-called convective Rossby number, Ro, which estimates the local convective scale ratio of inertial and Coriolis accelerations (Aurnou et al., 2020). When Ro $\lesssim$ 1, Coriolis accelerations dominate, generating rotationally aligned convective flow structures (e.g., Nakagawa and Frenzen, 1955). Here, the convective Rossby number value is estimated to be

$$Ro = \sqrt{RaEk^2/Pr} \simeq 0.1. \tag{7}$$

The Ra and Ro values are likely upper bounds since we use an impulsive flux of dye to force the flow in this experiment. Even so, Ro remains less than unity, such that we expect rotational effects to dominate the convection dynamics. Furthermore, the Ra, Ek and Ro values employed in this experiment are in adequate agreement with the deep ocean convection simulations carried out by Jones and Marshall (1993); Klinger and Marshall (1995) and Pal and Chalamalla (2020).

Rotationally dominated convection occurs in the form of tall columnar flows that can be $O(H)$ in axial extent. In contrast, these columnar structures are narrow in the cross-axial, or horizontal, direction. At the onset of convection, linear theory predicts the horizontal scale of the convective cells will have a radius of

$$r_{conv} = 1.2 Ek^{1/3} H = 1.2 \left(\frac{\nu}{2\Omega H^2}\right)^{1/3} H = 1.2 \left(\frac{15\nu H}{\pi \mathcal{N}_{RPM}}\right)^{1/3}, \tag{8}$$

(Julien and Knobloch, 1998; Horn and Aurnou, 2022). For our dye-driven rotating convection experiment, we predict that $r_{conv} \simeq 0.43$ cm, such that we estimate that 17 structures will form across the

r_{patch} ≃7.5 cm dye patch (Figure 5A and its inset). These initial convective structures later 'plump up', as shown in Figure 5B, to a larger, turbulent horizontal scale once the convection has become fully developed (Fernando et al., 1991; Guervilly et al., 2019; Aurnou et al., 2020; Bire et al., 2022).

Figure 6 shows images of rotating convection forming from a dense dye patch sprayed at the top surface of the fluid layer. The top row shows top view images at two points in time; the bottom row show the accompanying, contemporaneous side view images. Also see Supplementary Movie 1, from which these images are derived. Panels a) and c) show the dye field roughly 10 rotation periods after the emplacement of the dye. Panels b) and d) show images acquired roughly 45 rotation periods after dye emplacement. The dye converges in downwelling plumes, each of which act to generate positive axial vorticity via stretching of the background vorticity. This positive local vorticity causes the dye to swirl counter-clockwise, in the same direction as the tank is rotating. Approximately 15 - 20 structures span the diameter of the dye patch in panel a, in adequate agreement with (8). In panels b) and d), the dye extends across the entire depth of the fluid layer, forming a well-defined dye "chimney". The chimney as well as the individual convective flow structures within the chimney remain aligned along the direction of the rotation axis. Roughly 6 or 7 convective structures span the dye patch, showing that the horizontal scaleincreases as flow becomes fully developed, in qualitative agreement with theory. Unlike the upright convective structures, the diameter of the larger-scale chimney remains the same throughout this experiment.

3.2 Thermally-driven annular flows

After the initial upright convection stage of deep ocean convection (Figure 1A) there exists a cold chimney of fluid that spans the full depth of the ocean. This is represented in our table-top experiments by the dense dye chimney in Figure 6D. This dye chimney will continue to evolve, developing azimuthal thermal winds and baroclinic instabilities given sufficient time (e.g., Maxworthy and Narimousa, 1994). Strongly unstable dye-driven baroclinic flows would, however, require us to either use denser dye or to continually flux dye into the patch. Instead, in the following experiments, we simulate the later, post-upright-convective stages of deep ocean convection (Figures 1B, C) by replacing the dye chimney in Figure 6D with a comparable radius can, or jar, of ice water that generates strong thermally-driven flows around its edge, as shown schematically in Figure 1B.

The existence of the centered cold source changes the geometry of the experiment. The working fluid is no longer simply connected and exists now in the form of a cylindrical annulus, corresponding to the classical configuration known as Hide's annulus (e.g., Ghil et al., 2010). The radius of the centralized cold can sets the inner radius of the fluid annulus, R_i, while the tank sidewall sets the fluid's outer annular extent, R_o. The fluid that sits laterally adjacent to the ice-filled can at $r \simeq R_i$ represents the dense fluid in the outer part of the deep ocean convective chimney. The warmer fluid further away in radius represents the surrounding ambient ocean water. Estimates for the input scales in the annulus experiments are provided in Table 1.

3.3 Experiment 2: Axisymmetric thermal wind flows

The Rossby number in all three experiments is small, $Ro \lessapprox 1$, which implies that Coriolis accelerations dominate the dynamics. Thus, the leading order terms in the momentum balance represent a geostrophic balance between Coriolis and pressure gradient forces, and the leading order terms in the vorticity equation are the Coriolis

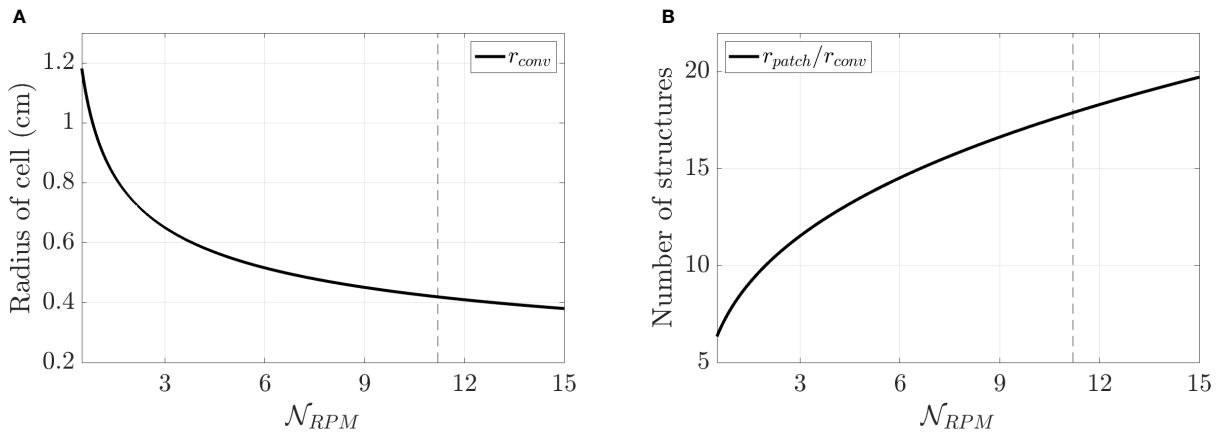

FIGURE 5
(A) Linear stability predictions of horizontal cell radius r_{conv} of rotating convective flows plotted versus the tank's rotation rate given in terms of $\mathcal{N}_{RPM}$. **(B)** Estimated number of rotating convection structures, r_{patch}/r_{conv}, forming out of the emplaced dye patch versus $\mathcal{N}_{RPM}$. In this experiment, the diameter of the dye patch is $2r_{patch}$ = 15 cm and the fluid layer depth is H = 10 cm. The vertical dashed line indicates the $\mathcal{N}_{RPM}$ = 10.26, which corresponds to the rotation rate of the upright convection experiment presented herein.

10.3389/fmars.2023.1192056

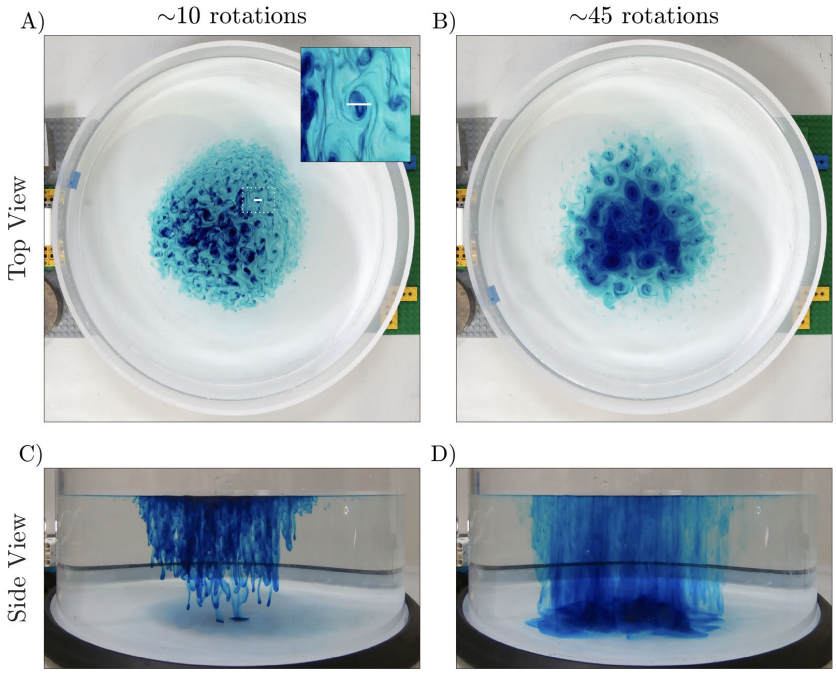

FIGURE 6
Table-top experimental simulation of the initial upright convective phase of deep ocean convection. The water depth is H = 10 cm; the rotation rate is 11.2 RPM such that τ_Ω = 5.36 s. The patch of dye at the fluid surface has an approximate diameter of 15 cm. **(A, C)** Top and side views, respectively, of the intial downwelling flow pattern roughly 10 τ_Ω after dye patch emplacement. **(B, D)** Fully-developed flow $\approx 45\tau_\Omega$ after dye emplacement. (Still images harvested from Supplementary Movie 1.).

and buoyancy terms:

$$2\Omega \cdot \nabla u = -g \times \nabla(\rho/\rho_o), \tag{9}$$

which is referred to as a geostrophic balance (McWilliams et al., 2006; Cushman-Roisin and Beckers, 2011; Marshall and Plumb, 2016). In (9), Ω is the system's rotational angular velocity vector, u is the fluid velocity measured in the rotating frame, g is lab gravity, ρ is the fluid density, and ρ_o is a reference density of the ambient fluid. In right-handed cylindrical coordinates (r, θ, z), the angular velocity and gravity vectors are axial, $\Omega = \Omega\hat{z}$ and $g = g\hat{z}$, allowing (9) to be recast as

$$2\Omega \frac{\partial u}{\partial z} = -\frac{g}{\rho_o}(\hat{z} \times \nabla\rho), \tag{10}$$

TABLE 1 Parameter estimates for the annular thermal wind (TW) and baroclinic instability (BCI) experiments.

Parameter	Value	Description
α	2×10^{-4}1/K	Thermal expansion coefficient of water
g	9.8m/s^2	Gravitational acceleration
R_i	5.25 cm	Inner radius
R_o	17.25 cm	Outer radius
H	10 cm	TW fluid layer depth
$\mathcal{N}_{RPM}$	1.46	TW rotation rate (RPM)
ΔT	2.7 ± 0.2K	TW temperature difference, $T_i - T_o$
$4R_{def}$	25 cm	TW radius of deformation estimate (> L_{gap})
H	5 cm	BCI fluid layer depth
$\mathcal{N}_{RPM}$	3.9, 11	BCI rotation rates (RPM)
ΔT	2.9 ± 0.3K	BCI temperature difference, $T_i - T_o$
$4R_{def}$	8.4, 3.0 cm	BCI radius of deformation estimates (< L_{gap})

known as 'thermal wind' balance. The left hand side of (10) describes vorticity generation by stretching of the so-called planetary vorticity, $2\mathbf{\Omega}$, and the right hand side is the baroclinic torque generated by lateral gradients in fluid density.

In the absence of salt the incompressible equation of state for water is

$$\rho(T) = \rho_0(1 - \alpha(T - T_0)), \tag{11}$$

where $\alpha \simeq 2 \times 10^{-4}$ 1/K is its thermal expansion coefficient, T is the fluid temperature, T_0 is ambient temperature, and $\rho_o = \rho(T_o)$ is the ambient density. Substituting (11) into (10) then yields

$$\frac{\partial u}{\partial z} = \frac{\alpha g}{2\Omega}(\hat{z} \times \nabla T). \tag{12}$$

Lastly, taking into account that the temperature gradient in our cylindrical annular experiments is predominantly radial, $T \approx T(r)$, the thermal winds will satisfy

$$\frac{\partial u_\theta}{\partial z} = \frac{\alpha g}{2\Omega}\frac{\partial T}{\partial r}. \tag{13}$$

The above equations show that horizontal density gradients lead to a vertical shearing of the horizontal flow fields in rapidly rotating fluids, as illustrated in Figure 1B. In a non-rotating system, a radial density gradient would generate an axisymmetric, meridionally-overturning circulation. In rapidly rotating low Ro systems, the radial density gradients generate baroclinic torques that drive an axially-shearing azimuthal velocity field, du_θ/dz. The thermal wind shear in right-handed systems ($\Omega > 0$) is positive $du_\theta/dz > 0$ since $dT/dr > 0$. From (13), the azimuthal thermal wind velocity at the top of the fluid layer will super-rotate with respect to the tank, and the fluid at the bottom of the fluid layer will tend to sub-rotate relative to the tank. Thus, in an experiment with a right handed angular rotation velocity, a dyed column of fluid observed in the rotating frame should tend to be sheared in a right handed sense as well, with the fluid at the top precessing in the prograde + $\hat{\theta}$-direction. The $\partial u_\theta/\partial z$ shearing of the thermal wind field will act to continually wrap the dye column around the domain, so long as the compositionally-dense dye doesn't settle under its own weight and the effects of Ekman pumping. Thus at the bottom of the tank, the fluid processes about the baroclinic cone in the retrograde direction. This non-intuitive axial shearing of the azimuthal thermal wind flow field is the rotating fluid analog to the precession of a tipped, rapidly rotating gyroscope (Haine and Cherian, 2013).

Figure 7 shows the results of a thermal winds experiment. The water depth in this experiment is $H = 10$ cm, with a rotation rate of approximately 1.46 RPM. The system was allowed to spin up without ice in the inner can for approximately 30 minutes to allow for solid body rotation. Ice, salt, and water were added to the can after spin-up and the system was allowed to establish a thermal gradient for approximately 5 minutes. To estimate the timescale that the thermal wind flow will take to wrap around the can in this experiment, we calculate thermal wind velocity U_{TW} and determine the time τ_{TW} that it takes to flow around the $R_i$radius can:

$$\tau_{TW} = \frac{2\pi R_i}{U_{TW}}. \tag{14}$$

The thermal wind velocity scales as,

$$U_{TW} = \frac{du_\theta}{dz}H = \frac{\alpha g}{2\Omega}\frac{\partial T}{\partial r}H \simeq \frac{\alpha g H \Delta T}{2\Omega \Delta R} \approx 1.5 \quad \text{cm/s}, \tag{15}$$

where we have used laboratory measurements of $\mathbf{\Delta}T = T_i - T_o = 2.7 \pm 0.2$ K (see Figure S4C in the Supplementary Materials) and $\mathbf{\Delta}R = R_o - R_i = 12$. Equations 14 and 15 then give the wrapping timescale,

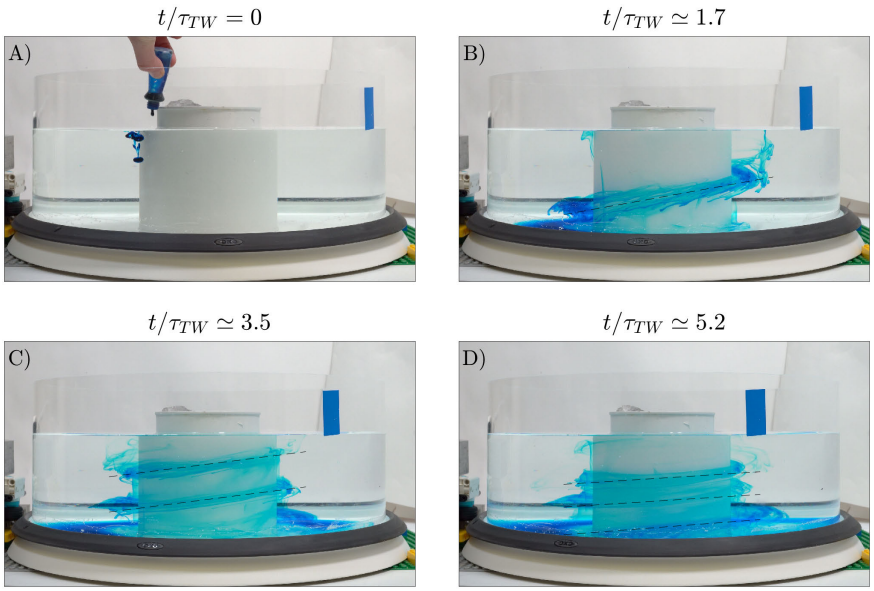

FIGURE 7
Side-view images showing evolution of an initially vertical dye line in a thermal wind flow field. **(A)** Initial dye emplacement adjacent to the cold central can. Panels **(B–D)** show successive wrappings of the dye around the can by the $\partial u\theta/\partial z$ thermal wind shear (13). (Still images harvested from Supplementary Movie 2).

$$\tau_{TW} = \frac{4\pi\Omega R_i}{\alpha g H(\partial T/\partial r)} \approx 23 \text{ s}, \tag{16}$$

over which the vertical thermal wind shear flow should wrap the dye once around the can.

Figure 7A shows the dye as it was dropped into the tank adjacent to the inner cylinder. The thermal wind vertically shears the dye, causing it to circulate in the prograde direction at the top of fluid layer and in the retrograde direction near the tank bottom. Over time, the thermal winds wrap the dye in successive windings around the inner cylinder. Figures 7B–D show the dye pattern at 2, 4, and 6 wrapping times, successively, which correspond to 40, 80, and 120 seconds after the dye is first added to the tank. The experimental measurements of the wrapping timescales are approximately one wrap at 26 s, two wrappings after 56 s, and a third wrapping at 82 s, giving an average experimental wrapping time of 28 ± 2 s, in good zeroth order agreement with the estimate given in (16).

There are several factors that affect the thermal wind wrapping timescale in any given experiment. The primary factor is the extent of the temperature gradient $\partial T/\partial r$. The approximation used here is that the temperature gradient covers the half the width of the tank. In contrast, if the temperature gradient is better described over the full width of the annulus, that would correspond to a doubling of the wrapping timescale. Additionally, we expect that the thermal gradient will change over time both as a consequence of the thermally-driven radial overturning circulation and due to the continual melting of the ice in the central cold can. As ΔT decreases over time, the wrapping timescale τ_{TW} will increase, which can eventually lead to baroclinic instability as considered in the following section.

3.4 Experiment 3: Baroclinic Instability

The Coriolis-dominated azimuthal thermal wind flow supports the colder, denser fluid adjacent to the central cylinder, nearly shutting down vertical motions in the fluid through hydrostatic balance. However, due to the sloping density surfaces, the density field stores gravitational potential energy. In some cases, this gravitational potential energy can be released through perturbations to the thermal wind flow via a process called barolinic instability (BCI) (e.g., Phillips, 1956; McWilliams et al., 2006; Vallis, 2017). When BCI occurs, the available potential energy is converted to kinetic energy in the form of "sloping convection". In our table-top rotating tank experiments, these BCI phenomena take the form of non-axisymmetric vortices, or eddies, which are easily visualized with dye.

The theory of BCI has been well studied in both atmospheric (e.g., Eady, 1949; Charney and Stern, 1962; Farrell, 1982; Eliassen, 1983), and oceanic frameworks (e.g., Gill et al., 1974; Robinson and McWilliams, 1974; Molemaker et al., 2005; Tulloch et al., 2011), as well as in other more exotic planetary and astrophysical settings (e.g., Tobias et al., 2007; Lonner et al., 2022). In this paper, we take advantage of the stability properties of the Eady problem (e.g., Eady, 1949; Vallis, 2017). As in Vallis (2017), we make the following assumptions to use stable solutions to the Eady problem: (i) there are no so-called β-effects, $\beta = 0$; (ii) the basic state has uniform shear; (iii) the motion is contained between a flat horizontal bottom and a flat rigid lid; and (iv) there is a constant vertical density stratification, $\partial\rho/\partial z$, of the fluid. Our *DIY*namics setup satisfies criteria (i)–(iii). It is possible that T, and thus ρ, evolve over time. However, the thermometry data in Supplementary Materials Section 3 shows that such secular changes in the mean temperature fields are small over the lifetimes of the experiments.

Linear analysis of BCI predicts its characteristic scale to be set by the Rossby radius of deformation, defined as

$$R_{def} = \frac{N_b H}{2\Omega}, \tag{17}$$

where

$$N_b = \sqrt{-\frac{g}{\rho_0}\frac{\partial\rho}{\partial z}} = \sqrt{\alpha g \frac{\partial T}{\partial z}}, \tag{18}$$

is the buoyancy, or Brunt-Vaisala, frequency (e.g., Sutherland, 2010; Cushman-Roisin and Beckers, 2011). By taking $\partial T/\partial z \approx \Delta T/H$ in (18) where $\Delta T = T(R_o) - T(R_i)$ is the temperature difference across the annular gap, the radius of deformation becomes

$$R_{def} = \frac{\sqrt{\alpha g \Delta T H}}{2\Omega} = \frac{15}{\pi}\frac{\sqrt{\alpha g \Delta T H}}{\mathcal{N}_{RPM}}. \tag{19}$$

Stability theory further predicts that baroclinic instabilities will develop with a characteristic time scale

$$\tau_{BCI} = 3\frac{R_{def}}{U_{TW}}, \tag{20}$$

with the prefactor value taken from Sloyan and O'Kane (2015). The diameter of the instability is determined by the fastest growing baroclinic mode to be $\approx 4R_{def}$ via analysis of the dispersion relationship to the linearized quasi-geostrophic equations (e.g., Vallis, 2017). Expressions (20) and (15) then yield

$$\tau_{BCI} \simeq \frac{3L_{gap}}{\sqrt{\alpha g \Delta T H}} \approx 22 \text{ s}, \tag{21}$$

in our annulus experiments, where $L_{gap} = R_o - R_i \simeq 12$ cm, $H = 5$ cm and we estimate $\Delta T \approx 2.9$ K based on the Figure 4D thermometry data in the Supplemental Materials. This τ_{BCI} value approximates the time over which thermal wind flows will tend to destabilize in the experiment. Note that the growth time scale does not depend on $\boldsymbol{\Omega}$, which implies that baroclinic instabilities should develop over roughly the same time period in all our annulus experiments since ΔT remains roughly constant and the fluid geometry is also held fixed in these cases.

In addition to requiring sufficient time for the instabilities to grow, there needs to be sufficient space in the fluid annulus as well. Thus, thermal winds can only become baroclinically unstable if the fluid gap is significantly larger than the instability scale $4R_{def}$. Alternatively, one can ensure that the thermal wind flow remains stable by using a small enough diameter tank. Conversely, in a large diameter tank (e.g. the HT3), a very slow rotation rate is necessary to maintain a balanced thermal wind flow.

We will estimate that baroclinic instability is possible in our tanks given the condition that

$$4R_{def} \lessapprox L_{gap}. \tag{22}$$

Recasting (22) in terms the system's angular rotation rate shows that BCI can only develop when the tank's rotation rate exceeds

$$\Omega^{crit} \approx 2\frac{\sqrt{\alpha g \Delta T H}}{L_{gap}}, \tag{23}$$

which corresponds to

$$\mathcal{N}^{crit}_{RPM} \approx \frac{60\sqrt{\alpha g \Delta T H}}{\pi L_{gap}} = 2.6, \tag{24}$$

where we have used H = 5 cm, L_{gap} = 12 cm, and $\Delta T \approx$ 2.9K based on Figure S4D. Below this rotation rate, the thermal winds in the table-top experiments should remain stable and nearly axisymmetric, whereas at higher rotation rates the thermal wind flow should break apart into a set of baroclinic eddies of diameter $\approx 4R_{def}$ on the τ_{BCI} scale (e.g., Eady, 1949; Pierrehumbert and Swanson, 1995; Read, 2001).

The BCI that develop in our experiments first develop adjacent to the cold source. To predict the number of initial structures that form, we use the inner radius as the radius of the cold boundary layer. At later times, the instabilities of the mean flow, visualized as eddies, will grow to fill the annulus. The initial number of baroclinic eddy structures is predicted to be

$$m_{BCI} \simeq \frac{2\pi R_i}{4R_{def}} = \frac{\pi R_i \Omega}{4\sqrt{\alpha g \Delta T H}} \approx \frac{\pi^2 R_i \mathcal{N}_{RPM}}{60\sqrt{\alpha g \Delta T H}}. \tag{25}$$

Figure 8 shows the results of two baroclinic instability experiments. The water depth in this experiment was 5cm, with two rotation rates of approximately 3.9 and 11 RPM. The system was allowed to spin up for approximately 10 minutes to achieve solid body rotation. Ice, salt, and water were added to the can after spin-up and the system was allowed to establish a thermal gradient for approximately 3 minutes ($\approx 9\tau_{BCI}$) before dye was added to the tank. A few drops of blue dye were then added adjacent to the cold can, and a few drops of red dye were added near the outer radius of the tank (see Supplementary Movies 3 and 4).

Figures 8A–C show the experiment run at 4 RPM, and Figures 8D–F show the BCI experiment at 11 RPM at $\tau_{BCI} \simeq 2, 4,$ and 10, respectively. (Also see Supplementary Movies 3 and 4 from which these figures are derived.) In both experiments, the flow is baroclinically unstable. Early stages of the experiment (t/τ_{BCI} = 2) show the baroclinic modes develop near the cold can with little perturbation of the red dye in the outer portions of the annulus. Three baroclinic modes develop in the 4 RPM experiment, whereas 5 modes develop in higher rotation rate experiment. The increase in baroclinic modes with rotation rate qualitative agrees with (24).

Figure 9 shows the predictions for our thermal wind flows and baroclinic instabilities plotted versus tabletop experimental measurements. Panel a) shows the number of dye wrappings as a function of time in the thermal winds experiment. The solid black line shows the predicted number of wrappings via (14) using the temperature gradient measured across the fluid gap in the thermometry experiment shown in Figure S4. The three black circles are our estimated wrapping time estimates made using the Supplemental Material's dye visualization movie 2.The dashed line shows the best fit inversion for the temperature gradient in the experiment.

Figure 9B shows the visual measurements of $m_{BCI}$from the Supplementary BCI movies plotted versus the rotation rate of the

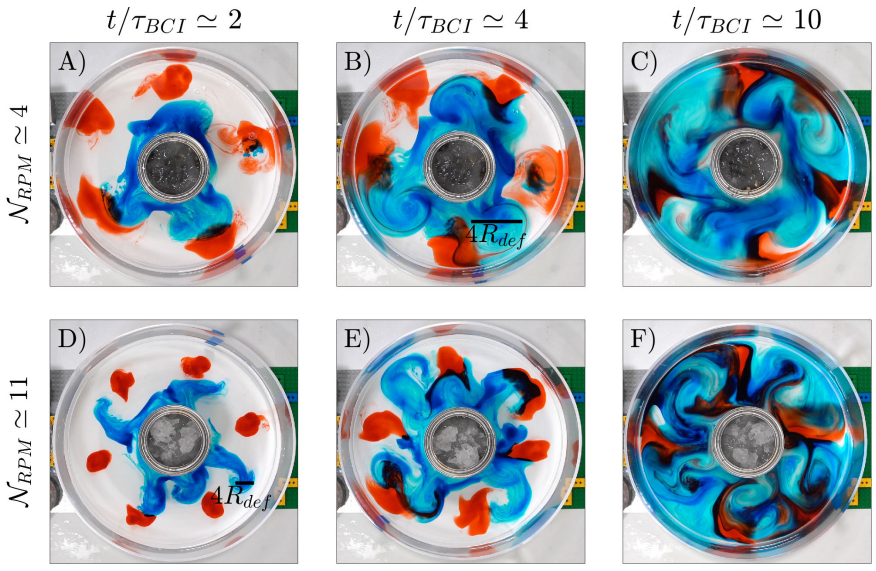

FIGURE 8
Top-view images of baroclinic instability experiments. The top row images **(A–C)** correspond to an experiment rotated at 3.9 revolutions per minute. The bottom row images **(D–F)** correspond to an experiment rotated at 11.0 revolutions per minute. In both rows, the time from ice emplacement in the central cylinder increases from left to right as **(A, D)** $t \simeq 2\tau_{BCI}$, **(B, C)** $t \simeq 4\tau_{BCI}$, and **(C, F)** $t \simeq 10\tau_{BCI}$. In both experiments, $H \simeq 5$, and $\tau_{BCI} \simeq 22$ s. The approximate length-scale twice the radius of deformation, $4R_{def}$ is annotated in panels **(B, D)**. (Images harvested from Supplementary Movies 3 and 4).

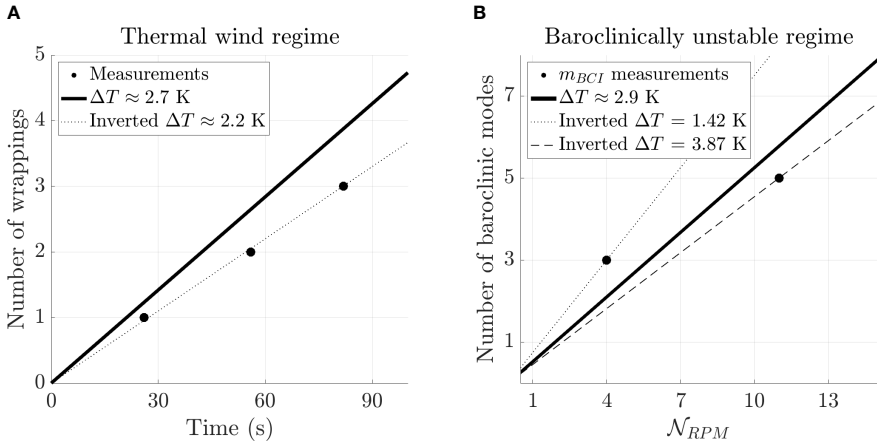

FIGURE 9
Quantitative comparisons between table-top thermal annulus experiments and theory. **(A)** Dye wrappings in Figure 7 dye to thermal wind shear. **(B)** Baroclinically unstable modes, m_{bci}, as a function of rotation rate.

tank in revolutions per minute (black circles). The solid black line denotes the theoretical prediction (24) $\Delta T = T_i - T_o = 2.9 \pm 0.3$ K measured in Figure S4D. The dashed and dotted lines show best fit ΔT estimates for the experimental cases.

While there is good agreement in Figure 9 between theory and observations, the inversions for both TW and BCI shows that our margin of error in ΔT ranges up to ≈ 1.5 K. This suggests that our assumption that the temperature gradient spans the entire annulus may be too simple. Despite this, Figure 9 demonstrates that our table-top geophysical fluids experiments yield results that can compared with theory.

4 Discussion

This study demonstrates that multi-scale deep ocean convection processes crucial to the behavior of deep ocean overturning and, thus, to global climate, can be successfully modeled using small-scale table-top LEGO-based hardware kits. Given the capabilities of our *DIY*namics setup, we model deep ocean convection through three controlled experiments: upright convection, thermal wind flows, and geostrophic adjustment through baroclinic instability. Linear theory is presented that adequately predicts the characteristic flows and flow structures.

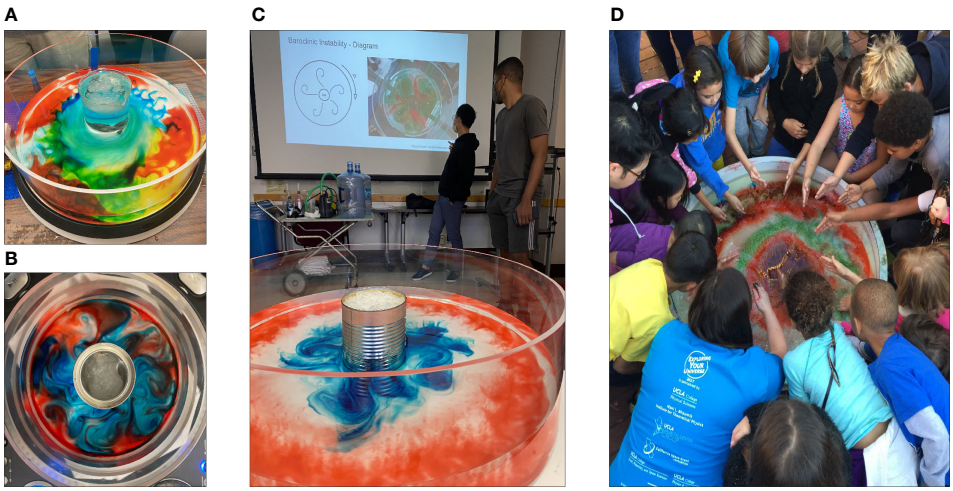

FIGURE 10
*DIY*namics in the wild. **(A)** Oblique view of a mixed thermal wind-evaporative convective multi-scale "ow in a LEGO tank in Fall 2022 AOS/EPSS M71 undergraduate computing class at UCLA. **(B)** Baroclinic instability (BCI) on the DJ table, top view image courtesy of Vincent Caiazzo. **(C)** Student-led HT3 BCI experiments in UCLA's Fall 2021 graduate-level Introduction to Atmospheric and Oceanic Fluid Dynamics (AOS 200A) course. **(D)** Early career scientists simulating Jupiter's great red spot at UCLA's 2018 Exploring Your Universe (EYU) science outreach event.

Our experiments have several tunable parameters that allow experimentalists to change dynamical regimes. In the experiments presented here, it is easiest to alter the depth of the fluid layer, H, and the rotation rate of the tank, N_{RPM}. It is however also possible to alter the temperature gradient by using different quantities of ice, for example. Furthermore, adding a vertical stratification profile to the working fluid creates a more realistic (and more complex) ocean model (e.g., Christin et al., 2021; Stewart et al., 2021).

Figure 10 shows the variety of *DIY*namics experiments already being carried 'in the wild.' With their relatively cost-effective materials, these kits can be used in classroom and outreach settings that would not normally have access to geophysical fluid dynamics and climate experimentation. Our experiments provide tangible, human-scale representations of phenomena essential to understanding global-scale climate and climate change. Further, they engage scientists, and future scientists, across all levels and encourage discussion in all the settings where they are used.

Towards that end, the Supplementary Materials contains a detailed, robust recipe for each of the three experiments presented here. Note though that there are innumerable ways to carry out these experiments. With experience, most users come up with their own individualized set of steps. The goal of this work is just to get everyone actively experimenting.

Data availability statement

The original contributions presented in the study are included in the article/Supplementary Material. Further inquiries can be directed to the corresponding author.

Author contributions

JM, RT, and JA designed the study, conducted all the experiments, created the figures, and wrote the manuscript. RT developed the current LEGO SPIKE kit, based on an initial design concept and fabrication by WC using a LEGO EV3 robotics kit. RT created build instructions, set-up the filming, and edited all movies. NK, SH, and JA developed the LEGO Series. HG, TL, and JA developed the DJ and HT Series *DIY*namics Kits. SC developed the *DIY*rotate software employed in the supplemental movies and the analysis thereof. All authors co-edited the manuscript. All authors contributed to the article and approved the submitted version.

Funding

We gratefully acknowledge the support of the National Science Foundation by awards OCE–PRF #2205637 (JM), EAR #1853196 and #2143939 (JA). In addition, our participation at the 2022 Earth Educators' Rendezvous was supported by NSF EAR and AGS funding. JM's development of undergraduate and graduate level *DIY*namics demonstrations was supported by UCLA's Center for the Advancement of Teaching's Instructional Improvement Program award #21-08.

Acknowledgments

We thank the organizers and participants of the Earth Educator's Rendezvous 2022 and of UCLA's Exploring Your Universe, and the UCLA students in (Fall 2021 AOS 200A and Fall 2022 AOS/EPSS M71. JM would like to thank Andrew Stewart and Gang Chen for co-sponsorship on her Instructional Improvement Grant. We would also like to thank Andrew Stewart, Marcelo Chamecki, and Jonathan Mitchell for furiously β-testing our experiments in their classes. Alex Gonzalez, J. Paul Mattern, Juan Lora, Hearth O'Hara , David James and Sam May are also warmly acknowledged for their various contributions. We also thank the two reviewers whose helpful comments and suggestions improved this manuscript.

Conflict of interest

The authors declare that the research was conducted in the absence of any commercial or financial relationships that could be construed as a potential conflict of interest.

Publisher's note

Supplementary material

The Supplementary Material for this article can be found online at: https://www.frontiersin.org/articles/10.3389/fmars.2023.1192056/full#supplementary-material

References

Aujogue, K., Pothérat, A., Sreenivasan, B., and Debray, F. (2018). Experimental study of the convection in a rotating tangent cylinder. *J. Fluid Mech.* 843, 355–381. doi: 10.1017/jfm.2018.77

Aurnou, J., Andreadis, S., Zhu, L., and Olson, P. (2003). Experiments on convection in earth's core tangent cylinder. *Earth Planet. Sci. Lett.* 212, 119–134. doi: 10.1016/S0012-821X(03)00237-1

Aurnou, J., Calkins, M., Cheng, J., Julien, K., King, E., Nieves, D., et al. (2015). Rotating convective turbulence in earth and planetary cores. *Phys. Earth Planet. Interiors* 246, 52–71. doi: 10.1016/j.pepi.2015.07.001

Aurnou, J. M., Horn, S., and Julien, K. (2020). Connections between nonrotating, slowly rotating, and rapidly rotating turbulent convection transport scalings. *Phys. Rev. Res.* 2, 043115. doi: 10.1103/PhysRevResearch.2.043115

Bire, S., Kang, W., Ramadhan, A., Campin, J.-M., and Marshall, J. (2022). Exploring ocean circulation on icy moons heated from below. *J. Geophys. Res.: Planets* 127, e2021IJE007025.

Boubnov, B., and Golitsyn, G. (1986). Experimental study of convective structures in rotating fluids. *J. Fluid Mech.* 167, 503–531. doi: 10.1017/S002211208600294X

Charney, J. G., and Stern, M. E. (1962). On the stability of internal baroclinic jets in a rotating atmosphere. *J. Atmos. Sci.* 19, 159–172. doi: 10.1175/1520-0469(1962)019<0159:OTSOIB>2.0.CO;2

Christin, S., Meunier, P., and Le Dizès, S. (2021). Fluid–structure interactions of a circular cylinder in a stratified fluid. *J. Fluid Mech.* 915, A97. doi: 10.1017/jfm.2021.155

Cushman-Roisin, B., and Beckers, J.-M. (2011). *Introduction to geophysical fluid dynamics: physical and numerical aspects* (Boston: Academic Press).

Duck, P., and Foster, M. (2001). Spin-up of homogeneous and stratified fluids. *Annu. Rev. Fluid Mech.* 33, 231–263. doi: 10.1146/annurev.fluid.33.1.231

Eady, E. T. (1949). Long waves and cyclone waves. *Tellus* 1, 33–52. doi: 10.3402/tellusa.v1i3.8507

Eliassen, A. (1983). "The charney–stern theorem on barotropic–baroclinic instability," in *Instabilities in continuous media* (Springer), 563–572.

Farrell, B. F. (1982). The initial growth of disturbances in a baroclinic flow. *J. Atmos. Sci.* 39, 1663–1686.

Fernando, H. J., Chen, R.-R., and Boyer, D. L. (1991). Effects of rotation on convective turbulence. *J. Fluid Mech.* 228, 513–547. doi: 10.1017/S002211209100280X

Flór, J. B., Ungarish, M., and Bush, J. W. (2002). Spin-up from rest in a stratified fluid: boundary flows. *J. Fluid Mech.* 472, 51–82. doi: 10.1017/S0022112002001921

Ghil, M., Read, P., and Smith, L. (2010). Geophysical flows as dynamical systems: the influence of hide's experiments. *Astron. Geophys.* 51, 4–28. doi: 10.1111/j.1468-4004.2010.51428.x

Gill, A., Green, J., and Simmons, A. (1974). "Energy partition in the large-scale ocean circulation and the production of mid-ocean eddies," in *Deep sea research and oceanographic abstracts*, vol. 21. (Elsevier), 499–528.

Guervilly, C., Cardin, P., and Schaeffer, N. (2019). Turbulent convective length scale in planetary cores. *Nature* 570, 368–371. doi: 10.1038/s41586-019-1301-5

Haine, T. W. N., and Cherian, D. A. (2013). Analogies of ocean/atmosphere rotating fluid dynamics with gyroscopes. *Bull. Am. Meteorol. Soc.* 94, ES49–ES54.

Haine, T. W., and Marshall, J. (1998). Gravitational, symmetric, and baroclinic instability of the ocean mixed layer. *J. Phys. oceanogr.* 28, 634–658. doi: 10.1175/1520-0485(1998)028<0634:GSABIO>2.0.CO;2

Hide, R., and Ibbetson, A. (1966). An experimental study of "taylor columns". *Icarus* 5, 279–290. doi: 10.1016/0019-1035(66)90038-8

Hill, S. A., Lora, J. M., Khoo, N., Faulk, S. P., and Aurnou, J. M. (2018). Affordable rotating fluid demonstrations for geoscience education: the diynamics project. *Bull. Am. Meteorol. Soc.* 99, 2529–2538. doi: 10.1175/BAMS-D-17-0215.1

Horn, S., and Aurnou, J. M. (2022). The elbert range of magnetostrophic convection. i. linear theory. *Proc. R. Soc. A* 478, 20220313.

Illari, L., Marshall, J., Bannon, P., Botella, J., Clark, R., Haine, T., et al. (2009). "Weather in a tank"–exploiting laboratory experiments in the teaching of meteorology, oceanography, and climate. *Bull. Am. Meteorol. Soc.* 90, 1619–1632. doi: 10.1175/2009BAMS2658.1

Illari, L., Marshall, J., and McKenna, W. (2017). Virtually enhanced fluid laboratories for teaching meteorology. *Bull. Am. Meteorol. Soc.* 98, 1949–1959. doi: 10.1175/BAMS-D-16-0075.1

Jacobs, P., and Ivey, G. (1998). The influence of rotation on shelf convection. *J. Fluid Mech.* 369, 23–48. doi: 10.1017/S0022112098001827

Jones, H., and Marshall, J. (1993). Convection with rotation in a neutral ocean: a study of open-ocean deep convection. *J. Phys. Oceanogr.* 23, 1009–1039. doi: 10.1175/1520-0485(1993)023<1009:CWRIAN>2.0.CO;2

Julien, K., and Knobloch, E. (1998). Strongly nonlinear convection cells in a rapidly rotating fluid layer: the tilted f-plane. *J. Fluid Mech.* 360, 141–178. doi: 10.1017/S0022112097008446

Killworth, P. D. (1983). Deep convection in the world ocean. *Rev. Geophys.* 21, 1–26. doi: 10.1029/RG021i001p00001

Klinger, B. A., and Marshall, J. (1995). Regimes and scaling laws for rotating deep convection in the ocean. *Dyna. atmos. oceans* 21, 227–256. doi: 10.1016/0377-0265(94)00393-B

Kundu, P. K., Cohen, I. M., and Dowling, D. R. (2015). *Fluid mechanics* (Academic press).

Lappa, M. (2012). *Rotating thermal flows in natural and industrial processes* (John Wiley & Sons).

Lonner, T. L., Aggarwal, A., and Aurnou, J. M. (2022). Planetary core-style rotating convective flows in paraboloidal laboratory experiments. *J. Geophys. Res.: Planets* 127, e2022JE007356.

Mackin, K. J., Cook-Smith, N., Illari, L., Marshall, J., and Sadler, P. (2012). The effectiveness of rotating tank experiments in teaching undergraduate courses in atmospheres, oceans, and climate sciences. *J. Geosci. Educ.* 60, 67–82. doi: 10.5408/10-194.1

Marshall, J., and Plumb, R. A. (2016). *Atmosphere, ocean and climate dynamics: an introductory text* (Academic Press).

Marshall, J., and Schott, F. (1999). Open-ocean convection: observations, theory, and models. *Rev. geophys.* 37, 1–64. doi: 10.1029/98RG02739

Matulka, A., Zhang, Y., and Afanasyev, Y. (2016). Complex environmental β-plane turbulence: laboratory experiments with altimetric imaging velocimetry. *Nonlinear Processes Geophys.* 23, 21–29. doi: 10.5194/npg-23-21-2016

Maxworthy, T., and Narimousa, S. (1994). Unsteady, turbulent convection into a homogeneous, rotating fluid, with oceanographic applications. *J. Phys. Oceanogr.* 24, 865–887. doi: 10.1175/1520-0485(1994)024<0865:UTCIAH>2.0.CO;2

McWilliams, J. C. (2006). *Fundamentals of geophysical fluid dynamics* (Cambridge University Press).

Molemaker, M. J., McWilliams, J. C., and Yavneh, I. (2005). Baroclinic instability and loss of balance. *J. Phys. oceanogr.* 35, 1505–1517. doi: 10.1175/JPO2770.1

Nadiga, B. T., and Aurnou, J. M. (2008). A tabletop demonstration of atmospheric dynamics: baroclinic instability. *Oceanography* 21, 196–201. doi: 10.5670/oceanog.2008.24

Nakagawa, Y., and Frenzen, P. (1955). A theoretical and experimental study of cellular convection in rotating fluids. *Tellus* 7, 2–21. doi: 10.3402/tellusa.v7i1.8773

Orlanski, I., and Cox, M. D. (1973). Baroclinic instability in ocean currents. *Geophys. Fluid Dyna.* 4, 297–332. doi: 10.1080/03091927208236102

Pal, A., and Chalamalla, V. K. (2020). Evolution of plumes and turbulent dynamics in deep-ocean convection. *J. Fluid Mech.* 889, A35. doi: 10.1017/jfm.2020.94

Pedlosky, J. (1964). An initial value problem in the theory of baroclinic instability. *Tellus* 16, 12–17. doi: 10.3402/tellusa.v16i1.8892

Phillips, N. A. (1956). The general circulation of the atmosphere: a numerical experiment. *Q. J. R. Meteorol. Soc.* 82, 123–164. doi: 10.1002/qj.49708235202

Pierrehumbert, R., and Swanson, K. (1995). Baroclinic instability. *Annu. Rev. fluid mechanics* 27, 419–467. doi: 10.1146/annurev.fl.27.010195.002223

Read, P. (2001). Transition to geostrophic turbulence in the laboratory, and as a paradigm in atmospheres and oceans. *Surveys Geophys.* 22, 265–317. doi: 10.1023/A:1013790802740

Robinson, A. R., and McWilliams, J. C. (1974). The baroclinic instability of the open ocean. *J. Phys. oceanogr.* 4, 281–294. doi: 10.1175/1520-0485(1974)004<0281:TBIOTO>2.0.CO;2

Rodda, C., Borcia, I.-D., Le Gal, P., Vincze, M., and Harlander, U. (2018). Baroclinic, kelvin and inertia-gravity waves in the barostrat instability experiment. *Geophys. Astrophys. Fluid Dyna.* 112, 175–206. doi: 10.1080/03091929.2018.1461858

Rossby, C. (1937). On the mutual adjustment of pressure and velocity distributions in certain simple current systems. *J. Mar. Res.* 1, 15–27.

Sloyan, B. M., and O'Kane, T. J. (2015). Drivers of decadal variability in the tasman sea. *J. Geophys. Res.: Oceans* 120, 3193–3210. doi: 10.1002/2014JC010550

Stewart, K. D., Shakespeare, C. J., Dossmann, Y., and Hogg, A. M. (2021). A simple technique for developing and visualising stratified fluid dynamics: the hot double-bucket. *Experiments Fluids* 62, 103. doi: 10.1007/s00348-021-03190-y

Stone, P. H., and Nemet, B. (1996). Baroclinic adjustment: a comparison between theory, observations, and models. *J. Atmos. Sci.* 53, 1663–1674. doi: 10.1175/1520-0469(1996)053<1663:BAACBT>2.0.CO;2

Sutherland, B. R. (2010). *Internal gravity waves* (Cambridge: Cambridge university press).

Tobias, S. M., Diamond, P. H., and Hughes, D. W. (2007). β-plane magnetohydrodynamic turbulence in the solar tachocline. *Astrophys. J.* 667, L113. doi: 10.1086/521978

Tulloch, R., Marshall, J., Hill, C., and Smith, K. S. (2011). Scales, growth rates, and spectral fluxes of baroclinic instability in the ocean. *J. Phys. Oceanogr.* 41, 1057–1076. doi: 10.1175/2011JPO4404.1

Vallis, G. K. (2017). *Atmospheric and oceanic fluid dynamics* (Cambridge: Cambridge University Press).

Warn-Varnas, A., Fowlis, W., Piacsek, S., and Lee, S. (1978). Numerical solutions and laser-Doppler measurements of spin-up. *J. Fluid Mech.* 85, 609–639. doi: 10.1017/S0022112078000828

Zhang, Y., and Afanasyev, Y. (2021). Rotating thermal convection: surface turbulence observed with altimetry and thermal radiometry. *Geophys. Astrophys. Fluid Dyna.* 115, 499–522. doi: 10.1080/03091929.2021.1939326

Frontiers in Marine Science

Explores ocean-based solutions for emerging global challenges

The third most-cited marine and freshwater biology journal, advancing our understanding of marine systems and addressing global challenges including overfishing, pollution, and climate change.

Discover the latest Research Topics

See more →

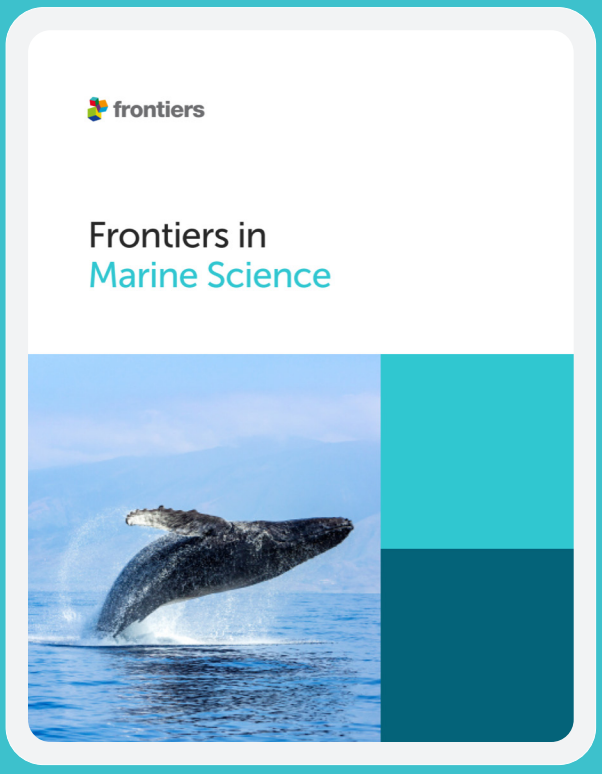

Frontiers

Avenue du Tribunal-Fédéral 34
1005 Lausanne, Switzerland
frontiersin.org

Contact us

+41 (0)21 510 17 00
frontiersin.org/about/contact